Durham University

Doctoral Thesis

Structure and Functionality of Novel Nanocomposite Granules for a Pressure-Sensitive Ink with Applications in Touchscreen Technologies.

Author:
Sarah Jessica Dempsey

Supervisor:
Prof. Del Atkinson and Dr. Marek Szablewski

A thesis submitted in fulfilment of the requirements for the degree of Doctor of Philosophy

in the

Centre for Materials Physics
Department of Physics

April 2016

Abstract

Tactile sensors are now ubiquitous within human-computer interactions, where mouse and keyboard functionality can be replaced with a trackpad or touchscreen sensor. In most technologies the sensor can detect the touch location only, with no information given on the force of the touch. In this thesis, functional components of a novel nanocomposite ink are developed, which when printed, form a pressure-sensitive interface which can detect both touch location and touch force. The physical basis of the force-sensitive response is investigated for the touchscreen sensor as a whole, as well as the intrinsic force-sensitivity of the ink components. In an earlier form the nanocomposite ink, that was the starting point of this study, contained agglomerates of conductive nanoparticles which were formed during blending of the ink, and provided the electrical functionality of the sensor. Here, novel nanocomposite granules were pre-fabricated prior to inclusion in the ink. The granules were designed such that they exhibited well-defined size, structure and strength. Control of these parameters was achieved through selection of the granule constituents, as well as the energy and duration of the granulation process. When incorporated into the ink and screen-printed to form a pressure-sensitive layer in a touchscreen test device, the functional performance could be assessed. Sensors containing pre-formed granules showed improved optical transmission, compared to sensors containing the same mass loading of nanoparticles forming spontaneous agglomerates. Agglomerates tend to create a larger number of small scattering centres which scatter light to larger angles. The spatial variation in the force-resistance response, as well as the sensitivity of this response, was also linked to the distribution of the granules within the pressure-sensitive layer. The physical basis of the force-resistance response is two-fold. Firstly, mathematical simulations showed that deflection of the upper electrode increased the number of granules contacted with increasing applied force and therefore decreased the resistance through the sensor. Secondly, a force-sensitive resistance of the granules themselves was also observed, at high forces. Analysis of the non-linear current-voltage characteristics suggested the presence of non-linear conduction pathways within the granules. Using a random resistor network model, the non-linear current contribution decreased after approximately 0.7 N force. To understand this effect, a model based on the physical basis of quantum tunnelling mechanisms was also applied, however this provided a poor fit to the data and no further understanding could be gained.

Declaration of Authorship

Unless explicitly stated otherwise, the work presented in this thesis is solely that of the author and has not been submitted for examination for any other degree at any University.

This research was supported through the Knowledge Transfer Partnership (KTP) scheme, part-funded by Innovate UK (EPSRC) and Peratech Ltd, which helps UK businesses to innovate and grow. The research was also partly funded by the Department of Physics, Durham University.

Acknowledgements

There are many people who I would like to thank for their support during my PhD studies. First and foremost to my supervisors, Professor Del Atkinson and Dr Marek Szablewski, who were both fundamental in setting up the Knowledge Transfer Partnership, and who provided excellent supervision throughout the duration of my studies. Thanks also go to Richard Parker-Smith, Jon Dean and Annisa Crich for their support throughout the KTP project.

I would also like to thank all staff, past and present, at Peratech Holdco Ltd. Particular thanks go to David Lussey, Dr Adam Graham, Dr Paul Laughlin and Professor David Bloor for initiating the KTP project and helping to promote a strong link with Durham University. More recently, thanks must also be given to Jon Stark for maintaining this link in recent times. Thanks also go to Matt Gospel, for screen-printing the inks developed in this thesis, as well as Kelly Grace and David Carrick for help in performing some of the analysis.

Characterising the granules in terms of their strength was not possible without the facilities in the Institute of Particle Science and Engineering at Leeds University. Specifically, thanks go to Professor Mojtaba Ghadiri and Dr Umair Zafir, who were instrumental in facilitating these measurements. Similarly, the electrical noise measurements could not have been performed without the expertise of Dr Chris Groves and Kenichi Kaku in the School of Engineering and Computer Science.

The SEM imaging and FIB milling performed in this thesis would not have been possible without the high standard of training I received from Leon Bowen, in the GJ Russell Microscopy Facility. The mechanical workshop team must also be thanked for their patience in drilling impossibly small holes, and Adam Poole for help with beam deflection calculations and MATLAB coding.

Size analysis techniques also played a key part in the analysis performed in this thesis. I would like to thank Simon Rundstrom and Sven Bremenfeld from Retsch Technology, and Andrew France from Sympatec GmbH, for allowing me to perform several demonstrations using their size analysis equipment.

I would like to thank all colleagues in Room 12, for making the past four years an enjoyable experience. Finally, thanks go to my family for their support and encouragement throughout the last four years.

Abbreviations

ADC	Analogue to digital converter
APR	Alcohol and petrol resistant
ATO	Antinomy doped tin dioxide
CAT	Computerised axial tomography
CB	Conduction band
CGSD	Cumulative granule size distribution
CPC	Conducting polymer composite
CQ	ColorQuest (spectrophotometer)
DAC	Dual asymmetric centrifuge
DIA	Dynamic image analysis
DRRN	Dynamic random resistor network
DSC	Differential scanning calorimetry
EM	Electromagnetic
ET	Everhart-Thornley
FIB	Focussed ion beam
F-R	Force-resistance
FSR	Force sensitive resistor
GEM	Generalised effective medium
GSD	Granule size distribution
HCI	Human-computer interaction
HPC	Hydroxypropyl cellulose
HPMC	Hydroxypropyl methyl cellulose
IR	Infrared
ITO	Indium tin oxide
I-V	Current-voltage

IZO	Indium zinc oxide
LCD	Liquid crystal display
LVDT	Linear variable displacement transducer
LW	Line-writing
NIR	Near infrared
NLRRN	Non-linear random resistor network
(O)LED	(Organic) light emitting diode
P3HT	Poly(3-hexylthiophene-2,5-diyl)
P-Cap	Projected capacitive
PDMS	Polydimethylsiloxane
PEDOT	Poly(3,4-ethylenedioxythiophene)
PEG	Polyethylene glycol
PET	Polyethylene terephthalate
PMMA	Polymethyl methacrylate
PS (layer)	Pressure sensitive/sensing (layer)
PSD	Particle size distribution
PSRT	Pressure sensitive resistive touchscreen
PVDF	Polyvinylidene fluoride
PVP	Polyvinylpyrrolidone
QTC	Quantum tunnelling composite
RRN	Random resistor network
SCTP	Spring contact test probe
SE	Secondary electron
SEM	Scanning electron microscope/microscopy
SIA	Static image analysis
SUV	Shimadzu UV-3600 (spectrophotometer)
SWCNT	Single-walled carbon nanotube
TCO	Transparent conducting oxide
UV	Ultraviolet
XRCT	X-ray computed tomography
XRT/XMT	X-ray microtomography

List of Publications

Tactile sensing in human-computer interfaces: The inclusion of pressure sensitivity as a third dimension of user input

S. J. Dempsey, M. Szablewski and D. Atkinson

Sensors and Actuators A: Physical, vol. 232, pp. 229–250, 2015.

Printable, transparent force sensing resistive materials for touchscreen applications

S. J. Dempsey, M. Szablewski, D. Bloor and D. Atkinson

Key Engineering Materials, vol. 644, pp. 120–124, 2015.

Vapor sensing properties of a conductive polymer composite containing Nickel particles with nano-scale surface features

S. J. Dempsey, A. J. Webb, A. Graham, D. Bloor, D. Atkinson and M. Szablewski

13th IEEE Conference on Nanotechnology (IEEE-NANO), pp. 665–670, 2013.

A novel screen-printed multi-component nanocomposite ink with a pressure sensitive electrical resistance functionality

A. J. Webb, S. J. Dempsey, D. Bloor, A. Graham, P. Laughlin, D. Lussey, M. Szablewski and D. Atkinson

13th IEEE Conference on Nanotechnology (IEEE-NANO), pp. 671–674, 2013.

List of Conferences

15th European Microscopy Congress,
September 2012
Manchester, UK.

6th International Granulation Conference,
June 2013
Sheffield, UK.

13th IEEE Conference on Nanotechnology,
August 2013
Beijing, China.

4th International Conference on Materials and Applications for Sensors and Transducers,
June 2014
Bilbao, Spain.

Electronic Displays Conference,
February 2015
Nuremberg, Germany.

Contents

Chapter 1

Introduction

1.1 Introduction to thesis and Peratech (Holdco) Ltd.

Tactile sensors have a wealth of applications, allowing the detection of touch in fields as diverse as robotics, biomedical engineering and human-computer interactivity [1–3]. Typically, tactile sensors comprise a force or pressure transducer, which converts a touch event into an electrical signal. There is a growing demand of tactile sensing within the field of human-computer interactivity, and specifically for consumer electronic devices, where the impetus is on replacing the peripheral mouse or keyboard with in-built trackpads and touchscreens. For example, in smartphones and tablets touch is detected through a transparent touchscreen which is overlaid on top of the display unit, allowing direct interaction with the icons shown on the display. Smartphones are ubiquitous in everyday life, and the market continues to grow. Currently about half of the adult population own a smartphone, and by 2020 this figure is expected to increase to 80 % [4].

Currently, tactile sensing within these examples is concerned with detecting the presence and location of a touch event, with no information given on the force or pressure that the user imparts to the interface. However, by measuring the touch force a new dimension of user input can be realised. For example, touch force may enable pressure-based text entry, where a harder press types a capital letter, or in handwriting or signature recognition where the force of the touch controls the thickness of the pen stroke. Additionally, touch force may be used to define force-enhanced gestures for scrolling, zooming and image manipulation on an underlying display. Introducing a third dimension of user input in the form of force or pressure sensing is a key focus of many leading consumer electronics companies, including Apple, Samsung and LG. Apple have recently released their 'ForceTouch' concept, which enables users to interact with Apple devices by applying varying degrees of force on the

touch interface [5]. As a result of this, the interest in force-enhanced interactivity has grown rapidly as developers look for new and intuitive ways for the user to interact with their devices.

The primary focus of this thesis is the development and physical understanding of functional components of a nanocomposite ink which, when printed, forms a transparent pressure-sensitive layer. This layer, when incorporated into a touchscreen sensor, allows both touch location and touch force to be detected. The transparent, screen-printable ink was developed and patented by Peratech Holdco Ltd ('Peratech') [6].

Peratech were founded in 1996 by David Lussey. Initially, Lussey patented a novel conducting polymer composite, comprising micro-sized nickel particles embedded in a silicone rubber matrix [7]. This bulk material exhibited unusual electrical properties, where the resistance dropped over several orders of magnitude when the composite was compressed [8, 9]. This feature was attributed to the spiky surface morphology of the nickel particles, which promoted field-assisted quantum tunnelling mechanisms, and from this the QTC® (quantum tunnelling composite) brand was developed. The material had primary applications in the detection of touch-force, although vapour sensing applications were also explored [10, 11].

Changing markets and consumer demands led away from the bulk composite material and into printable applications. Because of this, a screen-printable nanocomposite ink was developed, which possessed similar electrical characteristics to the bulk material [12], that is it exhibited a force or pressure-sensitive electrical resistance. The nanocomposite ink can be screen-printed in a thin layer between two electrodes to form a thin, lightweight force sensor. Peratech then developed a novel transparent version of their screen-printable ink, and it is this material which provides the focus of this thesis. The primary application of this sensor is in the field of human-computer interactivity, where the touch force can be used to open up new and intuitive methods of interaction between user and device. In particular, because the composite is optically transparent, it has key applications in the touchscreen industry. However, it is important to note that force or pressure sensors also have extensive applications in fields such as robotics and biomedical science. The printable nature of the sensors lends to easy integration into any device architecture.

The printable nature of this sensor is also highly advantageous. The benefits of printable electronics include low-cost, high throughput manufacture of integrated systems onto a variety of substrates [13]. The additive process of printing a circuit, sensor, transducer or other form of electrical system reduces the process complexity and allows integration of several electrical components onto the same substrate. Printed sensors are of particular interest because, often, they do not require complicated circuitry or complex lithographic structures, and as such are well suited to the printing process. In other words, the printed sensor exhibits functionality without the need for a high print resolution. Examples of printed sensors include glucose

biosensors [14, 15], printed antennae for remote sensing [16], and sensors for the detection of light [17], moisture [18, 19] and harmful vapours [20, 21], as well as tactile sensing which is the scope of this thesis.

1.2 Aims of the thesis

This thesis considers the design and development of new ink components for resistive touchscreen sensors, building on those developed by Peratech. The ink is then screen-printed between two transparent electrodes to form a pressure-sensitive layer. In a touchscreen format, the pressure-sensitive layer allows quantification of the applied force. In its current configuration, this layer contains micro-sized agglomerates of conductive nanoparticles, which are formed spontaneously during blending of the ink constituents. These agglomerates provide the functional, pressure-sensitive response.

In this thesis, the spontaneous agglomerations of nanoparticles have been replaced with novel nanocomposite granules, which can be mixed directly into the transparent ink base. Prefabrication of the granules is highly beneficial as it allows the controlled manufacture of the functional ink components prior to inclusion in the ink. The properties of the granules (for example their size, structure and strength) can be modified by control of the fabrication process. This was not possible when the agglomerates were spontaneously formed during blending.

This thesis also considers the physical basis of the pressure-sensitive response of the touchscreen sensors. Currently, the electrical functionality of the agglomerates or granules within the pressure-sensitive layer is poorly understood. The resistance through the layer may depend on the electrical contact created between the electrode and the granule ensemble, as well as any intrinsic pressure-sensitivity within the granules. It is important to understand any fundamental differences between the electrical and optical properties of pressure-sensing layers containing either the pre-formed granules or spontaneously formed agglomerates.

With this in mind, this thesis is broadly split into two key aims, although there is significant linkage between the two. The thesis is therefore divided into two parts. The first part of the thesis relates to the design, fabrication and analysis of the conductive nanocomposite granules. The aim is to develop a method to manufacture the granules with specific physical properties, including size, shape, porosity and strength, in a controllable and repeatable process. These parameters may be key to understanding the electrical conduction through the granules, and also through the touchscreen device as a whole. An understanding of how the method of fabrication (in this case a process called granulation) relates to the final properties of the granules is key to this aim. In addition to this, it is important to develop

a series of experiments which can accurately and reliably measure the granule properties. This includes measuring the size distribution of the granules, visualising and quantifying the granule internal structure and finally assessing their mechanical properties, including the fracture strength.

The second aim relates to the functional performance of the touchscreen device as a whole, and understanding the physical basis of the conduction processes within the pressure-sensitive layer. Of particular interest is the difference in functional response between a touchscreen containing pre-fabricated granules and one containing spontaneously formed agglomerates. This functional response includes both the transmission of visible light through the pressure-sensitive layer and the electrical conduction through the layer. In the former case, the aim is to understand how the number and size of the granules affects the scattering of visible light through the touchscreen assembly. In terms of electrical conduction, it is important to understand and characterise the two contributions to the force-resistance response, that is the effect of increasing the number of granules in contact with the electrode with increasing force, and any intrinsic pressure sensitivity within the individual granules. The latter effect links directly with the internal structure of the granules, covered by the first aim of this thesis.

Ultimately, it is hoped that a full understanding of how the granule size, structure and strength impacts on the functional performance of the touchscreen as a whole is created. This would then open up the possibility of tailored granules for particular applications, where the granule properties determine the sensitivity and range of the touchscreen resistance response.

1.3 Thesis outline

In line with the thesis aims as set out above, this thesis is split into two main parts. Part I, comprising chapters 3–7, details the fabrication and structural analysis of the granules whereas part II, comprising chapters 8–12 describes the incorporation of the granules into a touchscreen device. The properties of touchscreens containing both pre-formed granules and spontaneously formed agglomerations are compared, and a detailed study is presented on the origin of the force-sensitive response.

Prior to part I, chapter 2 gives a broad overview of the field of tactile or touch sensing within the field of human-computer interactivity, specifically within consumer electronics applications. This helps to define the scope of this thesis, as it relates the current state-of-the art within the field. The physical basis behind a range of touchscreen technologies is described, along with recent research efforts into the incorporation of force sensing. Because most innovation in this field is commercially driven, the relevant patents are reviewed. The

chapter concludes with a description of the novel touchscreen design developed by Peratech, from which this thesis is built upon.

Within part I, chapter 3 begins by giving a detailed account of the process of granulation, which converts small, cohesive particulates into larger granules bound by the presence of a liquid binder. This process is used to create the pre-formed granules which are later incorporated into the force-sensing touchscreen, and as such an understanding of this process is key to designing functional granules with the desired physical properties. A detailed literature review follows, describing how the granulation process can be used to tailor the final granule properties, namely their size and shape, internal structure and strength, by altering both the constituent material properties and the process conditions.

In order to fabricate and analyse the nanocomposite granules, a number of key techniques are developed. Chapter 4 introduces the methodology of granule fabrication and subsequent analysis. The raw materials, in this case conductive nanoparticles and electrically insulating polymer binder, are described along with the process by which the granules are formed. This is followed by a discussion of the concepts and theoretical underpinnings of each analytic technique used to assess the granule properties, including a comparison of methods for measuring the granule size distributions. The technique of focussed ion beam milling, used to expose the internal structure of the granules, is described, along with the methods used to determine the granule mechanical behaviour. In combination, these techniques provide a powerful tool to assess a range of granule properties (i.e. their size, structure and strength) as a function of different constituent materials and a range of operating conditions. Then, direct linkage can be made between the observed granule properties and the theory of granulation.

Chapter 5 provides a short, comparative study of the different size analysis techniques, and gives a critical analysis of each method. For the remainder of the thesis, scanning electron microscopy and manual image analysis form the basis of granule size measurements, and it is therefore imperative to understand the advantages and limitations of such a technique in comparison with automated size analysis techniques.

In chapter 6 the effect of changing the physical properties of the constituent materials of the granules is investigated. This includes the effects of nanoparticle shape and the binder composition and quantity on the size distribution, porosity and strength of the resultant granules. In chapter 7 an investigation into altering the operation variables of the granulating equipment is presented. This includes the effect of changing the energy and duration of the mixing process on the granule properties. In both of these chapters, links are made to the granulation process in the context of the current understanding of granulation mechanisms. Ultimately, these chapters develop a ‘recipe’ which can be used for the controlled fabrication of nanocomposite granules with well-defined physical properties. These granules can then be incorporated into the touchscreen device.

Part II is focussed on understanding the functional performance of both the granules and the overall touchscreen device. Ultimately, the conductive properties of the granules may control the functional response of the touchscreen sensor as a whole, so it is imperative to understand the nature and mechanisms of any intrinsic conduction processes. The granules themselves can be defined as conducting polymer composites, as they are formed of both conductive and insulating phases. In chapter 8, electrical conduction through composite materials is reviewed. This includes the theory of electron transport through conductors, semiconductors and insulating materials. Emphasis is given to charge transport mechanisms through conducting polymer composites, including models used to describe the macroscopic conduction behaviour, such as percolation theory and random resistor network models. Fluctuations in electrical conductivity, manifested as flicker noise, are also described, along with relevant works which link flicker noise in composite materials to the nature and type of electrical conduction.

Chapter 9 relates the experimental procedures used to formulate the transparent, screen-printable ink containing the nanocomposite granules, and the deposition of this ink into a touchscreen assembly by a screen-printing process. The methods of characterising the touchscreen performance, in terms of its force-resistance response and its optical transmission are described. The experimental design for assessing the conductive properties of the granules themselves is also explained.

In chapter 10, the functional performance of the fabricated touchscreens, containing both agglomerations and pre-formed granules, is assessed. The electrical resistance is measured as a function of applied force, and parameters are defined which allow a quantitative comparison between different test devices. The optical transmission through the touchscreens is assessed in terms of the transmission profile (as a function of wavelength) and the optical haze. Links are made between the distribution of granules and both the electrical and optical performance of the touchscreen.

Finally, chapters 11 and 12 present a detailed study of the nature of the force-sensitive response of both the touchscreen as a whole, and the individual nanocomposite granules. In chapter 11 a simulation is developed, where from the geometry and mechanics of the touchscreen assembly the number of granules contacted by the electrode can be calculated as a function of applied force. This allows the surface-area contribution to the force-resistance response to be assessed. Meanwhile, chapter 12 investigates any intrinsic force-sensitivity of the granule electrical resistance. This is achieved through removing the surface-area effect and compressing the granules directly. Lastly, chapter 13 summarises the key conclusions of both part I and part II of this thesis. The impact of these results on the direction of future touchscreen devices is also discussed.

Chapter 2

Pressure Sensitive Touch Technology for Tactile Sensing in Human Computer Interactivity

2.1 Introduction

Tactile sensing has become increasingly important in human-computer interactions (HCI) as it introduces new and intuitive ways for users to interact with a computer interface. In touch interfaces a variety of physical principles are used to detect the location of a touch and this information is then relayed to the device to provide a certain functionality. As examples, the touch surface may be a computer keyboard, a trackpad integrated into a laptop computer or a touchscreen overlaid on top of a display. In the latter case, a touchscreen may be defined as a transparent overlay located directly above a display unit such as an LCD (liquid crystal display) or (O)LED (organic light emitting diode) display. The touchscreen market has grown significantly from 0.31 billion units produced in 2007 to 1.32 billion units produced in 2012. In 2017 a further increase to 2.41 billion units is forecast [22]. Touchscreens are found in a wide range of applications including smartphones and tablets, as well as machinery control panels, ATMs and point-of-sale kiosks. They eliminate the requirement to have a separate touch interface, as the user can interact directly with icons shown on the underlying display. Currently, most touch interfaces are capable of detecting the location of a touch (or several simultaneous touches) but yield no information on the force or pressure of the touch. However, recently there has been increasing interest in detecting the touch force as it introduces a third dimension of user input alongside the two coordinates of touch location.

The printable, resistive ink components that are the focus of this thesis have pressure-sensing applications useful in this field. Hence, a full understanding of all current research and innovation with the addition of force or pressure-sensitivity is needed to understand what such a sensing material should be capable of achieving. However it is important to note that force or pressure-sensitive tactile sensors are not limited to the field of HCI, as they also have extensive applications in robotics and biomedical science. In robotics, force or pressure sensors may be incorporated into electronic skin to mimic the sensing capability of human skin, including its ability to sense touch pressure [23, 24]. In biomedical research, tactile sensors incorporating force or pressure sensitivity can be used in bite-force measurement in dentistry or in human gait analysis [25, 26]. There are many review articles which summarise the important research and innovation within these applications [1, 2, 27–29].

A force sensor may be defined as giving a constant reading as a function of applied force, independent of the contact area. Conversely, a pressure sensor will give, with a constant applied force, a reading which is inversely proportional to the area over which the force is applied. The technologies described in this chapter may be a combination of both physical principles although the term 'force sensitive' is often used in the literature and especially in the patents describing these devices. Often, these terms are used interchangeably. The touch interface should be able to detect varying *levels* of applied pressure or force. The software can then execute a specific response depending on the force level, such as a light touch or a hard press. For the purpose of touch interfaces in HCI, a light touch may be of the order of 0.1 N and a hard press anything greater than 5 N. Assuming a human fingertip to have a constant area of approximately 100 mm^2 this corresponds to touch pressures from 1×10^{-3} $\mathrm{N\,mm^{-2}}$ (light touch) to 0.05 $\mathrm{N\,mm^{-2}}$ (hard press). By detecting a range of input forces or pressures, many new and exciting applications can be introduced, including pressure based text entry [30], menu selection [31] and handwriting/signature recognition [32], and force enhanced gestures for scrolling, zooming and image manipulation [33, 34].

As mentioned previously, the majority of touch interfaces are currently only capable of detecting the location of the touch, where the location sensing mechanism may use a range of physical principles. Many resources describe the various principles behind touch sensing interfaces, including resistive, capacitive, optical, infra-red and acoustic sensing [22, 35–37]. Currently, location and pressure sensing capabilities exist for piezoelectric, capacitive and resistive sensing mechanisms and these are discussed in sections 2.2, 2.3 and 2.4 respectively and compared in section 2.5. Finally, the resistive pressure sensing touch interface developed by Peratech Holdco Ltd., which provides the basis for this thesis, is described in section 2.6.

2.2 Piezoelectric pressure sensing in HCI applications

Piezoelectricity is caused by the coupling of elastic and dielectric properties of a crystalline material, where an applied stress causes a change in the surface charge density. This is due to either the formation or realignment of induced electric dipoles within the material, which changes the electric polarisation. As such, the crystal structure must be non-centrosymmetric. For an applied stress, σ, the polarisation, P, of the internal charges is given by:

$$P = \sigma d + E\varepsilon_0\chi, \tag{2.1}$$

for the one dimensional case when P and σ are parallel, where d is the piezoelectric strain constant, E is the electric field and χ is the dielectric susceptibility [38]. Common piezoelectric materials include SiO_2 (quartz), lead ziroconate titanate (PZT) and ZnO. The piezoelectric strain constant d for SiO_2 crystals and ZnO thin films are of the order of 2 $\mathrm{pC\,N^{-1}}$ and 11 $\mathrm{pC\,N^{-1}}$ respectively [39, 40].

Polyvinylidene fluoride (PVDF) is a semicrystalline ferroelectric fluoropolymer which is capable of a large piezoelectric response and can be printed to form a transducer or pressure sensing device [41–43]. For the case where the applied force is parallel to the direction in which charge is measured (in this case through the thickness of a printed film) d values of -33 $\mathrm{pC\,N^{-1}}$ are reported [44]. The copolymer P(VDF-TrFE) (polyvinylidene fluoride–tri–fluoroethylene) is often used as it enhances the crystallinity of the polymer and increases the value of d to -38 $\mathrm{pC\,N^{-1}}$ at room temperature [45]. Alignment of the hydrogen and fluorine atoms within the crystals results in a permanent electric dipole moment. The dipole moments within the nanocrystals can be aligned by applying an external electric field greater than the coercive field strength in a process called electrical poling. This is shown in the inset of Fig. 2.1(a). Under an applied force the orientation of the dipoles within the film is altered, inducing a voltage on the connecting electrodes which is proportional to the stress applied.

Rendl *et al.* and Zirkl *et al.* demonstrated a prototype of a pressure-sensing touch interface utilising an array of piezoelectric sensors [46, 47]. Fig. 2.1(a) shows the structure of the pressure-sensitive array. The piezoelectric layer contained nanocrystals of the copolymer P(VDF TrFE), where d was 20–30 $\mathrm{pC\,N^{-1}}$, and was printed at a thickness of 5 µm onto a carbon electrode. The top and bottom electrodes were connected perpendicularly so that a voltage signal could be read out from each electrode-PVDF-electrode intersection. Hence each intersection was capable of measuring a touch force. The pressure-voltage response of the sensor array is shown in Fig. 2.1(b), reproduced from data provided in [46]. It can be seen that applied pressures in the range 0.12–0.29 $\mathrm{N\,mm^{-2}}$ produce a highly linear voltage output. Here, pressure was applied using a test probe of diameter 4.5 mm giving an applied

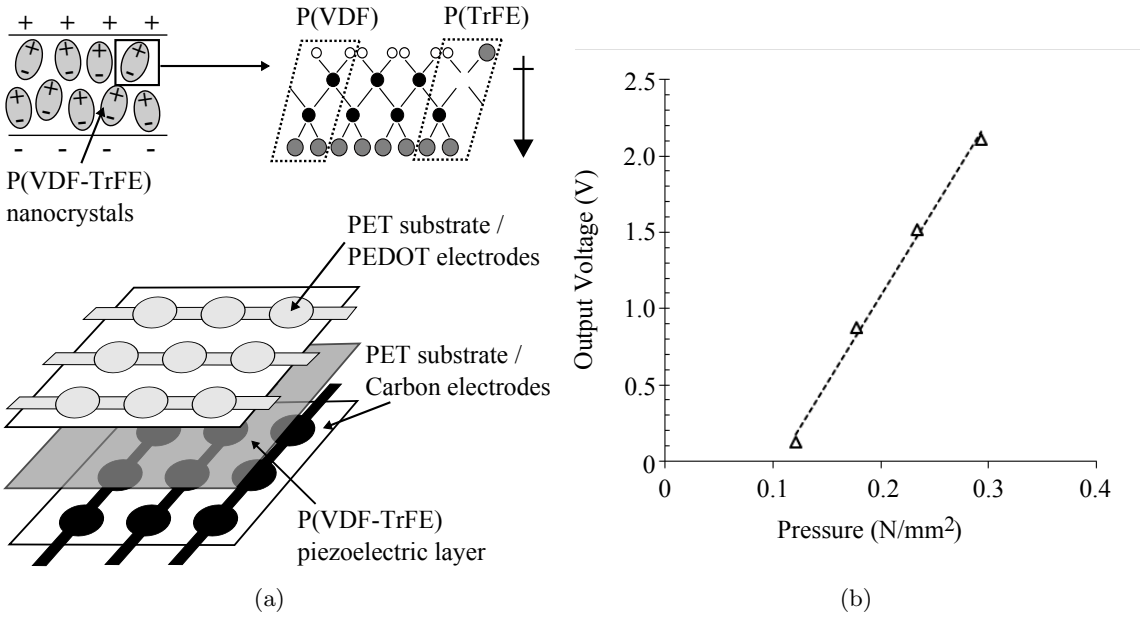

(a) (b)

FIGURE 2.1: (a) Schematic of piezoelectric touch interface, comprising a piezoelectric layer containing P(VDF-TrFE) nanocrystals located between two electrode arrays. The left hand inset shows the alignment of nanocrystals within the film achieved through a poling process. The right hand inset shows the atomic arrangement within a nanocrystal, where the arrangement of carbon (black circles), fluorine (grey circles) and hydrogen (white circles) atoms creates a permanent dipole moment. (b) Graph showing the output voltage as a function of applied pressure for a piezoelectric sensor array, reproduced from data provided by Rendl *et al.* [46]. The output voltage is linearly dependent on the applied pressure in the range 0.12–0.29 $\mathrm{N\,mm^{-2}}$.

force of 1.9–4.7 N. However, after the PVDF is touched the induced voltage discharges over a short time-scale through the internal resistance of the PVDF layer. The discharge has an exponential function of the form $\exp\left(\frac{-t}{\tau}\right)$ where the time constant τ was 17.7 ms [47].

In its current format, this sensor cannot detect a static force unless complex signal processing algorithms are used. Also, background noise may be introduced by the infra-red component in ambient lighting, and from cross-sensitivity between the piezo- and pyroelectric responses. This can complicate the detection of multiple adjacent touches. However, this technology shows potential in that the highly linear response facilitates mapping of pressure levels to the required applications. Each component of the piezoelectric sensor can be printed onto a flexible substrate, leading to potential applications in flexible electronics. A transparent sensor may be produced by replacing the carbon electrodes with a transparent alternative such as poly(3,4-ethylenedioxythiophene) (PEDOT) or indium doped tin oxide (ITO).

2.3 Capacitive tactile sensing in HCI

Capacitive touch sensing involves the measurement of the capacitance of one or two electrodes which are embedded in the touch interface. When the interface is contacted by a conductive object, the capacitance associated with these electrodes may change, allowing a touch to be registered. Capacitive touch sensing can be split into several types, depending on how the capacitance of the sensor or sensor array is measured and whether one or two electrodes are present in each sensor element. A critical review of all types of capacitive touch interfaces can be found in the literature [22, 35–37]. Here, the focus is on 'pressed' capacitive and projected (mutual) capacitive touch interfaces, and the inclusion of pressure-sensitivity into these.

2.3.1 Pressed capacitive touch interfaces

The capacitance between two parallel conducting plates can be increased by either increasing the overlapping area of the plates or by decreasing the plate separation. A pressed capacitive tactile sensor uses one or both of these effects. For touchscreen applications, the pressed capacitive tactile sensors can be incorporated into the display module, rather than being a separate sensing module above the display. For example, in an LCD display the electrodes are incorporated onto the colour filter glass and the thin film transistor layer which is found beneath the liquid crystal array. Often, a column spacer is used to prevent full contact between the two electrodes. This layout is shown in Fig. 2.2(a). Rigid layers of protective covering, usually required in most applications to prevent damage to the display, cannot be used here as the inflexibility of this layer would prevent the necessary deformation. The touch resolution depends on the number of display pixels per sensor (and therefore the total number of touch sensors present in the entire display). This is typically in the range of 4:1 (high touch resolution) to 16:1 (lower touch resolution) [35].

H. Kim *et al.* designed and fabricated a 20 × 20 array of pressed capacitive sensors [48, 49]. Indium zinc oxide (IZO) electrodes were deposited onto flexible polycarbonate films, and an insulating layer of the polymer SU-8 (an expoxy-based photoresist) was deposited at a thickness of 5 µm onto the lower electrode. The two electrodes were separated using spacer columns of SU-8, creating a void space 8 µm in height between the electrodes. The total thickness of the sensor array was 253 µm and the average optical transmittance in the visible light range was 86 %. The capacitance is plotted as a function of pressure in Fig. 2.2(b), which is replicated from results found in [48]. The capacitance increases from an initial value of 0.9 pF at no pressure to 4.5 pF at a pressure of 0.1 $\mathrm{N\,mm^{-2}}$, after which the capacitance output saturates. Numerical modelling of the system confirmed that a pressure of 0.07 $\mathrm{N\,mm^{-2}}$ caused maximum deflection of the upper electrode at 8 µm, leading to no further increase in capacitance.

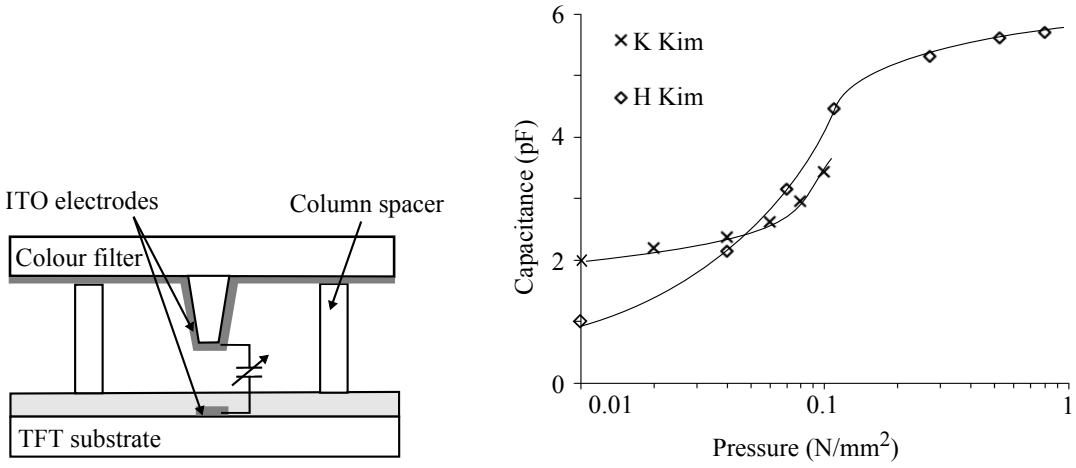

(a) (b)

FIGURE 2.2: (a) Schematic of a pressed capacitive touch interface incorporated directly into the LCD display. The touch electrodes are deposited on the thin film transistor and colour filter substrate. When the top surface of the LCD is pressed the colour filter substrate deforms, reducing the distance between the two electrodes and causing an increase in the mutual capacitance. (b) Graph showing capacitance as a function of applied pressure for two pressed capacitive transparent touchscreens developed by H. Kim (open diamonds) and K. Kim (black crosses) [48, 50].

K. Kim *et al.* designed a similar sensor where the perpendicular electrode arrays were fabricated by scribing and patterning single wall carbon nanotube (SWCNT) films. The electrodes were separated by a 500 µm thick layer of compressive silicone gel [50]. The optical transmittance at a wavelength of 550 nm was 81 %. The capacitance output as a function of pressure is also shown in Fig. 2.2(b), reproduced from data provided by K. Kim *et al.* [50]. The capacitance increases from an initial value of 1.92 pF at zero pressure to 3.42 pF at a pressure of 3.5 $\mathrm{N\,mm^{-2}}$.

The magnitude and sensitivity of the response is highly dependent upon the electrode separation and the mechanical flexibility of the upper substrate. The maximum pressure that can be detected is that which results in a vertical displacement of the electrode equal to that of the electrode separation. The minimum pressure that can be detected is dependent upon the read-out electronics, as the small change in capacitance must be detectable above any background noise. When the touchscreen is incorporated into a device, background noise is introduced through capacitive coupling of other device components, for example the display and charging circuitry. It becomes very difficult to extract the required signal when the background noise itself is also dependent on the changing separation of the components.

Due to the lack of a protective layer (or cover glass) the pressed capacitive touch interface can suffer from poor durability. The flexible upper substrate may cause flexing and cracking of the ITO electrodes and may damage the LCD display. Applying pressure directly to the

LCD display can cause image artefacts and lead to short product lifetime. Despite these limitations, a pressed capacitive touchscreen can be found in several camera touchscreen displays manufactured by Samsung (models ST550 and TL220) although the pressure sensitive capabilities are not currently utilised [51].

2.3.2 Mutual projected capacitive touch interfaces

Mutual capacitive touch interfaces comprise an array of spatially separated electrode pairs, for example a series of rows and columns which overlap to form intersections, as shown in Fig. 2.3. Each electrode pair has a mutual capacitance. When a conductive object, for example a fingertip, approaches the electrodes then capacitive coupling occurs between the object and the electrodes and this results in a decrease in the mutual capacitance. Each electrode intersection is scanned by a controlling unit and the location of the touch can be determined from the change in capacitance measured at the corresponding intersection.

Mutual projected capacitive (often termed 'p-cap') is the dominant sensing mechanism used in capacitive style touch interfaces and is commonly found in transparent touchscreens in smartphones and tablets. This is because each electrode intersection is capable of sensing an independent touch event, such that multiple simultaneous touches can be detected. Because no deformation is required the touchscreen is rigid and durable. However, only touch from conductive objects can be detected and the touch response is sensitive to screen contaminants or surface moisture.

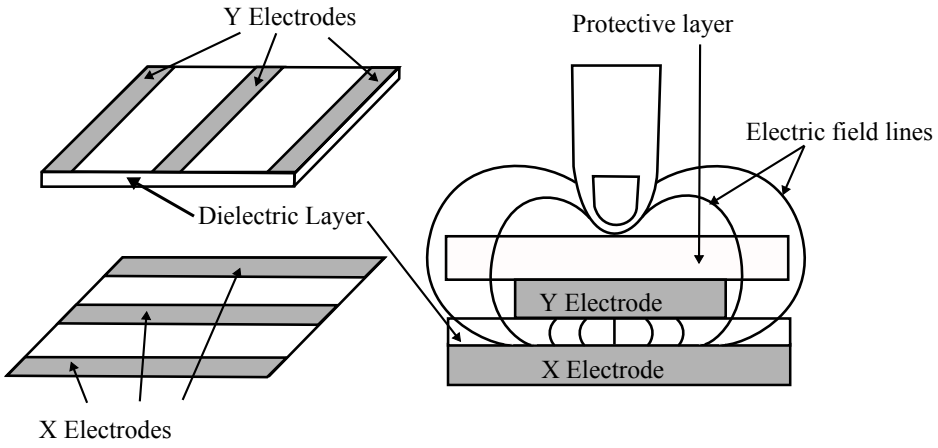

FIGURE 2.3: Schematic of a projected mutual capacitive touch interface which comprises two sets of perpendicular electrodes to create an array of electrode intersections. The approach of a conductive object such as a finger reduces the charge stored between the electrodes, resulting in a change in capacitance. Each electrode intersection is capable of measuring a change in capacitance and hence a touch event.

The lack of moving mechanical parts also means that an alternative approach to pressure sensitivity must be used. There are three ways this can be achieved: by algorithms relating the size of the contact area to the force applied, by using discrete force sensors external to the location sensing surface or by using a pressure-sensitive stylus.

2.3.2.1 Relating size of contact area to touch force

The touch force may be approximated by measuring the size of the contact area. A harder press will result in a greater contact area between finger and interface due to the compliant nature of the human fingertip. A larger contact area means that more electrode intersections are triggered and by integration of the capacitance values recorded at each intersection the contact area can be calculated. This approach has been demonstrated [52, 53]. The difference in contact area may also be used to differentiate between adult and child input and to adjust the device functionality accordingly [54]. However, this approach requires additional calibration to compensate for variation in user finger sizes and has limited accuracy. For example, without user calibration the method cannot distinguish between a hard press from a small finger and a light touch from a large finger. It is difficult to detect anything beyond a moderately hard press, beyond which the touch area does not increase significantly, and of course stylus input is not supported.

2.3.2.2 Using separate, discrete force or pressure sensors in the touch interface

The touch force may be measured independently of touch location by using several discrete small-area force or pressure sensors placed underneath the touch interface, where the touch interface is comprised of any capacitive touch system as described in section 2.3.

In fact, one type of touch interface, usually termed 'force-based' in the touch technology industry, utilises discrete force sensors underneath the touch surface to measure both the location and the force of a single touch. An example of this is shown in Fig. 2.4 where the force sensors are placed underneath each of the four corners of the touch surface. The force sensors may be strain gauges, piezoresistive, piezoelectric or capacitive sensors. Despite the simplicity of the concept very little success was achieved due to its limitations, including errors in location sensing due to the noisy, dynamic output from the force sensors, and the unwanted detection of lateral forces [55]. Several attempts have been made to overcome the latter problem, including beam-mounting of the sensors or using a spring-loaded suspension system [56–58]. Despite these improvements this technology can only detect the force and location of a single touch. Touching the interface in more than one location will return the centroid of the applied forces and hence return an erroneous location.

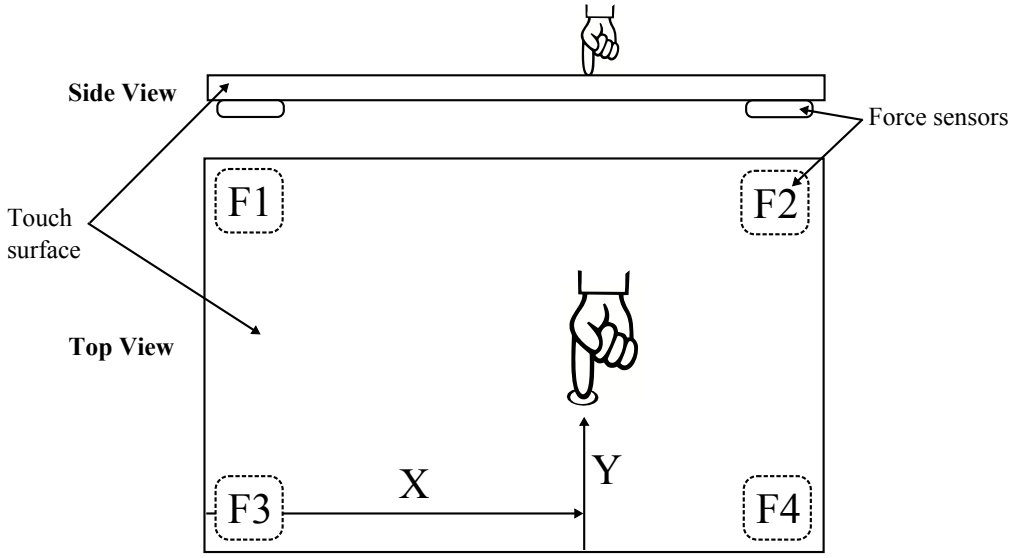

FIGURE 2.4: Schematic of a touch interface with four discrete force or pressure sensors (F1 to F4), underneath each corner. Analysis of the force or pressure recorded at each sensor provides information on both the location and the force of the touch. In 'hybrid' devices, touch location may be detected by a p-cap sensor, where the force sensors provide independent information on the touch force.

However, by incorporating force sensors beneath a capacitive location sensing interface, both multi-touch location sensing and force sensing can be achieved. These 'hybrid' touch interfaces provide a solution for applications such as smartphones and tablets where multi-touch is standard. This approach has already achieved commercial successes, for example in the ForcePad™ V.4 produced by Synaptics, Inc [59] comprises four force sensors underneath the corners of the trackpad. This allows the sensing of up to 1000 g from up to five fingers simultaneously with 15 g resolution, and 64 discrete force levels. The force-sensitivity can be used to define force-sensitive multi-touch gestures [60, 61] and is also used to redefine the click function. The hinge mechanism of the standard trackpad (which allows for click input) is not required as the user can click anywhere on the trackpad by applying a force above a predetermined threshold. In this case, the lack of moving mechanical parts may enhance the product lifetime. The hybrid approach can also be found in the new generation of Apple MacBook laptop trackpads [62] and also the newly released Apple Watch touchscreen [5] through their patented 'ForceTouch' technology [63, 64].

2.3.2.3 Using pressure sensors in a stylus device

Touch force or pressure can also be determined through the use of an active stylus. These are commercially available for devices such as smartphones, tablets and graphic tablets. The stylus requires power in order to operate, which can either be drawn from the device or provided by an internal battery. To detect the force the user is imparting to the interface,

the stylus has an internal force or pressure sensor, which is usually connected to the stylus nib such that retraction of the nib triggers the sensor. The sensor may detect pressure through a change in inductance [65], capacitance [66, 67], resistance [68, 69] or light intensity [70, 71].

These devices can typically differentiate between 256 and 2048 levels of pressure. Because only a single sensor is required, and the housing is large (the size of a typical pen) there is less constraint on the physical dimensions of the sensor. However, the stylus use and performance is also dependent on the display, chip, controller and driver support of the device it is used with. A stylus will work only on specifically designed applications which utilise its pressure sensitivity.

2.4 Resistive tactile sensing in HCI

In resistive touch sensing a change in resistance is measured between two electrodes, caused by the contact and deformation of an interface. An example of this is the resistive touchscreen, as shown in Fig. 2.5(a). In this case, a transparent electrode material such as ITO is used and the electrodes are separated by an array of micro-sized transparent polymer beads ('spacer dots'). Metallic X and Y contacts are deposited at the edges of the substrate. When the deformable upper substrate is pressed the ITO electrodes come into contact and a current can be measured. The resistance of the ITO layer acts as a voltage divider, as shown in Fig. 2.5(b). First, a voltage, V_{Xref}, is driven through the X contacts and one of the conductive bars in the Y layer is connected to an analogue-to-digital converter (ADC) through large impedance. By measuring the voltage V_Y the location along the x axis, x, can be determined using the equation:

$$\frac{x}{width} = \frac{X}{ADC_{Xmax}} = \frac{V_Y}{V_{Xref}} = \frac{R_1}{R_1 + R_2} \tag{2.2}$$

Similarly, the y coordinate of the touch, y, is measured by driving a voltage, V_{Yref}, through the Y contacts and measuring the voltage V_X through high impedance. The Y coordinate is then given by:

$$\frac{y}{height} = \frac{Y}{ADC_{Ymax}} = \frac{V_X}{V_{Yref}} = \frac{R_3}{R_3 + R_4} \tag{2.3}$$

Where the width and height are that of the touch surface, X and Y are the digital values read from the ADC converter at driving voltages V_{Xref} and V_{Yref} respectively, and ADC_{Xmax} and ADC_{Ymax} are the maximum ADC values for x and y readings.

In this 'four-wire' format, only a single touch can be detected at a given time. However, it is possible to create an array of ITO electrodes similar to that used in capacitive touchscreens. Then a touch can be registered at each intersection simultaneously. This approach has been

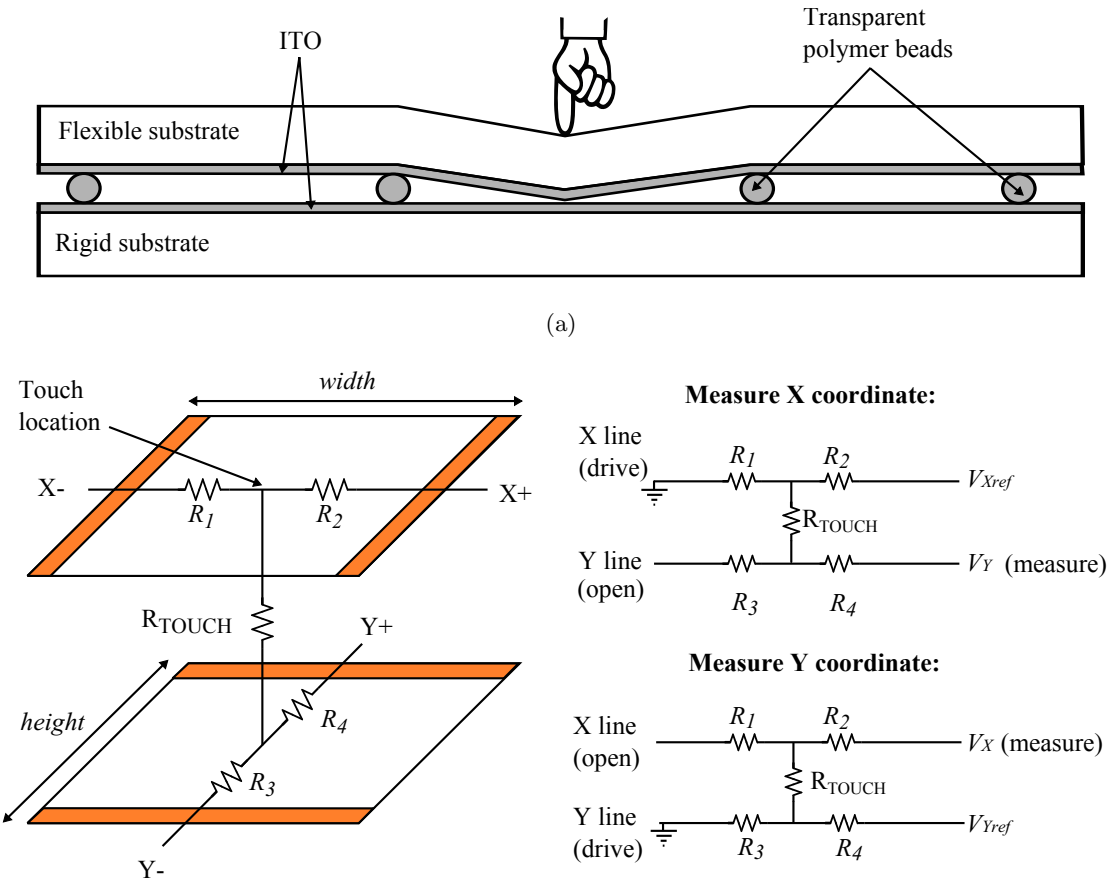

FIGURE 2.5: (a) Schematic of a resistive touchscreen comprising two substrates, one of which is flexible, coated in a transparent conductor such as ITO and with X and Y contact electrodes. The substrates are initially separated by an array of insulating transparent polymer beads ('spacer dots'). When the flexible substrate is pressed the ITO electrodes make contact allowing current to flow. The resistance of the ITO acts as a potential divider, as shown in (b), which allows the touch coordinates to be measured by driving a voltage through the X electrodes and measuring a voltage at a Y electrode, and vice versa.

developed by the company Stantum under the name Interpolated Voltage Sensing Matrix (iVSM) [72].

The advantages of resistive touch interfaces are that a touch from any object can be registered, whether conductive or insulating. They are cheaper to manufacture and the power consumption is lower than that of capacitive touchscreens as current flows only when the interface is touched. However, the ITO electrodes suffer from poor durability due to repeated flexing of the electrode. This can cause the ITO layer to crack and flake [73]. The touch interface can be insensitive to low applied forces because a minimum force is required to cause initial contact between the ITO electrodes.

In resistive touch interfaces, pressure-sensitivity may be achieved by the incorporation of

a conducting polymer composite (CPC) layer between the electrodes, which modifies the resistance between the electrodes as a function of the applied force or pressure. The CPC layer must also have high optical transmission so as not to impact on light transmission from the underlying display. In the literature there are very few examples of such an approach and the few examples that exist are described in patents or patent applications such that technical details are often obscured. However, the general approach of these examples is summarised below. Each example comprises a functional CPC layer, however the geometry of this layer is different in each case. These concepts relate directly to the conceptual approach discussed in this thesis.

2.4.1 Pressure sensing using a percolative network of conductive particles

Li *et al.*, in association with Motorola Inc., produced a prototype resistive pressure-sensing touchscreen. A CPC layer 1 µm thick was screen-printed between two electrodes. The electrodes comprised orthogonal rows and columns such that a touch at any electrode intersection could be independently registered [74]. The CPC layer comprised conductive nanoparticles less than 100 nm in size, e.g. ITO, tin dioxide or zinc oxide, dispersed in a translucent insulating polymer, where the particulate loading was 20–30 % by volume [75]. A schematic of this is illustrated in Fig. 2.6(a). When the CPC is compressed, more conductive pathways form in the particle network, reducing the resistance through the layer. This effect can be explained by percolation theory and quantum tunnelling, both of which are described later

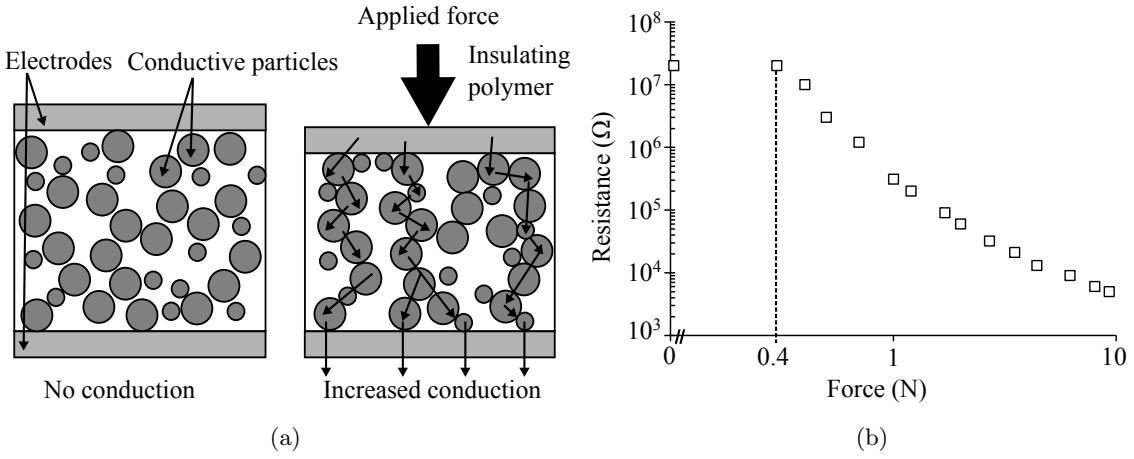

FIGURE 2.6: (a) Schematic of a conducting polymer composite layer comprising a network of conductive particles dispersed in an insulating polymer. Under applied force the composite compresses and the number of conductive pathways increase, causing a decrease in resistance through the composite. (b) Force-resistance response of prototype pressure-sensitive resistive touchscreen demonstrated by Li *et al.* [74]. Under application of 0.4–10 N applied force the resistance decreases over four orders of magnitude, where the dotted line represents the activation force needed to initiate pressure sensitivity.

in chapter 8, section 8.3.1. The optical transmission through the CPC layer was reported as 94 % with respect to transmission through the glass substrate. Fig. 2.6(b) shows the force-resistance response, reproduced from the data provided in [74]. The resistance decreases over three orders of magnitude with applied force, dropping from 20 MΩ at zero load to less than 5 kΩ for a 10 N load. However, a minimum force of 0.4 N is required to cause a decrease in resistance. This 'activation' force means that, in its current form, this composite is insensitive to light touches.

2.4.2 Pressure sensing using magnetically aligned conductive particles

Goncalves *et al.* developed a CPC layer for use in a pressure-sensitive resistive touchscreen which currently has a patent pending [76]. The conduction pathways are constrained in the vertical (z) axis through application of an external magnetic field during the fabrication stage. The CPC comprised magnetic, conductive nickel particles of diameter 2–5 µm, dispersed in an insulating polymer matrix such as silicone or polyurethane. The particulate loading was 0.3–10 % by volume. The composite was deposited as a 50–100 µm thick film and an external magnetic field of strength 3–10 mT was applied. The magnetic nickel particles were aligned to form columns spanning the thickness of the printed film, as shown in Fig. 2.7(a). This effect has been previously studied for composites containing nickel particles [77] and carbon

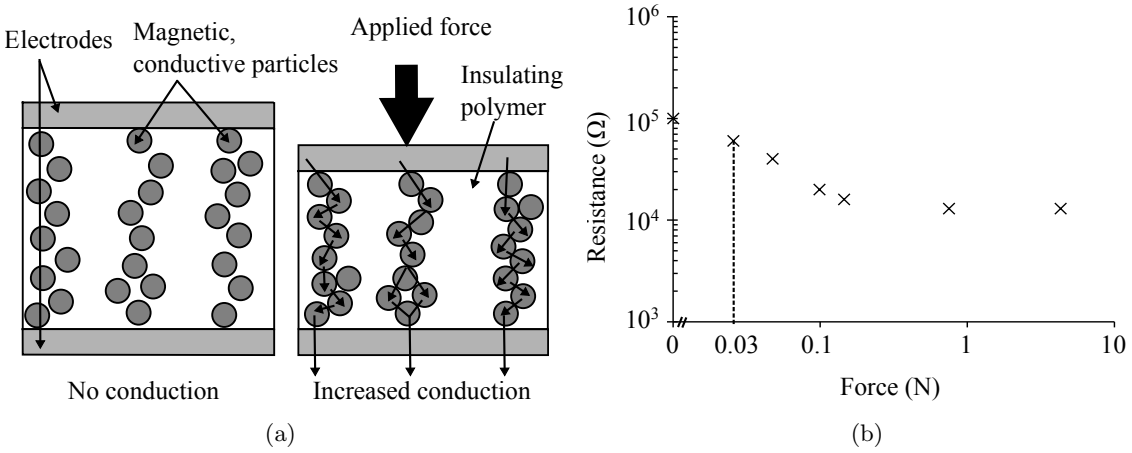

FIGURE 2.7: (a) Schematic of conducting polymer composite layer comprising columns of conductive, magnetic particles aligned through the application of an external magnetic field. Under applied force the composite compresses and the number of conductive pathways through the columns increase and field-assisted quantum tunnelling between particles may occur, causing a decrease in resistance through the composite. (b) Force-resistance response of a pressure-sensitive resistive touchscreen, demonstrated by Goncalves *et al.*, redrawn from data provided in the patent application [76]. The resistance through the composite decreases by a factor of 10 for applied forces up to 1 N, beyond which the resistance remains almost constant. The activation force of 0.03 N is shown by the dashed line.

nanotubes [78, 79]. The cross-sectional diameter of the columns was controlled by the strength of the applied magnetic field and was on average 20–25 µm.

The nickel particles had a spiky surface structure, with some surface protrusions exceeding 1 µm in length. CPCs containing these particles are of particular interest due to their enhanced pressure-sensitivity [8, 9]. It is shown that conduction between two spatially separated particles may occur through a quantum tunnelling mechanism which is further enhanced by the build-up of electric fields on the tips of the particles. Such field-enhanced quantum tunnelling is further discussed in chapter 8, section 8.4.3.2.

Force applied to the upper electrode compresses the CPC and decreases the particle separation within each column. Percolative conduction pathways are formed and conduction through field-assisted quantum tunnelling may occur. A force-resistance response for this composite is shown in Fig. 2.7(b), redrawn from data provided in the patent application [76]. In its unloaded state the composite exhibits a resistance in excess of 100 kΩ and the resistance begins to decrease at a force of 0.03 N. Increasing the load to 1 N decreases the resistance to the order of 10 kΩ but beyond this the resistance decreases marginally for loads up to 5 N. This insensitivity to applied forces larger than 0.1 N may limit its applicability in HCI applications as in this format it is unable to differentiate anything beyond a light touch.

By decreasing the number of particles in the composite and constraining them to vertical columns it is expected that the optical transmission would be enhanced, when compared to a composite of the same thickness but with a random network of unconstrained particles. However in practice it is likely that the large film thickness of 50–100 µm will, overall, have a detrimental effect on the optical transmission, although no details of this have yet been reported.

2.4.3 Pressure sensing using a single layer of particles spanning the CPC thickness

Divigalpitiya *et al.*, in association with 3M Innovative Properties Company ('3M'), have developed a CPC layer which comprises a single layer of conductive particles that spans the thickness of the layer, as shown in Fig. 2.8(a). This layer was patented for use in both force sensitive membranes [80] and resistive touchscreens [81]. Rather than conduction occurring through a convoluted vertical network of many small particles, here each individual particle acts as an electrical bridge between upper and lower electrodes. The upper electrode was initially separated from the CPC layer, for example using an array of spacer dots to maintain an electrically insulating air gap. When the upper electrode is pressed, the contact area

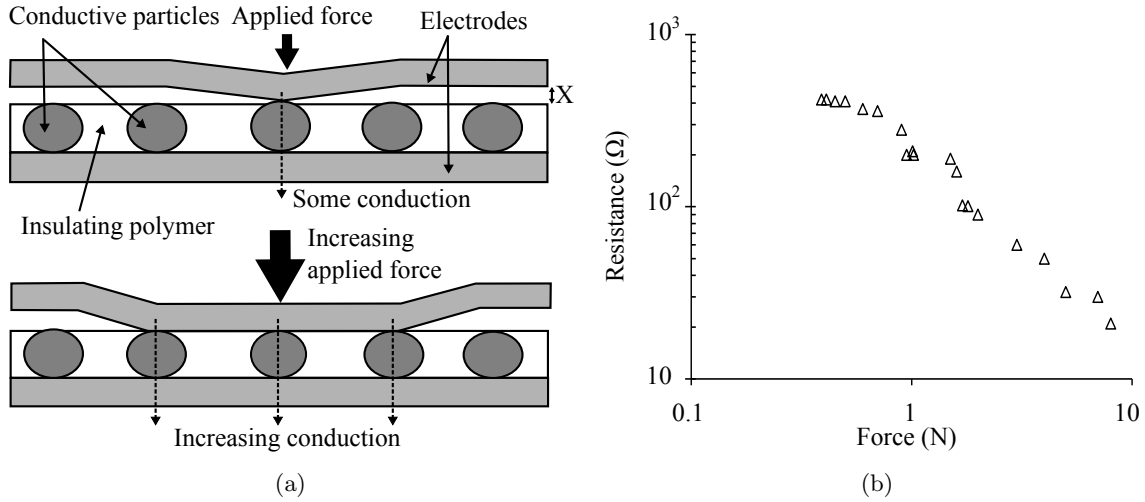

FIGURE 2.8: (a) Schematic of a conducting polymer composite layer comprising a single layer of conductive particles whose diameter is similar to the thickness of the layer. The upper electrode is initially separated from the CPC by an air gap of thickness X. Under applied force the upper electrode deforms. The contact area between electrode and CPC increases with force, contacting an increasing number of particles and decreasing the resistance through the layer. (b) Graph showing the force-resistance response of a pressure-sensitive interface developed by Divigalpitiya *et al.*, redrawn from data provided in the patent application [81].

between the upper electrode and CPC layer increases with increasing applied force. The number of particles contacted by the electrode increases, thus decreasing the resistance measured between the electrodes.

For a transparent touchscreen application, the CPC layer may comprise ITO particles or silver-coated glass beads dispersed in a single layer throughout an insulating elastomeric polymer. No information is given on the particle loading within the layer although it is justified within the patent to be low enough to allow high optical transmission.

A force-resistance response for a composite containing ITO-coated glass fibres deposited in a silicone rubber film of thickness 25 µm is shown in Fig. 2.8(b), which is reproduced from data provided in [81]. The resistance decreases from 10 kΩ at a force of 0.4 N to approximately 20 Ω at a force of 8 N. Resistance values for less than 0.4 N are not reported. Whilst no optical data was provided for this particular sensor, the transmission through a similar sensor comprising 43 µm diameter silver-coated glass beads dispersed into a 60 µm thick film at a particle loading of 140 particles mm^{-3} was reported to be 91 % over the visible wavelengths 400–700 nm.

The relationship between force, F, and resistance, R, was described by the equation:

$$R = \frac{A}{F^n}, \tag{2.4}$$

where A and n are constants. The value of n indicates the sensitivity of the response, where a larger n results in a greater decrease in resistance for a given increase in force. For the force-resistance response shown in Fig. 2.8(b) n is 1.02. The sensitivity can be controlled by the thickness of the air gap, that is the spacing between the surface of the CPC layer and the upper, flexible electrode. Fig. 2.9 shows the value of n calculated for three insulating air gap depths (denoted X in Fig. 2.8(a)) using data provided in the patent [80]. By increasing the air gap n also increases.

2.4.4 Force sensitive resistors

Conducting polymer composites are also used in Force Sensitive Resistors (FSRs), which were first patented by Franklin Eventoff in 1977 [82]. FSRs are typically small, discrete sensors used in non-transparent applications. The CPC layer is screen-printed onto a flexible substrate and separated from a set of inter-digitated electrodes by a spacer layer, as shown in Fig. 2.10(a). In another format the CPC is printed directly onto one electrode and separated from the other by the spacer layer. When the top layer is pressed the electrode(s) deforms into the spacer layer and force is applied to the CPC.

In the CPC, conductive particles are dispersed into a printable base polymer. When printed, this layer can exhibit micro- or nano-scale surface protrusions. The resistance through the FSR sensor is determined by both the increase in contact area between FSR and electrode and any intrinsic force-sensitive resistance of the CPC as governed by percolation theory and quantum tunnelling mechanisms. Conductive particles used have included tin oxide [83], carbon black [84] and titanium dioxide nanorods with a conductive coating [85]. As well as modifying the CPC layer, the sensitivity of the response can be further controlled by the number and spacing (pitch) of the inter-digitated electrodes and the flexibility of the deformable electrode.

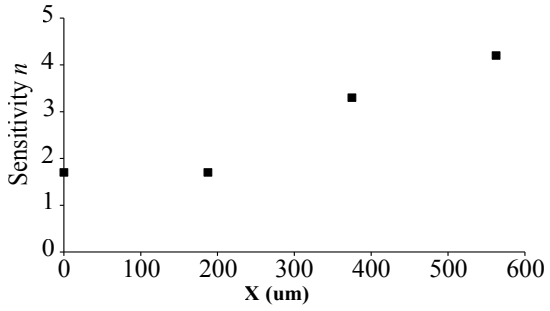

FIGURE 2.9: Graph showing the sensitivity, n, of the force-resistance response as a function of the depth of the air gap between electrode and CPC layer. By increasing the air gap, the sensitivity of the force-resistance response also increases.

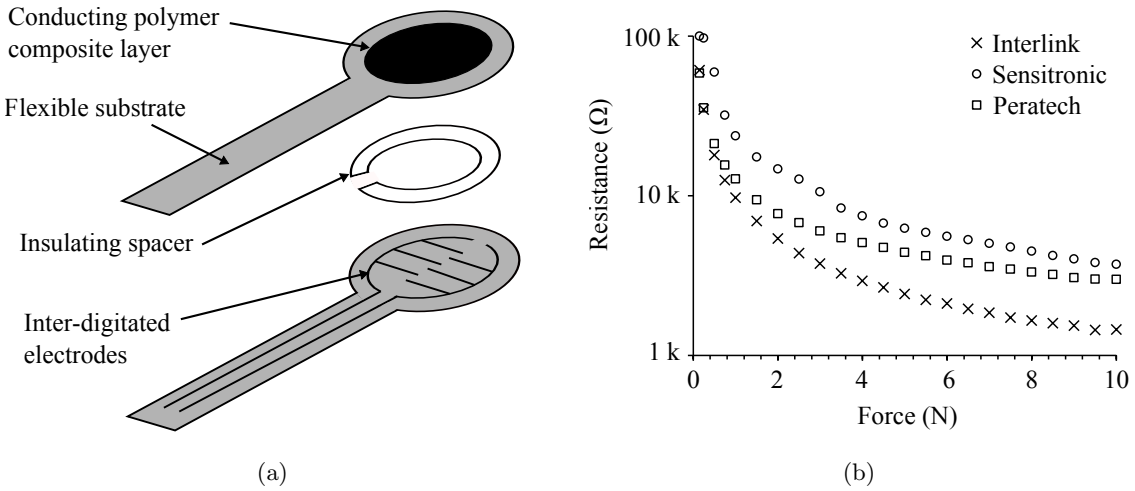

(a) (b)

FIGURE 2.10: (a) Schematic of a Force Sensitive Resistor (FSR) comprising a conducting polymer composite layer printed onto a flexible substrate, separated from a set of inter-digitated electrodes by an insulating spacer ring. When pressed, contact is made between the CPC layer and the electrodes. (b) Graph showing the force-resistance profile of three commercial FSR sensors sourced from Interlink Electronics, Sensitronic LLC and Peratech Holdco Ltd. For each FSR, the resistance decreases by over three orders of magnitude for up to 10 N applied force.

Fig. 2.10(b) compares the force-resistance responses of three commercial FSR sensors manufactured by Interlink Electronics, Sensitronics LLC and Peratech Holdco Ltd. In each case, the active layer is printed onto inter-digitated electrodes as shown in Fig. 2.10(a) and the sensor was loaded with forces up to 10 N using a load cell with a rubber probe of diameter 8 mm. For each sensor the resistance varies over three orders of magnitude when forces up to 10 N are applied. The sensors respond to forces as low as 0.15 N however for the Peratech and Sensitronics sensors the response appears to approach saturation at higher forces.

The benefits of FSR technology include the low-cost large-area manufacture methods (e.g. screen-printing) and the lightweight, thin geometry of the sensors. The sensitivity can be controlled by the mechanical design of the sensor. The sensors are insensitive to high frequency vibrations and electromagnetic noise interference. However, the resistance response can be highly variable, for example caused by hysteresis effects due to mechanical relaxation of the host polymer.

Applications of FSR sensors include biomedical sensing such as pressure mapping whilst walking [86], robotics [87] and musical synthesisers [88]. Reviews of FSR sensors in these applications have been conducted [89–92]. FSR sensors can be found in some computer keyboards and laptop trackpads, such as the VersaPad® trackpad where two large electrode/CPC substrates are separated by an array of spacer dots. The UnMousePad, developed by TouchCo,

Inc. in 2009, is a multi-touch location and pressure sensing trackpad using FSR technology [93] and the Microsoft Touch Cover is a pressure sensitive keyboard used with Microsoft Surface tablets. Here, the pressure sensitivity is used to dismiss light touches as accidental and for rejecting unintended touch from the palm of the hand (palm rejection). Other possible uses detailed in the relevant patent include using force to change the size, colour or case of text input and also for gaming applications [94].

2.5 Comparison of pressure-sensing in HCI applications

To quantitatively compare the force-sensitive touch interface approaches discussed in this chapter a basic response parameter was calculated as:

$$Response = \frac{X_i - X_{min}}{X_{max} - X_{min}} \times 100\%, \tag{2.5}$$

where X_i is the ith value of a measurable quantity X, for example resistance, capacitance or voltage, and X_{min} and X_{max} are the minimum and maximum values of X, respectively.

Fig. 2.11 compares the response of all the force-sensitive touch technologies discussed in this chapter, where data is available. This includes the piezoelectric pressure-sensing interface demonstrated by Rendl *et al.* and Zirkl *et al.* [46, 47], the pressed capacitive interfaces demonstrated by H. Kim *et al.* and K. Kim *et al.* [48, 50], the three transparent resistive sensors developed by the companies Motorola, Inc., Stantum and 3M Innovative Properties Company [75, 76, 81] and the FSR, where the sensor commercialised by Interlink is chosen as a representative example. Note that for the pressed capacitive sensors shown in Fig. 2.2(b), the pressure has been converted to an applied force using available information on the dimensions of the test probe.

Fig. 2.11 shows the force range over which each force-sensitive touch technology is sensitive. FSR sensors, as well as the resistive touchscreens demonstrated by 3M and Motorola, cover most of the range between a light touch (0.1 N) and a hard press (>5 N), although both resistive touchscreens fall short of being able to detect a true light touch, instead requiring a minimum force of around 0.4 N. Both the resistive touchscreen demonstrated by Stantum and the pressed capacitive touch interface demonstrated by H. Kim *et al.* are sensitive to very low levels of applied force (0.03 N), but in their current format they cannot distinguish a touch force greater than 1 N. Also, the piezoelectric pressure sensor cannot detect less than 2 N applied force.

In Table 2.1 the response percentage at an applied force of 1 N is compared for each force-sensitive technology. The piezoelectric sensor is not responsive at this force, whereas the response for the pressed capacitive (H. Kim) and the resistive touchscreens demonstrated by

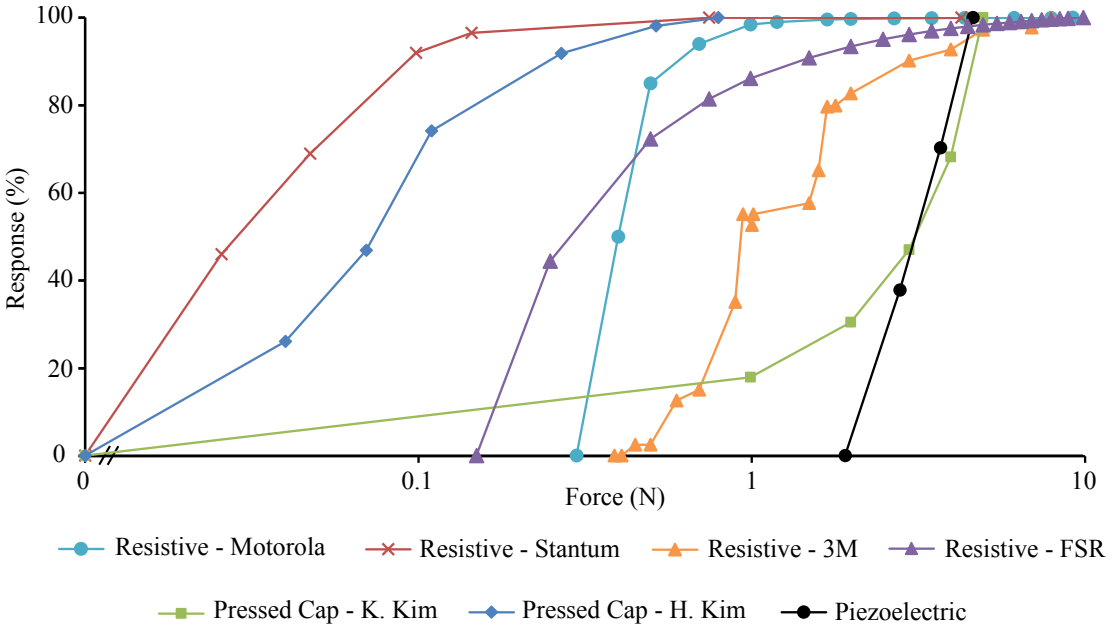

FIGURE 2.11: Force-sensitive response for all touch interfaces discussed in this chapter, including the piezoelectric sensor developed by Rendl *et al.* [46], the pressed capacitive sensors demonstrated by K. Kim *et al.* and H. Kim *et al.* [48, 50], the transparent resistive touchscreens patented by Motorola, Inc., Stantum and 3M Innovative Properties Company [75, 76, 81] and a force sensitive resistor commercialised by Interlink Electronics. Data points are connected by straight lines as a guide to the eye.

Stantum and Motorola is already saturated, indicating that they are unresponsive to further applied force. Here, the response may be defined as 'switch-like', in that it exhibits a very large change in resistance at low applied forces with a negligible decrease at higher applied forces. In this case the sensor is more suited to switching applications rather than the detection of an extended range of applied pressure. However, a controlled resistance decrease over a range of applied forces is ideal for sensing a multitude of applied force levels, as demonstrated by the FSR sensor and the resistive touchscreen demonstrated by 3M, which have a response at 1 N of 86 % and 53 % respectively. The pressed capacitive sensors demonstrated by K. Kim *et al.* and H. Kim *et al.* show very different responses at 1 N of 18 % and 100 %. This demonstrates the importance of the sensor structure, where the force range of the response can be controlled by the mechanical properties of the deformable substrate. Furthermore, the response for the latter sensor shows no sign of saturation, indicating that the full force range of this sensor has not been assessed.

Sensor	Response at 1 N force
Piezoelectric	0%
Pressed capacitive (K. Kim)	18%
Pressed capacitive (H. Kim)	100%
Resistive - Motorola	98 %
Resistive - Stantum	100 %
Resistive - 3M	53%
Resistive - FSR	86%

TABLE 2.1: Response of pressure–sensing tactile technologies at an applied force of 1 N.

2.6 Peratech Holdco Ltd, QTC™ Clear and the scope of this thesis

Peratech Ltd. (renamed Peratech Holdco Ltd. in 2014) have developed a transparent resistive touch technology which utilises a CPC layer similar to that developed by Divigalpitiya *et al.* as described in Section 2.4.3 [6]. However, here the CPC layer comprises a single layer of conductive *agglomerates*, where each agglomerate is comprised of a network of smaller, conductive particles. The agglomerates are dispersed into an insulating polymer and printed such that the size of the agglomerates is roughly equal to the thickness of the printed layer. However, this spontaneous agglomeration has many inherent disadvantages, including the lack of control over the agglomerate size and shape, which can impact the optical transmission through the CPC layer.

An alternative approach is to pre-form the agglomerates before they are dispersed into the polymer during a separate manufacture process. These pre-formed agglomerates are henceforth called granules. There are many advantages of using pre-formed granules instead of an uncontrolled agglomeration process. Firstly, it is possible to control both the size and shape of the granules through the process by which they are fabricated. This process is explained fully in chapter 3. Through this process, granules of a specific size and shape can be produced before they are incorporated into the CPC.

The internal structure, porosity and strength of the pre-formed granules can also be controlled through the manufacture process. These factors could have important implications on the granule functionality. For example, by controlling the size of the granules the optical properties through the CPC layer can be optimised, as the amount of light transmitted and absorbed by the layer is strongly dependent on the size of the particles within the CPC. This is explored further in chapter 10. Additionally, the size of the granules determines their electrical functionality because those equal to or larger than the CPC layer thickness contribute to the electrical conduction when the layer is compressed. Smaller granules are completely

wetted by the polymer and do not contact the electrodes, although they still contribute to the absorption of light through the CPC layer. By pre-forming the granules to a well-defined size range this problem can be overcome. The strength of the pre-formed granules dictates their durability and the range of applied forces they can withstand. Granule breakage is disadvantageous because it may lead to a loss of electrical conductivity and structural degradation of the CPC layer.

Finally, the resistance of the granules themselves may be inherently pressure sensitive, potentially extending the functional range of response. During the manufacture of the granules the constituent particles are mixed with an insulating polymeric binding agent. Hence the internal structure of the granule mirrors that of a CPC similar to that shown in Fig. 2.6(a). In this case it is expected that when compressed more conduction pathways are formed within the granule, leading to a decrease in resistance. The conduction mechanisms that may be present in such a composite are investigated in chapter 12. The presence of internal voids within the granule may aid this process and hence the granule porosity is also an important parameter to control.

2.7 Chapter summary

This chapter discussed various methods of incorporating pressure-sensitivity into sensors which previously could only detect the location of a touch event, and the benefits and limitations of each method were explained. Piezoelectric pressure sensors using the polymer PVDF can be printed in an array of sensors, each of which is capable of detecting a touch force. Pressed capacitive touch interfaces can measure a touch force through the increase in capacitance associated with deforming the upper electrode. For projected capacitive interfaces, where there are no moving parts, pressure sensitivity may be realised through the addition of separate, discrete force sensors or through the use of a pressure-sensitive stylus. For resistive touchscreens, a pressure sensitive layer can be printed onto one electrode, which acts to modify the resistance through the layer as a function of applied force. Three different pressure sensitive layers, comprising conducting polymer composites, have been compared here. Finally, the pressure-sensing resistive touchscreen patented by Peratech Holdco Ltd has been introduced as the focus for this thesis.

Chapter 3

Theory of Granulation

3.1 Introduction

In this chapter the theory of granulation processes are described. Granulation is a key process within this thesis as it allows controlled design and formation of the nanocomposite granules which are then incorporated into the touchscreen devices. Granulation may be defined as the agglomeration of primary particles to form semi-permanent aggregates (or granules), where the constituent particles can still be distinguished. In wet granulation, a liquid binder is used to bind the particles together. Granulation is a useful procedure as the resultant granules have a higher density than the cohesive powder. This results in improved flow characteristics which is especially useful for industries handling large amounts of powders, where problems such as caking of powders and the inhalation and explosion risks from these powders are reduced [95]. Granulation is a beneficial process for drug manufacture in the pharmaceutical industry as it can lead to a more efficient tabletting process and can be used to control the dissolution rate of the final product [96, 97]. Granulation is also an important process in food [98], agriculture [99], mineral processing [100] and the chemical industry [101].

Another benefit of granulation is the ability to produce a composite material whose properties are dependant on the exact blend of the starting components. In most of the applications highlighted above, the functionality of the granule is determined by the particle component only and the binder plays little or no role beyond that of binding the required particles together. However, for the purpose of this thesis, the process of granulation is used to produce nanocomposite granules comprised of conductive nanoparticles and electrically insulating polymer binder. Here the binder can act as a modifier to the electrical behaviour of the particles. The composite granules may then exhibit non-linear electrical resistance as a

function of applied force. More detail on this is given in chapter 8 which describes the conduction mechanisms in such composite materials.

In the field of granulation the properties of the granules are tailored to suit the application. By altering both the starting materials and the process variables the final properties of the granules, namely the average size and size distribution, surface morphology, internal porosity and strength can be controlled. Material variables include the quantity, viscosity and surface tension of the binder and the size, shape and surface chemistry of the primary particles, while important process variables include the granulator type and size, the duration and the energy of the mixing process. The aim of this chapter is to outline and summarise the theoretical granulation processes relevant to this work, namely nucleation, growth and breakage and to explain the key concepts of these processes. By understanding these processes it may be possible to predict how modifications to both the materials and process variables can change the resultant granule properties. This understanding will aid in the manufacture of the electrically functional nanocomposite granules which are the subject of this thesis.

The vessel in which granulation occurs (the granulator) may be a tumbling mixer (drum or low-shear granulation) or a mixer vessel with one or several impellers or choppers (high-shear granulation). Mixing may also occur in a fluidised-bed, where the binder is sprayed onto a bed of particles which are constantly agitated by air flow. Whilst the focus here is on high-shear granulation, results obtained using other types of granulator have been included where they can be generalised to high-shear granulation.

The chapter is split into three parts. Firstly, there is a summary of the three main granulation processes which are nucleation, growth and breakage. Then follows a discussion on how altering the materials and the process variables will impact the resultant granule characteristics, such as the size and shape, porosity and strength. Finally, the size parameters most commonly used in order to classify granule dimensions are defined.

3.2 Granulation processes

Granulation is a complex series of processes in which small changes on the micro-scale can result in large changes in the macroscopic properties of the resultant granules. To understand granulation it is convenient to split it into three processes: nucleation, growth and breakage. In the nucleation stage a liquid binder is brought into contact with the constituent particles and small granule nuclei are formed. Granule growth may be defined as a process which increases the overall size of the granule. This includes both coalescence and layering mechanisms. Often, granule consolidation is also included in this stage as it acts as a pre-cursor to growth. Granule breakage is defined as any process which reduces the granule size. Whilst

these processes may be described individually, it is important to note that in reality they may occur simultaneously during granulation, especially breakage and growth. The duration of the nucleation stage often depends on the extent of the binder addition phase and growth and breakage will often begin during the nucleation phase.

A detailed account of all aspects of granulation can be found in the literature. This includes the mathematical description of rate processes from the micro- to the macro-scale, from the theoretical description of individual particle-binder liquid bridges to the macro-scale growth kinetics of the system [102–104].

3.2.1 Wetting and nucleation

Wetting and nucleation may be regarded as the first stage of the granulation process where the liquid binder is brought into contact with the dry powder and is initially distributed during the mixing process. It is an important stage in granulation as the initial nuclei properties will affect the properties of the end-point granules, for example a broad size distribution of nuclei typically results in a broad distribution of end-point granules.

Granule nuclei form in the nucleation or wetting zone, which is defined as the region of the granulation vessel where binder and particles first come into contact. Ideally, during contact the binder should spread over and wet the surface of the particle. Whether this is energetically favourable is governed by thermodynamics and can be calculated from the surface free energies of the constituents. The wetting behaviour can be understood from surface energy studies. Fig. 3.1(a) shows a liquid droplet in contact with a smooth, non-porous solid surface and a vapour phase (i.e the surrounding air). At equilibrium the droplet forms a contact angle, θ, with the solid surface. For a flat surface, $0 < \theta < 180°$, where $\theta = 0°$ results in perfect wetting and angles greater than 90° result in the formation of liquid

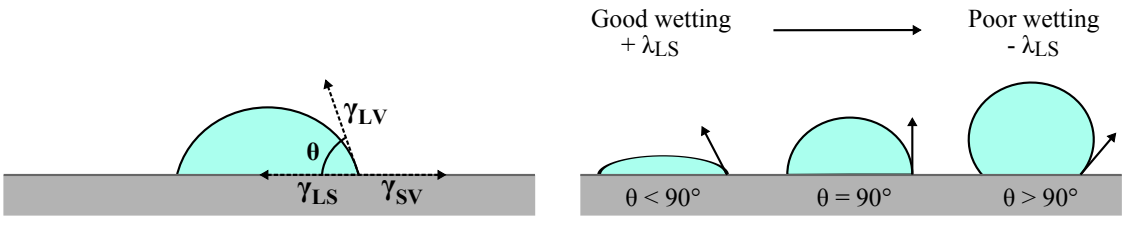

FIGURE 3.1: (a) Schematic showing a liquid droplet incident on a smooth, non-porous solid surface with a contact angle, θ, between the solid and liquid phase. The surface free energy between the phases is given by γ, where the subscripts L, S and V denote the liquid, solid and vapour phases respectively (b) Good wetting occurs for $\theta < 90°$ and leads to a positive spreading coefficient, λ_{LS}, between liquid and solid. Poor wetting occurs for $\theta > 90°$ and this leads to a negative λ_{LS}.

'beads' on the surface. In general terms, the smaller the contact angle, the greater the affinity between liquid and solid indicating good wetting, as shown in Fig. 3.1(b). For a water binder, good and poor wetting are described by the terms hydrophilic and hydrophobic, respectively. The Young-Dupré equation relates θ to the surface free energy γ between interfaces:

$$\gamma_{SV} = \gamma_{LS} + \gamma_{LV} \cos\theta, \tag{3.1}$$

where the subscripts S, L and V denote the solid, liquid and vapour phases respectively. Note that γ_{LV} is also called the surface tension [105]. The spreading coefficient, λ, is defined as the difference between the work of cohesion and the work of adhesion of the liquid/solid interface and is given by:

$$\lambda_{LS} = \gamma_{LV} \left(\cos\theta - 1\right). \tag{3.2}$$

When λ_{LS} is positive, spreading of the liquid over the solid is energetically favourable. For granulation, a positive λ_{LS} means that the liquid binder will spread over the primary particles and form liquid bridges, resulting in a stronger granule nucleus. Conversely if λ_{LS} is negative, or if λ_{SL} (the spreading coefficient of the solid over the liquid) is positive then the binder does not spread over the particle and liquid bridges will only form between the initial points of contact between binder and particles. This results in a weaker nucleus.

The method by which the binder is initially introduced into the granulation vessel is also important as it controls the size of the liquid binder droplets when they reach the nucleation zone. Schæfer and Mathieson proposed two different mechanisms by which nucleation may occur in melt pelletisation (a process where the binder is added in solid form and then melted by subsequent heating) [106]. The process depends on the size of the binder droplets relative to the primary particles. The *immersion* mechanism occurs when the binder droplets are much larger than the particles, so that the particles become immersed in the large droplet, as shown in Fig. 3.2(a). The *distribution* mechanism occurs when relatively small binder droplets are distributed onto the surface of larger particles as shown in Fig 3.2(b). These mechanisms were generalised for any wet granulation process by Scott *et al.* [107].

Practically, there are three main ways of introducing the binder to the granulation vessel: pouring, spraying and melt pelletisation. The effect of the binder introduction method is discussed in section 3.3.2 of this chapter.

3.2.2 Granule growth

Granule growth is defined as the increase in size of the granules. Coalescence is the mechanism by which two granules collide and stick together whilst layering is the adhesion of fine particulate material onto the surface of an existing granule. The difference between these

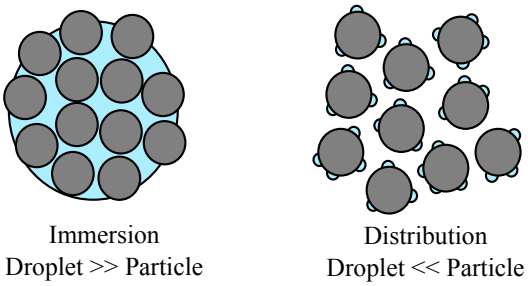

FIGURE 3.2: Schematic showing the immersion and distribution nucleation mechanisms first proposed by Schæfer and Mathieson [106]. (a) If the binder droplet size is much larger than the particle size then particles become immersed within the binder droplet. (b) If the binder droplet size is much smaller than the particle size then the droplets are distributed amongst the particles and adhere to the particle surfaces.

two processes is somewhat arbitrary, depending on what is classed as fine material. Growth begins during the nucleation stage and can continue for a long time after all the binder has been added. The amount of binder often determines the final granule size, to the point where insufficient binder may limit growth such that the nucleation kinetics have the largest impact on the final granule size.

For successful coalescence between two granules, the granules must collide, stick together and not separate. This behaviour is heavily influenced by the presence of binder on the granule surface and the strength of the wet granules, as this determines the degree of deformation during collisions. During mixing, the liquid binder may be squeezed out from the central nucleus to the surface in a process known as consolidation. The degree of consolidation further affects the wet granule strength.

The following subsections firstly describe granule strength and consolidation, before discussing growth by coalescence and layering. Note that the wet granule strength defined here should not be confused with dry granule strength (i.e. the strength of the resulting granules after drying or curing).

3.2.2.1 Wet granule strength

Newitt and Conway-Jones first described the various states of liquid saturation of granules as shown in Figure 3.3 [108]. When the constituent particles are connected at their contact points by a liquid bridge then this is the pendular state. The capillary state occurs when the granule is saturated by binder such that all pores are filled and the binder is pulled back into the pores through capillary action. The intermediate state between pendular and capillary is known as the funicular state, where some pores may remain unfilled. In the droplet state,

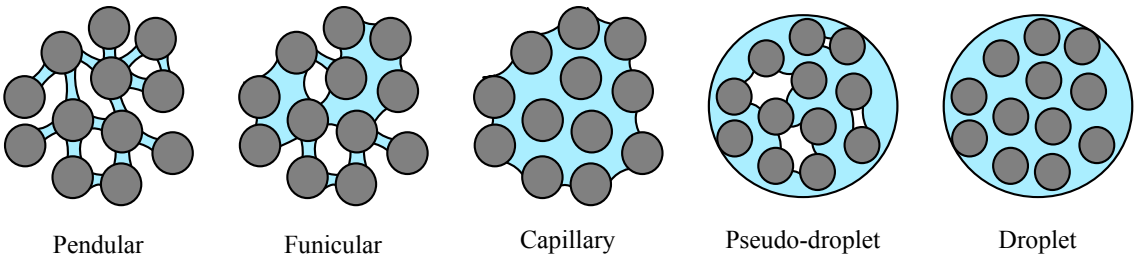

FIGURE 3.3: Schematic illustrations of the various states of liquid saturation within a granule as described by Newitt and Conway-Jones [108]

the particles are held within a binder droplet. The pseudo-droplet phase may form if there is poor wetting between the solid particles and liquid binder, resulting in trapped air pockets within the granule.

Wet granule strength is governed by capillary, viscous and frictional forces. The liquid bridges between constituent particles provide a static surface tensional force and a dynamic force relating to the binder viscosity. The surface tension itself has two components – a capillary suction pressure which is caused by the curvature of the liquid interface and an interfacial surface tension force acting on the perimeter of the liquid bridge cross-section.

Willet *et al.* found that the experimentally measured total bridge force is directly proportional to the liquid adhesion tension of the binder material ($\gamma_{LV} cos(\theta)$) [109]. The dynamic strength of a liquid pendular bridge, associated with the shear stress resulting from a changing separation between two liquid-bound particles, is proportional to the binder viscosity and the length of the liquid bridge. Finally, frictional forces arise from contacting particles. Other forces such as electrostatic and van der Waal's forces may also have a small effect for particles less than 10 µm in size.

The peak yield stress of a wet granule increases with decreasing primary particle size. This is because for smaller primary particles there are more inter-particle contacts per unit volume. Additionally, the average size of the pores between particles decreases, which increases the capillary and viscous forces and so increases the granule strength. The pore size can also be reduced when using primary particles with a wide size distribution, as the range of particle sizes promotes a high packing efficiency.

In 1962, Rumpf proposed a model for predicting the tensile static strength of a wet granule [110]. Granules were modelled as a collection of equal-sized particles of diameter d_p granulated with a binder of surface tension γ_{LV} to produce granules in the funicular or

capillary states. The static tensile strength, σ_t, is given by:

$$\sigma_t = Cs\frac{1-\varepsilon}{\varepsilon}\frac{\gamma_{LV}\cos\theta}{d_p}, \tag{3.3}$$

where s is the liquid pore saturation (that is the fraction of the total pore space filled with liquid binder), C is a constant depending on the geometry of the system (equal to 6 for uniform spheres) and ε is the granule porosity. The model is useful for qualitatively predicting the effect of material and process parameters on the granule strength, but quantitative predictions are usually incorrect because the model assumes failure is by the simultaneous rupture of the liquid bridges between all particles. In reality, breakage is most likely to occur by crack growth along defects such as pores or micro-cracks within the granule.

3.2.2.2 Consolidation

Granule consolidation occurs as the granules collide with each other or with the walls of the vessel during the mixing process. This causes the granules to be compacted and reduces the size of inter-particle voids, forcing the liquid binder towards the granule surface. The porosity of the granule thus decreases, as shown in Fig. 3.4.

During consolidation the inter-particle friction and viscous forces increase. This is because there is both a greater number of inter-particle contacts and smaller pores between the particles. These forces are dissipative, i.e. they resist consolidation of the granule. The capillary force also increases until the granule becomes fully saturated. This force is conservative and always acts to pull particles together and thus aids consolidation. The granules will continue to consolidate until these forces resist further compaction, and a minimum porosity occurs at dynamic equilibrium between the forces.

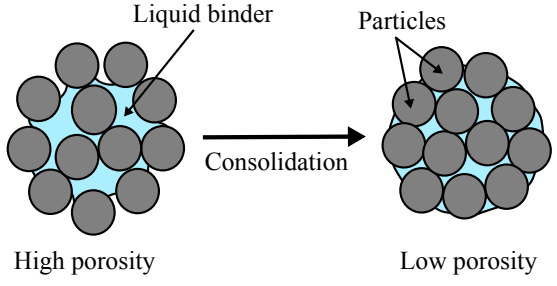

FIGURE 3.4: Schematic showing the process of granule consolidation. Repeated collisions between granules or with the walls of the granulating vessel causes densification of the granule, where porosity decreases and binder is squeezed to the granule surface. If sufficient consolidation occurs, the presence of binder on the granule surface may promote rapid growth by coalescence.

An empirical model for granule consolidation was first described by Iveson *et al.* in 1998 [111], who postulated that the rate of consolidation, k, is inversely proportional to the granule porosity, ϵ, at that time, as given by the equation:

$$\frac{\varepsilon - \varepsilon_{min}}{\varepsilon_0 - \varepsilon_{min}} = \exp\left(-kN\right), \tag{3.4}$$

where ε_0 is the initial granule porosity, ε_{min} is the minimum, end-point porosity and N is the number of revolutions of a drum granulator (proportional to the duration of the mixing process). The consolidation rate is also proportional to the size of the primary particles although this is not incorporated into equation 3.4.

Consolidation can directly impact granule growth. It has been observed in many systems that after nucleation the granules may show a period of little growth, often termed the induction or compaction phase. Following sufficient consolidation the binder is squeezed to the granule surface and further granule growth may follow.

Consolidation also affects the granule strength, which can then impact on granule growth. A decrease in granule porosity generally causes the granules to behave more rigidly, such that upon collision very little deformation occurs and the granules are more likely to separate than coalesce. However, low granule porosity also suggests that there may be more binder present at the granule surface which can then aid coalescence. The net effect of consolidation on granule growth is therefore complex and difficult to predict.

3.2.2.3 Coalescence and layering

For coalescence to occur the granules must first collide and stick together and not rebound. The amount of binder present on the granule surface can influence this process. Ennis *et al.* devised a model based on the collision between two solid particles of (average) radius r with surface protrusions of characteristic height h_a, covered with a uniform layer of liquid binder of thickness h as shown in Fig. 3.5(a) [112]. An assumption is made that the particles are not plastically deformed during impact (i.e. for low impact forces and rigid particles).

The model predicts that coalescence will occur if the kinetic energy of the impact is completely dissipated by viscous dissipation in the binder layer. The ratio of the collisional kinetic energy to the viscous dissipation is given by the viscous Stokes number, St_V:

$$St_V = \frac{8\rho r u}{9\mu}, \tag{3.5}$$

where ρ is the particle density, r is the harmonic mean radius of the two particles, u is half of the relative velocity of the impact and μ is the binder viscosity. Successful coalescence

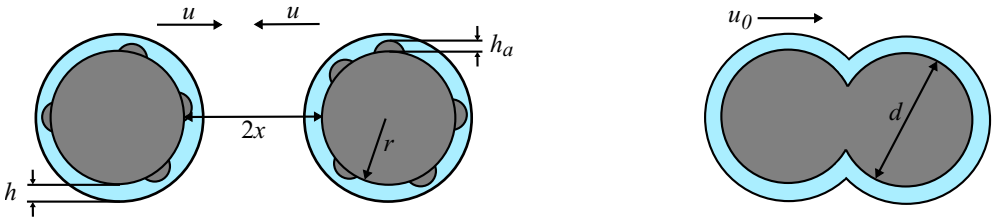

(a) (b)

FIGURE 3.5: (a) Schematic illustration showing (a) coalescence of two elastic particles separated by a distance $2x$, each of which has a radius r and surface asperities of height h_a, with a layer of binder of depth h, described in model proposed by Ennis *et al.* [112]. (b) Coalescence of two granules which may undergo plastic deformation upon impact, as described in the model proposed by Liu *et al.* [113].

occurs when St_V is less than the critical Stokes number, St_V^*, which is given by:

$$St_V^* = \left(1 + \frac{1}{e}\right)\left(ln\frac{h}{h_a}\right), \tag{3.6}$$

where e is the coefficient of restitution of the particle. Hence, growth by coalescence is most favourable when St_V is low and St_V^* is high.

Because this model is dependent on the size of the particles (through the harmonic mean r) three regimes are predicted:

1. The *non-inertial regime* occurs when $St_V \ll St_V^*$ so that all collisions are successful, regardless of the particle size.

2. The *inertial regime* occurs when $St_V \approx St_V^*$ so that the probability of a successful collision depends on the particle size. Because r is biased towards smaller particles, coalescence between two small particles or one small and one large particle is more likely than between two large particles.

3. The *coating regime* occurs when $St_V \gg St_V^*$ so that all collisions are unsuccessful, regardless of particle size.

Whilst this model is very simplistic, it may be used to predict the maximum size of granules produced although it can give no quantitative prediction of the rate of growth. It assumes that the granules do not plastically deform and that the capillary forces are negligible. Because the granules are already considered to be surface-wet, the effect of consolidation is ignored and the model does not cover surface-dry granules where the collisions do not result in coalescence but may aid consolidation. Furthermore, both the values of h and u are hard to predict. Realistically there will be a large range of collision velocities inside the granulator and this is

not easily calculable from the rotation or impeller speed. However, the model may be useful in predicting the effect of changing the material or process variables by assessing their net impact on the values of St_V and St_v^*.

Liu *et al.* extended the Ennis model by including the effects of plastic deformation of the colliding granules [113]. They define two types of coalescence. Type I occurs when the granule collisional velocity reduces to zero before the granules collide and rebound, due to viscous dissipation through the surface binder layer. For Type I:

$$St_V^* = ln\frac{h}{h_a}. \tag{3.7}$$

This is similar to the Ennis model, except that the mechanical properties of the granule do not have an effect. Type II coalescence occurs when the collisional velocity reduces to zero after the granules collide, deform and rebound, as shown in Fig. 3.5(b). Here the Stokes deformation number is defined as the ratio of the collisional kinetic energy to the plastic deformation for two colliding granules and is given by:

$$St_{Def} = \frac{mu_0^2}{2d^3Y_d}, \tag{3.8}$$

where d and m are the harmonic mean granule diameter and mass respectively, u_0 is the collisional velocity and Y_d is the plastic yield stress of the granule.

For initially surface-wet granules, at low St_{Def} the collisions are purely elastic and the coalescence probability is only dependent on St_V^* as in the Ennis model and equation 3.6. As St_{Def} increases the granule may plastically deform. This aids coalescence by dissipating some of the impact energy and by creating a flat contact area between granules so that there is a greater viscous dissipation force during rebound. In this case, coalescence occurs over a greater range of St_V values. Conversely to the Ennis model, increasing the collisional velocity (energy of mixing) may lead to an increase in coalescence growth due to the plastic deformation of the granules producing a flat contact layer. In the Ennis model, velocities above a critical value always result in granule separation.

For initially surface-dry granules, the model predicts that at low values of St_{Def} the granules do not plastically deform and no liquid binder is squeezed to the granule surface so that coalescence does not occur. Above a critical value of St_{Def} the probability of coalescence is a function of St_V, as in the surface-wet case. Whilst this is an improvement over the Ennis model, as granule deformation is taken into account, it still neglects the effect of capillary forces. It is also limited to small granule deformations as at high deformations the possibility of granule breakage is not taken into account.

Granule growth is usually assessed by measuring the granule size distribution at time intervals during the granulation process and plotting the average granule size as a function of time. Iveson and Litster [114] postulated that growth occurs by one of two mechanisms depending on the nature of the particle and binder constituents. The *induction growth* regime is characterised by an average granule size which remains fairly constant with limited growth. During this time consolidation may occur, as described in section 3.2.2.2. If sufficient consolidation occurs such that binder is squeezed to the granule surface this may be followed by a period of rapid growth by coalescence. This is most likely for strong granules that resist deformation, for example fine, widely-sized particles with a viscous binder. In the *steady growth phase*, growth may occur through the crushing and layering mechanism or by granule deformation leading to coalescence. This is most likely for weak, deformable granules or high impact velocities, or for coarse particles with low viscosity binder.

Iveson and Litster stated that the growth mechanism is dependent on two parameters: the Stokes deformation number St_{Def} and the maximum granule pore saturation s_{max}, that is the minimum porosity which the granules achieve during granulation. These are are given by:

$$St_{Def} = \frac{\rho_g u_0^2}{Y_g} \tag{3.9}$$

$$s_{max} = \frac{w\rho_s(1-\varepsilon_{min})}{\rho_l \varepsilon_{min}}, \tag{3.10}$$

where ρ_g, ρ_s and ρ_l are the densities of the granule, solid and liquid phase respectively, w is the mass ratio of solid to liquid and ε_{min} is the minimum porosity reached by the granules. u_0 and Y_g are the collisional velocity and the dynamic yield stress of the granules. They plotted the growth behaviour as a function of both s_{max} and St_{Def} on a regime map, an adaptation of which is shown in Fig. 3.6 [114]. The regime map shows a number of distinct phases. For insufficient granule strength the granules are constantly breaking and reforming into a crumb-like mixture. If there is too much binder in the system an over-wetted paste or slurry is formed. The model may be used to retrospectively define boundaries between regimes. It cannot be used as a predictive tool because *a priori* knowledge of ε_{min} is required.

The regime map was initially validated for the granulation of sand with water or ethanol binders and for glass ballotini (beads) with a glycerol binder in a drum granulator. Further work involved validating the model for a number of particle/binder systems in both drum and high-shear granulators [115]. Whilst the boundaries between regimes could be calculated for the drum granulator, problems were encountered in extending the quantitative assessment to high-shear granulators. The problem was that the collisional velocity was difficult to predict in high-shear mixers and over-estimation led to high St_{Def} values. Furthermore, additional analysis led to the conclusion that the boundaries between regimes were also dependent on additional parameters which were not included in the original model, such as binder viscosity.

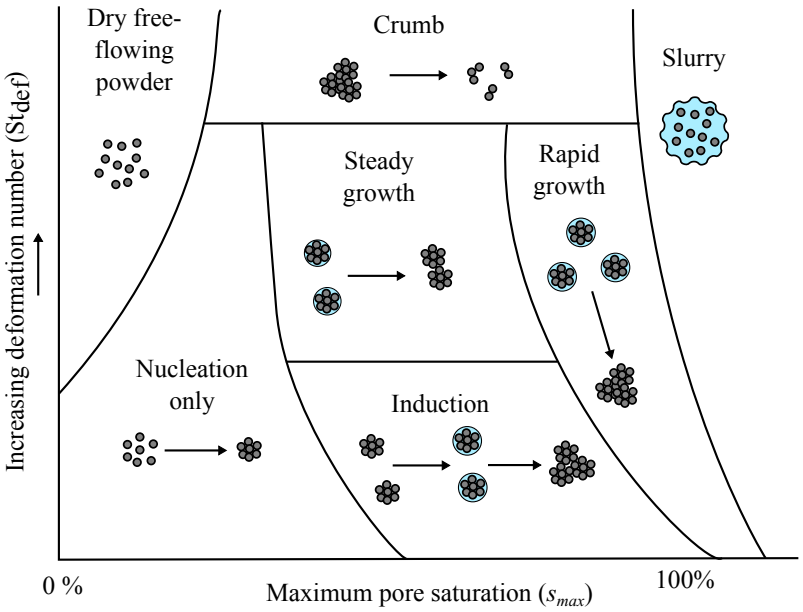

FIGURE 3.6: Granulation regime map as a function of the maximum pore saturation, s_{max}, and the Stokes deformation number, St_{Def}. Figure adapted from that of Iveson and Litster [114].

3.2.3 Granule breakage

During granulation the wet granules may break apart or alternatively the granules may dry during the process and subsequently fracture. Breakage of wet granules may be beneficial as it aids distribution of the binder and it can be used to control the final granule size. However, the breakage of dried granules tends to create small, dry particle fragments which are not recycled back into the growth phase.

The breakage of wet granules is very difficult to observe experimentally. Breakage is more likely to occur in high-shear granulation due to the high process energy. An increase in granulation energy has been shown to decrease the final granule size (this is explored further in section 3.3).

In some studies coloured tracer particles were incorporated into the granules (or binder) in order to verify whether breakage of wet granules was occurring in the granulation process [116, 117]. However very little quantitative theory exists that can predict either the breakage rate or the conditions for which breakage will occur. One model, developed by Tardos *et al.*, predicts that granules will break in a shear field if they have sufficient externally applied kinetic energy [118]. Similar to the theory developed by Liu on the deformation leading to coalescence of granules, Tardos *et al.* proposed that breakage occurs if St_{Def} exceeds a

critical value. In this case, they proposed that St_{Def} was defined as:

$$St_{Def} = \frac{m_p U_0^2}{2V_p \tau(\dot{\gamma})}, \tag{3.11}$$

where m_p and V_p are the granule mass and volume, U_0 is the relative particle velocity and $\tau(\dot{\gamma})$ is a characteristic stress within the granule. The model predicts that breakage will occur for granules above a maximum size and this decreases with increasing shear rate. This model is severely restricted as it only accounts for granule breakage due to shear flow and does not take into account breakage due to collisions with the impellers or the sides of the granulating vessel. For instance, in a high-shear mixer it is often observed that broken granular material forms a paste on the walls of the granulating vessel. This is because a granule exhibiting plastic behaviour is more likely to smear than break when its yield stress is exceeded. Other models relate the collisional kinetic energy to the energy absorbed by plastic defomation of the granule [119].

3.3 Control of granulation

The aim of any granulation process is to convert the starting materials into granules with tailored properties such as size, strength and porosity. The ultimate goal of granulation theory is to be able to accurately predict and control the outcome of the granulation process by control of the material and process variables. Rather than producing granules through trial and error, if the effects of changing the material and process variables were predictable then achieving the desired end-point granule becomes easier. There is a large volume of existing work which aims to fulfil this aspiration. Unfortunately, as of yet a universal theory does not exist and most results are specific to the particular particle/binder system or to the type of granulating vessel used. In this section, the effect of changing the material and process variables on the outcome (the size, strength and porosity) is explored and linked back to the theory discussed in section 3.2. Whilst emphasis is given to high-shear granulation, results are also quoted for other types of granulators where the principles may be transferred.

3.3.1 Effect of binder/particle surface energy

As described in section 3.2.1 the surface energy of both binder and particle can strongly affect the nucleation kinetics during granulation. By choosing a binder and particle combination with a favourable spreading coefficient, λ_{LS}, it is possible to control the nucleation rate and therefore the size, morphology and strength of the resultant granules. It is predicted that a positive λ_{LS} will lead to stronger, less deformable granules.

Ho *et al.* investigated the effect of granulating both untreated and silanised particles of D-mannitol (a sugar alcohol commonly used as a drug bulking agent) of diameter 75–180 µm with a Polyvinylpyrrolidone (PVP) binder [120]. λ_{LS} was positive for the untreated D-mannitol/PVP system and large and negative for the silanised D-mannitol/PVP system. Granules were prepared using different ratios of untreated to silanised D-mannitol. An increase in silanised D-mannitol (corresponding to increasing hydrophobicity) resulted in a larger fraction of smaller granules and an increase in the span of the distribution, as well as an increase in the granule porosity. Furthermore, it was found that with an increasing percentage of silanised D-mannitol (i.e. decreasing λ_{LS} from positive to negative) the granules exhibited a lower Young's modulus. Thielman *et al.* obtained similar results when granulating hydrophobic ($-\lambda_{LS}$) and hydrophilic ($+\lambda_{LS}$) particles with a hydroxy propyl-cellulose (HPC) binder [121]. Hydrophobic particles led to granules with a wider size distribution and a higher proportion of smaller granules than for hydrophilic particles. Zhang *et al.* granulated various pharmaceutical compounds with either pure water or a solution of 20 vol. % ethanol in water [122]. In both cases λ_{LS} was negative, but for the water/ethanol solution λ_{LS} was higher (less negative). For the latter case the resultant granules had a higher density, a lower porosity and a lower friability (higher strength) when compared to granules made with pure water binder. Scanning electron microscopy showed that the water/ethanol granules had a smoother and more homogeneous morphology than when granulating with pure water. Planinšek *et al.* obtained similar results when lactose or pentoxyfilline particles were granulated with a PVP or HPMC (polymer) binder [123].

The increase in granule strength with increasing λ_{LS} may be attributed to a larger work of adhesion between binder-particle bridges. Poor wetting between particle and binder also leads to more voids within the granules which decreases the granule strength. Poor wetting between particle and binder means that the binder droplet does not completely wet the particle surface. During particle collisions there are fewer sites where viscous contacts are formed and the collisional kinetic energy can be dissipated. Therefore there is a decreased likelihood of coalescence and a higher probability of separation. Hence a low or negative value of λ_{LS} can lead to smaller granule sizes. When λ_{LS} is positive the binder spreads over the particle surface increasing the amount of binder present for viscous dissipation during coalescence. Furthermore, a positive λ_{LS} decreases the capillary suction pressure and inter-particle friction, increasing the rate of consolidation and subsequent growth.

3.3.2 Effect of binder distribution method

The method by which the binder is introduced to the particles (or vice versa) can be critical as it controls the nucleation mechanism in the early stages of granulation, as described in section 3.2.1. In granulation experiments the binder is usually introduced into the vessel by

either pouring, spraying or melting. For the latter case, often termed melt pelletisation, the binder is introduced into the powder as solid pellets and then melted during the granulation process.

Inhomogeneity in the binder distribution is found to promote bimodal granule size distributions, especially in the early stages of granulation. Analysis of the liquid-to-solid ratio in the resulting granules often shows that larger granules contain a higher proportion of binder than smaller granules. This indicates that preferential growth occurs in binder-rich regions and this result has been found for high-shear granulation using both pouring and melting methods of binder distribution [124–127]. For the pouring method, the bimodality may persist even after long granulation times. For example, Scott *et al.* granulated calcium carbonate powders with polyethylene glycol (PEG) using both a pouring and melting binder addition method [107]. In both cases the granule size distribution was bimodal in the early stages (4 minutes). However, after 24 minutes the melting method produced a unimodal granule size distribution, whereas for the pouring method the granule size distribution remained bimodal. Analysis of granule porosity showed that the pouring method produced lower porosity granules, where the porosity was also found to increase with increasing granule size.

Pouring the binder onto the powder bed (or pouring the powder onto the binder) results in a larger binder droplet size compared to the particle size, thus promoting the immersion method of nucleation. This results in distinct 'binder-rich' and 'binder-dry' regions which leads to the observed bimodality demonstrated above. Spraying of the binder onto the particles results in liquid droplets which are smaller or similar to the particle size, so that nucleation occurs through the distribution mechanism. Here, the binder droplet size can be used to control the size of resultant granules [128]. Melt pelletisation can result in either mechanism depending on the size of the pellets used – larger pellets may promote the immersion mechanism and smaller pellets the distribution mechanism. For example, Schæfer and Mathieson found that increasing the size of the binder pellets increased the initial nuclei size and the granulation rate [106].

An understanding of the effect of binder introduction is of great importance, because the method of granulation employed in this thesis requires a pouring method of binder addition (see chapter 4, section 4.2.3). Understanding how this affects the resultant granule properties will aid the understanding of how optimum granules may be produced.

3.3.3 Effect of binder quantity and viscosity

The Ennis model described in section 3.2.2.3 cannot account for binder viscosity, as this has no predictable effect on St_{Def} and s_{max}. The effect of binder viscosity is also dependent on the binder amount and also on the primary particle size. With more liquid binder, the

inter-particle friction is reduced as there is more lubrication. However viscous forces increase due to the larger volume of binder squeezing through the pores. The rate of consolidation may therefore increase or decrease, depending on whether inter-particle or viscous forces dominate. Viscous forces are most likely to dominate for high viscosity binders.

Iveson and Litster, and Iveson *et al.*, investigated the relationship between binder quantity and viscosity when granulating 19 µm glass ballotini with water and glycerol mixtures in a drum granulator [111, 129]. For lower viscosity binders the minimum porosity of the end-point granules decreased with increasing binder content, suggesting that the extent of consolidation increased with binder content. For higher-viscosity binders the minimum porosity was found to increase with binder amount, suggesting the extent of consolidation decreased with increasing binder content. Increasing the percentage of viscous glycerol in the binder mix increases the viscous forces within the granules. Viscous forces were therefore more likely to dominate over inter-particle forces and decrease the rate of consolidation.

Similar results were found by Keningley *et al.* when granulating calcium carbonate powders with silicone binder of viscosity ranging from 1 mPa s to 56 Pa s [119]. They investigated the minimum and maximum binder content to achieve non-granulated powder and over-wet slurry respectively as a function of binder viscosity. At binder viscosities below 1 Pa s the minimum and maximum binder contents were viscosity-independent. They concluded that in this regime inter-particle frictional forces were dominant and consolidation was reduced. Above 1 Pa s the minimum binder-particle ratio remained unchanged but the maximum value increased dramatically. This was attributed to both viscous and inter-particle forces controlling the consolidation rate. Mills *et al.* discovered that the growth mechanism of 90–180 µm silica sand particles granulated with a silicone binder of viscosity ranging from 20–500 mPa s was dependent on binder viscosity [130]. At viscosities less than 100 mPa s granule growth occurred through a layering process. Increasing the binder viscosity up to 100 mPa s increased the growth rate. For viscosities above 100 mPa s growth occurred by coalescence and the growth rate decreased with increasing binder viscosity.

The effect of binder viscosity and binder particle size in a fluidised bed melt pelletisation process was investigated by Zhai *et al.*, using polymer binder and glass ballotini of size 150–250 µm [131]. For a larger binder particle size the onset of granulation (defined as the time taken for the ungranulated fraction to significantly decrease) decreased with increasing binder viscosity. For a smaller binder particle size the onset of granulation increased when the binder viscosity was also increased. For a smaller binder particle size, the growth was dependent on the distribution of the melted binder through the particles. In this case a high viscosity binder slowed down the binder distribution and resulted in a longer onset time before growth occurred. For larger binder particle sizes, the agglomerate growth was not limited by the distribution of the binder but instead by collisions between particles wetted by the

melted binder. Because a higher viscosity binder increases the dissipative energy losses upon collision, particles wetted by a more viscous binder were less likely to rebound. Hence in this case an increased binder viscosity resulted in an increased coalescence rate and a decrease in the onset time for granulation.

Johansen and Schæfer, and Johansen *et al.*, concluded in their work that the issue of unequal binder distribution amongst the size classes of resultant granules (tested with calcium carbonate particles and PEG binder in a high shear mixer) was dependant upon both the particle size and binder viscosity [132–134]. When using a small particle size with a low binder viscosity, or a large particle size with a high binder viscosity, the binder tended to be equally distributed amongst the size classes. However, when small particles were granulated with a high viscosity binder then the binder was unevenly distributed among the size classes – larger granules contained a higher proportion of binder. This was attributed to the immersion mechanism of nucleation which dominated when there was a large binder droplet size.

In summary, it is often impossible to predict the effect of binder viscosity without first understanding the relationship between binder content and viscosity. Similarly, increasing the binder quantity cannot be understood without first understanding the effect of the binder viscosity.

3.3.4 Effect of primary particle size, shape and distribution

Decreasing the particle size is expected to decrease the rate of consolidation because the number of inter-particle contacts increases and the pore diameters decrease. However, the extent of consolidation (i.e. the minimum porosity achieved) increases because granule strength is predicted to increase with decreasing particle size.

Mackaplow *et al.* investigated the effect of different sizes of lactose monohydrate powders in a high-shear granulator [135]. The particles had varying volume mean diameters (defined later in section 3.4.2) but similar packing densities due to the shape of the particles. Increasing the particle size did not affect the binder distribution in the resultant granules. However, the granule porosity decreased with increasing particle size, which is in opposition to the predictions stated above. As well as the average particle size, factors such as the particle size distribution (i.e. the span) and the particle shape were also predicted to have an effect.

Johansen and Schæfer investigated three grades of calcium carbonate powders granulated with PEG in a melt pelletisation process in a high-shear mixer [132]. The median particle size across the three grades was roughly 4–5 µm however the size distribution and particle shape were different in each case. The powders were either angular and rough, round and

smooth, or needle-shaped (acicular) and the packing efficiency was lowest for the needles and highest for the angular particles. The span of the distribution was largest for the angular particles and roughly equal for the round and acicular particles. The high packing efficiency of the angular particles was attributed to the large span of the distribution. There was an observed trend between the packing efficiency and the binder requirement for granulation. The particles with the highest packing efficiencies required the least amount of binder for successful granulation due to the decrease in the void size between particles.

Ramachandran *et al.* granulated three grades of D-mannitol with an aqueous polymer solution in a fluidised bed granulator [136]. Whilst the average particle size and shape was kept constant, the size distribution of the particles was different for each grade, corresponding to narrow, medium and wide size ranges. There was very little effect of the particle size distribution (PSD) on the corresponding granule size distributions. In all cases, granule porosity decreased with increasing granule size. However, this decrease is less pronounced for the narrow PSD and most pronounced for a widest PSD. The percentage of coarse, medium and fine primary particles in each granule size class was determined. There were more fine particles found in the largest granules, but in the other granule size classes the proportion of primary particle sizes was roughly equal.

In summary, the effect of the size of primary particles is also strongly linked to the shape of the particles and the PSD. Assessing the effect of changing one of these variables is only effective when keeping the other two constant. For example, whilst decreasing the particle size should in theory increase the strength of the granules, this is not always observed experimentally. Instead, it is found that packing efficiencies for wide PSDs are higher and this can lead to an increase in granule strength and a decrease in porosity. The shape of the particles can also affect the packing efficiency. In this thesis, both acicular and spherical shaped particles are used and it is important to understand how not only the shape but the size and span of the particle distribution may affect the resultant granules.

3.3.5 Effect of speed/energy of mixing

Knight *et al.* reported on the effect of increasing the rotational speed of the impeller in a high-shear mixer when granulating calcium carbonate powder with PEG binder in a melt pelletisation process [137]. The granule growth was reported as a function of time in the granulator, for three impeller speeds of low (450 rpm), medium (800 rpm) and high (1500 rpm). The growth rate was slowest at the low impeller speed and fastest for the medium impeller speed. At the high impeller speed the growth rate was intermediate and this was explained by increased granule breakage at high speeds. The fraction of smaller granules was observed to decrease with time irrespective of impeller speed. This was attributed to growth

by coalescence. For each impeller speed the granule size distribution started off as bimodal, but the bimodality persisted after long mixing times which is unusual even after accounting for the effects of an initially inhomogeneous binder distribution. For larger impeller speeds the bimodality became skewed towards smaller granule sizes and this was attributed to granule breakage. This was supported by scanning electron microscope images that showed that granules produced at low and medium impeller speeds were rounder and smoother in shape whereas those produced at high impeller speeds had irregular shapes suggestive of breakage.

Oulahna *et al.* found similar results using sericite powder granulated with PEG, water and ethanol mixtures in a high-shear mixer, where the resultant granule porosity, friability and binder content were also assessed [138]. At a low impeller speed (100 rpm) there was a higher proportion of fine granules and a wider granule size distribution. This was attributed to binder inhomogeneity due to low energy input. At medium (500 rpm) and high (1000 rpm) speeds the distributions became narrower. However, at high speed the percentage of finer granules was higher than for the medium impeller speed and again this was attributed to breakage. Furthermore, the granule porosity decreased with increasing impeller speed. Increasing impeller speed increased both the collisional velocity and the frequency of collisions, both of which increased the rate of consolidation. Because of this, granules produced at high impeller speeds were less friable (i.e. they were stronger). Rahmanian *et al.* achieved similar results for calcium carbonate particles granulated with an aqueous solution of PEG in high-shear mixer, where the granule strength increased with increasing impeller speed [139, 140]. Furthermore, a more homogeneous internal structure was produced from higher impeller speeds. In disagreement with the results of Oulahna, granules produced at higher impeller speeds had a smoother, rounder morphology indicating that breakage had not yet occurred in this system.

To summarise, an increase in agitation energy, for example caused by increasing the impeller speed of a high-shear mixer, increases the rate of consolidation and leads to faster growth of less porous, stronger granules. However, granule breakage becomes more common at higher energies which may or may not be beneficial depending on the application. The granulation method used in this thesis, as described later in chapter 4, allows control over the speed of rotation of a high–shear mixer. Whilst the mixer used in this work contained no impellers, the principles discussed above are transferable.

3.4 Granule size and shape parameters

3.4.1 Size parameters of individual granules

Granules often have a complex shape which makes characterisation by a single size parameter very difficult. In fact only a sphere can be completely characterised by one parameter. Nevertheless, it is often useful to be able to characterise the granules with a meaningful parameter as it allows a quantitative comparison. The method used to measure the granule often imposes its own limitations on what properties of the granule can be measured. Granules which have the same diameter can have vastly different shapes. If theoretically one could measure all dimensions of a granule, then it is possible to define a volume or surface diameter which is the diameter of a sphere having the same volume or surface area of the granule respectively. However, for imaging techniques such as optical and scanning electron microscopy the image represents a 2D projection of the granule. Furthermore, granules are measured at one orientation. Usually the samples are prepared in such a way that the granules rest in a stable equilibrium on a flat surface and the largest dimensions are parallel to the plane of the image. Because the image gives a 2D projection of each granule this means there can be a bias towards measuring the larger dimensions of the granules.

The diameter of a circle of equal projection area, d_{EQPC}, is the diameter of a circle which has an area equal to the projected area of the granule, as shown in Fig. 3.7(a). The perimeter equal diameter, d_{EQPC}, is the diameter of a circle with the same perimeter as the projected image of the granule as shown in Fig. 3.7(b). However d_{PED} may give an over-estimation of the granule size if the granule has an irregular, non-spherical shape.

The Feret X and Y diameters, $d_{f,x}$ and $d_{f,y}$, are the maximum size of the granule measured in the X or Y orientation, as shown in Fig. 3.7(c). In principle it is possible to measure a Feret diameter at every orientation in the 2D plane from 0° to 180°. Then the maximum Feret diameter, $d_{f,max}$, can be determined. The Martin diameter is the diameter which bisects the total granule area for a specified orientation. Fig. 3.7(d) shows the Martin diameter for the X orientation.

3.4.2 Size parameters for granule distributions

Once a set of granule diameters has been measured, the mean granule size may be calculated in one of several ways. The mean $\bar{x}$ of a set of numbers x, where n_i numbers have a value of x_i is given by:

$$\bar{x} = \frac{\sum x_i^k x_i^r n_i}{\sum x_i^r n_i}, \tag{3.12}$$

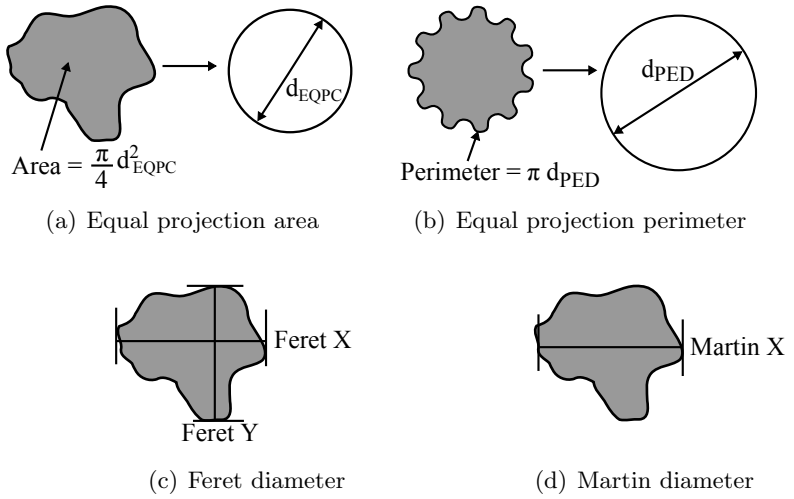

(a) Equal projection area (b) Equal projection perimeter

(c) Feret diameter (d) Martin diameter

FIGURE 3.7: Schematic of diameters used to characterise granules, where (a) d_{EQPC} is the diameter of a circle with the same area as the projected area of the granule (b) d_{PED} is the diameter of a circle with the same perimeter as the projected perimeter of the granule (c) the Feret X and Y diameters, $d_{f,x}$ and $d_{f,y}$, are the maximum granule sizes measured in the X and Y orientations (b) the Martin diameter is the diameter measured at a specified orientation which bisects the total granule area, where in this case the X orientation is shown.

where r may be equal to 0, 1, 2 or 3 for number, length, surface or volume weighted means and k may be equal to -1, 0, 1 or 2 for harmonic, geometric, arithmetic or quadratic means etc. The most common mean values used in granule size analysis are the arithmetic mean ($k = 1$, $r = 0$), denoted $D(1,0)$, the arithmetic surface mean $D(3,2)$ (where $k = 1$, $r = 2$), and the arithmetic volume mean $D(4,3)$ (where $k = 1$, $r = 3$) which are given by:

$$D(3,2) = \frac{\sum x_i^3}{\sum x_i^2}, \tag{3.13}$$

$$D(4,3) = \frac{\sum x_i^4}{\sum x_i^3}, \tag{3.14}$$

where the bracketed numbers are used as shorthand to denote the exponent of x_i in the numerator and denominator respectively. $D(3,2)$ and $D(4,3)$ are known as moment means and are analogous to the moment of inertia as they indicate at what point (i.e. what surface area or volume) the granule size distribution would rotate. The advantage of using a measurement system where either $D(3,2)$ or $D(4,3)$ are calculated is that no knowledge of the particle count is required.

Different size analysis techniques will report a different mean value for the same set of granules. For example, analysis of scanning electron or optical microscope images may give a set of granule diameters (for example the Feret diameter). Adding these diameters and dividing by the total number of granules gives $D(1,0)$. However, image analysis software may be used to determine the projected area of each granule. By dividing the sum of the projected areas

of a number of granules and taking the square root $D(2,0)$ is obtained. A Coulter counter measures the change in resistance measured in a narrow channel passing between two electrodes, where particles are dispersed in an electrolyte which is passed through the channel, causing a change in the measured resistance proportional to the particle volume. Hence in this case $D(3,0)$ is measured. Laser diffraction (described in chapter 4) measures the $D(4,3)$ value, that is the volume percentage of granules which scatter light by a certain intensity. Size analysis by sieving also measures $D(4,3)$ as the total mass in each sieve fraction is measured. For constant granule density this is equivalent to the volume.

Fig. 3.8(a) shows a granule size distribution obtained by measuring the maximum Feret diameter of 330 granules. To obtain the granule size distribution (GSD) the frequency of granules residing in each bin was calculated as a percentage of the total number of granules measured. $D(1,0)$ was calculated as 5.4 µm. The mode of the distribution is the most common granule size and this is the bin from 4–5µm. The cumulative granule size distribution (CGSD) is shown in Fig. 3.8(b). This shows the total percentage of granules measured below a certain size. It can be used to define the percentiles of the distribution. For example D_{10} is the size below which 10% of the total granules are measured. Other commonly used percentiles in particle size analysis are D_{90} and D_{50} where the latter is the median of the distribution. In this case, D_{10} is 2.8 µm, D_{50} is 5.1 µm and D_{90} is 8.1 µm.

The span S of the distribution may be defined as:

$$S = \frac{D_{90} - D_{10}}{D_{50}} \tag{3.15}$$

and this gives a useful measure of the width of the distribution. In this example the span is equal to 1.0. The smaller the S value the more monodisperse the distribution. Merkus

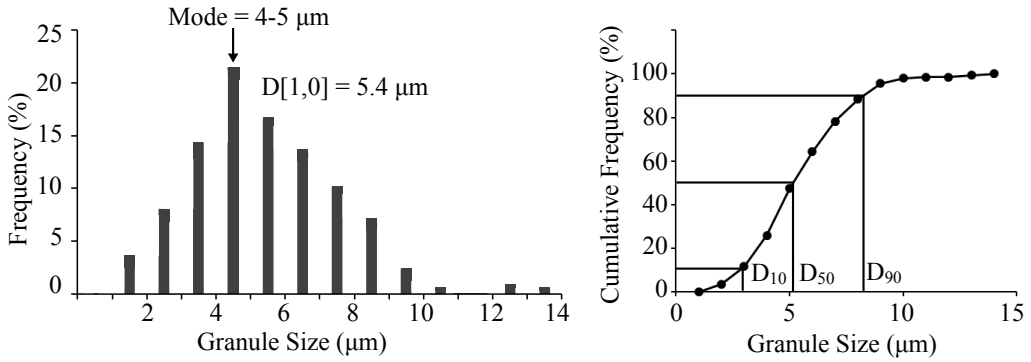

(a) (b)

FIGURE 3.8: (a) A granule size distribution (GSD) obtained from measuring the maximum Feret diameter of 330 granules. (b) The cumulative granule size distribution (CGSD) of the same granules, showing the median (D_{50}) and the 10th and 90th percentiles (D_{10} and D_{90}).

D_{90}/D_{10}	Distribution
< 1.02 (ideally 1.00)	Monodisperse
1.02–1.05	Ultra-narrow
1.05–1.5	Narrow
1.5–4	Medium
4–10	Broad
> 10	Very broad

TABLE 3.1: Classification of granule size distributions according to the ratio of the 90th to the 10th percentile of the distribution, according to Merkus [141].

adopted a different approach, where the width of the distribution was calculated as the ratio of D_{90} to D_{10} [141]. Then, the distribution can be classified into one of several categories as described in Table 3.1.

In the case of area or volume frequency distributions, the percentage of the total area of volume is calculated for each area or volume class. To express this as a diameter often a single granule shape is assumed, e.g. a circle or sphere. Fig. 3.9 shows the same set of granules analysed in terms of number (as in Fig. 3.8(a)), area or volume. The GSD is dramatically different in each case and will give different calculated values of $D(X,0)$, D_{10}, D_{50} and D_{90}. For example the $D(1,0)$, $D(2,0)$ and $D(3,0)$ mean values are 5.4, 5.8 and 6.2 µm for the number, area and volume distributions respectively. One 100 µm granule has the same volume as 1000 10 µm granules or 10^6 1 µm granules. Therefore a number distribution is always dominated by the fine fraction whilst a volume distribution is dominated by the coarse fraction of the sample. For a bimodal granule size distribution, even a couple of large granules may heavily affect the surface or volume size distribution. For this reason, number distributions are used throughout the thesis, with the caveat that the secondary mode associated with a bimodal distribution is non-negligible. In this thesis, to overcome

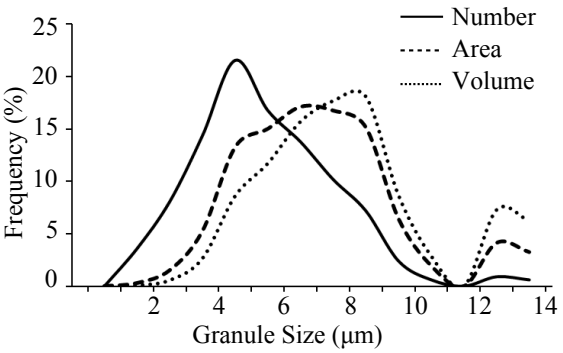

FIGURE 3.9: Granule size distributions calculated for same set of granules, where the frequency weighting by number, area and volume are compared. Area and volume weighting are biased towards larger granules compared to number weighting. For ease of comparison the lines show the envelope of the measured GSDs.

this issue the granules were often sieved in order to remove the large fraction, prior to their incorporation into an ink.

3.5 Chapter summary

Granulation is a key process used in this thesis to produce nanocomposite granules. It is very important to understand the processes and theory of granulation as this enables the design of granules with the required characteristics, for example size, strength and porosity. Here, the nanocomposite granule size must be carefully matched to the thickness of the printed ink, and the strength and porosity of the granules may have important ramifications in their electrical functionality. By understanding the theory behind granulation and having a detailed comprehension of the relevant research in this field, the effect of changing both the starting material properties (e.g. binder type and quantity, particle size and shape) and the process variables (e.g. the granulation energy and duration) can be predicted.

Chapter 4

Experimental Details of Granule Fabrication and Analysis

4.1 Introduction

This chapter describes the methodologies and relevant theory behind the techniques used in the fabrication and subsequent analysis of the physical structure of the nanocomposite granules, which are later incorporated into the transparent pressure-sensitive ink. First the method of granule manufacture is described, beginning with details of the primary components of the granules, which were conductive nanoparticles and electrically insulating polymer binders. The mixing protocol using a dual asymmetric centrifuge is also explained and compared to conventional granulation vessels. This chapter also describes a variety of different size analysis techniques used to measure the size distribution of the granules, where various types of instrument were trialled in order to compare and contrast each method for this particular application. Following this, the methodology of focussed ion beam milling, which was used to characterise the internal granule structure and porosity, is described. Finally the procedure used to measure the mechanical properties of individual granules is detailed.

4.2 Granule constituents and fabrication

In granulation processes it is the properties of the primary particles which dictate the functionality of the resulting granule. As an example, pharmaceutical granules contain an active ingredient (i.e. the functional drug) which is granulated with other 'bulking' components and a suitable binder. For the purposes of this thesis the nanocomposite granules should be electro-active and ideally should have an electrical resistance which is dependent on the force

applied. In order to achieve this, the primary particles used are semi-conductive by nature and the polymer binder is electrically insulating. Possible conduction mechanisms in such a composite material are described later in chapter 8.

4.2.1 Properties of conductive nanoparticles used in granulation

The primary particles for granulation were antimony-doped tin dioxide (ATO) nanoparticles which were either spherical or acicular (needle-like). Scanning electron microscopy (SEM) images of agglomerated clusters of the particles are shown in Fig. 4.1 and the properties of these particles are compared in Table 4.1. Here the powder resistivity was measured by compressing the powder into a tablet at 9.8 MPa. These particles are the same as those used by Peratech in formulations of the ink in which agglomerates were formed during the mixing process. By granulating these same particles, a comparison can be made between inks containing pre-formed granules and those containing spontaneously formed agglomerates. In principle (and in any extension of the work presented in this thesis) other sizes, shapes and types of semiconducting or conducting particles may also be trialled.

Tin dioxide (SnO_2) is a direct band gap semiconductor which has a tetragonal crystal structure. It has a band gap of 3.6 eV [142] and the Fermi level is situated 0.427 eV into the band gap. The valence band is composed of mainly oxygen 2p states, whereas the conduction band is a mix of tin 5s and 5p states and oxygen 2p states [143]. Oxygen vacancies or interstitial doping results in a free electron concentration of the order 10^{20} cm^{-3}.

The electron concentration can be increased by n-type doping with antimony (Sb). For example, ATO thin films produced using a spray pyrolysis technique have shown an increase

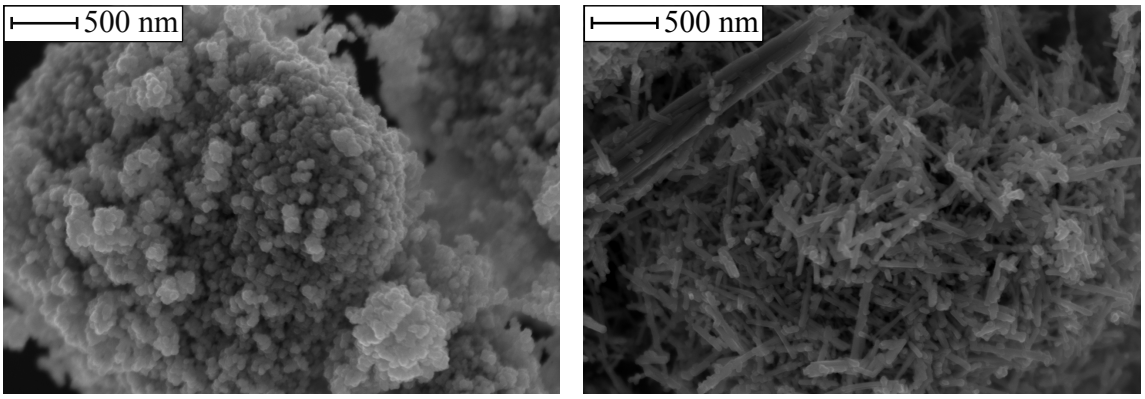

(a) (b)

FIGURE 4.1: SEM images of (a) agglomerated spherical ATO nanoparticles of diameter 10–30 nm (b) acicular ATO nanoparticles of diameter 10–20 nm and length 0.2–2 µm.

Particles	Diameter (nm)	Length (µm)	Powder resistivity (Ωcm)	Density ($g\,cm^{-3}$)	Specific surface area ($m^2\,g^{-1}$)
Acicular	10–20	0.2 – 2.0	100	6.6	25–35
Spherical	10–30	–	1–5	6.6	70–80

TABLE 4.1: Details of antimony doped tin dioxide nanoparticles used in granulation

in conductivity from 67 $S\,m^{-1}$ for no doping to 170 $S\,m^{-1}$ for doping with 10 Mol.% antimony. [144]. This is because doping with antimony causes the Sb^{5+} electronic levels to overlap the bottom of the conduction band, raising the Fermi level into the conduction band [145]. This conductivity is much larger than the powder conductivity of the spherical and acicular ATO used here (the reciprocal of the powder resistivity given in Table 4.1) which is 0.2–1 $S\,cm^{-1}$ and 0.01 $S\,cm^{-1}$ respectively. This is because even for highly compacted particles, voids between the particles act to increase the resistance through the tablet. ATO nano- or micro-sized particles can be produced by various methods including solid-state synthesis [146], co-precipitation [147, 148] and hydrothermal reactions [149].

4.2.2 Properties of polymer binders used in granulation

The binders used in the granulation process were either carbon-based, water-based or addition-curable silicone. The carbon-based (organic) binder was an alcohol/petrol resistant (APR) varnish. This was chosen due to its hardness and resistance to mechanical abrasion. The viscosity was measured to be 5.5 Pa s. The water-based binder was a commercial transparent screen-printable ink containing no organic solvent, which cures through evaporation in 20–30 minutes [150]. The viscosity was measured at 4.3 Pa s. It was chosen as a non-organic alternative to the APR varnish.

The silicone binder was a two-part translucent high consistency rubber of which the main constituent was polydimethylsiloxane (PDMS). High consistency rubber is distinguished from other silicones by its high degree of polymerisation (typically 5000 to 10000) and a molecular weight of 370–740 $\times\ 10^3$ Da. The basic structure of PDMS is shown in Fig. 4.2(a). It consists of an inorganic silicon-oxygen backbone with organic side groups. In the silicone binder used, a large proportion of the polymer chains were terminated with a dimethylvinyl group. This introduced cross-linking sites throughout the polymer chain. The silicone was used in conjunction with a curing agent which caused hardening of the silicone through an addition curing (hydrosilylation) process. This involved the addition of a silicon hydride molecule to an unsaturated carbon-carbon bond, for example in a side group containing vinyl, as shown in Fig. 4.2(b). The process was catalysed by a noble metal catalyst such as platinum. The

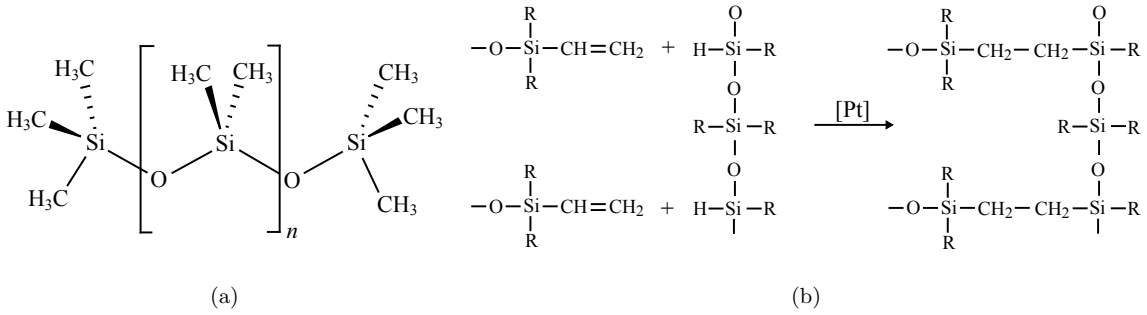

FIGURE 4.2: Schematic showing (a) the molecular arrangement of the polymer polydimethylsiloxane (PDMS) which was present in the silicone binder used for granulation. The polymer comprises an inorganic backbone of silicon and oxygen atoms and organic side groups, in this case methyl (b) The addition curing process, where a silicone hydride molecule is added to an unsatured carbon-carbon bond.

viscosity of the silicone binder was 70 Pa s. When the curing agent was added at a ratio of 10:1 by weight the viscosity decreased to 37 Pa s [151].

Silicone was chosen as a binder for granulation for a number of reasons. It has a low surface tension due to the methyl groups pointing outwards from the polymer chain, meaning it is capable of wetting most solid surfaces. From chapter 3 it is known that good wetting between particle and binder promotes efficient nucleation and granulation processes. After curing, it had a hardness of 40 on the Shore A scale and a tensile strength of 6.7 MPa, indicating resistance to mechanical abrasion. Its viscoelastic properties suggest that a granule containing a sufficient amount of this binder may also have some degree of compressibility and this in turn may have important implications if the granules were found to exhibit pressure-sensitive electrical conduction. Finally, the silicone binder had a significantly higher viscosity than the carbon and water-based binders, which allowed the effect of binder viscosity to be investigated.

4.2.3 Granulation of components using a dual asymmetric centrifuge

The granules were fabricated in cylindrical non-reactive polypropylene containers of diameter 38 mm and height 40 mm. First the binder was added to the base of the container, where the binder mass was measured at a precision of ± 0.01 g. For the lower viscosity binders (carbon and water-based) the binder spread to cover the entire base of the container. The high viscosity silicone binder did not spread over the base. For the silicone binder, the curing agent was added by allowing droplets to fall from a thin wooden stick onto the binder, whilst recording the change in mass. The curing agent was in all cases added at a ratio of 10 parts silicone to one part curing agent by weight and this corresponded to 4–5 droplets. When calculating binder/particle ratios the mass of the curing agent was considered negligible. The particles

(either spherical or acicular) were added on top of the binder in the cylindrical container, where the typical quantity used was 2.00 ± 0.01 g. This method of binder introduction may have important implications for the nucleation stage of granulation. As explained in chapter 3, this method favours the immersion mechanism of granule nucleation which can promote bimodal granule size distributions.

The granulating vessel was a SpeedMixer™ DAC 150.1 FVZ dual asymmetric centrifugal laboratory mixer (DAC). The mixing container was attached to an arm inclined at 40° to the horizontal which spun around a central rotational axis, as shown in Fig. 4.3. The DAC also incorporated a secondary rotation as the sample container rotated around its own centre at a direction opposing the main rotational direction.

During operation the sample material was subject to high centripetal force. The effect of the main rotation was to push the material to the outer edges of the container. Because of the secondary rotation the material was also subject to a secondary centrifugal force which modified the flow pattern such that there was a high-shear flow of material moving towards and away from the sides of the container. This promoted rapid homogenisation of the sample without the incorporation of air bubbles. This method of mixing has successfully been applied to fields as diverse as liposome and fat emulsification [152, 153] and the formation of composite materials such as dental adhesives [154], carbon nanotube-reinforced epoxy adhesives [155] and magnetic silicone composites [156]. However this type of equipment has not, to date, been used as a granulation vessel for the purpose of fabricating granules.

The angular velocity of the main rotation was set from 300–3500 rpm which corresponded to tangential velocities in the range 2.5–29.3 $\mathrm{m\,s^{-2}}$. The angular speed of the secondary rotation was 25% that of the main rotation and in the opposite direction. The mixing time was set up to a maximum of 5 minutes. For longer mixing times, the timer was reset after each 5

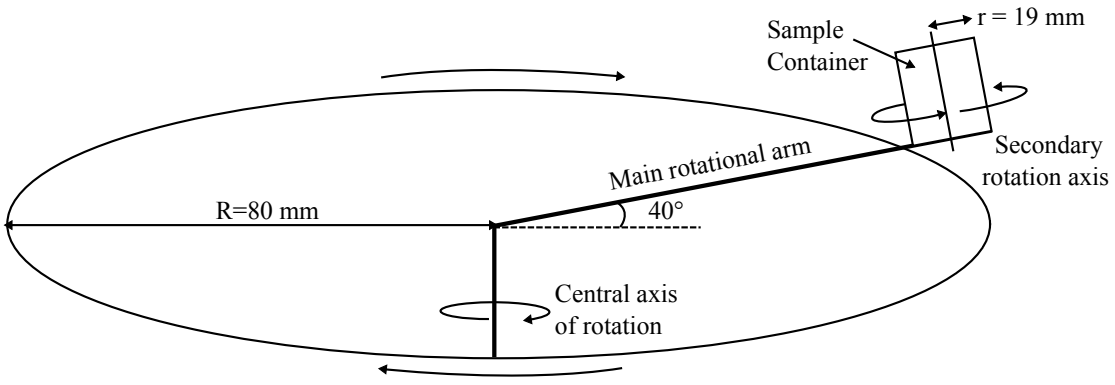

FIGURE 4.3: Schematic of the Dual Asymmetric Centrifuge (DAC). The sample is simultaneously spun around two axes of rotation as indicated. This leads to high-shear flow of the sample within the sample container and promotes rapid homogenisation.

minute interval. For example, for a 6 minute mixing time, the sample was first mixed for 5 minutes and then immediately for a further 1 minute.

After mixing, a loose granular powder was present at the bottom of the container and granular residue was adhered to the sides of the container. The residue extended to a maximum height of 13 mm up the walls of the 40 mm high container, which was independent of both the mixing speed or mixing time. The thickness of the residue layer increased with increasing height up the sides of the container, where towards the base there was little or no residue on the walls. This suggested that the residue closest to the bottom of the container was reincorporated into the granules.

The Froude number of a granulator with a characteristic radius r and angular velocity ω in units of $\mathrm{rad\,s^{-1}}$ is defined as:

$$Fr = \frac{\omega^2 r}{g} \tag{4.1}$$

and is a measure of the centripetal acceleration acting on the sample as a ratio of the gravitational acceleration g [116]. It is often used when attempting to scale up a granulation process [157–159]. Theoretically, by keeping the Froude number constant the flow properties of the powder within should be similar and hence the resulting granules are similar regardless of batch size. On a simpler level, the Froude number can be used to compare the energy of granulation for each type and dimension of granulation vessel.

The Froude number of drum granulators are typically very low, for example Walker *et al.* report Froude numbers of 0.2 and 0.1 [160]. A Froude number of less than one indicates that the gravitational force dominates over the centripetal force, leading to a tumbling action of the material within the drum. The Froude number of high-shear granulators incorporating a rotating impeller are usually of the order of a few hundred or less, for example Cavinato *et al.* report values up to 144 for various speed settings on a high-shear granulator [161]. Because of the squared dependency on the rotational or impeller speed, the highest speeds result in rapidly rising Froude numbers. Knight *et al.* report a large Froude number of approximately 270 when using a high-shear granulator capable of impeller speeds of 1500 rpm and they note that typical Froude numbers for high-shear granulators are usually less than 30 [137].

The DAC had variable speed settings from 300 to 3500 rpm. The Froude number as a function of the main rotational speed is shown in Fig. 4.4 as the solid black line. It can be seen that at the highest speed of 3500 rpm an exceedingly large Froude number of 1096 is calculated. Froude numbers this large are extremely unusual, perhaps even impossible, in high-shear granulators using impeller blades. Use of a DAC as a granulation vessel has not previously been reported in the literature. Furthermore, the secondary rotation (at 25% of the main rotational speed) of the DAC can also be assumed to have its own Froude number. This maximum and minimum perturbation around the main rotational Froude number is shown

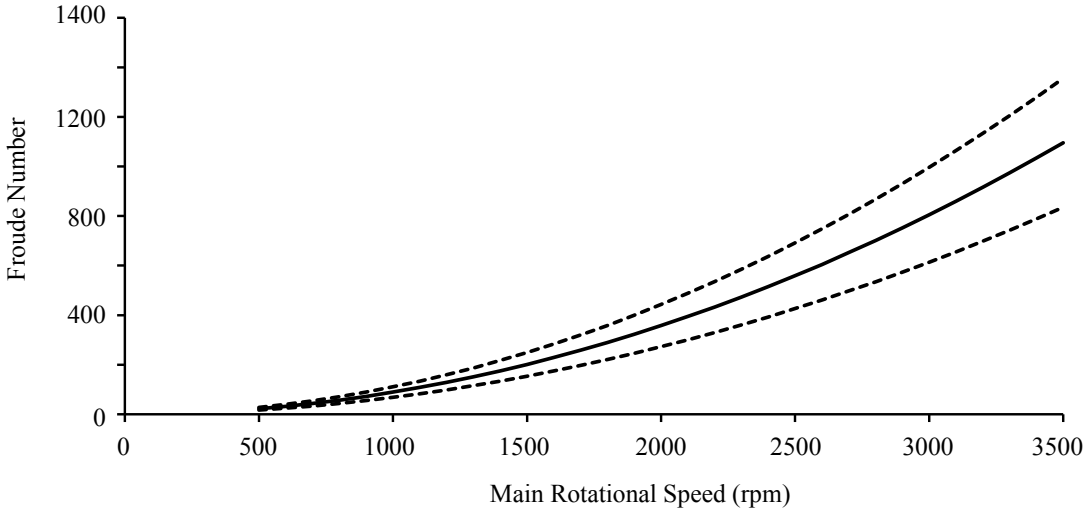

FIGURE 4.4: Graph showing the Froude number as a function of the main rotational speed of the DAC (solid black line). Perturbations in this number may result from the secondary rotation of the sample container about its own axis. The perturbation as a function of speed is shown as a maximum and minimum envelope function (dashed black lines).

as the dotted black line in Fig. 4.4. It is possible that this causes unusual perturbations in the powder flow.

4.2.4 Post-granulation curing and sieving

The resultant granules were removed from the mixing container into a heatproof open-topped tin. After removal of the loose granules a residue was also found adhered to the base of the container. Care was taken not to remove any of the residue from the sides or base of the container. The granules were cured in a convective oven at 90 °C for a minimum of 90 minutes in order to remove surplus solvent or water content, in the case of carbon or water-based binders, or to speed up the addition curing process in the case of the silicone binder.

Unless stated otherwise, all granules were sieved through a 75 µm sieve prior to imaging or incorporation into the ink. This was performed manually, where the granules were agitated over the sieve surface for at least 5 minutes. No external implements (e.g. brushes) were used as this may have caused attrition of the granules. The sieving process removed any large granular material or residue left from granulation. In some cases, the granules were sieved using an automated sieve shaker. Here, the sieve was vibrated such that the material was repeatedly passed over the entire surface of the sieve. The amplitude of vibration was set from 40–100 mm/g. The sieves used had mesh sizes of 100 µm, 75 µm, 45 µm and 20 µm, allowing the granules to be selected by various size fractions. After sieving, the granules were stored in airtight containers until required.

4.3 Size analysis of granules

Measurement of the granule size distribution was important in order to understand the effect of altering the material and process variables on the resultant granule size. Understanding exactly how these factors affect the resultant granule size distribution was beneficial as it allowed the manufacture of optimum granules which had the desired properties suitable for incorporation into the transparent resistive sensors. In this application it is desirable that the granules are matched to the thickness of the printed ink and hence should be less than 10 µm in size. Furthermore, some imaging techniques also allowed visualisation of the granule shape. Again, this could give insight into the granulation process. A number of size analysis techniques were trialled, including static image analysis, dynamic image analysis and laser diffractometry. In static image analysis, the granules were analysed whilst in static equilibrium, for example dispersed on a horizontal stage. The longest axis of the granule lies parallel to the stage surface, which means that there is an inherent bias towards measuring the longest dimension of the granule. The images taken represent a projected area of each granule, i.e. the granules are reduced to a two dimensional shape. Both optical microscopy and scanning electron microscopy were used to image the granules prior to performing image analysis and these methods are described in sections 4.3.1 and 4.3.2 respectively. In dynamic image analysis the granules are imaged as they are moving through a sensing zone as part of an aerosol jet or a liquid flow. All orientations of the granule are presented to the sensor, removing the orientation bias associated with static image analysis. This technique is described in section 4.3.3. Finally, in laser diffractometry the light scattering intensity of the volume proportion of granules in each size range is detected. This is described in section 4.3.4. A detailed discussion on the principles and limitations of these methods can be found in the review literature and in books [141, 162–164].

4.3.1 Static image analysis by optical microscopy

In order to measure granule size distributions using static image analysis (SIA), an automated, optical microscopy imaging system was used. This was the Malvern Morphologi G3, which was used in collaboration with the Institute of Particle Science and Engineering at Leeds University. The physical principle of this instrument is shown in Fig. 4.5.

The granules were dispersed in a single layer onto the sample stage using the in-built dispersion unit. This dispersed loose agglomerates of the granules which would otherwise be falsely classed as large, single granules. The dispersion of granules onto the slide controlled the measurement time and the total number of granules measured. If the granule distribution across the slide was too low there would be large empty spaces between granules and fewer

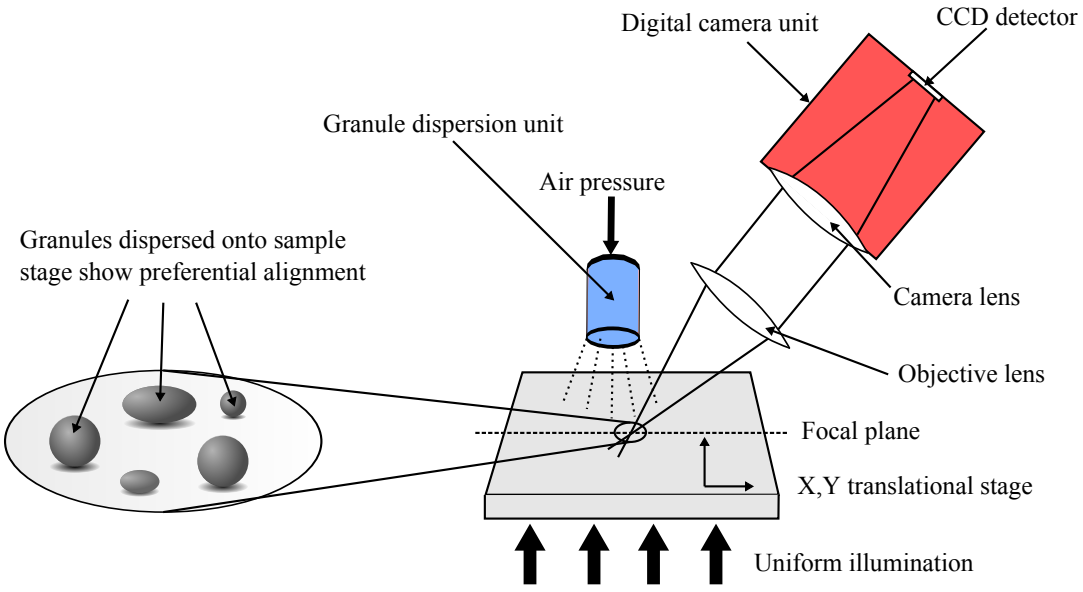

FIGURE 4.5: Schematic of static image analysis using optical microscopy and digital image capture. Granules are dispersed on a horizontal stage and illuminated from below. The objective lens is chosen for optimum magnification. A CCD detector records an image of each granule. The stage is automatically translated so that each granule can be imaged.

granules would be measured per unit time. For more efficient dispersion the granule spacing decreases and more granules are measured per unit time. However if the granules overlap they cannot be distinguished as individual entities. Granule dispersion was controlled by the application of air pressure to a sealed unit containing the granules. A granule volume of 7 mm^3 was placed in the dispersion unit and sealed. The application of 1 bar of pressure ruptured the foil seal of the unit and dispersed the granules over the microscope slide.

An optical microscope with a CCD digital camera was used to take a digital image of each granule. The stage height was set so that the granules lie in the focal plane of the objective lens. The lens could be changed to give a magnification ranging from 2.5x to 50x, allowing granules from 0.5 µm to 1 mm to be resolved. The focal depth decreased with increasing lens magnification and this means that at high magnifications only a small vertical depth of the granule was in focus. Automatic translation of the stage along the X, Y coordinates ensured that each granule was imaged. Using this method, between 30 000 and 70 000 granules were imaged. Subsequent automated image analysis characterised the granules in terms of their diameter of equal projection area d_{EQPC} and the D_{10}, D_{50} and D_{90} percentile values, as defined previously in chapter 3.

The benefit of SIA is that each granule could be fully characterised by a range of size and shape parameters. Details of the best practice for static image analysis are given in ISO 13322-1:2014 [165]. This explains that SIA may only provide accurate results for particle size distributions limited to less than one order of magnitude between minimum and maximum

particle size. In order to comply with this standard, measurements from a minimum of 6000 particles are required to reliably calculate the volume mean diameter and to calculate the percentiles of the distribution at least 61 000 particles should be measured. Automatic operation is advantageous as it removes the need for an operator to be present throughout the measurement. However, the measurement time may still be long, depending on the granule size and dispersion.

4.3.2 Static image analysis by scanning electron microscopy

A Hitachi SU-70 scanning electron microscope (SEM) was also used to acquire images of granules. The SEM uses a focussed beam of primary electrons to probe a sample surface. A schematic of a typical SEM beam column is shown in Fig. 4.6. The electron beam can be created by thermionic or field emission of electrons from the electron gun. In the Hitachi SU-70 a Schottky field emission electron source was used. This consisted of a tungsten wire with a tip diameter less than 100 nm through which a high electric field was passed. The electric field at the tip can be in excess of 10^7 V cm^{-1} and this promotes field-assisted quantum tunnelling of electrons [166]. Through this, a high brightness (defined as the current density per unit solid angle) of 10^9 A cm^{-2} sr^{-1} and a low energy spread of 0.3 eV can be achieved [167].

The SEM chamber was kept under high vacuum, typically around 10^{-7} Torr, to prevent the electrons from colliding with and scattering from atoms within the SEM chamber. This also

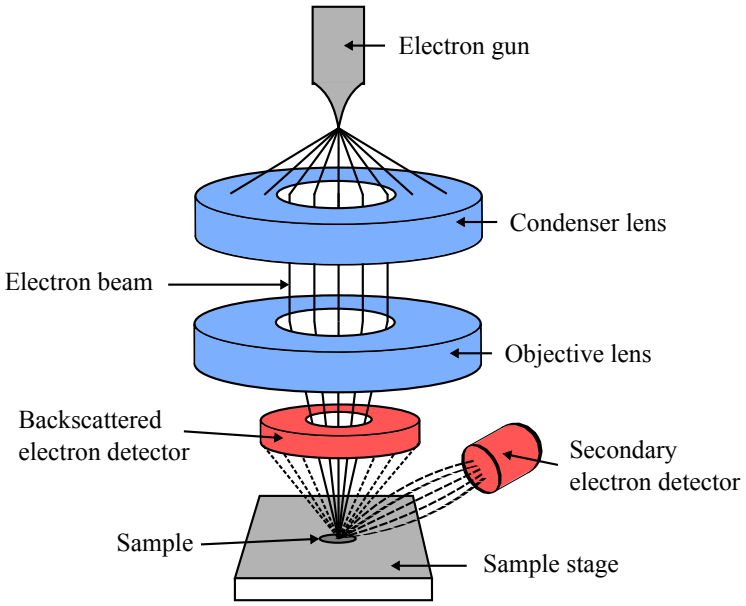

FIGURE 4.6: Schematic of SEM column showing the main components including the backscatter and secondary electron detectors. The SEM chamber itself is under vacuum at a pressure of approximately 10^{-7} Torr.

promoted efficient and stable electron emission from the electron source, as here the presence of contaminants on the tungsten surface may increase the work function and hence decrease the electron emission.

The primary electrons are accelerated towards an anode to the required energy. After filtering, the emitted electrons are focussed into a narrow beam by a series of electromagnetic condenser and objective lenses. These decrease the diameter of the electron beam to the order of a few nm to give high resolution images of the sample surface. This effect is ultimately limited by the effects of spherical and chromatic aberration and astigmatism of the condenser lens. Even if these effects are corrected for the beam diameter is fundamentally limited by diffraction of the electrons. The diffraction limited beam diameter d_{diff} of an electron beam focussed to an angle of α and of energy-dependent wavelength λ is given by:

$$d_{diff} = \frac{1.22\lambda}{\sin\alpha}. \tag{4.2}$$

Hence the beam diameter decreases for increasing electron energy (decreasing λ) and decreasing angle α. For typical values of $\lambda = 0.0037$ nm and α =0.1 rad the diffraction limited beam diameter is 0.02 nm which is smaller than the size of a single atom [168]. Hence electron microscopy fundamentally offers much greater resolution than optical microscopy techniques.

When the electrons reach the sample surface they interact with the sample within the interaction volume. Here the incident electrons may elastically collide and scatter from the electrons within the sample, or inelastically scatter with the orbital electrons and be ejected from close to the sample surface as secondary electrons (SE), which typically have low energies of less than 20 keV. If the collision is elastic the incident electrons are scattered to high angles and may leave the sample as backscattered electrons. SE detection is most commonly used for high-resolution topographical imaging. This is because low-energy SEs are highly susceptible to inelastic scattering and rapidly attenuate in energy. The probability of escape p is given by:

$$p \propto \exp\left(\frac{-z}{l}\right) \tag{4.3}$$

where z is the vertical depth below the sample surface where the SEs are generated and l is the mean free path of the electrons, which is dependent on their energy. The lower the electron energy, the closer to the surface the SE needs to be in order to have a high probability of escape and detection. Because only SEs close to the surface escape and can be detected this leads to high-resolution imaging of the topographical details of the sample surface. This is almost independent of electron beam energy.

SE detection is by a specialised sensor such as an Everhart-Thornley (ET) detector. This is a scintillator-photomultiplier system. The electrons impinge on a scintillator material

which then emits light. The light is transmitted into a photomultiplier which converts the photons into electrons. These are then amplified and used to modulate the intensity of the corresponding pixel in the image. The electron beam is scanned over the sample surface in a raster pattern and the ET detector detects the SE intensity at each position on the sample surface. This is used to create an image as a grey-scale representation of the sample surface.

The depth-of-field achievable in SEM is typically 10–100 times greater than for optical microscopy [166] and it can be increased by increasing the working distance (that is the distance between the sample and the final objective lens). A decreased working distance gives a higher resolution but a narrower depth-of-field. For the size analysis of granules a low magnification was necessary. The working distance was typically 14 mm as this led to a large depth-of-field giving a high level of detail on the 3D granular structure. The beam energy was set in the range 1.5–5.0 keV to minimise electrical charging of the sample surface.

4.3.2.1 SEM sample preparation

Prior to SEM imaging, the granules were dispersed onto an aluminium 'stub' for mounting onto the sample stage in the SEM chamber. A conductive carbon-based adhesive pad was placed on the stub and granules were dispersed onto the pad using a cotton bud. The stub was gently tapped to ensure adhesion of the granules and a low-pressure nitrogen gas was passed over the surface to remove unattached granules.

For non-conductive samples electrical charging of the sample surface may occur during SEM imaging. This is because the incident electrons are not conducted through the sample to earth and this can result in imaging artefacts, such as glowing of the surface due to the trapped electrons. Because the granules contained a proportion of non-conductive polymer binder it was necessary to coat them with a thin layer of carbon in order to circumvent this problem. The samples were coated by evaporation of carbon onto the stub by passing a large current through a carbon rod placed directly above the samples in a vacuum chamber. In this way a carbon layer of thickness 10–30 nm was deposited onto the granules prior to SEM imaging.

4.3.2.2 SEM image analysis

The SEM image magnification used depended on the granule size and ranged from 800x to 1500x for smaller granules (typically less than 20 µm) and 50x to 200x for larger granules (typically larger than 20 µm). It was observed that the smaller granules were poorly dispersed and often agglomerated into large structures. In these cases, it was assumed that the agglomerated structure was a weakly bound collection of granules and each granule within was measured individually.

Image processing software (ImageJ) was used to measure the granule dimensions. Because the granules often overlapped or formed agglomerated structures it was not always possible to automate this process. Instead, the maximum Feret diameter of a minimum of 300 granules was manually assessed for each sample. The maximum Feret diameter (as defined in section 3.4.1) was subjectively assessed by eye where it was assumed that any error associated with this technique would be small. In some cases automated measurement of the granule shape and size was possible, for example for larger granules which were dispersed with minimal overlapping. Collation of the granule sizes allowed the calculation of average diameters, size distributions and cumulative size distributions in an automated process.

4.3.3 Dynamic image analysis

In dynamic image analysis (DIA) the granules are measured in dynamic flow as they move past the detector in a liquid suspension or aerosol jet. As a granule moves it may rotate through any plane and hence the granule orientation at the time of measurement is statistically random. A pulsed light source is used to illuminate the granules and a high-resolution CCD detector images the projection of the granule shadows. Some systems may also incorporate an additional pulsed light source and a zoom camera which has a smaller field-of-view which is optimised to image small granules at a high resolution [169]. The system may operate in transmission or reflection mode dependent on the location of the pulsed light source and CCD detector. The transmission mode is shown in Fig. 4.7. Here, the light source is opposite to the detector such that a projection of the granule shadows is recorded by the CCD. In

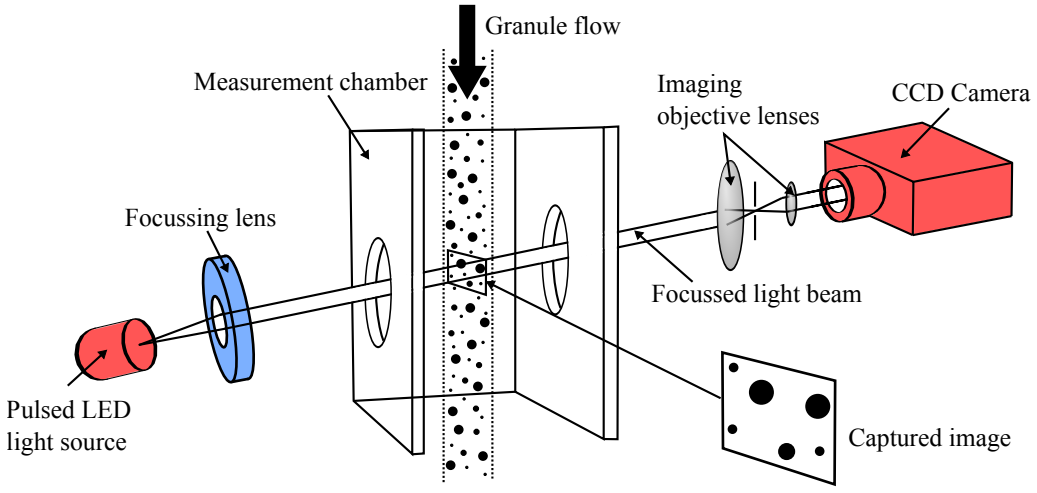

FIGURE 4.7: Schematic of a dynamic image analysis system. Granules flow through the sample chamber, dispersed as an aerosol jet or in solution. A pulsed LED light source is used to illuminate the granules and the CCD detector images the projection of the shadows of the granules at a high frame rate.

reflection mode, the light source and detector are next to one another such that the reflected light from the granule surface is detected by the CCD. Both DIA systems used here operated in transmission mode.

The pixel size of the CCD detector defines the smallest feature size measurable and this is usually of the order of 1 µm. A pulsed light source is used so as to reduce the motion blur caused by imaging fast-moving granules. For a high-speed granule travelling at 100 $\mathrm{m\,s^{-1}}$, typical for a high pressure aerosol, pulsed light exposures of 1 ns are necessary in order to reduce the motion blur to below the 1 µm resolution limit of the CCD detector. The CCD detector can capture images at up to 450 frames per second. This allows for the detection and measurement of very large numbers of granules in a short time. For example, if 50 granules are detected per frame and 450 frames are collected per second then almost 23 000 granules can be imaged per second.

A potential issue for DIA is ensuring that all measured granules are within the depth-of-field of the camera. The depth-of-field in the optical system, $DOF_{optical}$, for a given magnification M is given by:

$$DOF_{optical} = \frac{\delta z_{image}}{M^2}, \tag{4.4}$$

where δz_{image} is dependent on the aperture angle of the camera and the pixel size. $DOF_{optical}$ decreases with the square of the magnification and this can cause problems when imaging smaller granules where higher magnification objective lenses are likely to be used. For smaller granules, the flow has to be constrained to a small dimension parallel to the optical light beam in order to ensure that all granules are within the depth-of-field. Granules outside of this range are likely to be blurred.

One way to overcome this is by using a telecentric objective lens before the camera and CCD detector. In a standard objective lens, each point on the object plane is transferred to one point in the corresponding image plane and all light rays up to a maximum scattering angle pass through the lens, as shown in Fig. 4.8(a). However, for each distance between lens and object a multitude of image planes are created. The camera detector, placed at just one of the image planes, sees the corresponding granule in sharp focus but all other granules are defocussed and appear blurred. Hence, the depth-of-field is limited. Furthermore, the magnification of the image depends on the object position, i.e. a perspective image is formed. In a telecentric lens, an aperture is placed at the focal length of the lens, as shown in Fig. 4.8(b). Only rays which are near-parallel to the optical axis can pass through the aperture and light which is scattered or diffracted to large angles is blocked. A secondary lens is used to focus the light rays onto the image plane. In this case, light from a multitude of object planes is focussed onto a single image plane, thereby increasing the depth-of-field. The magnification of the image is independent of the object position, i.e. an orthographic image is formed.

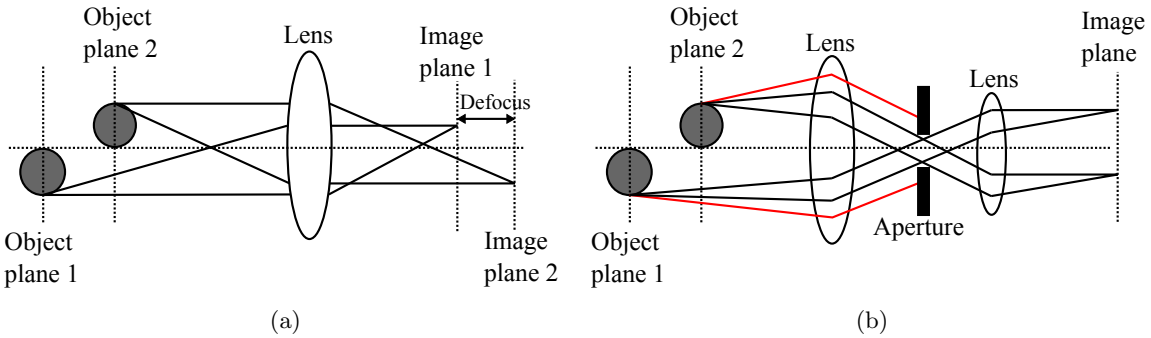

FIGURE 4.8: Schematic of (a) a standard imaging lens, where each granule in the object plane is focussed onto a corresponding image plane resulting in a small depth-of-field and (b) a telecentric lens, where an aperture stop is placed at the focal length of the first lens. Only light rays which are near-parallel to the optical axis are incident on the second lens. Each granule, in its own object plane, is focussed onto the same image plane resulting in a greater depth-of-field.

The imaged granules can be subsequently analysed in terms of a wide range of size and shape parameters, similar to SIA techniques. However, unlike SEM imaging, DIA in transmission mode cannot give detail on the granule surface structure.

4.3.3.1 Dry dispersion of granules prior to DIA

Dry dispersion of granules can be achieved by one of two methods. The granules can be subject to a gravity-induced flow or they can be dispersed in an aerosol jet. In the latter case, granule agglomerates can be dispersed through granule-granule collisions, collisions between the granules and the walls of the feed-pipe, or through turbulent flow caused by air velocity gradients. The high-speeds of the granules dispersed in an aerosol jet require high frame rates but result in very small measurement times.

Gravity-induced flow was used as the dry dispersion method for DIA used in this thesis, using the Camsizer XT instrument. Here, a vibrating feeder was used to slowly move the granules towards the feed-pipe of the instrument. The amplitude of vibration controlled the rate at which the granules passed over the edge of the feeder and into the instrument. However this dispersion method was unlikely to have been sufficiently energetic to break apart small, cohesive granule agglomerates. For this reason, a lower limit on the measurable granule size of 10 µm was imposed by the instrument manufacturer. A small sample size of less than 1 mm^3 was placed onto the vibrational feeder. The measurement time was limited by the rate at which the feeder dispersed the granules into the measurement chamber, where

each measurement typically took under 10 minutes. The resultant images were analysed automatically to extract the maximum Feret diameter.

4.3.3.2 Wet dispersion of granules prior to DIA

Wet dispersion of granules was achieved through mixing a small amount of granules (typically less than 1 g) into 50 mL of solvent. The solvent chosen was also used in the production of the screen-printable granular ink, as described in chapter 9. Subsequent imaging of these inks had shown that the granules did not dissolve in this solvent. However constant agitation of the solution was necessary to prevent granule sedimentation.

The solution was introduced into the measurement chamber of the instrument (in this case the QICPIC dynamic image analysis system) using a syringe, where the flow rate was controlled manually. Inside the instrument, the solution passed though a flow cell. The flow cell can have a range of optical path lengths (i.e. thicknesses) and in this case the cell width was 100 µm. This meant that granules larger than 100 µm could not pass through the flow cell and were not measured. The flow cell was positioned inside the measurement chamber such that the granule flow was focussed by the imaging camera. Because of the relatively slow movement of the granules through the flow cell, a low frame-rate of 50 frames per second was used. From the resultant images the maximum Feret diameter of the granules was automatically extracted.

4.3.4 Laser diffraction

Laser diffractometers use the principles of light scattering from a collection of particles in order to measure their size distribution. A schematic of a typical laser diffractometer is shown in Fig. 4.9. A He-Ne laser of wavelength 632.8 nm is passed through a lens in order to produce a plane wave. The laser beam is passed through a flow of granules in the measurement chamber and the light interacts with the granules in a number of ways. Diffraction and light scattering occur at the granule edges, light can reflect from or be absorbed by the granule surface and if the granule is optically transparent then refraction can also occur. The diffracted and scattered light from the granules is focussed onto a radial multi-element photo-detector and a spatial intensity profile is measured. Some diffractometers also incorporate an additional array of light detectors which record the intensity of backscattered light.

For monosized granules, scattering of light produces an Airy disk which has concentric rings of high and low intensity at radii r. The spatial intensity profile for a granule of size d is given by:

$$I(r) = I_0 \left(\frac{kd^2}{2}\right)^2 \left(\frac{J_1(krd)}{krd}\right)^2, \tag{4.5}$$

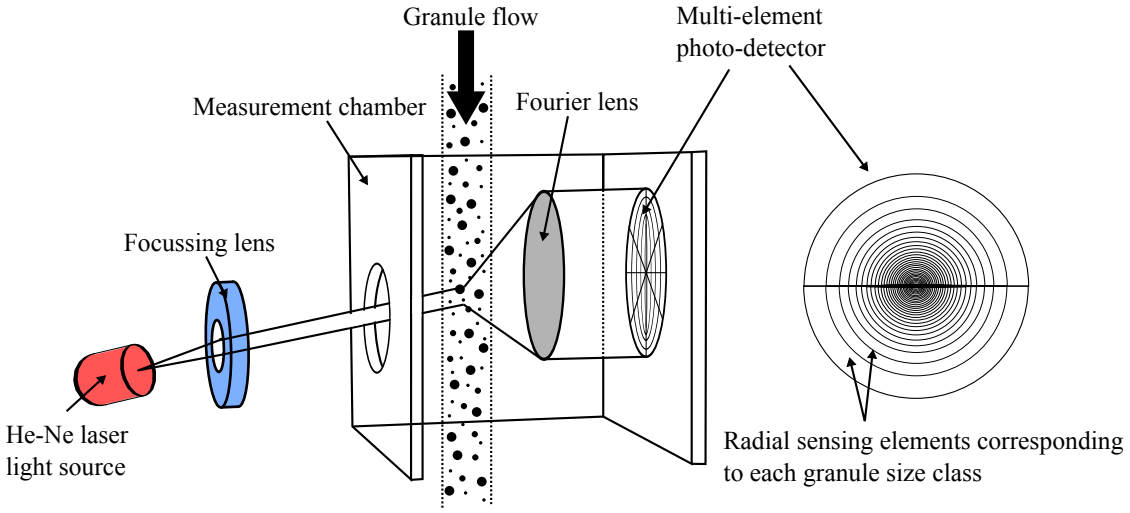

FIGURE 4.9: Schematic of a laser diffractometer used to determine granule size distributions. A laser light source is used to provide planar illumination of the granule flow. The light interacts with the granules by diffraction, scattering, absorption, reflection and refraction. Scattered and diffracted light is focussed onto a multi-element photo-detector which records the angular intensity profile. From this the proportion of granules in each size class can be determined.

where:

$$k = \frac{\pi}{\lambda f}. \tag{4.6}$$

Here, I_0 is the maximum intensity at $r = 0$, f is the focal length of the Fourier lens, λ is the wavelength of the light and $J_1(krx)$ is a first order Bessel function. Light scattering from both large and small granules and the corresponding intensity profiles are shown in Fig. 4.10. The distance r_0 to the first intensity maximum is given by:

$$r_0 = \frac{1.22 f \lambda}{d}. \tag{4.7}$$

Hence smaller particles scatter light at a lower intensity to larger angles (radii) and larger particles scatter light at a higher intensity to smaller angles (radii). The resulting intensity profile measured on the detector is a superposition of scattered light from granules of all sizes.

Light scattered by angles greater than 90° cannot be focussed onto the photo-detector, imposing a lower limit on the smallest granule detectable. However, many laser diffractometers also include a series of backscattered light detectors such that highly scattered light can be detected. In practice, the lower limit on granule size is in the nm range. For very large granules which cause small-angle scattering, the scattered light must be distinguishable from the central intensity maxima which is produced by the undeflected laser beam striking the sensor. In practice the upper limit of the measurable granule size is of the order of a few mm.

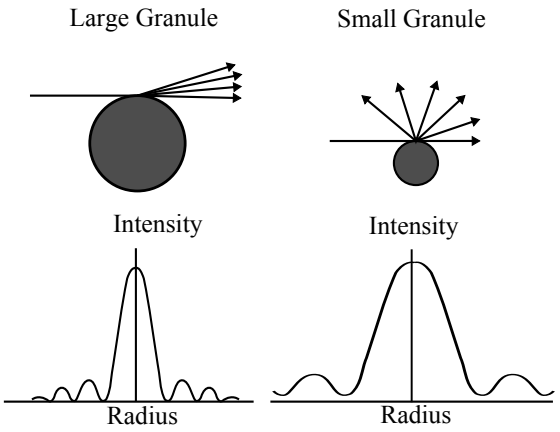

FIGURE 4.10: Schematic of light scattering from granules which are small and large compared to the wavelength of incident light. For large granules a high intensity of light is scattered to small angles. For small granules a lower intensity of light is scattered to larger angles. The corresponding maxima in the radial intensity profile occur at smaller radii for large granules and larger radii for small granules.

The multi-element photo-detector is comprised of a series of discrete, non-overlapping sensing elements which are arranged in a radial geometry as shown in Fig. 4.9. Due to the inverse relationship between particle diameter and the first intensity maximum the central sensing elements must be very narrow. Each sensing element represents a size class of granules that can be detected and typically up to 32 elements are used. The photo-sensor comprises a silicon photo-diode array, comprising an n-doped silicon substrate with sensing elements of p-doped silicon areas. This creates a built-in voltage across the p-n junction. Thin regions of silicon dioxide separate the sensing elements and prevent cross-talk. When light is incident on the p-doped silicon electron-hole pairs are produced, causing a current to flow which is proportional to the intensity of the incident light.

From the angular intensity profile measured at the photo-detector the size distribution of the granules can be determined by applying either a Fraunhofer or Mie theory of light scattering. The Mie parameter, a, is defined as:

$$a = \frac{\pi x}{\lambda}. \tag{4.8}$$

Mie scattering theory is a general approach applicable to all granule sizes and light wavelengths and it describes the solution to Maxwell's equations for the scattering of an electromagnetic plane wave by a homogeneous sphere, where the solution comprises an infinite series of spherical partial waves [170]. The application of Mie theory is also necessary if the granules are optically transparent as it includes the effect of light refraction as well as light absorption. Using Mie theory requires knowledge of the optical properties of the granules, including the complex refractive index and absorption coefficient. More details on light scattering from large and small granules are provided in chapter 8.

For the special case where $a \gg 1$ a Fraunhofer approximation may be used. Here the refraction and absorption effects are neglected, and this is generally applicable for opaque granules. For a number density distribution $q_0(d)$ of N_{tot} number of granules, where each granule produces a radial intensity distribution $I(r, d)$ as given for each granule size d in equation 4.5 the total intensity profile is given by:

$$I(r) = \int_{d_{min}}^{d_{max}} N_{tot} q_0(d) I(r, d) dd. \tag{4.9}$$

This is solved using a linear system of equations, for example by using the approach of Phillips and Twomey [171, 172]. In practice, it is possible to successfully apply Fraunhofer theory for opaque granules down to 0.1 µm [173].

Here, the granules were dispersed in an aerosol jet prior to entering the laser diffraction chamber. The dispersion pressure was varied between 1.5 and 5 bar to investigate the effect of dispersion pressure on the measured size distribution. A small sample size, typically less than 1 mm^3, was used. The granules were assumed to be optically opaque and the Fraunhofer approximation was used to calculate the volume-weighted granule size distribution.

4.4 Structural analysis of granules by focussed ion beam milling

Understanding the internal structure of granules is beneficial for two reasons. Firstly, the internal structure of the granules can be used to gain insight into the granulation mechanisms occurring when the granules are produced. For example regions of high and low porosity, or low and high binder content can give physical insight on the processes which are occurring during granulation and how these are affected by changing the material and process variables during fabrication. The porosity of the granules may lead to enhanced compressibility, and the internal voids may also provide an insulating medium (i.e. air) between the conductive nanoparticles which can alter the conductive properties, as explained later in chapter 8.

Many methods exist by which to investigate the internal structure of granules. Macroscopic approaches to measuring granule porosity involve measuring both the mass and volume of the granules and comparing this to the theoretical mass of a granule with no internal pores. The volume of a granule ensemble can be determined using a displaced volume method, where the granules are dispersed into a liquid solution and the displacement of the liquid is measured [174]. Whilst giving an average porosity for the granule ensemble it can give no information on the pore distribution within individual granules.

Mercury intrusion porosimetry is often used to determine granule porosity [175–179]. This involves forcing a non-wetting liquid such as mercury into the internal pores of a granule through the application of varying levels of pressure. The pore size distribution and the total porosity can be determined from the volume intruded at each pressure increment and the total mercury volume intruded. The smallest pore diameter measurable can be as small as 3 nm [180], however only pores present on or connected to the outside surface can be measured and completely enclosed pores are not assessed. The pore opening diameter is measured rather than the maximum internal pore diameter which can lead to an underestimation of pore size when compared to direct image analyses of porosity [181]. Additionally, no visual data is given on the granule structure and the method is insensitive to pores filled with binder.

The technique of X-ray microtomography (XRT or XMT) or X-ray computed tomography (XRCT) has also been used to image the internal structure of granules [177, 178, 182] and has also been used simultaneously with mercury porosimetry [183]. This technique evolved from the principles of computerised axial tomography (CAT) which has extensive applications in medical imaging [184]. Here, X-rays from synchrotron radiation are used to probe the internal structure of a granule. X-ray absorption is measured as a function of depth through the material and this is used to build up a 3D picture of the granule interior [185]. Whilst these techniques allow the 3D visualisation of the entire pore network within granules a minimum resolution of several microns only is achievable. This method does not provide adequate resolution needed to characterise the internal structure of the granules produced in this thesis, which are often less than 10 µm in size.

SEM can also be used to investigate internal granule structure. Cross-sections of granules may be produced through mechanical abrasion techniques such as diamond polishing [176, 186, 187]. In this case, the resolution limit is determined by the mechanical abrasion technique. For example, abrading with diamond particles of minimum size of 1 µm means that granule structures less than 1 µm in size cannot be resolved upon subsequent imaging. Focussed ion beam (FIB) milling, which is the technique used throughout this thesis, has previously been demonstrated for revealing the internal structure of granules [176]. Whilst in this case a single cross-section through the granule was imaged, it is also possible to image the 3D internal structure using a serial sectioning process where a thin layer of material from the cross-section is milled and then imaged using SEM. This is repeated through the depth of the material [188]. This approach allows both high-resolution milling and imaging of the granule whereby structures as small as tens of nm can be resolved.

4.4.1 Focussed ion beam milling principle of operation

An FEI Helios Nanolab DualBeam 600 was used to analyse the internal granule structure and porosity, where Focussed Ion Beam (FIB) milling was used to expose the internal structure. The system comprises a vertical electron beam column, as shown in Fig. 4.6 and an ion beam column which is inclined at 52°, as shown in Fig. 4.11(a). The structure and principle of the ion beam column is similar to that of the electron beam column except that a gallium ion source is used instead of an electron gun. A tungsten tip coated in liquid gallium is exposed to a large electric field which causes gallium ions to be emitted from the source through field emission. The gallium ions are accelerated and focussed by a series of electromagnetic lenses.

During milling the sample was aligned perpendicular to the ion beam, that is at 52° to the electron beam. Imaging through the electron beam was used to locate and align a sample prior to milling. During the FIB milling process the gallium ion beam was focussed onto the sample surface and causing localised sputtering of the sample surface. Gallium ions also become implanted in the surface and sputtered material may be redeposited back onto the sample. These processes are shown schematically in Fig. 4.11(b). The milling rate is dependent on the beam current (dose) and the atomic properties of the sample, as different elements and crystallographic planes are sputtered at different rates. This can lead to uneven

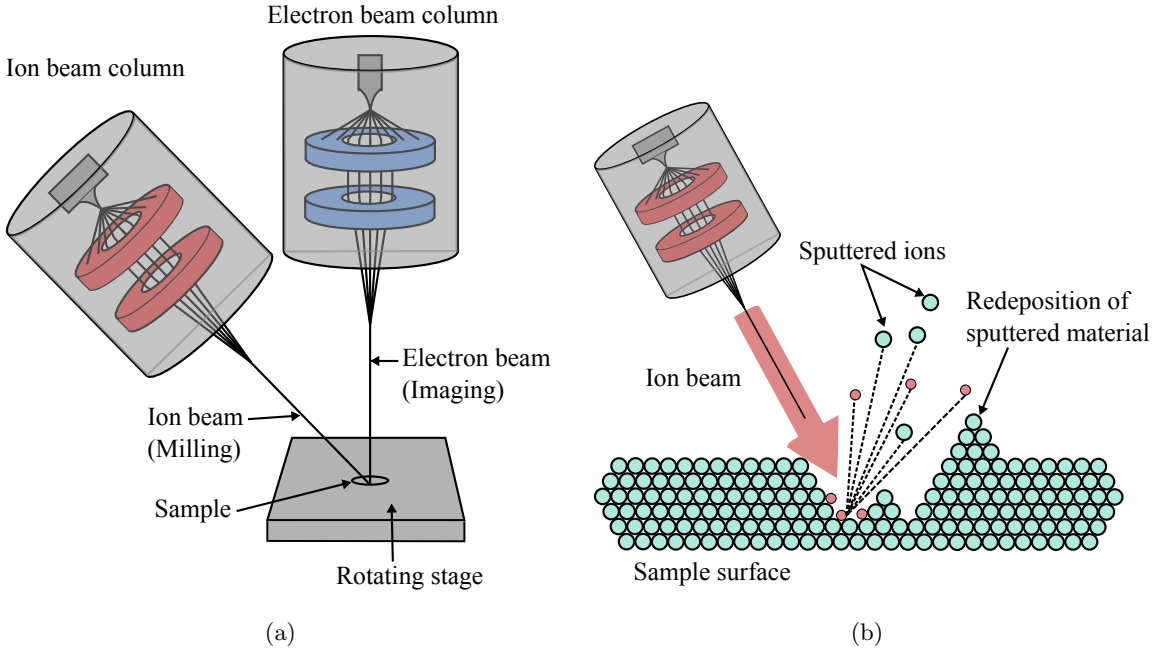

FIGURE 4.11: Schematic showing (a) the FEI Helios Nanolab DualBeam 600, which includes both an electron beam and a gallium ion beam column at an angle of 52° (b) Ion interaction with the sample surface during FIB milling. The sputtered material is ejected from the sample surface and may be redeposited. Gallium ions may also become implanted into the sample surface.

milling effects. To counteract this a final milling stage, using a low ion dose, was used to 'polish' the previously cut surface and to reveal the internal structure of the granule.

4.4.2 Sample preparation and milling procedure

The granules were first securely attached to a thin polyethylene terephthalate (PET) substrate using a strong cyanoacrylate adhesive. A thin layer of the adhesive was blade-coated onto the PET using a razorblade. Using a cotton bud, the granules were dispersed onto the adhesive layer and the sample was then allowed to dry. Excess loose material was removed by passing a low-pressure nitrogen flow over the surface. The PET was then attached to an aluminium stub and carbon-coated before mounting onto the FEI Helios stage.

After location and alignment of a suitable granule, a platinum capping layer was deposited on top of the granule using a localised chemical vapour deposition method. The platinum protected the surface underneath from sputter damage so that only the required area was milled. A SEM image of such a capping layer is shown in Fig. 4.12(a). A cross-section through the granule was milled using a high-energy, high-dose ion beam (16 keV and 0.47 nA), as shown in Fig. 4.12(b). Then, a low-dose ion beam (16 keV and 0.22 nA) was used to polish the milled surface to reveal the internal structure of the granule, as shown in Fig. 4.12(c). After milling, the exposed granular interior was imaged using the SEM system.

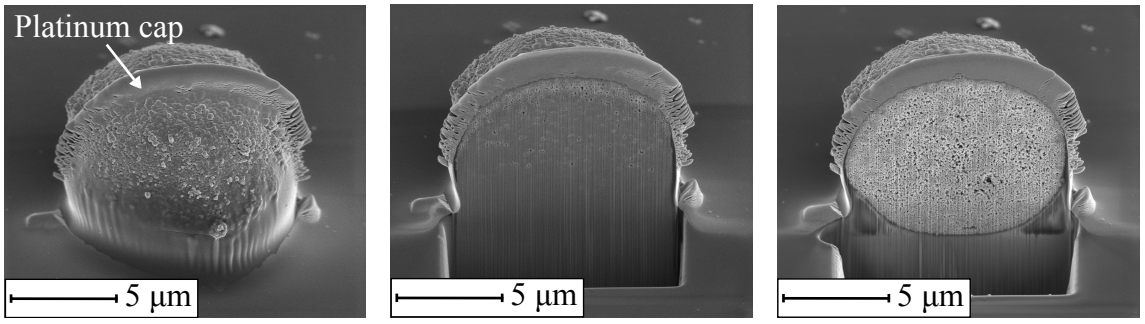

(a) (b) (c)

FIGURE 4.12: SEM images of a granule during FIB milling, showing (a) a platinum capping layer deposited on the granule surface in order to protect the surface prior to FIB milling (b) A rough cross-section through the granule, milled using a high-energy, high-dose ion beam and (c) the polished cross-section through the granule, milled using a low-dose ion beam, revealing the internal granule structure.

4.4.3 Image analysis

For each FIB milled granule, a series of images were taken at a high magnification across the milled surface. In order to calculate the internal granule porosity the cross-sectional images were analysed using image analysis software (ImageJ). An automated procedure was defined which extracted the pore size distribution and the average porosity of each image. This procedure consisted of five steps:

1. The image was normalised in terms of brightness and contrast, such that the image histogram (which shows the pixel count for each grey-scale value) was stretched and the full range of grey-scale shades were used.

2. A median filter was applied over a two pixel radius, where each pixel was replaced with the median grey-scale value of its neighbouring pixels. This removed extreme pixel values associated with noise. A cross-sectional image with an applied median filter is demonstrated in Fig. 4.13(a).

3. The image was thresholded to produce a black and white binary image. Pixel values below the pixel value threshold were coloured black (representing pores) and pixel values above the threshold were set to white (representing particles). To determine the pixel threshold value the method proposed by Deshpande *et al.* was used [189]. A range of threshold values were sampled and the number of pores with an area less than 4 square pixels was determined. The results are shown in Fig. 4.14. At the critical threshold the number of small-area pores drastically increased and this occurs at a pixel value of 120. It was assumed that this threshold value was the same for each image analysed. An example of a thresholded image is shown in Fig. 4.13(b).

4. Morphological opening was performed through application of an erosion and then a dilation step. Here, a layer of pixels was removed from the perimeter of each pore (erosion) and then added to the perimeter of the remaining pores. This removed small or very thin pores whilst maintaining the original dimension of the larger pores.

5. The remaining pores were measured in terms of their area and maximum Feret diameter. The porosity was then defined as the ratio of the total pore area to the total image area. Fig. 4.13(c) shows the measured pore sizes overlaid onto the original cross-section image.

In some cases images were taken along the entire length of the cross-section such that the porosity could be calculated as a function of distance from the granule centre. In this case, each image was bisected lengthways and the porosity calculated using the method detailed above. The granule porosity was then recorded as distance through the granule.

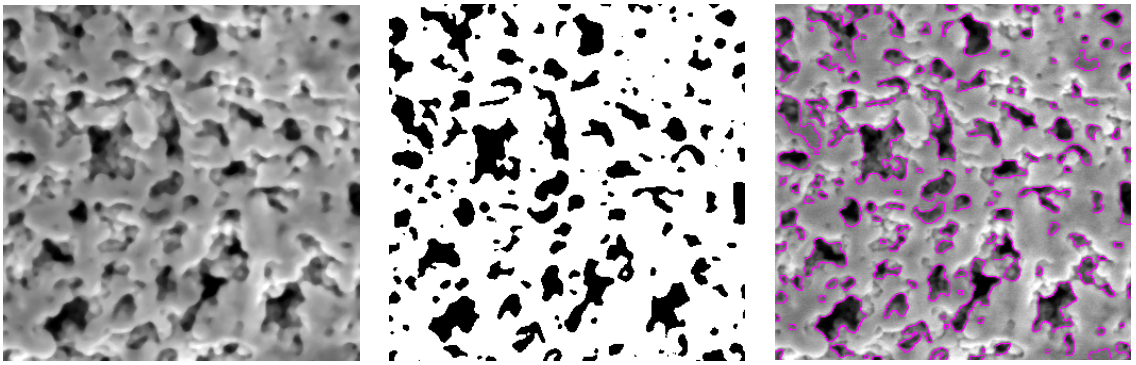

FIGURE 4.13: SEM images showing steps from the procedure by which the granule porosity was calculated from cross-section images through the granule. (a) Application of median filter over 2 pixel radius removed noise in the pixel values and produced a smoothed image (b) Image thresholding, where pixel values below the threshold value were converted to black and represent the pores inside the granule, and pixels above the threshold value were converted to white and represent the primary particles.(c) The measured pores, which have been overlaid onto the original image.

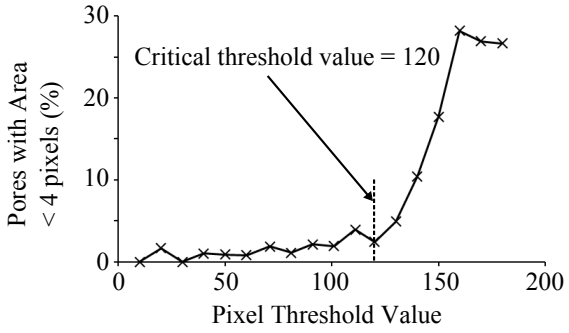

FIGURE 4.14: Graph showing the number of pores with less than 4 pixel area measured for various threshold values. Above the critical threshold value (in this case at 120) the number of pores rapidly increases. This method was adapted from that of Deshpande *et al* [189].

4.5 Mechanical properties of granules

Analysis of the mechanical properties of granules is important as it can give insight into the effects of changing the process and material parameters on the resultant granule strength. For example, the effect of changing the binder type, the granulation energy and the granulation duration on the granule strength could be investigated and then linked to the theoretical understanding of granulation presented in chapter 3. An understanding of the granule strength also allows an understanding of the failure mechanisms by which granules may ultimately break. It allows the estimation of an average force value above which the compressive yield strength of the granule is exceeded. This may help in understanding and perhaps preventing

any durability issues of the transparent resistive sensor containing these granules. For example, if each granule is loaded to above its compressive yield strength during operation of the sensor the granules may break and their electrical functionality may be compromised. This would have a negative impact on the repeatability of the response of the resistive sensor.

The mechanical characteristics of granules or agglomerates can be investigated using one of several methods. A common procedure for granules which are larger than 1 mm in size is impact or collision testing [190–192]. Here, the granules are accelerated towards a stationary plate, and the impact is recorded using a high-speed video camera. This gives a real-time analysis of fracture and crack propagation and the resulting granule fragments can be analysed to determine the breakage mechanisms. However, due to the imaging technique, this method is suitable only for larger granules and hence cannot be used to characterise the small granules typically less than 100 µm produced here.

Indentation (or nanoindentation) methods can also be used to investigate the mechanical properties of granules [193, 194]. An indenter probe fabricated from a very hard material such as diamond is pressed into the granule surface. Use of a nanoindenter allows mechanical properties such as the hardness, elastic or Young's modulus and the yield stress of the granule to be determined. For a brittle material the nanoindenter may be used to investigate the fracture behaviour resulting from microscale fractures. The indenter tip is typically less than 10 µm in size allowing even very small granules to be analysed [195, 196].

Crush tests may also be performed. Here an individual granule is compressed between two plates, one of which is fixed and the other is moveable. A force is applied through the moveable plate until the yield stress of the granule is reached, which is characterised by a sudden decrease in the load. Ultimately, the resolution of the test equipment determines both the smallest granule that can be compressed and the resolution at which the force is applied. Typically displacement resolutions of the order of several micrometers can be achieved for granules greater than 500 µm in size [139, 140, 187, 197–200]. Analysis of the force-displacement data gives information on elastic and plastic deformation regimes, Young's modulus and the breakage point. Here, a similar testing method was used in which the granules were compressed between the sample stage and the probe. The equipment was specially designed for the testing of small granules, that is those above 75 µm in size, where both high resolution force and displacement could be measured.

4.5.1 NanoCrush test facility

In order to determine the mechanical properties of individual granules, specialised testing equipment at the Institute of Particle Science and Engineering at Leeds University was used. The equipment used was the 'NanoCrush', an early prototype which was custom-built in

collaboration with Micro Materials Ltd. It was specifically designed for measuring the crush strength of individual granules at sub-mN resolution. A schematic of the NanoCrush apparatus is shown in Fig. 4.15. The compressive loading on the sample is controlled by regulating the current through a coil, situated close to a permanent magnet, itself connected to a stiff ceramic beam and onto the sample probe. Increasing the coil current causes the beam to rotate through the pivot point such that the probe moves downwards towards the sample. The probe displacement is measured using a Linear Variable Displacement Transducer (LVDT). Specialised software records both the load applied and the displacement of the sample probe.

Prior to testing, the NanoCrush apparatus first had to be calibrated. Load calibration was required in order to determine the relationship between the coil current and the load on the sample probe. To do this, three known masses were applied to the beam at a fixed location (denoted X on Fig. 4.15). The current required to balance this mass was then determined. The LVDT coil was internally calibrated upon assembly of the equipment and it was not necessary to recalibrate this before testing.

4.5.2 Sample preparation

Because of the nature of the equipment and the sample preparation method it was only possible to measure the mechanical properties of larger granules. The granules to be tested were first sieved, using the method outlined in section 4.2.4, to obtain the size fraction of

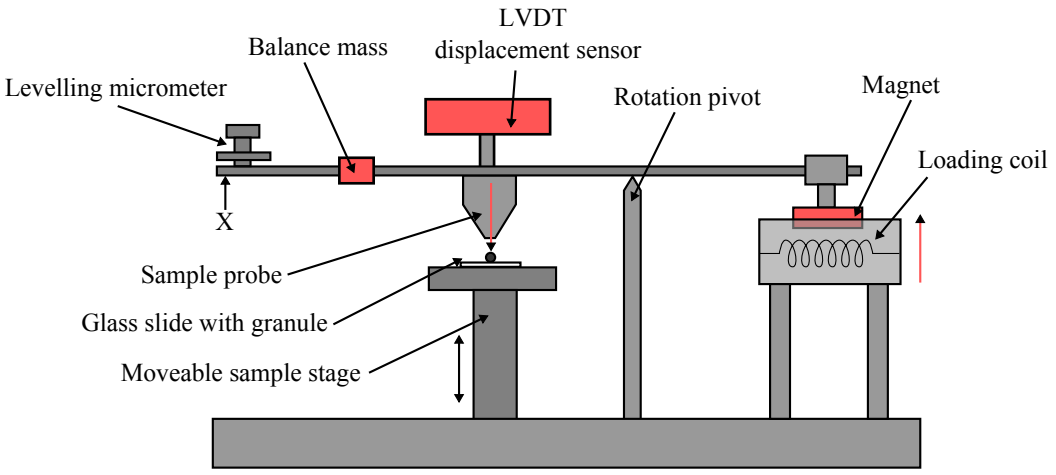

FIGURE 4.15: Schematic of the NanoCrush apparatus, which allowed measurement of the yield or fracture strength of individual granules. The force applied to the sample probe was controlled by regulating the current in a coil close to a permanent magnet, which controlled the force applied to a stiff ceramic beam. The probe displacement was measured using a Linear Variable Displacement Transducer (LVDT).

75–100 µm. A small circle matching the diameter of the crush probe tip was drawn on the underside of a glass microscope slide to demarcate the testing zone, which was then aligned underneath the crush probe prior to measurement. Granules were dispersed onto the slide using a cotton bud. A digital microscope with 40x magnification was used to obtain live imaging of the microscope slide and granules. A single granule was manipulated into the testing zone using a small blunt-ended wooden pick, as shown in Fig. 4.16(a). The remainder of the granules were removed from the vicinity of the test zone. The test zone was aligned underneath the crush probe, as shown in Fig. 4.16(b). During testing, increasing force was applied to the granule until breakage occurred. Breakage was characterised by a clear jump in the measured displacement at the characteristic force, as illustrated in Fig. 4.16(c).

4.6 Chapter summary

This chapter has described the experimental methods used to both fabricate and characterise nanocomposite granules. The physical principles of various size analysis techniques used to determine the granule size distribution have been described, as well as the process of focussed ion beam milling used to analyse the internal granule structure. The equipment used to characterise the granule mechanical properties was also discussed. Granule characterisation in terms of the granule size distribution, internal structure and mechanical properties is important because it allows corroboration of the theoretical understanding of the granulation process. For example, monitoring the effect on the granule size distribution, the internal structure and the mechanical properties allows a better understanding of the

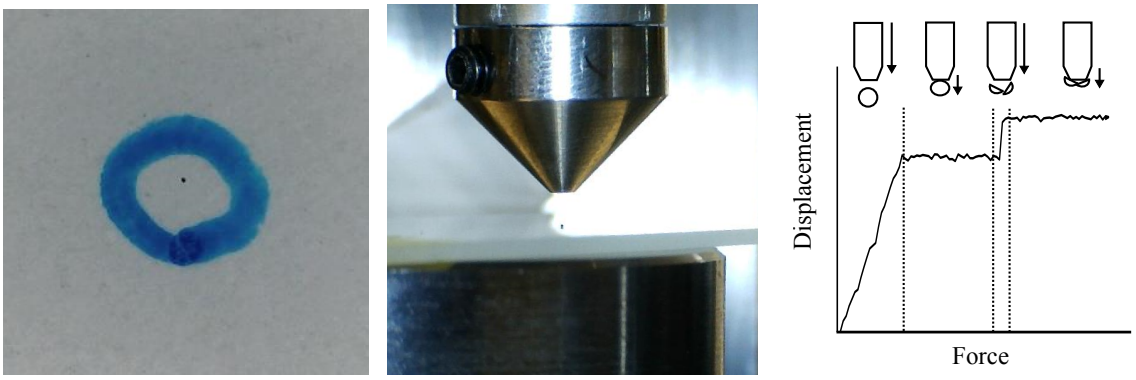

(a) (b) (c)

FIGURE 4.16: Photographs and schematic of the NanoCrush testing apparatus. (a) A single granule of size 75–100 µm was dispersed onto the testing zone. (b) The glass slide was positioned on the stage so that the testing zone lay directly beneath the crush probe. (c) As the force was increased the crush probe contacted the granule and applied increasing force until the granule compressive yield stress was exceeded resulting in granule breakage.

effects of changing either the material properties or the process variables during the granule fabrication stage. Furthermore, these parameters are also of great importance in order to characterise the granules prior to their incorporation into the screen-printable ink and subsequently the resistive pressure-sensing touch interface. Here, the granule size, porosity, compressibility and strength may play an important role in the pressure-sensing capabilities of the resistive touch interface.

Chapter 5

Comparative Study of Size Analysis Techniques

5.1 Introduction

Counting and measuring granules is a statistical problem, where enough granules need to be measured in order to obtain an accurate representation of the granule size distribution (GSD). There are many techniques which can be used to measure large numbers of granules (ideally in a short period of time) through either static or dynamic image analysis or by laser diffraction. These techniques have been discussed previously in chapter 4. These methods contrast with static image analysis using SEM, which is the only sizing technique available at Durham University that is suited to the measurement of granules in the size range 1–100 μm. Size analysis using SEM imaging is limited in that the image capture is manual and time consuming. The subsequent image analysis can only be automated for large, well dispersed granules so that in most cases the granule measurements have to be taken manually and the granule dimensions are approximated. Realistically only a very small number of granules can be measured and it is then assumed that these granules are representative of the entire granule batch.

This chapter compares the results obtained when measuring the size distribution of a granule batch using SEM image analysis and other forms of static and dynamic image analysis, as well as laser diffraction. Here, a granule batch is defined as a set of granules which have been produced using the same material properties and operating variables. Through this comparison, the advantages and limitations of each method are ascertained and more importantly the limitations inherent in SEM analysis can be better understood. This is important as SEM image analysis is used both qualitatively and quantitatively to assess the

nanocomposite granules produced for a range of material and process variables. The size analysis technique used therefore needs to be able to accurately and reliably quantify the effect of changing these variables.

5.2 Error on granule measurements using SEM imaging

When imaging the granules using SEM, the granules are often agglomerated or poorly dispersed. This is most likely for smaller granules less than 10 µm in size. As a result, subsequent image analysis cannot be automated as boundaries between the granules cannot be distinguished. Instead, measurements must be manually taken and this introduces some degree of subjectivity when measuring the granule dimensions. In order to quantify this error, two methods for determining the maximum Feret diameter $d_{f,max}$, were compared. First, measurements were taken by approximately measuring $d_{f,max}$ of 75 granules from granule batch A. This involved subjectively assessing the maximum dimension of the granule. Secondly, the outline of each granule was carefully traced such that an algorithm could then be used to accurately calculate $d_{f,max}$. From preliminary investigations, granule batch A was known to contain granules of a similar size (i.e. approaching unimodal) however the granules were not perfectly spherical in shape. These were chosen as the irregular shape could lead to large errors if $d_{f,max}$ was not accurately measured. These granules are shown in Fig. 5.1(a), where the outlines were used to accurately calculate $d_{f,max}$ and the straight lines represent the manual approximation of $d_{f,max}$.

Fig. 5.1(b) plots the automatic and manually determined values of $d_{f,max}$, where each data point represents a single granule. The solid black line represents perfect correlation indicating

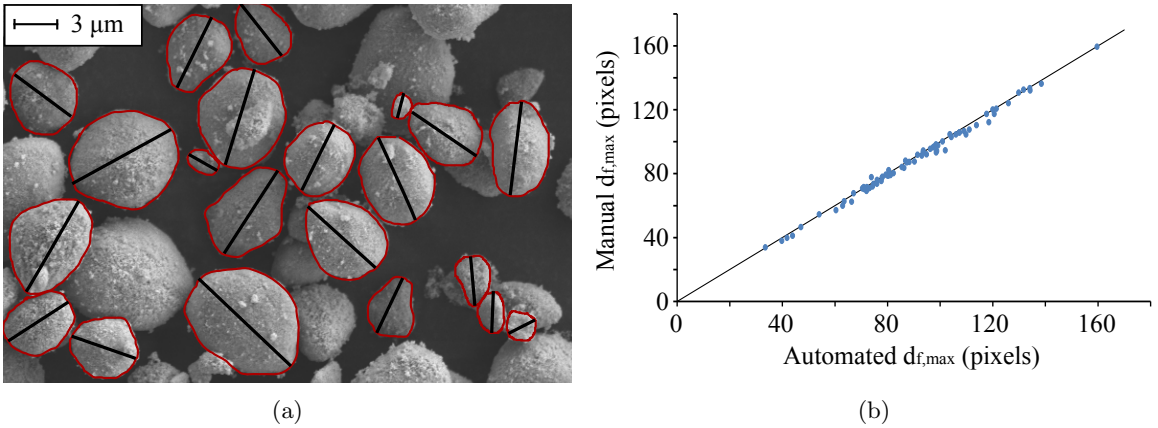

(a) (b)

FIGURE 5.1: (a) SEM image of granules, where the maximum Feret diameter, $d_{f,max}$ is manually approximated (black straight lines) and calculated exactly from the area of the granule (red perimeter) (b) Graph showing automatically and manually determined $d_{f,max}$ values, where the black line represents perfect correllation.

agreement between the methods. The maximum difference in granule size measured by the two methods was just 7 pixels. This can be converted to an error in size using the scale factor of the image. For the image shown in Fig. 5.1 this results in an error of 0.5 µm. This error scales with the magnification of the image, where lower magnifications results in a larger error on the measured granule size. In all subsequent measurements the error on the granule size was assumed to be 7 times the scale factor of the image.

5.3 Effect of number of granules measured on the granule size distribution using SEM imaging

The effect of the sample size (i.e. the number of granules measured) on the resultant GSD was analysed for granule batch A using SEM imaging. The $d_{f,max}$ value for each granule was measured and used to determine the GSD. Fig. 5.2(a) shows the GSD for sample sizes of 100, 200, 300, 400, 500, 750 and 1000 granules, where the percentage of measured granules is expressed as a function of granule size. The percentile values D_{10}, D_{50} and D_{90} of the distribution are compared in Table 5.1. Each data point on the GSD represents the upper limit of a granule size class and the percentage of granules within the size class. Lines are drawn between data points as a guide to the eye, but it is important to note that the GSD itself is not a continuous function. Representing the data in this way allows ease of comparison between multiple data sets.

Granule Batch	Measurement Technique	D_{10} (µm)	D_{50} (µm)	D_{90} (µm)
A	Manual SIA (SEM) - 200 granules	2.4	4.9	8.5
	Manual SIA (SEM) - 400 granules	2.3	5.3	8.2
	Manual SIA (SEM) - 750 granules	2.3	5.3	8.3
	Manual SIA (SEM) - 1000 granules	2.3	5.1	8.2
B	Manual SIA (SEM)	36.2	58.7	95.5
	Automated SIA	34.2	40.8	82.4
C	Manual SIA (SEM)	6.3	26.7	38.6
	Dry Dispersion DIA	58.8	113.5	211.1
	Wet Dispersion DIA	6.5	12.2	20.4
D	Laser Diffraction (1.5 Bar)	0.9	6.5	36.9
	Laser Diffraction (3.0 Bar)	0.8	5.8	33.5
	Laser Diffraction (5.0 Bar)	0.8	4.0	29.9
	Manual SIA (SEM)	5.7	13.6	38.7

TABLE 5.1: Percentile values for granule batches A–D measured using static image analysis (manual and automated), dynamic image analysis (wet and dry dispersion) and laser diffraction (dry dispersion).

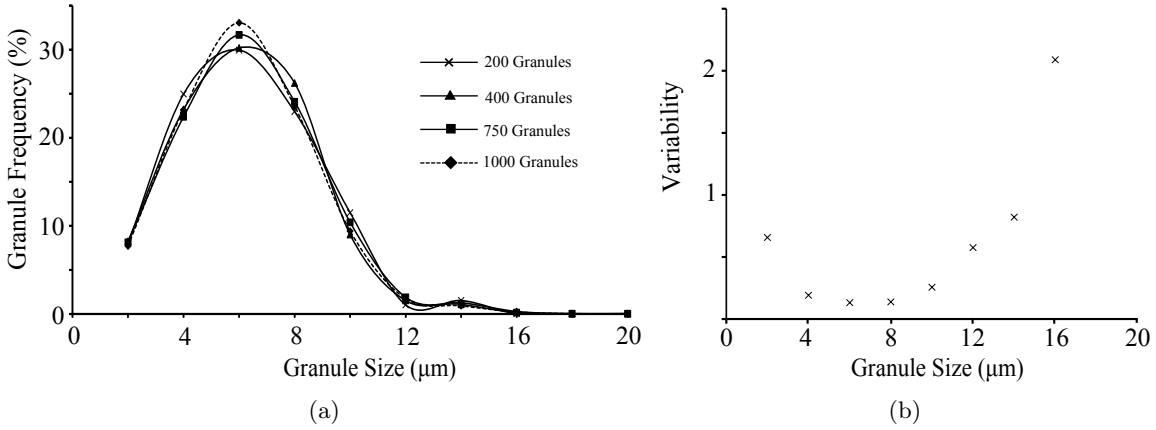

FIGURE 5.2: Graphs showing (a) GSD measured for a unimodal granule batch as a function of sample size ranging from 100–1000 granules. (b) The variability in the frequency of granules measured in each size range for each sample size, plotted against granule size.

Fig. 5.2(a) shows that the GSDs are very similar regardless of the sample size, where the modal value occurs at 4–6 µm and a secondary mode is apparent at 12–14 µm. The percentile values are very close, where for each sample size the difference is 0.1, 0.4 and 0.3 µm for D_{10}, D_{50} and D_{90} respectively.

A sampling error as a function of granule size can be defined. For each sample size a granule frequency was measured for each granule size range in order to produce the GSD. The sampling error was defined as the difference between the minimum and maximum frequency in these sets of values, divided by the average frequency. This is calculated for each granule size class and plotted in Fig. 5.2(b). For example, in the modal size class of 4–6 µm, the granule frequency was measured as 32.0, 30.0, 29.0, 30.3, 31.7 and 33.1 % for sample sizes of 100, 200, 300, 400, 500, 750 and 1000 granules respectively, with an average value over all sample sizes of 30.9 %. The sampling error in this case is (33.1 - 29.0) / 30.9 = 0.13.

Fig. 5.2(b) shows that the largest sampling error occurs at large and small granule sizes, i.e. furthest away from the mean size. For wide or bimodal distributions, the few numbers of large granule measured may not provide a representative sample of the true GSD. This is confirmed by the ISO 13322-1:2006 standard which states that static image analysis can only give accurate results for GSDs limited to less than one order of magnitude between the minimum and maximum granule size when a minimum of 6000 granules are measured [165]. Such a large sample size is infeasible when the measurements must be taken manually.

As can be seen in Fig. 5.2(a), for the case of a unimodal GSD increasing the sample size gives little improvement in the resulting GSD but requires a longer measurement time. Therefore measuring in excess of 400 granules has a limited advantage and is assumed to be unnecessary in order to provide an accurate representation of the true GSD. Henceforth, for manual

measurements a sample size of a minimum of 300 granules is defined as giving the optimum results between accuracy and measurement time.

5.4 Comparison of static image analysis using SEM and optical microscopy

Fig. 5.3(a) shows the GSD obtained from using both manual and automated SIA (using SEM and optical microscopy respectively), when sampling granule batch B. In both cases $d_{f,max}$ of the granules was measured and a bin size of 1 µm was used to calculate the GSD. For the automated optical microscopy system 30 000 granules were measured, in comparison with over 700 granules measured using SEM. Here, 700 granules were measured to ensure minimum error due to sampling size, where it was previously shown that a minimum of 300 granules was required for a unimodal size distribution. Because the automated system gave volume-weighted results, the results from SEM image analysis were also converted to a volume-weighted distribution. This type of distribution was discussed previously in chapter 3. Both GSDs have a similar range and a modal value at 40 µm. However the proportion of large and small granules varies for each method used, as is shown by the large discrepancy between the percentile values which are given in Table 5.1. Here, the percentile values differ by 2.0, 17.9 and 13.1 µm for (D_{10}, D_{50} and D_{90} respectively. The large discrepancy in D_{50} and D_{90} indicates that each method measures a different (volume) proportion of granules which are greater than 35 µm in size.

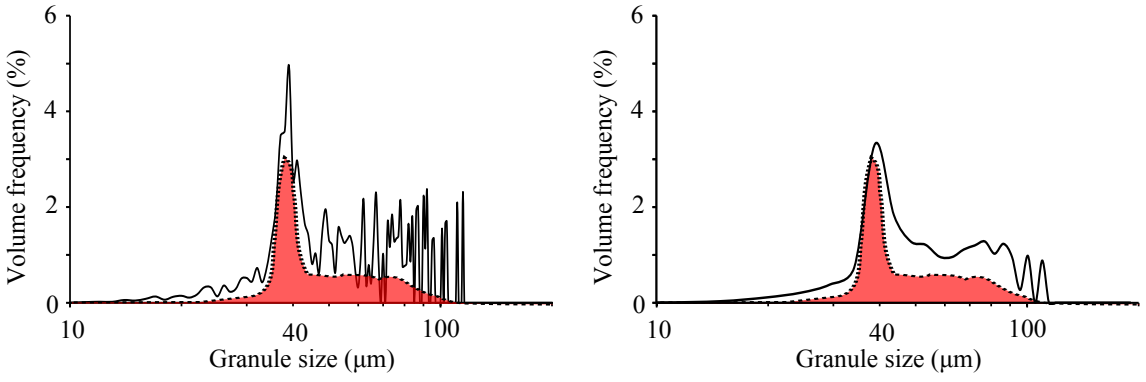

FIGURE 5.3: Graphs showing (a) GSD of granules measured with static image analysis techniques using SEM imaging (shown by the solid black line) and optical microscopy (shown by the red shaded area), where in both cases the bin size was 1 µm. The optical microscopy technique is automated allowing a large sample size to be measured in a short period of time resulting in a smooth GSD. Discontinuities in the GSD for manual SEM image analysis result from the small sample size (b) The bin size for SEM image analysis is increased to 5 µm, smoothing the resultant GSD.

Because the SEM GSD is volume-weighted the distribution appears discontinuous at large granule diameters and is characterised by a number of sharp, closely-spaced peaks. This occurs because not all granule size classes have been sampled due to the small number of granules measured. This may result in an over-estimation of the D_{50} and D_{90} percentiles because the majority of the volume of the system is contained in a very small number of large granules. It is expected that by increasing the sample size the GSD will approach that of the automated SIA system. This effect may be minimised by increasing the bin size at which frequency values are calculated. Fig. 5.3(b) shows the GSD for the SEM image analysis where this time the bin size was increased to 5 µm. This smooths out some of the discontinuity present in the distribution.

5.5 Comparison of dynamic image analysis techniques with SEM imaging

Fig. 5.4 shows a comparison of dynamic image analysis (DIA) techniques with SEM imaging. DIA was performed using both a wet and dry dispersion of granule batch C. This batch had a bimodal distribution where many granules were larger than 20 µm in diameter. This batch was chosen because the dry dispersion system could not resolve granules less than 10 µm in size. When performing DIA the GSD is volume-weighted, hence the GSD from SEM analysis was also calculated using volume weighting. The percentile values of each GSD are shown in Table 5.1 and the large difference in these values reflects the differences between the GSDs.

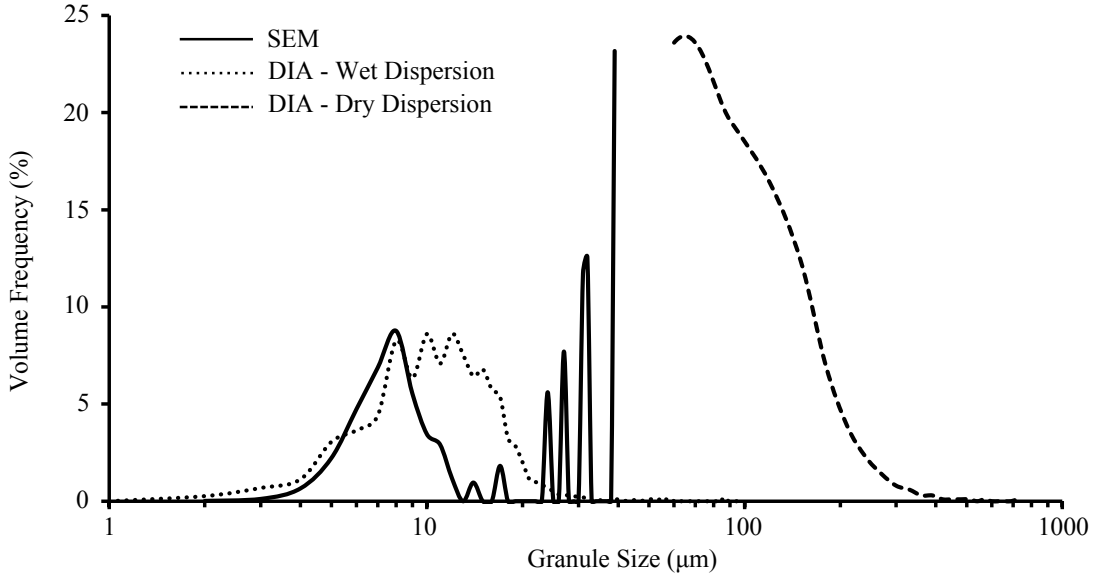

FIGURE 5.4: GSD of granule batch C measured with SEM imaging and dynamic image analysis using both a dry and wet granule dispersion.

SEM image analysis shows a bimodal distribution. Whilst there are a large number of small granules less than 10 µm in size, when plotted as a volume distribution the larger granules dominate. The dry dispersion method cannot measure granules which are less than 10 µm in size and so this peak is missing in the corresponding GSD. This results in larger calculated values for D_{10}, D_{50} and D_{90}. Furthermore, there were issues with the focussing of the camera onto the granule flow in the DIA system. Fig. 5.5(a) shows an example image taken when using the dry DIA method where it can be seen that only the granules in the forefront of the vertical flow are in focus.

The GSD obtained using wet dispersion shows a peak with a modal value around 10 µm which is slightly larger than that measured using SEM analysis. Additionally, no granules larger than 30 µm were measured. As mentioned in chapter 4, the cuvette used in the wet dispersion method was of a size that discounted granules greater than 100 µm from the measurement chamber. This could explain why the peak at large granule sizes in the GSD is not present. However, this does not explain the absence of granules in the range 30–100 µm. Again, this could be due to issues with poor focussing. Analysis of the images taken during the measurement process show that sometimes a larger granule may be split into several small granules due to poor focussing when the image is taken. When the image is subsequently thresholded lighter regions may be misclassified as empty space. An example of this is shown in Fig. 5.5(b).

Whilst poor focussing in both the wet and dry DIA methods is an issue it does not fully explain the discrepancy in the GSDs when comparing to the results from SEM image analysis. As mentioned previously, this is largely due to the fact that the dry dispersion DIA system cannot resolve particles less than 10 µm in size and the wet dispersion DIA system cannot measure

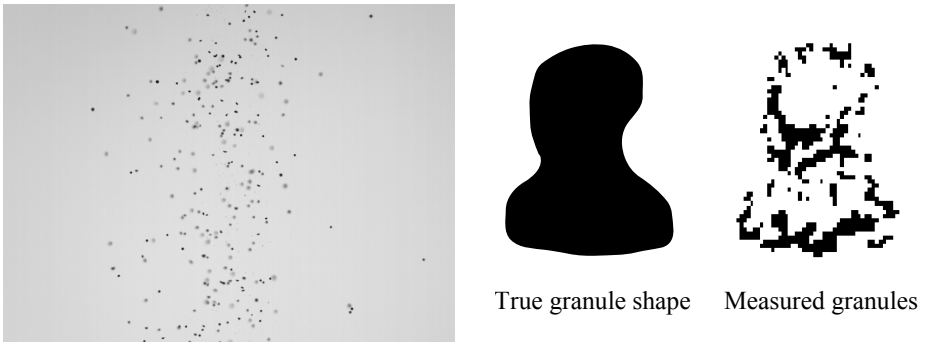

(a) (b)

FIGURE 5.5: (a) Image taken using DIA method with dry dispersion of granules, where the granular flow is top to bottom due to gravity. Only the granules in the forefront of the image are properly focussed. (b) Example of poor focussing of a granule, leading to the misclassification of a large granules into several smaller granules.

granules greater than 100 µm in size. Furthermore, when imaging bimodal distributions using SEM imaging, poor sampling leads to misrepresentation of the peaks.

5.6 Comparison of laser diffractometry and static image analysis by SEM imaging

5.6.1 Effect of dispersion pressure on laser diffraction results

As described previously in chapter 4, prior to laser diffractometry the sample was dispersed though air pressure. The air pressure controls the energy of the collisions between granules and the dispersion chamber walls. If the pressure is insufficient, granule agglomerates are not dispersed and if the pressure is too high breakage of individual granules may occur. Therefore, the dispersion pressure can affect the measured GSD.

Fig. 5.6 shows the effect of altering the dispersion pressure on the GSD during laser diffractometry, for granule batch D. SEM imaging indicated that these granules had a bimodal size distribution. However the GSD obtained using laser diffractometry shows three peaks at granule diameters of 1, 8 and 30 µm, where the peak height is dependent on the dispersion pressure. As the dispersion pressure increases the modal value remains constant at 6 µm. However, the proportion of large granules decreases whilst the proportion of smaller granules increases. Table 5.1 shows the percentile values for each dispersion pressure. With increasing pressure the D_{10}, D_{50} and D_{90} values decrease, indicating that the GSD shifts towards smaller particle sizes with increasing dispersion pressure. Kippax states that this is

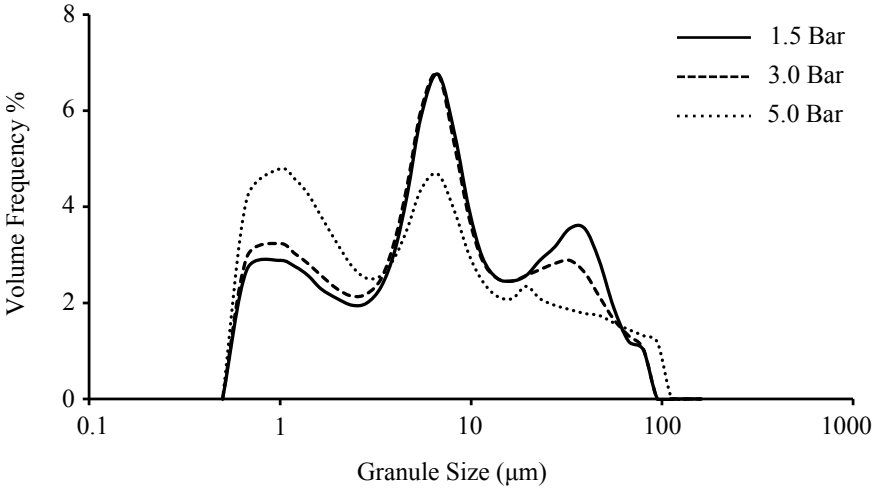

FIGURE 5.6: GSD obtained using laser diffractometry as a function of the air pressure used to disperse the granules

a common issue in laser diffractometers when the particles are dispersed in an air jet [201] and can be caused by one of two processes. Firstly, it is possible that increasing the dispersion pressure breaks apart loose agglomerations of granules. This is a favourable process as large agglomerates can then be correctly classified into their constituent granules. However, a high dispersion pressure may also lead to granule breakage. SEM analysis of the same granules (see the following section) showed no evidence of (whole) granules less than 2 µm in size as the minimum size was nearer to 5 µm, even when imaging using a high magnification capable of resolving much smaller granules. Therefore it is more likely that high dispersion pressures lead to granule breakage. This effect needs to be fully assessed before accurate results can be obtained using the laser diffractometry technique. For example, taking repeat measurements of the same sample may indicate whether the granule size decreases with each repeat, as would be characteristic of breakage. Another possibility is the effect of 'ghosting'. Here, sharp edges on angular granules scatter light to large angles and this can be erroneously attributed to scattering from small spherical particles [202].

5.6.2 Comparison to static image analysis using SEM imaging

Fig. 5.7 compares the GSD produced using both laser diffraction and SEM image analysis techniques, where both are represented as volume distributions. For the former, a dispersion pressure of 3.0 Bar was chosen as a compromise between the effects of agglomeration dispersion and granule breakage.

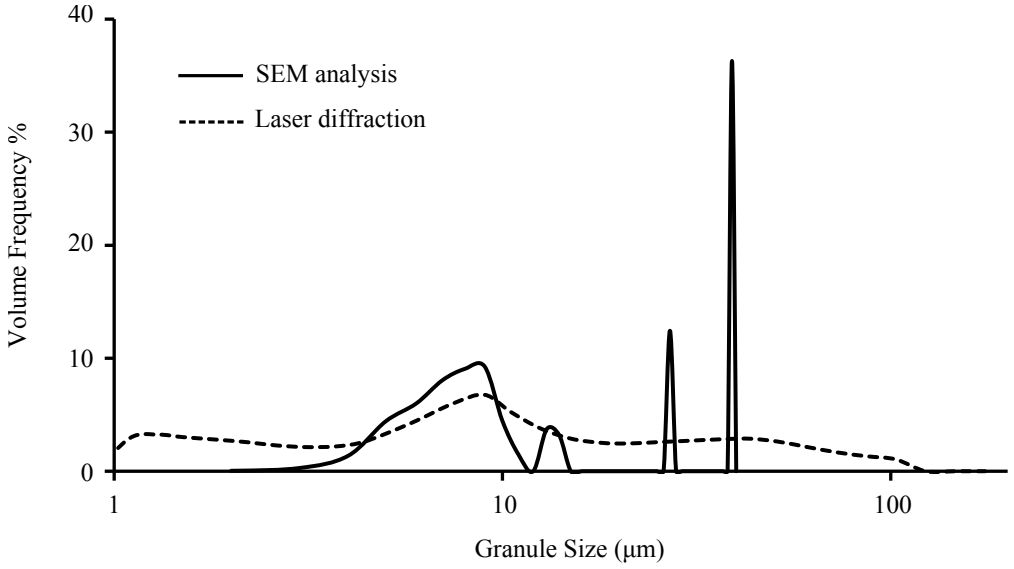

FIGURE 5.7: Graph showing the GSD obtained for both a laser diffractometer measurement system and static image analysis by SEM imaging.

Both GSDs show a peak close to 10 µm, however for SEM analysis this peak is a secondary mode because most of the volume is contained in two large granules of diameter 27 and 38 µm. As a result the percentile values, shown in Table 5.1, are very different. This highlights the issue of representing granule sizes measured using SEM analysis with a volume weighted distribution, as here just two granules out of a sample size of 350 dominate the distribution. As mentioned in the previous section, the cause of the peak in the laser diffraction GSD at 1 µm could either be a real effect (for example small granule nuclei) or fragments of larger granules which have been broken during the dispersion process. For SEM image analysis, the dispersion during sample preparation is low-energy and therefore breakage is unlikely. Additionally, broken granules can easily be identified and discounted due to their jagged, uneven morphology associated with dry particle attrition. However, one of the benefits of laser diffractometry is that a large size range can be measured, and bimodal or polydisperse GSDs can be accurately characterised. This is in contrast to the technique of SEM image analysis where bimodality is very difficult to assess.

5.7 Chapter summary

This chapter has highlighted the differences between GSDs obtained using different measurement principles. By comparing these techniques the benefits and limitations of SEM imaging (i.e. a manual SIA technique) can be assessed.

From the results shown here, the main issue with SEM analysis is that the small sampling size leads to difficulty in accurately determining a bimodal GSD. It has been shown that a smaller sample size does not have a significant, negative impact for narrow, monodisperse GSDs. However, for bimodal or polydisperse distributions a low granule count can cause the distribution to appear discontinuous. This effect is magnified when the GSD is volume weighted, where, a small number of large granules may represent the majority of the volume of the system and therefore dominate the GSD. However, if the GSD is not weighted then the few larger granules are not visible within the GSD. The image magnification can also affect the number of small and large granules measured in bimodal distributions. If the SEM images are taken at high magnification, small granules can be resolved but large granules are unlikely to be sampled. Conversely, at a low magnification more large granules are sampled but the small granules cannot be resolved. Furthermore, the error in single granule measurements is amplified at low magnifications.

Whilst in this regard SEM imaging is disadvantageous, it is important to note that other size analysis techniques are not without their limitations. Whilst in principle dynamic image analysis is capable of measuring a large range of granule sizes, often the operation variables and set-up of the equipment impose limits on the size range that can be measured. For

example, the size of the cuvette used in wet dispersion DIA imposed an upper limit of 100 µm. The low-energy dispersion used in the dry dispersion DIA technique meant that granules less than 10 µm could not be detected. Both of these systems can produce effects related to the poor focussing of the granule images. Only laser diffraction is capable of measuring a large range of granule sizes simultaneously. However, the energetic dispersion principle used here may lead to granule breakage. Additionally, each of these techniques cannot give precise detail on the shape, morphology and surface roughness of the granules.

In conclusion, whilst SEM imaging is used to determine granule properties throughout the rest of this thesis, the above limitations should be noted. Most importantly, when imaging bimodal distributions a secondary mode at a larger granule size may not always be apparent in the number-weighted GSD. In practice, this is circumvented by sieving the granules before inclusion into the transparent screen-printable ink. By sieving at 20 µm or even 45 µm, the secondary mode in granule size can be removed.

Chapter 6

The Effect of Constituent Material Properties on Granulation

6.1 Introduction

In this chapter, the effect of the constituent material properties upon the resultant granules is investigated. As explored in chapter 3, granulation processes are controlled by a vast range of factors, all of which interact and result in a complex process that is not yet fully understood. Whilst this thesis does not aim to present a comprehensive review of the granulation of ATO nanoparticles, nevertheless an in-depth understanding is required in order to better control the properties of the final granules. These granules are incorporated into an ink and printed to create a transparent touch interface which has a pressure-sensitive resistance response. As such, the properties of the granules will play an important role in the pressure-sensitive touch behaviour of the interface. The granules span the thickness of the printed CPC layer, and for this reason granules less than 10 µm in size were favoured. To this aim, the formation of the granules and their structural properties were investigated in detail and the results are presented in this chapter and the next. This brings together extended studies of the effect of changing the ATO particle shape, the type of binder and the amount of binder on the granulation processes. The next chapter extends these studies by investigating the effect of process variables on the granulation mechanisms, namely the speed of the DAC and the granulation duration.

Here, granules were fabricated from a range of starting material properties and the resultant granules were analysed in terms of their size distribution, internal structure and mechanical properties. In section 6.2, the shape of the ATO nanoparticles, which were either spherical or acicular, is studied. The effect of the type of binder used is investigated in section 6.3.1, where

the binders had either a carbon-based, water-based or silicone-based chemical composition and each had a different viscosity. Finally, in section 6.4 the quantity of binder used is altered and the effect on the resultant granules characterised. Throughout these investigations, SEM was used to image the granules and enable measurement of the GSD. The advantages and disadvantages of this process over other size analysis techniques was discussed previously in chapter 5. FIB milling was used to reveal the internal granule structure, a tool which is invaluable in assessing the effect of changing each variable on the internal properties of the granules. Finally, the mechanical properties of selected granules were also assessed using the specialised NanoCrush test equipment at Leeds University. These techniques were described fully in chapter 4. Combined, they allow an in-depth understanding of not just the outward appearance of the granules, but also their porosity and mechanical strength.

6.2 Effect of ATO particle shape on granulation mechanisms

Both spherical and acicular ATO particles, as described in chapter 4.2, were combined with silicone binder at a ratio of 10% binder with respect to the particle mass, and granulated at a speed of 2000 rpm for up to 10 minutes in the DAC. In both cases the cured granules were sieved to remove agglomerates greater than 75 µm. This large material component was comprised of a residual paste-like substance which had formed on the sides and base of the container during granulation.

6.2.1 Granules comprising spherical ATO nanoparticles

To measure the size distribution of the granules, SEM images were collected and the maximum Feret diameter of a minimum of 300 granules was measured for each sample. Representative SEM images at each time interval are shown in Fig. 6.1. Fig. 6.2 shows the corresponding GSD for each mixing time. For ease of comparison, data points are joined by lines, as a guide to the eye. At short mixing times granule nuclei are formed by the initial contact between the nanoparticles and the silicone binder. Here, granule nuclei are defined as granules with a size less than 15 µm. Any granule over 15 µm in size is classed as a large granule.

During fabrication, the primary particles were poured onto the binder, and this was expected to promote nuclei formation through the immersion mechanism. Here, the binder droplets are much larger than the particles so that the particles become immersed in the binder at localised regions, resulting in binder-rich and binder-poor areas. It is predicted that preferential growth will occur in the binder-rich regions, resulting in a bimodal size distribution of granules. Fig. 6.1(a) and Fig. 6.1(b) show granule nuclei produced after 1 and 2 minutes mixing in the DAC where a bimodal size distribution was observed. As shown in Fig. 6.2, the

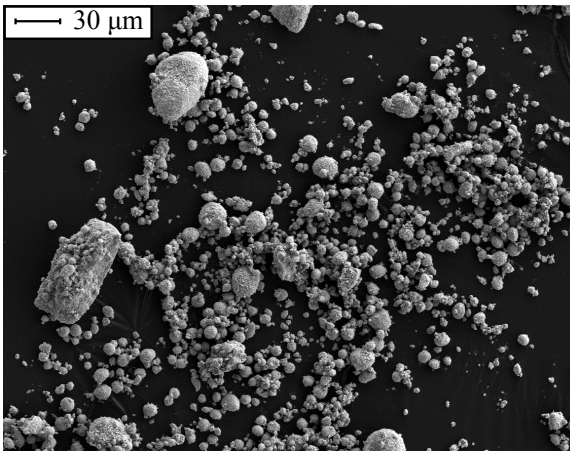

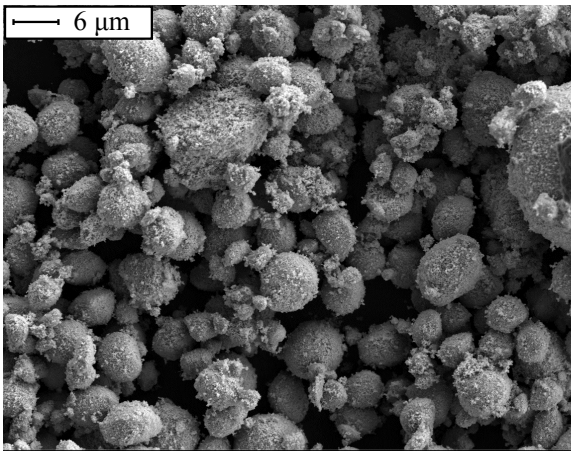

(a) 1 minute

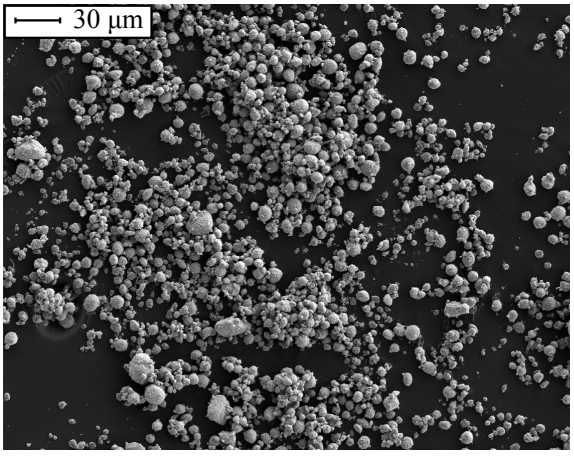

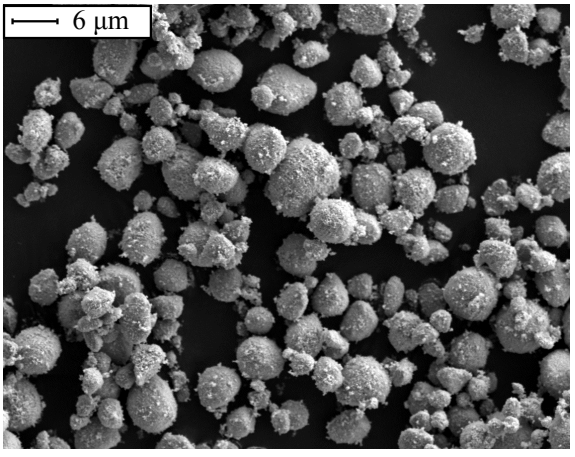

(b) 2 minutes

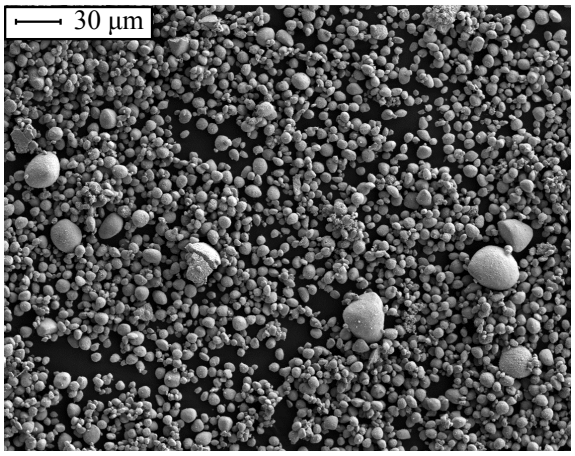

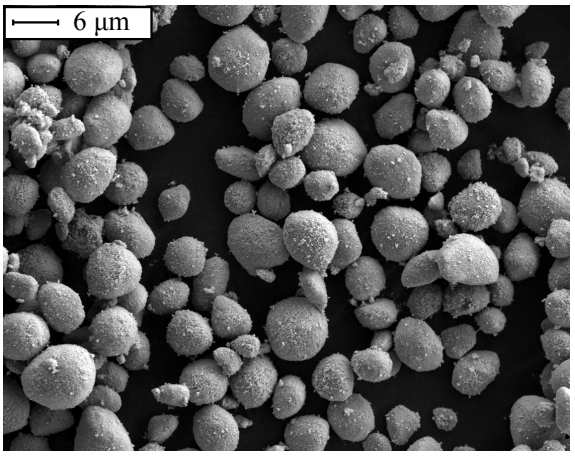

(c) 4 minutes

FIGURE 6.1: SEM images of granules produced using spherical ATO nanoparticles and 10 % silicone binder, granulated at 2000 rpm in the DAC for a range of mixing times. For each time, low and high magnification images are shown. The figure continues overleaf.

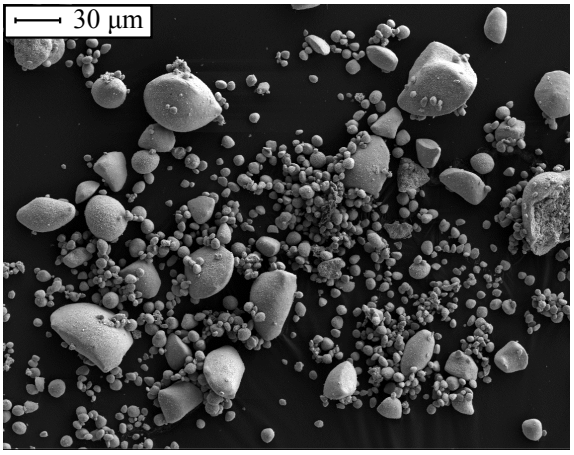

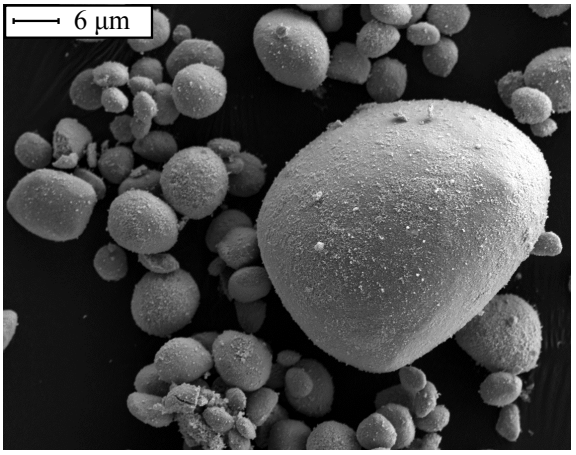

(d) 6 minutes

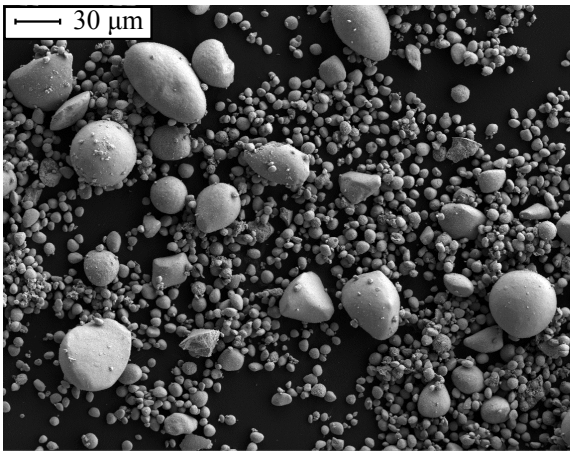

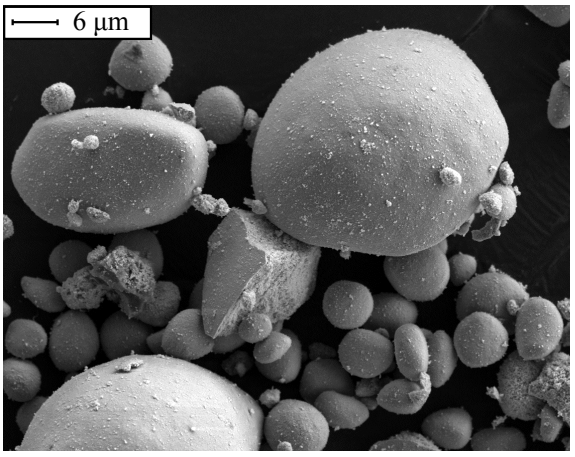

(e) 10 minutes

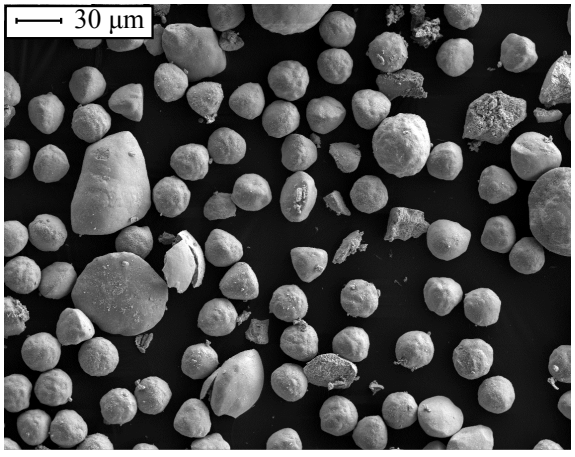

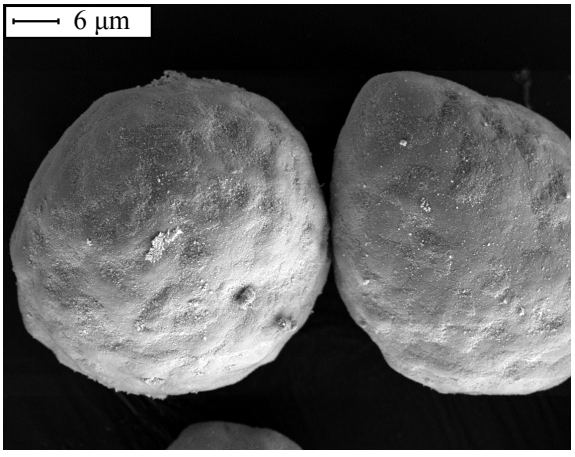

(f) 15 minutes

FIGURE 6.1: Continued

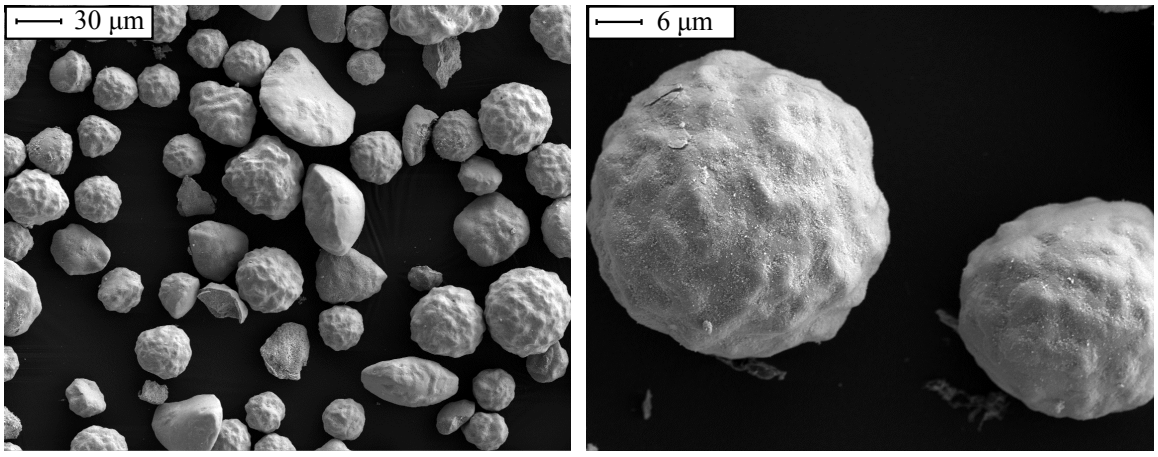

(g) 20 minutes

FIGURE 6.1: Continued

majority of the granule nuclei are less than 10 µm in size, with a peak in the distribution at 4 µm. Analysis of the SEM images showed that the larger granules have a maximum size of around 70 µm, corresponding to the sieve size of 75 µm used to process the granules. These larger granules are poorly represented on the number-weighted GSD. This limitation of size analysis through SEM imaging was discussed previously in chapter 5. Granule nuclei may be adhered to the surface of larger granules, either superficially or perhaps during early stages of continued growth by coalescence. The smaller granules are themselves cohesive and may be agglomerated into loose structures. Closer inspection shows that the smaller granules have roughly structured surfaces, where primary particles may be adhered to the surface but not yet fully incorporated into the granule structure. This indicates that the granules themselves are not fully compacted, as here it would be expected that the granule surface would be smoothed through repeated collisions.

With increasing mixing time from 2 to 10 minutes the granule nuclei become increasingly surface-smooth, as can be seen by comparing nuclei in Fig. 6.1(c), Fig. 6.1(d) and Fig. 6.1(e). In Fig. 6.2, the peak of the corresponding GSD moves from 4 µm for 1 and 2 minutes, to 5 µm after 4 minutes, and 6 µm after 6 and 10 minutes. Whilst the majority of the granules remain less than 10 µm in size, it was also observed that the proportion of larger, surface-smooth granules increased. This may be due to the continued preferential growth of the binder-rich regions and coalescence and the layering of fine material onto the binder-rich granules.

After 15 minutes of granulation in the DAC, an important phenomenon occurred. Rapid granule growth had occurred so that now the majority of granules are larger than 15 µm. These granules are shown in Fig. 6.1(f) and Fig. 6.1(g). The GSD in Fig. 6.2 shows a strong peak at 24–30 µm after 15 minutes, where 76 % of the total number of granules are greater

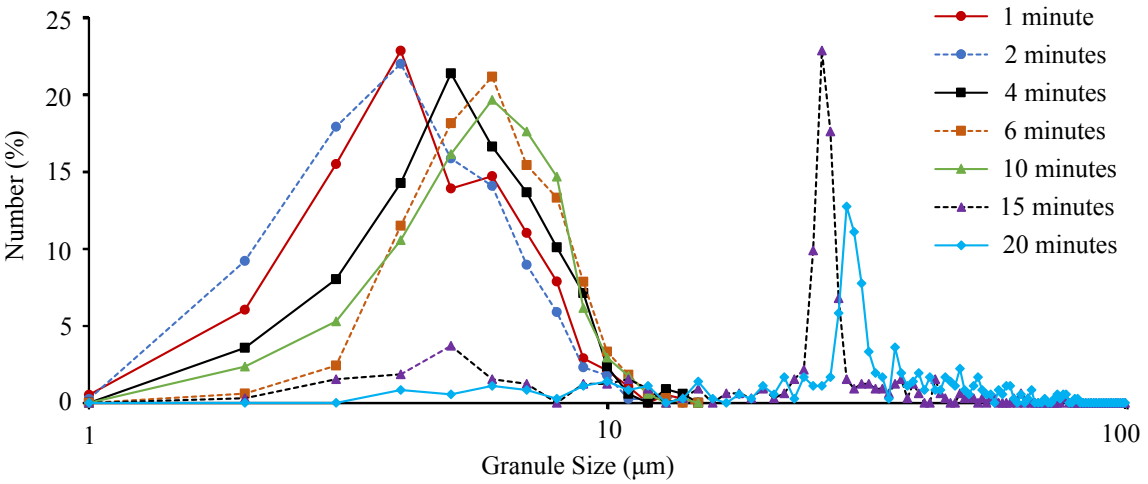

FIGURE 6.2: Graphs showing GSD for granules comprising spherical ATO particles and 10 % silicone binder, granulated at a speed of 2000 rpm for 1 to 20 minutes. Lines between data points are drawn as a guide to the eye.

than 24 µm in size. After 20 minutes there is a strong peak at 27-33 µm where 80 % of granules are greater than 27 µm in size. The smaller granules had an angular jagged shape suggestive of granular breakage, and few rounded, smooth nuclei remained.

A finite period of little or no growth, followed by rapid growth, is indicative of an induction process. As described previously in chapter 3, during the induction phase the granules consolidate and liquid binder is squeezed to the granule surface as a result of granule collisions and decreasing porosity. During the induction phase, the granules are surface-dry and little growth occurs through coalescence. When binder is finally squeezed to the granule surface rapid growth may occur by coalescence and layering. This process is not instantaneous and happens over a finite time-scale. It is proposed that this is responsible for the increasing number of large granules with granulation times up to 15 minutes, and the rapid growth that is observed after 15 minutes in the DAC. It was also noted that irregularities in the granule shape occur after 15 and 20 minutes, characterised by indentations and protrusions on the surface of the the granule. This 'golf-ball' effect can be seen in Fig. 6.1(f) and Fig. 6.1(g) and is discussed further in chapter 7.

6.2.1.1 Internal structure of granules comprising spherical ATO nanoparticles

To better understand granule growth, the internal structure of granules produced after 1 minute were cross-sectioned via FIB milling. Fig. 6.3(a) shows the cross-section of a granule nucleus and high-resolution detail of the internal pore network is shown in Fig. 6.3(b). The internal structure shows a network of pores between ATO nanoparticle agglomerates, where the pore distribution appears homogeneous throughout the cross-sectioned surface. The

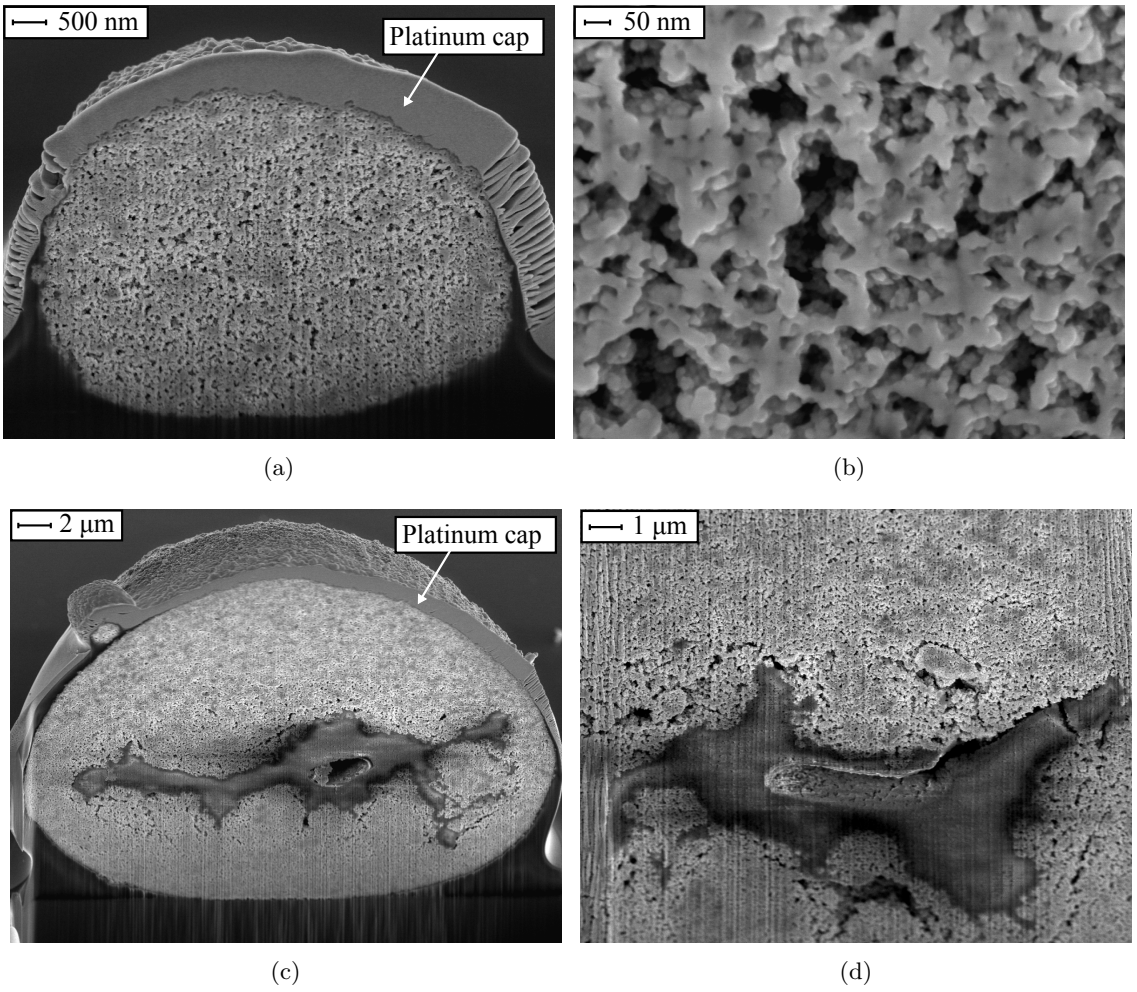

FIGURE 6.3: SEM images of (a) cross-section of a granule nucleus formed after 1 minute, and (b) high-magnification detail of the particle-pore system, which appeared homogeneous across the cut surface. The internal structure of larger granules > 30 µm also produced after 1 minute are shown in (c) and (d), where a binder-rich core was observed

average porosity was determined using the method developed and described in chapter 4. By averaging over images taken from 5 granule nuclei with diameters of 5–8 µm, the average porosity was calculated to be 20 ± 2 %.

Large granules present in the bimodal distribution after 1 minute were also cross-sectioned. Fig. 6.3(c) and Fig.6.3(d) show cross-sectioned surfaces through granules of diameter 31 and 35 µm respectively. Here, the darker regions found in the centre of the granule are large deposits of the silicone binder. The presence of a binder-rich core is evidence supporting the idea that preferential growth in the early stages of granulation occurs in binder-rich areas. This can be explained by the immersion model of nucleation which produces both binder-rich and binder-poor areas. The porosity of the granule (discounting the central area comprising binder only) was measured at 19 ± 2 %, averaged over three areas of the cross-section. This agrees, within error, to the measured porosity of the small granule nuclei which

formed after the same time. It suggests that the degree of compaction, in these early stages of granulation, is similar for these granules despite their difference in internal composition. The effect of granulation time on the internal structure of granules is explored further in chapter 7.

6.2.2 Granules comprising acicular ATO nanoparticles

The size distribution of granules containing acicular ATO nanoparticles was assessed by measuring the maximum Feret diameter of a minimum of 300 granules. These granules contained 10 % silicone binder and were fabricated using the same method as for the spherical ATO nanoparticles, allowing direct comparison to be made. Representative SEM images for different times in the granulation process are shown in Fig. 6.4. When compared against

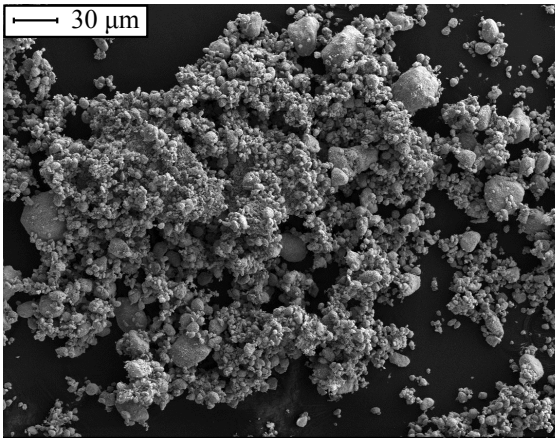

(a) 1 minute

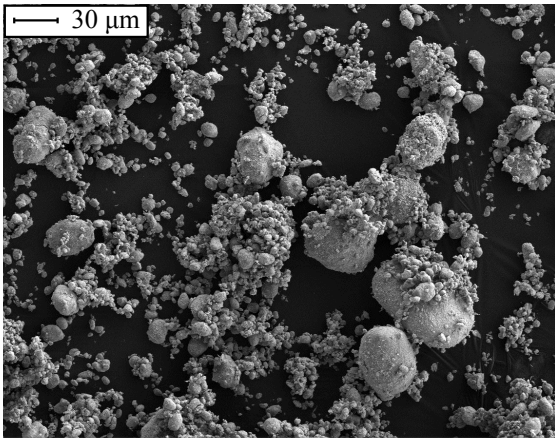

(b) 2 minutes

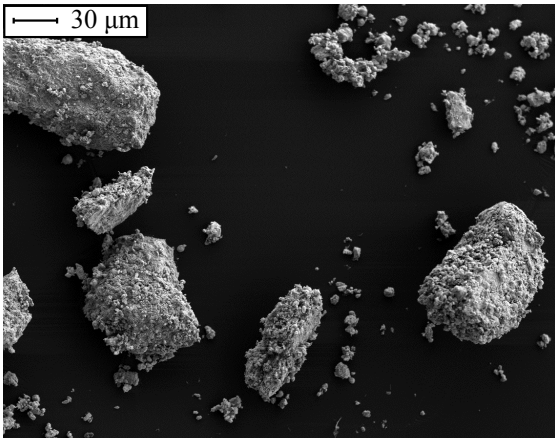

(c) 6 minutes

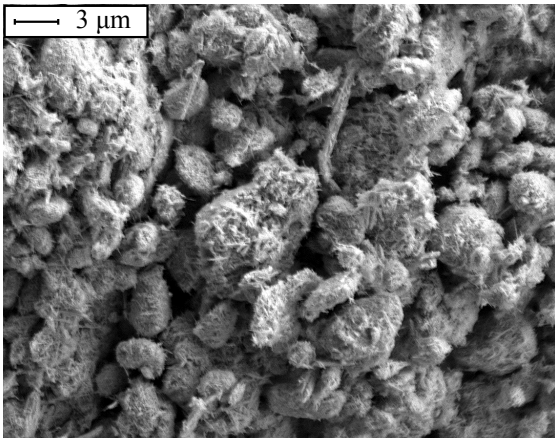

(d) 10 minutes

FIGURE 6.4: SEM images showing granules fabricated with 10 % silicone binder and acicular ATO nanoparticles, mixed at 2000 rpm in the DAC for (a) 1 minute (b) 2 minutes (c) 6 minutes and (d) 10 minutes.

the corresponding images for spherical nanoparticles shown in Fig. 6.1, these images show evidence of a very different granulation process. Fig. 6.4(a) and Fig. 6.4(b) show granule nuclei which were formed after 1 and 2 minutes respectively, where the nuclei are heavily agglomerated into large clusters.

The GSD of the individual nuclei within these clusters are shown in Fig. 6.5. Here, most nuclei were less than 10 µm in size and the peaks of the distributions occurred at 3 µm. This is similar to granules comprising spherical nanoparticles, where the peak in the distribution occurred at 4 µm. After 2 minutes, large, smoother granules greater than 30 µm in size can also be seen along with the smaller granule nuclei and nuclei agglomerations. After 6 minutes, most granule nuclei are incorporated into larger structures such as those shown in Fig. 6.4(c). Fig. 6.4(d) shows a close-up image of the surface structure of such a granule, produced after 10 minutes. It comprises a densely packed agglomeration of smaller granules suggesting the dominance of growth by coalescence. The indented 'golf-ball' appearance shown by the granules comprising spherical nanoparticles did not occur for acicular particles. Due to the extent of the granule growth and the extreme bimodality of the distributions after 2 minutes, calculation of the GSD for these times was not possible

6.2.2.1 Internal structure of granules comprising acicular ATO nanoparticles

Fig. 6.6(a) shows a cross-section through a granule fabricated with acicular ATO nanoparticles. The granule, of diameter 43 µm, was produced after 2 minutes mixing and appeared surface-smooth, although several granule nuclei were adhered to the surface. FIB milling revealed a complex internal structure consisting of many coalesced nuclei and regions of high

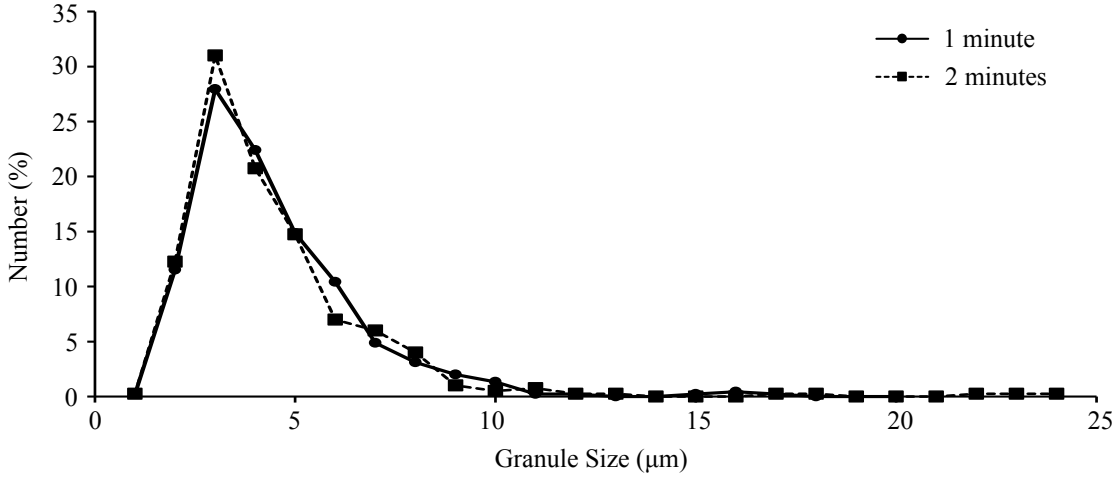

FIGURE 6.5: Graph showing the GSD of granules comprising acicular ATO nanoparticles and 10% silicone binder, mixed at 2000 rpm for 1 and 2 minutes.

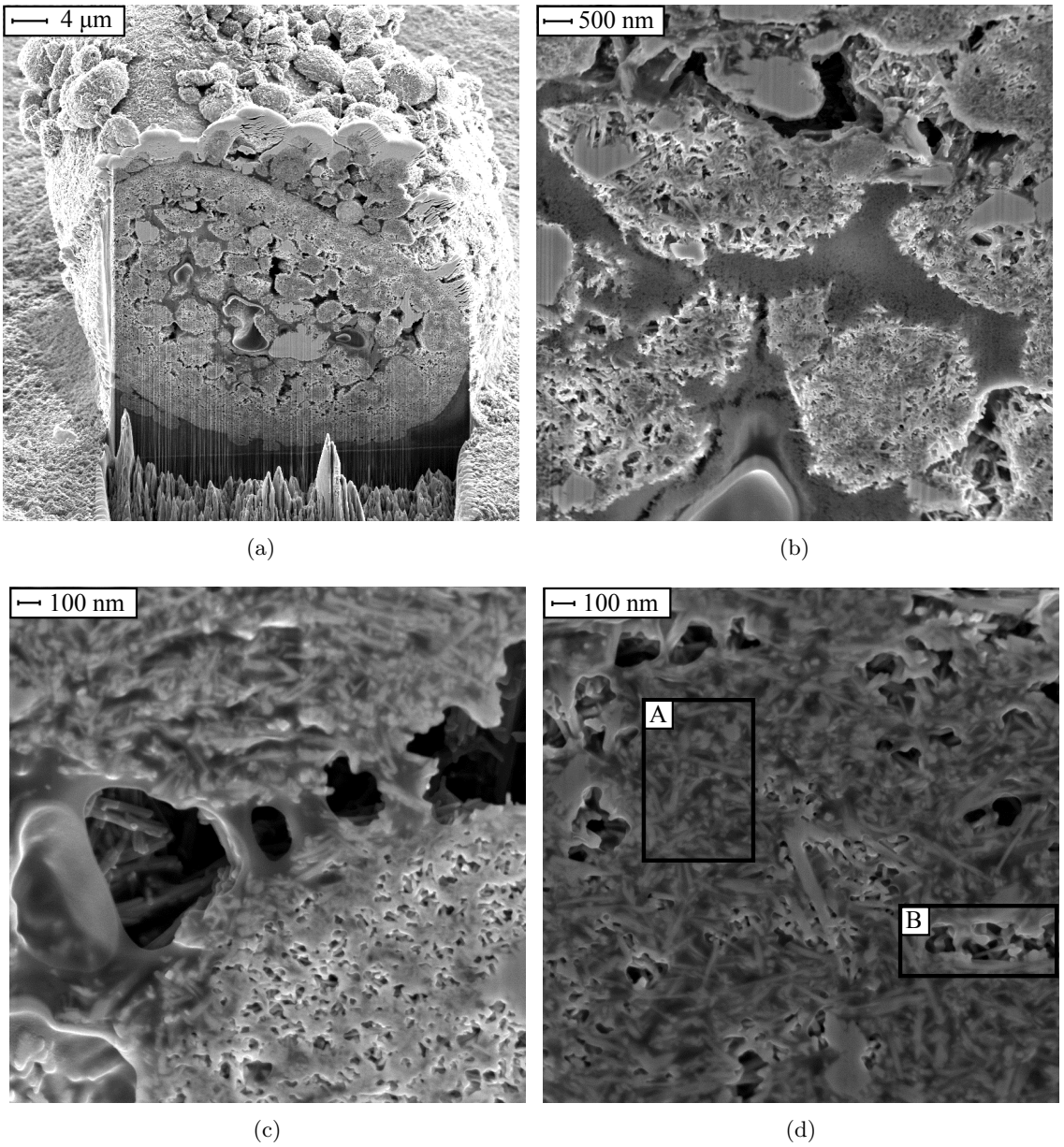

FIGURE 6.6: SEM images showing FIB cross-sections through a large granule agglomerate, comprising acicular ATO nanoparticles and 10 % silicone binder, granulation for 2 minutes at 2000 rpm in the DAC. (a) overview of the milled surface (b) close-up detail of coalesced nuclei bound by binder-rich regions (c) solidified liquid bridges formed between adjacent nuclei (d) the porosity of a single nuclei, where region A shows binder-filled pores and region B shows open, air-filled pores.

binder content, as well as macro-pores between individual nuclei. Towards the surface of the granule a continuous layer of particles was present, which is indicative of a layering mechanism. This gave the granule its outwardly smooth appearance. This structure is very different to granules comprising spherical ATO nanoparticles.

Fig. 6.6(b) shows the coalescence of several small nuclei within the large structure. The dark

regions between nuclei indicate a high content of the silicone binder. This evidence supports the surface-wet coalescence models proposed by Ennis *et al.* and Liu *et al.*, as described in chapter 3. However, it is not possible to confirm whether or not the nuclei have been plastically deformed during the process. Fig. 6.6(c) shows evidence of solidified liquid bridges between two granule nuclei which further supports growth by coalescence.

This structure is very different to that of the large, surface-smooth granules which appeared in the early stages of granulation using spherical ATO particles. In that case, the granules had a binder-rich core that was surrounded by a continuous deposition of particles, and there was no evidence of coalesced nuclei. If these examples are representative of the entire granule batch, then it may be inferred that for spherical particles, the small granule nuclei and the large binder-rich surface-smooth granules form simultaneously but independently. In the case of acicular particles, the presence of nuclei inside the large surface-smooth granules formed at early stages in the granulation process suggests that formation of nuclei and the formation of large smooth granules are sequential. This in turn suggests faster growth mechanics, where nuclei form prior to one minute mixing and are then incorporated into the larger structures observed here.

The internal structure of the individual granule nuclei was also different to that of nuclei containing spherical ATO (see Fig. 6.3(b)). In the case of spherical ATO the cross-sectional image of the nucleus could be split into two phases, particle or (air-filled) pore. For acicular ATO nuclei a third phase was also present in the form of binder-filled pores. For example, in region A in Fig. 6.6(d) the voids between particles are filled with binder. In region B the pores remain empty. The porosity algorithm as described in chapter 4 was modified in order to discount these binder-filled pores. Here, an estimated porosity was measured by changing the threshold value between 50 and 70. At 50, no binder-filled pores were included in the calculation. At a threshold value of 70, all unfilled pores and some binder-filled pores were included. The true porosity lies between the porosity calculated at these two threshold values and was calculated to be between 6 % and 14 %. Even at the highest value, this porosity is lower than the corresponding porosity for spherical ATO nuclei, which was 20 $\pm$ 2 %. This can be attributed to the presence of the binder in the majority of the pores between particles.

6.2.3 Comparison between spherical and acicular nuclei

Here, granule nuclei are of most interest because they fall within the size criteria required for the incorporation of the granules into the resistive touchscreen. For this application, the granules should ideally be less than 10 µm in size. The granule nuclei produced at 1 and 2 minutes for both spherical and acicular ATO granules fall mainly within this size range. However, the degree of agglomeration of the acicular ATO nuclei was significantly higher

than for the spherical nuclei and this is suggestive of a strong cohesive nature in the former case. This could partly be due to the shape of the constituent particles. The length of the acicular rods was 0.2–2 µm and protrusions from the granule surface may promote interlocking between adjacent nuclei. SEM images of the surfaces of both spherical and acicular nuclei are compared in Fig. 6.7, where the greater surface roughness of the acicular granules is evident. The heavily agglomerated nature of the ATO nanoparticle granules is not conducive to efficient dispersion when the granules are subsequently incorporated into the transparent, pressure-sensitive ink. In this regard, nuclei comprising spherical ATO particles may be most beneficial.

Furthermore, the granules comprising spherical ATO particles showed slower growth kinetics. The bimodal distribution produced at early granulation times is due to poor binder distribution as a result of the immersion mechanism of nucleation, and FIB analysis showed that large granules have a high binder content. Granule nuclei remain until the period of induction growth ends, in this case after 10 minutes in the DAC. During induction the nuclei become more surface smooth. FIB analysis showed a homogeneous internal structure with an average porosity of 20 ± 2 %. For granules comprising acicular ATO particles, fast growth occurred by coalescence and layering from early stages of granulation. Granule nuclei were formed after 1 minute but were heavily agglomerated. FIB analysis of larger granules showed they consisted of both coalesced nuclei and large binder-rich regions. The average porosity of the individual nuclei was estimated to be between 6 and 14 %, which is lower than for spherical ATO particles. This was due to the presence of binder-filled pores and is suggestive of energetically favourable wetting between binder and particle. The induction period was much shorter as granule coalescence produced very large structures after just 2 minutes. Granule

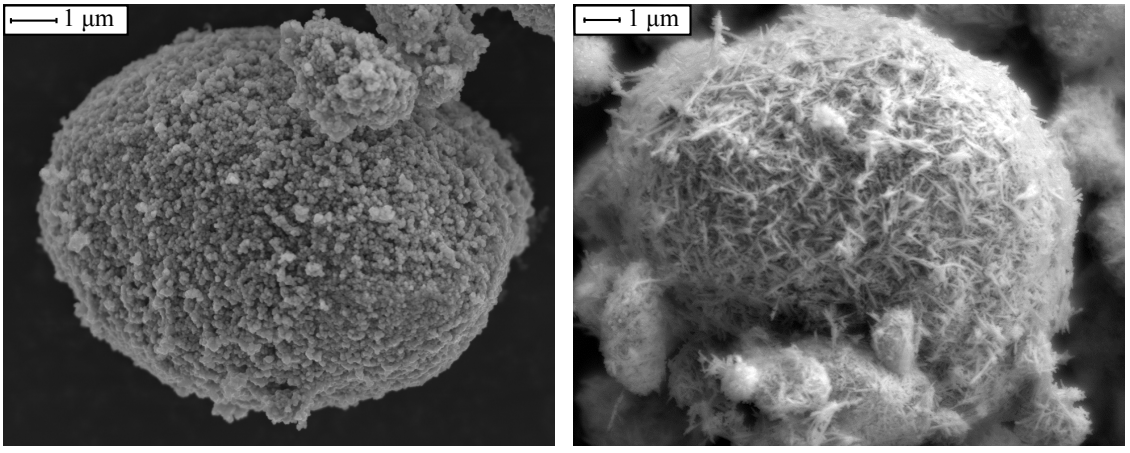

(a) (b)

FIGURE 6.7: SEM images showing surface detail of granule nuclei comprising 10 % silicone binder and (a) spherical ATO nanoparticles (b) acicular spherical nanoparticles, produced after 1 minute mixing at 2000 rpm in the DAC.

porosity is believed to have some importance for the application of nanocomposite granules in a pressure sensitive resistive layer, as it may lead to compressibility of the granule. For this reason, and the greater degree of control possible for spherical granules due to the longer induction phase, spherical ATO particles are used henceforth for all future granules.

6.3 Effect of binder type on granulation mechanisms and granule fracture strength

To investigate the effect of granulating with different binders, spherical ATO particles were combined with carbon-based, water-based and silicone binders, the properties of which were detailed in chapter 4. Here, changing the binder type alters two process variables. Firstly, each binder has a different chemical composition and hence can affect the wetting kinetics between binder and particle. Secondly, each binder had a different viscosity. The carbon and water-based binders had relatively low viscosities of 5.5 and 4.3 Pa s respectively. The two-part addition cure silicone binder had a much larger viscosity of 37 Pa s. In the literature, high viscosity silicone fluids were defined as having a viscosity greater than 1 Pa s [119]. Above this value, it is predicted that the viscous force contribution to the strength of dynamic liquid bridges formed between particles outweighs the capillary force from the surface tension of the binder, and leads to a slower rate of consolidation.

Each binder was granulated with spherical ATO at a ratio of 10 % binder to particle mass, at a speed of 2000 rpm for mixing times up to 10 minutes. Representative SEM images from each stage in the granulation process for each binder are compared in Fig. 6.8. Fig. 6.9 shows the corresponding GSD and CGSD at each mixing time. The granulation process for granules containing silicone binder mixed at 2000 rpm in the DAC was previously reported in section 6.2.1. SEM images are also shown in Fig. 6.8(i) to Fig. 6.8(l) for a qualitative comparison with the other binders used. Similarly, the GSD for mixing times up to 10 minutes were previously reported in Fig. 6.2. Note that in the GSD histograms reported here, all granules greater than 15 µm in size are represented by the last column.

For each type of binder, granule nuclei are produced at early stages of granulation after 2 minutes. Fig. 6.8(a), 6.8(e) and 6.8(i) show SEM images of the granule nuclei for carbon-based, water-based and silicone binders respectively. At this stage, the GSD as shown in Fig. 6.9(a) show close similarity. For carbon-based binder a peak in the distribution is spread over the size range of 2–6 µm whilst for water-based and silicone binder a peak is observed at 2–3 and 3–4 µm respectively. The CGSD shows that granules containing silicone binder are on average smaller than for carbon and water-based binders. Agglomerations of granule nuclei are relatively common during these early stages for each binder type, however the

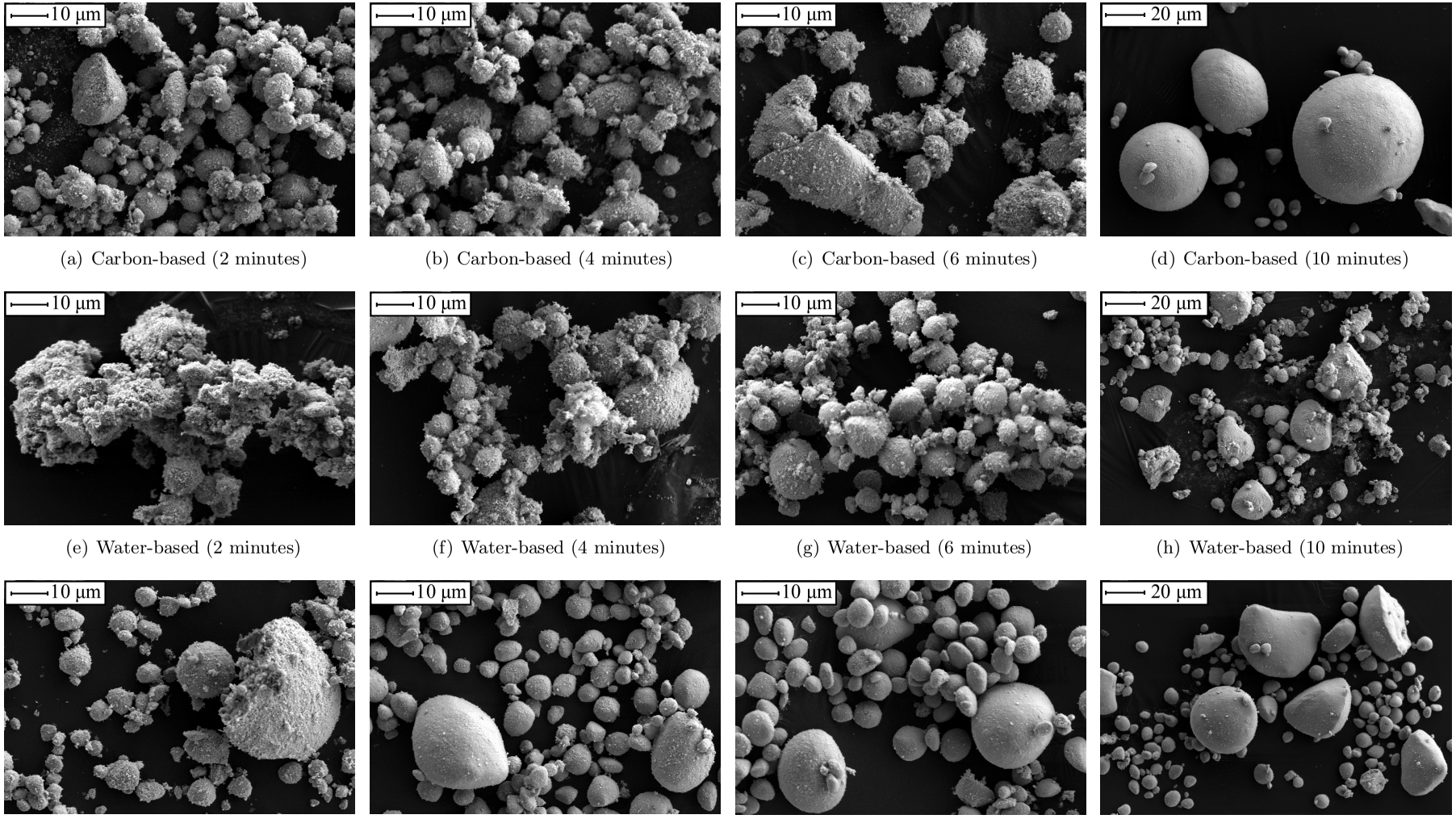

(a) Carbon-based (2 minutes) (b) Carbon-based (4 minutes) (c) Carbon-based (6 minutes) (d) Carbon-based (10 minutes)

(e) Water-based (2 minutes) (f) Water-based (4 minutes) (g) Water-based (6 minutes) (h) Water-based (10 minutes)

(i) Silicone (2 minutes) (j) Silicone (4 minutes) (k) Silicone (6 minutes) (l) Silicone (10 minutes)

FIGURE 6.8: SEM images of granules comprising spherical ATO particles and (a)–(d) carbon based binder, (e)–(h) water-based binder and (i)–(l) silicone binder, granulated at a speed of 2000 rpm in the DAC for 2, 4, 6 and 10 minutes.

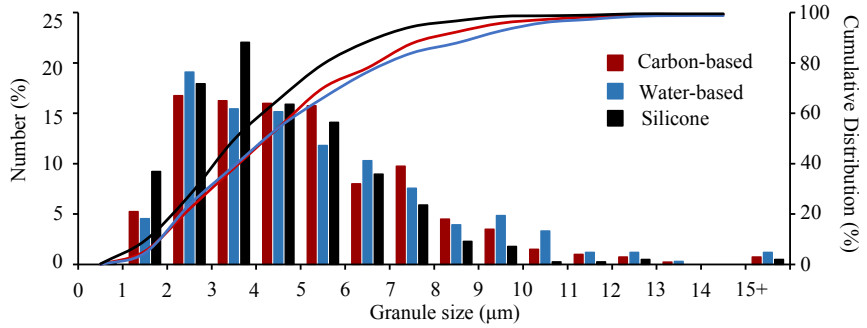

(a) 2 minutes

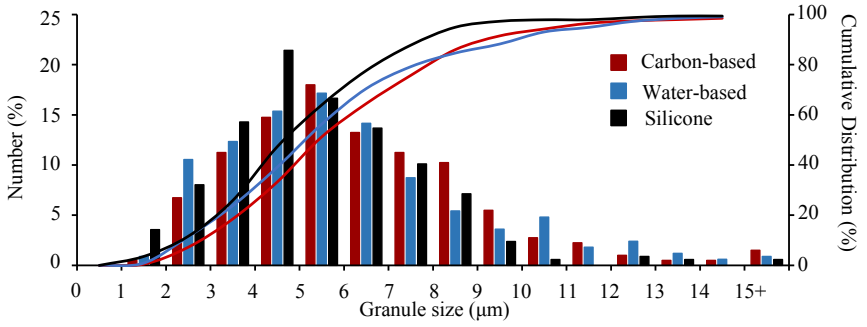

(b) 4 minutes

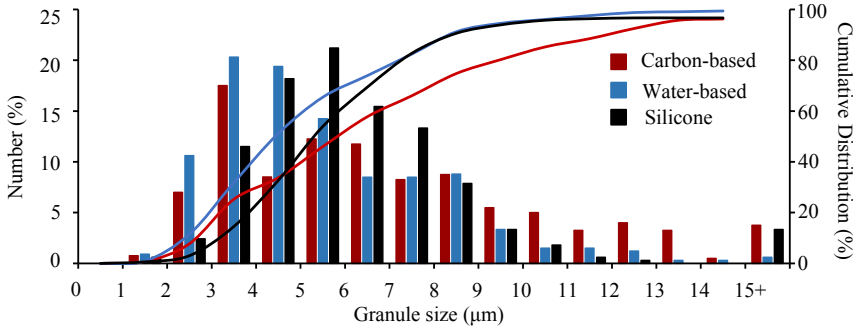

(c) 6 minutes

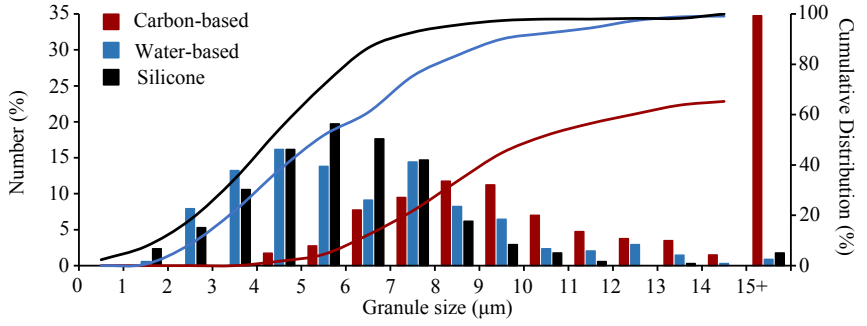

(d) 10 minutes

FIGURE 6.9: Graphs showing the GSD and cumulative size distributions for granules comprising spherical ATO nanoparticles with either carbon-based, water-based or silicone binder, produced after (a) 2 minutes (b) 4 minutes (c) 6 minutes and (d) 10 minutes.

water-based nuclei seemed to show the highest levels of agglomeration. Large granules above 15 µm in size are found to occur for all binder types, which is a typical occurrence related to poor binder distribution in early stages of granulation, as previously discussed.

After 4 minutes, the GSD as shown in Fig. 6.9(b) are still very similar. Some growth has occurred, indicated by the shift of the modal value to higher granule sizes. Here, silicone binder produces a peak at 4–5 µm whilst carbon and water-based binders produce a peak at 5–6 µm. Only after 6 minutes mixing in the DAC do the granules show any significant differences, as can be seen in Fig. 6.9(c). The number of larger granules, that is those above 15 µm which can be said to have 'outgrown' the nucleation stage, has increased for silicone and carbon-based binder but still remains low for water-based binder. For the latter case there remains a strong peak in the GSD at 3–4 µm indicating the prevalence of granule nuclei at this stage. The increase in the number of large (non-nuclear) granules indicates the conclusion of the induction process, where consolidation squeezes liquid binder to the granule surface and causes the onset of rapid growth. Here, it can be inferred that water-based binder results in a longer induction stage.

After 10 minutes, rapid growth has occurred for granules containing the carbon-based binder, as can be seen by the large peak at granule sizes larger than 15 µm in Fig. 6.9(d). There is also a shift towards larger granule sizes for those less than 15 µm in size compared to water-based and silicone binders. The corresponding SEM image in Fig. 6.8(d) shows a bimodal distribution of granule sizes, where large near-spherical granules are produced. Whilst an increase in large non-nuclear granules is also seen in the case of the silicone binder, it is to a lesser extent. It has been shown previously that in this case, rapid growth occurs at 15 minutes mixing (as shown in Fig. 6.1(f) and the corresponding GSD in Fig. 6.2).

Fig. 6.10 shows the evolution of the percentile values D_{10}, D_{50} and D_{90} for each binder type as a function of mixing time. The data points represent the median value (D_{50}) whilst the vertical bars represent the D_{10} and D_{90} values. This provides further support of the theory that induction growth occurs soonest for carbon-based binder and after 10 minutes for both water-based and silicone binders. During induction, little or no growth of the granule nuclei occurs and the span of the distribution is narrow because in most cases D_{10}, D_{50} and D_{90} all lie below 10 µm. However, for carbon-based binder rapid growth had occurred after 10 minutes, leading to an increase in D_{90} to 63 µm, whereas D_{10} and D_{50} remain low at 7 and 11 µm respectively. This is strong indication of either a polydisperse or a bimodal distribution, where a significant fraction of granules are greater than 10 µm in size.

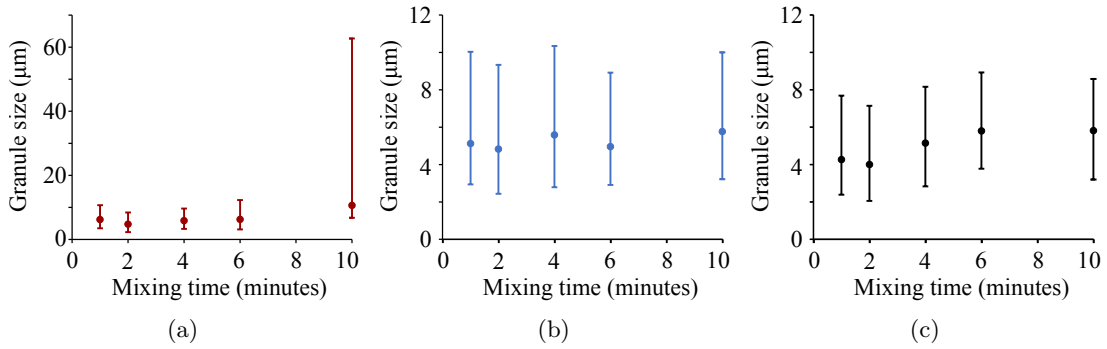

FIGURE 6.10: Graphs showing the percentile values of the GSD for granules produced using (a) carbon-based, (b) water-based and (c) silicone binder with spherical ATO particles for mixing times up to 10 minutes. The data points show the median value ($D(50)$) and the positive and negative vertical bars represent the $D(90)$ and $D(10)$ values respectively.

6.3.1 Effect of binder type on compressive fracture strength of granules

Granules comprising 10 % binder (carbon-based, water-based and silicone) and spherical ATO nanoparticles, mixed at 10 minutes in the DAC at 2000 rpm, were assessed for their fracture strength using the NanoCrush test facility as described in chapter 4. The fracture strength indicates the maximum force that can be applied to the granule before breakage occurs. This indirectly relates to the response of the granule-containing layer in the resistive touch interface which is the focus of the second part of this thesis. Here, granule breakage due to repeated or high-intensity testing is disadvantageous as it can affect the stability of the pressure-sensitive resistance response of the layer.

The granules were selected in the sieve fraction of 75–100 µm. Fig. 6.11(a) shows a typical force-displacement curve obtained when operating the NanoCrush equipment, in this case for a carbon-based granule. Initially, the test was performed with no granule present in order to measure the distance from the sample probe to the surface of the glass slide. This distance is shown as a dotted line at a displacement of 350 µm and allows an estimation of the granule size in subsequent tests. During the test, force was applied to the sample probe, causing downward displacement onto the granule surface. At an applied force of approximately 8 mN the probe contacts the granule surface. The granule size can be estimated at this point and in this example was 117 µm. After initial contact, the displacement rate decreased as the granule was compressed by the probe. At 19 mN applied force, the displacement shows a sudden increase which indicated fracture of the granule. After this, the granule fragments were then compressed by the probe. Fig. 6.11(b) shows a close-up of the compressive region between 8 and 19 mN. Theoretically, the slope of the associated stress-strain curve can be used to determine the mechanical properties of the granules including the Young's (elastic) modulus, the plastic yield strength and the hardness, as described previously in chapter 4.

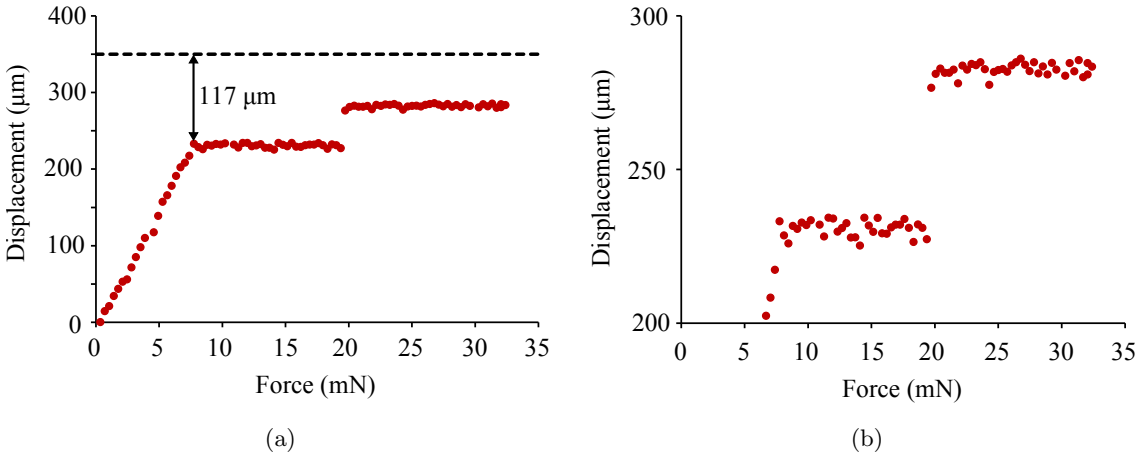

FIGURE 6.11: Graphs showing (a) force-displacement data obtained for a granule containing carbon-based binder, where the dashed line represents the surface of the sample stage and can be used to obtain an estimate of the granule size, in this case 117 µm. Initially the probe is displaced towards the granule and contact is made at an applied force of 8 mN. At 19 mN the large increase in displacement implies granule fracture. (b) Close-up of the region where load is applied to the granule up until the fracture point.

Unfortunately, here the noise on the displacement (measured by a LVDT coil) means that extraction of the gradient is not possible. However, by the near-horizontal appearance of the force-displacement curve it can be inferred that the elastic modulus is very high. The Young's modulus was roughly estimated by fitting a line of best fit to the corresponding stress-strain graph using a least squares regression model. From calculation of the gradient, a value of 2 GPa $\pm$ 3 GPa was estimated. A maximum Young's Modulus of 5 GPa can be inferred, however the minimum value cannot be determined due to the large error value. Furthermore, this average value was roughly constant for a range of granule properties and process conditions, and any distinction between the mechanical properties of granules produced using various operating variables or material properties is beyond the capabilities of the NanoCrush test equipment for this particular application. In the literature, the Young's modulus of granules have been reported in the range of 1.2 GPa for glass beads granulated with PVP polymer binder [194], 2.5–12.6 GPa for a range of granules used in the coating industry [196], 2–12 MPa for aluminosilicate zeolite [200] and 0.3–1.8 GPa for a range of pharmaceutical excipients [203].

The fracture strength of the granules can be read from the force-displacement data as the point at which the displacement rapidly increases, due to brittle failure of the granules (for the granule in Fig. 6.11(a) this is 19 mN). For each binder type used, the fracture strength of 5 granules was determined. The results are plotted in Fig. 6.12. SEM images of a representative granule in the size range 75–100 µm are also shown.

Granules containing silicone binder exhibit a greater fracture strength, with an average value of 33 $\pm$ 6 mN. Granules comprising carbon-based and water-based binders had an average

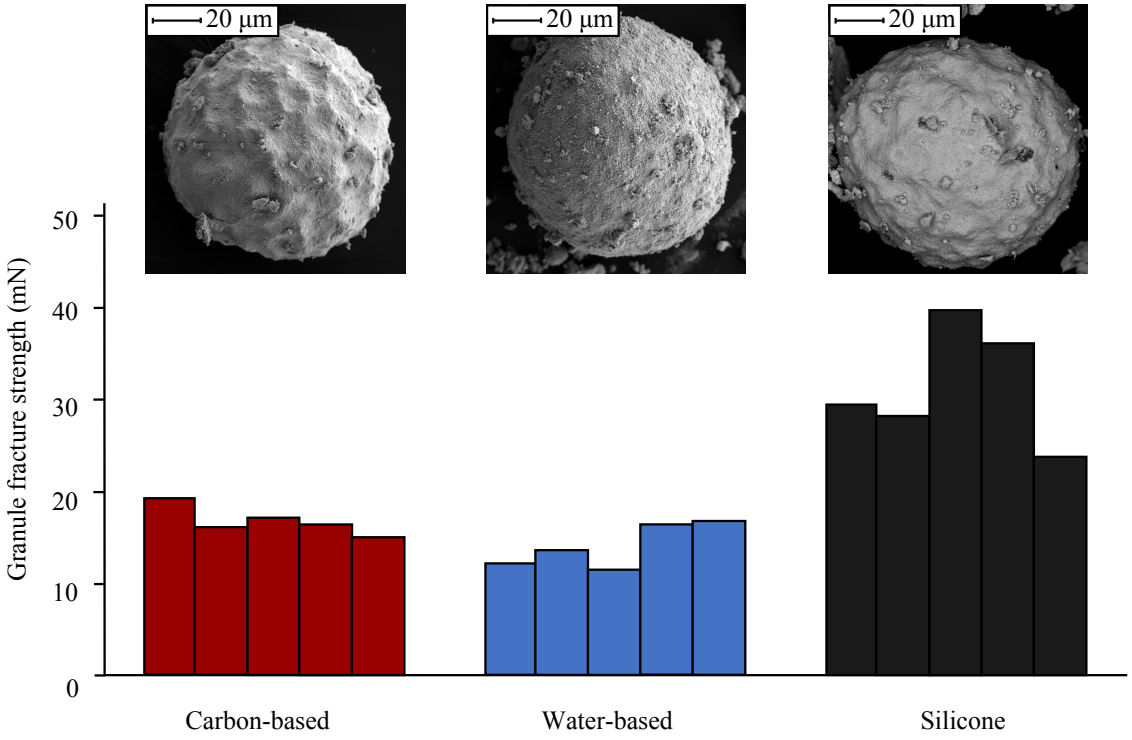

FIGURE 6.12: Granule fracture strength of granules comprising carbon-based, water-based and silicone binder with spherical ATO nanoparticles, granulated at 2000 rpm in the DAC for 10 minutes.

fracture strength of 17 ± 2 mN and 14 ± 2 mN respectively. It can be concluded that the granules containing silicone binder, in the size range 75–100 µm can withstand greater applied force before fracture than when using carbon and water-based binders.

The higher strength exhibited by granules containing silicone binder could be caused by either the difference in surface chemistry between binder and particle, or the large viscosity exhibited by the silicone binder. The average granule strength is plotted as a function of binder viscosity in Fig. 6.13, which shows that increased binder viscosity leads to an increase in the average fracture strength exhibited by the granules. The dashed line shows a logarithmic dependency.

Rahmanian *et al.*, investigated the effect of PEG binder viscosity on the granulation of calcium carbonate powders [140]. Here, increasing the viscosity of the PEG aqueous solution in the range 0.100–0.424 Pa s decreased the average strength of the granules when mixing at low speed in a high-shear mixer. This was attributed to the dominance of decreased granule deformability over the increased strength of dynamic liquid bridges which occurs when binder viscosity is increased. The decreased granule deformability lead to a decrease in the rate of consolidation, a decrease in the granule porosity and hence a lower fracture strength. This is in line with the predictions of Keningley *et al.* who predicted that an increase in viscosity would decrease the consolidation rate [119].

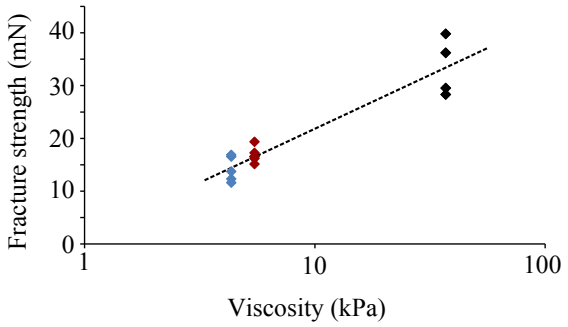

FIGURE 6.13: Granule fracture strength as a function of the measured viscosity of each binder used in granulation. Here, carbon-based, water-based and silicone binders are represented by the red, blue and black data points respectively. The dashed line shows a logarithmic dependency between strength and viscosity.

However, the results presented here are in opposition to this theory. Here, the highest viscosity binder produces granules with the greatest fracture strength. Later in chapter 7 it is also shown that the porosity of silicone-containing granules decreases as a function of mixing time, showing that consolidation is occurring and a low porosity is reached after 10 minutes of mixing. This is perhaps due to the layering mechanism which occurred after longer mixing times. The highly intensive mixing process in the DAC may play some part in counteracting the retarded rate of consolidation expected for high-viscosity binders, however further evidence is needed to confirm this.

When granules are dried or cured, liquid bridges between the constituent particles solidify, producing permanent bonds between the particles which contribute to the granule strength. Hence the formation of liquid bridges through coalescence is also an important mechanism to consider. In the model proposed by Ennis *et al.*, as described by equation 3.5, coalescence is promoted by a low Stokes deformation number, which in turn is promoted by a high binder viscosity. Hence a high viscosity may lead to increased granule strength through the number of inter-particle solid bridges. Of course, this analysis is simplified by neglecting the wetting characteristics of each binder. This itself may play a role in the observed difference in granule fracture strength with each binder type used. However, in order to understand this effect it is necessary to determine the exact wetting coefficients and contact angles between spherical ATO nanoparticles and each of the liquid binders, which was beyond the scope of this thesis.

For the purposes of this thesis, the granules which were incorporated into the resistive touchscreen devices comprised spherical ATO nanoparticles and silicone binder. This was largely due to the increased fracture strength exhibited by the granules which was believed to promote high durability in the resultant touchscreen. Granules comprising carbon-based granules were not carried forwards into this stage, because of two reasons. Firstly, the faster growth kinetics when compared to silicone binder meant a lesser degree of control over the nucleation

stage of granulation. Secondly, the carbon-based binder was also used as a base material in the transparent granule-containing ink and it was not confirmed whether the granules would redissolve when dispersed in the same material. Despite the lower fracture strength of the water-based granules, the growth kinetics were favourable to the control of nucleation, and whilst not further investigated in this thesis, this should not be fully discounted in any future investigations.

6.4 Effect of binder quantity on granulation

To investigate the effect of the binder quantity on the resultant granule properties, silicone binder at mass percentages of 2.5, 5.0, 10.0, 15.0 and 20 % were granulated with spherical ATO nanoparticles, at 3500 rpm in the DAC. Fig. 6.14 shows representative SEM images and the corresponding GSDs for granules produced after 1 minute for each binder quantity.

As binder quantity increases, the GSDs are shifted toward larger granule sizes. For 2.5, 5.0 and 10.0 % of binder, a minimum of 97 % of the number of granules measured are less than 10 µm in size. With 15.0 and 20.0 % silicone, only 64 % and 42 % are less than 10 µm in size, respectively. Therefore, in terms of nuclei production, less binder is favourable. The granule growth was further monitored for up to 10 minutes of mixing time. Fig. 6.15 shows the change in the median granule size, D_{50}, for each binder amount as a function of time.

For binder fractions up to and including 10.0 %, the growth behaviour obeys a similar trend. After 1 minute, binder nuclei are formed, after which rapid growth occurs and a peak in the median value is seen at 6 minutes. There appears to be no correlation between the amount of silicone binder and the extent of the growth between 1 and 2 minutes, where it can be seen that at 2 minutes granules containing 2.5 % binder have the largest median size, followed by 10.0 and then 5.0 % binder. After 6 minutes, the median value decreases indicating the dominance of a breakage mechanism over subsequent granule growth. Evidence of breakage was observed via SEM imaging; as an example Fig. 6.16 shows the presence of granule fragments amongst whole, spherical granules after mixing for 6 minutes for 2.5 %, 5.0 % and 10.0 % binder. Whilst such granule fragments have been observed at all mixing times above 2 minutes, after 6 minutes the proportion of fragments outweighs that of large, intact granules and the average size of the distribution decreases. Furthermore, the intact granules produced at 6 minutes show indented surfaces. The presence of surface indentations is explored further in chapter 7, however it should be noted here that the surface indentations appear deeper and are more pronounced for 2.5 % binder and are the least pronounced for 10.0 % binder. If the surface indentations are caused by plastic deformation during collisions it can be inferred that granules containing 2.5 % binder are the most deformable. Wet granule strength is controlled by two competing mechanisms. Viscous force contributions

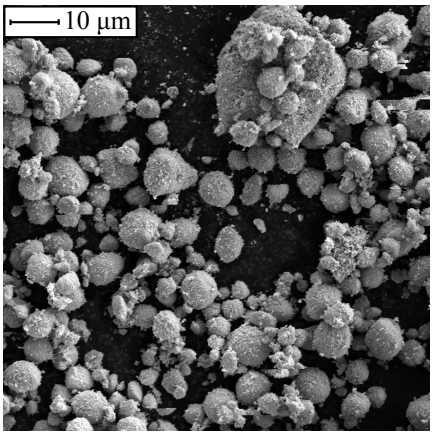

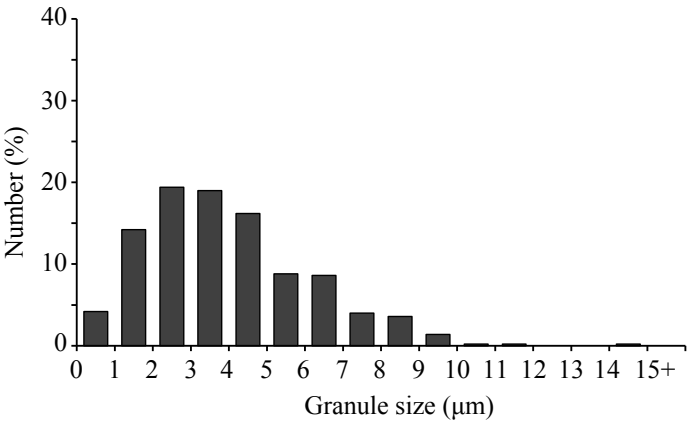

(a) 2.5 % silicone

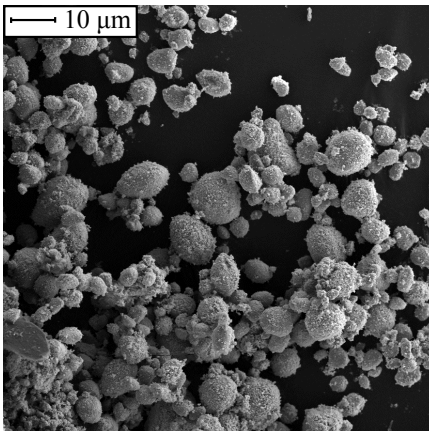

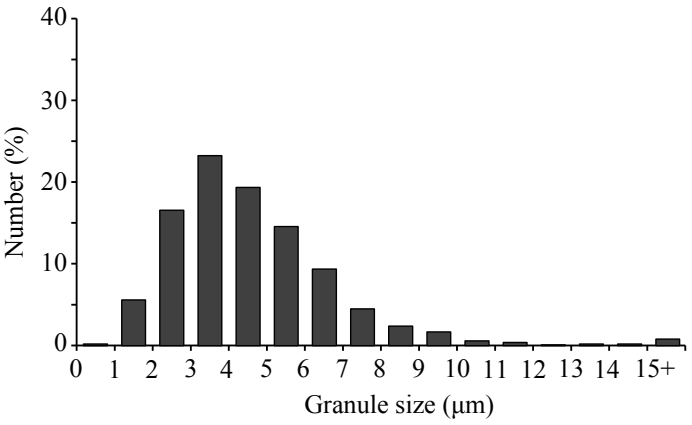

(b) 5.0 % silicone

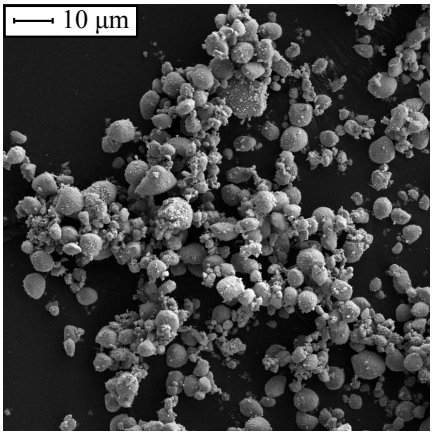

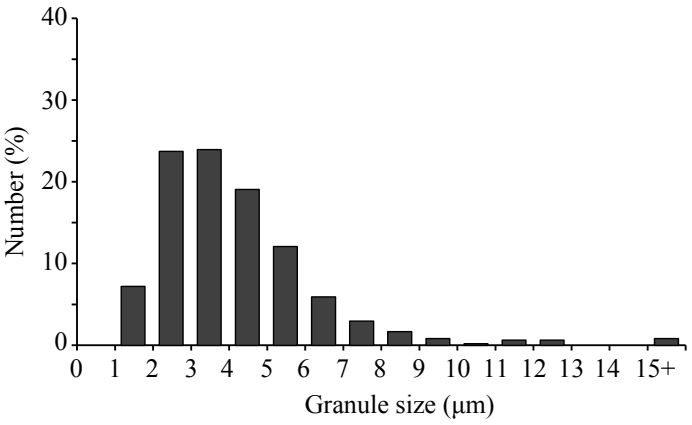

(c) 10.0 % silicone

FIGURE 6.14: SEM images and GSD for granules produced after 1 minute at a speed of 3500 rpm, where the granules comprise spherical ATO nanoparticles and (a) 2.5 % (b) 5.0 % (c) 10.0 % (d) 15.0 % and (e) 20.0 % silicone binder. Figure is continued overleaf.

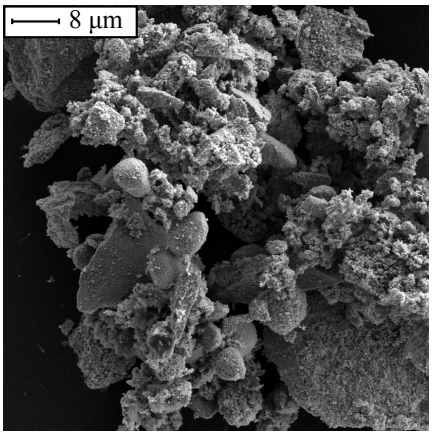

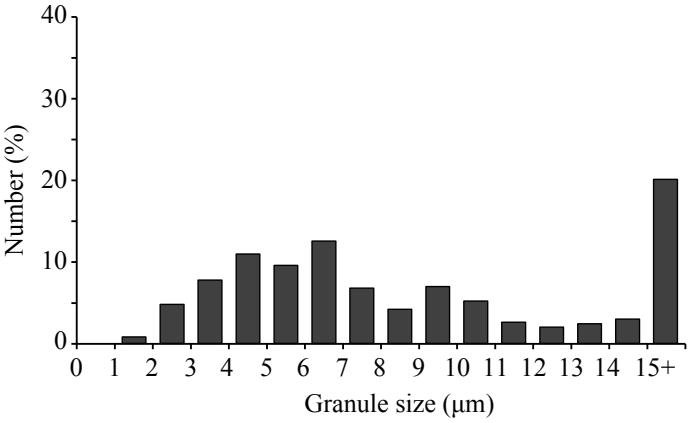

(d) 15.0 % silicone

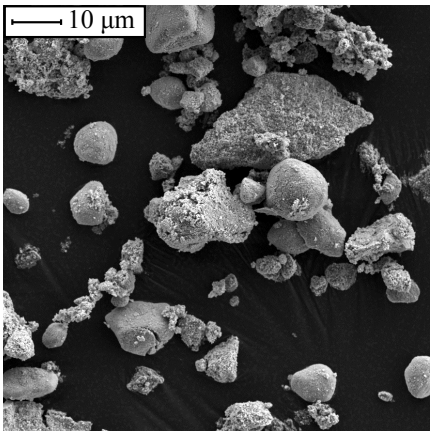

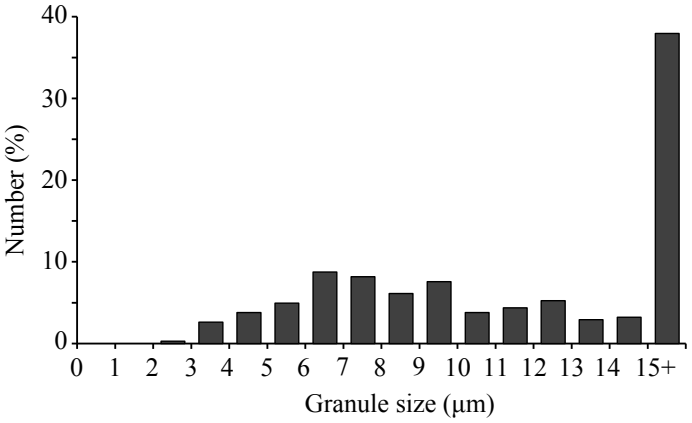

(e) 20.0 % silicone

FIGURE 6.14: Continued

to the dynamic bridge strength dominate the wet granule strength at high viscosities, and resist granule deformation. However, for decreasing binder content the number of these liquid bridges is reduced and thus the granule may be expected to be more deformable.

For high binder quantities of 15.0 % and 20.0 %, a different growth pattern is observed. In the case of 15.0 % binder, the growth appears to be slow and steady throughout the entire granulation process. After an apparent sharp increase after 2 minutes, the median value for 20.0 % silicone also follows this trend. Analysis of the SEM images shows that the reason for the small median granule sizes is the overwhelming prevalence of fragmented material, an example of which is shown in Fig. 6.17(a) and Fig. 6.17(b), produced after 6 minutes for 15.0 and 20.0 % silicone respectively.

As explored in chapter 3, by increasing the binder content in a granulation process it is expected that the inter-particle frictional forces are lessened, due to the increase in lubrication between primary particles. Whilst this aids granule consolidation, it must overcome the conflicting increase in the viscous force of the liquid bridges between particles. For high

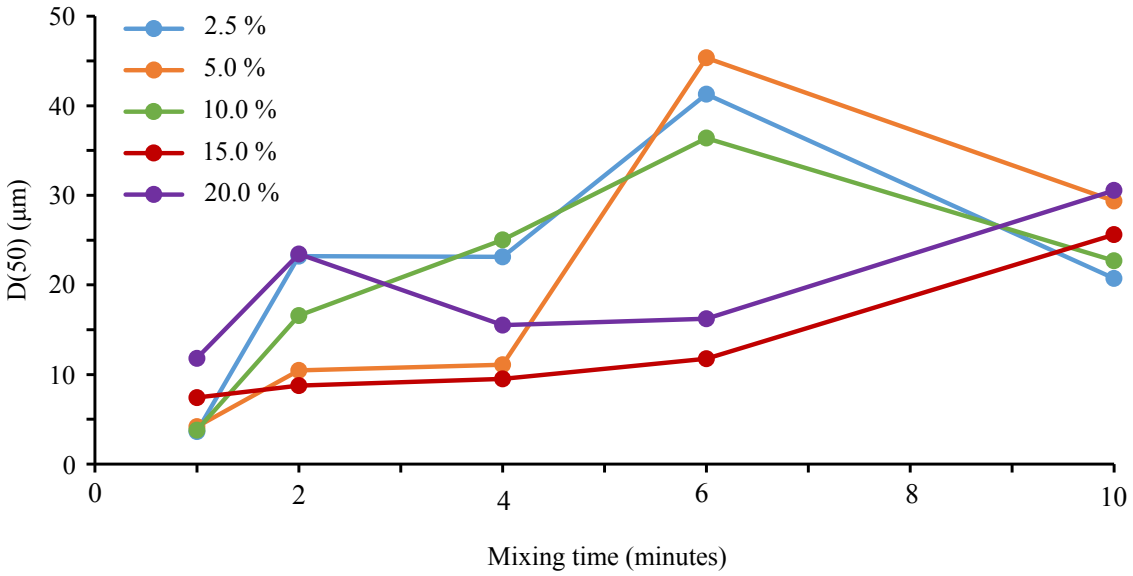

FIGURE 6.15: Graph showing the median granule size, D(50), as a function of granulation time for granules comprising spherical ATO nanoparticles and 2.5 %, 5.0 %, 10.0 %, 15.0 % and 20.0 % silicone binder.

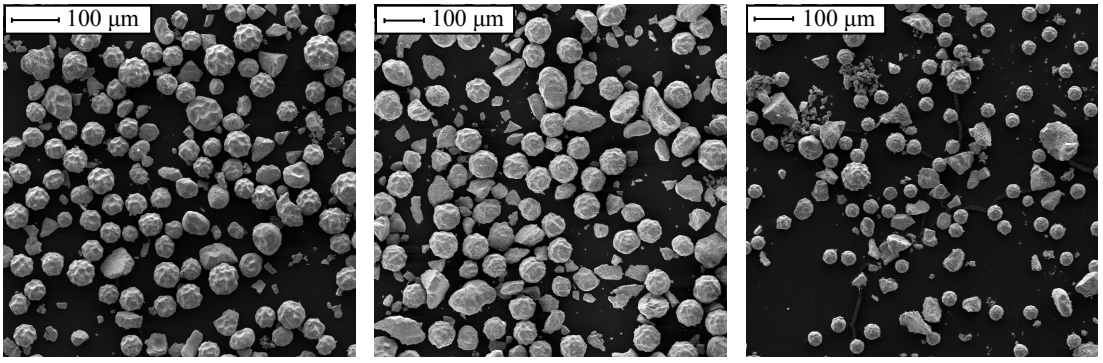

(a) (b) (c)

FIGURE 6.16: SEM images of granules produced after 6 minutes, where the granules comprise (a) 2.5 % (b) 5.0 % and (c) 10.0 % silicone binder.

viscosity binder it is generally accepted that this is not the case. In this case, it is expected that increasing the binder amount would act to decrease the rate of consolidation and thus extend the induction phase. Keningley *et al.* attribute this reasoning to their observed result that for silicone binder viscosities of 12.2 and 55.7 Pa s, a maximum liquid-to-solid ratio of 0.8 and 1.1 still produced a stable granule formulation [119]. This is because low consolidation rates are unlikely to result in surface-wet granules. The lack of a stable granulation formation observed here is contrary to this result, however this may be partially due to the high energy mixing dynamics of the DAC. In Keningley's experiment a low impeller speed of 1000 rpm, corresponding to an impeller tip speed of 10 m s^{-1}, was used. Here, at 3500 rpm the tangential velocity of the main rotation is 29 m s^{-1} and this promotes a faster rate of consolidation

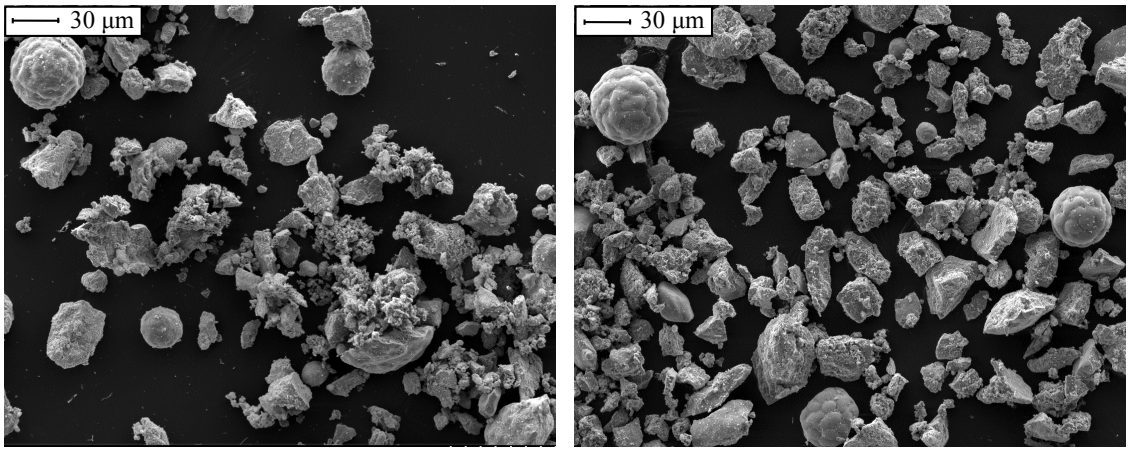

(a) (b)

FIGURE 6.17: SEM images of granules produced after 6 minutes, where the granules comprise (a) 15.0 % (b) 20.0 % silicone binder. Here, a large proportion of granule fragments result from breakage processes are observed.

through more frequent and higher energy collisions between granules. This effect may be enough to counteract the slow rate of consolidation and produce unstable granule formulations at high binder contents.

Whilst the growth process is not fully understood, it is evident that high binder contents are not conducive to the controlled production of granule nuclei less than 10 µm in size, which are required for incorporation into the resistive sensor that is the focus of this thesis. For the remainder of this thesis, granules were made with 10 % silicone binder. This was a compromise between a stable granule formulation and limiting the propensity for breakage. Additionally, with a higher binder content there is an increased fraction of electrically insulating material, which may allow modification of the conductive properties of the nanocomposite granule.

However, in future work lower binder quantities should not be discounted. Furthermore, the interplay between other process variables means that a binder content of 10 % will not always be optimal. For example, granulation at 2000 rpm, using 10 % silicone binder was reported earlier in section 6.2.1. Comparing the SEM images shown in Fig. 6.1(d) for 2000 rpm with Fig. 6.16(c) for 3500 rpm clearly demonstrates the effect of changing the speed of the DAC whilst maintaining the binder quantity. It is also worthwhile to note that the trends observed when granulating a range of binder concentrations at 3500 rpm may be very different to the trends produced when granulating at 2000 rpm.

6.5 Chapter summary

This chapter described the effect that changing the primary particle shape, and the type and quantity of the liquid binder, had on the resulting granules, in terms of their size distribution, porosity and mechanical properties. It is important to understand the effects of these parameters in order to fully appreciate the granulation process. From these results, a 'recipe' for producing granules optimised for incorporation into the resistive touchscreen which is the focus of this thesis. From this recipe, precise control over the granule nuclei may be achieved through changing the operating conditions of the DAC, which is investigated in the next chapter.

Here, it was found that granulating spherical ATO nanoparticles resulted in a well-defined granulation process, with a long induction stage when mixing at 2000 rpm. Significant granule growth did not occur until after 15 minutes and prior to this point the majority of granule nuclei were less than 10 µm in size. However, for acicular particles a different growth process occurred, where granule growth by the coalescence of nuclei was promoted during the early stages. These agglomerated nuclei are not conducive to effective dispersion when the granules are subsequently incorporated into the screen-printable ink. Granules containing silicone binder showed on average the largest fracture strength, compared to those comprising carbon and water-based binders. Furthermore, the growth kinetics were also altered where rapid growth of carbon-based binder occurred soonest. Silicone binder was deemed preferential for this application because of the higher fracture strength of the resultant granules. Lastly, there was a complex reaction to the quantity of silicone binder used for granulation at 3500 rpm. For binder quantities up to and including 10 % a stable, predictable granulation process of nucleation, growth and then breakage occurred. However for larger binder quantities an unstable formulation was produced where granule breakage dominated even at early stages of the process.

Chapter 7

Effect of Process Variables on Granule Structure and Morphology

7.1 Introduction

In the previous chapter, it was found that spherical ATO nanoparticles granulated with 10 % silicone binder were the optimum materials for a granulation process which was controllable and could be understood in terms of granulation theory. Here, this granule composition was further investigated by altering the operating variables, specifically the duration of the granulation process and the rotational speed of the DAC. Whilst some preliminary results for the evolution of granule size through time was presented early in chapter 6, here the results are extended to include the granule shape and surface-roughness, internal structure and the mechanical fracture strength as a function of granulation time, in sections 7.2.2, 7.2.3 and 7.2.4.

The effect of the rotational speed of the DAC granulator was investigated by changing the speed of the main rotation of the DAC in the range of 1600–3500 rpm (with tangential velocities of 13.4–29.3 $\mathrm{m\,s^{-1}}$). This corresponds to Froude numbers in the range 229–1095 and, as described in chapter 4, this has the potential to be far in excess of any Froude numbers reported in the granulation literature. This indicated that the centripetal acceleration of the DAC is extremely large and this contributes to the superior mixing properties of the DAC. In section 7.3.1, the effect of increasing the speed, and therefore the energy of the granulation process, was investigated and is linked to the induction growth of granule nuclei. The mechanical fracture strength as a function of speed is reported in section 7.3.2.

Finally, the temperature inside the DAC was monitored as a function of time. In the curing process, the cross-linking of the silicone binder can be accelerated by raising the temperature.

Therefore it was important to understand how a temperature increase during the temperature process may affect the properties of the silicone binder.

7.2 Time evolution of granule properties during granulation

7.2.1 Granule size and morphology as a function of time

The evolution of granule morphology and the GSD for spherical ATO nanoparticles granulated with 10 % binder at 2000 rpm was reported previously in chapter 6.2.1, where SEM images were shown in Fig. 6.1 and the GSD for each granulation time were compared in Fig. 6.2. For clarity, a summary of the key findings is also presented here.

Nuclei are formed after 1 minute of granulation from the initial contact between the nanoparticles and the silicone binder, where 97 % of the number of granules measured were less than 10 µm in size. The remainder of the granules were much larger, reaching sizes of up to 50 µm and indicating a bimodal size distribution. FIB cross-sectional analysis, shown in Fig. 6.3(c) and Fig. 6.3(d), revealed a binder-rich core which further supported the immersion mechanism of nucleation and poor binder distribution. Granule nuclei persisted for up to 10 minutes. Throughout this interval, the nuclei appeared increasingly surface smooth which indicated some level of compaction, perhaps caused by repeated collisions. On average, the nuclei size increased incrementally, evidenced by the shifting peak of the GSD from 4 µm at 1 and 2 minutes, to 5 µm after 4 minutes, and 6 µm after 6 and 10 minutes. Qualitatively, it was observed that the number of larger non-nuclear granules increased throughout this time.

After 15 minutes, rapid granule growth had occurred and the majority of granules were now larger than 10 µm. The peak of the GSD occurred at 24–30 µm and 76 % of the total number of granules were greater than 24 µm in size. After 20 minutes there was a strong peak at 27-33 µm where 80 % of granules are greater than 27 µm in size. Very few granule nuclei remained, and these sub-10 µm granules had an angular, jagged shape suggesting that they were fragments of a larger granule which had broken apart during granulation. Rapid growth was attributed to an induction mechanism. It was proposed that for times up to 15 minutes, granule consolidation caused binder to migrate towards the granule surface. During this process little growth occurred. When binder finally reached the surface, rapid growth occurred through either surface-wet coalescence or by a layering mechanism. Of course, this process does not occur simultaneously for all granules and the increase in the number of large non-nuclear granules up until 15 minutes can also be attributed to the induction process.

In the next section, the induction process is investigated further by monitoring the surface-roughness of the granule nuclei, as well as changes in the internal structure of granules before and after rapid growth has occurred.

7.2.2 Evolution of granule nuclei surface roughness and granule shape

Granule surface-roughness results from sub-micron protrusions on the granule surface. Surface-roughness was quantitatively assessed by measuring the ratio of d_{EQPC} to d_{PED} for granule nuclei, which assesses the roughness of the edge of the 2D projection of the granule shape. These diameters were defined in chapter 3. The magnification of the SEM images was maintained at 1500x, corresponding to a scale of 15 pixels per µm. For a perfect circle (and assuming infinitely small pixel size) the values of d_{EQPC} and d_{PED} are equal. With increasing surface roughness both d_{EQPC} and d_{PED} increase, however the effect is significantly larger for d_{PED}. Hence with increasing surface roughness the ratio $\frac{d_{PED}}{d_{EQPC}}$ is expected to increase.

Fig. 7.1(a) shows the average surface roughness as a function of granulation time up to 10 minutes, beyond which few granule nuclei remained. For each sample, 10 granule nuclei with $d_{f,max}$ in the range 4–13 µm, were analysed. The error on each measurement was taken as 0.05, which corresponded to the deviation from unity of $\frac{d_{PED}}{d_{EQPC}}$ for a pixellated circle of diameter 13 µm. However, the error bars shown here represent the minimum and maximum surface roughness measured for that particular sample and indicate the spread of the results. The ratio $\frac{d_{PED}}{d_{EQPC}}$ decreases with increasing granulation time, indicating that the granule surfaces do indeed become smoother with increasing time. A power-law relationship has been fitted to the data where the exponent is -0.08 ± 0.01. The error bars on the data also become narrower with increasing time, indicating a smaller spread in the measured smoothness values and therefore a greater degree of homogeneity of the granule surfaces. The measurable decrease in the surface roughness over time is evidence of granule compaction and smoothing through repeated collisions. At early granulation times, i.e. 1 and 2 minutes, primary particles may be loosely adhered onto the surface of a nucleus causing a high degree of roughness. With increasing time, and increasing number of collisions within the DAC, the nuclei surface becomes compacted resulting in a smoother surface. This is in line with theoretical models which suggest that granule consolidation increases with residence time in the granulating vessel. If consolidation of the nuclei is occurring then it is expected that the internal nuclei porosity would also decrease over time.

The aspect ratio can give an indication to the macro-scale shape of the nuclei. It is independent of the perimeter length and hence the surface roughness. The aspect ratio is the ratio of the major to the minor axis of an ellipse fitted to encompass the projected granule area. For a perfectly circular granule projection, the encompassing ellipse is also circular and

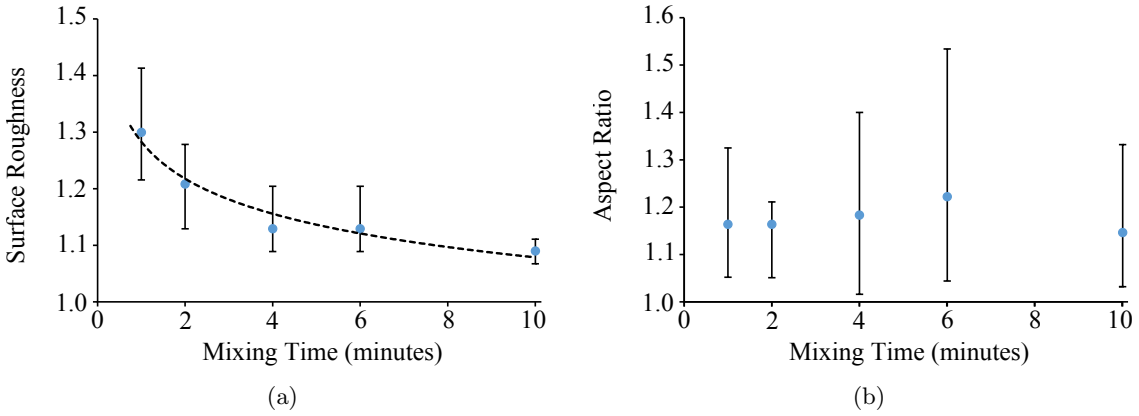

FIGURE 7.1: Graphs showing (a) the decrease in surface roughness with increasing mixing time, where the dotted line shows a power law relation with exponent -0.08 ± 0.01. (b) nuclei aspect ratio as a function of mixing time. There is no discernible change in nuclei shape over time, where the aspect ratio fluctuates around an average value of 1.2 ± 0.1.

the aspect ratio is 1. The larger the aspect ratio, the more elongated the particle shape. Fig. 7.1(b) shows the average aspect ratio as a function of granulation time up to 10 minutes. For granule nuclei, there is no discernible trend of changing shape over time and the aspect ratio varies within an average of 1.2 ± 0.1. This corresponds to the observed nuclei shape which is not spherical but rather a slightly elongated ellipsoid, regardless of granulation time.

7.2.3 Internal structure of granules as a function of time

7.2.3.1 Internal structure of granule nuclei

The internal structure of granule nuclei was investigated as a function of granulation time using FIB milling to obtain cross-sections of representative granules. The internal structure of a granule nucleus produced after 1 minute was previously shown in Fig. 6.3(a) and Fig. 6.3(b). FIB cross-sections for 4 and 6 minutes are shown in Fig. 7.2. Similar to structures formed after 1 minute, the pore network appears homogeneous across the entirety of the cross-sectioned surface. To calculate the average porosity, a minimum of three separate images from the central region of three different nuclei were analysed.

The pore size distribution is shown for 1, 4 and 6 minutes in Fig. 7.3(a), where d_{EQPC} of each pore was measured. The average porosity is plotted against time in the inset. The majority of the total number of pores measured have a d_{EQPC} in the range 10–30 nm. Pores with $d_{EQPC} < 30$ nm tend to be found within individual nanoparticle clusters. The distribution of these micro-pores in one FIB cross-section is shown in Fig. 7.3(b). These clusters are separated by larger dendritic pore networks, to form the overall nucleus. Such macro-pores,

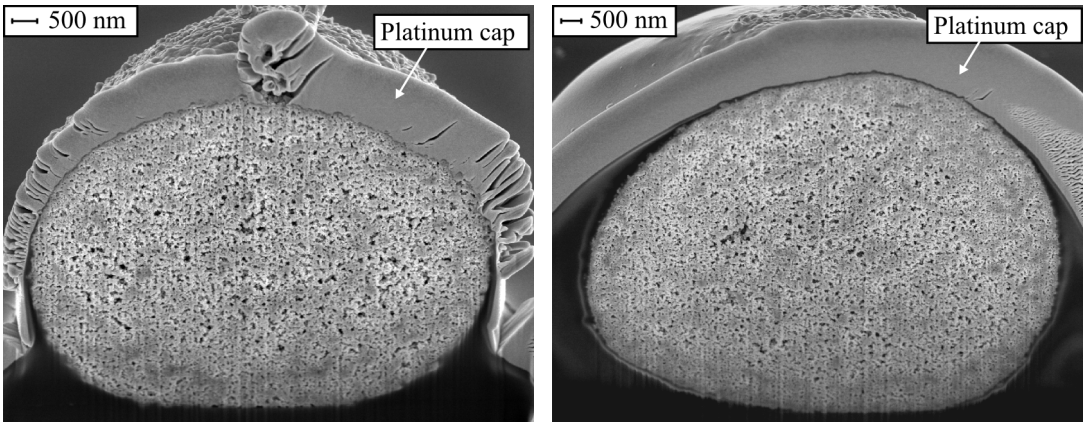

(a) (b)

FIGURE 7.2: SEM images showing a FIB-milled cross-section through granule nuclei, produced after (a) 4 minutes and (b) 6 minutes mixing in the DAC. The porosity appears homogeneous over the entire cross-sectioned surface.

defined as having $d_{EQPC} > 30$ nm, contribute significantly to the overall porosity and their distribution is highlighted in Fig. 7.3(c). For example, for the granule shown in Fig. 7.2(a) the overall porosity was 23.5 %, with 2.0 % from micro-pores and 21.5 % from macro-pores. The slight increase in pore size observed at 6 minutes is likely to be an artefact resulting from the limitations of the algorithm used to determine porosity. Whilst re-normalisation of the pixel value histogram does remove some discrepancy caused by difference in brightness and contrast, smaller or shallower pores can be under-represented if there is insufficient contrast between them and the surrounding particulate material.

The decrease in the average porosity between 1 and 4 minutes is further evidence of granule compaction, which was also responsible for decreasing the surface roughness of the nuclei. After 6 minutes, it appears that no further compaction occurs, although the surface roughness continues to decrease, as in Fig. 7.1(a). To understand this further, the porosity of the nuclei produced after 6 minutes was measured towards the edge of the granule. As an example, for one nucleus the central porosity (averaged across three locations) was 15.7 % whilst the porosity near to the granule surface (averaged across three locations) was 12.9 %. Here, granule compaction causes the greatest decrease in granule porosity near to the surface.

7.2.3.2 Internal structure of granules after induction

Granules produced after 15 minutes were cross-sectioned in order to better understand the growth mechanisms in the later stages of granulation. Rather than a uniform internal appearance, there was a greater variability between these granules, where the porosity was not constant throughout the granule. Fig. 7.4 shows a small selection of the observed internal

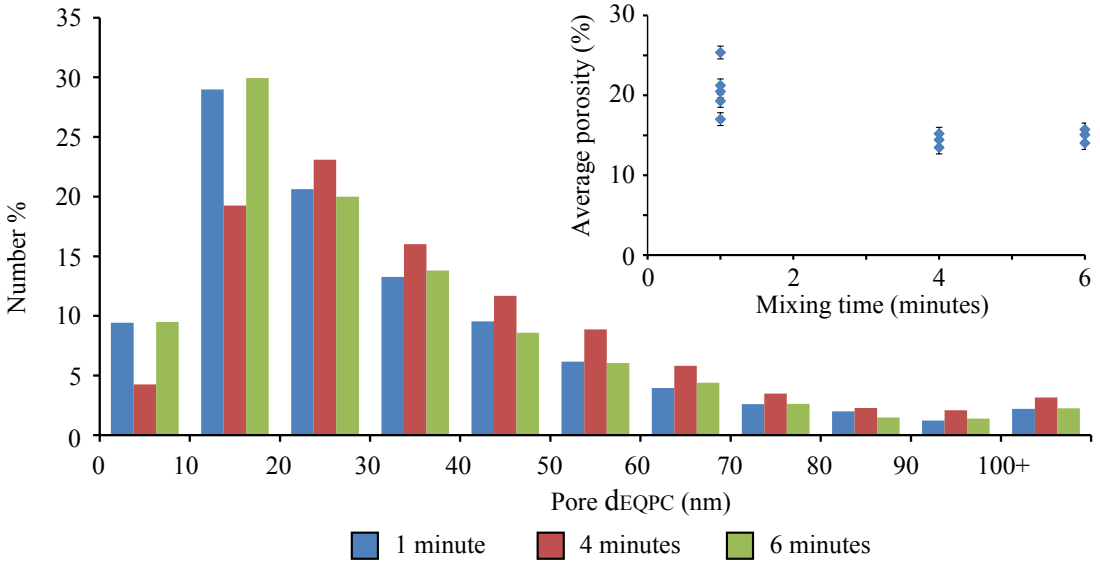

(a)

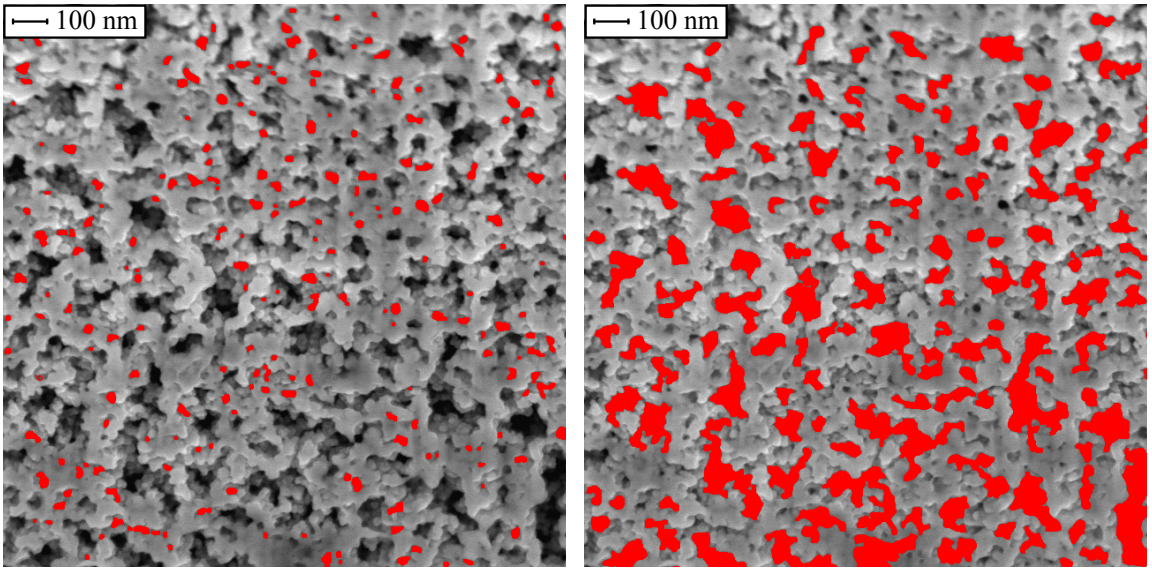

(b) (c)

FIGURE 7.3: (a) Graph showing the pore size distribution as a function of granulation time. The inset shows the change in average porosity as a function of mixing time. SEM images (b) and (c) show the distribution of micro-pores, with $d_{EQPC} < 30$ nm, and macro-pores, with $d_{EQPC} > 30$ nm, within a granule nucleus.

structures which were discovered. In Fig. 7.4(a) and Fig. 7.4(b), which show 66 and 47 µm granules produced after 10 minutes, the central region consists of several coalesced nuclei, regions of high binder content and large internal voids. In Fig. 7.4(c) and Fig. 7.4(d), which show granules produced after 15 and 20 minutes, the internal structure comprises concentric rings of high binder content and deposited material around a central region.

Because of the complex internal structure the granule porosity was calculated as a function

of distance from the granule centre. A number of high-resolution SEM images were taken along a continuous strip passing through the granule centre. The strip was split into a number of thresholded images, from which the average porosity was calculated. This process is exemplified in Fig. 7.5 for granules with a concentric ring structure.

In Fig. 7.5, the central region of the 25 µm granule has a peak porosity of 17.5 %, whilst at the edges the porosity is much lower at 5.3 and 4.2 %. Similarly, the central region of the 28 µm granule has a high porosity of 24.1 % whilst the edges have low porosities of 8.1 and 1.6 %. In the latter case, the particularly low porosity is caused by a high proportion of binder close to the granule surface. In both cases, the higher porosity of the central region (similar to that of granule nuclei produced after 1 minute), coupled with the diameter of the region

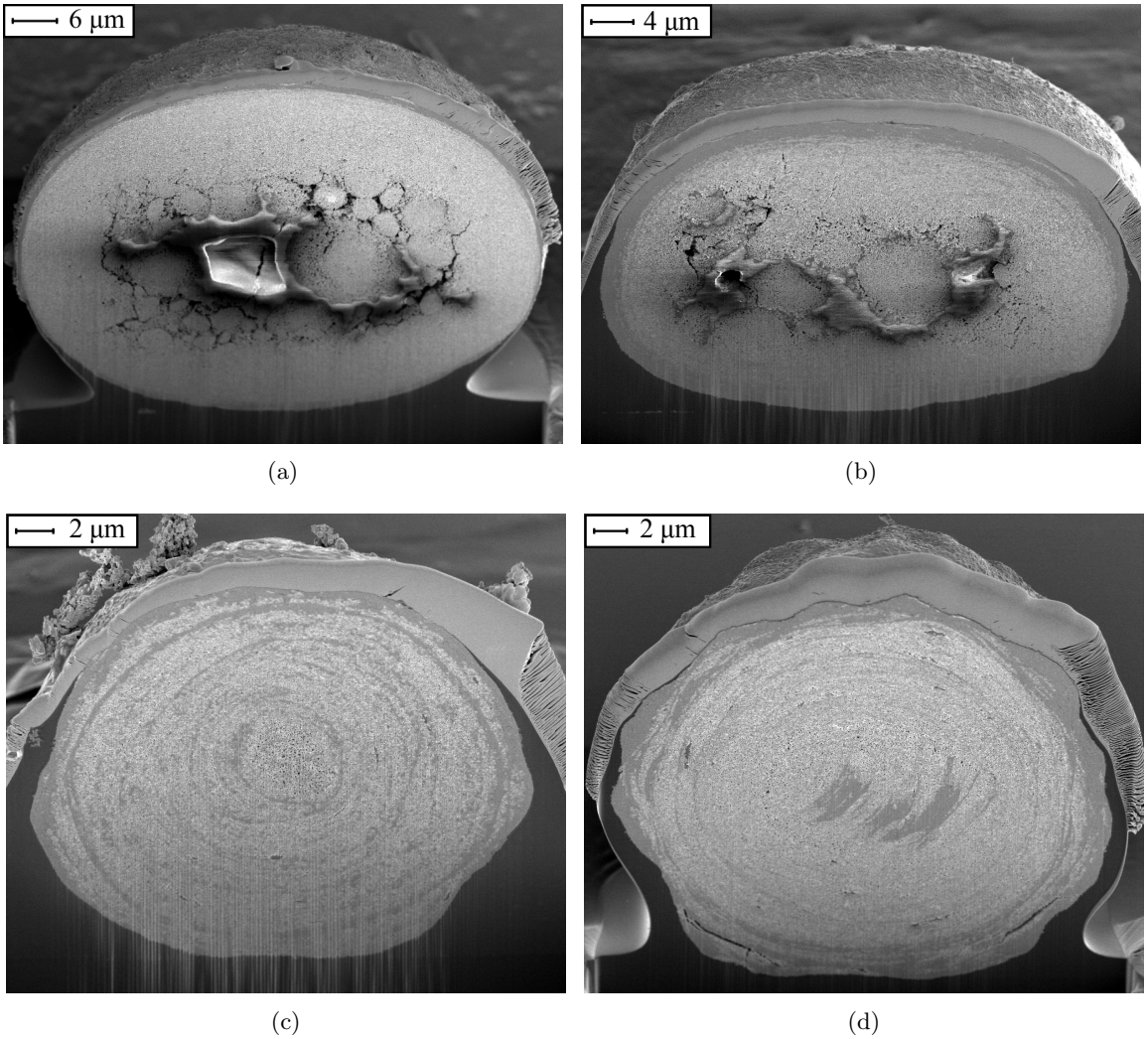

FIGURE 7.4: SEM images showing a FIB-milled cross-section through various granules: (a) and (b) 66 and 47 µm granules produced after 10 minutes, showing a binder-rich core and evidence of coalesced nuclei (c) and (d): 25 and 28 µm granules produced after 15 and 20 minutes respectively, showing a central nuclear core and concentric rings of binder and deposited material.

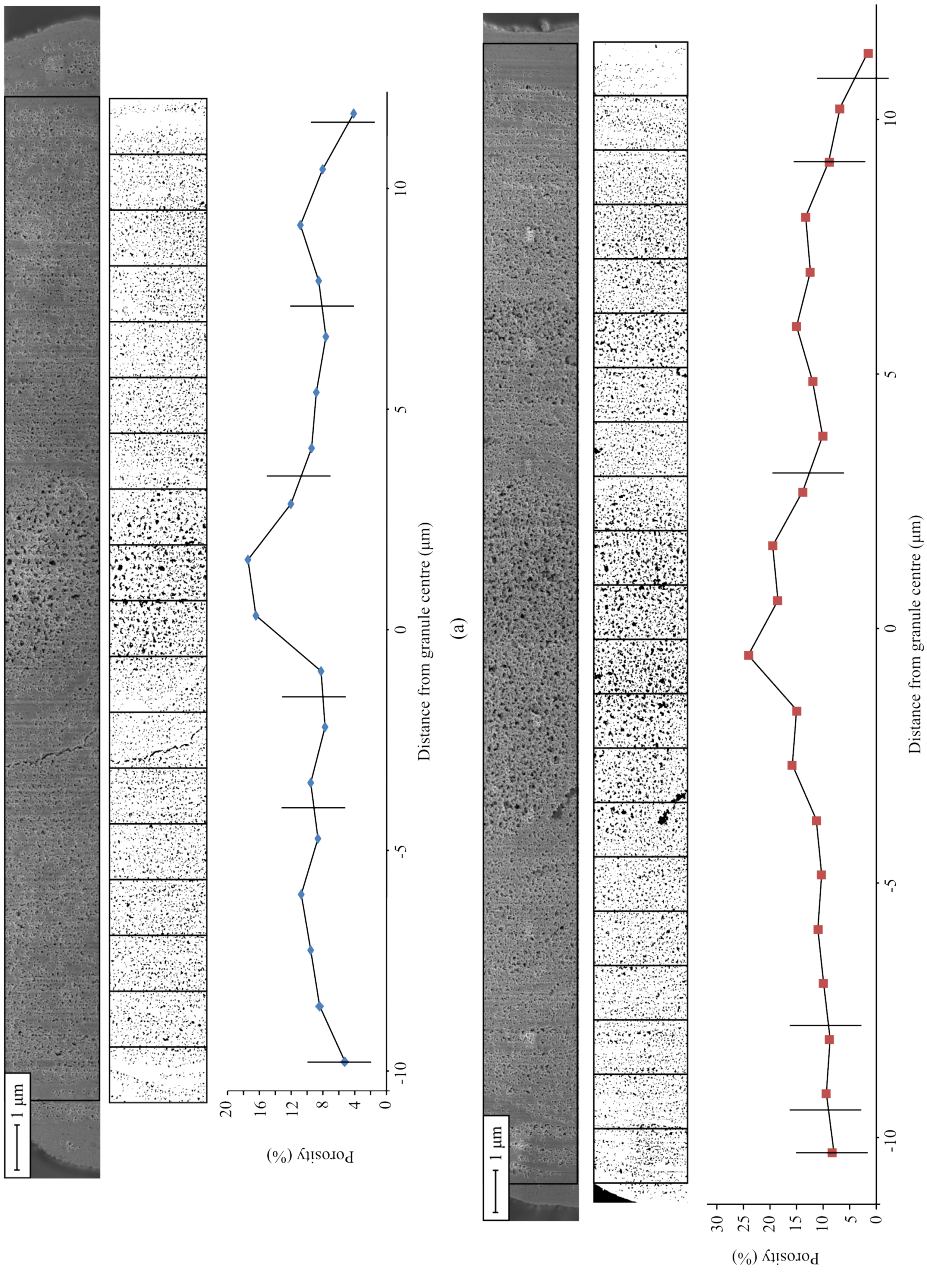

FIGURE 7.5: Porosity profiles through (a) 25 µm and (b) 28 µm granules produced after 15 minutes, as a function of distance from the granule center. The image sequences were partitioned into numerous segments, thresholded according to the procedure outlined in chapter 4 and the porosity of each was calculated. The vertical lines on the graph are drawn at distances from the granule centre where concentric binder rings occur.

(4.5 and 8.0 µm) is suggestive of granule nucleus which has then grown by the addition of successive layers of particulate material. Vertical lines are drawn on the porosity profile to indicate the presence of a binder-rich ring of material. This would be expected to lower the porosity of the image segment it is found in. It can be seen that these lines approximately correspond to local minima in the porosity profile.

FIB milling also revealed granules which contained no central high porosity nuclear region. For completeness, the porosity profile of two granules of diameter 26 and 29 µm are shown in Fig. 7.6. The porosity exhibits localised maxima and minima but with no overall trend. However, common to all granules presented above is the existence of concentric rings of binder progressing outwards from the granule center. This was observed in all cross-sections of granules produced at 15 and 20 minutes. This structural phenomenon is magnified in Fig. 7.7(a), which shows how the rings become more frequent toward the granule edges. Fig. 7.7(b) shows that inside the rings both the micro- and macro-pores have been filled with silicone binder. This structure is strong evidence that the process of layering is responsible for granule growth at long granulation times. Binder, squeezed from the interior of the granule, reaches the granule surface and a short period of granule growth occurs by a layering mechanism, where fine particulate material is deposited onto the granule surface. After a short period of time, the liquid binder is again squeezed to the new surface and the next layer is deposited.

Aside from a layering mechanism, evidence for granule growth by coalescence was also discovered. The FIB cross-sections shown in Fig. 7.4(a) and 7.4(b) show internal structures consisting of a central region of coalesced granule nuclei, alongside regions of high binder content and large internal voids. The porosity profile of a 34 µm granule produced after 10 minutes, with this type of internal structure, is shown in Fig. 7.8. The porosity reaches

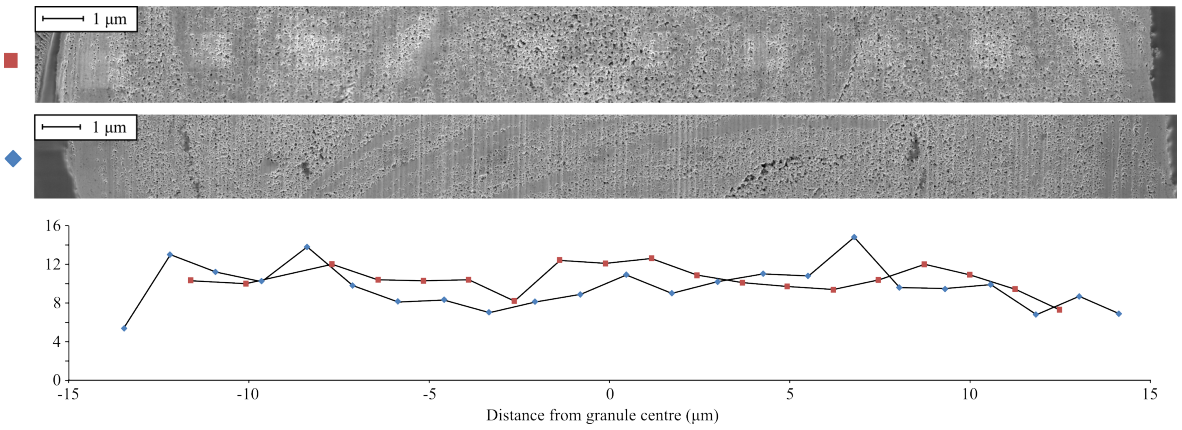

FIGURE 7.6: Porosity profiles of two granules of diameter 26 (red squares) and 29 µm (blue diamond) produced after 20 minutes. Here, the porosity exhibits localised maxima and minima throughout the granule cross-section although there is no overall trend.

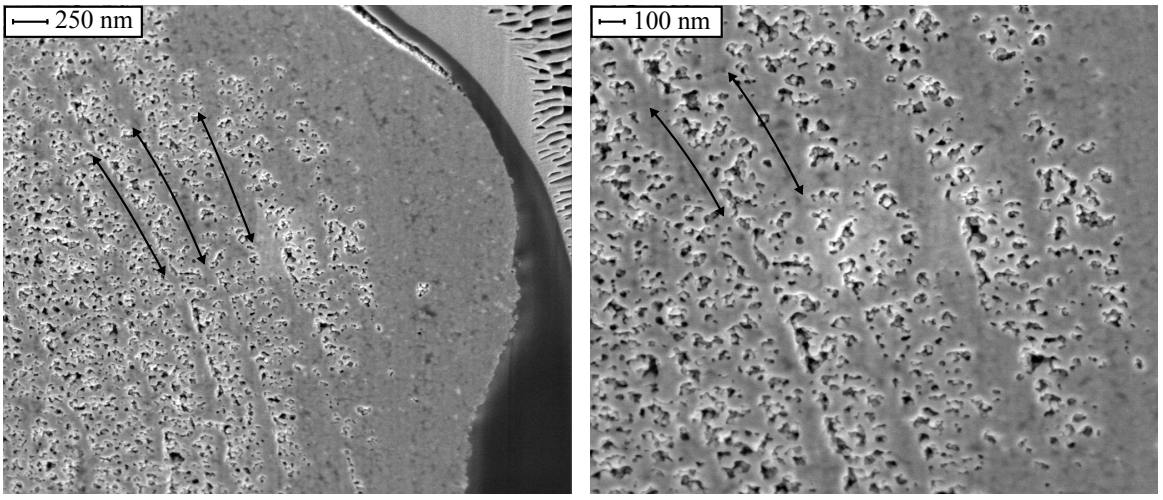

(a) (b)

FIGURE 7.7: SEM images detailing the concentric ring structure found in all FIB-milled cross-sections of granules produced at 15 and 20 minutes, where the arrows indicate the circumference of successive rings. (a) The rings become more frequent towards the surface of the granule. (b) Inside the rings, the inter-particle pores are filled with silicone binder.

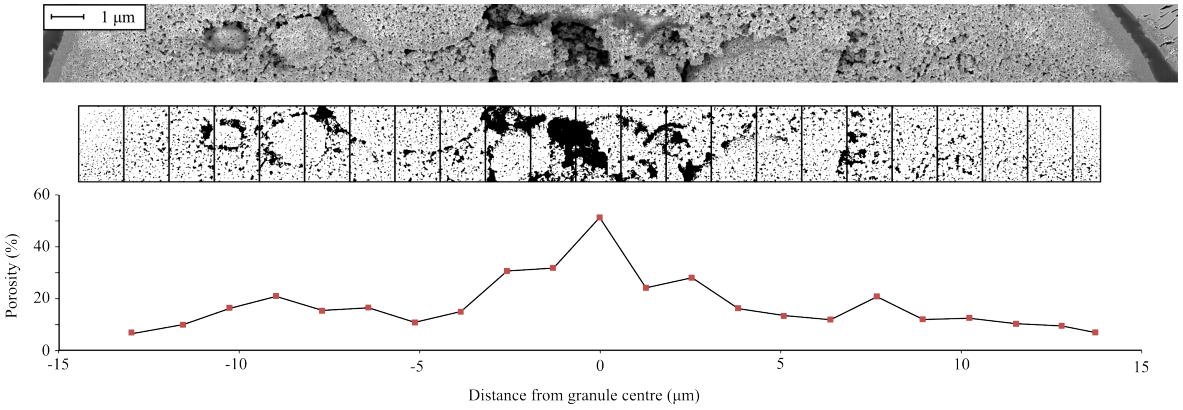

FIGURE 7.8: Porosity profile of a granule of Feret diameter 34 µm produced after 10 minutes, comprising a core of coalesced nuclei, areas of high binder content and large internal voids. The porosity reaches a peak value of 51.3 % at the granule centre, caused by a large internal void.

a peak value of 51.3 % at the granule centre due to the presence of a large internal void. Overall, the porosity decreases towards the edges of the granule where continuous material is deposited on to the coalesced nuclei, reaching a minimum of 7% at the edges of the granule.

7.2.3.3 Average porosity as a function of time

To calculate the average porosities of the complex granule structures described previously, regions within the granule were chosen which were relatively homogeneous. For example,

regions outside of the coalesced nuclei core, or the single nuclear core, yet not at the surface of the granules as this tended to have a high binder content and therefore low porosity. The average porosity was calculated from a minimum of three images of such regions inside each granule, for each granulation time. The results are appended onto those obtained for the granule nuclei produced prior to 10 minutes and are shown in Fig. 7.9(a). A logarithmic trendline is fitted, suggesting a power law dependence of porosity on granulation time.

As described in chapter 3, Iveson *et al.* proposed an empirical consolidation model for drum granulation described by equation. 3.4 [111]. This proposed an exponential relationship between the change in porosity (as a fraction of the overall change in porosity) and the number of revolutions of the drum, where the equation constants were expected to be complex functions of other granulation parameters. This model can be adapted to high shear granulation in the DAC as the number of revolutions is simply the speed setting of the DAC (in rpm) multiplied by the granulation time in minutes. This model is fitted for the result obtained here in Fig. 7.9(b). A linear relationship would indicate agreement with the model. Whilst this may be true within error, the large spread around the line of best fit indicates that the complexities observed here are not precisely described by this simplified model. Iveson *et al.* proposed that each granule produced at a certain time has a well-defined porosity. Whilst this may be true for the granule nuclei produced here, granules produced after rapid growth has occurred have a complex internal structure for which it is difficult to define an average porosity. Also, Iveson *et al.* pre-wetted the glass ballotini with a glycerol binder prior to granulation. Here, binder dispersion is an important process and has already been shown to result in an initial bimodal distribution of granule sizes. The model does not account for this early stage of granulation.

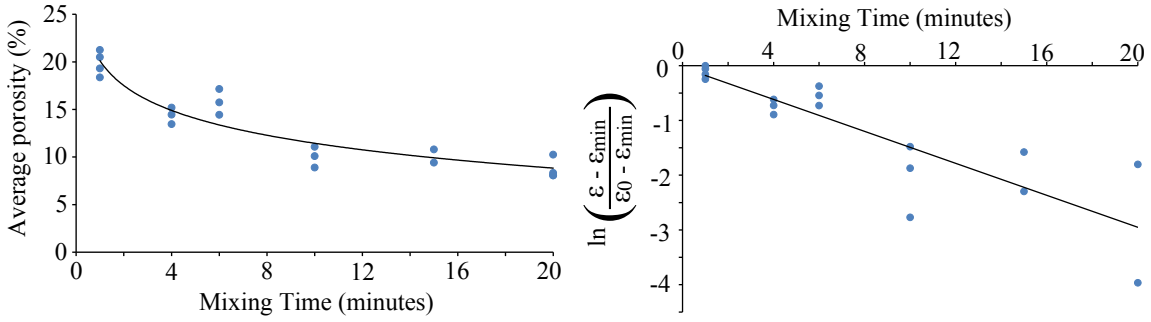

FIGURE 7.9: Graphs showing (a) the decrease of average porosity as a function of granulation time, where the solid black line shows a logarithmic relationship between porosity and time (b) data fit to the consolidation model predicted by Iveson *et al.* [111] with a linear line of best fit.

7.2.4 Mechanical properties of granules as a function of time

Granules produced after 1 to 20 minutes were tested for their fracture strength using the NanoCrush test facility, as described in chapter 4. Granules in the size range 75–100 µm were chosen. An understanding of the fracture strength of the granules as a function of granulation time is beneficial as it may provide an understanding of the behaviour of granules under load in a resistive touchscreen, which is the focus of the second half of this thesis.

Fig. 7.10 shows the fracture strength of granules as a function of the mixing time. SEM images of representative granules for each mixing time, of size 75–100 µm, are shown in the inset. Between 4 and 15 minutes, the average granule fracture strength was 11 ± 2 mN, irrespective of granulation time. However, after 20 minutes the fracture strength of the granules had increased to 33 ± 8 mN. The large error reflects the spread in the measured fracture strengths, however this still represents a significant increase in the strength of the granules.

The overall trend of increasing strength fits with general granulation theory whereby a decrease in porosity results in stronger granules. A decrease in porosity with increasing mixing time was shown earlier in Fig. 7.9(a). Granule strength as a function of fractional porosity, ρ, is shown in Fig. 7.11(a). It can be seen that lower porosity granules exhibit the largest values

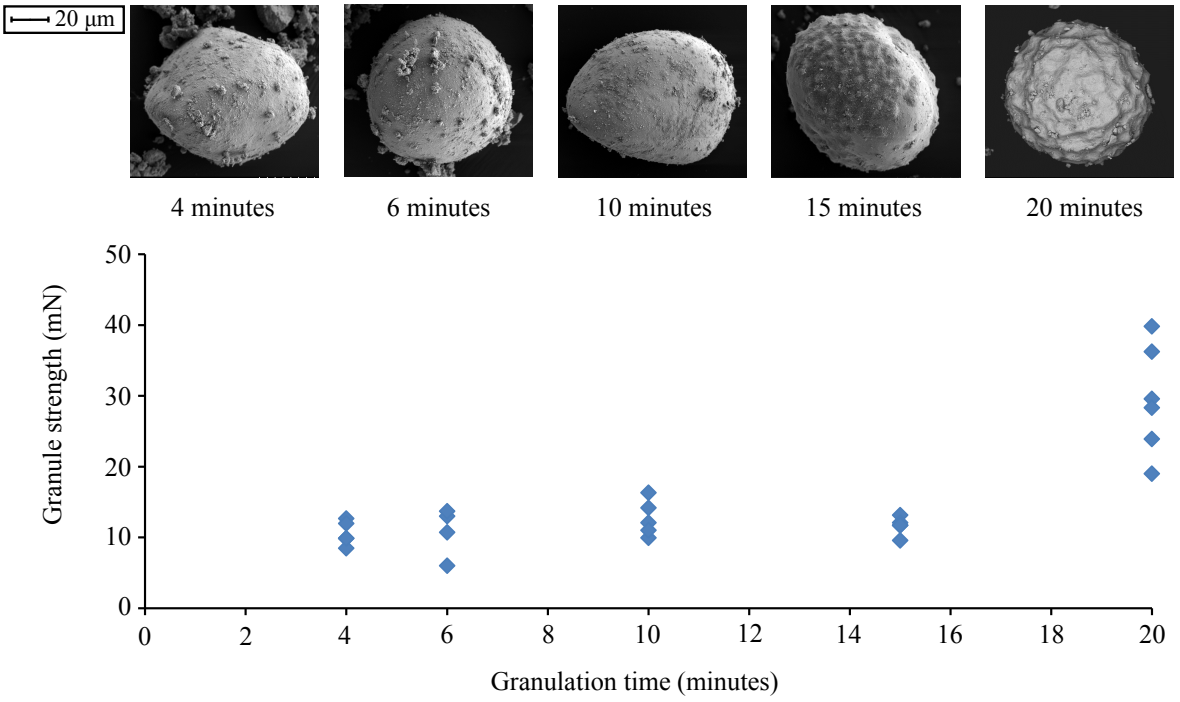

FIGURE 7.10: Graph showing the effect of granulation time on the granule fracture strength of granules of size 75–100 µm produced at 2000 rpm. The SEM images show characteristic granules produced after each time.

of fracture strength. In the Rumpf model of wet granule strength [110], the tensile strength σ is proportional to $\frac{1-\rho}{\rho}$. The tensile strength can be related to the compressive granule fracture strength measured here. Bika *et al.* argue that during uniaxial, unconfined, compression tests such as the diametrical compression test utilised in the Nanocrush, the stress required to break the granule can be equated to the tensile stress [194]. With the further assumption that the wet granule strength can be assumed proportional to the cured granule strength, the average fracture strength is plotted against the factor $\frac{1-\rho}{\rho}$ in Fig. 7.11(b).

The absence of a linear relationship suggests that the Rumpf model cannot describe the results observed here and a more complicated relationship exists between the granule strength and porosity. The Rumpf model is often criticised because it predicts that granule breakage occurs by the simultaneous rupture of all interparticle bonds within the granule. However the granules produced here undergo a brittle breakage mechanism, whereby fracture occurs through crack propagation at weak points in the granule structure. This is evidenced by the existence and appearance of granule fragments during SEM imaging, especially after longer mixing times where hemispherical fragments, or shell fragments from the core-shell structure are observed. It is also evidenced by the individual force-displacement curves obtained during strength measurements where breakage is sudden and preceded by very little granule deformation.

Furthermore, the granule strength calculated here may not be representative of the granules for which the porosity was measured, despite being produced at the same granulation time. For up to 6 minutes the porosity of granule nuclei typically less than 10 µm in size was

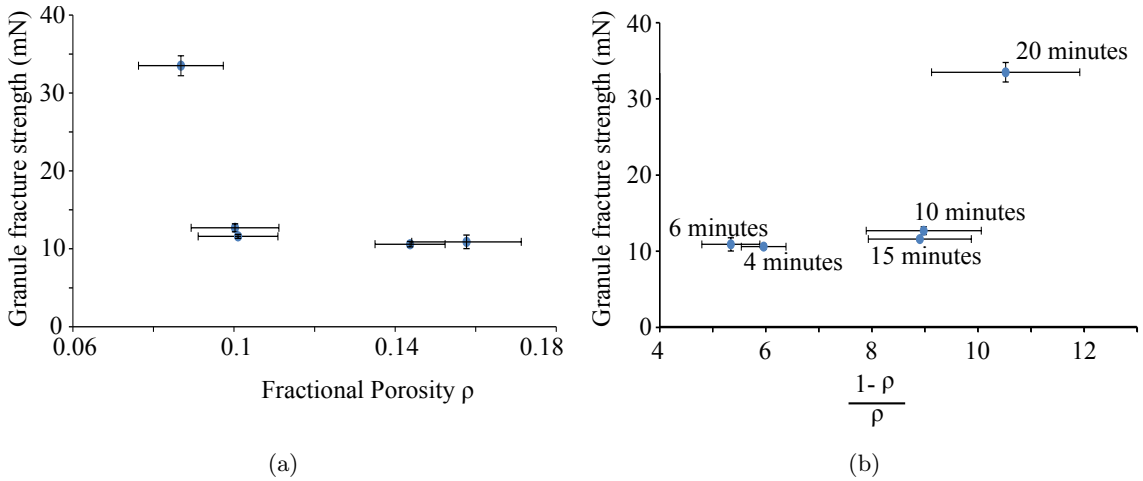

FIGURE 7.11: Graphs showing (a) the relationship between granule strength and porosity, where the lowest porosity granules show the largest granule fracture strength. (b) Application of the Rumpf model of granule strength [110], where a linear relationship would indicate a good fit of the data to the model.

measured, reflecting the prevalence of the nuclei at these times. For 15 and 20 minutes, after rapid growth had occurred, most granules were greater than 10 µm in size and so the porosity of these granules were analysed. By selecting the size fraction 75–100 µm for strength measurements, the granules tested may not be representative of the majority of granules which are produced at that time. As an example, large non-nuclear granules produced at short mixing times are likely to contain a binder-rich core and large internal voids, such as the granules shown in Fig. 6.3(c) and Fig. 6.3(d). Here, the granule porosity may be much larger than for the granule nuclei. On the other hand for granules produced at 15 and 20 minutes, FIB analysis of granules of size 23–24 µm showed evidence of binder distribution through the presence of concentric rings of binder progressing outwards from the granule centre. These granules had a distinctive 'golf-ball' shape, which is also evident in the granule size fraction 75–100 µm used for strength measurement. Hence it is a likely assumption that these granules possess a similar internal structure. Cross-sectional analysis through FIB milling showed that at later times there was a high binder concentration near to the granule surface and this may have added to the strength of the granule. However, this is currently inconclusive and further testing is necessary in order to better understand the cause of the increase in strength after 20 minutes.

7.3 The Effect of DAC speed and the link to granulation time

7.3.1 Effect of DAC speed on the induction process

To further understand the granulation processes the influence of DAC speed was investigated. The link between DAC speed and the onset of rapid growth after the induction period was of particular interest, as here the DAC speed offers another degree of control over the development of granule nuclei.

The speed of the main rotation was altered between 1600 rpm and 3500 rpm, corresponding to tangential velocities of 13.4 – 29.3 $\mathrm{m\,s^{-1}}$ and Froude numbers in the range 229–1095. In all cases, the secondary rotation remained at 25 % that of the main rotation, in the opposite direction. Granules comprising spherical ATO nanoparticles and 10% silicone binder were produced at different DAC speeds, for times in the range 1–20 minutes.

Fig. 7.12 shows SEM images of granules produced after 2 and 15 minutes, as a function of DAC speed. At 1600 rpm, surface-rough granule nuclei are present after 2 minutes (Fig. 7.12(a)). After 15 minutes (Fig. 7.12(b)), surface-smooth granule nuclei are predominant and rapid growth has not occurred. Fig. 7.12(c) and Fig. 7.12(d) show that, at 2000 rpm, the granule

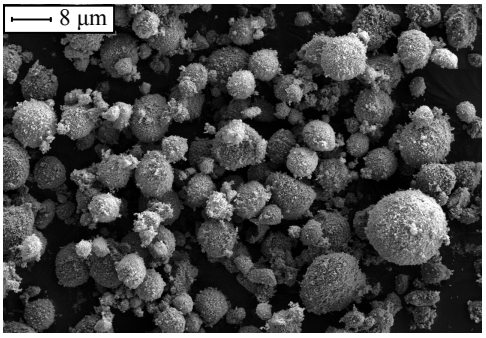

(a) 1600 rpm, 2 minutes

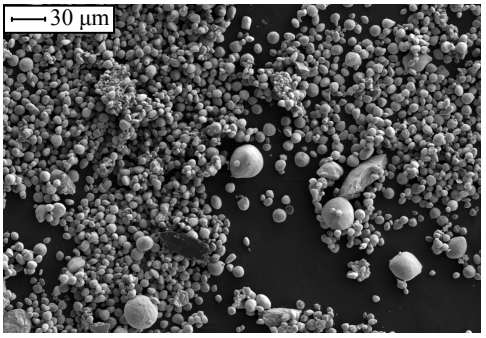

(b) 1600 rpm, 15 minutes

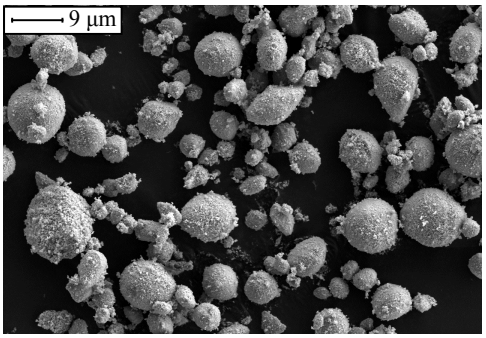

(c) 2000 rpm, 2 minutes

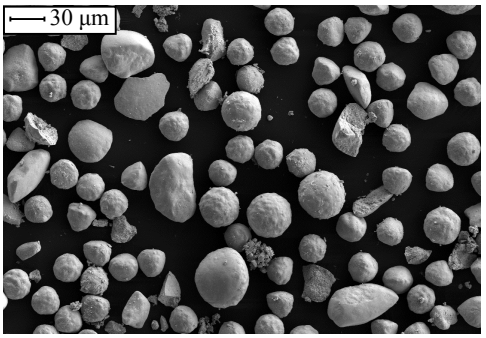

(d) 2000rpm, 15 minutes

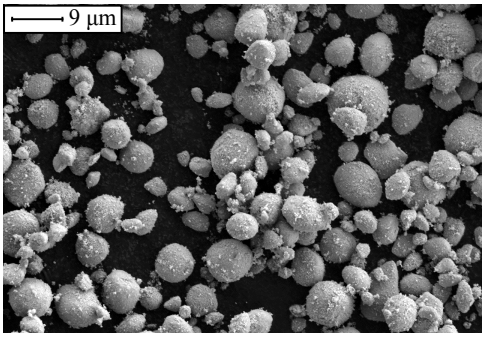

(e) 2500 rpm, 2 minutes

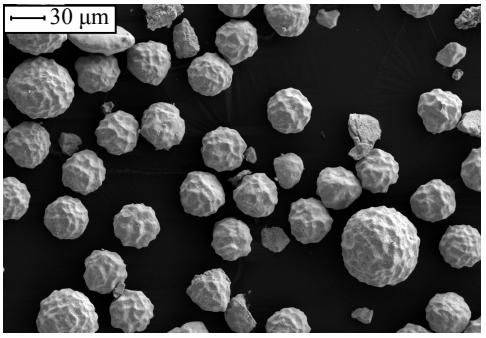

(f) 2500 rpm, 15 minutes

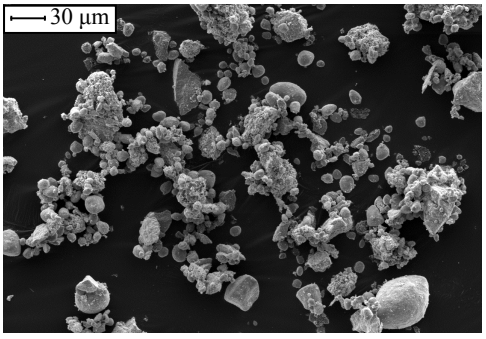

(g) 3500 rpm, 2 minutes

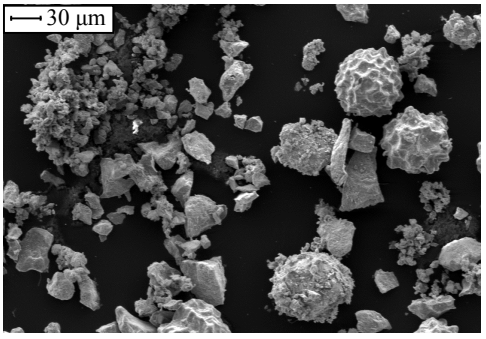

(h) 3500 rpm, 15 minutes

FIGURE 7.12: SEM images showing granules produced at DAC speeds from 1600 rpm to 3500 rpm, at granulation times of 2 minutes and 15 minutes.

nuclei which are observed after 2 minutes have undergone rapid growth after 15 minutes. Here, the large granules show very shallow surface indentations. Fig. 7.12(e) and Fig. 7.12(f) show, at 2500 rpm, the granule nuclei present at 2 minutes have undergone rapid growth by 15 minutes, and also exhibit the distinctive 'golf-ball' effect. At 3500 rpm after 15 minutes, whilst there are some large, heavily indented granules there is also a large proportion of granule fragments suggestive of increased granule breakage.

These images suggest that the onset of rapid growth, and the onset of granule surface indentations, can be controlled through the speed of the DAC. Increasing the rotational speed of the DAC increases both the frequency and the energy of collisions between granules and the container, which results in a faster rate of consolidation. Liquid binder is squeezed through the internal macro- and micro-pores and reaches the granule surface, promoting rapid growth by coalescence and/or layering mechanisms, as was observed previously in section 7.2.3. The effect of increasing the DAC rotational speed and time of granulation are closely linked. The same extent of consolidation can in theory be achieved through a range of granulation speeds and time.

In order to understand this effect, a speed-time regime map was produced by collating results across all granulation experiments for a range of DAC speeds and granulation times. For each speed, the size distribution and average size of granules produced for up to 20 minutes was calculated. Fig. 7.13 shows the results. Each granulation event is plotted according to the speed setting of the DAC and the granulation time. The marker identifies the average size of the resultant granules, where green represents granules with an average size less than 10 µm, yellow for 10–20 µm, orange for 20–40 µm and red for $>$ 40 µm. The green markers are of most interest as they correspond to the granule size range most suited for incorporation into the resistive pressure sensing touchscreen developed in Part II of this thesis.

This regime map is similar to that devised by Iveson and Litster [114], shown in Fig. 3.6. It predicts the result of changing the granulation speed and time on the size of the resultant granules, based on empirical evidence. However, it is only applicable for the individual case where granules are fabricated using spherical ATO nanoparticles and 10 % silicone binder. It does not predict the effect of changing the binder concentration or viscosity, or the primary particle size. In order to calculate the parameters St_{Def} and S_{max}, knowledge of the granule porosity, density and strength are required for every point on the phase diagram. Such detailed analysis is beyond the scope of this thesis.

However, the diagram does show various granulation methodologies which result in the production of granules less than 10 µm in size. For example, granulating at both high speeds and short mixing times, or low speeds and long mixing times, will result in final granules which have not outgrown the nucleation phase. This is demarcated as region I in the diagram.

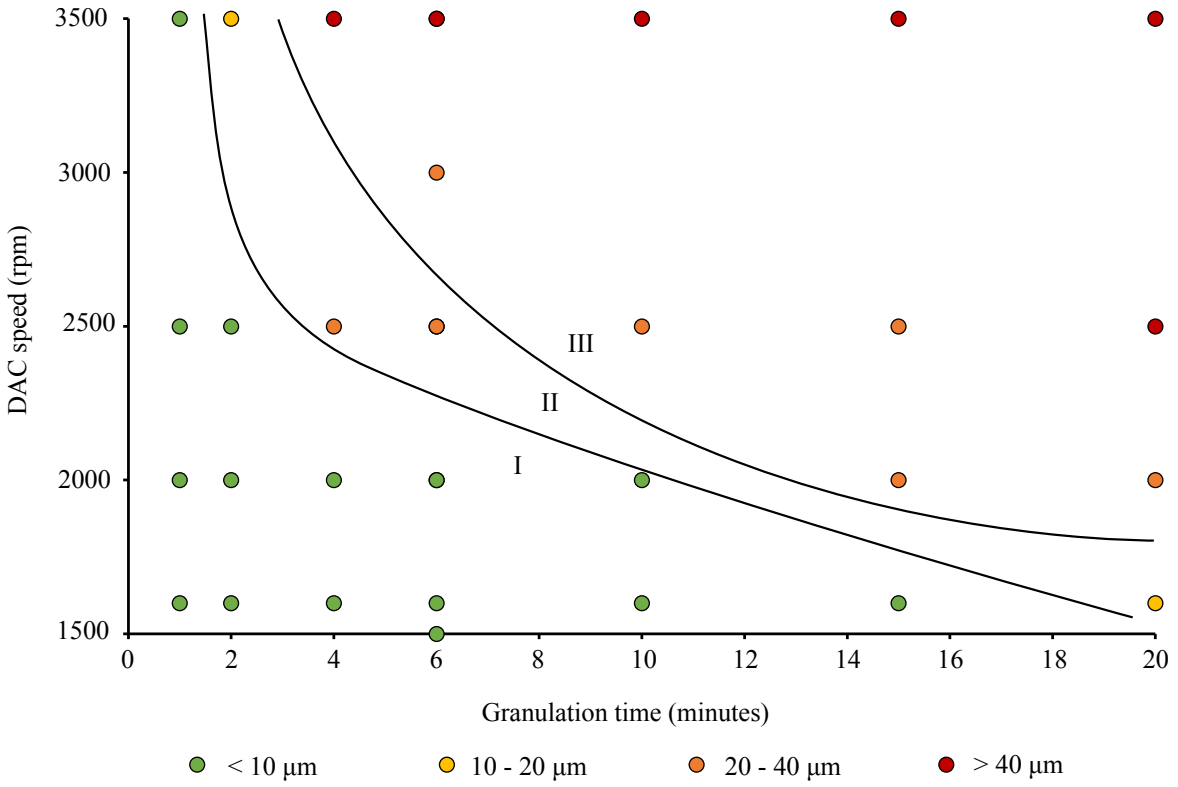

FIGURE 7.13: Graph showing the relationship between the DAC operating parameters (rotational speed and granulation time) and the size of the resultant granules. Three regimes are identified. In region I, the resultant granules have not outgrown the nucleation phase and on average are less than 10 µm in size. In region II, rapid growth after the inductance phase occurs producing larger, surface-smooth granules that are typically 20-40 µm in size. In region III, the resultant granules possess surface indentations, giving them a cratered, 'golf-ball' appearance.

Fig. 7.14 plots the effect of granulation speed on the induction time. Here, the induction time is taken as the time after which the average size is greater than 10 µm.

Furthermore, within region I, whilst the resultant granules have fixed average size, other properties such as their surface-roughness and internal porosity will change as a function of the granulation speed and time. For example, for the granule subset produced at 2000 rpm, the surface roughness of the nuclei was shown to decrease with granulation time, and the porosity decreased. This gives an opportunity to fine-tune the granule properties. In future work, it is envisaged that the effect of granule porosity on any pressure-sensitive electrical conduction mechanisms through the granule may be fully understood. This regime map is the first step in identifying how granules with specific size and porosity may be fabricated for this purpose.

Region II marks the onset of rapid growth, signalling the end of the induction phase. Here rapid growth, promoted by surface-wet granules, increases the average size to 20–40 µm and the granules have a surface smooth appearance. Region III identifies the granules which

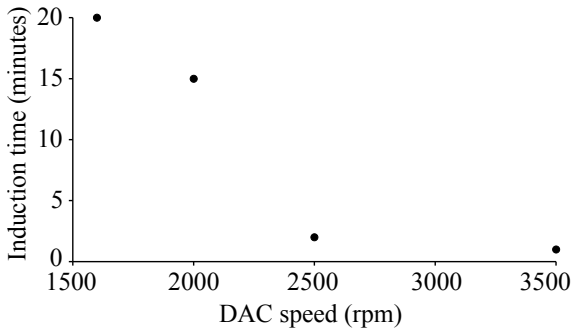

FIGURE 7.14: Graph showing the effect of DAC rotational speed on the length of the induction phase. The induction time, defined as the time after which the average size of the granules has exceeded 10 µm, increases with decreasing DAC speed.

show surface indentations or protrusions, or the 'golf-ball' effect. Here, indentations and protrusions appear on the granule surface producing a dimpled effect. These effects appear at larger granulation speeds or for granules mixed for a long duration. It is important to note that this feature is not limited to a small proportion of granules in each batch. As long as breakage is not dominant, in region III the vast majority of granules produced will show this effect. For example, the granules shown in Fig. 7.15(a) show the predominance of these structures. Fig. 7.15(b), Fig. 7.15(c), Fig. 7.15(d) and Fig. 7.15(e) show examples of exceptionally structured granules.

This behaviour is specific to the granulation process used here, and has not been observed in any granulation process appearing in the literature. Whilst non-spherical granule shapes are common, and many granules do have an irregular or angular geometry, to date there are no public examples of granules which possess the specific geometry shown here. The exact cause of this feature is not fully understood, but it must be related to granule collisions in the DAC. Collisions between two large, deformable granules may not be energetic enough to cause breakage but may cause plastic deformation resulting in 'impact craters'.

Whilst these structures are not directly relevant to this thesis (their large size makes them unsuitable for printing in a thin layer) it is not infeasible to suggest a range of possible applications which make use of their unusual features. It is possible that it is the specific mixing procedure of the DAC, as described in chapter 4, which results in the observed shape rather than the particle and binder properties. If this were the case then in theory any granule made using a DAC may possess this feature. The main advantage of such a granule is its increased surface area. Assuming each granule of diameter R contains a number N of hemispherical indentations of radius r the total surface area of the granule is $4\pi R^2 + N \times \pi r^2$. Applications where granule surface area is important include pharmaceutical granules, where an increased surface area leads to an increased rate of dissolution [204, 205], and also

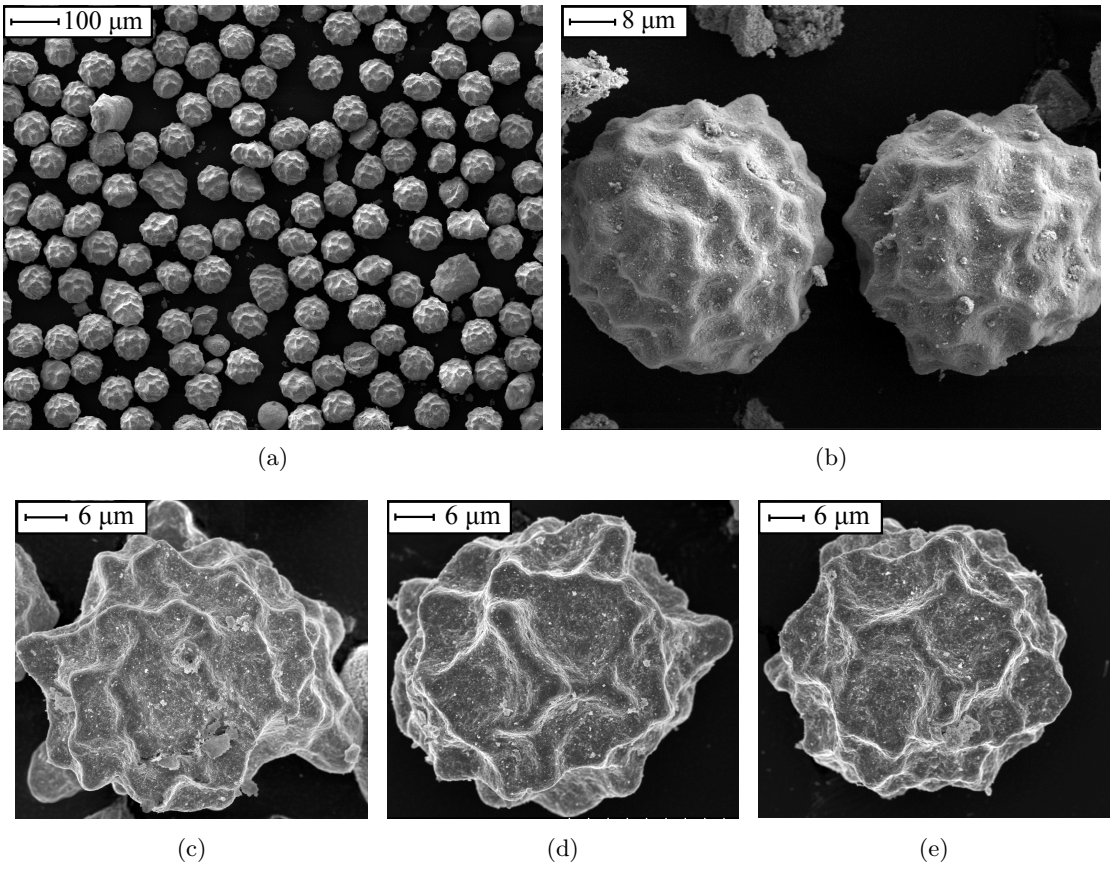

FIGURE 7.15: SEM images showing warped granule structures produced at long granulation times or high DAC rotational speeds.

granulated chemical catalysts where increased surface area leads to an increase in the number of chemical reaction sites [206].

7.3.2 Granule mechanical properties as a function of DAC speed

Fig. 7.16 shows the granule fracture strength as a function of DAC rotational speed. The granulation time was kept constant at 10 minutes. For each speed, a minimum of 4 granules in the size range 75–100 µm were tested. Representative granules for each speed, in this size range, are also shown in the figure.

With increasing DAC speed, the fracture strength of the granules also increases.This increase is marginal for speeds between 1600 and 2500 rpm, and ranges between 10.6–19.2 mN. However, the fracture strength increases to 27.0–40.7 mN at 3000 rpm and 3500 rpm.

This trend is in agreement with observations in the granulation literature, all of which report a general increase in granule strength with increasing granulation energy, usually by increasing the impeller speed in a high-shear granulator. Oulahna *et al.* reported that for increasing the

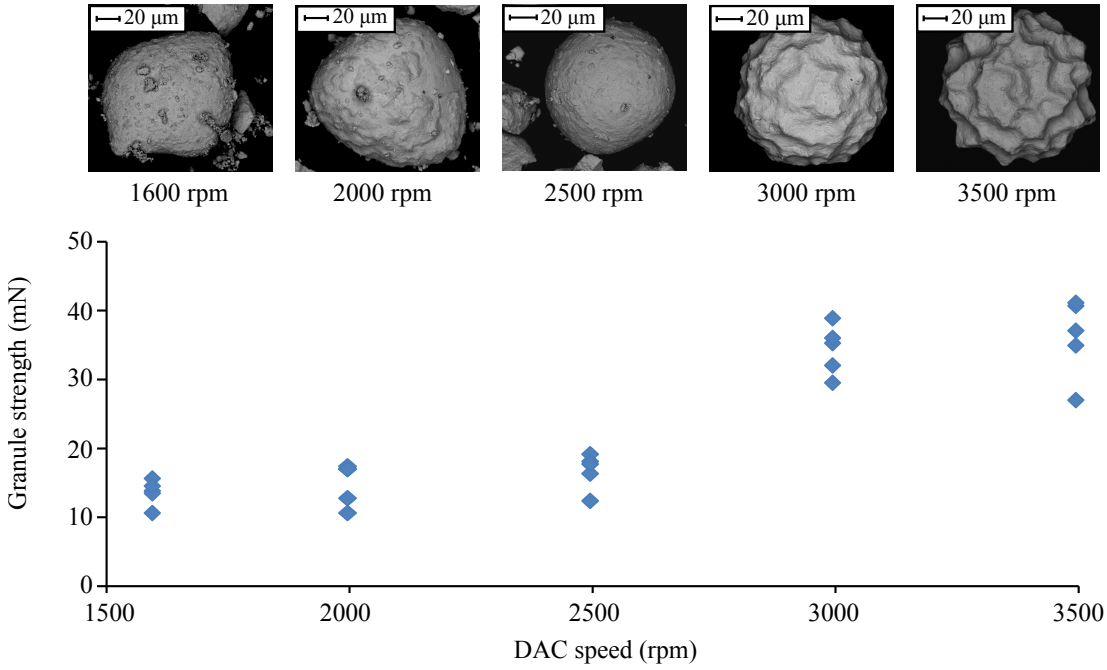

FIGURE 7.16: Graph showing the effect of DAC rotational speed on the fracture strength of granules in the size range 75–100 µm produced after 10 minutes. The insets show SEM images of representative granules produced at each speed.

impeller speed of a high-shear granulator from 100 rpm, to 500 and then 1000 rpm the porosity of the resultant granules decreased and the friability of the granules decreased [138]. Here, the friability measured the propensity of the granules to break during subsequent tumbling in a rotating drum. Furthermore, the friability was assessed as a function of granule sieve fraction, where it was found that for all speeds, granule strength was highest for the smallest and largest granules and at a minimum for the intermediate granule sizes. Rahmanian *et al.* also reported an increase in granule fracture strength with increasing impeller speed from 3.50 to 5.39 $\mathrm{m\,s^{-1}}$, above which the strength remained constant [139, 140]. The granules were found to have a core-shell structure, where the core comprised a particularly large primary particle. The strength increase was then attributed to densification of the shell and therefore reduction in porosity. Maximum strength was realised at minimum porosity, beyond which a further increase in impeller speed had no effect. At the highest impeller speeds the fracture strength distribution is narrowest, suggesting the granules produced at high speeds are more uniform in structure and strength.

Here, granule strength shows no sign of reaching a maximum value at the highest speeds, despite the increased rotational speeds used here compared to those sampled by Rahmanian *et al.* By Rahmanian's analysis, this would imply that the granules had not yet reached minimum porosity. However, it was previously shown that at 2000 rpm the porosity decreases only incrementally after 10 minutes, whilst the granule strength increases significantly between 15

and 20 minutes. The increase in strength seen here cannot be attributed to a decrease in porosity. Instead, this may be related to the binder distribution within the granule. At 2000 rpm, after 15 minutes, binder migration out from the granule centre resulted in a high concentration of binder at the granule edges. At higher speeds it is likely that this effect is accelerated. Post-curing, a high binder content at the granule surface may result in increased hardness and therefore a larger force is required to fracture the granule.

Finally, one important caveat of these results is that the granules selected for size analysis may not be representative of the entire granule batch. At low speeds, the average size of the granules produced after 10 minutes is typically less than 10 µm. The few granules in the size range 75–100 µm may have an entirely different internal structure such as high binder content, large internal voids, and coalesced nuclei. Furthermore, at high granulation speeds granule breakage causes fragmentation of the weakest granules. The large granules that remain have a high-strength as they have withstood breakage. Hence care must be taken when generalising these results to all granules produced at that speed.

7.4 Influence of process temperature on granulation

During granulation, collisions between granules and the container cause an increase in the temperature inside the DAC. The rise in temperature is dependent on both the residence time in the granulator, if the heating rate exceeds the rate of cooling, and the collisional energy. The temperature of the granules immediately after granulation was monitored using an infra-red (IR) camera. After granulation, the container was removed from the DAC and the lid removed. The IR camera was used to image the inside of the container, from which the average temperature of the granule ensemble could be calculated. Due to the enclosed nature of the DAC, temperature monitoring *in situ* was not possible.

The rise in the average temperature of the granule ensembles is shown as a function of granulation time, for DAC speeds of 2000 and 3500 rpm, in Fig. 7.17(a). The temperature of the granules reaches in excess of 35 °C after 20 minutes. Up to 10 minutes the temperature increases at an approximately linear rate of 1.0 ± 0.1 °C min^{-1}. After 10 minutes the temperature increases at a slower rate of 0.2 ± 0.1 °C min^{-1}. The effect of the DAC speed on the temperature is shown in Fig. 7.17(b), for granules produced after 6 minutes. When granulating at 3500 rpm, the temperature of the granules can reach 57 °C. The rate of temperature increase is approximately linear with a 6.6 ± 0.8 °C increase in temperature each time the rotational speed is increased by 500 rpm. The errors bars are propagated from the spread of temperature around the average value and the associated cooling error caused by the finite time between the end of granulation and the actual measurement. For high speeds when the temperature increase is largest, the cooling rate is also larger, resulting in a greater error.

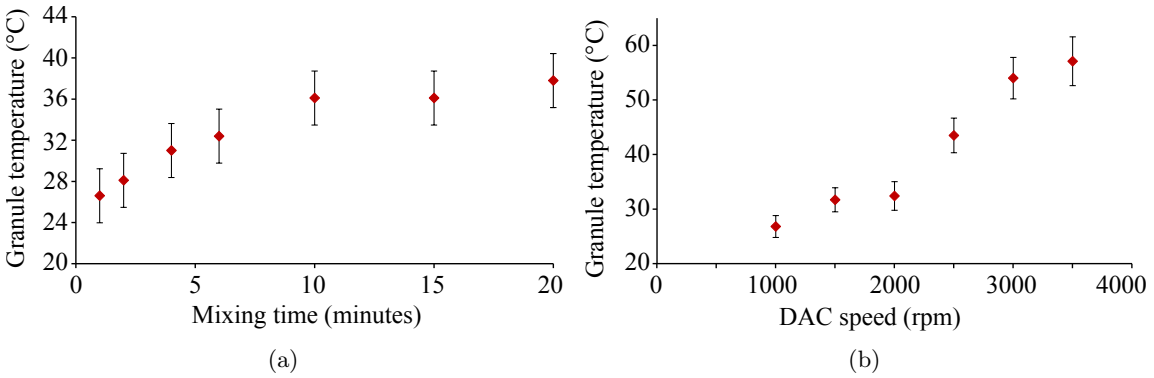

FIGURE 7.17: Graphs showing (a) the temperature increase in the DAC as a function of time, for a speed of 2000 rpm (b) the temperature increase as a function of DAC rotational speed, for granules produced after 6 minutes.

The rise in temperature observed in the DAC may itself affect the granulation processes. The silicone binder used here cures through an addition reaction, as described in chapter 4. The recommended curing conditions for the silicone used are 25 °C for 24 hours, although heating the silicone will accelerate the curing process.

Andersson and Hjertberg investigated the addition curing properties of a number of two-part silicones, one of which was similar to the silicone binder used throughout this thesis [207]. The heat of curing (that is the total heat required to complete the curing process) was investigated using differential scanning calorimetry (DSC). This enabled the curing reaction to be studied as a function of time and temperature. It was found that the addition curing process followed an Arrhenius relation and was strongly temperature dependent. For silicone similar to that used here, the curing time decreased exponentially with increasing temperature. At 20 °C, the total curing time was approximately 42 hours. At 30, 40, 50 and 60 °C the curing time decreased to 15, 5.6, 2.2 and 1.2 hours respectively. Furthermore, the time at which the maximum cure rate was achieved was 3.4 hours at 40 °C, 50 minutes at 55 °C and 14 minutes at 70 °C.

The results of Andersson and Hjertberg suggest that there is a strong possibility that curing of the silicone binder is initiated during the granulation process, and the extent of curing increases with increasing temperature inside the DAC. During addition curing, cross-linking of polymer chains increases the viscosity of the silicone binder. Therefore, the silicone viscosity does not remain constant throughout the granulation process. This adds a further complication to an already complex granulation process. Bardin *et al.* define a reactive binder as one which undergoes a physical or chemical reaction, resulting in either a change in binder viscosity or quantity [208]. Examples of processes which may cause these effects include the evaporation of solvent, formation of crystalline hydrates, chemical reactions between binder and solid and binder phase change from a liquid to crystalline phase.

For reactions which increase the binder viscosity, the rate of consolidation is predicted to decrease with increasing binder viscosity. The concentric binder rings, apparent in the FIB-milled cross-sections of granules produced at 2000 rpm at 15 and 20 minutes, may provide evidence for this process. The concentric rings became more frequent towards the edges of the granule, as shown in Fig. 7.7(a) and near to the granule surface there is a high concentration of binder. This is consistent with a process for which the consolidation rate is decreasing with time. As viscosity increases, the binder is squeezed a lesser distance towards the granule surface. This causes the reduction in the concentric ring spacing near to the granule surface. Eventually a point is reached when the binder viscosity is sufficiently high to prevent further consolidation and at this point the granule reaches a maximum size.

For granulation at 2000 rpm, the temperature rise for up to 10 minutes is just 15 °C above room temperature. Here, the extent of binder curing is likely to be minimal. However, the process described above effectively limits the granule growth. In future work it may be worthwhile to investigate a granulation system in which the temperature can be adjusted, or to investigate the effect of pre-curing the silicone binder to a lower viscosity state before initiating granulation. This may offer a further degree of control over nuclei growth kinetics.

7.5 Summary and conclusions for part I

Part I of this thesis was concerned with the fabrication and structural analysis of nanocomposite granules for the inclusion into a pressure sensitive resistive touchscreen. Ideally, the nanocomposite granules should be less than 10 µm in size in order to match the printed thickness of the pressure-sensitive layer within the touchscreen. Furthermore, importance is placed on understanding the structural and mechanical properties of the granules, including their porosity and mechanical fracture strength. These parameters may give important contributions to the electrical functionality and the durability of the granules, and hence of the resistive touchscreen.

A granulation process was used to fabricate the nanocomposite granules. The theoretical processes of granulation, as were described in chapter 3, are complex and as yet not fully understood. Furthermore, applications of granulation are usually chemical, pharmaceutical and agricultural. Here, the primary particles used are typically of a similar size to the end-point granules created here - it is very unusual to granulate nanoparticles in order to produce micron-sized granules. Additionally, the DAC was shown to be capable of extremely high Froude numbers in excess of those found in the literature, which indicated that the mixing intensity in the DAC far exceeded what is commonly used in granulation elsewhere. Both of these factors mean that here, granulation is used in a novel and unconventional application, and some of the results described here reflect this fact.

Throughout this thesis, static image analysis through SEM imaging and subsequent image analysis was used to determine the GSD. This technique was critically compared with other size analysis techniques in chapter 5, in order to better understand the limitations of the method used here. It was found that SEM imaging did not allow for the measurement of large sample sets, so that a full statistical interpretation was not feasible. Bimodal distributions could not be represented on either number or volume weighted distributions due to this sampling issue. Despite this, the additional detail acquired through SEM imaging, allowing visualisation of granule structure and surface texture, offered significant advantages over other techniques.

In chapter 6, the effect of altering the material properties of the granule components was investigated, including the effect of changing the particle shape, binder type and binder amount, allowing the determination of an optimum 'recipe' for granulation. It was found that acicular ATO nanoparticles were not conducive to controllable granule growth. For spherical ATO nanoparticles an inductive model of granule growth could be applied. Here, granule growth during the early stages of granulation was limited by consolidation. As the granules consolidated, liquid binder was squeezed to the granule surface. When binder reached the surface, a period of rapid growth through coalescence and/or layering occurred. Silicone was chosen as the optimum binder as this resulted in granules with the largest mechanical fracture strength. The effect of binder amount was difficult to quantify, as this parameter was also dependent on binder viscosity. The interplay of both of these factors determines whether interparticle friction or dynamic viscous forces are dominant. However, 10 % binder was used for all subsequent granulation experiments.

Once the basic granule 'recipe' was finalised, the effects of the DAC rotational speed and the granulation time on this granule formulation were investigated. FIB milling was used to reveal the internal structure of the granules as a function of granulation time. It was found that granule nuclei had a homogeneous porosity profile, and a high porosity compared to later stages of granulation. After rapid growth had occurred the porosity profile became more complex. The internal structure shed light on possible growth mechanisms, for example concentric rings of binder progressing outwards from the granule center indicated growth by consolidation and layering. Some granule interiors were found to comprise several nuclei, indicating growth by coalescence. At later stages in granulation, deep surface indentations developed, leading to a 'golf-ball' appearance. The granule fracture strength was largest for granules produced after 20 minutes. It was found that altering the rotational speed of the DAC allowed further control of the induction time before rapid growth occurred. At lower speeds, the granulation process progressed at a slower rate. Production of a detailed regime map for speed and time identified an optimum regime where granule nuclei less than 10 µm in size could be produced. This important result allows the controlled formation of granule

nuclei, where it is envisaged that the properties of these nuclei, including their porosity and surface-smoothness, are themselves a function of the granulation time and speed.

In part II of this thesis, the optimum granule nuclei were incorporated into a screen-printable ink and then deposited by printing a thin layer between two ITO electrodes, in order to produce pressure-sensitive resistive touchscreen devices. The optical properties of these devices were investigated. An understanding of the electrical properties and the pressure-sensitive nature as a function of the granule loading is attempted. Furthermore, the electrical functionality of the granules themselves was investigated through force-resistance measurements and studies of the intrinsic flicker noise. A model simulation of a resistive touchscreen containing these granules was also developed in order to interpret the observed results.

Chapter 8

Electrical Transport and Optical Transmission through Pressure-Sensitive Resistive Touchscreens

8.1 Introduction

In this chapter, the physical principles behind the electrical conduction and optical transmission through pressure-sensitive resistive touchscreen (PSRT) devices are described. In terms of electrical conduction, the pressure sensitive mechanism is shown in Fig. 8.1. Firstly, increasing the force applied on the upper, deformable ITO electrode increases the number of granules contacted. The physics behind this mechanism is explored in section 8.2, which uses the engineering principles of beam deflection under load to relate the applied force to the area of contact with the pressure sensitive (PS) layer. Later in chapter 11, computational simulations are performed using this approach, in order to develop a model for the force-resistance behaviour of the PSRTs.

In addition, it is also possible that the nanocomposite granules are inherently pressure sensitive, that is the conduction through the granules is dependent on applied force. The nanocomposite granules were designed to contain conductive ATO nanoparticles and electrically insulating silicone polymer binder. The properties of similar composite materials display non-linear conduction mechanisms which are sensitive to applied force. Phenomenological models describing this behaviour are described in section 8.3. These models relate observed macroscopic properties of the composite-containing device to linear or non-linear

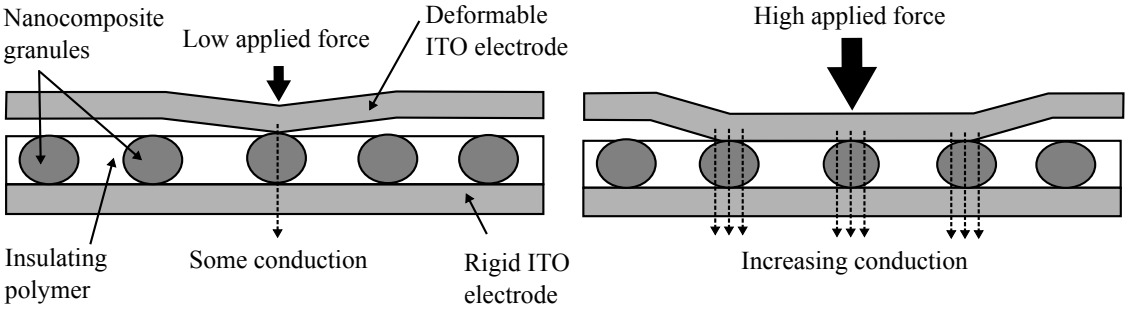

FIGURE 8.1: Schematic showing the proposed conduction mechanisms of the pressure sensitive resistive touchscreen produced in this thesis. There are two contributions to conduction. Firstly, increasing the applied force to the flexible ITO electrode increases the number of granules contacted by the electrode. Secondly, the nanocomposite granules themselves may exhibit a pressure sensitive electrical resistance, such that at higher applied force there is an increase in conduction.

conduction mechanisms, and include percolation theory, effective medium models and random resistor networks. Beyond this the models cannot explicitly predict the form of the non-linear conduction occurring within the composite.

The composite itself may be modelled as a series of semiconductor-insulator-semiconductor interfaces. Physical conduction mechanisms through such composite materials are described in section 8.4. This is split into current emission from a semiconductor, current injection into an insulator and quantum tunnelling mechanisms in semiconductor-insulator-semiconductor junctions. This links with the physical structure of the nanocomposite granules used in this thesis; of semiconducting ATO nanoparticles and insulating silicone binder. Current flow from, and into, each of these components should be considered. Finally, the effect that these conduction mechanisms may have on the macroscopic electrical properties of the device is explored. Previous works which relate such conduction mechanisms to current-voltage characteristics are described.

Optical transmission through the touchscreen assembly is considered in section 8.6. High optical transmission is a necessity for applications of touchscreens as an overlay onto a high-resolution display. Both Rayleigh and Mie scattering theory are used to determine the angular-dependent intensity of light scattering from particulate material within the pressure sensitive layer, where the particles are both large and small compared to the wavelength of the incident light.

8.2 Electrical conduction as a function of contact area

For the touchscreen structure shown in Fig. 8.1, the upper electrode (PET/ITO) can be considered as a supported flexible beam. Application of force to the beam causes deformation and bending, where the vertical deflection depends on the the applied force. Bending causes the upper surface of the beam to become concave and the lower surface to become convex. A neutral axis within the beam exists, where above the material is compressed and below the material is stretched. For a symmetrical beam cross-section the neutral axis passes through the centre of the beam in both the x and y directions.

The deformation of the flexible electrode can be modelled as a function of applied force, W, where at a certain force the deformation is sufficient to create contact with the PS layer which is fixed at a set distance below the flexible electrode. This distance is set by the 'air-gap' between the PS layer and electrode. Increasing the force acts to increase the contact area between electrode and PS layer. This can be used as the basis of modelling the area-sensitive resistance response. For simplicity, the system is considered in one dimension only where the electrode is fixed at both ends. A schematic of this model is shown in Fig. 8.2. The curvature of the deflected electrode, which is the reciprocal of the radius of curvature R, can be approximated by:

$$\frac{1}{R} = \frac{d^2y(x)}{dy(x)^2} = \frac{M(x)}{EI} \tag{8.1}$$

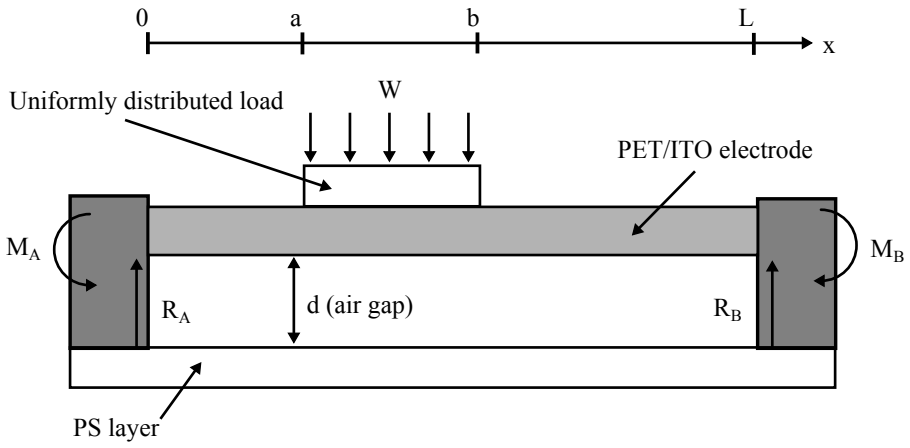

FIGURE 8.2: Schematic of the model used for predicting the vertical deflection, y, of the flexible PET/ITO substrate at a distance x along the electrode, for a uniformly distributed load W. M_A and M_B are the bending moments at points A and B, at each end of the beam, and similarly R_A and R_B are the reaction forces.

where y is the vertical deflection of the electrode as a function of position x, M is the applied bending moment, and E and I are the Young's modulus and the moment of inertia of the PET/ITO substrate respectively [209]. Here, the load W is uniformly distributed over a finite width $b-a$. In reality, this may correspond to the finite width of a fingertip or stylus device. The full derivation of the deflection is given in Appendix A, with the final result that the deflections y_1 (for $0 \leq x \leq a$), y_2 (for $a \leq x \leq b$) and y_3 (for $b \leq x \leq L$) are given by:

$$\begin{aligned} y_1 &= \left[\frac{M_A x^2}{2} + \frac{R_A x^3}{6}\right] \times \frac{1}{EI} \\ y_2 &= \left[\frac{M_A x^2}{2} + \frac{R_A x^3}{6} - \frac{w\,(x-a)^4}{24}\right] \times \frac{1}{EI} \\ y_3 &= \left[\frac{M_A x^2}{2} + \frac{R_A x^3}{6} - \frac{w\,(x-a)^4}{24} + \frac{w\,(x-b)^4}{24}\right] \times \frac{1}{EI} \end{aligned} \tag{8.2}$$

where:

$$\begin{aligned} M_A &= \frac{-w}{L^2}\left[\frac{L^2}{2}\left(b^2-a^2\right) - \frac{2L}{3}\left(b^3-a^3\right) + \frac{1}{4}\left(b^4-a^4\right)\right] \\ R_A &= \frac{w}{L^3}\left[L^3\,(b-a) - L\left(b^3-a^3\right) + \frac{1}{2}\left(b^4-a^4\right)\right] \end{aligned} \tag{8.3}$$

Equations 8.2 and 8.3 allow the determination of the PET/ITO deflection as a function of distance along the electrode under a variety of different conditions. Using these equations, mathematical simulations of the model for PET/ITO parameters such as thickness and Young's modulus can be compared. Furthermore, by comparing the deflection with the size of the air-gap between the PET/ITO and PS layers a model for predicting the point of first contact and the subsequent decrease in resistance with increasing contact area can be calculated. Details of the modelling procedure and results of the simulations are presented in chapter 11.

8.3 Conduction mechanisms in conducting polymer composites - phenomenological models

8.3.1 Percolation theory

Percolation theory is used to predict the transition point between two phases or states of matter. The concept of percolation was first introduced by Flory in 1941, who described the transition between small branching molecules into a larger macromolecule by the formation

of chemical bonds (gelation) [210]. A more mathematical approach was derived by Broadbent and Hammersley in 1957 [211].

Percolation theory is also widely used to describe the electrical conductivity of composite systems, where conductive components are embedded into an insulating medium. The composite is divided into a lattice, where each lattice site is either conductive (fraction p) or insulating (fraction (1-p). For a given p there is a defined probability that a conductive pathway is formed between two points in the composite. For increasing p it is more likely that conductive pathways are formed through the composite, as illustrated in Fig. 8.3. At a critical filler content, called the percolation threshold p_c, conduction pathways begin to form and the electrical resistance is highly sensitive to any small change in p. Below the percolation threshold the filler particles are widely spaced resulting in few, if any, conductive pathways. Well above the percolation threshold, an extensive conductive network is formed and the resistance is less sensitive to small changes in p. The general trend of conductivity with increasing filler volume fraction is shown in Fig. 8.4 for filler content above p_c. Below p_c it is predicted that the composite is electrically insulating. For $p > p_c$, the conductivity σ is described by:

$$\sigma \propto (p - p_c)^t \tag{8.4}$$

where the exponent t, at least theoretically, depends upon the dimensionality of the system, the number of particle clusters formed and a relevant scaling law. For example, for 3D systems a universal value of $t = 1.9$ is predicted. However, experimentally, values of t in the range $1 - 6.27$ have been reported [212]. Likewise, the value of p_c is theoretically dependent on the particle coordination number, the dimensionality of the system and the filling factor of the particle. Theoretically, for 3D systems a value of $p_c = 0.16$ is predicted [213]. However,

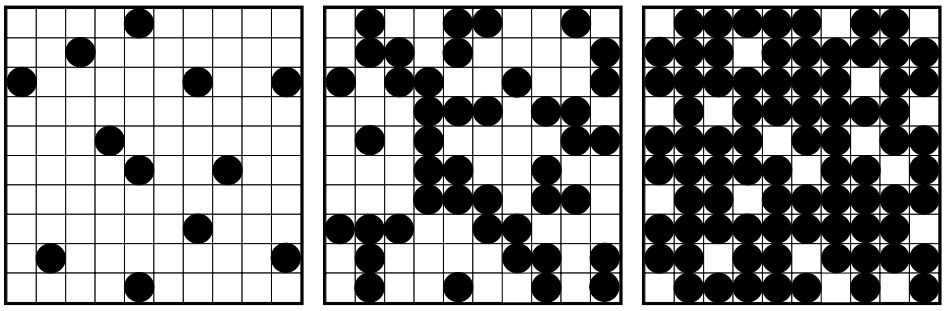

(a) $p < p_c$ (b) $p \approx p_c$ (c) $p > p_c$

FIGURE 8.3: Schematic showing the increase in conductivity with increasing p in a conducting polymer composite, where the black circles represent conducting elements in an insulating matrix. In (a) no conducting pathways are formed, and in (b) the percolation threshold is reached and conductive pathways begin to form. In (c) the system is above the percolation threshold and the conductivity is less sensitive to small changes in filler content.

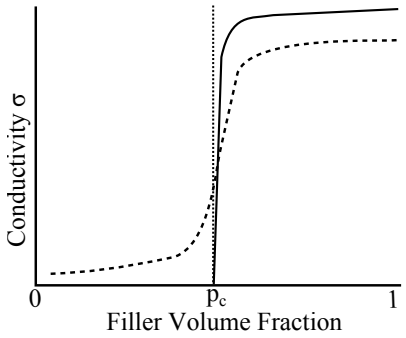

FIGURE 8.4: The conductivity of a conductive polymer composite as predicted by percolation theory (solid line) and using an effective medium model (dashed line). Near to the percolation threshold p_c, the conductivity is highly sensitive to small changes in the filler loading.

experimentally p_c is found to be dependent on the particle shape, the ratio of filler to matrix particle sizes and interactions between particles.

Percolation theory has been used to model the conductivity of various composites, examples of which include polymer/carbon nanotubes [214], rubber/carbon black [215] and polymer/metal systems [216]. It was found that the value of p_c is often lower for composites containing nanoparticles [217]. For fibrous or acicular filler particles, percolating networks may form at low filler contents due to elongated shape of the particles [218, 219]. Percolating systems are intrinsically pressure sensitive, as for $p \approx p_c$ deforming the composite can result in large changes in the electrical conductivity, due to the decreasing distance between adjacent conductive particles which increases the number of conductive pathways formed. Hence percolating composites have extensive force or pressure sensing applications [220, 221].

The electrical conductivity of percolating composite systems is often analysed as a function of conductive particle loading or applied force. For example, for carbon nanofibres embedded in an epoxy matrix, current-voltage analysis showed Ohmic behaviour where the conductivity increased with carbon nanofibre content above p_c [222]. However, many percolating systems also exhibit non-Ohmic current-voltage characteristics that cannot be fully explained by percolation theory and instead suggest quantum tunnelling conduction mechanisms [223, 224]. Detailed investigations into the electrical properties of conducting polymer composites use an extended theoretical approach which may include effective medium models and quantum tunnelling behaviour.

8.3.2 Further modifications to percolation theory

The effective medium model extends percolation theory by removing the sharp transition from insulating to conductive behaviour and considering the conductivity below the percolation threshold. Here the resistance between pairs of nearest neighbours within the insulating

matrix is calculated, resulting in a network of randomly positioned particles with a random distribution of resistances. The average resistance of the ensemble is used to characterise the effective medium, which has the same overall macroscopic properties as the percolation model [225]. The development of a generalised effective medium (GEM) model allows for the conductivity contribution from the shape of the filler particles as well as their size and orientation [226]. The finite conductivity of the insulating phase is also accounted for. The conductivity predicted by an effective medium model is compared to that predicted by percolation theory in Fig. 8.4. The effective medium model can be used to predict the conductivity of a composite over the entire range of filler contents for a range of particle shapes.

In the Links-Nodes-Blobs model proposed by Lin and Lee, clusters of conductive material (blobs) are joined by chains of single particles (links) which intersect at nodes [227]. The distribution of links, blobs and nodes controls the mechanical properties of the composite. This was further extended to include the effect on the electrical properties of the composite [228]. Across the blobs, conduction is through a large number of parallel pathways leading to a low electrical resistance. The links are comprised of a chain of single particles in series, and have a much higher resistance. The overall resistance of the composite is therefore dominated by the number of complete links.

Additionally, Gupta and Sen extended the percolation model to include a third phase in the form of a quantum tunnelling bond [229]. This was linked to random resistor networks, described in the next section, and quantum tunnelling mechanisms as described in section 8.4.3. However, whilst the models presented above extend the applicability of percolation theory, they still offer no physical insight into the nature of any non-linear contribution to the conductivity which is often seen in composite materials.

8.3.3 Random resistor network models

Random resistor networks were first described by Gefen and Shih in an attempt to model the macroscopic current-voltage behaviour of discontinuous thin gold films with observed percolation threshold behaviour [230]. The percolating system was modelled as a network of conductive and non-conductive elements, where the conductive elements had either a linear or non-linear resistance.

In a non-linear random resistor network (NLRRN) each resistor has a small, non-linear component, for example caused by Joule heating, and the macroscopic current-voltage (I-V) relationship is:

$$V = rI + CI^{\alpha}, \tag{8.5}$$

where C and r are constants and the exponent $\alpha > 1$. It is often found that the non-linearity increases with increasing applied voltage. For low values of current (or voltage) the behaviour can be considered as linear. A crossover current, I_c, can be defined beyond which the overall conductance deviates from linear behaviour.

In the dynamic random resistor network (DRRN) model, each resistor initially has a linear I-V response but for a sufficiently high electric field a non-linear term is introduced, for example caused by electron tunnelling through narrow insulating regions. Below this critical field, the material exhibits Ohmic behaviour given by $I = \Sigma_1 V$ where Σ_1 is the linear conductance. For both NLRRN and DRRN models, it is predicted that I_c follows a scaling relationship according to:

$$I_c =\sim \Sigma_1^x. \tag{8.6}$$

The exponent x is linked to the spatial dimension d and and the type of model used to describe the non-linearity of the percolating medium. Gefen *et al.* determined that the exponent x obeyed the following relationships:

For the NLRRN:

$$x \lesssim \frac{v}{t}(d-1). \tag{8.7}$$

For the DRRN:

$$x \lesssim 1 + \frac{v}{t}, \tag{8.8}$$

where v is the correlation length critical exponent and t the exponent in percolation conductivity according to Equation 8.4 [230]. In three dimensional systems commonly accepted values are $v = 0.89$ and t=1.7 [231]. Hence for the NLRRN $x \lesssim 1.05$ and for the DRRN $x \lesssim 1.52$.

In order to apply this model, the function:

$$I = \Sigma_1 V + \Sigma_2 V^2 \tag{8.9}$$

is often fitted to the I-V curves obtained for a particular device, where Σ_2 is the quadratic (or non-linear) conductance. This model has been successfully applied for epoxy resin/graphite flake composites [231], carbon/wax composites [232] and more recently by Webb *et al.* for a nanocomposite pressure sensitive material [233]. In the latter case, the nanocomposite material was also manufactured by Peratech Holdco Ltd, however it has a different composition than the ink and sensor presented in this thesis and is primarily used in non-transparent pressure sensing applications. Webb investigated the relationship between Σ_1 and Σ_2 with force applied to the composite. It was found that Σ_1 increased for up to 10 N, however the quadratic conductance G_2 increased for up to 1 N only and subsequently decreased. This was

attributed to the increasing number of Ohmic contacts formed between the conductive particles within the ink with the increase in applied force. At higher forces the Ohmic behaviour outweighed the contribution from non-linear conduction mechanisms.

It should be noted that the quadratic term in equation 8.9 is somewhat arbitrarily chosen to represent all non-linearity within the I-V curve. Celzard *et al.*, Lin *et al.* and He and Tjong [223, 231, 234] also used a cubic term instead of quadratic, in addition to the linear term, with excellent results.

Here, the PS layer within the resistive touchscreen contains nanocomposite granules, where each granule may behave as a conducting polymer composite, that is a network of conductive nanoparticles embedded in an electrically insulating polymer matrix. The conductivity through such a composite may be modelled as having a linear conductance term through direct percolation between individual nanoparticles spanning the thickness of the pressure sensitive layer, and also a quadratic term adding a non-linear conductivity. For the NL-RRN model, this non-linearity may be inherent within the granules with no dependence on the applied field. Alternatively, for the DRRN model this non-linearity may stem from the formation of additional conduction pathways through quantum tunnelling or similar. Beyond this, the model gives no further information on the nature of any non-linear conduction pathways.

8.4 Electrical conduction between metals, semiconductors and insulators

In order to understand charge transport mechanisms within the nanocomposite granules, the charge transport mechanisms of semiconductors and insulators are now discussed. Within the granules, the nanoparticles used are antimony doped tin oxide, a degenerate semiconductor [143]. The electrons within the conduction band (CB) are free to be emitted into another host media providing certain conditions are met. The processes of thermionic emission, Schottky emission and the image field potential for semiconducting materials are described below. The nanocomposite granules contain a silicone polymeric binder, which is electrically insulating. In insulating materials there is a large difference in energy between the valence band and the conduction band, such that in equilibrium the Fermi level lies in the forbidden gap. However, unlike for semiconductors, the gap between Fermi level and conduction band is large and thermal excitation of charge carriers across the band gap is unlikely, leading to low electrical conductivity. Nevertheless, charge may be injected into insulating materials in the same way as charge can be injected into a vacuum by thermionic emission. The following sections also describe the injection and subsequent transport of charge in insulating material.

8.4.1 Emission of electrons from semiconductors

8.4.1.1 Thermionic emission

Thermionic emission is the process by which an electron may leave a surface or a potential well as a result of it possessing sufficient thermal energy. The minimum energy the electron requires in order to leave the surface is given by the work function ϕ of the material. Here, the work function is the energy difference between the Fermi level, E_F of the semiconductor and a zero potential vacuum, as shown in Fig. 8.5(a). If an electron possesses a thermal energy which is greater than the work function, the resultant current density J_{th} is a function of the temperature T and is described by Richardson's law:

$$J_{th} = (1 - R)\frac{4\pi e m_e}{h^3}(k_B T)^2 \exp\frac{-\phi_c}{k_B T}, \tag{8.10}$$

where e is the electron charge and m_e is the effective mass of an electron in the conduction band [235]. The fraction R represents the proportion of electrons reflected at the interface.

8.4.1.2 Image field potential

An electron leaving a charged metal or semiconducting surface is subject to a potential created by the image charge effect. There is an electrostatic charge between the surface and the escaping electron. This can be modelled by replacing the charged surface with a point charge located at an equal distance inside the surface as the electron is outside the surface.

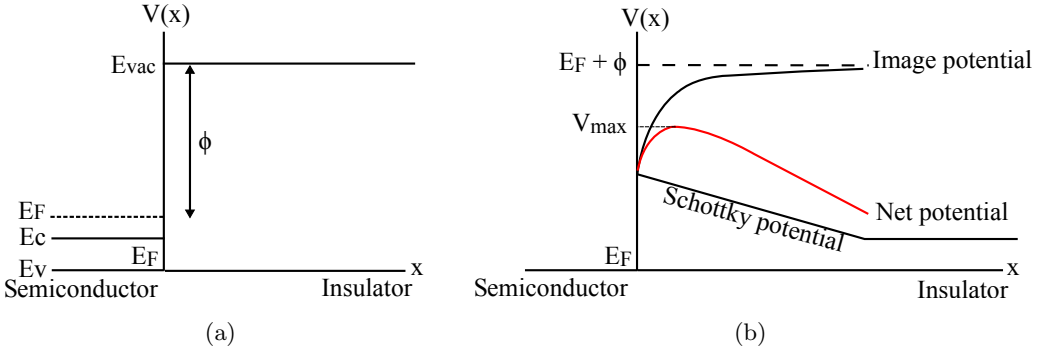

FIGURE 8.5: Schematic showing (a) the interface between a doped semiconductor and the vacuum, where a minimum energy equal to the work function ϕ is required for an electron at the Fermi level E_F to be emitted into the vacuum. Here, in the doped semiconductor, E_F lies above the conduction band, E_c. (b) The potential experienced by an emitted electron as a function of the distance from the surface. The resultant potential is the sum of the Schottky and image field potentials experienced by the electron.

The electron experiences a potential given by:

$$V(x) = \frac{-e^2}{16\pi\varepsilon_0 x}, \tag{8.11}$$

where ε_0 is the permittivity of free space, and x is the distance between each charge and the surface. This creates a potential barrier which the electron must overcome in order to escape the metal and be injected into the polymer.

8.4.1.3 Schottky effect

An external applied electric field acts to alter the shape of the potential barrier an electron must overcome in order to leave the surface. The potential $V(x)$ associated with a (constant) electric field E is given by:

$$V(x) = -eEx, \tag{8.12}$$

where x is again the distance between the electron and the surface. This is the Schottky effect which leads to Schottky field emission of electrons. The result is to lower the potential required for electrons to leave the surface. The potentials induced for both the image field potential and the Schottky potential are shown in Fig. 8.5(b). Overall, the electron has to overcome a lower potential to be successfully emitted from the surface of the metal and the emission is increased. Including these effects, the thermionic current density is given by:

$$J_{th} = \frac{4\pi em}{h^3}(k_B T)^2 \exp\frac{-\Phi_c - V_{MAX}}{k_B T}, \tag{8.13}$$

where V_{max} is as defined in Fig. 8.5(b). This equation is applicable for electric field strengths up to the order of 10^8 $\mathrm{V\,m^{-1}}$. Above this, the field emission dominates over the thermionic emission, and other emission processes including field-assisted (or Fowler-Nordheim) quantum tunnelling become significant.

8.4.2 Injection of electrons into insulators

8.4.2.1 Space charge limited injection

In a perfect insulator there are no energy traps for electrons and there is a negligible concentration of free charge carriers in thermal equilibrium. All injected electrons reside in the conduction band and contribute to space-charge. For Ohmic contacts, charge injection into a trap-free polymer is eventually limited when the injected charge carrier density becomes so large that the field due to the carriers themselves is dominant over the applied bias, and no

further injection occurs. The trap-free space charge limited current density, J_{TFSCL} is given by the Mott-Gurney law:

$$J_{TFSCL} = \frac{9}{8}\varepsilon_0\varepsilon_r\mu\frac{V^2}{d^3} \tag{8.14}$$

where ε_0 and ε_r are the relative permittivity and the permittivity of free space, μ is the electron mobility and d is the distance between the two electrodes (or the insulator thickness) [235]. This predicts a quadratic dependence of the current on the voltage and a strong $1/d^3$ dependence on material thickness. Of course, in reality most insulators contain electron trap sites. The above equation will then apply for an imperfect insulator at applied voltages which are sufficiently high so that the number of injected electrons exceeds the number of initially empty electron traps, and all traps are filled.

8.4.2.2 Charge hopping and the Poole-Frenkel effect

Electron traps in insulators can be in the form of chemical impurities and structural imperfections. The presence of these traps, as well as phonon collisions, limits the flow of space charge. For example, physical defects within the insulator structure may create empty energy levels into which injected electrons can be trapped. Shallow traps are found just below the conduction band such that a small injection of energy is required to promote the electron into the conduction band. Deep traps are located close to the valence band, below the Fermi level. Injected charge may leave the trap by thermal excitation. If the electron gains enough thermal energy to overcome the potential barrier imposed by the trap it may be promoted to the conduction band and contribute to the conductivity. Additionally, in a process known as variable charge hopping, charge may be transferred from one localised trap site to another, through the absorption of phonons (lattice vibrations). This is shown in Fig. 8.6(a).

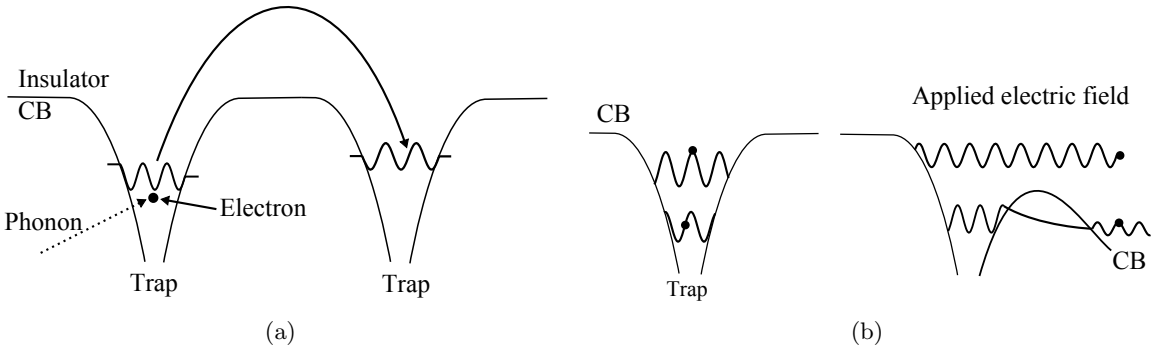

FIGURE 8.6: Schematic showing (a) the charge hopping mechanism between trap sites in an insulating material. Absorption of a phonon or photon allows charge to transfer from one trap site to another. (b) The Poole-Frenkel effect, where an externally applied electric field causes reduction of the potential barrier in one direction. This allows charge trapped within the site to flow out or tunnel through the remaining barrier.

Alternatively, an external electric field can reduce the energy the electron must exceed in order to escape the trap, similar to the Schottky effect for potential barriers in semiconductors. The electric field lowers the trapping potential at one side of the trap, so that charge can flow out of the trap or tunnel through the reduced potential barrier, as shown in Fig. 8.6(b). This is known as the Poole-Frenkel effect [236]. Murgatroyd derived the current density as a function of voltage for an insulator containing traps which limit the current by a fraction θ_0 to be [237]:

$$J_{PF} = \frac{9}{8}\varepsilon_0\varepsilon_r\mu\theta_0\frac{V^2}{d^3}\exp\left[\frac{0.891}{k_BT}\left(\frac{Ve^3}{\pi\varepsilon_0\varepsilon_r d}\right)^{\frac{1}{2}}\right]. \tag{8.15}$$

8.4.3 Quantum tunnelling between semiconductor particles separated by a potential barrier

The previous sections described how electrons may be injected into a semi-conductor or insulator, providing they have sufficient energy to overcome the potential barrier. The potential barrier is increased by the image field potential and decreased in the presence of an external electric field. Classically, if the electrons do not possess sufficient energy then they cannot overcome the potential barrier. However, electrons are also described as quantum mechanical entities with a wave function. When the wave function reaches the potential barrier, if the potential barrier is too high to overcome, the wavefunction will decay exponentially to zero amplitude. If there is another energy band, separated from the potential by a distance d (e.g. two metal particles separated by a thin layer of insulating material) the amplitude of the wavefunction may be non-zero by the time once it reaches the far side of the potential barrier and the electron may tunnel into the adjacent conduction band with no loss of energy.

8.4.3.1 Simple quantum tunnelling

In the simplest case, an electron of mass m_e and energy E_x may be trapped in a one-dimensional potential barrier of uniform barrier height V_0, where $V_0 > E_x$, and width b as shown in Fig. 8.7. The potential barrier may be caused by a finite region of insulating material, such as the silicone binder present between ATO nanoparticles within each nanocomposite granule. The wavefunction of the electron, Ψ, is a solution to the time independent Schrödinger equation:

$$\frac{-\hbar^2}{2m}\frac{d^2\Psi(x)}{dx^2} + V(x)\Psi(x) = E\Psi(x). \tag{8.16}$$

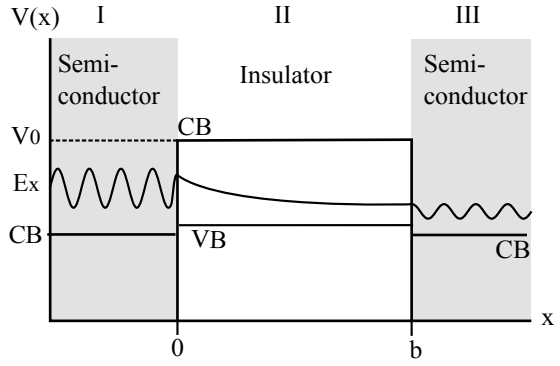

FIGURE 8.7: Schematic showing the quantum tunnelling mechanism between two semiconductive particles (regions I and III) separated by an insulator (region II) which presents a potential barrier of height V_0. The wavefunction of an electron of energy E_x initially found in I decays exponentially when it reaches the barrier with II, so that there is a finite probability that the electron may be found in region III provided that the potential barrier width b is sufficiently small.

This equation may be solved separately for the wavefunction of the electron in each region in Fig. 8.7 (denoted Ψ_I, Ψ_{II} and Ψ_{III}) yielding the solutions:

$$\Psi_I(x) = A \exp ikx + B \exp -ikx, \tag{8.17}$$

$$\Psi_{II}(x) = C \exp \mu x + D \exp -\mu x, \tag{8.18}$$

$$\Psi_{III}(x) = E \exp ikx + F \exp -ikx. \tag{8.19}$$

where:

$$\begin{aligned} k &= \frac{\sqrt{2mE_x}}{\hbar}, \\ \mu &= \frac{\sqrt{2m(V_0 - E_x)}}{\hbar}. \end{aligned} \tag{8.20}$$

The general solutions to the time-independent Schrödinger equation are wavefunctions representing reflected and transmitted parts of the wave. However, in region III only transmitted waves exist and the coefficient F for Ψ_{III} in equation 8.17 is equal to zero. In region II it can be assumed that the electron wave reflected from the right edge of the barrier is also negligible, so that C is also zero. Therefore, inside region II (the classically forbidden zone) the wavefunction exponentially decays with increasing distance through the barrier.

The transmission probability τ, that is the probability that an electron will be found on the far side of the potential barrier of width b, is given by the ratio $\mid E \mid^2 / \mid A \mid^2$. By applying continuity conditions for the wavefunctions, where at the edge of each region both the wavefunctions and the second order differential of the wavefunctions must be equal in value, the coefficients A and E can be determined, giving [238]:

$$\tau = \frac{|\ E\ |^2}{|\ A\ |^2} = \frac{16\mu^2 k^2 \exp -2\mu b}{(k^2+\mu^2)^2} = 16\left(\frac{E_x}{V_0}\right)\left(1-\frac{E_x}{V_0}\right)\exp -2\mu b \tag{8.21}$$

The tunnelling probability exponentially decays with increasing barrier width b and is also reduced for larger barrier heights V_0.

8.4.3.2 Field-assisted quantum tunnelling

As was described in the preceding sections, the potential barrier an electron must overcome can be reduced through the image field potential, the Schottky effect or the Poole-Frenkel effect. Modelling of the potential barrier as rectangular is not accurate in the presence of an external electric field. Instead an electric field modifies the barrier height, as shown in Fig. 8.8(a) and this gives rise to field-assisted quantum tunnelling effects.

To calculate the tunnelling probability through a triangular potential barrier, the barrier is treated as a series of infinitesimally small rectangular barriers, provided that the slope of the barrier is sufficiently low. This is the Wentzel-Kramers-Brillouin approximation [239]. For a triangular barrier the resultant current density J_{FAQT} is given by:

$$J_{FAQT} = A\exp\left[\frac{-4}{3}\left(\frac{2m}{\hbar^2}\right)^{\frac{1}{2}}\frac{b\,(V_0-E_x)^{\frac{3}{2}}}{eE}\right]. \tag{8.22}$$

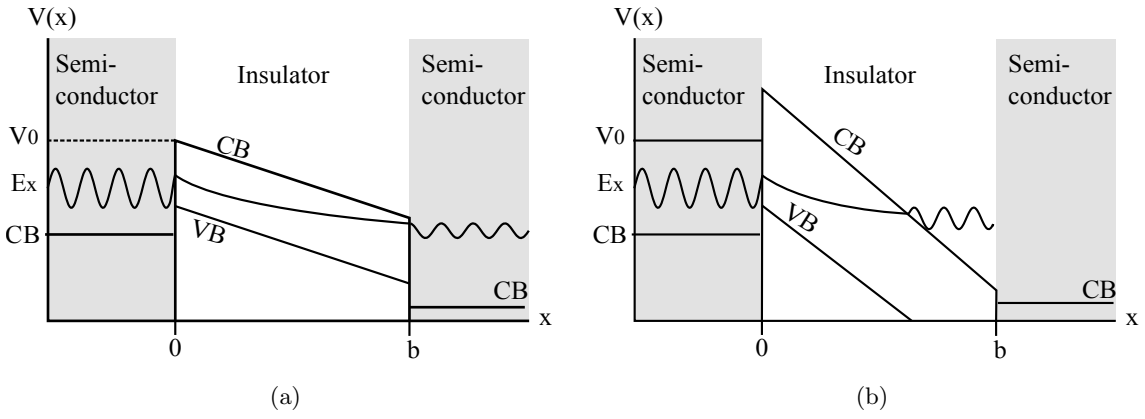

FIGURE 8.8: Schematic showing field assisted quantum tunnelling mechanisms. In (a) the potential barrier created by the insulator interface is lowered through an external electric field. The probability of transmission for an electron to tunnel between the conduction bands (CB) of the semiconductor regions is increased. In (b) the potential barrier has been drastically distorted by the electric field such that an electron from the semiconductor CB can now tunnel into the insulator CB, in a process known as Fowler-Nordheim tunnelling.

In Fowler-Nordheim tunnelling, a large electric field distorts the potential barrier to such an extent that the electrons tunnel from the conduction band of the semiconductor into the conduction band of the insulator, as shown in Fig. 8.8(b). In this case, the current density is modified by the transport of the electrons within the insulator following the Mott-Gurney law. Neglecting the effect of the image force on the potential barrier, and the temperature dependence of the electron energy, the current density J_{FN} can be written in the form [240]:

$$J_{FN} = \frac{q^3 E^2}{8\pi h\phi} \exp\left[\frac{-4(2m)^{\frac{1}{2}}\,(V_0 - E_x)^{\frac{3}{2}}}{3\hbar q E}\right]. \tag{8.23}$$

8.4.4 Linking conduction mechanisms to macroscopic current-voltage relationships

The current-voltage (I-V) behaviour of a material can be used to probe the electrical conduction mechanisms. By relating the current I to the current density J (where J is simply the current per unit area) and the applied voltage to the electric field within the sample then non-linear current transport mechanisms may be determined. For a flat sample with Ohmic contacts to two electrodes the electric field may be approximated as $E = \frac{V}{d}$, where d is the separation between electrodes (i.e. the sample thickness). In previous sections, the conduction mechanisms between semiconductors and insulators were described. The J-E characteristics all have the basic form:

$$J \sim AE^m \exp -BE^n, \tag{8.24}$$

where A and B are constants, and m and n may take the values shown in Table 8.1 for each of the charge transport mechanisms described in the previous sections.

By analysing the slope of the log$J$-log$E$ characteristics, the dominant conduction mechanism may be determined. For example, Niklasson and Brantervik found that a metal-insulator thin film consisting of Co-Al_2O_3 had a space-charge limited current density with a steep

Conduction Mechanism	m	n
Ohmic	1	0
Space charge limited	2	0
Poole-Frenkel charge de-trapping	2	1/2
Field-assisted quantum tunnelling	0	-1
Fowler-Nordheim quantum tunnelling	2	-1

TABLE 8.1: Coefficients m and n for equation 8.24 describing conduction mechanisms between semiconductor/insulator composites

rise in current at high fields caused by the approach to the trap-filled limit [241]. Similarly, Chiguvare *et al.* studied conduction through an ITO/P3HT/aluminium thin film, where charge was injected through the aluminium contact. At low field the J-E response was Ohmic. With increasing field the slope of the logJ-logE plot increased to > 2, indicating the presence of traping sites [242]. Chiou *et al.* investigated the Fowler-Nordheim tunnelling behaviour in metal oxide/semiconductor capacitors, where the pre-factors of the quadratic-E dependence and the exponential 1/E dependence in equation 8.23 were determined from analyis of the I-V response [243]. In polyvinyl alcohol/glycogen blends, I-V analysis showed charge transport through Poole-Frenkel de-trapping and Schottky emission, dependent on the blend composition and temperature. At low voltages a space charge contribution was also present [244].

For analytical purposes it may be assumed that conduction through a composite material comprising conductive and insulating phases has both a linear and a non-linear component, as described by:

$$J = \sigma_0 E + AE^m \exp\left(\frac{-B}{E}\right), \tag{8.25}$$

where σ_0 is the linear conductivity and A_1 and B are constants. The non-linear term may account for field-assisted or Fowler-Nordheim tunnelling. Webb *et al.* used this model to determine the temperature dependent conduction mechanisms through a pressure sensitive nanocomposite sensor also developed by Peratech [233, 245]. The linear component was attributed to direct charge transfer between contacting conductive particles, and the non-linear term was attributed to tunnelling conduction through the insulating phase. Webb *et al.* found that increasing the force applied to the composite increased both σ_0 and A. It was inferred that compression of the composite both increased the number of direct contacts (as for percolation theory) and decreased the potential barrier width for quantum tunnelling through the insulating phase. Later work showed the coefficient B was temperature dependent [246]. Additionally, He and Tjong used equation 8.25 and also the random resistor network approach exemplified by equation 8.9 to describe non-linear conduction through high-density polyethylene/carbon nanofibre composites [223]. It was found that the former model provided the better fit to the observed data where non-linearity was created by the formation of field-enhanced tunnelling pathways.

8.5 Flicker noise within conducting polymer composites

8.5.1 Theory of noise

Electronic noise may be defined as a random fluctuation in a measurable quantity such as voltage or current, which results from the random movement of charge carriers within a device. This is intrinsic to the device and is not caused by any external noise source such as electromagnetic interference. For any quantity that fluctuates over time, a power spectrum can be calculated which quantifies the noise in the frequency domain. For example for a signal $X(t)$ which fluctuates around a zero mean value the power spectrum is expressed as the amplitude squared of the Fourier transform of the signal $X(t)$:

$$S(f) = \lim_{T\to\infty} \frac{1}{2T} \left| \int_{-T}^{T} X(t) exp(-2\pi i f t)\, dt \right|^2. \tag{8.26}$$

The Weiner-Khintchine theorum states that the power spectrum is also the Fourier transform of the autocorrelation function $C(\tau)$, where:

$$C(\tau) = \lim_{T\to\infty} \frac{1}{2T} \int_{-T}^{T} X(t+\tau)X(t)\, dt. \tag{8.27}$$

The three main types of intrinsic noise are thermal (Nyquist), shot and flicker noise (also called excess or 1/f noise). Thermal noise is caused by thermal excitation of charge carriers within the device. The spectral power, defined in equation 8.26, is independent of the both the current and the frequency and depends only on the temperature T and resistance R of the device, as:

$$S(f) = 4k_B T R. \tag{8.28}$$

Shot noise is a result of discrete electronic carrier motion in a device and is also independent of frequency. It causes a fluctuation in the measured current which is proportional to the charge q of the charge carrier and the current I through the device:

$$S(f) = 2qI. \tag{8.29}$$

These noise forms have limited applicability in the investigation of material properties. Whilst thermal noise may provide an estimate of the effective electron temperature, it cannot distinguish between for example, a metal and a carbon resistor if they both have the same R value. Shot noise may indicate the charge value of the charge carrier, but is only visible at

temperatures low enough for thermal noise to be negligible. However, flicker noise has extended applicability in materials characterisation because it probes the underlying conduction mechanisms.

Flicker, or excess noise was so-called because it was found in excess of the thermal and shot noise within a current-carrying device, where the spectral power $S(f)$ scales as V^2. The fluctuating variable has a finite relaxation time which can be expressed by a relaxation function $\varphi(t)$. The power spectrum then becomes:

$$S(f) = C \int_{-\infty}^{\infty} \varphi(t) exp(-2\pi i f t)\, dt. \tag{8.30}$$

For example, the Debye relaxation function for a single relaxation time τ is $\varphi(t) = exp(-i/\tau)$. The power spectrum becomes a Lorentzian function:

$$S(f) \propto \frac{2\tau}{1 + (2\pi f \tau)^2}. \tag{8.31}$$

For a distribution of such Lorentzian functions, with varying time constants τ, the integration of these gives the total power spectrum:

$$S(f) \propto \int_{0}^{\infty} \frac{2\tau}{1 + (2\pi f \tau)^2}\, dt \tag{8.32}$$

In this case, $S(f)$ now has a $1/f$ dependency. This is illustrated in Fig. 8.9 which shows five Lorentzian functions with different τ values, the summation of which tends towards to the

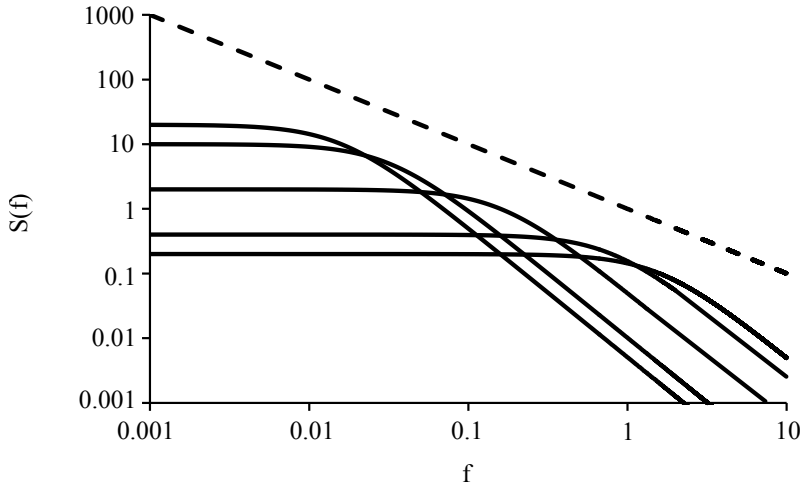

FIGURE 8.9: The power spectrum for several Lorentzian functions resulting from Debye functions with a variety of relaxations times τ. The dashed line shows a $1/f$ relationship. For a system in which the fluctuating variable is caused by a process with several characteristic relaxation time, the power spectrum may become frequency dependent.

$^1/_f$ relationship such that the power spectrum is now frequency dependent. The flicker noise is often written as $\frac{1}{f^\gamma}$, where $\gamma \approx 1$. The noise may also be expressed as a root mean square (rms) fluctuation of the measurement variable x, defined between a bandwidth of f_{min} and f_{max} as:

$$< (\delta x)^2 >= \int_{f_{min}}^{f_{max}} S(f)\, dt \tag{8.33}$$

As of yet, there is no universally accepted theory describing the origin of flicker noise. Theories tend to split depending on whether the noise originates in the bulk or the surface of the sample and also depend upon the nature of the sample. Generally, flicker noise exists in disordered systems leading many to believe it is defect driven [247]. The following section describes flicker noise measurements and suggested theories for conducting polymer composites, where the noise is usually measured as a function of increasing conductive particle content. Aside from conductive composites, flicker noise measurements have also been used to probe the charge transport mechanisms in metallic and metallic oxide films [248], semiconductors [249] and low-dimensional carbon systems such as graphene and carbon nanotubes [250, 251].

8.5.2 Applications in conducting polymer composite characterisation

Due to the inhomogeneous nature of conducting polymer composites the current pathways within the composite are non-uniform. The resultant conduction is inherently susceptible to fluctuation and noise effects. For composites adequately described by percolation theory, the noise is strongly dependent on the filler volume fraction close to the percolation threshold. For non-linear I-V behaviour the flicker noise may be strongly influenced by the nature of the conduction mechanism causing the non-linearity. Hooge predicted a behaviour of the generalised noise amplitude Υ of the form:

$$\Upsilon = \frac{S_R}{R^2} = \frac{S_V}{V^2} = \frac{S_I}{I^2} = \frac{V^\Theta}{f^\gamma} R^\omega, \tag{8.34}$$

where S_x represents the power spectrum for voltage, current or resistance fluctuations over time, denoted by the subscripts V, I and R respectively [252]. V, I and R represent the average values of these quantities. The exponent Θ is believed to be 0 for equilibrium resistance fluctuations where the current acts only as a probe. Non-zero values of Θ indicates that the noise is a driven phenomenon dependent on the current. The exponent w is usually close to 2 [253]. In percolating systems where $R \sim (p - p_c)^{-t}$ (from equation 8.4), it is often found that Υ diverges as the percolation threshold is approached from the conductive side. From equation 8.34:

$$\Upsilon \sim (p - p_c)^{-\kappa} \sim R^\omega, \tag{8.35}$$

where $\omega = \frac{\kappa}{t}$. Hence for increasing the conductive content p above the percolation threshold, it is expected that the value of Υ will decrease. Experimentally, and of relevance here, the value of p may be altered by compression of the composite, as compression acts to decrease the spacing between conductive particles and so increase the number of particles per unit volume. In terms of conduction mechanisms, the power law dependence of Υ on the resistance, as in equation 8.34, predicts classical percolation through linear conduction. However, Breeze *et al.* predicted an exponential dependence for non-linear conduction, for example through quantum tunnelling [254]. When investigating the flicker noise characteristics of carbon black/polyethylene composites, Breeze *et al.* found that at high resistivity the flicker noise showed exponential dependency on the resistivity, indicating quantum tunnelling transport mechanisms. A transition to power-law behaviour occurred as the composite approached the percolation threshold, where direct conduction occurred between particles. Hence the transition from quantum to classical behaviour occurred when the length scale for percolation was comparable to the length scale for the disorder within the composite.

In addition to the above analysis, the value of γ can also reveal important physical detail of the composite. As mentioned previously, $\gamma \approx 1$ leads to the 1/f frequency dependence characteristic of flicker noise. However, deviations away from unity may relate to trapping mechanisms within a disordered system. From equation 8.31 it is seen that a single trap with a single relaxation time produces a $1/f^2$ dependency. A smaller γ indicates an increasing number of trap states with an associated set of oscillators. Williams *et al.* investigated the noise characteristics of P3HT/polystyrene blends, where the proportion of the conductive P3HT represented the p fraction in the composite [255]. By decreasing p it was found that γ increased. This was attributed to a reduction in the number of conduction pathways with decreasing p, so that the charge carriers encounter fewer trapping sites.

8.6 Optical transmission through resistive touchscreens

The resistive touchscreen comprises two key layers, namely the PET/ITO flexible electrode and the pressure sensitive layer printed onto a glass/ITO electrode. Between these two layers there is an air gap of finite depth. The optical transmission through this assembly is complex. For a complete analysis scattering and absorption from each of the layers must be considered as well as interface effects. This section describes the theory of some of these processes and how they may be measured.

In order to simplify the problem, only the glass/ITO/pressure sensing layer is considered here. The focus is on the pressure sensitive (PS) layer, which comprises a single layer of granules or particle agglomerates dispersed within a thin (< 10 µm) polymer layer, as was shown in Fig. 8.1. To simplify this further, the scattering effects of the polymer are neglected and the

focus is on the particle ensemble only. Of course, in reality the polymer itself scatters and absorbs incident light, where the amount of scattering is linked to the molecular weight of the polymer chains [256]. Here, this effect is assumed to be negligible compared to the scattering contribution from the particulate material. The maximum transmission through the PS layer is equal to the transmission of the substrate, in this case the glass/ITO electrode.

The scattering of light from particles was briefly described in chapter 4 in relation to the technique of laser diffractometry. Here, the theory is expanded in relation to scattering of light from particulate material within the PS layer of the resistive touchscreen. Within the PS layer it is assumed the polymer matrix has a refractive index similar to that of glass, i.e.$\sim$ 1.5. The granules and particles are assumed to be spherical and homogeneous and remain intact when mixed into the ink prior to printing, such that the minimum granule size is of the order 1 µm. In order to understand the optical benefit of size-controlled pre-formed granules, the optical properties of this system can be compared to that of a PS layer containing ungranulated ATO nanoparticles. In this case, the PS layer contains particulate material with a range of sizes, from unagglomerated ATO nanoparticles of size 10 nm, small nanoparticle clusters, and larger agglomerates similar in size to that of the pre-formed granules, i.e. $>$ 1 µm. A dimensionless size parameter α can be defined in relation to the size of the particle, d, the refractive index of the surrounding medium m, and the wavelength of incident light in a vacuum, λ_0:

$$\alpha = \frac{2\pi dm}{\lambda_0}. \tag{8.36}$$

The ATO particles themselves have a complex refractive index, $m = n - i\kappa$, where n is the refractive index and the extinction coefficient κ relates to the absorption coefficient as $\xi = \frac{4\pi\kappa}{\lambda}$. Giraldi *et al.* measured refractive indices in the range 0.40–0.45 for nanostructured ATO films of thickness 150 and 998 nm respectively [257]. From theoretical considerations of band structure within bulk ATO, Li *et al.* reported an extinction coefficient κ of approximately 0.3 (taken from readings of the absorption coefficient ξ at a wavelength of 440 nm [143]).

8.6.1 Scattering of light from unagglomerated nanoparticles

Rayleigh scattering theory describes the scattering of light from molecules, however it can be extended to particles so long as α <1. For particulate material embedded in the PS layer, and for a characteristic wavelength of 550 nm this relation holds true for ATO nanoparticles or nanoparticle clusters less than 60 nm in size.

In the Rayleigh approximation, the particle is sufficiently small such that it encounters a uniform electric field from the incident electromagnetic (EM) radiation, and the penetration time for the electric field is much less than the period of oscillation of the EM wave. The

EM wave interacts with electrons within the particle, inducing a dipole moment which is proportional to the (constant) electric field experienced by the particle. The induced dipole radiates light in all directions with the same phase. For unpolarised incident light, the intensity of light scattered at angle θ, I_θ, detected at a distance R from the particle, is the average of the parallel and perpendicularly polarised components and is given by:

$$I_\theta = I_0 \frac{8\pi^4 P^2}{R^2 \lambda^4} \left(1 + \cos^2 \theta\right), \tag{8.37}$$

where I_0 is the intensity of the incident light and P is the polarisability of the particle [258]. This is shown schematically in Fig. 8.10(a). The scattered light intensity is equal in the forward and backward directions. There is also a strong wavelength dependence where shorter wavelengths scatter more than long wavelengths.

8.6.2 Scattering of light from nanoparticle agglomerates and granules

For agglomerates of nanoparticles greater than 60 nm in size $\alpha > 1$ and Rayleigh scattering theory cannot be applied. Hence for the case of nanoparticle agglomerates and nanocomposite granules Mie scattering theory must be used. This covers the scattering characteristics of

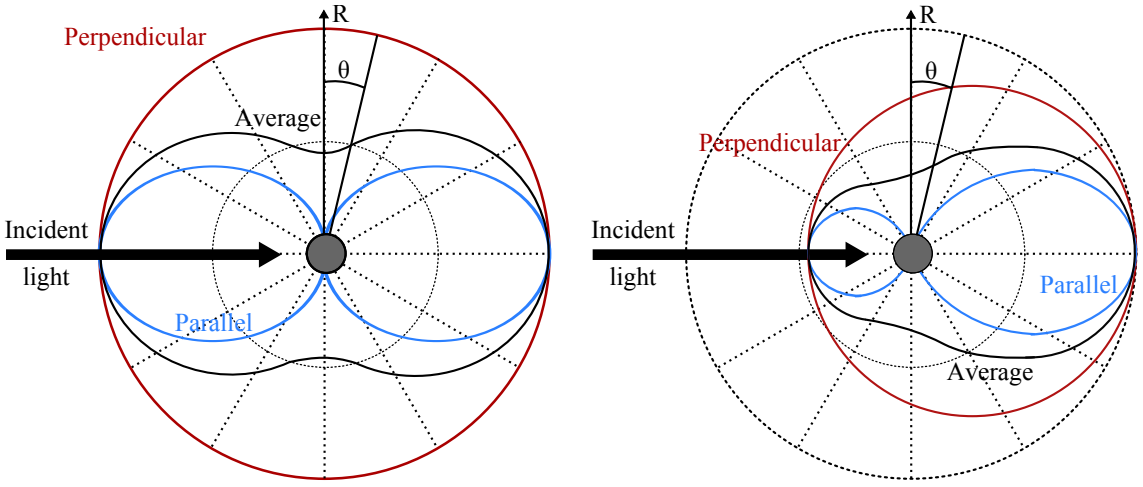

FIGURE 8.10: Schematic showing parallel, perpendicular and average light scattering from (a) a particles with $\alpha < 1$ where Rayleigh scattering theory can be applied. Here, the intensity of forward and backscattered light is equal (b) a particle with $\alpha > 1$, where Mie scattering theory must be applied. Here, scattering is predominantly in the forward direction.

particles of a wide range of sizes and refractive indices. Its complex derivation is outside the scope of this thesis but is described in detail elsewhere [258, 259].

For a spherical, homogeneous particle which is no longer small compared to the wavelength of the incident light, the light scatters from many different parts of the particle. The particle itself consists of an array of dipoles and the incident electric field can no longer be considered constant. Furthermore, the phase of the electric field is not uniform over the particle and this results in spatial and temporal phase differences between the emitted waves. As the scattered waves radiate they experience destructive interference causing a reduction in measured intensity. The interference depends on the wavelength of the incident light, the size and refractive index of the particle and the path difference travelled by the ray (which is dependent on the scattering angle). It is found that the intensity of scattered light observed at angle θ has both perpendicular and parallel polarised intensity contributions $I_\perp$ and $I_\parallel$ given by:

$$\begin{aligned} I_\perp &= E_\perp \frac{\lambda^2}{4\pi^2} i_1 (\alpha m \theta), \\ I_\parallel &= E_\parallel \frac{\lambda^2}{4\pi^2} i_2 (\alpha m \theta), \end{aligned} \tag{8.38}$$

where the intensity functions i_1 and i_2 are given by:

$$\begin{aligned} i_1(\alpha, m, \theta) &= \left| \sum_{n=1}^{\infty} \frac{2n+1}{n(n+1)} (a_n \Pi_n + b_n \Gamma_n) \right|^2, \\ i_2(\alpha, m, \theta) &= \left| \sum_{n=1}^{\infty} \frac{2n+1}{n(n+1)} (a_n \Gamma_n + b_n \Pi_n) \right|^2. \end{aligned} \tag{8.39}$$

The intensity functions i_1 and i_2 represent an infinite series which converges slowly. When α <1 and $m \approx 1$ the first term in the series corresponds to Rayleigh scattering. The terms Π_n and Γ_n provide the angular (θ) dependency and are Legendre polynomials. The terms a_n and b_n are dependent on both α and m and comprise half-integer-order Bessel functions. For unpolarised light, the scattering intensity is simply the average of the perpendicular and parallel contributions.

The angular dependence of the scattering is highlighted in Fig. 8.10(b), where it can be seen that the proportion of light forward scattered is much greater than is backscattered. Fig. 8.11 shows calculated values of the scattering intensity as a function of scattering angle, for a system comprising 10 nm ATO nanoparticles, 100 nm nanoparticle agglomerates and large agglomerates or granules of size 1 and 10 µm, dispersed into the PS layer at a concentration of 200 mm^{-3}. The calculations were performed using open source software [260]. Here, the

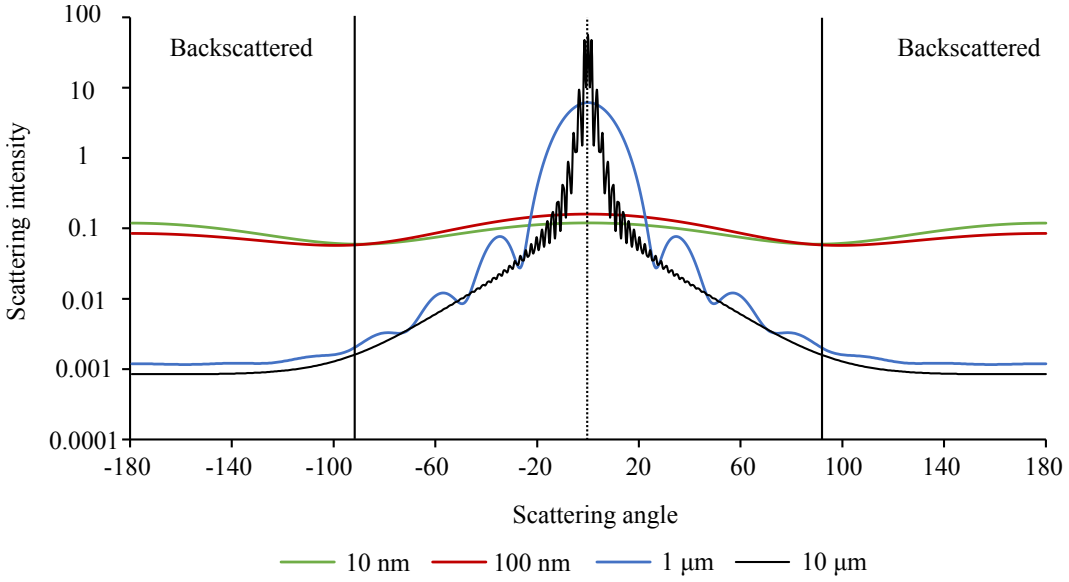

FIGURE 8.11: Graph showing the scattering intensity as a function of angle for a range of ATO particle/agglomerate sizes, calculated using Mie scattering theory. For 10 and 100 nm particles scattering intensity is approximately equal in all directions, and a Rayleigh approximation may be used. For larger agglomerates and granules the scattering intensity is significantly larger in the forward direction.

optical properties of the ATO nanoparticles were assumed to be equal to that of bulk or thin-film ATO, as described previously. As the particle size increases there is an increasing ratio of forward scattering to backscattering, resulting in the growth of the forward lobe in Fig. 8.10(b) and the large intensities predicted for small scattering angles in Fig. 8.11.

Note that for nanocomposite granules and agglomerates which can be approximated as optically opaque and non-absorbing Mie theory tends towards the principles of Fraunhofer diffraction. This was described previously in chapter 4 with reference to its use in laser diffraction particle measurement systems. Extension of Mie theory to include non-spherical particles, an absorbing particle medium and aggregrates of spheres has also been attempted [261].

8.6.3 Measurement of optical properties of touchscreens

In order to quantify the effects of scattering within the PS layer, the haze through the layer is measured. Haze, h, is defined as:

$$h = \frac{T_d}{T_t}, \tag{8.40}$$

where T_d is the diffuse transmission (the proportion of light scattered to greater than $\pm$ 2.5°), and T_t is the total transmission of light through the layer. The equipment and principles used to measure haze are reported in chapter 9. However, here it is useful to note that the

magnitude of light scattered to small angles increases for increasing particle size. Therefore, it is expected that by removing any particulate material less than 1 µm in size T_d would decrease. By pre-forming the granules prior to incorporation into the ink the fine particulate component is removed and haze is expected to decrease.

Additionally, the integrated transmittance, T_{INT} can be used to assess the transmission T of a layer over a specific wavelength range, and is given by:

$$T_{INT} = \frac{1}{b-a} \int_a^b T\left(\lambda\right)\, d\lambda, \tag{8.41}$$

where the limits a and b represent the upper and lower wavelengths for which the transmission is considered.

8.7 Chapter summary

Electric conduction through the pressure sensitive layer is a key process which determines the functional response of the touchscreen and its force-resistance characteristics. As such, understanding the origin of the pressure sensitive conduction is vital in order to control the touchscreen response. The nature of the pressure-sensitivity could stem from two sources, namely an area effect caused by increasing the number of granules contacted by the upper electrode, and intrinsic pressure-sensitive conduction within the nanocomposite granules. The former case can be understood by mechanical considerations of the deflection of the upper electrode with applied force. The intrinsic pressure sensitivity may be investigated through analysis of the current-voltage behaviour and flicker noise of the pressure sensitive layer. To this end, possible conduction mechanisms within the granules and the effect they have on the macroscopic current-voltage characteristics were described. Finally, in order to understand the effect of pre-formed nanocomposite granules on the optical transmission through the pressure sensitive layer, light scattering from particles both small and large in comparison to the wavelength of light were considered. It was predicted that pre-formed granules offer an advantage over spontaneous agglomeration of ATO nanoparticles, reducing the number of sub-micron sized particulates and reducing the Rayleigh scattering component in which incident light is scattered equally in all directions. For granules greater than 1 µm in size it is predicted that scattering is greatest at small angles in the forward direction. In the next chapter, the experimental procedures to investigate both the electrical conduction mechanisms and the optical transmission are described.

Chapter 9

Experimental Details of Fabrication and Functional Performance of Pressure Sensitive Resistive Touchscreens

9.1 Introduction

This chapter describes the experimental techniques used to fabricate and characterise the pressure-sensitive resistive touchscreen (PSRT) containing the nanocomposite granules which were fabricated during part I of this thesis. The PSRT offers dual functionality that can detect both the location of a touch and the touch force. Touch location can be calculated by the realisation of a voltage divider at the touch coordinates, as was described in chapter 2. The fabrication, characterisation and analysis of the PSRT is the focus of these next chapters.

The nanocomposite granules were formulated into a transparent, screen-printable ink which could be printed to form a pressure sensing (PS) layer onto a glass/ITO substrate. The addition of a flexible PET/ITO substrate on top of the PS layer completed the resistive touchscreen structure. Details on the ink formulation and the properties of the ITO substrates are given in sections 9.2.1 and 9.2.2 respectively. Details on the screen-printing process used to deposit the ink onto the glass/ITO substrate and the subsequent assembly of the PSRT are given in sections 9.2.3 and 9.2.4. As well as large-area PSRTs, the ink was also printed as small 6 mm sensors as described in section 9.2.5.

The optical properties of PS layer were assessed using two types of spectrophotometer utlising different measurement geometries. In particular, the total transmission through the layer as a function of incident wavelength and the haze contribution caused by diffuse scattering were investigated. The measurement principles are described in section 9.3.

Experiments were designed to measure and define the force-resistance (F-R) response of the PSRTs in order to assess their functional behaviour both spatially (many positions across the same sensor) and temporally (after repeated cyclic testing) so as to determine the variability and the durability of the functional response. These testing protocols are described in sections 9.4.1 and 9.4.2 respectively. In order to probe the fundamental conduction mechanisms as a function of applied force, current-voltage (I-V) properties and measurements of the flicker noise were taken (section 9.4.3). Finally, a testing facility was designed which allowed force to be applied directly to small discrete regions of the PS layer. This approach, described in section 9.4.4, allowed the force sensitive response of small numbers of granules within the PS layer to be assessed whilst simultaneously negating any effect due to increasing the number of granules contacted with increasing deformation of the PET/ITO substrate.

9.2 Fabrication of pressure-sensitive resistive touchscreens containing nanocomposite granules

9.2.1 Ink formulation

In principle, a wide range of varnish and solvents may be used to form the base ink material, as it is the nanocomposite granules which define the functionality of the printed layer. The particular formulation and methodology described below was developed by Peratech, to create an ink with a viscosity well-suited to the screen printing process (see section 9.2.3). The same formulation and methodology is continued throughout this thesis to enable comparisons to be made between inks containing nanocomposite granules and inks containing spontaneously formed nanoparticle agglomerates.

To form the screen-printable ink, the granules were dispersed into a pre-thinned transparent ink base. The ink base was a carbon-based alcohol and petrol resistant transparent varnish with a high solvent content of 73.4 %. After evaporation of the solvent a hard, abrasion-resistant surface was formed. This was beneficial in order to minimise damage to the screen-printed layer when incorporated into the resistive touchscreen. Here, mechanical stability is necessary in order to prevent or minimise damage caused by the contact of the deformable ITO electrode. The varnish was thinned by the addition of extra solvent. Here, a lower ink viscosity enabled levelling of the ink surface after passing through the mesh during the

screen-printing process. To form the ink base, solvent was mixed with the varnish at a mass ratio of 1:5, where a typical batch size comprised 50 g varnish and 10 g solvent. The total solvent content of the ink (accounting for both varnish and additional solvent) was 77.8 %. The varnish and solvent mixture was homogenised using a high energy mixing process in the DAC (3500 rpm for 1 minute) prior to the addition of granules.

Granules were added to the varnish/solvent mixture at the required loading and the ink was further mixed for 3 minutes at 3500 rpm to fully disperse the granules within the ink. The granule loading was typically 0.2–0.6 % by mass respective to the mass of the base varnish. Only a very low granule loading was required as when printed, the granules form a single layer in the varnish and it is not necessary to reach a percolation threshold associated with a 3D network of conductive particles. The ink was stored in airtight containers until printed. Immediately prior to printing, the ink formulation was re-mixed in the DAC for 1 minute at 3500 rpm. This re-dispersed any granules which may have sedimented to the bottom of the container.

9.2.2 ITO-coated substrates

Tin-doped indium oxide (ITO, or In_2O_3:Sn), was used as the transparent conductive electrodes within the resistive touchscreen. ITO is a Transparent Conducting Oxide (TCO). Aside from ITO, some of the most common TCOs include (doped) In_2O_3, SnO_2 or ZnO. TCOs are used as electrode material in a variety of applications, including solar cells, LCD or (O)LED displays and transparent touch panels, where both a high electrical conductivity and high optical transmission are required. TCOs are wide band-gap semiconductors which have a direct band gap in the range 3–4 eV. This is similar to the energy of visible light (1.8–3.1 eV). As no electron energy states lie in this gap, optical absorption processes are minimised leading to high optical transmission. In the absence of donor or acceptor states, thermal excitations across the band gap are minimal and the TCO is insulating. However, for shallow donors (which contribute energy levels just below the conduction band), thermal excitation can promote electrons into the conduction band. Shallow donors can occur naturally through oxygen deficiencies, however most TCOs are doped with extrinsic dopants that are substituted into the lattice at either the metallic or oxygen sites. For the case of ITO the un-doped In_2O_3 lattice has a cubic structure with a direct band gap of 3.75 eV [262]. When doping with tin (Sn), the In^{3+} anion is replaced with an Sn^{4+} ion. This leads to the formation of three impurity bands, one of which overlaps with the conduction band of the In_2O_3 [263]. With increasing number of dopant atoms the impurity energy band merges with the conduction band, so that the Fermi level is pushed into the conduction band and the electrical conductivity increases. The ITO now has a permanent population of free charge carriers and becomes conductive.

For ITO, there is a trade-off between optical transparency and electrical conductivity. Increased optical clarity can only be gained by the sacrifice of conductivity, and vice versa. For small-area touchscreen applications increasing the optical transmission can be more beneficial than increasing ITO conductivity. This is because the resistivity of the ITO does not control the charge injection into other layers, as is the case for applications such as OLEDS and solar cells. It is used only as a voltage divider, as described previously in chapter 2. Even with the addition of the PS interface, into which charge from the ITO is injected, there may be no negative effects so long as the resistance of the PS layer does not fall beneath that of the ITO. For applications in touchscreens the ITO is deposited at a thickness of 10–20nm on the rigid substrate, with a resistivity of 500–750 $\mu\Omega\,cm^{-1}$ and a sheet resistance of $\sim$ 200–650 $\Omega/\square$. The optical transmittance at 550 nm is typically in the range 89–93 % [264]. For the flexible ITO electrode a PET substrate is usually used, where the ITO is deposited at a thickness 15–25 nm with a sheet resistance of 250 $\Omega/\square$ and a transmittance at 550 nm of 85–88 %.

ITO thin films can be fabricated by a wide range of deposition techniques, including thermal evaporation, spray pyrolysis, chemical vapour deposition, sol-gel and spin coating, pulsed laser deposition, electron beam evaporation and both radio-frequency and direct current magnetron sputtering. For large-scale manufacture magnetron sputtering techniques are commonly used [265]. A review of the conductive and transmissive properties of ITO fabricated using these techniques is given elsewhere [266].

Whilst ITO benefits from extensive research into cost-effective fabrication techniques, as well as a high transmission and conductivity, alternatives to ITO are currently of much interest. One disadvantage of ITO, relevant to this thesis, is its brittleness and poor durability. Whilst ITO/glass electrodes exhibit long lifetime, ITO deposited onto a flexible substrate such as PET is known to crack and flake when flexed. This is a potential issue for resistive touchscreens which rely on the deformation of the transparent, flexible electrode. Cairns and Crawford found that the response of resistive touchscreens was negatively affected by an increasing number of flexing cycles on flexible ITO/PET electrode [73]. SEM microscopy of the ITO layer post-testing showed cracking of the ITO and adhesive wear of small ITO regions. They suggested a damage mechanism whereby the ITO on the PET substrate experienced both contact and tensile stresses due to deformation and contact with the lower ITO/glass substrate. After some time, patches of ITO had delaminated and transferred to the lower ITO/glass substrate. Sierros and Kukureka, and Sierros *et al.* also report similar results [267, 268]. Cairns *et al.* reported that the addition of a polyimide layer on top of the ITO/PET electrode increased the resistance to crack formation [269]. The poor durability of ITO has led to increasing research efforts into suitable replacements with increased durability, including carbon nanotube solutions [270, 271], metal nanowire meshes [272] and graphene [273].

Substrate	Composition	Total thickness (µm)	Sheet Resistance (Ω/□)
$B1$	ITO/glass	880	460
$T1$	ITO/PMMA	750	460
$T2$	ITO/PET	175	120
$T3$	PMMA	170	N/A

TABLE 9.1: Details of ITO electrodes used in touchscreen fabrication

Here, the ITO electrodes were formed on both glass and plastic substrates. The rigid, bottom glass substrate is denoted B and the topmost, flexible PET substrate T. The ITO was adjoined to printed silver conductive bars, which form either the X or Y electrodes of the device. The properties of the available ITO substrates used in the production of the PSRT are summarised in Table 9.1. Here, two possible T substrates were available, where $T1$ comprised a thicker PMMA substrate and ITO with a higher sheet resistance and $T2$ comprised a thin, PET substrate with low sheet resistance ITO. The layer $T3$ could be used in addition to either of the other T substrates but not on its own. It provided an additional protective PMMA layer used for enhanced durability of the touch interface.

9.2.3 Screen-printing of transparent layer containing nanocomposite granules

Flat-bed screen-printing was used to deposit a thin layer of the ink onto the rigid glass/ITO substrate. It was important that the printed PS layer had a uniform well-defined thickness that could be controlled by the printing process. Furthermore, the process had to deposit the nanocomposite granules contained within the ink to produce an even concentration of the granules throughout the PS layer.

The screen-printing process has five main components: ink, substrate, screen (and stencil), flood bar and squeegee. The screen comprises a close-knit mesh, with a stencil overlaid onto the mesh to define the pattern which is to be transferred to the substrate.

The flood bar dispersed the ink onto the mesh surface prior to printing, as shown in Fig. 9.1(a). During the print process the squeegee was drawn along the mesh surface at a fixed pressure, pushing the ink into the mesh openings and removing any excess ink from the surface of the screen. It also created a downward deflection of the screen, causing contact with the substrate and deposition of the ink. This process is shown in Fig. 9.1(b). As the squeegee progressed along the screen the mesh relaxed and returned to its original position, whilst the ink was deposited on the substrate in the shape of the stencil, as shown in Fig. 9.1(c). The final ink deposit on the substrate is shown in Fig. 9.1(d).

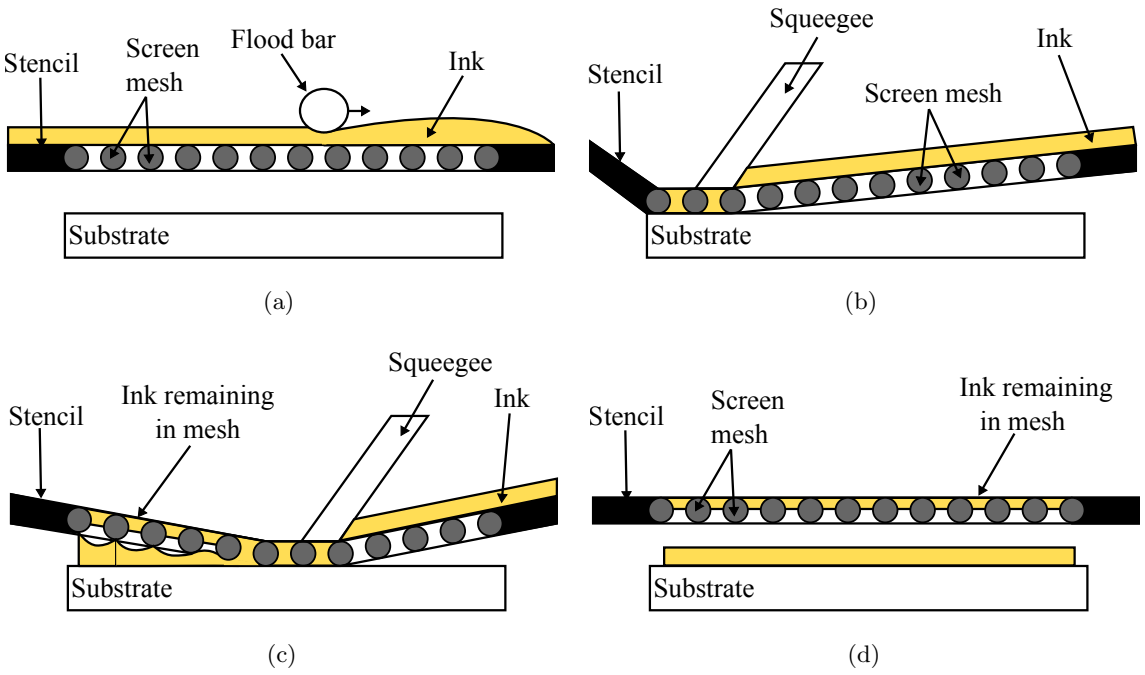

FIGURE 9.1: Schematic showing the screen-printing process. (a) A flood bar is drawn over the screen to provide an even covering of ink over the mesh. (b) The squeegee is drawn along the mesh, pushing the ink down into the mesh openings and deflecting the screen downwards to contact the substrate. (c) As the squeegee moves along the screen, the mesh relaxes upwards leaving the ink deposited on the substrate. (d) At the end of the print an even layer of ink is deposited on the substrate.

The screen comprised a woven mesh of material, usually either nylon, polyester or stainless steel depending on the application. Polyester is often favourable as it is strong and durable, with sufficient flexibility to print onto irregular surfaces. Unlike nylon, it is unaffected by environmental humidity [274]. The diameter of the individual threads in the mesh, along with the spacing between the threads (the thread count) determined the thickness of the wet printed layer. Other parameters, such as squeegee pressure and travel speed were optimised to fill the mesh openings and create contact between the screen and substrate and had no influence over the printed ink thickness.

The smallest feature size that can be screen-printed ultimately depends upon the resolution of the stencil within the screen mesh. For screen-printed electronics the stencil pattern is usually generated through a photoresistive screen coating. For commercial, high-speed screen-printing the resolution limit is of the order of 50 µm, although in research resolutions of less than 10 µm have been reported [13]. The main application of screen-printing is for large-area patterns and not high resolution details. As examples, screen-printing has been used to fabricate piezoelectric pressure sensors [46], supercapacitors for wearable electronics [275], large-area, flexible polymer solar cells [276] and silver and carbon electrodes on flexible organic thin-film transistors [277].

9.2.3.1 Calculation of printed ink thickness

The volume of ink printed is equal to the ink in the mesh at the start, IMS, minus the ink remaining in the mesh after printing, IME. IMS can be calculated by considering a unit square of the mesh comprising two interwoven threads of diameter D and spacing M, as shown in Fig. 9.2. The ink volume is simply the volume of the unit cell minus the volume of the two threads.

To a first approximation, assuming no compression of the threads during printing:

$$IMS = 2DM^2 - \frac{2\pi LD^2}{4} \tag{9.1}$$

As M is the reciprocal of the thread count (threads per unit length, or T), it can be shown that the ink deposited per unit area is:

$$\frac{IMS}{M^2} = 2D - \frac{\pi TD^2\sqrt{1+T^2D^2}}{2}. \tag{9.2}$$

In practice, at the thread intersections the thread diameter is slightly compressed. This is because during screen manufacture the interwoven threads are passed through heated rollers which compress and weld together the intersections. Additionally, during printing the mesh is stretched downwards toward the substrate, decreasing the number of threads per unit length. A more accurate approximation could be obtained by replacing the thread diameter with the compressed diameter and the thread count with the stretched thread count.

IME is empirically approximated as 30 % of the ink volume within the mesh. That is, during printing 70 % of the ink is transferred from the screen to the substrate [278]. Hence the theoretical volume of printed ink, TIV, is given by:

$$TIV = 0.7 \times \left(2D - \frac{\pi TD^2\sqrt{1+T^2D^2}}{2}\right). \tag{9.3}$$

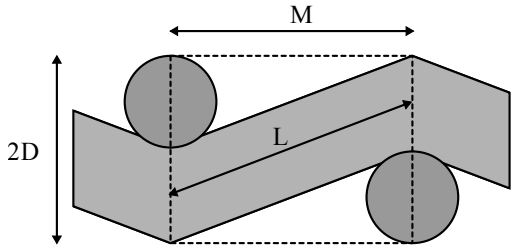

FIGURE 9.2: A unit cell of the woven mesh used in screen printing, consisting of interwoven wires of diameter D and spacing M.

Here, screen-printing was ideal for the large-area deposition of the transparent electro-active ink containing nanocomposite granules. A high print resolution was not required, and the thickness of the ink could be easily controlled using the thread diameter and thread count of the screen. The stencil used was a rectangle of dimensions 73 by 56 mm. The polyester screen had a mesh count of 120 cm^{-1} and a thread diameter of 34 µm. This corresponded to a thread spacing of 83 µm. This 'open area' of 49^2 µm allowed granules of maximum length (Feret diameter) of around 120 µm to pass through the screen. As the vast majority of granules were less than 20 µm in size, due to the fabrication procedure as well as post-fabrication sieving, the screen posed no obstacle to the passage of granules.

During printing, the screen was maintained at a tension of 18 $N\,cm^{-1}$ with an initial separation from the substrate of 2.5 mm. The squeegee was applied at an angle of 65° at a pressure of 300 kPa, and travelled over the screen at a speed of 0.14 $m\,s^{-1}$. These parameters were optimised by Peratech Holdco Ltd. to give optimum penetration of the ink into the mesh. From equation 9.3, the deposited ink volume was 31.1 µm per $µm^2$, which was dimensionally equivalent to the printed ink thickness. After printing, the glass/ITO/ink was cured for 90 minutes at 90 °C so the solvent could evaporate. The dried ink thickness can be approximately calculated by multiplying the theoretical wet ink thickness by the percentage of solids in the ink [279]. The transparent ink fabricated here has a total solvent content of 77.8 %, leaving a solid content of 22.2 %. Once dried, the ink formed a pressure sensitive (PS) layer with a theoretical thickness of 6.9 µm. The actual ink thickness was measured using FIB milling to cross-section the printed PS layer, using the same procedure outlined in chapter 4.

9.2.4 Assembly of touchscreens

Once printed and cured, the substrates were assembled into the PSRT device, as shown in Fig. 9.3. Electrical connections were made to the silver conductive bars using a pre-fabricated four-wire connection port. The port was aligned over the conductive bars on the glass/ITO/PS layer and heat was applied to melt a localised conductive adhesive and form the connection. Prior to assembly, an air-gap between the layers was introduced by carefully adhering a strip of Scotch™ tape around the edges of the PS layer on the glass/ITO substrate. The PET/ITO layer contained an adhesive strip around its outer edges so that when aligned with the glass/ITO/PS layer it was held in place by the adhesive strips. When assembled, the thickness of the tape (100 µm) introduced an air-gap between top and bottom layers. Finally, heat was applied through the top layer to the connection port beneath to heat the conductive adhesive and form an electrical connection between the port and the silver conductive bars on the upper PET/ITO substrate. As described in chapter 2, this sensor format allows both the touch location and the touch force to be determined.

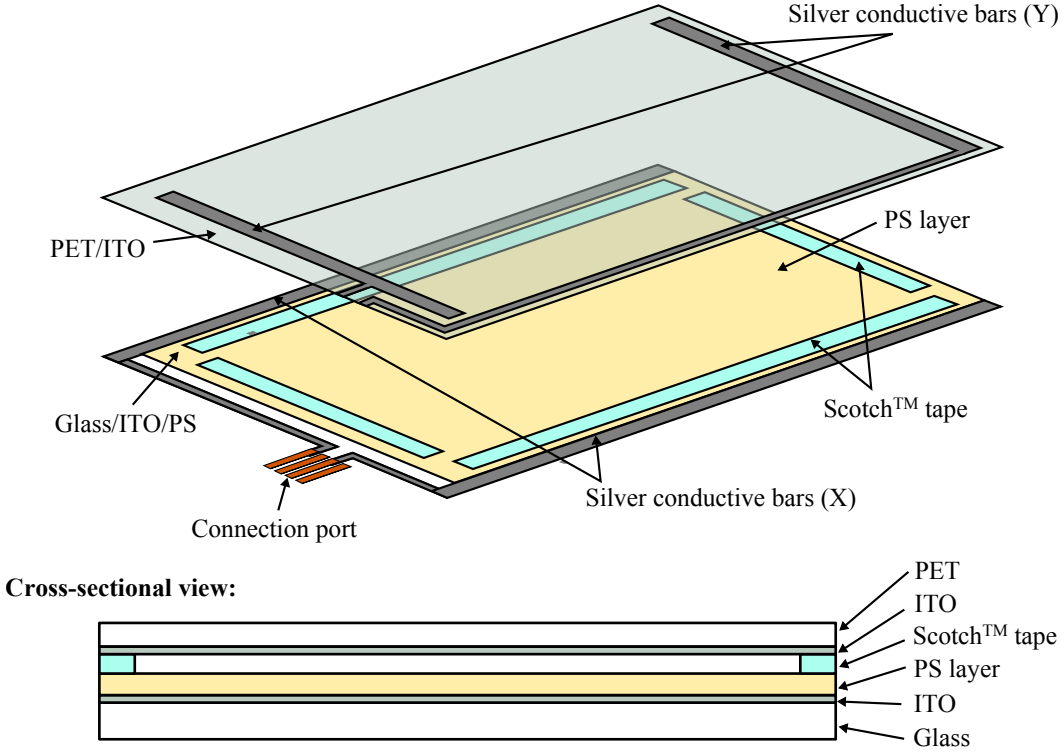

FIGURE 9.3: Schematic showing the assembly of the PSRT. Scotch™ tape was deposited around the edges of the PS layer, which was screen-printed onto a glass/ITO substrate. Electrical connections were made via a four-wire connection port adhered to each conductive bar using heat-activated conductive adhesive. Finally the PET/ITO substrate was attached using a non-conductive adhesive, which also prevented short-circuiting between the conductive bars on each substrate.

9.2.5 Fabrication of 6 mm transparent sensors containing nanocomposite granules

For some of the electrical testing, it was necessary to print the transparent ink into a different format than the large-area four-wire PSRT. In these instances, small discrete sensors were used instead. The transparent ink (containing nanocomposite granules) was printed in a 6 mm sensor format, as demonstrated in Fig. 9.4. First, silver connectors were printed onto a PET flexible sheet. ITO contacts were deposited on top of the silver contacts, in circles of 5 mm diameter. Then, the ink of interest was printed on top of the ITO contacts as for the standard four-wire format. Finally, an opposing contact was created by printing silver contacts/ITO electrodes in a mirror image to the first sheet. To assemble the sensors, the second ITO contact sheet was overlaid onto the ITO/ink sheet and a metal pin was crimped through each of the silver contacts. This design is similar to that of the FSR sensors described in chapter 2.

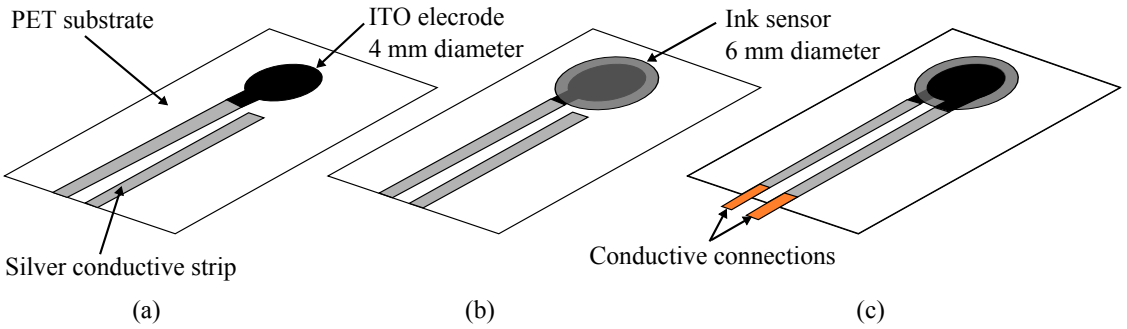

FIGURE 9.4: Schematic showing the fabrication steps for the 6 mm sensors: (a) Silver connectors are printed onto a PET substrate. An ITO electrode of diameter 4 mm is deposited which makes electrical contact with one of the silver connectors. (b) The ink is screen-printed on top of the ITO electrode at a diameter of 6 mm. (c) An opposing PET/silver/ITO sheet, which is a mirror image of the first, is placed on top of the first sheet. Lastly, a metal pin is crimped over each of the silver contacts.

9.3 Measuring the optical properties of the touchscreens

The inclusion of the PS layer within the resistive touchscreen assembly can negatively impact the transmission of (visible) light through the touchscreen. This is disadvantageous because in all applications, the touchscreen is overlaid directly onto a display. For applications using a high-resolution, colourful display it is of paramount importance that the touchscreen has minimal impact on the transmission of light from this display. The optical performance of the PS layer was characterised in terms of the transmission profile over a wavelength range (in this case corresponding to visible light) and the haze. Here, haze is defined as the percentage of forward-scattered transmitted light scattered by an angle greater than 2.5° [280]. The physical basis of these parameters was discussed in chapter 8. Here, the optical properties of the glass/ITO/PS layer were measured and compared to those of the glass/ITO substrate. This allowed the effect of the PS layer on the optical transmission and haze to be determined. These measurements were important for two reasons. Firstly, they allowed the optical effect of the inclusion of the PS layer into the touchscreen device to be characterised. Secondly, it allowed comparison between the two different methods of fabricating the PS layer, i.e. the incorporation of pre-formed granules of a well-defined size range and the spontaneous formation of agglomerates during the ink manufacture process. It was hoped that tailoring of the nanocomposite properties would allow some level of control over the optical properties.

Here, two spectrophotometers were used to characterise the sample, each of which used different measurement geometries. The ColourQuest XE spectrophotometer (CQ) measured transmission over visible wavelengths of 400-700 nm, with measurements taken every 10 nm. The components of this spectrophotometer are shown in Fig. 9.5. Radiation from a light source is passed through a colour filter in order to produce the standard 'D65' illuminant.

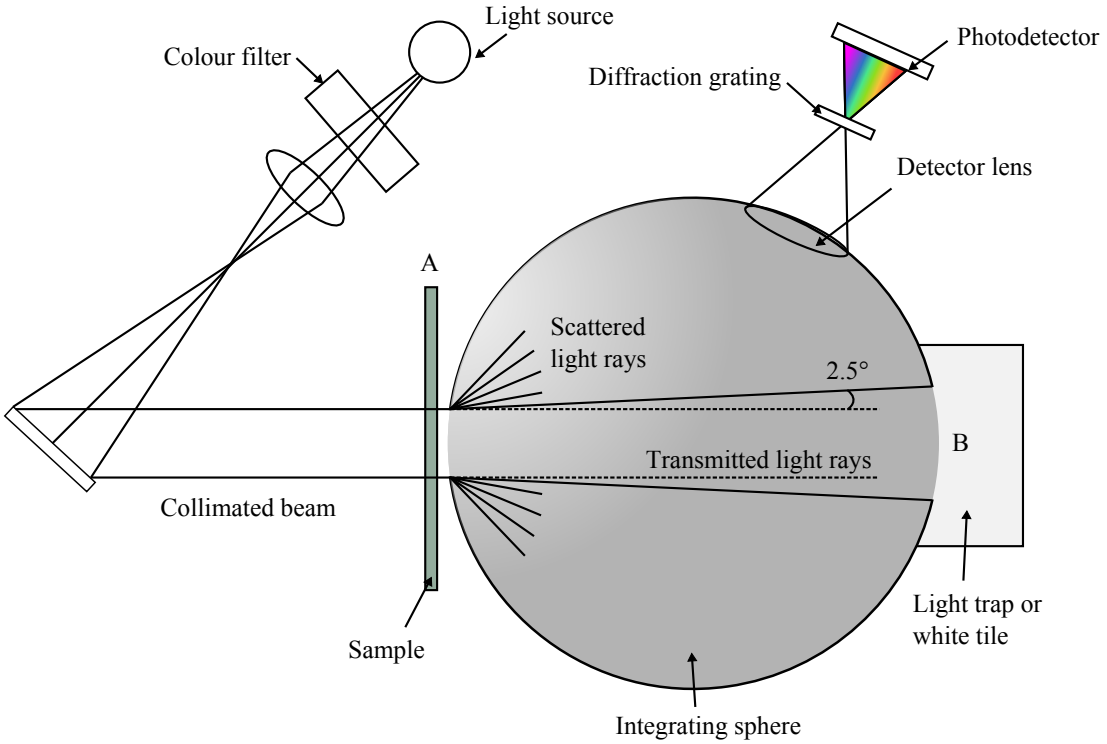

FIGURE 9.5: Schematic showing the components of the ColourQuest spectrophotometer used to measure the transmission and haze through PSRT samples.

The D65 function is a standard light spectrum replicating sunlight in western Europe. After passing through focussing optics, the collimated beam is then passed through the sample and into an integrating sphere. The interior surface of the integrating sphere is covered with a diffuse white coating which provides a uniform diffusing effect. Light rays incident upon any location on the sphere wall are distributed equally to all other points through multiple scattering events. A single detector inside the sphere measures the power of all light in the sphere, regardless of its spatial origin.

Referring to Fig. 9.5, the sample was placed at position A, flush against the entrance into the sphere. At point B is placed either a standard white tile or a light trap. Four measurements were taken, which are summarised in Table 9.2. The reflectance of the white tile (ideally) matched that of the surface of the integrating sphere, so that when the tile was placed at position B, all light transmitted into the sphere was detected. With no sample (M3), theoretically 100 % transmission should be measured. In practice this is less than 100 % due to inefficiencies in the detector and mismatch between the reflectance of the white tile with the walls of the integrating sphere [281]. With the sample in place the total transmission, T_{total}, is given by:

$$T_{total} = \frac{M2}{M1} \times 100\%. \tag{9.4}$$

Measurement	Position A	Position B
M1	No sample	White standard
M2	Sample	White standard
M3	No sample	Light trap
M4	Sample	Light trap

TABLE 9.2: Measurement protocol for determining haze of PSRT samples

With the light trap placed at position B, all light transmitted at angles $< 2.5°$ was deflected 90° by a mirror towards a light-absorbing material. The remaining light in the integrating sphere was scattered to angles greater than 2.5 %, contributing to haze. Measurement M2 determined the diffuse transmission through the sample and M1 recorded the 'background' diffuse transmission. The haze, h, can be calculated as follows:

$$h = \left(\frac{M4}{M2} - \frac{M3}{M1}\right) \times 100\% \tag{9.5}$$

A dual light beam was used in this spectrophotometer, which removed the need for additional measurement steps M1 and M3. Instead, a second beam is passed into the integrating sphere through a separate aperture and not through the sample. This combines the measurement steps M1 with M2, and M3 with M4 without the need for removing the sample. To measure the total transmission as a function of the visible light wavelength, a lens was used to divert the transmitted light to a diffraction grating which separated the light into its component wavelengths. The transmission for each wavelength was measured by a photodiode array.

The second spectrophotomer, the Shimadzu UV-3600 (SUV), was also dual-beam but had no integrating sphere. Two lamps were used to provide illumination from ultraviolet through to near-infrared wavelengths, and here the transmission was measured from 300–900 nm. A schematic of this spectrophotometer is shown in Fig. 9.6. Radiation from the light source was passed through a diffraction grating and then a 2 nm slit to select the wavelength and spectral width. The beam was split and simultaneously passed through the sample port and reference port (which was kept empty) before detection using a photomultiplier. Both path lengths were equal to minimise phase shift. A baseline scan is measured initially with the sample port empty, to correct for any variation in the emission intensity over the wavelength range. The transmission through the reference defined the maximum transmission through the sample. Because no integrating sphere was used only direct transmission was measured and haze could not be determined. However, the transmission spectra could be recorded at a wavelength intervals of 0.5 nm, offering greater resolution than the CQ spectrophotometer.

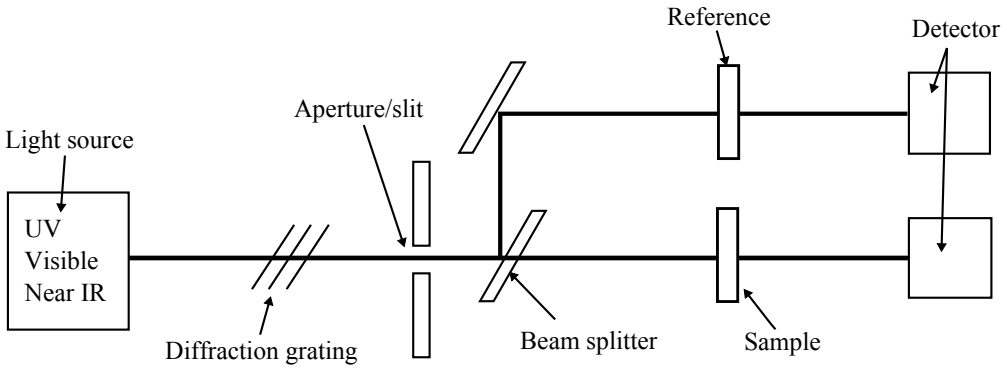

FIGURE 9.6: Schematic showing the Shimadzu UV-3600 spectrophotometer used to record the transmission spectra through PSRT samples over wavelengths of 300–900 nm.

9.4 Measuring the electrical functionality of the touchscreens

The electrical response of the PSRT was assessed using a number of methods which aimed to both characterise the device and reveal the underlying physical conduction mechanisms. The pressure-sensitive resistive functionality of the touchscreen is thought to comprise of two components. The deflection of the upper ITO/PET electrode causes increasing contact area with the PS layer with increasing applied force. Therefore the number of granules contacted also increases, reducing the resistance through the layer. Additionally, there is a possibility that the granules themselves are intrinsically pressure sensitive, each behaving as a pressure-sensitive conducting polymer composite. The electrical measurements performed here aim to determine the effect of these two components on the overall response of the PSRT. To this end, a series of experiments were devised to investigate the electrical transport mechanisms throughout the device, and through the granules individually (where the effect of increasing surface area was nullified). Also, by investigating the response of the PSRT to applied force using flicker noise measurements and current-voltage sweeps it was attempted to determine if the conduction mechanisms were influenced by applied force.

9.4.1 Force-resistance profiling

Force-resistance (F-R) profiling of each PSRT is an important characterisation test which describes the resistive behaviour of the touchscreen under applied force. As discussed in chapter 2, for applications in human-computer interactivity a light touch is of the order of 0.1 N and a hard press any force greater than 5 N. Here, the resistance of the PSRT was measured for applied forces from 0.1 to 10 N to cover this range. The F-R profile is the overall response of the PSRT to applied pressure, that is dependent on both the number of granules contacted (and therefore the geometry of the touchscreen and the mechanical properties of

the deformable electrode) and also any inherent pressure-sensitivity within the PS layer itself. Whilst it is not possible to determine the contribution of each of these to the overall F-R response, this test is nevertheless useful because it provides a benchmark through which the effect of other parameters may be assessed.

Force was applied using an automated mechanical testing rig (Instron model 5543). The rig comprised a single column load frame with a moveable crosshead, as shown in Fig. 9.7(a). A load cell attached to the cross head enabled vertical displacement to be converted to applied force. Here, compressive force was applied using a stylus attachment to the load cell. The stylus, comprised of a rigid plastic material, had a hemispherical tip of diameter 1.7 mm and exemplified the passive styli commonly used for the operation of resistive touchscreens. Whilst rubber test probes are available which mimic the compressive behaviour of the human fingertip, the plastic stylus was chosen as, due to its non-compliant nature, the contact area between stylus and PSRT remained constant throughout testing. This was necessary to

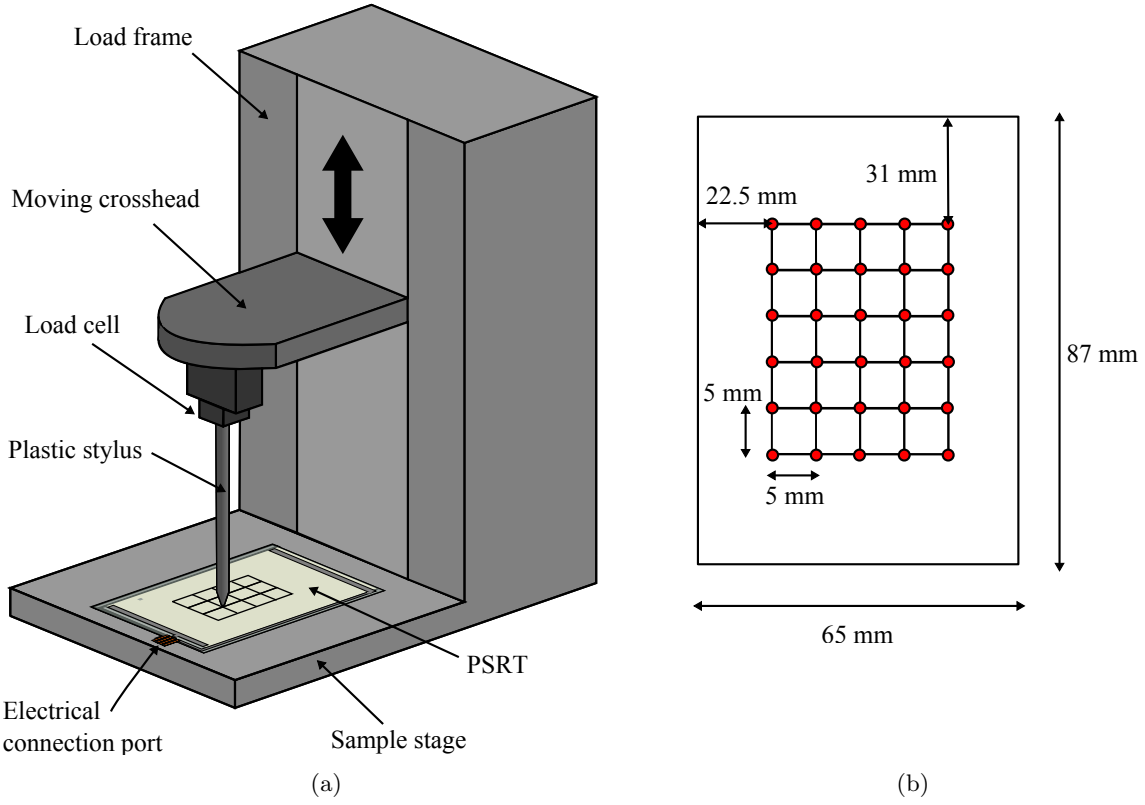

FIGURE 9.7: Schematic showing (a) the mechanical testing rig for force-resistance profiling of the PSRTs, comprising a load frame with moveable crosshead, attached to which is a load cell with plastic stylus attachment. Displacement of the crosshead causes a force to be applied to the PSRT via the stylus, where the force is measured by the load cell. (b) The test grid drawn onto the PSRT sample, comprising 30 positions which are tested using the mechanical testing rig. This enables force-resistance profiling across the central region of each PSRT.

enable comparison of the results to those obtained by model simulations, as investigated in chapter 11.

The load cell is a precise force measurement transducer, converting applied force into an electrical signal. Force is measured by a series of internal strain gauges. Pre-calibration of the strain gauge therefore allows compressive strain to be converted to an applied force. The load cell used here could measure forces up to 1 kN. Even when operating at up to 1 % of its capacity (i.e. forces up to 10 N) the load cell provides a small linearity error of just 0.25 %. The error on the force was therefore taken as ± 0.25 % of each reading.

The PSRT was secured onto a rigid plate at the base of the load frame. Prior to testing, a grid of 30 test points was drawn onto the PSRT over the central portion of the surface, as shown in Fig. 9.7(b). Electrical connections were made via the connection port on the PSRT. For each test, one point was manually aligned under the stylus tip. When the tip first contacted the PSRT surface the displacement was defined as zero. Any further downward deflection resulted in an applied force. The rate of downward deflection was set at 0.5 $\mathrm{mm\,min^{-1}}$. The stylus was deflected until a force of 10 N was reached, after which force was removed at the same rate. Automated data collection recorded values of the force versus the measured resistance, where the resistance was measured at a constant voltage of 4.5 V. Comparison of the calculated F-R profiles showed the variation in response over the 30 tested positions.

9.4.2 Durability testing

The durability of the PSRT can be defined as the change in its electrical functionality with repeated use. A loss in electrical functionality may result in a change in the observed F-R profile of the PSRT, for example a shift to higher resistances for each applied force. Such a response could indicate damage to the PS layer, or the ITO electrodes. ITO is known to degrade with repeated flexing, as was described in section 9.2.2. An investigation into the durability of the PSRTs was used to quantify the change in F-R behaviour in response to cyclic testing. Using SEM analysis of the ITO and PS layers in the touchscreen, the damage mechanisms could also be investigated.

In order to rapidly simulate a large number of touch events, a custom made sliding wear testing rig was developed at Peratech Holdco Ltd, as shown in Fig. 9.8(a). Sliding wear testing is a high impact procedure devised to test the limits of touchscreen performance under prolonged and heavy use. A pneumatic system was used to push a stylus attachment across the surface of the PSRT sample, whilst maintaining a constant compressive force of 5 N. Due to the sideways motion of the stylus both shear and compressive forces are imparted to the PSRT. Prior to testing, a grid comprising five parallel lines was drawn across the PSRT sample, as shown in Fig. 9.8(b). When a sample was placed onto the rig, the stylus

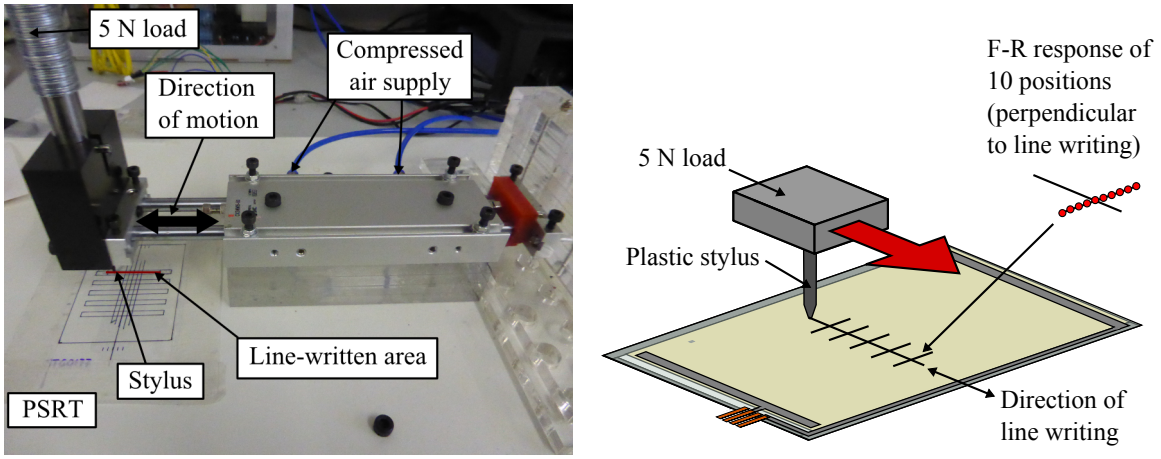

(a) (b)

FIGURE 9.8: Diagram showing custom-made line-writing test facility at Peratech Holdco Ltd (a) photograph of the equipment (b) Schematic of line-writing area on PSTS. After linewriting, 10 positions along 5 lines perpendicular to the line-written region are characterised in terms of their F-R response. In the diagram, one of these lines is shown where red circles represent the test location.

runs perpendicular to these lines, intersecting each one. A typically 'line writing' (LW) test comprises 30 000 cycles, where each cycle is defined as the stylus passing back and forth along the PSRT. Immediately after the LW cycles the F-R response was tested at 10 points along each line on the grid. This enabled comparison between the F-R response of the line-written region and the PSRT immediately outside of the test area. Damage to the PS layer could be quantified by the change in resistance.

9.4.3 Flicker noise measurements

As discussed previously in chapter 8, the flicker noise within an electronic system can give insight into electrical conduction mechanisms subject to relaxation processes. By measuring the flicker noise within PSRT test structures under increasing force, the nature of any force-sensitive conduction mechanisms can be probed. In order to measure this phenomenon it was important to minimise the length of the electrical interconnects into the system, as each of these also contributes to the flicker noise. Because of this, the transparent 6 mm sensors, as described in section 9.2.5, were used instead of large-area PSRT devices. A two-point probe measurement system was used, utilising the electrical connections on the 6 mm sensors. The electrical connections were kept short and low-noise coaxial cable was used in order to reduce their contribution to the electrical noise. It was assumed that the flicker noise of these connections did not significantly contribute to the observed results.

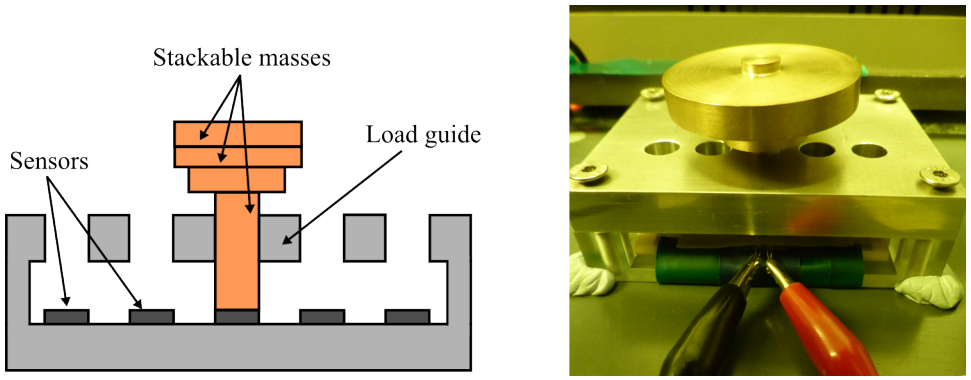

FIGURE 9.9: (a) Schematic of electrical testing rig used for noise measurements. Sensors (up to 5) are placed in the sample holder and secured into position. Load is applied by a series of cylindrical stackable masses through holes in the upper surface of the test rig which lie directly above the sample. (b) A photograph of the equipment. Crocodile clips are attached to the metal pins on the sensor.

The sensors were placed in a custom-made test rig, as shown in Fig. 9.9. The sensors (maximum five at one time) were placed into the rig and secured in position. Circular holes of diameter 8 mm in the upper plate of the rig allowed force to be applied vertically over the entire area of the sample through a series of cylindrical stackable masses. The holes were just larger than the diameter of the first cylindrical mass (10 g) such that a sliding fit was realised and friction was minimised. In this way masses ranging from 10 g to 1 kg were applied to the sensor.

The sensor was connected to a low-noise current pre-amplifier (Stanford Research model SR570) where a test bias could be set. It was important that the current did not exceed 2 mA due to the capabilities of the low noise pre-amplifier. I-V sweeps collected prior to testing allowed the determination of a suitable voltage. This was maintained at 2.5 V which, even at high compressions, did not result in a current flow exceeding 2 mA in any of the sensors tested. The current pre-amplifier provided a voltage output proportional to the input current (i.e. the current passing through the sensor). The gain, or sensitivity, of this conversion can be set in the range 1 pA/V to 1 mA/V. The digital noise of the instrument is dependent on the sensitivity. In order to minimise digital noise introduced by the equipment, the sensitivity was set at 1 mA/V or less. Here, the digital noise from the pre-amplifier is below 10^{-9} $A/\sqrt{Hz}$.

The low-noise pre-amplifier was connected to a PC with a 24-bit data acquisition card (National Instruments NI USB-4431) and automated measurements were taken using a custom designed LabView programme. Under application of a fixed voltage of 2.5 V the current fluctuations were recorded over a fixed time. Current data was acquired at a rate of 4000

measurements per second, for 2 seconds. This was repeated 10 times. The current power spectrum was then calculated according to equation 8.26.

9.4.4 Measuring the force-sensitive resistance of granules

The F-R response of the PSRT may be attributed to two components. The first is a surface effect, that is with increasing deformation of the upper electrode, more nanocomposite granules are contacted providing multiple conduction pathways through the PS layer to the rigid ITO electrode beneath. This effect can be modelled by assuming the upper, deformable electrode acts as a fully restrained beam, the deflection of which under a known force can be calculated, as was described in chapter 8. This approach was used to investigate the surface-component of the force sensitivity by using MATLAB to design a model simulation. The results of this are reported in chapter 11.

However, there is also a possibility that the granules themselves are intrinsically force-sensitive. The granules contain a network of conductive ATO nanoparticles which are bound together with an insulating material, and as such may behave as a conducting polymer composite, the electrical properties of which were described in chapter 8. In order to assess whether this mechanism contributes to the observed behaviour of the PSRT, it was necessary to negate the surface contribution of the F-R response. This was achieved by removing the deformable ITO electrode and depositing an electrode directly onto well-defined areas of the PS layer. This method also allowed the resistance of the sensing layer to be determined as a function of the contact area and the number of granules contacted. Additionally, I-V sweeps were also performed through the PS layer directly, in order to probe the origin of any non-linearity in the electrical conduction. These results are reported in chapter 12.

9.4.4.1 Preparation of samples

Electrical contacts were deposited by thermal evaporation onto the PS surface in a custom-built evaporation chamber using a mechanical shadow mask. The electrical contacts of varying diameter, as shown in Fig. 9.10, connected all granules contained within that diameter. This removed any surface effects when contacting these regions as each granule was electrically connected to all others within the area of the contact. Evaporation was chosen as it allowed an even layer of material to be deposited over a macroscopically rough region. A mask was designed which contained precision drilled holes of diameter 2.0, 1.0 and 0.5 mm. The mask was placed over the glass/ITO/PS substrate inside the chamber. Electrical contacts comprising 3 nm chromium, 100 nm copper and 5 nm gold were thermally evaporated onto the sample. Chromium was deposited onto the sample first as it facilitated adhesion of the subsequent layer of copper. Copper was chosen due to its high electrical conductivity, and

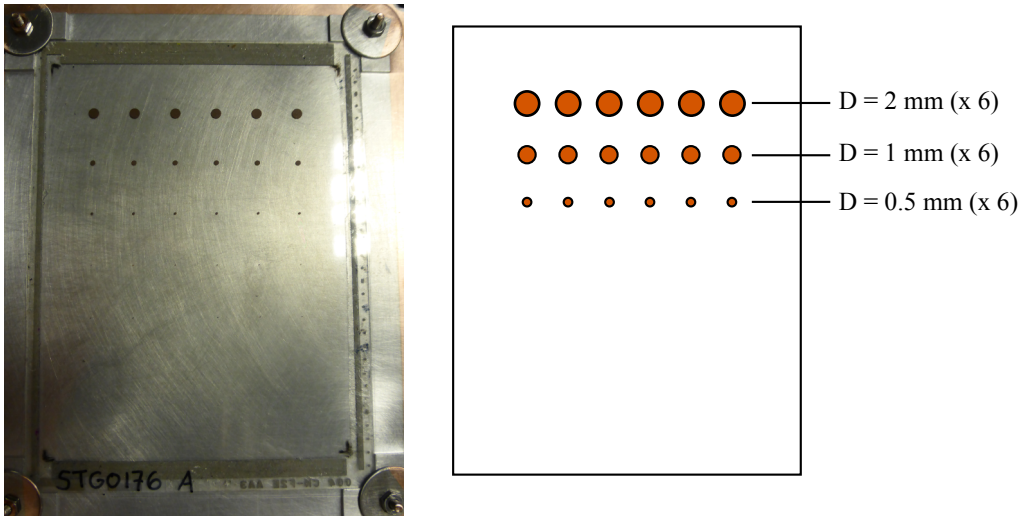

(a) (b)

FIGURE 9.10: (a) Photograph and (b) schematic of the PSRT sample (without PET/ITO upper electrode) and evaporated contacts of varying diameter, where the contacts consisted of 3 nm chromium, 100 nm copper and 5 nm gold.

the gold layer acted as a cap to prevent oxidation of the copper, which would have reduced its conductivity. On each PSRT sample, six contacts of each diameter of 2.0, 1.0 and 0.5 mm were deposited. This created 'capping electrodes' in intimate contact with the granules embedded in the PS layer.

Subsequent imaging of the capping electrodes using an optical microscope allowed the exact number, size and distribution of the granules within each contact to be determined. Example images are shown in Fig. 9.11(a) and Fig. 9.11(b) for 2 mm and 0.5 mm diameter contacts. A measure of the number of granules within each area covered by a capping electrode enabled the resistance of a single granule to be estimated from the relationship between contact resistance and electrode size. An SEM image of a 2 mm capping electrode is shown in Fig. 9.11(c). Surrounding the electrode, the image appears to glow and is distorted - this is an artefact caused by charge build-up on the insulating polymer, as the sample was not carbon-coated prior to imaging. Inside the electrode the granules appear well-coated by the Cr/Cu/Au, exemplified in Fig. 9.11(d) which shows an individual granule with an approximate size of 5 µm well coated with the electrode material.

9.4.4.2 Design of equipment for applying load to PSRT

In order to apply a known force to each evaporated contact on the PSRT sample a custom-built test rig was designed. The rig comprised spring-loaded contact test probes (SCTP)

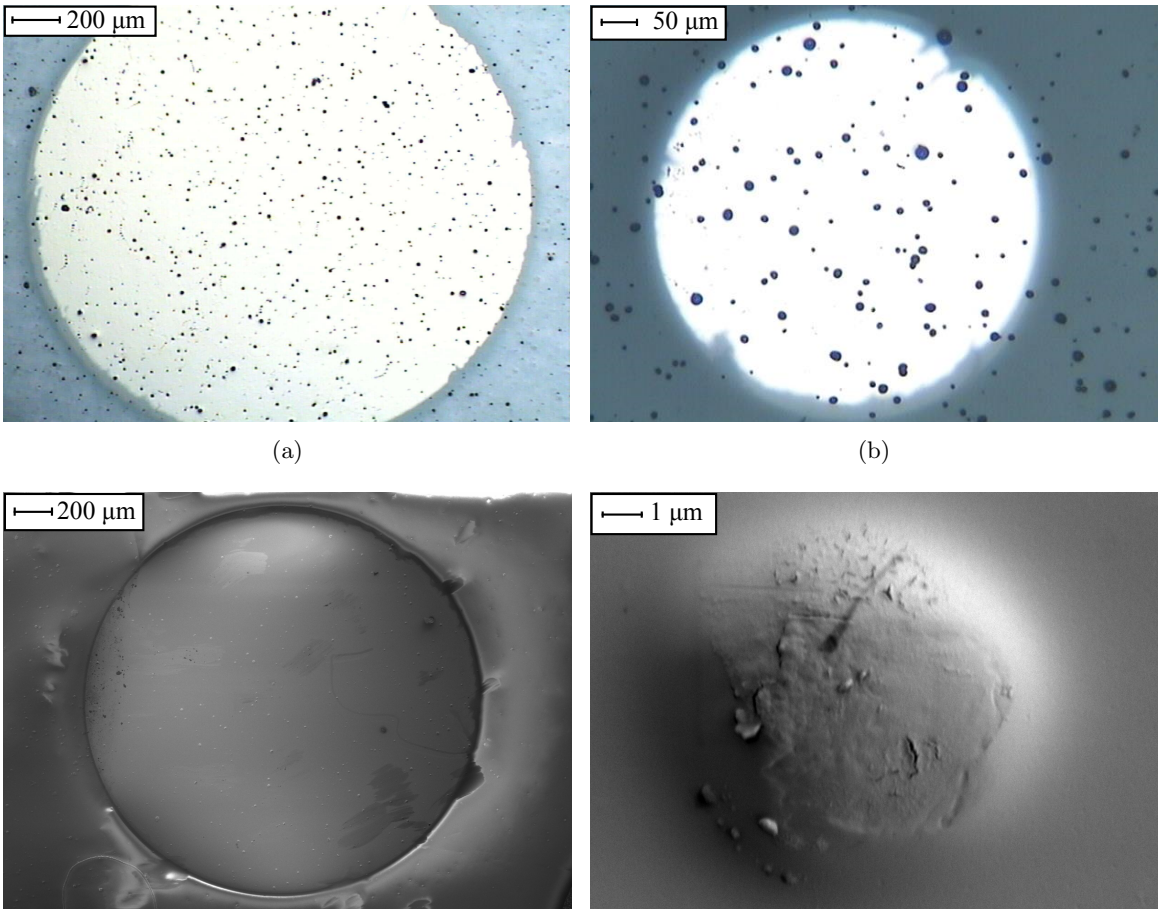

FIGURE 9.11: Figure showing optical microscopy images of the evaporated copper contacts with diameter (a) 2 mm and (b) 0.5 mm. From optical microscopy images, the number and sizes of the granules within each contact could be calculated. SEM images taken from a 2 mm contact showing (c) the entire contact and (d) detail of a single granule, where the contact coats the rough topography of the granule.

aligned with each capping electrode on the PSRT. The SCTP comprised a metal casing with contact plunger attached to the casing by a spring. These are typically used for providing electrical contact to a test surface at an indeterminate distance, for example testing the electrical functionality of printed circuit board components. Excellent electrical contact is ensured by the spring force when the plunger is depressed. In this case, the force-compression properties of the spring are utilised to apply a fixed force to each contact on the PSRT surface. Ideally, the SCTP diameter should be matched to the diameter of the capping electrodes. This was possible for the 2 mm and 1 mm electrodes, however the closest-matched flat-tipped SCTP available for the 0.5 mm electrodes had a larger diameter of 0.65 mm. Each of these SCTPs had a spring constant of 0.75 $\mathrm{N\,mm^{-1}}$ for up to 4 mm deflection of the spring, corresponding to a maximum applied force of 3 N.

A schematic of the custom-built test rig is shown in Fig. 9.12. The sample holder was an

acrylic base plate with a shallow groove matching the dimensions of the PSRT sample, firmly holding the sample in place. Electrical contact was made to the ITO electrode underneath the PS layer using the connections to the silver conductive bars adjoining the ITO layer. Bolts were screwed into the base, upon which the test bar was placed. The test bar comprised an acrylic bar through which the SCTPs were held in place. The SCTPs were located such that when assembled, the probes were precisely aligned with the capping electrodes on the sample beneath.

Tightening of the nuts above the test bar caused downward movement of the bar. When the SCTP first contacted a capping electrode a resistance was measured. At this initial contact, a small indeterminate force was applied to the electrode. All further deflection, and force, was measured with respect to this initial value. Subsequent deflection of the test bar downwards, caused by tightening of the nut, resulted in compression of the spring inside the SCTP and an increase in the force applied to the capping electrode. Prior to testing, the downward deflection of the bar was calibrated with the number of rotations of the nut on the bolt. The deflection could be controlled to within 1/6 of a turn of the nut, where each half turn corresponded to 0.23 ± 0.08 mm deflection. Using the known properties of the SCTPs this

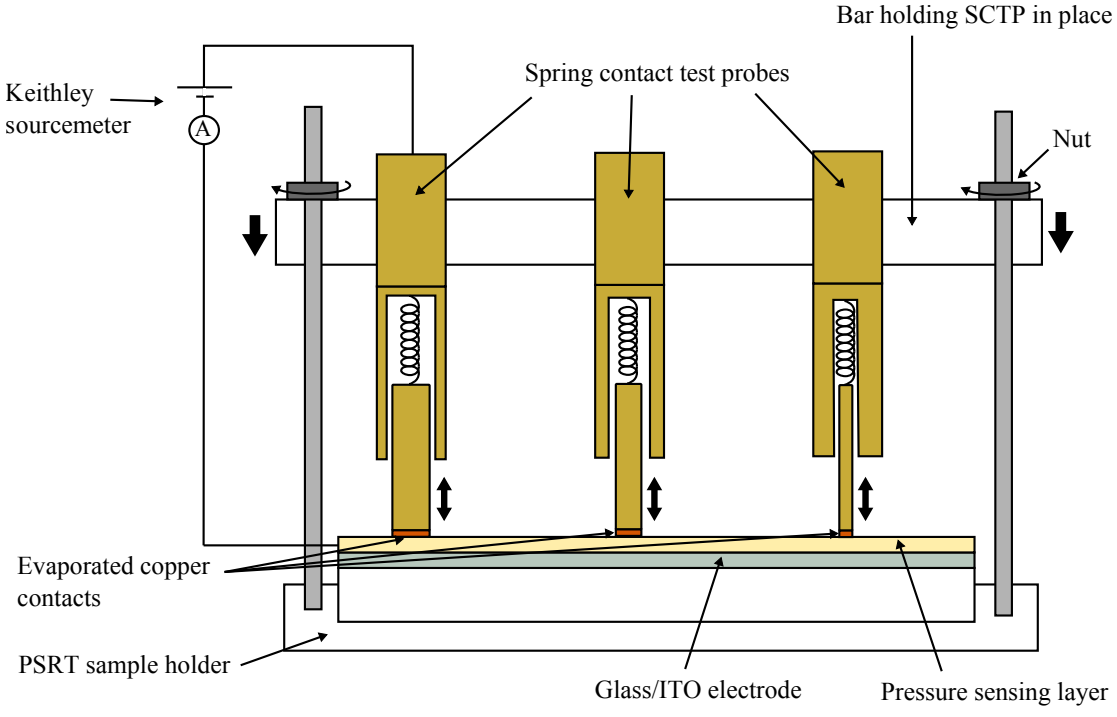

FIGURE 9.12: Schematic of the custom-built test rig used to measure the electrical properties of discrete areas on the PS layer capped with electrodes. The test rig comprised spring contact test probes mounted into an acrylic bar. Downward deflection of the bar was controlled through tightening of the nut on the bolt and this increased the force exerted on the PS layer test areas.

was converted to an applied force. Here, each half turn of the nut corresponded to a force increase of 0.17 ± 0.06 N. The resistance was measured using a two-point measurement, where probes were attached at the top of the SCTP and to the ITO beneath the PS layer. The resistance was recorded using a digital multimeter connected to automated LabView software.

Using the same experimental set-up, I-V sweeps were also performed through the capping electrode/PS layer areas at various levels of applied force. The IV behaviour can give information on the nature of the conduction mechanisms. For example, deviation from a linear I-V relationship (Ohm's law) can help to identify the conduction mechanisms, e.g. quantum tunnelling or field assisted quantum tunnelling, percolative networks, or Poole-Frenkel and space-charge limited regimes. As such, I-V sweeps are an important tool in understanding underlying conduction mechanisms within a device.

Here, the multimeter was used to apply voltage increments of 0.1 V, at which the current was measured. The voltage was sequentially ramped up to 10 V and then ramped back down to 0 V to complete the voltage sweep. Ten voltage sweeps were performed sequentially for each sample in order to ascertain whether there was any change in the I-V characteristics between each sweep. Such an occurrence could indicate the presence of charge trapping within the sensor [238]. Data was collected automatically using a custom-built LabView programme.

9.5 Chapter summary

This chapter described the experimental methods used to both fabricate and analyse pressure sensitive resistive touchscreens, containing the nanocomposite granules that were developed in part I of this thesis. These granules were formulated into a transparent ink and screen-printed onto glass/ITO substrates. Control of the screen parameters, including thread count and diameter, allowed control over the printed ink thickness. The theoretical dried thickness of the PS layer was calculated to be 6.9 µm. Pressure-sensitive resistive touchscreens were fabricated by the addition of a separate, flexible PET/ITO electrode. Additionally, small 6 mm circular sensors with a similar structure were also fabricated.

After assembly, the optical properties of the PSRTs were investigated using a spectrophotometer to measure the total transmission of visible light as well as the haze (resulting from diffuse transmission). High optical transmission and low haze are important for applications where the touchscreen is overlaid onto a high-resolution display, so as not to obscure the output from this display.

A series of experiments were designed to characterise and investigate the electrical functionality of the touchscreens and their pressure sensitive response. Measurements of force-resistance

profiles, over many positions on the same sensor and also as a function of cyclic testing, were performed to characterise the response of the devices. In order to understand the fundamental conduction behaviour of the PSRTs, flicker noise measurements were performed so as to extract information on the nature of conduction and whether this was affected by increasing the applied force to the device. A custom-built test rig utilising spring contact test probes was used to test the force-resistance response of the pressure-sensitive layer itself, removing the effect of increasing contact area associated with operating the full PSRT assembly. This was achieved by evaporating chromium/copper/gold contacts directly onto the pressure sensing layer containing the nanocomposite granules. I-V sweeps were also performed for varying applied force. This aims to show to what extent the role of any intrinsic granule force-sensitivity plays in the overall force-sensitivity of the granule-based touchscreen.

Chapter 10

Functional Performance of Touchscreens containing Nanocomposite Granules

10.1 Introduction

In this chapter, the functional performance of the pressure sensitive resistive touchscreens (PSRTs) is reported, in terms of their physical properties, optical performance and force-resistance (F-R) behaviour. The PSRTs contained either pre-formed nanocomposite granules as developed in part I of this thesis, or agglomerated ATO (antimony-doped tin oxide) nanoparticles formed during the ink manufacture stage. The latter system acted as a control sample for comparison with the performance of the granular-PSRTs developed in this study.

The physical properties of the PSRTs are discussed in section 10.2. SEM imaging was used to image the granules embedded in the host polymer in the pressure sensing (PS) layer, and optical microscopy used to measure the granule concentration within the layer. FIB milling, used to create a cross-section through the ink surface, allowed comparison of the ink thickness to the theoretical predictions outlined in chapter 9. The optical properties of the PS layers are examined in detail in section 10.3. A critical comparison is made between granulated samples and the control sample. Results from two spectrophotometers are compared and used to characterise the optical performance in terms of the transmission over visible wavelengths as well as the haze.

Finally, the electrical functional performance of the PSRTs is described in section 10.4.2. The F-R behaviour is quantified in terms of sensitivity, hysteresis and variability of the response.

A comparison is made between the control sample and samples containing granules. The effect of sieving to remove granules greater than 20 µm in size is also assessed. The durability of the PSRTs in response to high-impact sliding wear testing is examined in section 10.4.3.

10.2 Physical structure of ink through optical microscopy, SEM and FIB analysis

Fig. 10.1 shows the physical structure of a PS layer containing nanocomposite granules. Fig. 10.1(a) shows the distribution of granules within the ink for a granule loading of 0.4% with respect to the mass of the base varnish. Fig. 10.1(b) shows the same PS layer imaged at a higher magnification and an oblique incidence of 52°, highlighting the protrusion of the granules above the PS surface. Fig. 10.1(c), Fig. 10.1(d) and Fig. 10.1(e) show individual granules embedded into the insulating polymer. The granules protrude above the ink surface

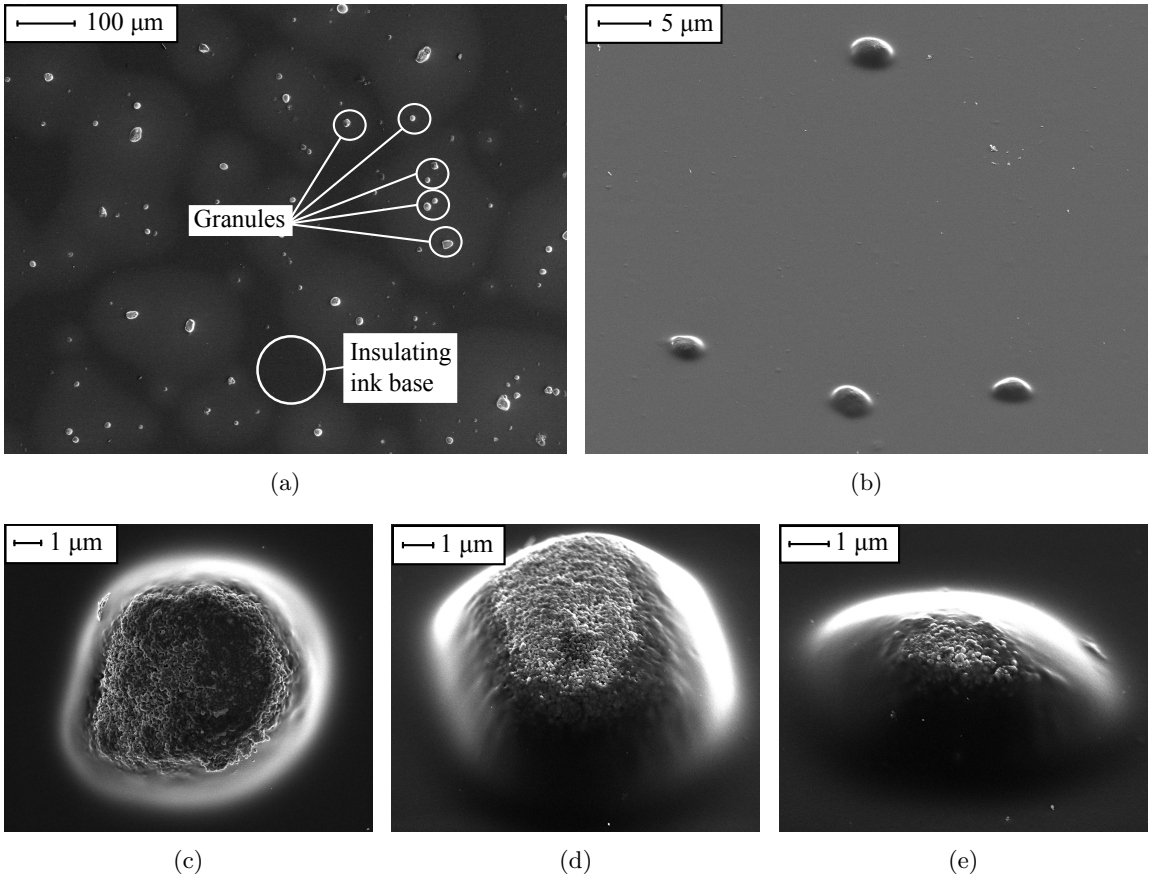

FIGURE 10.1: SEM images showing the physical structure of the printed PS layer (a) normal to the printed surface (b) at 52° to the printed surface, showing the granule protrusion above the surface. (c) (d) and (e) show individual granules embedded into the ink where the granule is not completely wetted by the base polymer.

and are not fully wetted by the base ink. This is crucial in providing a conductive surface for contact with the flexible electrode. The amount of conductive material exposed can vary from granule to granule. For example in Fig. 10.1(e) only a small percentage of the conductive granule surface is exposed, and the remainder resides below the ink surface. To measure the spatial distribution of granules within the PS layer optical microscopy was used to obtain nine images at random locations across the layer, using a 40x objective lens. The granule number density was defined as the number of granules measured per unit area, quoted here in mm^{-2}.

Fig. 10.2 shows a FIB-milled cross-section through the PS layer. The layer was first treated with a platinum capping layer to preserve the surface topography. To the right of the image is the edge of a granule embedded within the layer. The bright region at the bottom of the image is an artefact caused by charging of the insulating PET substrate, and the bottom of the PS layer can be observed just above this region. The PS layer thickness is 1.3 µm, significantly less than the theoretical value of 6.9 µm calculated in chapter 9. This could be due to an inefficient screen-printing process, for example poor flooding of the mesh prior to printing or insufficient squeegee pressure reducing the thickness of the printed layer, or an underestimation of the dried ink thickness after solvent evaporation. A large mis-match between granule size and PS layer thickness causes increased protrusion of the granules above the surface of the layer. This may have an adverse effect on the durability of the PSRT, as is explored further in section 10.4.3.

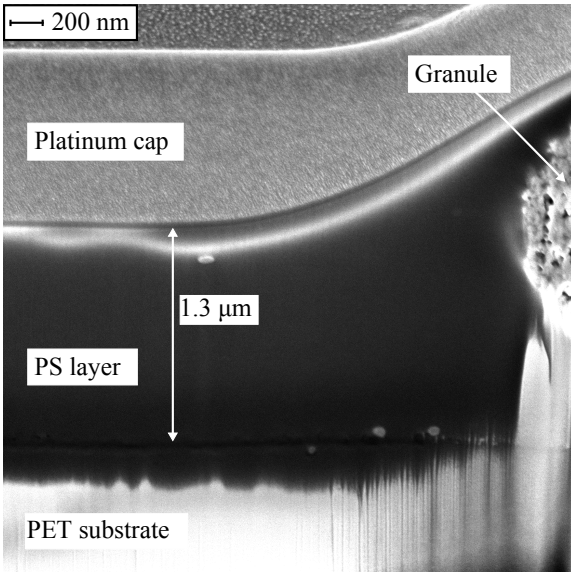

FIGURE 10.2: SEM image of a FIB-milled cross-section through a PS layer. A platinum cap was deposited to protect the surface prior to milling. The ink thickness was measured at 1.3 µm, much less than the theoretical dried ink thickness of 6.9 µm calculated in chapter 9.

10.3 Optical performance of touchscreens containing pre-formed granules

10.3.1 Comparison of techniques used to measure transmission

The optical transmission through the glass/ITO substrate $B1$ was measured using the HunterLab ColourQuest integrating-sphere spectrophotometer (CQ) described in chapter 8. This defines the maximum achievable transmission through the PS layer printed onto the glass/ITO substrate, and therefore allows the effect of the additional PS layer on the transmission and haze to be determined. Fig. 10.3(a) shows the total transmission as a function of incident light wavelength in the range 400–700 nm, corresponding to visible light. In all cases four measurements were taken, one in each quadrant of the sample. Error bars, representing the standard deviation of the measurements, are smaller than the data points. The haze, h, was $0.6 \pm 0.1\%$. The error of 0.1 % corresponds to the minimum resolution of the measurement as stated by the manufacturer and the spread in haze values measured over the four quadrants did not exceed this value. The transmission at 550 nm is 91.6 %. This matches typical values for glass/ITO substrates used in touchscreen assemblies, which are 89–93 % [264].

Fig. 10.3(b) shows the optical transmission profile (measured using the CQ spectrophotometer) for two samples, compared against that of the substrate $B1$. Lines are drawn between data points as a guide to the eye. Sample $G1$ contained nanocomposite granules at a loading of 0.2 % by mass of the base varnish. The granules themselves were fabricated using the optimum composition determined in chapter 6, specifically spherical ATO nanoparticles and 10 % silicone binder. They were granulated at 2000 rpm in the DAC for 4 minutes before curing and then sieving at 75 µm to remove large agglomerated material. Also shown is the

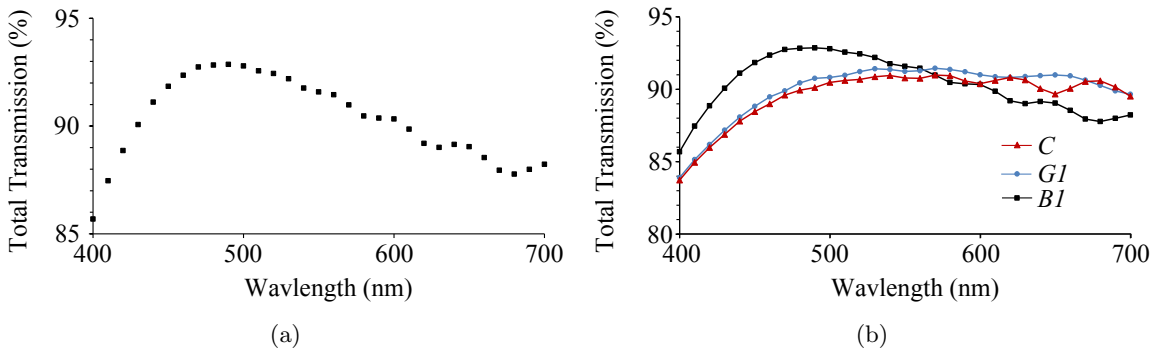

FIGURE 10.3: Graphs showing the transmission spectra over visible wavelengths measured using the CQ spectrophotometer for (a) the rigid glass/ITO substrate ($B1$) onto which all samples were printed (b) and the PS layers C and $G1$ printed onto substrate $B1$

control sample, C, in which an equal amount of ATO nanoparticles were dispersed directly into the base ink without the pre-granulation stage.

For both samples $G1$ and C, at wavelengths less than 550 nm, a slight decrease in the transmission was observed, with this effect minimised for $G1$. This suggests that scattering and absorption of light within the PS layer reduced the transmission through the assembly. However above 550 nm the transmission through both samples appears to exceed that of the substrate only. The difference in transmission is significantly higher than the error. It is possible that this phenomena is caused by poor calibration of the CQ spectrophotometer leading to larger measurement errors than anticipated. If this were a real effect it may be suggestive of a fluorescent mechanism, where shorter wavelengths (higher energies) are absorbed and then re-emitted at longer wavelengths (lower energies). To corroborate this result, the measurements were repeated on the Shimadzu UV-3600 (SUV) spectrophotometer, which offered greater wavelength resolution.

Fig. 10.4(a) shows the transmission through the $B1$ substrate measured using the SUV spectrophotometer, at wavelengths of 300–900 nm covering the ultraviolet (UV), visible and near infra-red (NIR) wavelengths. By measuring the transmission at an extended wavelength range it is possible to identify features such as the absorption edge due to the band gap of the ITO. As discussed in chapter 9, ITO has a band gap typically in the range 3–4 eV, corresponding to a wavelength of 310–410 nm. For photons below this energy ITO is non-absorbing, however above this photons may be absorbed in electron transitions, producing a sharp transition between absorbing and transparent regions in the transmission spectrum at wavelength corresponding to the band gap. In reality the transition is smoothed out over a

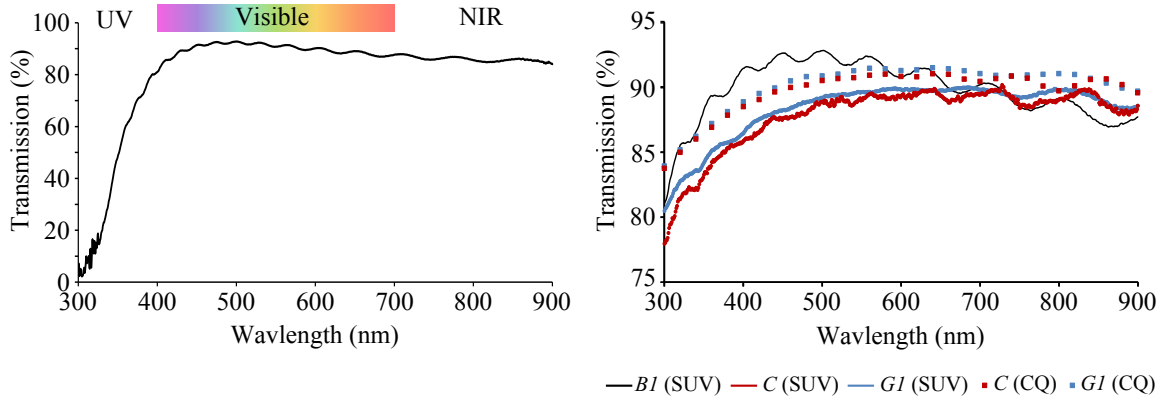

(a) (b)

FIGURE 10.4: Graphs showing the transmission spectra for (a) substrate $B1$ over ultraviolet/visible/near infra-red wavelengths from 300–900 nm measured using the SUV spectrophotometer and (b) samples $G1$ and C measured using both CQ and SUV spectrophotometers, compared against substrate $B1$ measured using the SUV spectrophotometer.

wider range of energies due to transitions involving impurity states or phonons. This effect is responsible for the decrease in transmission at wavelengths shorter than 400 nm, observed in Fig. 10.4(a). In the NIR region (> 700 nm) the transmission slowly decreases to 84.6 % at 900 nm. With increasing wavelength, the real part of the complex dielectric permittivity of the ITO decreases and at the plasma frequency it is equal to zero. Here, the ITO becomes highly reflective and the transmittance decreases. For higher carrier concentrations the plasma frequency may occur within long wavelengths in the visible range, causing the transmission to decrease at longer wavelengths. Another interesting phenomenon is the oscillations in the transmission occurring over all wavelengths > 350 nm, where the transmission exhibits multiple local maxima and minima. This feature is indicative of interference fringes generated by coherent and incoherent reflection of light at the interfaces of the PSRT structure, when compared to the reference sample. In this case, the reference was transmission through air, as the reference port in the SUV spectrophotometer was left empty.

Fig. 10.4(b) compares the transmission spectra obtained using both SUV and CQ spectrophotometers for the $B1$ substrate and samples C and $G1$, for visible wavelengths. The same shape of the transmission spectra is measured regardless of the instrument used, although the transmission measured using the CQ spectrophotometer produced a systematic shift to higher transmission values by approximately 1–2 %. This may be partly attributed to the integrating sphere attachment which collects all forward scattered light, whereas using the SUV spectrophotometer only directly transmitted light is collected. Furthermore, the light source is different in each instrument, where the colour filter used in the CQ spectrophotometer simulates daylight conditions and there is no such filter in the SUV spectrophotometer. Due to the general agreement between results, henceforth the transmission properties (e.g. the integrated transmission) are measured using the SUV whilst the haze is recorded using the CQ spectrophotometer. The increase in transmission for the PS layers above that of the substrate, if a real effect, may be caused by fluorescent effects. The source of the fluorescence may be the polymeric base varnish or the ATO nanoparticles. Whilst an interesting phenomenon, this is not explored further in this thesis.

10.3.2 Transmission and haze through pressure-sensitive layers

The transmission spectra for various samples are quantified in terms of their integrated transmittance, T_{INT} and the haze, h, and the results are compared in Table 10.1. The number density of granules is the number of granules per mm^2, and this is shown for each PS layer. The mass loading of granules into the ink, expressed as a percentage of the base varnish mass, is also shown. Samples with the same mass loading may have a different number density of granules. This is because the number density does not account for the size and therefore mass of individual granules - for the same mass loading it is possible to have either a high number

Sample	Granulation time (mins)	Sieve size (µm)	Substrate	Mass loading (%)	Number density (mm^{-2})	% < 5 µm	T_{INT} (%)	Haze (%)
B1	–	–	B1	–	–	–	90.07 ± 0.09	0.6 ± 0.1
C	–	–	B1	0.2	250 ± 70	74	87.7 ± 0.3	2.5 ± 0.1
G1	4	75	B1	0.2	54 ± 8	49	88.6 ± 0.1	1.3 ± 0.1
G2	4	75	B1	0.2	47 ± 6	56	88.78 ± 0.08	1.4 ± 0.1
G3	4	20	B1	0.2	190 ± 20	64	87.7 ± 0.2	2.1 ± 0.1
G4	4	20	B1	0.4	330 ± 10	64	86.8 ± 0.2	3.1 ± 0.1

TABLE 10.1: Optical properties of the $B1$ substrate, and PS layer comprising granules produced with a range of process variables and post-production sieve protocols.

density of small (low mass) granules or a low number density of large (higher mass) granules, or anything in between. Additionally, the percentage of granules that are 1–5 µm in size is also shown. Granules less than 1 µm could not be measured due to the resolution of the images and the thresholding algorithm used. Samples $G1$ and $G2$ are structurally identical, however $G2$ was printed 6 months after $G1$ using the same ink. The similarities in granule concentration and optical transmission suggest no degradation of the granules within the ink. For samples $G3$ and $G4$ the granules were passed through a 20 µm sieve before incorporation into the ink.

An important observation is that haze is minimised for pre-formed granules when compared to the control sample, which contained ungranulated ATO nanoparticles at the same mass loading. For example, sample C produced a haze of 2.5 %, whereas samples $G1$ and $G2$ produced a haze of just 1.3 and 1.4 % respectively. The haze and transmission properties can be linked to the size and number density of the granules within the PS layer. Fig. 10.5(a) shows the number density of granules plotted against h and T_{INT} for each PS layer. For a greater number of granules per unit area, h increases whilst T_{INT} decreases. The solid lines represent linear relationships. In Fig. 10.5(b) the percentage of granules in the size range 1–5 µm is plotted against haze. The horizontal error bars relate to the error in the determination of the granule size distribution when the size is altered by ± 1 pixel. Within error, haze increases with an increasing proportion of smaller granules within the PS layer.

These observations are in agreement with the theoretical predictions discussed in chapter 8. The scattered light intensity from granules or agglomerates within the PS layer is strongly dependent on their size and number. Generally speaking, granules less than 100 nm in size promote Rayleigh scattering and an approximately constant scattered light intensity is found independent of scattering angle. For larger particulates scattering is predominantly in the forward direction with a large scattering peak centred at 0°. Referring back to Fig. 8.11, the intensity of light scattered to small angles (i.e. less than 2.5°) is greater for 10 µm particles than it is for 1 µm particles. For example, sample C, which contained a larger number of smaller granules would be expected to scatter a lower intensity of incident light to less than

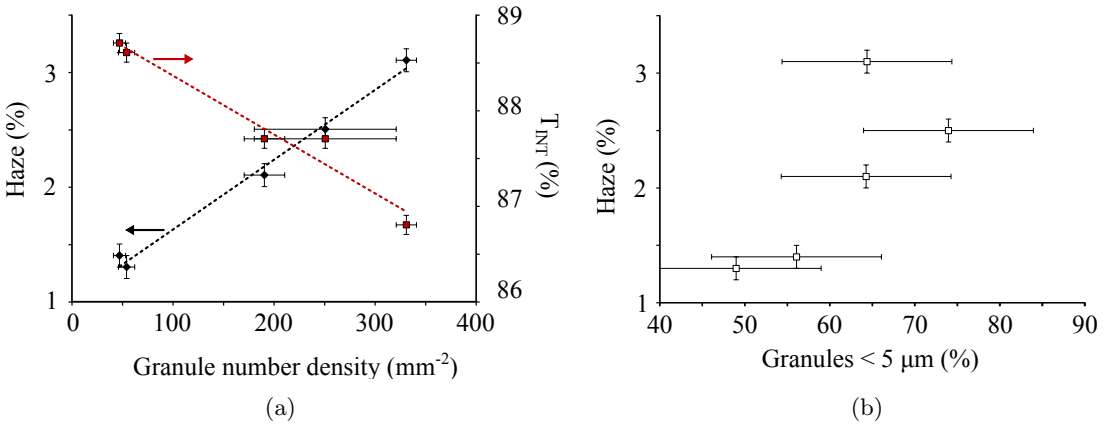

FIGURE 10.5: Graphs showing (a) the relationship between the granule number density within the PS layer with the measured haze (black data points) and integrated transmission (red data points), where the dashed lines represent linear trends. (b) shows the relationship between the haze and the proportion of granules of size 1–5 µm.

2.5°, whereas samples containing fewer and larger pre-formed granules would be expected to scatter a higher intensity of light to less than 2.5°. This is reflected in the measured haze values.

Referring to samples $G3$ and $G4$, it is clear that sieving the granules at 20 µm is detrimental to the optical properties of the PS layer. Sieving was performed in the hope of eradicating the minority of large granules reminiscent of the bimodal distribution promoted during granulation (see chapters 6 and 7). The large number density of granules in sample $G4$, compared to samples $G1$ and $G2$ which were sieved at 75 µm, suggests breakdown of individual granules during the sieving process. Doubling the granule loading at the ink manufacture stage, as for $G5$, produces a 1.7 factor increase in the measured granule concentration in the printed PS layer and further increases the haze.

In summary, it is shown that pre-formed granules offer a significant advantage over spontaneously formed agglomerates, in terms of the optical properties of the PSRT devices. This is because the granulation step effectively reduces the percentage of small granules < 5 µm within the PS layer, so that for the same mass loading the granules are on average larger with a correspondingly lower number density. Larger particles scatter predominantly in the forwards direction, with a strong transmission peak at low angles. This result is important as it allows minimisation of the optical haze for a given particulate loading by mass, if the particles are first granulated before incorporation into the ink.

10.4 Electrical functionality of touchscreens containing nanocomposite granules

10.4.1 Quantifying the force-resistance response of PSRTs

In the previous section it was shown that PS layers containing pre-fabricated granules offered a significant benefit over the control sample in terms of optical transmission through the layer. However, it is also necessary for the granulated samples to offer the same, if not improved, electrical functionality when compared to the control. In this section, the parameters used to quantify the functional response of the PSRTs are defined and compared for each PSRT.

To exemplify the typical F-R profile exhibited by the PSRT, the control sample C is chosen as a representative example. This sample contained unagglomerated ATO nanoparticles instead of pre-formed granules. Here, the PS layer was printed onto substrate B1 and then adhered to the PET/ITO flexible electrode $T1$.

10.4.1.1 Hysteresis in F-R behaviour

The F-R response at 30 positions on the test PSRTs was measured using the testing procedure outlined in section 9.4.1. To highlight the hysteresis in the response, the F-R response at one position is shown as an example in Fig. 10.6 for both loading and unloading of force up to 5 N, where the solid arrows indicate the loading and unloading cycles.

With increasing force the resistance drops non-linearly from 0.54 MΩ to the order of 1 kΩ. The resistance of 0.54 MΩ represents the maximum measurable resistance of the system and

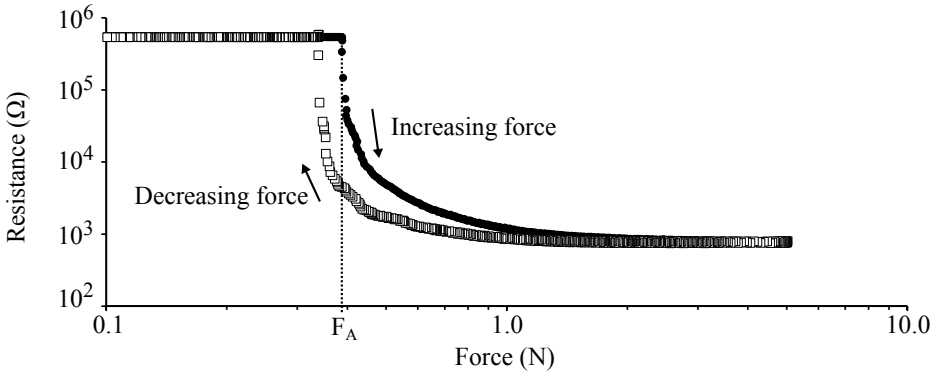

FIGURE 10.6: Graph showing the F-R response of sample C at one location. Hysteresis occurs between the increasing and decreasing force regimes shown by the black circles and white squares respectively, where the resistance is consistently lower when decreasing the applied force. The activation force, F_A, at which the resistance first drops to 0.4 MΩ, is shown by the dashed line.

not the off-state resistance of the PSRT. The activation force, F_A, is defined as the force required to cause a decrease in resistance to 0.4 MΩ, when increasing the force. For the test position shown in Fig. 10.6 F_A was 0.38 N. The greatest change in resistance is seen for forces up to 1 N, after which the resistance decreases at a slower rate. Furthermore, hysteresis between loading and unloading cycles is also evident, where decreasing the applied force results in a lower resistance than when increasing the force. To quantify this, a dimensionless hysteresis parameter, **H**, was defined as:

$$\mathbf{H} = \frac{R_{F,inc} - R_{F,dec}}{R_{F,inc}} \tag{10.1}$$

where $R_{F,inc}$ and $R_{F,dec}$ are the resistance values for increasing and decreasing applied force respectively, at force F. Unless otherwise stated, **H** was evaluated at 1 N. A **H** value of 0 represents no hysteresis. The larger the value the greater the hysteresis. Here, **H** is 0.23. When comparing the functional response of multiple PSRTs the average hysteresis parameter over the 30 tested positions is quoted, with an error given by the standard deviation over all positions. Hysteresis may be caused by one of two effects. Firstly, the flexible electrode has a finite relaxation time when the load is decreased by retracting the stylus. The flexible electrode does not immediately attain its equilibrium position when the force is removed, such that there is a lag between the force applied to the electrode by the test probe and the force applied to the PS layer by the electrode. The second possibility is an inherent hysteresis in the pressure-sensitive resistance response of the nanocomposite granules. This feature is explored later in chapter 12.

10.4.1.2 Variability of F-R behaviour over 30 tested positions

Considering increasing the applied force only, the F-R response for each of the 30 tested positions is shown in Fig. 10.7(a). A comparison over all locations allows the variability in the resistance response to be assessed using a dimensionless variability parameter, **V**:

$$\mathbf{V} = \frac{R_{F,max} - R_{F,min}}{R_{F,avg}} \tag{10.2}$$

where $R_{F,max}$, $R_{F,min}$ and $R_{F,avg}$ are the maximum, minimum and average resistance values at applied force F over the 30 positions tested (shown by the dashed lines in Fig. 10.7(a)). Unless otherwise stated, **V** is assessed at a force of 1 N. Ideally, $\mathbf{V} \approx 0$ is preferable as this represents an equal F-R response regardless of test location. For sample C, **V** is 0.43 corresponding to a spread in resistance values of 1200 Ω at 1 N. The variability in the response at less than 1 N is typically high and the spread of F_A across the 30 positions implies that the activation force is highly sensitive to the morphology of the PS layer. For

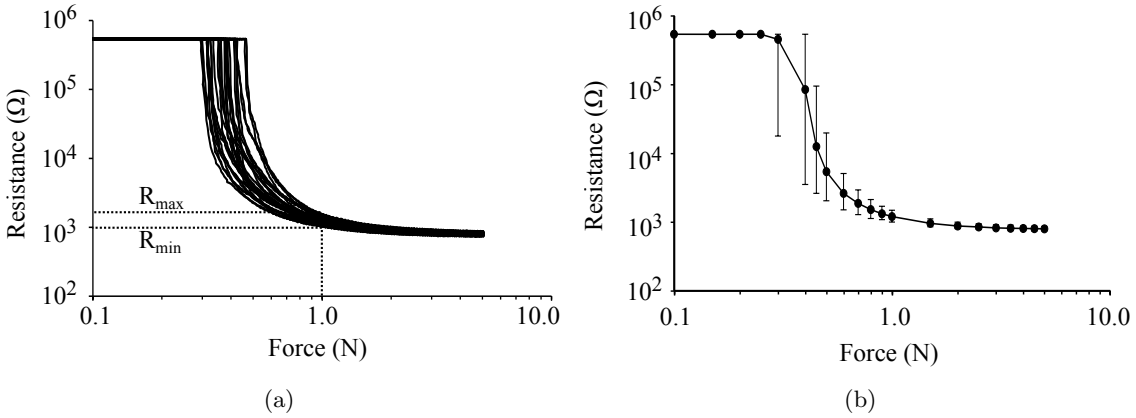

FIGURE 10.7: Graph showing (a) the F-R response over 30 positions on sample C (b) the average F-R response where the error bars represent maximum and minimum resistance values recorded over all positions.

PS localities where a larger granule protrudes well above the PS surface it is expected that the activation force may decrease in that region.

10.4.1.3 Average sensitivity of F-R behaviour

The average response of the PSRT is calculated by averaging the resistance values recorded at discrete sample forces. The average response for sample C is shown in Fig. 10.7(b). The error bars represent the maximum and minimum resistance values measured at that force over all positions. The large error bars at forces of 0.3–0.6 N are caused by the variation in F_A at each test location.

Ideally, the F-R response would show a decrease in resistance for applied force in the range of interest. In this case, the force range corresponds to a light touch (0.1 N) and a hard press (∼5 N). It is useful to define a dimensionless sensitivity parameter, **S**, which describes the rate of resistance decrease:

$$\mathbf{S} = \frac{\log R_{F_A} - \log R_{1N}}{\log R_{F_A} - \log R_{5N}} \tag{10.3}$$

Here, the denominator represents the total change in (the logarithm of) the resistance over the forces F_A to 5.0 N. The numerator represents the change in (the logarithm) of the resistance from F_A to 1.0 N applied force. It is important to note that a high value of **S** is not always beneficial. At low forces, an overly sensitive response will result in 'switch-like' behaviour, where initially the resistance drops rapidly but then is unresponsive to further application of force. Such a response may be useful in digital (on/off) applications but is not suited for continuous sensing of applied pressure. Here, an **S** value of 1 represents fully digital or switch-like behaviour where the response of the PSRT is fully saturated at 1 N.

For sample C, where the average F_A over 30 positions was 0.35 N, an **S** value of 0.93 was calculated.

10.4.2 Comparison of F-R response for different PS layers

In this section, the functional performance of several PSRTs are compared according to their force-resistance characteristics, quantified through the hysteresis, variability and sensitivity parameters as described above. These values are compared against those obtained for the control sample C.

10.4.2.1 Comparison of control sample with sample containing optimum granule composition

The optimum granule composition was investigated in part I of this thesis. It was found that silicone binder and spherical ATO nanoparticles allowed for a controllable granulation process where granule nuclei were formed for mixing times up to 10 minutes when granulated at 2000 rpm in the DAC. Furthermore, analysis of the granule structure determined the average porosity and strength of such granules. Here, the optimum granules produced after 4 minutes were incorporated into the PS layer. These granules had a GSD which was shown in Fig. 6.2 and the percentile values D_{10}, D_{50} and D_{90} of 3.6, 5.8 and 8.9 µm respectively. The average porosity of the nuclei was 16 ± 1 % and the average fracture strength (of the size fraction 75–100 µm) was 10.9 ± 0.9 mN.

A granule loading of 0.1 g in the PS layer was used to create sample $G1$, which was previously characterised in Table 10.1 in terms of the optical properties and the number density of granules per mm^2. The F-R profile measured at one location is shown in Fig. 10.8(a). The general trend of the F-R response is similar to that of sample C. The resistance drops from an initial value in excess of 0.5 MΩ to around 1 kΩ, with application of up to 5 N force. Here, F_A was 0.41 N. However, the F-R curve shown here exhibits an unusual bump at 1 N. Here, the F-R response prior to 1 N appears to level, and then decreases further just after 1 N. This feature appears in the F-R response over all 30 positions tested, although the exact force at which it appears shows some variation. The cause of the feature is not currently understood but may be caused by atypical mechanical properties of this particular PSRT assembly.

Similar to sample C, hysteresis is observed when increasing and decreasing the force. At this location **H** is 0.43. Fig. 10.8(b) shows the F-R response over all 30 positions. The average **H** is 0.37 ± 0.07. The variability **V** at 1 N over the 30 locations is 1.3. Here, the spread of resistance values around the average is greater than the average resistance itself and indicates

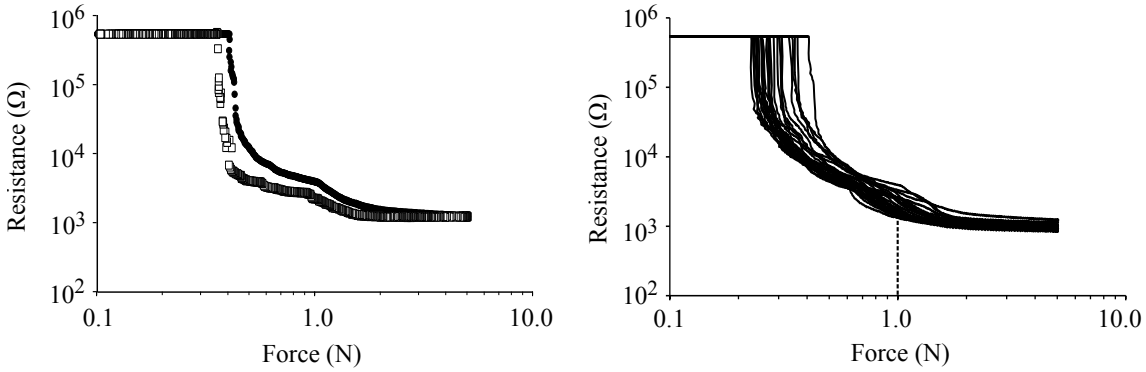

FIGURE 10.8: Graph showing (a) the F-R response at one position on sample $G1$, where the black circles and white squares represent increasing and decreasing the force respectively. (b) shows the F-R response over all 30 tested locations on sample $G1$.

large variation between tested locations on the PSRT surface. As for the control sample, the variability increases for forces less than 1 N, with a range of F_A values. The average response of sample $G1$ is compared to that of sample C in Fig. 10.9(a) and Table 10.2 compares the performance parameters for each PSRT discussed in this section. The error on the average activation force ($\bar{F_A}$) is taken as the standard deviation of the F_A values recorded over each test position, whereas ΔF_A gives the range between the maximum and minimum values recorded.

For sample $G1$ **V** is much larger than for sample C, however F_A and **H** are similar considering their statistical variations. Additionally, for $G1$ **S** is calculated as 0.88, which is lower than that of sample C (0.93). Fig. 10.9(b) shows the change in resistance as a function of applied force, i.e. the gradient of Fig. 10.9(a), for both samples. It can be seen that in the force range F_A to 0.65 N, the change in resistance is lower for sample $G1$ than it is for sample C. This highlights the lower sensitivity for $G1$ at lower applied forces, where it behaves less 'switch-like' when compared to sample C.

It is apparent that by replacing the spontaneous ATO agglomerates with pre-formed granules, the overall response of the PSRT remains comparable to the control C. The F-R response becomes less sensitive, or 'switch-like', at low applied forces however **V** is greatly increased.

Hence it can be concluded that pre-formed granules can offer the advantage of a less sensitive, or 'switch-like' response when compared to spontaneous agglomerates, in addition to enhancing the visible light transmission through the PS layer. However the drawback to a lower number density of granules is the increased spatial variation in response over the PS surface, which can be a disadvantage in large-area applications.

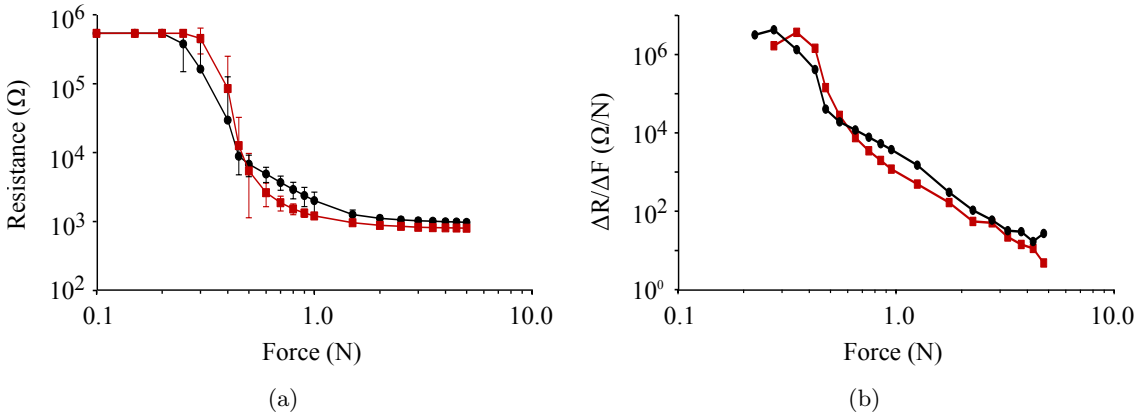

(a) (b)

FIGURE 10.9: Graph showing (a) the average F-R response over 30 positions for samples C (red) and $G1$ (black), where the error bars represent the standard deviation over the 30 tested locations. (b) shows the gradient of the F-R response as a function of force for samples C (red) and $G1$ (black) where it can be seen the rate of decrease of resistance with force is lesser for sample $G1$ for forces between 0.65 and 5 N.

10.4.2.2 The effect of sieving the granules to a maximum size of 20 µm

During granule fabrication a granulation regime was selected which produced granule nuclei typically less than 20 µm in size. However, due to the method of binder dispersion a bimodal size distribution of granules was promoted where a small fraction (by number) were greater than 20 µm. Whilst all granules were sieved at 75 µm before inclusion into any ink, this does not remove any intermediate sized granules from 20–75 µm. Such granules in the PS layer may be disadvantageous. Initial contact between the flexible electrode and large granules may delay any subsequent contact with surrounding smaller granules and produce an overly sensitive, 'switch-like' response.

To negate this possibility the optimum granules (as described above) were sieved at 20 µm prior to inclusion in the ink at 0.1 g loading ($G3$) and 0.2 g loading ($G4$). The F-R response over the 30 tested positions is shown in Fig. 10.10(a) for sample $G3$ and in Fig. 10.10(b) for sample $G4$. The performance parameters are listed in Table 10.2. Interestingly, the average

Sample	$\bar{F}_A$ (N)	ΔF_A (N)	**H**	**V**	**S**
C	0.35 ± 0.05	0.24	0.26 ± 0.04	0.43	0.93
G1	0.27 ± 0.05	0.29	0.37 ± 0.07	1.3	0.88
G3	0.34 ± 0.06	0.31	0.27 ± 0.06	0.66	0.95
G4	0.24 ± 0.07	0.27	0.23 ± 0.04	0.37	0.97

TABLE 10.2: Performance parameters for PSRT functional response, including the average activation force, $\bar{F}_A$ and the spread of the activation force over 30 tested locations, ΔF_A, as well as the hysteresis (**H**), variability (**V**) and sensitivity (**S**) parameters. **H** and **V** were assessed at a force of 1 N.

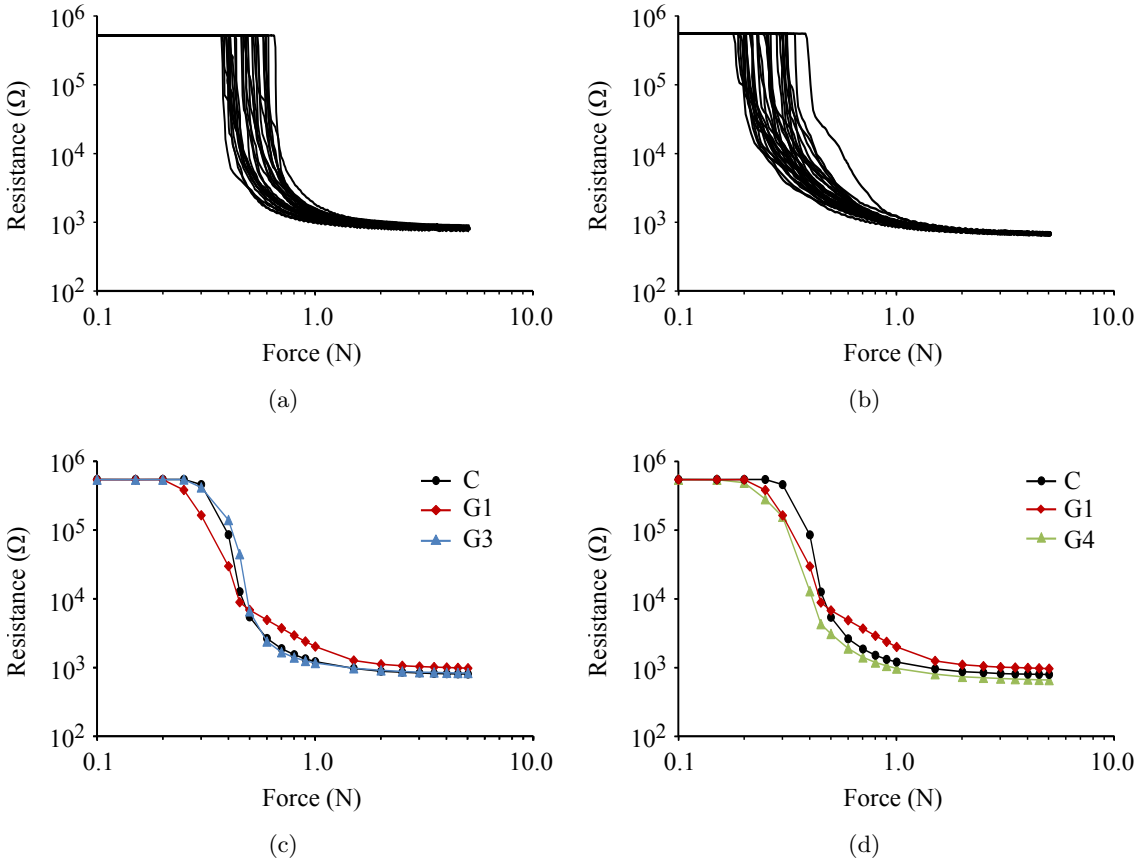

FIGURE 10.10: Graph showing the F-R response over 30 positions for sample (a) $G3$ and (b) $G4$ and the average F-R response compared against $G1$ and C for (c) $G3$ and (d) $G4$.

F-R response bears more similarity to that of C rather than $G1$ and the values of $\mathbf{H}$, $\bar{F}_A$ and ΔF_A are comparable with those of sample C. Fig. 10.10(c) and Fig. 10.10(d) compare the average response for $G3$ and $G4$ against C and $G1$ respectively, where the F-R curve for $G3$ lies almost on top of that produced by C. The $\mathbf{S}$ parameter is similar to that for C whilst the variability $\mathbf{V}$ lies between the values obtained for C and $G1$. Meanwhile, sample $G4$ shows an increased $\mathbf{S}$ and a reduced $\mathbf{V}$, whilst $\mathbf{H}$ remains comparable.

These results indicate that sieving the granules before ink manufacture has a negative impact on the F-R response because it increases the sensitivity of the response to that approaching sample C. Meanwhile, $\mathbf{V}$ decreases with increased granule loading. The number density of granules per mm^2 was shown in Table 10.1. Sieving the granules at 20 µm increased the granule concentration, a fact which was attributed to causing the observed deterioration of optical performance. Sieving the granules therefore appears to break down the pre-formed granule structure. When sieving the granules, it was noted that the granules quickly blocked the sieve openings. This phenomena, known as sieve blinding, can result from granules larger than the sieve size becoming lodged in the mesh openings. For granules below the mesh size,

blinding can occur if there are too many granules on the surface of the sieve. This phenomena is exacerbated for sieve openings less than 100 µm in diameter [282]. Increased mechanical agitation may free the sieve openings but may also result in granule attrition and breakage, which is detrimental in this application.

10.4.2.3 Linking PSRT performance to granule distribution within the PS layer

It is hypothesised that the differences in the variation and sensitivity of the F-R response observed for samples $G1$ to $G4$ can be linked with the distribution of granules within the PS layer. As can be seen from Table 10.1, the number density of granules in the PS layer is much larger for sample C and $G3$ than for $G1$, for the same mass loading of solids into the base ink. This can be attributed to the formation of a greater number of smaller agglomerates or granules in the former case, and fewer but larger granules in the latter case. When the number density of granules within the PS layer is lower, the F-R response may become more sensitive to local fluctuations in the granule number, as fewer granules are responsible for the overall conduction through the PSRT. This may explain the observed increase in variability. Furthermore, because there are fewer granules per unit area the sensitivity of the response may improve, i.e. become less 'switch-like'. For a large number of granules contacted by the flexible electrode the resistance may quickly saturate to a minimum value. For a lower concentration of granules the rate of saturation may decrease, thus decreasing the sensitivity.

V and **S** are plotted as a function of granule number density in Fig. 10.11(a) and Fig. 10.11(b) respectively. It can be seen that in both cases there is a correlation, where **V** decreases with increasing granule number density and **S** increases with number density. In both instances a linear trend may be used as a first approximation, although more data points are needed to clarify the exact form of the relationship. This result supports the above hypothesis and indicate that there is indeed a trade-off between improving the sensitivity of a PSRT and improving the spatial variation in the F-R response.

In summary, the electrical properties of the PSRT containing nanocomposite granules is comparable to that of the control sample containing spontaneously formed agglomerates. Whilst pre-formed granules result in an improvement of the sensitivity of the F-R response, spatial variation across the layer also increased. When the granules were sieved at 20 µm, the response approached that of the control sample. It was found that the sensitivity increased (i.e. became more 'switch-like') with an increasing number density of granules within the PS layer, whilst the variability of the response decreased.

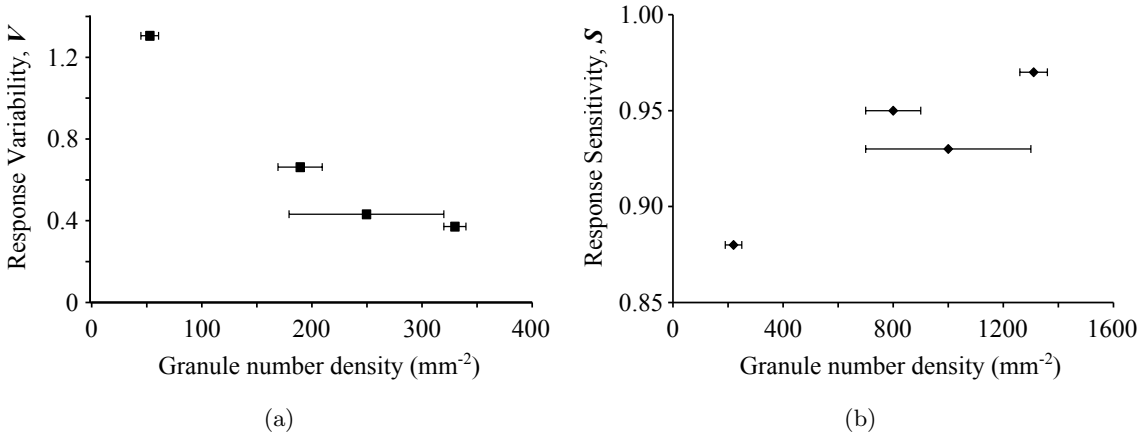

FIGURE 10.11: Graph showing the correlation between the number density of granules within the PS layer and the (a) variability (**V**) and (b) sensitivity (**S**) parameters of the F-R response.

10.4.3 Durability of PSRTs

Durability is important in device applications because the response of the device must remain unaltered with repeated use. Here, it is observed that after repetitive F-R testing, the response shifts towards higher resistances. The durability of a PSRT after a large number of testing cycles was assessed using the sliding wear procedure outlined in chapter 9. By subjecting the PSRT samples to this high-energy testing procedure it is possible to investigate both the damage mechanisms and possible methods of circumventing the problem through the touchscreen assembly. Sample *G*1 is used as an example to quantify the effects of the line-writing procedure.

10.4.3.1 Assessing the effects of the line-writing test

Prior to testing, 15 locations close to the LW region were tested and an average F-R curve was calculated. After 30 000 line-writing cycles, 50 positions corresponding to 5 lines of 10 points crossing the line-written region (as shown in Fig. 9.8(b) were tested for their F-R response. Fig. 10.12(a) shows the resistance measured at 1 N applied force, at each of the 10 points on the line perpendicular to the line-written area. Results for each of the 5 perpendicular lines are shown. The horizontal dashed line shows the average resistance at 1 N measured prior to line-writing, and also accounts for the inherent variability, **V**, in the F-R response. The peak values of resistance along each line were used to determine the location of maximum deviation from the pre-line writing F-R response, shown by the vertical dashed lines in the figure. The F-R curves for these 5 locations are shown in red in Fig. 10.12(b). The black lines represent the tests outside the line-written area which showed no change in

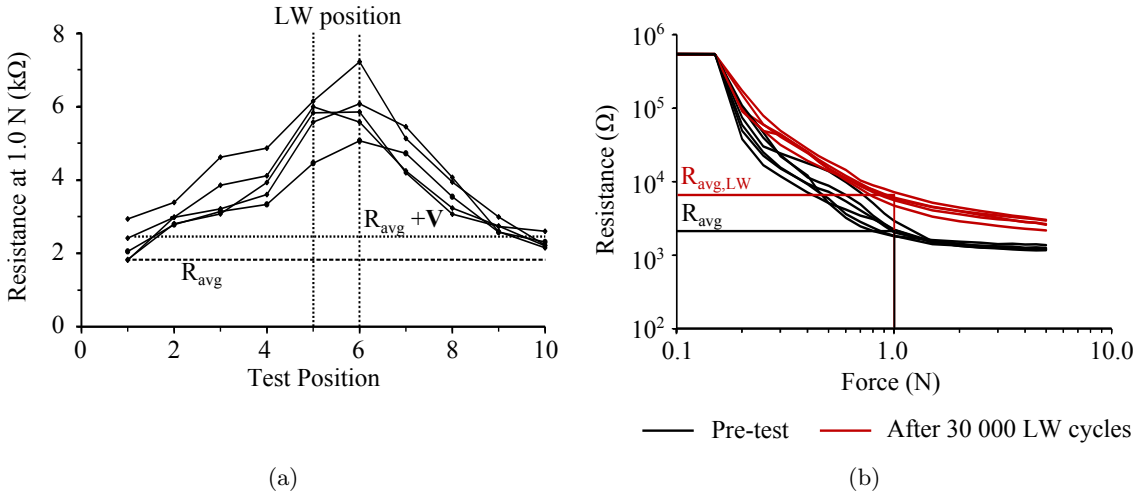

(a) (b)

FIGURE 10.12: Graphs showing the effect of sliding wear or 'line writing' tests on the functional performance of a PSRT. (a) The resistance measured at 1 N for 10 positions along a test line perpendicular to the line-written region, with 5 test lines measured in total. The horizontal dashed lines represent the average resistance measured at 1 N prior to line-writing, and the inherent spatial variability in the F-R response. The 5 maxima represent 5 locations corresponding to maximum deviation away from pre-line-writing F-R behaviour, contained within the vertical dashed lines representing the line-written region. (b) The F-R curves at maximum deviation are shown in red, whilst the black lines represent the F-R response away from the line-written area, corresponding to the minima shown in (a).

F-R response when compared to the pre-test results, i.e. the minima in Fig. 10.12(a). A durability parameter, **D**, was defined as:

$$\mathbf{D} = \frac{R_{LW,max}}{R_{avg}} \tag{10.4}$$

where $R_{LW,max}$ is the average peak resistance post-LW measured at 1 N as shown in Fig. 10.12(a), and R_{avg} is the average resistance pre-LW at 1 N. For **D** =1, there is no shift to higher resistances after line-writing and the touchscreen has ideal durability. Realistically, **D** >1 where a higher value represents poorer durability. For **D** < 1 this would indicate that the post-LW resistance was lower than the pre-LW resistance, although this has not been observed experimentally. Note that for the durability to be measurable against the inherent spatial variability of the F-R response then $\mathbf{D} > 1 + \mathbf{V}$. For sample $G1$ presented here, **D** is 3.2, which is distinguishable from the inherent variability of 1.3.

The durability of samples $G3$ and $G4$ were also assessed using the same procedure. Fig. 10.13 shows the effect of 10 000 line-writing cycles. Note that for both of these samples the resistance shift is approximately a factor of 10 larger than for $G1$. The durability parameters of all samples are compared in Table 10.3. Also shown are the **H** and **S** parameters. These were averaged over the five F-R curves at the line-written location and also calculated for

the average F-R response prior to line-writing. The **H** and **S** values outside the line-written region may not match those calculated in section 10.4.2, as in the latter case the results were obtained over a large area of the PS layer, whereas here only a small locality was tested. The values of **S** and **H** before and after line-writing allow further characterisation of the effect of the sliding-wear test.

The **D** values for $G3$ and $G4$ are a factor of 10 larger than for that of $G1$, indicating a large shift to higher resistances after the LW procedure for the 20 µm-sieved granules. In all cases, **H** increases after LW which suggests that the hysteresis may be partly intrinsic to the PS layer. This is because if the hysteresis was caused by the mechanical properties

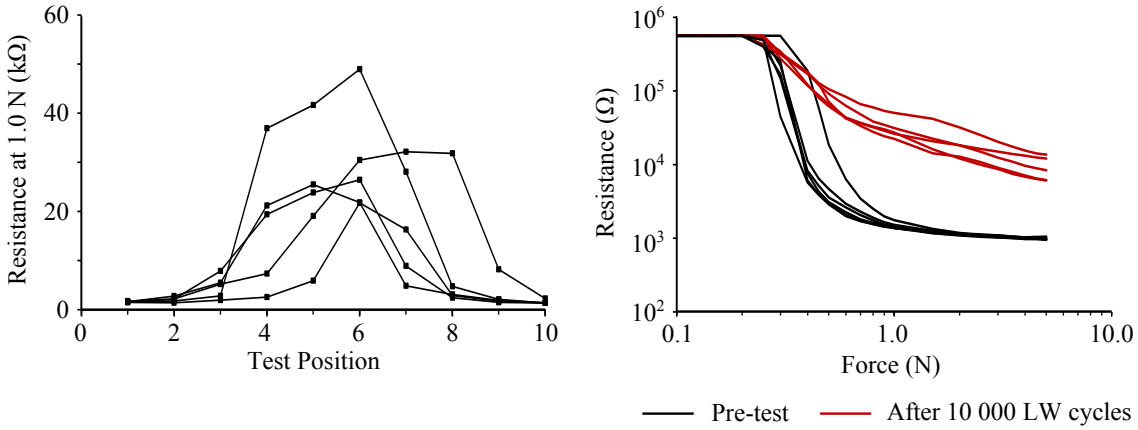

(a) Resistance at 1 N for $G3$

(b) F-R response pre- and post-LW for $G3$

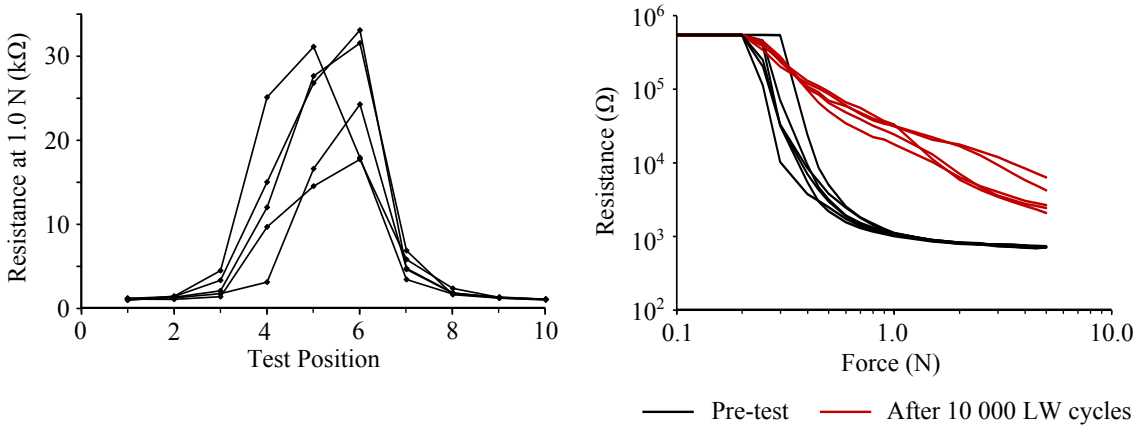

(c) Resistance at 1 N for $G4$

(d) F-R response pre- and post-LW for $G4$

FIGURE 10.13: Graphs showing (a) the effect of the line-writing test on the resistance at 1 N applied force on 10 positions along five test lines perpendicular to to the line-written area for sample $G3$, where lines between data points are shown as a guide to the eye. The peak values correspond to the position on the sample where line-writing produced the largest shift in resistance. (b) shows the F-R response at the five positions closest to the line-writing area, compared to those furthest from the tested area. Graphs (c) and (d) show the same process for sample $G4$.

Sample	**D**	**S** (Pre-LW)	**S** (Post-LW)	**H** (Pre-LW)	**H** (Post-LW)
G1	3.2	0.90	0.84	0.38 ± 0.09	0.53 ± 0.03
G3	25.5	0.93	0.68	0.29 ± 0.07	0.51 ± 0.08
G4	24.9	0.94	0.57	0.25 ± 0.04	0.7 ± 0.1

TABLE 10.3: The change in F-R characteristics as a result of the line-writing test procedure, where the durability parameter, **D**, is calculated along with the sensitivity, **S**, and the hysteresis, **H** before and after the line-writing test.

of the PET/ITO electrode only then this would remain unaffected by the LW test, unless significant damage to the PET was evident. After all durability tests conducted here, no obvious damage to the PET substrate was observed. For $G1$, **S** decreased post-LW by 7 %. In comparison, the sensitivity decreased by 27 and 39 % for $G3$ and $G4$ respectively. This is apparent from Fig. 10.13(b) and Fig. 10.13(d) as the resistance post-LW saturated to a higher value at 5 N. This affect may be attributed to damage to the PS layer and damage to the ITO coating on the flexible electrode, both of which may interrupt the flow of charge through the assembly. The poor response of samples $G3$ and $G4$, compared to the response of $G1$, may be attributed to the possibility that these granules were structurally compromised by the sieving procedure, as explored earlier in section 10.4.2.2. For fractured or broken granules, the sliding wear test may cause a greater amount of damage compared to whole, structurally sound, granules.

After LW testing, both the surface of the PS layer and the ITO electrode in the location corresponding to the line-written region were imaged using SEM. Fig. 10.14(a) and Fig. 10.14(b) show the effect of line-writing on the PS layer. Lower magnification images showed no discernible damage to the overall structure of the PS layer and the insulating polymer had not been observably marked. However closer inspection of individual granules showed a flattened surface and some smearing of granular matter. Damage to the ITO took the form of delamination of regions of ITO, as shown in Fig. 10.14(c) and 10.14(d). This is consistent with results obtained by others [73, 267, 268].

10.4.3.2 Extended durability through altering the build of the PSRT

Cairns *et al.* reported that the durability of a resistive touch interface could be enhanced by adding a polyimide layer on top of the flexible electrode, which acted to reduce crack formation in the ITO layer [269]. Here, the durability of the PSRT may be enhanced through the addition of the layer $T3$ on top of the original PET/ITO electrode. $T3$ comprised a transparent PMMA layer approximately 0.17 mm thick. Each of the PS layers discussed here was deposited on the glass/ITO substrate $B1$. Samples $G5$ and $G6$ comprised a granule loading of 0.1 g, whereas samples $G7$ and $G8$ had a loading of 0.26 g. F-R graphs before and

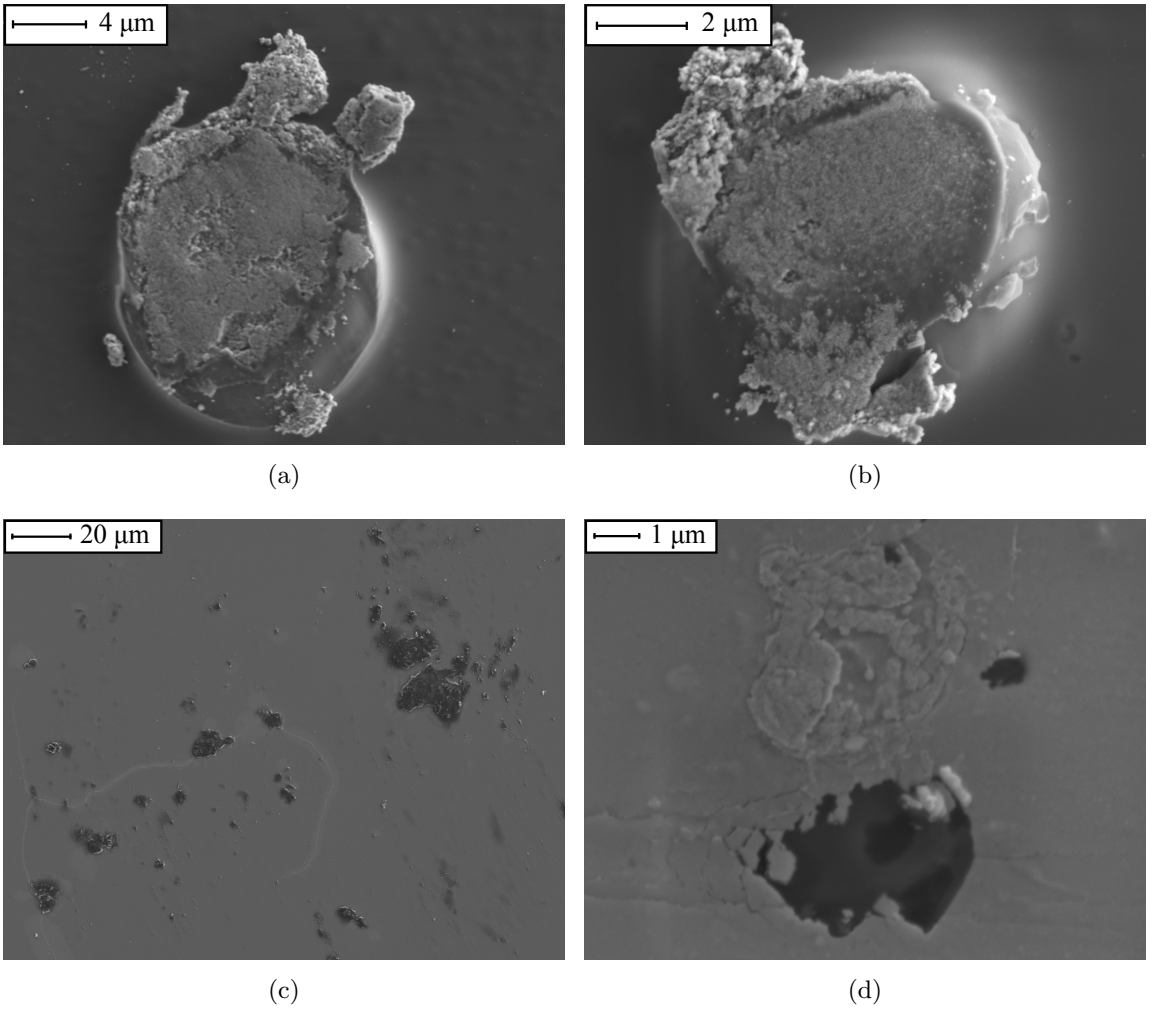

FIGURE 10.14: SEM images showing the effect of line-writing on the PS layer and ITO electrode. (a) and (b) show individual granules within the PS layer with a flattened surface profile and smearing of granular matter. (c) and (d) show damage to the ITO electrode in the form of delaminated flakes of material.

after line-writing are compared in Fig. 10.15 for the four samples. The build parameters and the results of the line-writing test are summarised in Table 10.4.

In all cases, the addition of the $T3$ layer on top of the flexible electrode ($T1$ or $T2$) gave a significant improvement in durability. For example, for samples $G5$ and $G6$, which are identical other than the inclusion of $T3$ in the latter case, **D** decreased from 8.7 to 3.7. With increased granule loading (which increases the number density of granules in the PS layer) the addition of the $T3$ layer, as in sample $G7$, produced the most favourable durability conditions, with the lowest **D** value implying the smallest shift in resistance in response to the line-writing test. The decrease in **S** post-LW was also minimised for this sample. However sample $G8$, assembled using the PET/ITO $T2$ substrate and the $T3$ layer, showed a variable F-R response both before and after line-writing, as shown in Fig. 10.15(d). The exact reasons

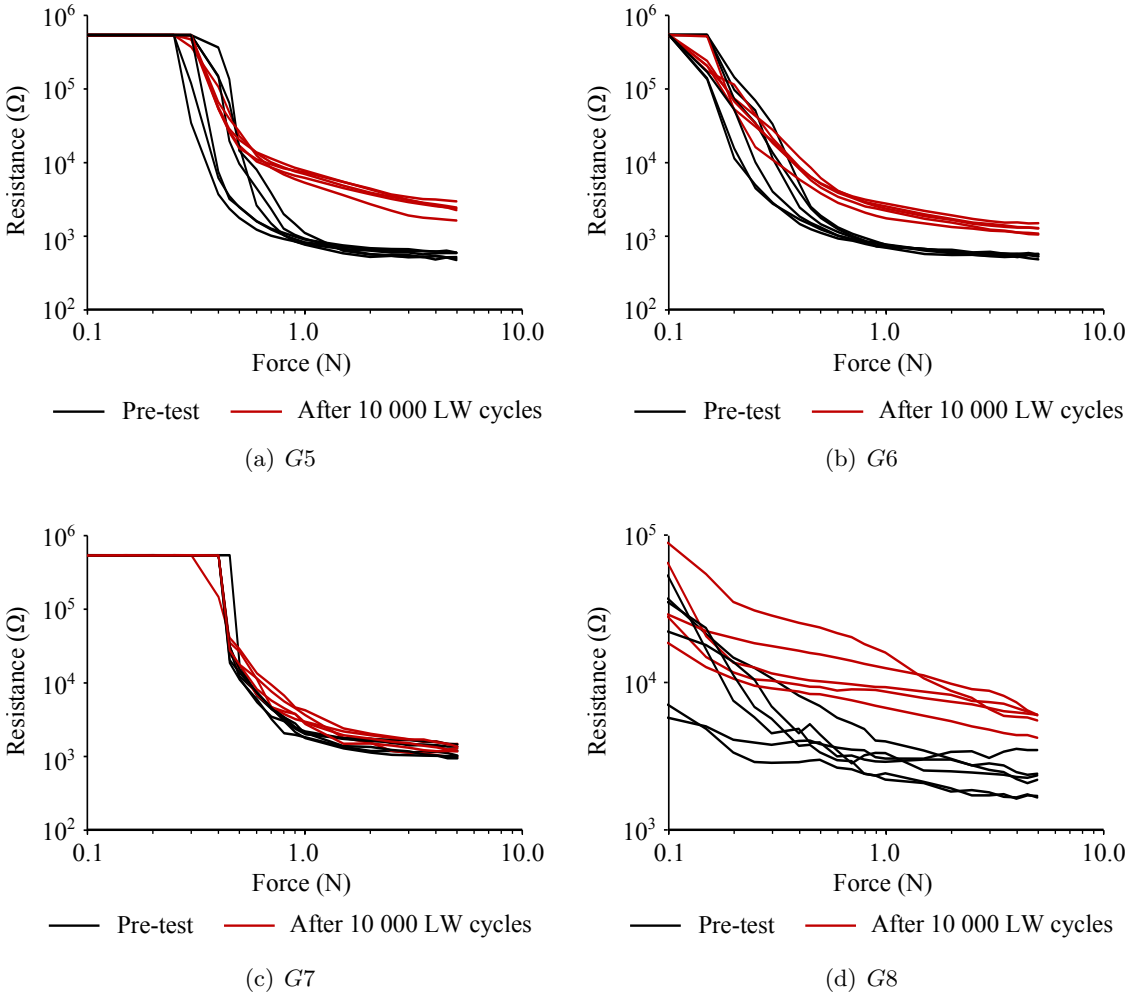

(a) $G5$ (b) $G6$

(c) $G7$ (d) $G8$

FIGURE 10.15: Graphs showing the effect of the line-writing test on the F-R response of samples (a) $G5$ (b) $G6$ (c) $G7$ and (d) $G8$

for this remain unclear although it could in part be due to the overall thinness of the build, as the substrate $T2$ was just 175 µm thick.

With the addition of the $T3$ layer, the flexible electrode becomes thicker and thus decreases the deflection for a given applied force. If less force is exerted on the granules then granule breakage is less likely to occur. Similarly, by increasing the granule loading the pressure on the granules is decreased, as the electrode is in contact with a larger number of granules at any given time. Again, this would be expected to increase the durability of the PSRT. The effect of increasing the electrode thickness is explored further using the simulation developed in chapter 11.

In summary, the addition of $T3$ onto $T1$ enhances the durability, and the durability is fundamentally improved for an increased granule loading. However, it should be noted that the addition of a further layer in the assembly may impact on the optimum transmission and

Sample	Granule Loading (g)	Build	**D**	**S** (Pre-LW)	**S** (Post-LW)
*G*5	0.1	B1, T1	8.7	0.95	0.79
*G*6	0.1	B1, T1 + T3	3.7	0.97	0.89
*G*7	0.26	B1, T1 + T3	1.2	0.85	0.83
*G*8	0.26	B1, T2 + T3	2.9	0.90	0.85

TABLE 10.4: Durability, **D** and the sensitivity, **S**, before and after line-writing, as a function of PSRT build.

the overall build thickness. Hence for any application, there must be a trade-off between the durability of the device to repeated testing and the optical transmission through the touchscreen assembly.

10.4.4 Comparison of PSRTs containing nanocomposite granules with other force sensing technologies

In chapter 2, a comparison was made between different technologies allowing the detection of force on a touch interface. These included piezoelectric and capacitive sensors, as well as piezoresistive conducting polymer composites and force sensitive resistors. Particular emphasis was made on the detectable force range, from a light touch (0.1 N) to a hard press (5 N). A comparison of all technologies was presented in Fig. 2.11.

Fig. 10.16 shows a comparison of these technologies with the response of the PSRTs developed in this chapter. The F-R response of sample *G*1 was chosen as a representative example, and the response parameter was calculated according to equation 2.5. Here, the activation force of the PSRT comprising layer *G*1 was 0.41 N. This is similar to that of the FSR and the resistive touch interface developed by Stantum. In its current form, the PSRT cannot detect light touches of 0.1 N. However, this is much improved over the resistive touch interface demonstrated by 3M (with a minimum detectable force of 0.5 N), and the piezoelectric touch interface (1.9 N). Similarly, the response range of the resistive touchscreen developed by Stantum, and the pressed capacitive touchscreen demonstrated by H. Kim operate in the low force region only, with maximum response achieved by approximately 0.8 N. In this regard, the PSRT demonstrated here is beneficial as it shows a response from 0.4 N to approximately 1 N, a closer match to the requirements for touch sensing in HCI applications. However, in its current form the PSRT does not fully cover the touch requirements for HCI applications. Future work may look to extend the force sensitivity to below 0.4 N, and above 1 N.

It should be noted that the sensitivity of the response, and the range of detectable forces may be further controlled through the build parameters of the device. For example, for the 3M touch interface the sensitivity of the response may be controlled by altering the depth of the air-gap between electrode and sensing layer, as was demonstrated in Fig. 2.9. Here, the

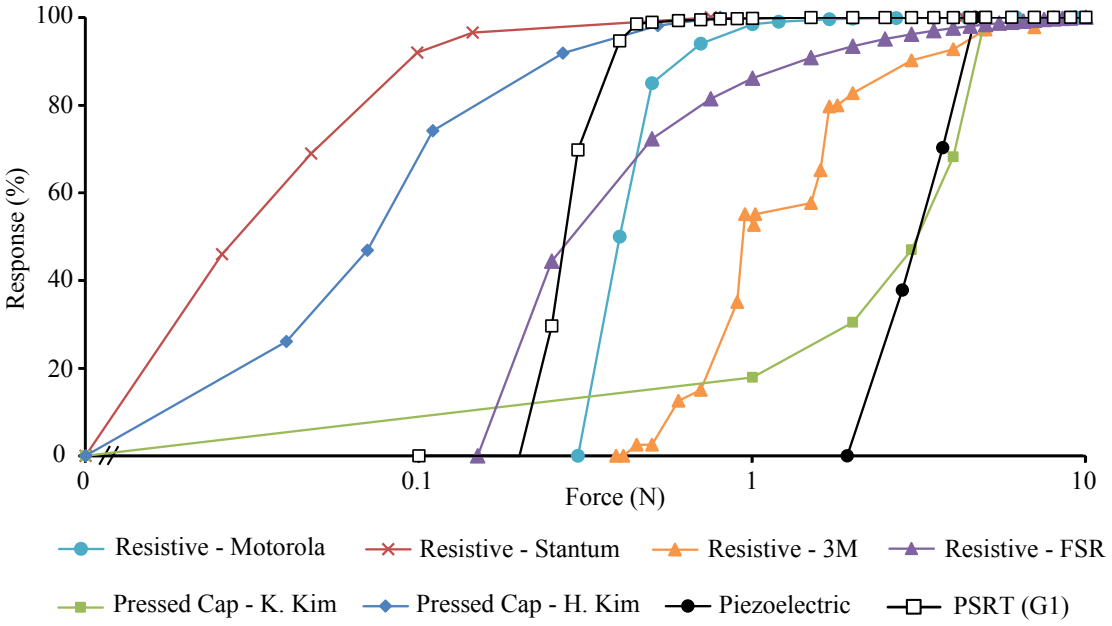

FIGURE 10.16: Graph showing the force sensitive response of the PSRT device comprising the PS layer $G1$, compared against the response of other force sensing technologies described in chapter 2 of this thesis, including a piezoelectric sensor developed by PyzoFlex, pressed capacitive sensors developed by H. Kim and K. Kim, piezoresistive conducting polymer composites developed by Motorola, Stantum and 3M and force sensitive resistors developed by Interlink Electronics.

sensitivity increased with increasing air-gap. Other build parameters which may affect the functional performance of the device include the thickness and mechanical properties of the electrode substrate. The effect of these parameters are explored in the next chapter.

10.5 Chapter summary

In this chapter the functional performance of PSRTs containing nanocomposite granules was compared against that of a control sample containing spontaneously agglomerated ATO nanoparticles. For samples containing the same solid loading by mass, those containing the optimum granules (developed in part I) exhibited improved optical transmission and reduced haze, over the visible wavelengths. Hence by pre-fabricating the granules prior to inclusion into the ink, the optical performance is enhanced. This was linked to the granule size and number density of granules within the PS layer. For pre-formed granules there were fewer granules per unit area and a smaller percentage less than 5 µm in size. From the theory of light scattering, larger particles scatter predominantly in the forward direction and thus minimise the haze. This result is important as, for a given granule loading, the haze can be minimised by pre-forming the ATO nanoparticles into granules before incorporation into the

ink. The optical performance of touchscreens should be optimised for high-end applications where obstruction of the underlying display needs to be minimised and granulation provides a route for achieving this.

The F-R response of a number of PSRTs was quantified in terms of the hysteresis produced when increasing and decreasing the force in a test cycle, the spatial variation in the F-R response and the sensitivity of the average F-R response. It was found that PSRTs containing pre-formed granules showed a comparable response to PSRTs containing spontaneously agglomerated ATO nanoparticles. Overall, the sensitivity of the PSRT containing granules was lower, resulting in a less 'switch-like' response which is important for pressure-sensing applications where a number of discrete pressure levels must be differentiated. However, the PSRTs containing granules showed a higher spatial variation in F-R response. Furthermore, sieving the granules at 20 µm prior to their inclusion into the ink produced adverse effects, showing a greater number density of granules than the unsieved sample. It was hypothesised that the sensitivity and variability were inherently linked to the number density of granules within the PS layer, where it was found that for a lower number density of granules the sensitivity decreased and the variability increased.

Finally, the durability of the PSRTs was assessed before and after the line-writing procedure. By repeated testing at high force, it was found that the resistance shifted to a higher value for a given applied force. This shift could be quantified by a durability parameter. SEM analysis showed a flattening of the granule structures within the tested regions, as well as delamination of the ITO on the electrode. The effect of line-writing test could be minimised through the inclusion of an additional protective layer adhered on top of the flexible electrode.

Chapter 11

Modelling the Force-Resistance Behaviour of the PSRT Response

11.1 Introduction

This chapter describes the model which was developed in order to predict the force-resistance (F-R) behaviour of the pressure-sensitive resistive touchscreens (PSRTs). This model assumes that the force-sensitive response is caused by an increased contact area between the flexible PET/ITO electrode and the pressure sensitive (PS) layer, which in turn increases the number of granules that provide conductive pathways through to the lower ITO/glass substrate. The conductive nature of the granules themselves is neglected, where instead it is assumed that each granule, if contacted, behaves as a linear (Ohmic) resistor. The resistance through the PS layer can then be calculated as each granule provides a parallel resistance. Any intrinsic pressure sensitivity of the granules is ignored.

In section 11.2, a model simulating the F-R behaviour is developed using the theory discussed in chapter 8. This simulation predicts the F-R response by calculating the increase in contact area between electrode and PS layer, and uses this as a basis for calculating the resistance response. The effect of the touch location on the flexible electrode deflection is studied in section 11.3. The simulation also allows the effect of other parameters, including the granule loading and the individual granule resistance, as well as the depth of the air-gap and the thickness of the PET/ITO electrode to be assessed, and these are explored in section 11.4. Finally, the results of the model are compared with experimental data in section 11.5.

11.2 Development of the model

As described in chapter 8, the deflection of a beam which is fully restrained at both ends can be calculated using mechanical principles using equations 8.2 and 8.3. Here, to a first approximation, the PSRT was modelled as a two dimensional flexible PET/ITO electrode, fully fixed at both ends and positioned above the PS layer which was assumed to be non-deformable.

With regards to equation 8.2 and 8.3, the following parameters were set. The total length L of the flexible electrode was 80 mm, the width W was 65 mm and the thickness d was 1 mm. This corresponds to the PSRT dimensions outlined in Fig. 9.3, accounting for the finite width of the Scotch™ tape which also acted as a fixed support at each end of the electrode and produced an air-gap of depth ~100 µm. To simplify matters, it was assumed that the electrode was fixed lengthways only. The Young's modulus of PET was taken to be 3.3 GPa [283, 284] and the effect of the thin layer of ITO was neglected.

Fig. 11.1(a) shows the deflection of the PET/ITO electrode as a function of applied force, where the force is applied to the centre of the electrode over a finite width of 2 mm. This is similar to the dimensions of the stylus tip used in experimental testing. With increasing force, the maximum deflection also increases. Of course, the deflection is limited by the rigid PS layer. This is shown on the graph as a dashed line at a vertical depth of 100 µm. This air gap corresponds to that produced experimentally through the use of Scotch™ tape as described in chapter 9. As a simple approximation, a contact length can be defined by the

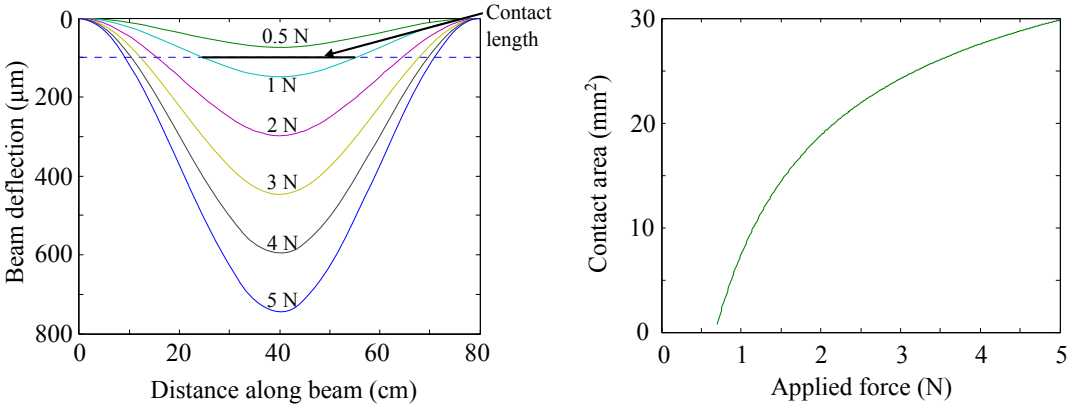

FIGURE 11.1: Graphs showing (a) the deflection of the flexible PET/ITO electrode with increasing centrally applied force. The intersection of each deflection curve with the dashed line representing the rigid PS layer can be used to define a contact length between electrode and PS layer, from which contact area can be estimated. (b) The contact area as a function of applied force.

two intersections of the deflection curve with the dashed line representing the rigid PS layer, for each value of applied force. As an example, the contact length for 1 N is shown on the graph. Overall, the contact length increases with applied force, as would be expected. By assuming that the deflection is symmetrical along the length and breadth of the electrode the contact length can be equated to the diameter of the contact area made between electrode and PS layer. The increase in contact area with applied force is shown in Fig. 11.1(b). From the contact area, the resistance through the layer may be approximated by knowing the resistance of each granule and the spatial distribution of the granules within the layer.

The granules spanning the PS layer were modelled as resistors in parallel. When contact is made between the flexible electrode and N granules of resistance r_i, the total resistance R_{TOTAL} is given by:

$$\frac{1}{R_{TOTAL}} = \sum_{i=1}^{N} \left(\frac{1}{r_i} \right). \tag{11.1}$$

Assuming for all granules $r_i = R_g$, i.e. each granule within the layer contributes the same resistance value, R_{TOTAL} is given by:

$$R_{TOTAL} = \frac{R_g}{N} \tag{11.2}$$

where N is simply the product of the contact area, and the number density of granules within the PS layer, i.e. the number of granules per unit area.

Fig. 11.2(a) shows the effect of the individual granule resistance on the resultant F-R relationship. Here, granule resistance is set in the range of 10 kΩ to 100 MΩ and the granule number density in the PS layer is kept constant at 5.4×10^7 m^{-2}. This corresponds to the actual number density measured for the PS layer $G1$. Actual values of granule resistances are discussed further in chapter 12. In Fig. 11.2(b) the granule number density is set in the range 1×10^6 to 5×10^7 m^{-2}, for a granule resistance of 1 MΩ. Due to the nature and assumptions of the model, changing the granule resistance and the granule number density bears no effect on the overall shape of the curve and produces a vertical translation only. The model therefore predicts that for a larger intrinsic granule resistance, the minimum resistance achievable through the PS layer increases. Similarly, for a higher number density of granules within the PS layer, the minimum resistance decreases. It is important to note that the model predicts no effect on the values of $\mathbf{S}$ and the activation force, F_A, that is the minimum force required to produce contact between flexible electrode and PS layer.

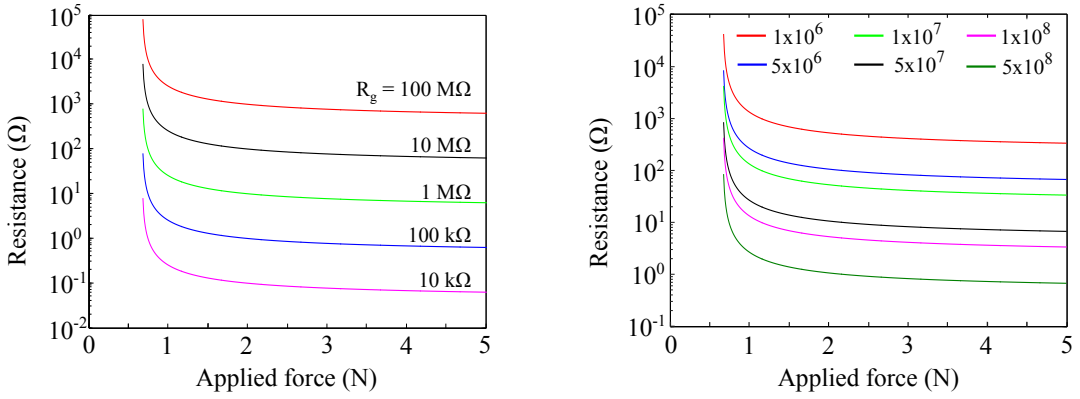

(a) (b)

FIGURE 11.2: Graphs showing F-R profiles obtained by converting the contact area between electrode and PS layer into a resistance, based on the granule concentration and the individual granule resistance. In (a) F-R curves are shown for a granule concentration of 5.4×10^7 m^{-2} for five different granule resistances ranging from 10 kΩ–100 MΩ. In (b) the F-R curve is shown for 5 different granule number densities, for a granule resistance of 1×10^6 Ω. In both cases, changing these variables does not alter the shape of the F-R curve and produces a translation along the y axis only.

A normalised change in resistance can be defined as the ratio of the resistance to the resistance R_{F_A}, that is the resistance measured at the activation force F_A:

$$R_N = \frac{R_i}{R_{F_A}} : \tag{11.3}$$

This removes the dependency on the initial resistance value of a single granule, as well as the number density of the granules within the PS layer. Each of the data series in Fig. 11.2(a) and Fig. 11.2(b) map onto a single F-R curve when the normalised resistance R_N is plotted.

11.3 The effect of touch location on the F-R response

Because the flexible electrode is fully constrained at both ends, the maximum deflection is dependent on where the force is applied. For example, closer to the restrained edges of the electrode, the maximum deflection will be less for a given force, than in the centre of the electrode. Fig. 11.3(a) shows the deflection of the flexible electrode for two cases. In the first case, a force of 1 N is centrally applied. In the second case, the 1 N force is applied at a distance of 15 mm from the left hand support. The horizontal line represents the rigid PS layer, positioned 100 µm below the flexible electrode. For a centrally applied load, the maximum displacement of the electrode is greater than the depth of the air gap such that contact is created between the electrode and the PS layer. However, for the same applied

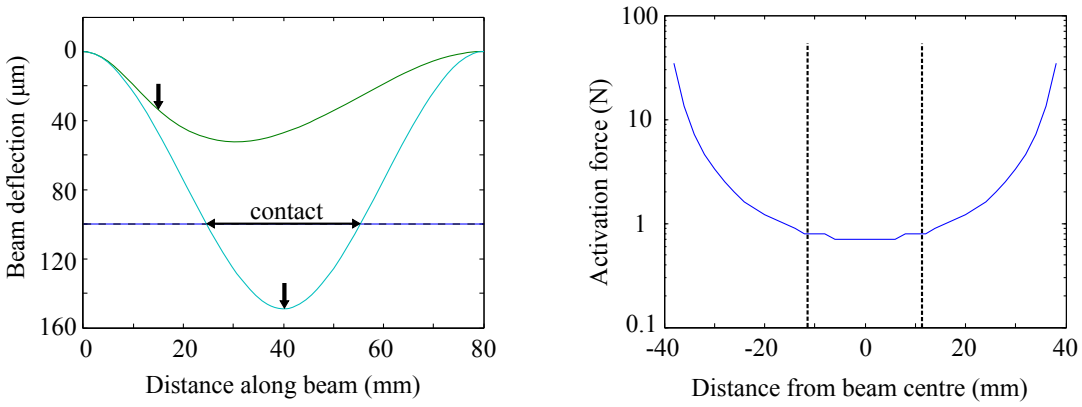

FIGURE 11.3: Graphs showing (a) a simulation of the flexible electrode deformation when a 1 N force is applied both centrally (blue solid line) and offset towards the leftmost support (green solid line). The exact location of applied force is shown by the solid black arrows. The horizontal dashed line represents the position of the rigid PS layer, positioned 100 microm below the flexible electrode. (b) The activation force (the minimum force required to cause contact between flexible and rigid electrode) as a function of the location of the applied force along the flexible electrode. The region inside the dashed lines corresponds to the regions which are tested experimentally.

force at 15 mm from the left support, the additional constraint supplied by the support means that the deflection is insufficient to produce contact. The activation force, F_A, measures the minimum force necessary to achieve contact between the flexible electrode and PS layer. F_A is plotted as a function of the distance from the electrode centre at which the force is applied in Fig. 11.3(b). It can be seen that the activation force rises rapidly when approaching the edges of the electrode, and is a minimum in the electrode centre. This can lead to intrinsic variation of the measured F-R response which is independent of the PS layer properties.

In the previous chapter, it was seen that variation in F-R response was measured over 30 tested positions. However, as described in chapter 9, the measurement grid used for F-R testing covered the central 30 % of the PSRT surface only, corresponding to approximately the central 20 mm of the electrode considered in this simulation. This region is represented by the vertical dashed lines in Fig. 11.3(b). Within this region, F_A is expected to vary in the range 0.7–0.8 N. This small variation cannot fully account for the variation in the F-R response observed over the 30 tested positions, which was reported in chapter 10. Hence, the variation observed experimentally cannot fully result from the additional constraint when approaching the edge of the flexible electrode, and rather must also be caused by intrinsic variation in the PS layer itself.

It is worthwhile to note that in real world applications, the air-gap in resistive touchscreens is created with an array of spacer dots (polymeric beads) between the ITO electrodes, as described in chapter 2. The deflection of the ITO electrode then becomes a complex function

of the distance from the touch location to the nearest spacer dots. However, this approach removes the edge effects resulting in the spread of activation forces seen here.

11.4 The effect of PSRT build parameters on the functional performance

The model can be used as a predictive tool to investigate the role of the build parameters of the PSRT device on the functional F-R performance. The model allows parameters such as the depth of the air-gap between the flexible electrode and PS layer to be altered, as well as the thickness of the PET/ITO electrode.

Fig. 11.4(a) shows the effect of altering the depth of the air-gap on the resultant F-R behaviour. This could be achieved experimentally by successive layers of Scotch™ tape. Note that here the normalised resistance as defined in equation 11.3 is plotted. The graph shows that increasing the depth of the air-gap reduces the sensitivity of the response whilst simultaneously increasing the activation force required to cause initial contact. For air-gaps of 50, 75 and 100 µm F_A was below 1 N and **S** could be calculated according to equation 10.3. For air-gaps of 50, 75 and 100 µm F_A was 0.34, 0.51 and 0.68 N and **S** was 0.87, 0.81 and 0.71 respectively. Similarly, Fig. 11.4(b) shows the effect of altering the thickness of the PET/ITO electrode from 0.2 to 1.0 mm. Again, increasing the thickness causes a decrease in **S** and an increase in F_A. The decrease in sensitivity is attributed to a lower dynamic range of response observed when decreasing the electrode thickness. For example, at a thickness of 0.2 mm the resistance change is less than one order of magnitude, whereas for 1 mm the resistance decreases over 2 orders of magnitude.

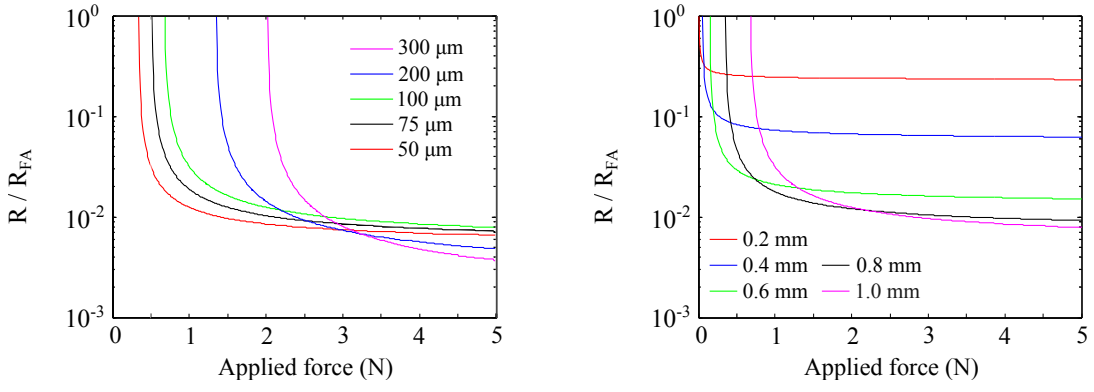

(a) (b)

FIGURE 11.4: Simulations of the F-R response for PSRTs with (a) varying air-gap depths between PET/ITO electrode and PS layer and (b) varying PET/ITO thickness.

Hence a trade-off is predicted between the sensitivity and the activation force. Here, an overly sensitive response is not beneficial as it results in digitisation of the response - i.e. rapid switching between high and low resistance with limited intermediary stages. This is not conducive to the detection of multiple pressure levels. In order to achieve a response which is less 'switch-like', the model predicts that this must be at the expense of reducing the functional force range of the PSRT such that low force, light touch, sensing is limited. Additionally, increased build thickness can be undesirable in real-world applications as it adds bulk and weight to the overall device dimensions.

11.5 Comparison of model and experiment

In Fig. 11.5(a) the F-R curve obtained experimentally for the $G1$ PS layer is compared with a model simulation. For the simulation the granule number density was set as 5.4×10^7 per m^2 (the same as was measured using optical microscopy for sample $G1$) and the granule resistance was arbitrarily set to 1 MΩ, where it was noted previously that these parameters did not affect the normalised resistance. The resistance for sample $G1$ was also converted to a normalised resistance to allow comparison. The simulation gives the correct form of the F-R response observed experimentally. However, the simulation overestimates the activation force, and underestimates the magnitude of the response.

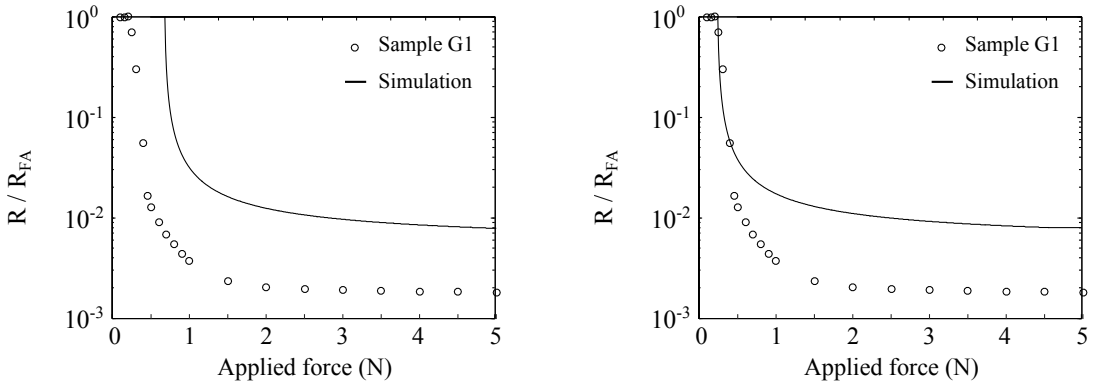

FIGURE 11.5: Graphs showing (a) the simulated force-resistance response for a PS layer with a granule concentration of 54 mm^{-2}, where each granule has an arbitrarily assigned resistance of 1 MΩ (black line), compared against the F-R response of sample $G1$ (open circles) where the (normalised) resistance is expressed as a fraction of the resistance at the activation force. In (b), the simulation is adjusted to match the activation force F_A observed in sample $G1$.

For the simulation, an activation force of 0.7 N is predicted, compared to 0.4 N observed experimentally. This may be due to a number of reasons. Firstly, the simulation does not account for the protrusion of granules above the surface of the PS layer. As can be seen in Fig. 10.1 the granules do not lie flush with the surface and this acts to decrease the depth of the air-gap. However, this effect is marginal as the granules protrude typically less than 5 µm above the surface. Another possible cause is the compressibility of the supports, that is of the adhesive layers and the Scotch Tape™ that hold the PSRT together and create the air-gap. For compressible supports the air-gap itself is dependent on the applied force. Fig. 11.5(b) compares model and experiment, removing the shift associated with the higher activation force.

Of greater interest is the underestimation of the magnitude of the response calculated using the simulation. Using the model, the resistance is predicted to decrease up to $1 \times 10^{-2} \times R_{F_A}$ at 5 N applied force whereas experimentally the resistance decrease approaches $1 \times 10^{-3} \times R_{F_A}$ after 5 N, a further factor of 10 lower. It is unlikely that this is caused by an underestimation of the contact area between flexible electrode and PS layer. Indeed, the simulation may actually overestimate the contact area. This is because, for a small stylus width with a constant tip diameter, once first contact has occurred applying a greater force is unlikely to cause a large increase in the contact area. However, the force applied to the established contact area increases. Furthermore, the simulation was developed considering deflection in the longitudinal axis only (i.e. along the PSRT length) and it was assumed that the lateral axis (along the PSRT width) was unconstrained, whereas in reality the flexible electrode is constrained along both dimensions. The effect of the additional constraints would be to limit the contact area in the lateral dimension (width) such that instead of being a circular contact zone the true shape would become elliptical, decreasing the area and therefore the number of granules contacted. Hence this effect cannot explain the underestimation of the resistance decrease.

The model also fails to predict the experimental observation that an increased sensitivity is observed for an increase in granule number density. The model predicts that the granule concentration has no effect on the shape of the F-R curve (although both start and end resistance are affected). The model assumes that each granule has a fixed resistance independent on the applied force, and the pressure-sensitivity of the PSRT is realised through the increase in the number of granules contacted with applied force only. The effect of any pressure-sensitive conductive pathways within the nanocomposite granules is neglected. The investigation into possible pressure-sensitive conduction pathways throughout the granules is the focus of the next chapter.

11.6 Chapter summary

This chapter detailed the development of a model to predict the force sensing capabilities of PSRT devices. This was achieved by modelling the flexible PET/ITO electrode as a two dimensional flexible beam, fully constrained at both ends and separated from the rigid PS layer by an air-gap. Applying force to the flexible electrode caused downward deflection, and for sufficient force created contact with the PS layer. The contact area could be estimated from the overlap between the flexible electrode and PS layer, and the resistance estimated from the granule resistance and granule number density.

The deflection of the flexible PET/ITO was dependent upon the distance of the touch location to the constrained end of the electrode, where a closer distance resulted in less deflection for a given force. This property can cause variation in the resultant F-R response of the PSRT, as the activation force increases for touch locations closer to the edges of the electrode. Experimentally, the F-R response of PSRTs was tested over the central 30% of the surface, and it was shown that over this region the change in activation force was minimal and could not account for all of the variation in F-R response demonstrated previously in chapter 10.

The model was used to predict the effects of granule number density, granule resistance, air-gap depth and electrode thickness on the F-R response. It was found that the granule number density within the PS layer had no effect on the overall shape of the curve, instead producing a vertical translation only. The model could not explain the observed trend that the sensitivity of the F-R response increased with increasing granule number density, as reported previously in chapter 10.

When comparing the model predictions to F-R curves produced experimentally, it was found that the activation force was overestimated by the model. A possible reason for this is that the adhesive used to constrain the flexible electrode is likely to be slightly compressible, which would act to reduce the activation force. The magnitude of the response was underestimated by the model by a factor of 10. This may be because the model fails to account for any variation in granule resistance, for example through any pressure-sensitivity intrinsic to the granules themselves. This effect is investigated in the following chapter.

Chapter 12

Pressure Sensitive Conduction in Nanocomposite Granules

12.1 Introduction

The focus of this chapter is an experimental investigation into any pressure-enhanced electrical conduction within the nanocomposite granules. In chapter 10 the force-resistance response of the entire PSRT system was assessed, where it was found that as force was applied to the touchscreen devices the resistance decreased. This force or pressure-sensitive response may originate from two mechanisms. The first is caused by an increase in the contact area between the flexible ITO electrode and the PS layer. The PS layer exhibits anisotropic conduction, such that each granule provides a means of charge flow from bottom to top electrode, however there is no charge flow through the plane of the PS layer. Thus, with increasing applied force a greater number of granules are contacted by the electrode and can then contribute to the conduction. This effect was simulated through assessing the mechanical deflection of the flexible electrode under applied force, and the results were presented in chapter 11. It was found that, whilst this effect could account for a significant proportion of the observed F-R response of the PSRT devices, the model in its current form could not account for the magnitude of the F-R response observed experimentally in PSRT devices. Thus, it is possible that the granules themselves behave as pressure-sensitive entities, exhibiting an increase in the number of intra-granule conduction pathways with increasing force. This chapter details the experimental work performed in order to isolate and investigate this effect.

To do this, a chromium/copper/gold capping electrode was deposited onto the PS layer to define a 'test area', as described in chapter 8. These 'capping electrodes', with diameters of 2, 1 and 0.5 mm, intimately coated each granule within the test area, creating electrical

connectivity within the plane of the PS layer. Then, spring-contact test probes (SCTP), with a diameter comparable to that of the test areas, were used to press down on the capping electrode with a known force. This methodology ensured that the number of granules contributing to electrical conduction was the same for each force applied, i.e. the effect of increasing the number of granules in electrical contact with the probe was negated. By decreasing the test area, the number of granules within that area decreased. This is the subject of section 12.2. Assuming that each granule protrudes the same height from the PS surface, the force exerted by the probe is distributed equally between these granules. Thus, for smaller test areas, each granule experiences a larger force. The force-resistance response of the granules within each test area is discussed in section 12.3. Then, by performing current-voltage sweeps on the test areas, the conduction mechanisms of the granules was probed. This is described in section 12.4. Finally, measurements of the electrical flicker noise within pre-prepared sensors (see section 9.2.5) are presented in section 12.5. Note that the sensors used for the noise measurements are those described in section 9.2.5, and the test procedure was different to that described above, and as explained in section 9.4.3.

12.2 Contact area vs number of granules

After depositing the capping electrodes onto the test areas, the exact number of granules within each test area was determined using optical microscopy. The number of granules within each test area, for samples $G3$ and $G4$ are shown in Fig. 12.1(a) and Fig. 12.1(b) respectively, where each data point represents an individual test area. Note that test areas of 0.2 and 0.1 mm diameter were also deposited for the purposes of this calculation. Samples $G3$ and $G4$ were as defined previously in Table 10.1. The granule concentration within these test areas was measured at 200 $\pm$ 100 per mm^2 for sample $G3$ and 400 $\pm$ 100 for sample $G4$. Within error, this matches the values found previously for samples $G3$ and $G4$ presented in Table 10.1. Here, the large error is a result of inhomogeneous granule distribution when sampling small areas. The number of granules within each test area is used later to determine the force imparted to each granule by the SCTP.

12.3 Force-resistance measurements of test areas

The testing procedure for investigating the force-sensitive resistance of small areas of the PS layer was described fully in chapter 9 and the apparatus used shown in Fig. 9.12. The key features of the experimental design were that a capping electrode was deposited onto discrete test areas of the PS layer, short-circuiting each of the granules within that layer in the x/y dimension. Force was imparted to these regions using spring-contact test probes

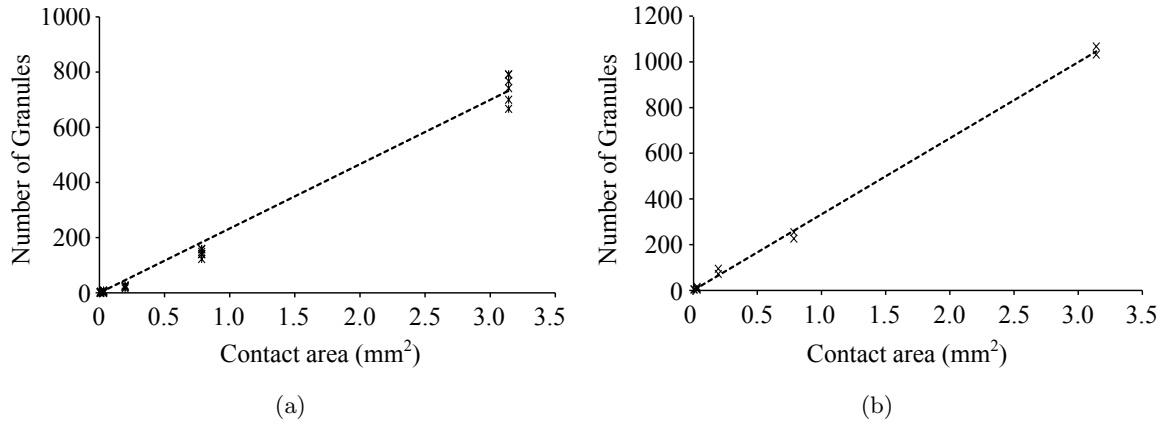

FIGURE 12.1: Graphs showing the number of granules found within each capping electrode as a function of electrode area, for samples (a) $G3$ and (b) $G4$. The granule number density per mm^2 matches that found measured previously in chapter 10.

(SCTPs). Through this, the effect of sampling a greater number of granules with increasing applied force was negated. Any measured resistance change could then be attributed to the intrinsic resistance of the PS layer. The size of the capping electrode (2 mm, 1 mm and 0.5 mm) changed the number of granules sampled during the measurement, and hence the force experienced by each granule. Tightening of a bolt threaded onto a screw caused compression of the spring within the SCTP. Due to its geometry, the rotation of the bolt could be set to an accuracy of 1/6 turns.

Initial contact between the probe and the capping electrode was made when the resistance through the probe/capping electrode/PS layer could be recorded using the digital multimeter. A small amount of force was necessary to create first contact, and all subsequent force increments were measured relative to this. Once first contact was made it required 11 1/2 rotations of the bolt to reach the full working travel of the SCTP, that is 5.3 mm. Therefore each 1/6 turn of the bolt corresponded to a vertical displacement of 0.077 mm and this was taken as the achievable resolution of the displacement. The spring constant of the test probe was 0.75 N mm^{-1} and therefore each half rotation of the bolt corresponded to a force increase of 0.17 $\pm$ 0.06 N.

Fig. 12.2 shows a schematic of the (idealised) test procedure, highlighting the resistances involved in the measurement. Initially, it is assumed that the probe is perfectly flat and that each granule protrudes the same height above the PS surface. Thus, the SCTP contacts each granule simultaneously. Additionally, it is assumed that the capping electrode creates a uniform, unbroken film across the granule surface with negligible resistance. The resistance through the SCTP (R_{SCTP}), was measured from the uppermost electrical connection to the base of the spring-loaded plunger, and was just 0.5 Ω and therefore considered negligible.

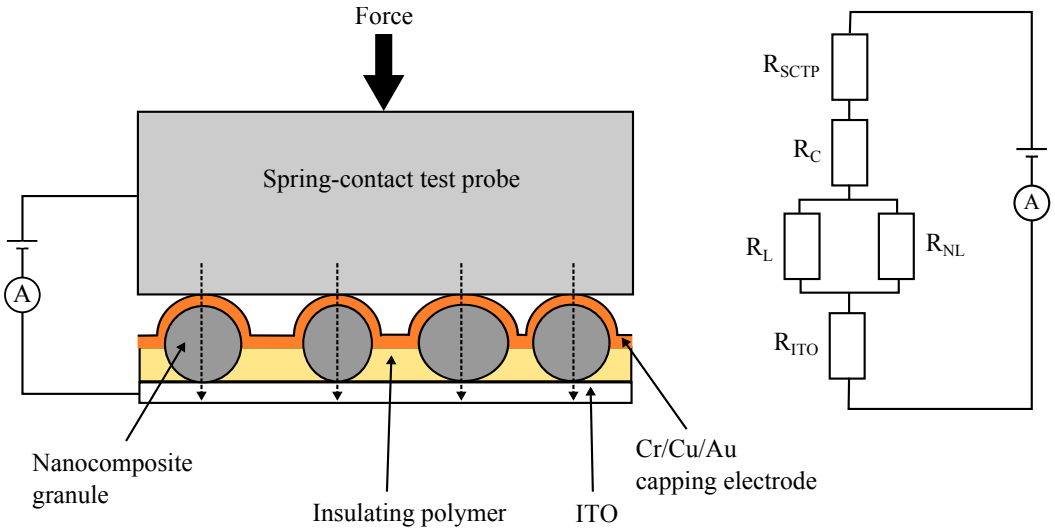

FIGURE 12.2: Schematic showing the ideal electrical contact created between SCTP and the capping electrode, which intimately coats the nanocomposite granules (not to scale) within the PS layer. The probe creates a two-point resistance measurement. An equivalent circuit is also shown, based on that suggested by He and Tjong [223]. In the ideal scenario, resistance contributions from the SCTP (R_{SCTP}), the contact between SCTP and capping electrode (R_C) and the ITO electrode (R_{ITO}) are assumed to be negligible when compared to the linear and non-linear resistance contributions of the granules (R_L and R_{NL}).

Due to the geometry of the sample and the test equipment, a two-point probe sensing mechanism was used to measure resistance, where voltage and current were measured simultaneously by the terminals (in this case the SCTP and the ITO). Using this method, the contact resistance R_C between SCTP and capping electrode cannot be disregarded. In reality, the measured resistance comprises the contact resistance, R_C as well as the intrinsic resistance of the granular array. In the models which are applied later in this chapter, it is assumed that the resistance of the granule consists of a linear and a non-linear contribution, R_L and R_{NL}, the magnitude of which may or may not depend on the force applied via the SCTP. Initially, it is assumed that the capping electrode makes Ohmic contact with both the SCTP and the PS layer, such that R_C is small compared to the resistance through the PS layer, and independent of the force applied. This assumption is examined in detail later in section 12.3.2.

12.3.1 F-R response of PS layer

The resistance through the granules was measured by applying a constant current through the SCTP and measuring the change in voltage over a period of 60 seconds. It was assumed the I-V response was approximately linear and resistance was calculated using Ohm's law. The I-V properties of the PS layer are discussed in more detail in section 12.4. It quickly became apparent that the resistance was not constant and instead tended to drift throughout

the measurement time. To account for this variation, the average resistance was quoted with an error calculated from the range of resistance values. The force was sequentially increased and the average resistance was recorded at each force. Once maximum force was reached the force was then sequentially reduced back to the starting value (i.e. initial contact).

The F-R response of all test areas (2, 1 and 0.5 mm diameter) are compared in Fig. 12.3. Here, the solid black lines indicate increasing force and the dashed black lines represent decreasing force. Error bars are shown, representing the range of resistance values measured. In the following discussion, the change in resistance when increasing the force is discussed. Later, in section 12.3.2, the resistance when removing the force is analysed, along with the repeatability of the resistance response between each test area, and for subsequent force sweeps on a single test area.

The F-R response of the 2 mm diameter test areas are shown in Fig. 12.3(a), Fig. 12.3(b), Fig. 12.3(c) and Fig. 12.3(d). At initial contact, a resistance in the range 1–6 kΩ was recorded. In 3 of the 4 test areas the resistance decreased when increasing the force. Here, the total change in resistance at the maximum force of 1.38 N was 65, 90 and 650 Ω for test areas 1, 2 and 3 respectively. However, in Fig. 12.3(d), the 4th test area showed no overall decrease in resistance. Instead, the final resistance was approximately 250 Ω larger than resistance at initial contact. With knowledge of the number of granules within the test area it was possible to obtain a crude estimate of the force that each individual granule may experience over the course of the experiment. On average there were 1050 $\pm$ 25 granules within each 2 mm test area. Assuming that the SCTP contacts each granule simultaneously such that load is distributed equally, each granule within the test area will then experience 1.31 $\pm$ 0.04 mN force when the SCTP is applying a force of 1.38 N.

By decreasing the test area diameter the force experienced by each granule was increased. For the 1 mm diameter contacts, the average number of granules within each contact was 240 $\pm$ 20. Hence, when the SCTP applied a force of 1.38 N to the test area, each granule within experienced 5.8 $\pm$ 0.5 mN force. The F-R behaviours of four different test areas are shown in Fig. 12.3(e), Fig. 12.3(f), Fig. 12.3(g) and Fig. 12.3(h). At initial contact, the resistance through the test area was in the range of 5–12 kΩ. Note that this was larger than for the 2 mm test area – because the granule array in the test area can be seen as a collection of parallel resistors, by decreasing the number of granules the overall resistance will increase. Here, as force was increased there was an observable decrease in resistance. The change in resistance at the maximum force was 5500, 330, 1200 and 1400 Ω for test areas 1, 2, 3 and 4 respectively. This resistance decrease was larger than that of the 2 mm test areas. This fact can be attributed to the greater force each individual granule experienced, which may be sufficient to cause an increase in the number of pressure-activated conduction pathways through the granules.

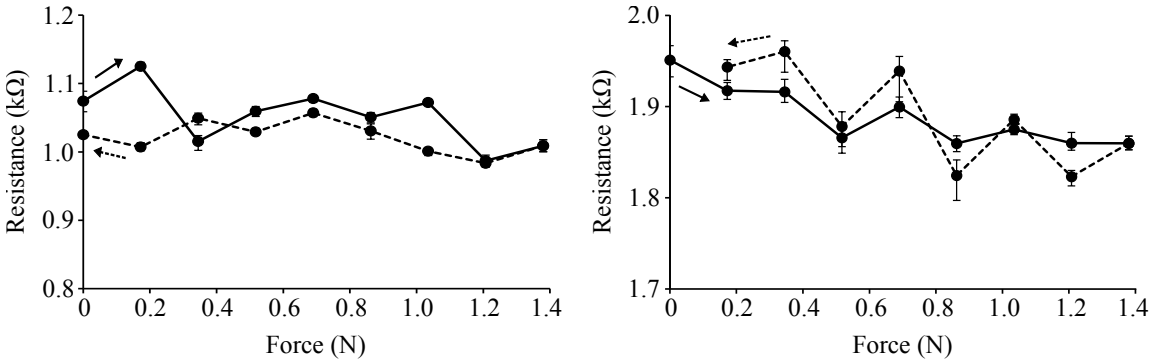

(a) 2 mm (1)

(b) 2 mm (2)

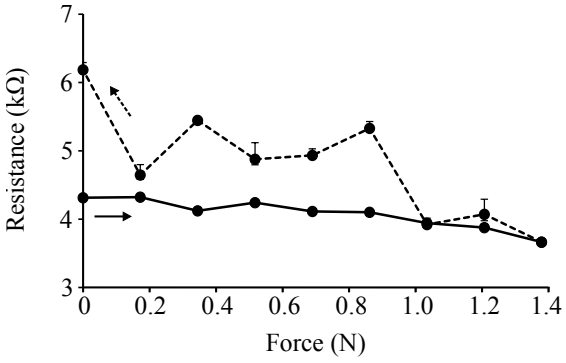

(c) 2 mm (3)

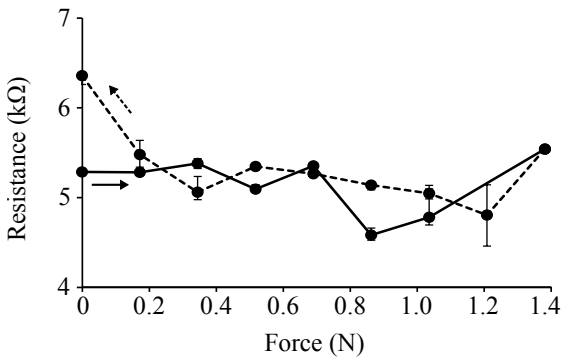

(d) 2 mm (4)

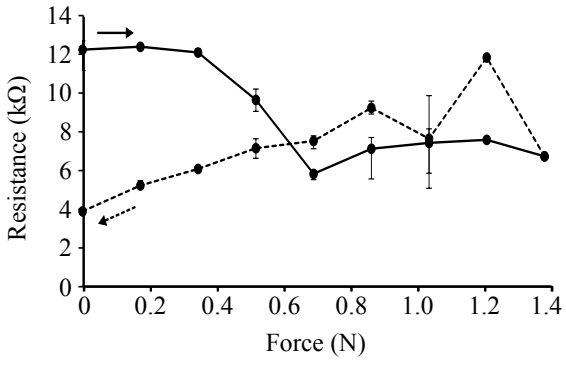

(e) 1 mm (1)

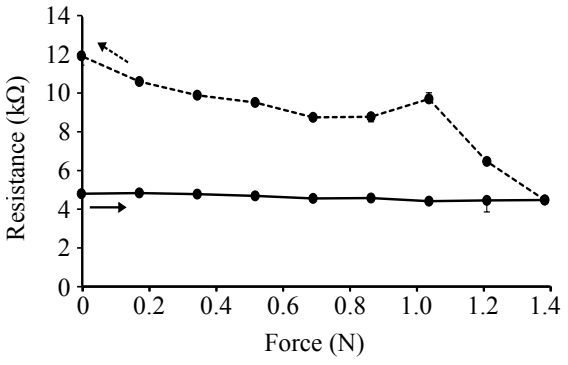

(f) 1 mm (2)

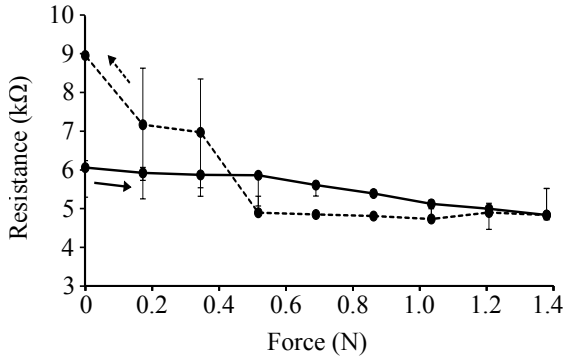

(g) 1 mm (3)

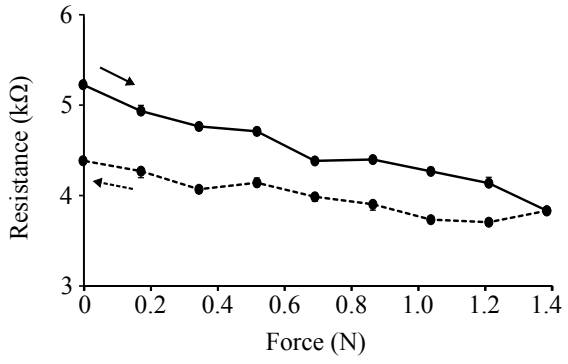

(h) 1 mm (4)

FIGURE 12.3: Graphs showing the F-R response of PS layer test areas of various diameter, where the solid lines represent increasing force and the dashed lines represent decreasing the force. Error bars represent the range of resistance values measured and are often smaller than the data points.

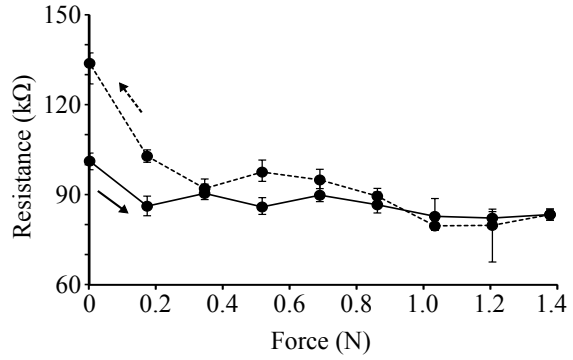

(i) 0.5 mm (1)

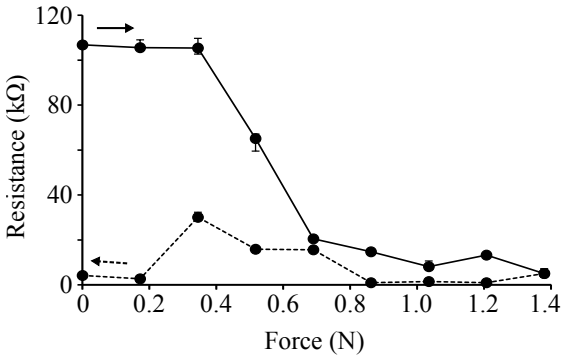

(j) 0.5 mm (2)

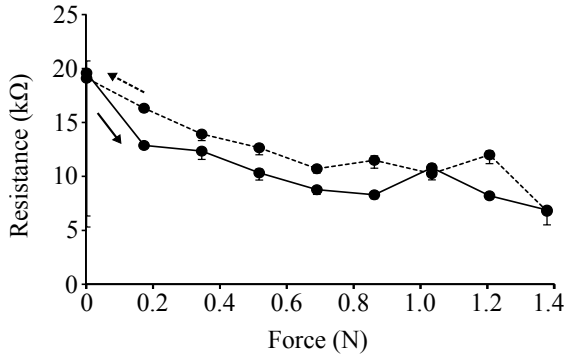

(k) 0.5 mm (3)

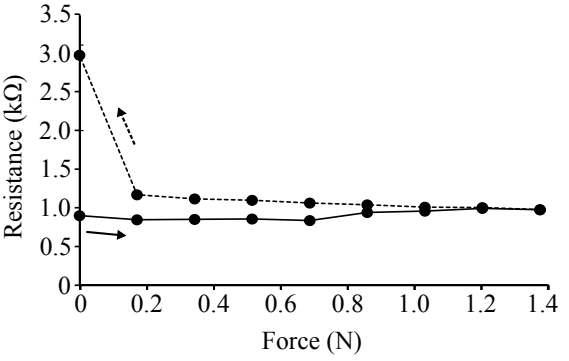

(l) 0.5 mm (4)

FIGURE 12.3: Continued from previous page

For the 0.5 mm diameter test areas, each area contained an average of 84 ± 16 granules. At a maximum SCTP force, each individual granule experienced 16 ± 4 mN force. The F-R response of four individual test areas are shown in Fig. 12.3(i), Fig. 12.3(j), Fig. 12.3(k) and Fig. 12.3(l). The resistance at initial contact was highly variable, ranging from approximately 100 kΩ for Fig. 12.3(i) and 12.3(j), to 20 kΩ for Fig. 12.3(k) and just 1 kΩ for Fig. 12.3(l). However, again a decrease in resistance was observed with increasing force. The change in resistance was 18, 102 and 13 kΩ for contacts 1, 2 and 3 respectively. This is by far in excess of the resistance decrease observed in the larger test areas and again can be linked to the increased force acting on the individual granules.

In order to compare the F-R response for each test area, the above results are replotted in Fig. 12.4. This shows the force experienced by each granule - i.e. the SCTP force is normalised according to the number of granules within the test area. The resistance change from initial contact to maximum force is expressed as a percentage of the initial resistance, along with the associated error. This resistance change was almost always positive (i.e. the resistance decreases with increasing force) however negative values arose in the case where the test area showed an increase in resistance with force (i.e. see Fig. 12.3(d) and Fig. 12.3(l)).

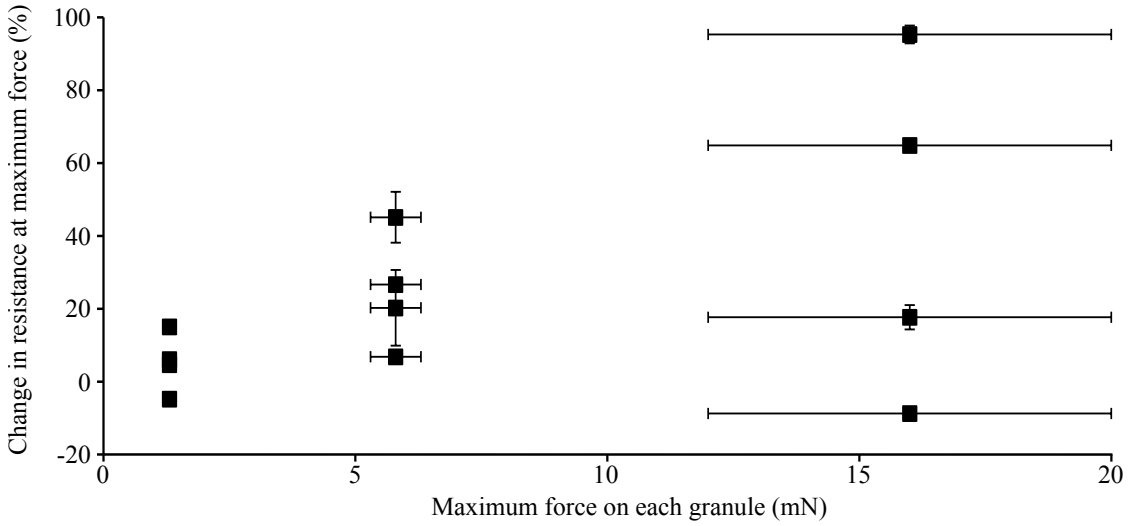

FIGURE 12.4: Graph showing the change in resistance from initial contact of the SCTP to the resistance at maximum force, as a function of the maximum force experienced by each individual granule within the test areas. As a greater force is applied to the individual granules, the % change in resistance also increases. Error bars, calculated by propagating the errors on the individual resistance measurements, are also shown.

On average, it can be seen that as the maximum force acting on each individual granule increases, the overall change in resistance also increases. This is supportive of the theory that increased force on the granule enhances or opens up force/pressure-sensitive conduction pathways within the granule. Earlier in chapter 7 it was seen that these granules possessed a porous internal structure, where 17 % of the cross-sectional area comprised empty space. The high porosity lends itself to the idea of granule compressibility. It is envisaged that compression of the granule reduces the overall void space and increases the number of interparticle contacts. Increased electrical conduction may occur through direct percolative transport between adjacent particles within the granule, or by a quantum tunnelling mechanism (field-assisted or otherwise) for finite interparticle distances. The exact nature of the conduction is explored further through the current-voltage behaviour of the granules in section 12.4.

12.3.2 Repeatability of F-R response

In the previous section, the response of the test areas to increasing applied force was discussed. However, from the graphs presented in Fig. 12.3 it is clear that in most cases, when the force is removed from the test area the resistance seldom returns to its original value. As an example consider Fig. 12.3(c), which shows a 2 mm test area. When the force on the test area is increased, overall the resistance through the test area decreased, with a 15 % change in resistance at the maximum force. However, when the force was then subsequently removed, the resistance remained consistently higher. The final resistance was 6.2 kΩ, significantly

larger than the original resistance at initial contact of 4.3 kΩ. A similar phenomenon was also found for the test areas shown in Fig. 12.3(f), Fig. 12.3(i) and Fig. 12.3(l).

However, in other test areas the opposite situation was observed. When removing the force the resistance was consistently lower then when force was applied. As examples, see Fig. 12.3(h) and Fig. 12.3(j). Here, the final resistance was significantly lower than the resistance at initial contact. Other test areas showed a fluctuating resistance as force was removed. In Fig. 12.3(e), at high forces the resistance when removing the force was larger than when increasing the force. At approximately 0.6 N, the resistance steadily declined upon further removal of the force, and the final resistance value was three times smaller than the resistance at initial contact. Conversely, in Fig. 12.3(i) at high forces the resistance upon removal of force was lower than for when increasing the force. At approximately 0.3 N the resistance rapidly increased upon further reduction of force, and the final resistance was in excess of the initial resistance.

The above observations highlight both the variation in the resistance measurements for increasing and decreasing load, and also the variation in response between different test areas of the same size. To further investigate the repeatability of the resistance measurements, repeated force cycles were tested sequentially on the same test areas. Fig. 12.5 shows repeated force sweeps performed on test areas of 2, 1 and 0.5 mm diameters. The graphs show that poor repeatability is also a feature of repeated force sweeps on the same test area.

Repeated cycles on the 2 mm test area is shown in Fig. 12.5(a). On the first sweep the resistance fluctuates around 5 kΩ when both increasing and decreasing the force, although the final resistance at initial contact is greater than the initial value. No obvious force sensitivity is observed. On the second force sweep, the resistance is consistently higher for the increasing force cycle, and again higher when decreasing the load. A similar trend is observed for the 1 mm test area shown in Fig. 12.5(b). Whilst the resistance for the second increasing force cycle closely matches that of the decreasing force cycle of the first sweep, subsequent removal of force resulted in a larger measured resistance. Fig. 12.5(c) shows three force sweeps on a 0.5 mm diameter test area. Here, the resistance values for both the increasing and decreasing force during the second sweep closely match that of the decreasing force regime of the first sweep. However, during the third force sweep the resistance was once again observed to increase. The greatest variation in the resistance values was seen at low forces, typically less than 0.7 N.

The common feature to all of the results described above is that with repeated testing on the same test area, overall the resistance is larger with each successive sweep. An overall increase in resistance during testing may indicate a degree of physical change or degradation of the granules or the capping electrode. Granule degradation may also explain the variability in resistance between increasing and decreasing force regimes.

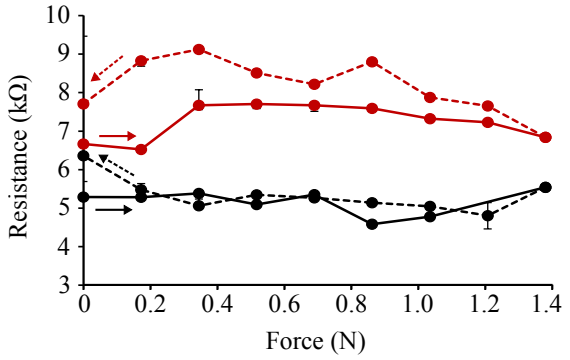

(a) 2 mm test area

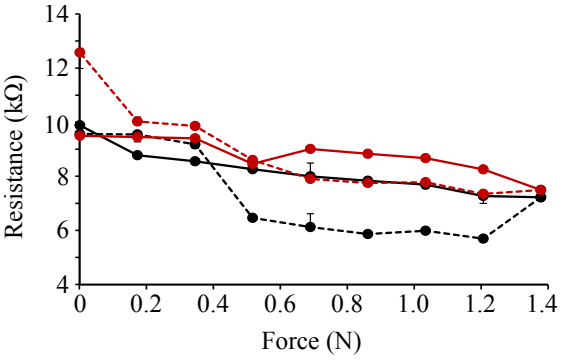

(b) 1 mm test area

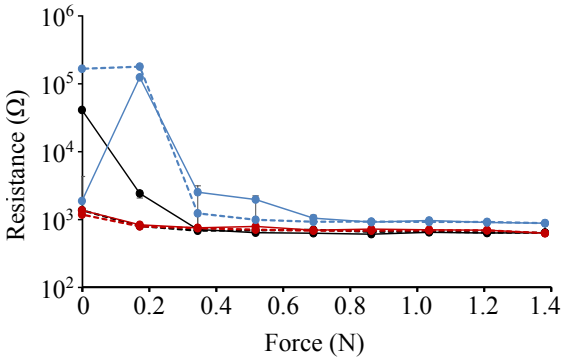

(c) 0.5 mm test area

FIGURE 12.5: Graphs showing multiple force sweeps conducted on the same test area, for test areas of (a) 2 mm (b) 1 mm and (c) 0.5 mm diameter. The first force sweep is indicated by the solid black line (increasing force) and dashed black line (decreasing force). The second sweep is shown by the red solid and dashed lines, and in the case of (c) a third sweep is shown by the blue solid and dashed lines. Error bars relating to the minimum and maximum resistances recorded during the measurement are also shown.

The fracture strength of granules was assessed in chapter 7. For the granules present in the sample tested here ($G3$), the average fracture strength of granules of size 75–100 µm was 10.6 ± 0.3 mN. From this, it follows that the maximum force imparted to the granules in the 2 and 1 mm contacts (1.31 ± 0.04 and 5.8 ± 0.5 mN respectively) may not be sufficient to cause granule fracture. However, the force imparted to granules in the 0.5 mm contact was estimated at 14–20 mN, much greater than the average fracture strength of the granules. Unfortunately, this does not account for the observations made here, where poor repeatability of the F-R response is inherent for all sizes of test area. One possibility is that the fracture strength of 5–15 µm granules is less than what was measured for the 75–100 µm granules, and that the granules break or plastically deform at forces much less than 10.6 mN. As discussed in chapter 7, an assumption is made that the granules within the PS layer (5–15 µm) show similar breakage characteristics to the 75–100 µm size fraction.

To complicate matters further, the granules are constrained within the PS layer, so whilst the

granules may fragment it is expected that these fragments may remain *in situ* such that some conduction can still occur. As force is applied, the granule may fracture but the compression means that each fragment remains in contact. As force is removed, the fragments may relax and separate. This would result in an overall higher resistance when decreasing the force, as is seen in Fig. 12.3(c), Fig. 12.3(f) and Fig. 12.3(k). Alternatively, the granules may plastically deform upon compression. Then, when force is removed the granules do not attain their original form and pressure-sensitive conduction pathways remain open. The resistance would thus remain at a low value when force is removed, as was seen in Fig. 12.3(a), Fig. 12.3(h) and Fig. 12.3(j). Of course, this hypothesis cannot be fully tested until a method of measuring the fracture strength of small granules less than 20 µm in size is devised.

An additional point is that, whilst pressure sensitive behaviour of the granules is suggested, the force that the granules in the 0.5 mm contacts were subjected to is much larger than what may be expected during standard operation of a PSRT device. In chapter 11, a model describing the force-dependent area of contact between electrode and PS layer was developed. Using this model, the highest force exerted on a granule may occur at the instance of first contact between the electrode and the PS layer, where contact area is smallest. As a rough calculation, assume that this occurs upon application of 0.7 N force. This is similar to the activation force predicted for model PSRTs geometrically and mechanically similar to those developed experimentally. At this force, a contact area of approximately 75 mm^2 is predicted. For 190 granules per square mm (as for sample $G3$) each granule experiences just 0.05 mN. Compare this to the force per granule for the 0.5 mm contact, which was 16 mN. Hence, in the experimental design, the granules in the 0.5 mm contact experience a force which is approximately 300 times larger than they may experience during normal operation of the PSRT. In conclusion, although evidence suggests that the granules may be intrinsically pressure sensitive, this may only be activated at high forces beyond those imparted during use of the touchscreen.

To fully understand the processes occurring here, it is important to note that in reality the PS layer contains an array of granules each of a different size (i.e. protrusion height above the PS surface) and a range of fracture strengths, and as such is a highly complex system. The idealised system was shown in Fig. 12.2. In comparison, Fig. 12.6 shows a more realistic scenario where the granules protrude above the ink surface at a range of heights. Thus, when the test area is contacted by the SCTP, initial contact is first created between the SCTP and the largest granules, and it is these granules which are initially compressed. Application of further force may create contact with progressively smaller granules, and these granules are then compressed. This means that each granule within the test area may not experience the same force profile as its neighbours. Additionally, realistically the granules have a range of fracture strengths and granule breakage is not universal at a particular applied force. Of course, for reasons described above, even if granule breakage does occur it is likely that

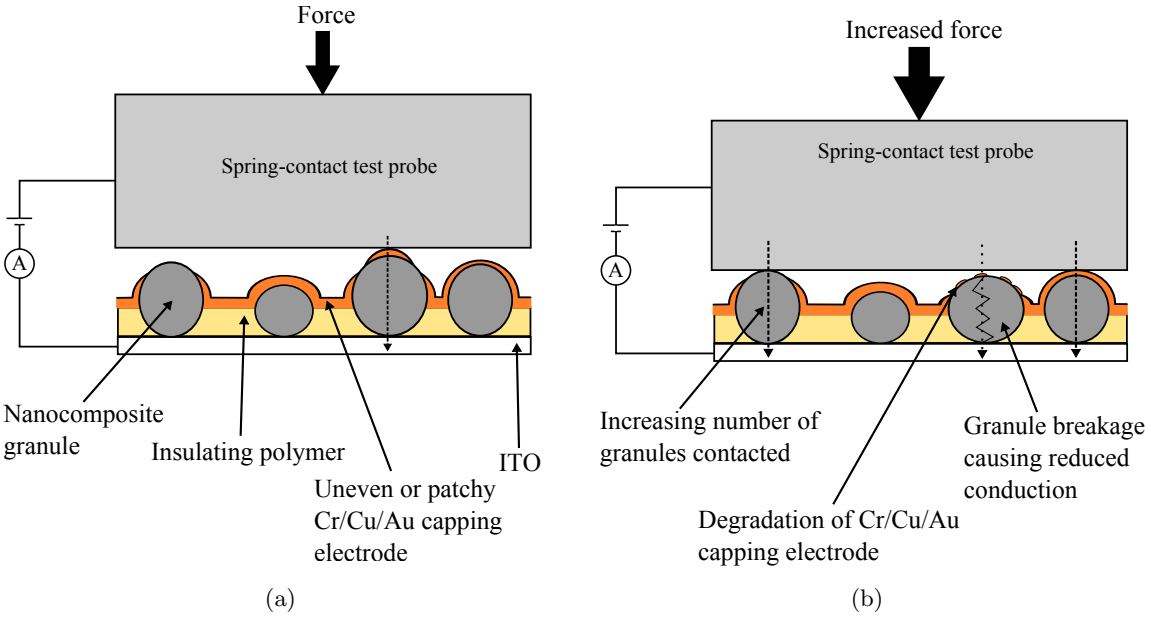

FIGURE 12.6: Schematics showing the complex interaction between the granules within the PS layer and the SCTP. In (a) initial contact is first created between the largest granule and the SCTP, and this granule is compressed first. The capping electrode may be uneven across the curved granule topography. In (b) increasing force increases the number of granules contacted and subsequently compressed by the SCTP, and may also cause degradation of the capping electrode.

the fragments still allow some electrical conduction between the electrodes. Finally, it was assumed that the capping electrode created Ohmic contact to both the SCTP and the PS layer, and had a small, constant contact resistance. In reality, the capping electrode may not be uniform across the complex granule topography and may degrade with repeated or prolonged contact with the SCTP. Furthermore, for two rough surfaces pressed into contact, the contact resistance is often found to be dependent on the contact force, as this determines the size-dependent constriction resistance which is created by the micro-contacts formed between the two opposing surfaces [285–287].

In summary, all of these considerations mean that it becomes very difficult to reliably link the F-R profile of the collective system with the F-R profile of the individual granules. Nevertheless, the F-R profiles obtained for the 0.5 mm test area showed a large percentage decrease in resistance with increasing force, and this is suggestive of some form of pressure or force-sensitive conduction within the granules. In order to investigate the nature of any pressure sensitive conduction channels, I-V sweeps were performed on the test areas. This is the focus of section 12.4.

12.3.3 Predicting the resistance of a single granule

From the F-R response of each test area, and by knowing the number of granules within each test area, it is possible to estimate the resistance of a single granule. When initial contact is made between the SCTP and the test area, each granule within that area can act as a conduction pathway to the lower ITO electrode. This is possible because the capping electrode coats the PS surface and therefore electrically links each granule within the test area. The number of granules contributing to the measured resistance depends upon the size of the contact area, as discussed in section 12.2. Fig. 12.7 plots the number of granules within each test area against the average value of the resistance recorded at initial contact with the SCTP. The error bars represent standard deviations on the average values on both axes. The dashed line represents a power law relationship. Extrapolating the power law relationship allows the resistance of a single granule to be estimated in the range 0.5–30 MΩ. The large variation on this result is caused by the large spread in the resistance values measured at first contact. In chapter 11, Fig. 11.2(a) plotted the simulated F-R curves for a variety of granule resistances. An estimation of the granule resistance, determined experimentally, may be useful in any future work where this simulation is developed further.

12.4 I-V behaviour of the test areas

Previously, it was shown that the 0.5 mm test areas showed a large fractional decrease in resistance at maximum applied force. Due to the design of the experiment, this effect was separated from the F-R mechanism associated with increasing the number of granules contacted with applied force. The force exerted on each individual granule was predicted

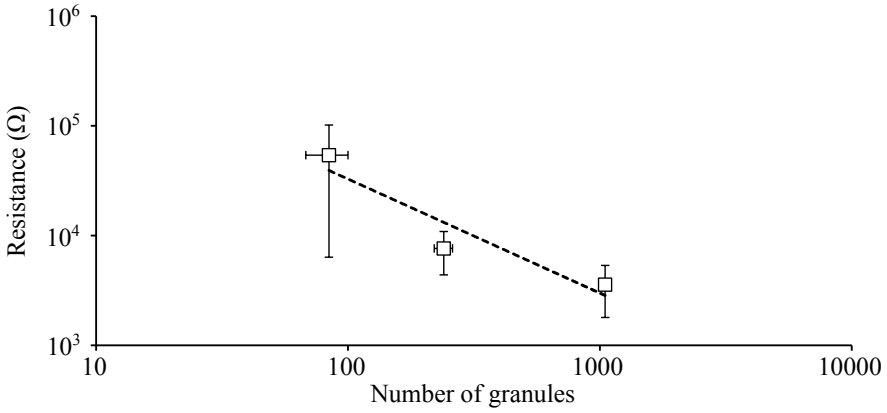

FIGURE 12.7: Graph showing the average initial resistance measured as a function of the average number of granules within the test area. Error bars represent the standard deviations on both axes and the dashed line represents a power law relationship. Using this relationship the resistance of a single granule may be estimated in the range 0.5–30 MΩ.

to trigger force-sensitive conduction pathways within the granules. To investigate the origin of the force-sensitive conduction, the current-voltage (I-V) behaviour of the test areas was measured using the experimental procedure outlined in chapter 9.

First, the I-V behaviour of the ITO electrode was tested by increasing the voltage between the two conductive bars on the ITO electrode (see Fig 9.3) and measuring the current. The I-V responses at forces of 0, 1.7 and 3.5 N are shown in Fig. 12.8. The behaviour indicates that there is no increase in current with increasing force. The linear I-V response indicates Ohmic behaviour. The inverse of the gradient yields the resistance of the ITO between the conductive bars, which was 409.0 Ω. Hence it was confirmed that the ITO electrode does not contribute any non-linear I-V effects, and exhibits no pressure-sensitive resistance response for up to 3.5 N force.

In the next section, the electrical hysteresis present in the I-V behaviour is discussed for all test areas. Later in section 12.4.2, the force-dependent I-V response observed for the 0.5 mm test area is examined in detail.

12.4.1 Hysteresis in I-V sweeps

In most I-V sweeps measured for the PS layer, some degree of electrical hysteresis was present. This takes the form of a difference in current measured when ramping-up and ramping-down the voltage. Examples of I-V hysteresis in 2 mm test areas are shown in Fig. 12.9, which shows the first and last I-V sweeps (out of a total of ten) obtained at both initial contact with the SCTP and at the maximum force of 1.38 N. Note that the I-V curves shown here represent the general trend of all I-V curves generated, that is a non-linear I-V relationship with some degree of electrical hysteresis. The errors on the individual data points are smaller than the symbols.

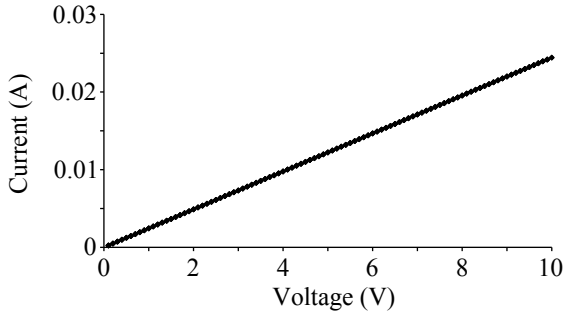

FIGURE 12.8: Graph showing the linear I-V characteristics of the ITO electrode under applied forces of 0, 1.7 and 3.5 N. For each force the I-V sweeps overlap and the error bars are smaller than the data points.

For the first I-V sweep obtained at initial contact (shown in Fig. 12.9(a)), the hysteresis is prominent. For example, at 4 V there is difference in current of 1.1 mA between increasing and decreasing voltage ramps. For less than 5 V, the current for the up ramp is less than for the down ramp. This is typical of charge trapping mechanisms, which have been observed in other conducting polymer composites [238, 245]. Here, the current flow as voltage is increased is limited by the presence of trapping sites within the composite. Trapping sites, as described in chapter 8, create a potential well where the trapped electron must have sufficient energy in order to escape the trap. As the voltage is increased these trapping sites are filled by electrons. Here, the hysteresis diminishes after 5 V, suggesting that trap sites are filled. Once filled, subsequent electrons can contribute to the transport of charge. When ramping down the voltage, the filled traps no longer act as a sink for electrons, resulting in a larger current flow and a smoother I-V curve. If no charge leakage occurs (or occurs over sufficiently long time-scales) then all subsequent I-V sweeps would be expected to show minimal hysteresis.

Fig. 12.9(b) shows the tenth I-V sweep obtained at initial contact with the 2 mm test area. The degree of hysteresis is much smaller than for the first sweep, for example at 7 V the difference in current between up and down ramp is just 0.52 mA. In fact, in all subsequent I-V sweeps at each level of force, the degree of hysteresis is less than for the first sweep at initial contact. This is consistent with the charge trapping hypothesis. This is exemplified by Fig. 12.9(c) and Fig. 12.9(d) which show the 1st and 10th I-V sweeps obtained at the maximum applied force of 1.38 N, where again there is minimal hysteresis. Interestingly, in these subsequent sweeps it is common for the current in the up ramp to exceed the current in the down ramp. This does not fit with the charge trapping hypothesis, which predicts the opposite trend. Instead, this phenomena is suggestive of a non-steady current flow, where the current decreases over the measurement period.

Similar observations can be made for the I-V sweeps performed on the 1 mm test areas, which are also shown in Fig. 12.9. Maximum hysteresis is observed for the first I-V sweep performed at initial contact with the SCTP, as can be seen in Fig. 12.9(e). Here, the I-V response is very noisy but settles down in repeated measurements. Again, the hysteresis has diminished at the 10th sweep at initial contact, shown in Fig. 12.9(f), and for all subsequent sweeps at increased force, such as those shown in Fig. 12.9(g) and Fig. 12.9(h).

For both 2 mm and 1 mm test areas, analysis of the I-V response at each force shows that the current passing through the test area is dependent on voltage only and shows little change with increasing force. For example, consider the 2 mm test area: At initial contact the current at 8 V is around 11 mA. Similarly, at the maximum force of 1.38 N the current at 8 V is again close to 11 mA. For the 1 mm test area, after the initial noisy I-V sweep measured at initial contact, each subsequent sweep shows a current of around 2 mA at 8 V irrespective of

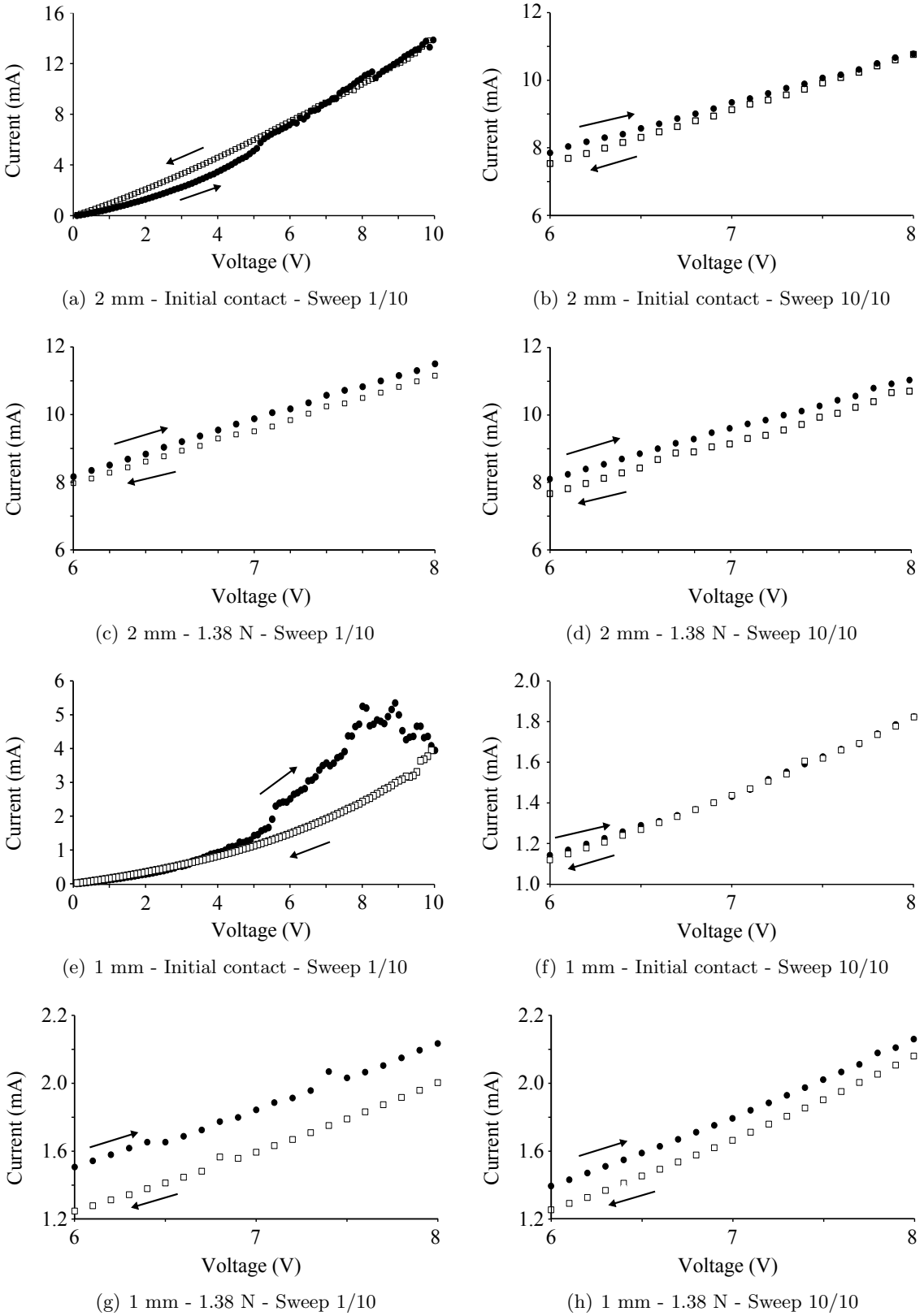

(a) 2 mm - Initial contact - Sweep 1/10

(b) 2 mm - Initial contact - Sweep 10/10

(c) 2 mm - 1.38 N - Sweep 1/10

(d) 2 mm - 1.38 N - Sweep 10/10

(e) 1 mm - Initial contact - Sweep 1/10

(f) 1 mm - Initial contact - Sweep 10/10

(g) 1 mm - 1.38 N - Sweep 1/10

(h) 1 mm - 1.38 N - Sweep 10/10

FIGURE 12.9: Graphs showing the electrical hysteresis in the first and last I-V sweeps performed for 2 mm and 1 mm test areas, at both initial contact between test area and SCTP, and the maximum applied force of 1.38 N. Black circles and open squares represent ramping up and ramping down the voltage respectively, and arrows also show the direction of the sweep. Errors on the measured current are smaller than the symbols.

force. These observations link to the observed F-R behaviour of the test areas. As described in section 12.3, the 2 and 1 mm test areas displayed a limited force-sensitive resistance.

Selected I-V sweeps for the 0.5 mm test area are shown in Fig. 12.10, for forces up to 3.45 N. The first, fifth and tenth I-V sweeps are shown by the red, blue and black lines respectively. The data is represented as solid lines for ease of comparison, and where hysteresis is evident the direction of the sweep is indicated by arrows. For these test areas a force-sensitive resistance response was observed and this is reflected by the increase in current flow with

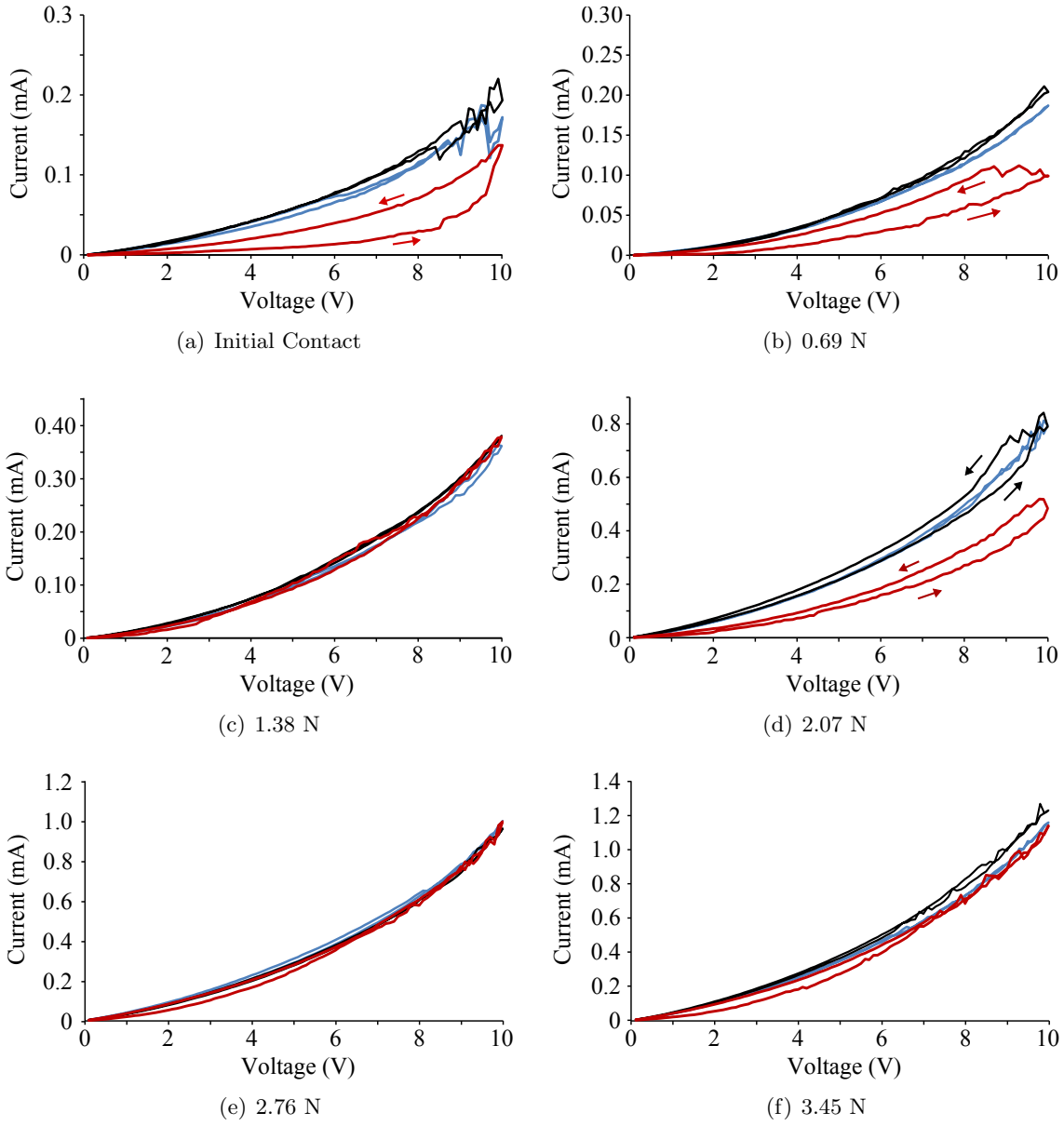

FIGURE 12.10: Graphs showing I-V response of 0.5 mm test area under a range of applied forces. For each force, the first (red), fifth (blue) and last (black) I-V sweep performed on the area is shown. Where hysteresis is evident, arrows show the direction of increasing and decreasing voltage.

applied force. For example, at initial contact (Fig. 12.10(a)) the maximum current at 10 V was approximately 0.2 mA. At 3.45 N (Fig. 12.10(f)) the maximum current had increased to 1.2 mA.

Compared to the 2 and 1 mm test areas, the 0.5 mm test areas show a larger degree of hysteresis, which persists beyond the first sweep at initial contact. Specifically, large hysteresis is also observed in the first sweep at further force increments, for example at 0.69 N (Fig. 12.10(b)) and 2.07 N (Fig. 12.10(d)). Where hysteresis is evident, the current when increasing the voltage is less than when decreasing the voltage, which is consistent with the charge trapping mechanism described previously. The persistence of hysteresis at later sweeps suggests leakage of trapped charge over short time scales, although this effect is not explored further in this thesis. Additionally, the current is seen to increase with progressive sweeps at the same force. This in turn implies that the resistance through the test area has not reached a stable value and continuously increases during the measurement. Fluctuations in the current value can be observed in several of the I-V sweeps and tend to happen at higher voltages, for example see sweeps 5 and 10 in Fig. 12.10(a) and sweeps 1 and 10 in Fig. 12.10(f).

In summary, electrical hysteresis is present in most I-V sweeps performed on the 2, 1 and 0.5 mm test areas. In the larger test areas (2 and 1 mm) hysteresis is largest in the first sweep at initial contact between test area and SCTP, and diminished in all subsequent sweeps. This is consistent with a charge trapping mechanism where trap sites are filled during the first I-V sweep and remain so for all subsequent sweeps. For the 0.5 mm test area hysteresis is also common in the repeated sweeps at each force applied. This suggests charge leakage from trap sites. Here, the maximum current is dependent on the force applied which is consistent with the F-R behaviour observed for test areas of this size. The force-dependence of the I-V behaviour in this case is explored in the following section.

12.4.2 Force-dependent I-V behaviour

As mentioned previously, only the 0.5 mm test areas showed clear evidence of a force-sensitive resistive behaviour. For this reason, I-V sweeps were performed up to a maximum of 3.45 N - the maximum force that could be applied using the SCTP. In this section, the force-dependence of the I-V response is analysed for the 0.5 mm test area, yielding physical insight into the nature of the force-sensitive conduction.

In the following analysis the 10th sweep measured at each force is analysed, considering the decreasing voltage ramp only. This is due to charge trapping effects sometimes observed when increasing the voltage. Because the current was observed to drift to larger values with each subsequent sweep, it was felt that averaging all ten I-V sweeps would not give a precise representation of the current behaviour. Instead, the tenth sweep was chosen as

representative, as after ten sweeps the I-V behaviour had often stabilised, as evidenced by the frequent similarity in the magnitude of the current at the 5th and 10th sweeps, shown in Fig. 12.10. Above 8 V, fluctuations in the current were commonly observed. Therefore, when fitting physical models to the data, only voltages up to 8 V were considered.

Fig. 12.11 compares the tenth I-V sweep obtained at initial contact (IC) and selected forces of 0.345, 0.69, 1.38, 2.07, 2.76 and 3.45 N. The inset shows the current at 10 V as a function of force applied. Generally, the I-V curves show a progression towards higher current values (and therefore lower resistance) with increasing force. The exception to this is the I-V sweep at 0.345 N, which lies between those at 1.38 and 2.07 N. This results in a local maximum in the current at 10 V at 0.345 N, as shown in the inset.

12.4.2.1 Application of random resistor network model

An important feature of the I-V response is its intrinsic non-linearity. The response is not simply ohmic in nature, and instead the rate of current flow increases with voltage. In this section, the origin of the non-linearity is explored through application of a random resistor network (RRN) model. Before this model is applied, it is necessary to understand the possible sources of non-linearity within the nanocomposite granules present in the PS layer.

Early work presented in the first half of this thesis investigated the internal structure of the fabricated nanocomposite granules. It was found that the granules comprised three phases: conductive particles or particle clusters, air voids and insulating silicone binder. Conduction

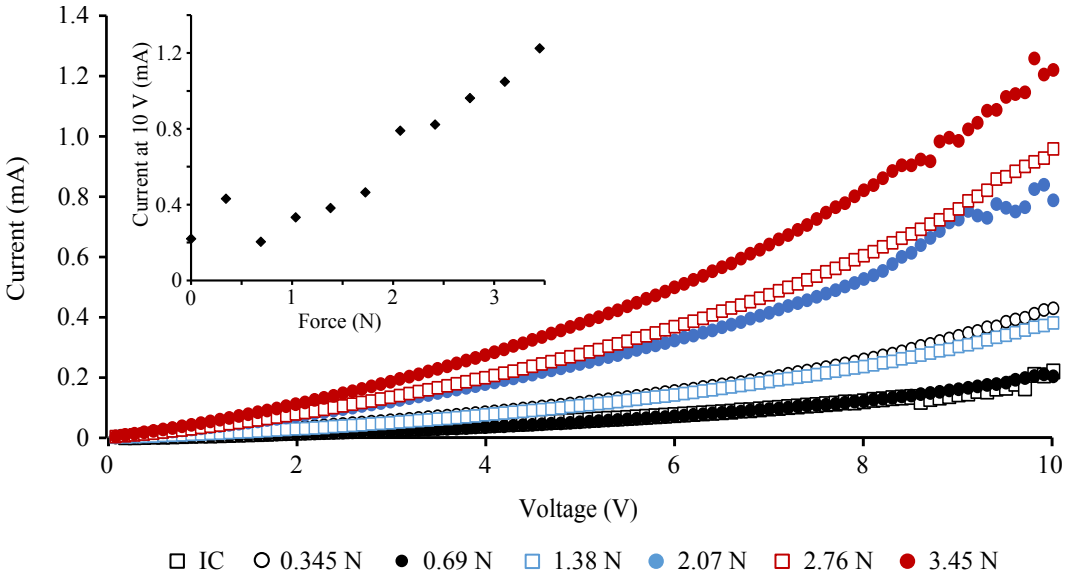

FIGURE 12.11: Graph showing the average I-V response as a function of force applied to the 0.5 mm contact.

within the granule may be split into linear and non-linear contributions. In the first instance, linear conductive pathways may form as a result of ohmic contact between adjacent particles. Non-linear conduction pathways may form between nearby particles separated by an insulating medium, which be air voids or polymer binder. Electrons may tunnel from one particle to the next providing the potential barrier created by the insulating medium is sufficiently narrow. Additionally, the number of non-linear conduction pathways may increase with voltage, due to field-assisted tunnelling mechanisms. Alternatively, instead of the formation of new, intrinsically non-linear pathways, initially linear pathways may themselves become non-linear. For instance, Joule heating at high current flow may lead to a reduced conduction. The aim of this section is to understand how the contribution of both linear and non-linear conduction channels depends upon the force applied to the nanocomposite granules.

To apply the RRN model, the I-V response was decomposed into a linear and a higher order polynomial contribution of the form $I = \Sigma_1 V + \Sigma_2 V^2$, where Σ_1 and Σ_2 are the linear and higher order conductances respectively. The model was fitted to the I-V sweeps using a least squares damped approach, using Origin® graph plotting software. As mentioned earlier, because of the current fluctuations frequently seen at higher voltages, only I-V data up to 8 V was considered when fitting the models.

An example fit using the linear/quadratic form of the RRN model is shown for the maximum force of 3.45 N in Fig. 12.12. Visual inspection shows good agreement between model and data, however the inset highlights deviations occuring at high voltages. In this example, Σ_1 and Σ_2 were $(3.67 \pm 0.06)\times10^{-5}$ S and $(7.96 \pm 0.09)\times10^{-6}$ S V^{-1} respectively. The goodness

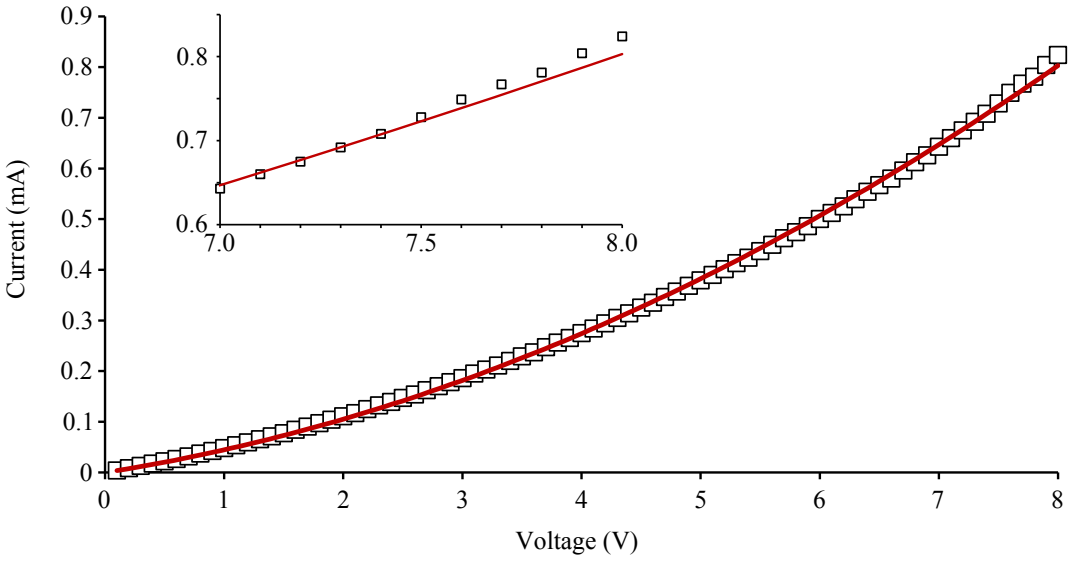

FIGURE 12.12: Graph showing the fit of a random resistor network model of the form $I = \Sigma_1 V + \Sigma_2 V^2$ to the 10th I-V sweep obtained at the maximum force of 3.45 N, with fit parameters Σ_1 and Σ_2 of $(3.67 \pm 0.06)\times10^{-5}$ S and $(7.96 \pm 0.09)\times10^{-6}$ S V^{-1} respectively.

of fit can be assessed from the adjusted R^2 value, which quantifies the correlation between model and data. The closer R^2 is to 1, the better the fit and in this example R^2 was 0.9996. In fact, the minimum value of R^2 over all I-V curves using this linear/quadratic model was 0.9990, indicating high correlation. Additionally, a linear/cubic variation of the RRN model, of the form $I = \Sigma_1 V + \Sigma_3 V^3$, was trialled. However, for the majority of the I-V curves this gave a poorer fit with a lower R^2 value than the linear/quadratic form. For the remainder of this analysis, the linear/quadratic form was used.

Of great interest is the contribution of the linear and quadratic terms to the total current flow through the test area. The linear and quadratic conductances Σ_1 and Σ_2 are plotted as a function of force in Fig. 12.13(a) and Fig. 12.13(b). It can be seen that Σ_1 increases by a factor of 8, and Σ_2 increases by a factor of 6 over the range of applied forces. Overall this accounts for the increased current flow observed at high forces. The local peak at 0.345 N for both Σ_1 and Σ_2 can be traced back to the I-V sweep performed at this force, which was shown in Fig. 12.11. Here, the maximum current peaked to a higher value. The exact cause of this is unconfirmed, however one possible scenario is an initially poor electrical connection between the probe and the test area.

The quadratic model presented here provides a phenomenological basis for understanding the conduction in terms of linear and non-linear components. The contribution of each to the total current measured depends on the voltage applied through the system. The linear and quadratic contributions to the total current, at the maximum applied force of 3.45 N are shown as a function of voltage in Fig. 12.14(a). As can be expected, the non-linear current increases with voltage, at the expense of the non-linear current. In terms of physical mechanisms, at high voltages additional, intrinsically non-linear conduction channels may form, for example through field-assisted quantum tunnelling mechanisms. In this process,

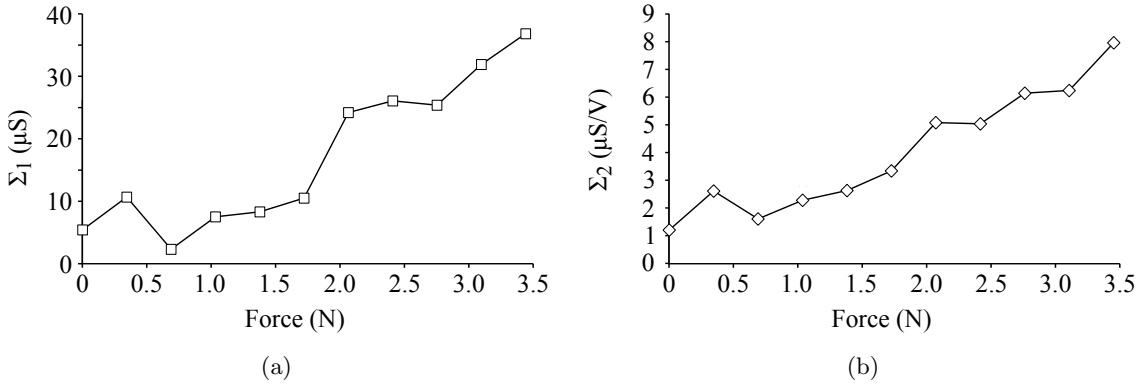

FIGURE 12.13: Graphs showing the fit parameters (a) Σ_1 and (b) Σ_2, representing the linear and quadratic conductances of the random resistor network model, as a function of force applied to the 0.5 mm test area. Lines are drawn between data points as a guide to the eye, and errors on the values are smaller than the symbols.

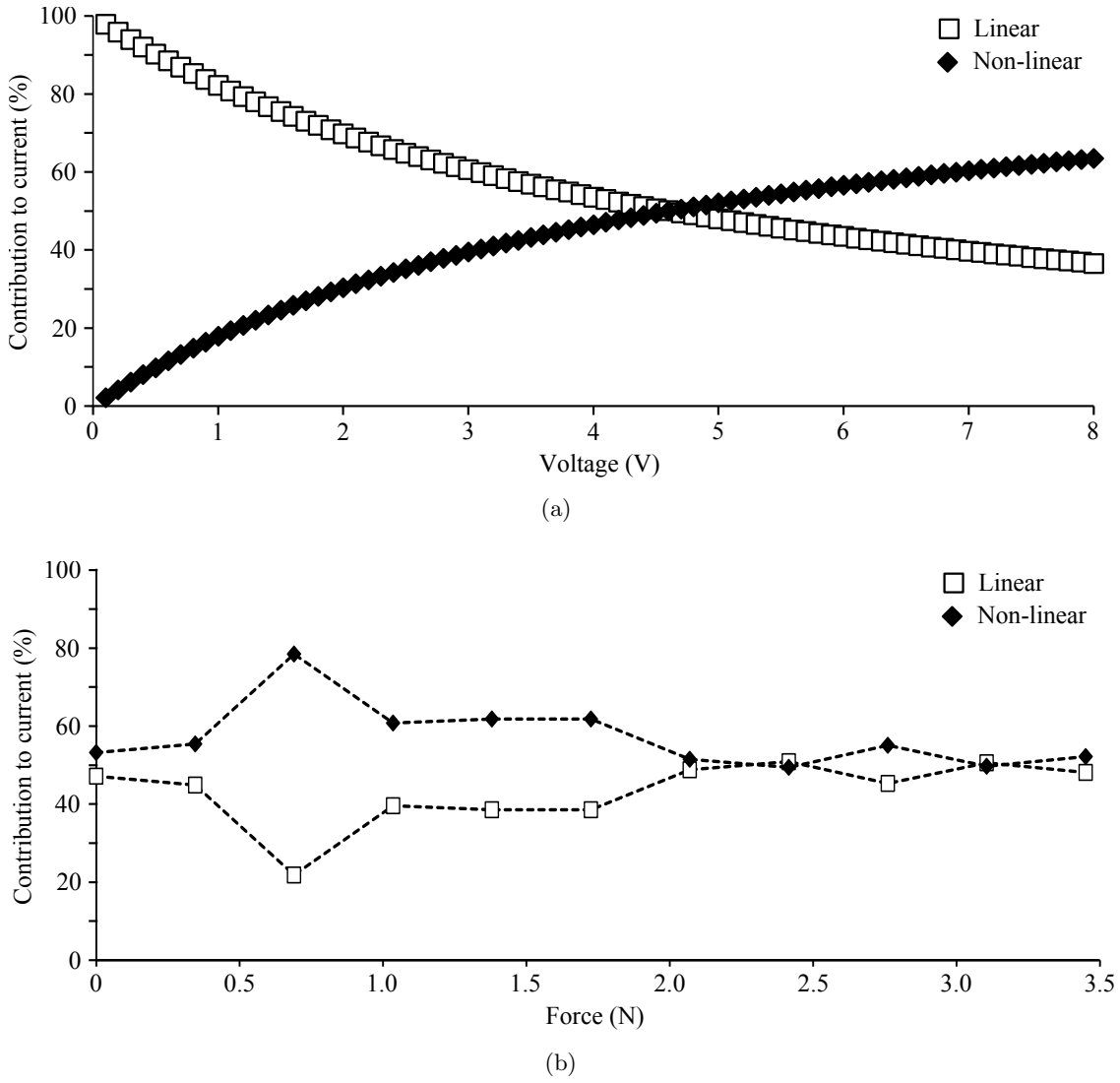

FIGURE 12.14: Graphs showing the linear and non-linear contributions to total current for (a) increasing voltage, at a fixed force of 3.45 N and (b) for increasing force, at a fixed voltage of 5 V, where the solid data points represent recalculated values of Σ_1 and Σ_2 at 0.345 N. Error bars are smaller than the data points.

described in chapter 8, a sufficiently high external electric field may distort a potential barrier such that electrons may pass through the barrier and contribute to conduction. This is the premise for the dynamic RRN model. Alternatively, at high currents (produced by a high voltage) an initially linear conducting channel may become non-linear, for example through Joule heating effects. Here conduction electrons collide with atoms in the conducting medium and generate heat through losses in kinetic energy. In the non-linear RRN model, non-linearities are expected to be a result of such mechanisms. This effect can not be ruled out in this system, as the small-area local contacts created between the SCTP and each granule within the PS layer may experience significant Joule heating effects.

Furthermore, Fig. 12.14(b) shows the linear and quadratic contribution to the current as a function of applied force, at a fixed voltage of 5 V. This voltage is similar to that used experimentally when measuring the F-R response of the PSRT samples. The general trend, after 0.7 N is of a decreasing non-linear component and an increasing linear component. At the maximum force both contributions are approximately equal. Because the granules are inherently porous, one possible explanation is that compression of the granules decreases the separation between neighouring particles, creating more linear conduction pathways. Additionally, particles originally separated by an air void may, under sufficient compression, come into direct contact and thus what was initially a non-linear conduction pathway would then become linear.

However, this mechanism does not account for the results obtained at forces less than 0.7 N. Here, forces from 0 to 0.7 N cause the linear component to decrease and the non-linear component to increase. There are two fundamental reasons why this could occur. The first is that the initial application of force decreases the interparticle separation within the granule, but does not create direct contact between particles. Non-linear conduction through quantum tunnelling would then increase, if the potential barrier width was sufficiently reduced. Then, at 0.7 N direct contact between neighbouring particles occurs and the linear conduction increases.

The second possibility relates to the resistance of the electrical connection between the SCTP and the capping electrode. There will be a finite resistance relating to the quality of contact between the probe and the capping electrode, which itself may decrease with increasing applied force. The limitations of the experimental procedure were previously described in section 12.3.2. Because of the ambiguity in the nature of the electrical contact created between the SCTP and the capping electrode, unfortunately this possibility cannot be ruled out without further investigation.

As a final remark on the application of the RRN model, in general a good fit was achieved between model and data, with an R^2 value very close to one. However, at larger voltages some deviation between model and data was seen, for example as shown in the inset of Fig. 12.12 for a force of 3.45 N. Residual analysis can also be used to assess the goodness of fit of the model. The residual is simply the difference between the observed data and the prediction of the model. Fig. 12.15 shows the residuals for the I-V sweep performed at 3.45 N. For a good fit, it is expected that the residuals are small and are randomly distributed around zero. Here, clear structure is observed and the magnitude rises sharply at higher voltages. This indicates that the model becomes a poor fit to the data at higher voltages, and that a better fit could be achieved through the addition of higher order terms in the model.

To summarise, the phenomenological RRN model was applied to the data, where the I-V response could be described by a sum of linear and quadratic terms. Analysis of the linear and

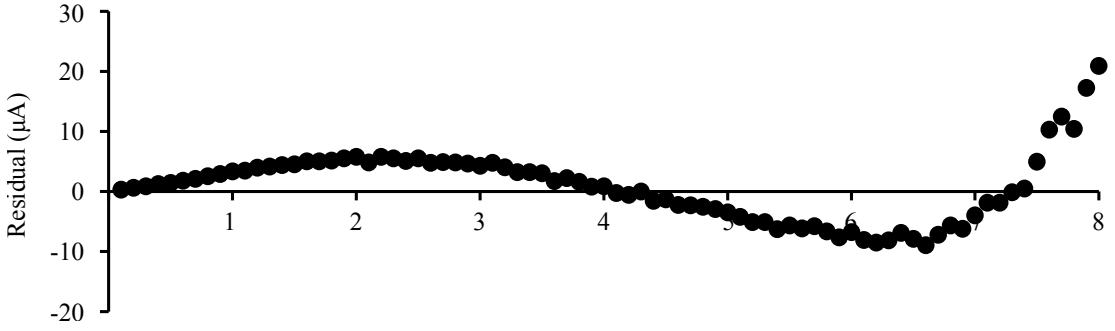

FIGURE 12.15: Graphs showing residual analysis of the fit of the RRN model to the I-V sweep performed at 3.45 N. Clear structure within the residuals indicates that a better fit may be achieved through the incorpoation of higher order terms into the model.

higher order conductances showed that both terms increased with increasing force, resulting in an increase in the total current flow with force. Furthermore, the linear contribution increased with force, above 0.7 N. This could be attributed to compression of the granules, which decreased the average interparticle distance and resulted in an increased number of percolative (ohmic) conduction pathways. The contribution from the higher-order conductance decreased with force, after 0.7 N. This was attributed to initially non-linear conduction pathways (e.g. from tunnelling or hopping of charge from particles separated by a potential barrier) becoming linear with increased granule compression. Below 0.7 N the system appeared more complex and limitations in the experimental set up may have contributed to this.

12.4.2.2 Application of a linear-exponential model

In the previous section, the phenomenological RRN model was applied to the I-V sweeps of the 0.5 mm test area. However, analysis of the residuals between model and data suggested that the inclusion of higher order terms in the model may yield a better fit. In this section, a model of the form $J(E) = \sigma_0 E + AE^m \exp(-B/E)$ was applied to the I-V response of the 0.5 mm test area. This model was described in detail in chapter 8. Again, the total current density comprises a linear and a non-linear term. However, the non-linear term is derived from the physical principles of quantum tunnelling mechanisms. Each parameter in the equation may be linked to the physical form of the conduction. Similar to the RRN model, the term σ_0 represents the linear conductivity. The value of A describes the magnitude of the non-linear conduction, and is related to the frequency of tunnelling events (the number of attempts per second made by the charge carrier to cross the potential barrier [223]). The exponent m usually takes the value 1–3, depending on the specific form of tunnelling and any corrections made to the model for the effects of the image field potential or Coulombic forces between the carriers. Table 8.1 listed values of m for specific non-linear conduction mechanisms. Specifically, when $m = 2$, this related to Fowler-Nordheim tunnelling. Finally,

B represents the effective height of the potential energy barrier between the insulating polymer and conductive particles within the nanocomposite granules. The factor $\exp(-B/E)$ therefore represents the tunnelling probability.

In order to apply this model, the measured current and voltage were converted to current density J and electric field E. To calculate the current density, it was assumed that the test area was perfectly circular. The PS layer, sandwiched by the capping electrode and the ITO, formed a parallel plate capacitor where the electric field could be approximated by $E = V/d$, where d was the spacing between the two electrodes. In chapter 10, the thickness of the printed layer was measured at 1.3 µm. However in order to account for the protrusion of the granules above the PS surface, d was estimated as 5 µm. Any reduction in d due to compression of the granules was neglected.

The model was applied using Origin® graphing software, and the parameters σ_0, A, m and B were optimised using a damped least-squares (Levenberg-Marquardt) algorithm. The parameters were constrained such that $\sigma_0 > 0$, $A > 0$, $B > 0$ and $1 < m < 3$, in line with the theory. Fig. 12.16 shows example fits of this model to I-V sweeps performed at selected forces. The blue and green dashed lines represent the linear and non-linear contribution to the total current density in each case. At first glance, the model appears to give a good fit to the experimental data. However, close inspection reveals deviations at low and high forces. Examples of this are shown in the insets of Fig. 12.16(d) and Fig. 12.16(f). In Fig. 12.16(d) and Fig. 12.16(f) the majority of the total current density can be attributed to the non-linear component, and the linear component is very small. At the other forces, there is a more even split between linear and non-linear components. However, as force is increased there is no obvious trend in the contribution from linear and non-linear contributions. This contrasts with the results found by He and Tjong for a range of conductive composite materials [223]. They found that, for increasing filler content (analogous to increasing force), the linear contribution increased at the expense of the non-linear component.

Here, the linear and non-linear contributions can be further analysed by studying the parameters σ, A, m and B as a function of applied force. The results are shown in Fig. 12.17. They reveal no apparent trend. In fact, the large errors associated with these parameters suggests that the model does not give a good representation of the data. Whilst a reasonable fit to the data is achieved, some parameters clearly give little or no input into the current density, and this is reflected by the large error bars on these parameters. For example for σ_0, which defines the linear contribution to J, the error at the maximum force of 3.45 N is very large. In this case, σ_0 may take a wide range of values with no significant impact on the overall current density. As can be seen from Fig. 12.16(f), in this case the observed $J - E$ data can be well represented by the non-linear term only. A similar scenario is also seen for parameter A, which defines the magnitude of the non-linear response. A large error in the A

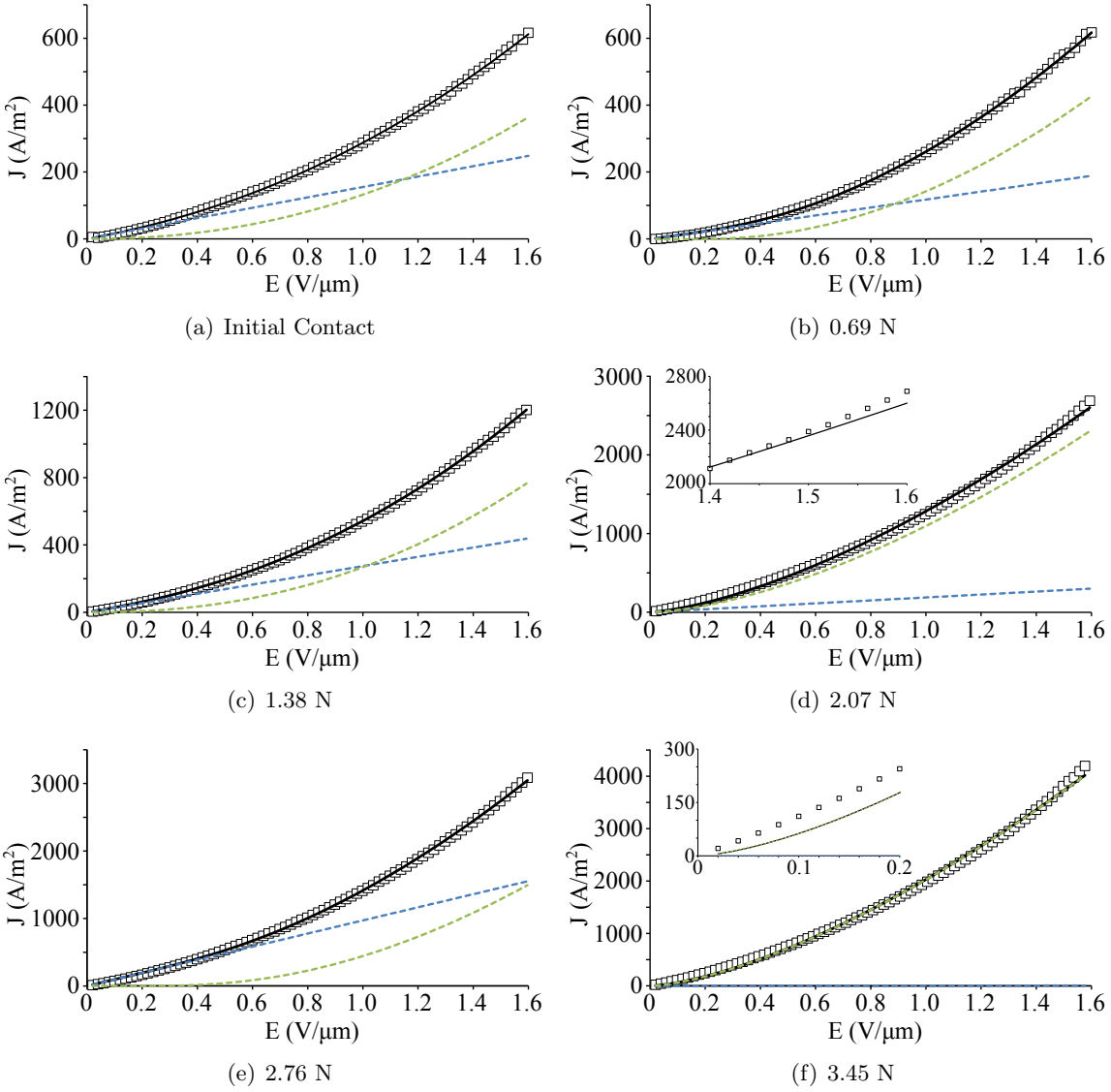

FIGURE 12.16: Graphs showing a fit of the model $J(E) = \sigma_0 E + AE^m \exp(-B/E)$ to I-V sweeps performed on the 0.5 mm test area. Experimental data is represented by the open squares, and the best fit of the model by the solid black line. The linear contribution to the total current density ($\sigma_0 E$) is shown by the dashed blue line and the non-linear contribution ($AE^m \exp(-B/E)$) is shown by the dashed green line.

value at the best fit of model to data suggests that this parameter plays no significant role in the measured $J - E$ response.

Parameter m shows no significant trend with applied force, instead fluctuating in the range 1.5–2.2. Here, m represents the type of non-linear conduction. For field-assisted or Fowler-Nordheim tunnelling $m = 2$, as described by equation 8.23. The fluctuation of m values observed here suggests no universal origin of non-linearity. Note that for $m > 2$ space-charge limited conduction is predicted [241].

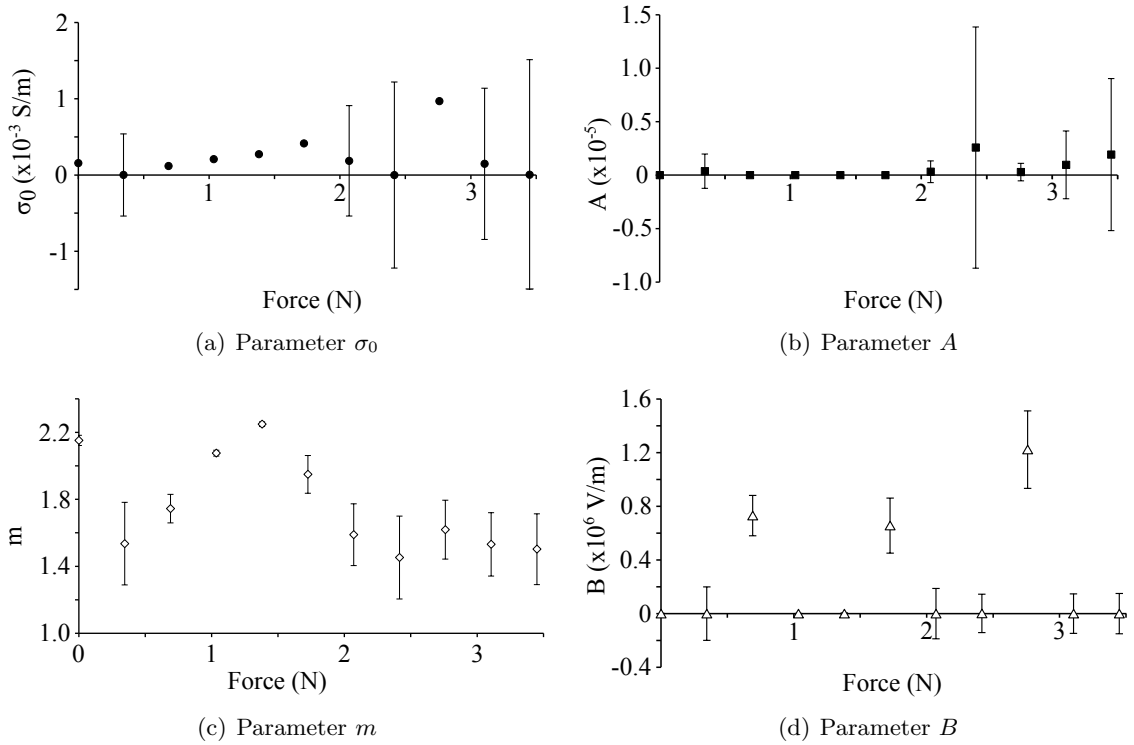

(a) Parameter σ_0 (b) Parameter A

(c) Parameter m (d) Parameter B

FIGURE 12.17: Graphs showing the relationship between the parameters σ, A, m and B to the force applied on the 0.5 mm test are. Where the associated errors are large, this indicates that this parameter plays no significant contribution to the current density at this force.

In the majority of the fits, the parameter B is close to zero, with large error. B is a measure of the potential energy barrier between the conductive particles, for example due to the presence of insulating silicone binder, or air voids. When B is zero the exponential yields 1, suggesting that in these cases the data can be modelled effectively without the input from the exponential term. For a finite value of B, the tunnelling probability, given by the exponential term, asymptotically approaches unity with increasing electric field. Therefore this term has greatest impact at low electric fields. When B is zero, or small compared to E then the probability of tunnelling events is very close to 1. Indeed, for any non-zero B, this term is most effective at low electric fields where the probability of field-assisted tunnelling decreases. In any physical system, a distribution of barrier heights is expected, however this does not account for the zero values sometimes predicted by this model.

The large errors in the fit parameters suggest that, in this case, the model is over-parameterised. As was shown in section 12.4.2.1, the I-V curves can be accurately and precisely fitted using a combination of linear and quadratic terms, i.e. two degrees of freedom. By increasing the number of parameters in the model, there is more leeway in the values each parameter may take. This is highlighted by Fig. 12.18 which shows two fits of the model to the same data (in this case the I-V sweep recorded at 3.45 N). The two fits appear almost identical and

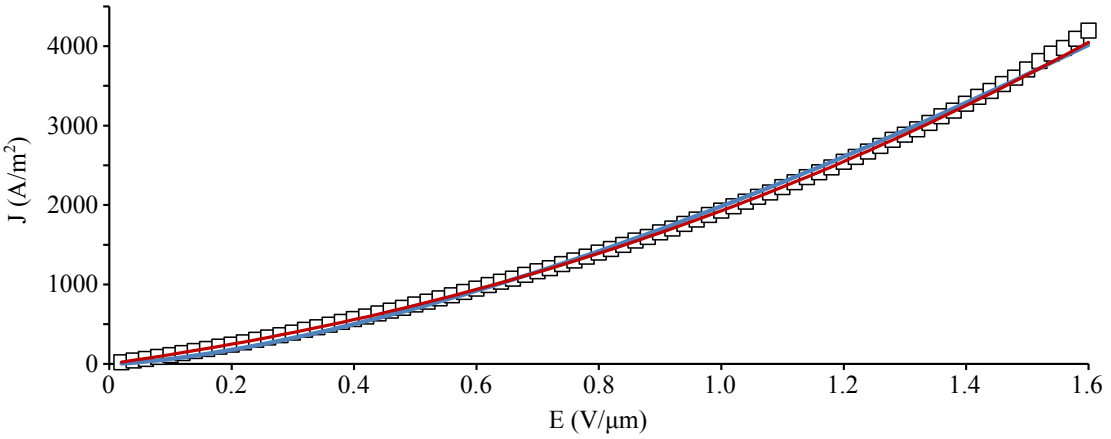

FIGURE 12.18: Graph showing two mathematical fits to the $J-E$ data obtained at a force of 3.45 N, where Fit 1 is shown by the blue solid line and Fit 2 is shown by the red solid line. Both fits appear visually identical and have similar adjusted R^2 values. The parameters for each fit are compared in Table 12.1. Here, over-parameterisation means a large amount of variation in the parameters can still result in good fits to the data.

have similar adjusted R^2 values, which indicates the goodness of fit. Table 12.1 compares the parameters obtained for each fit. It highlights large differences between the calculated parameters for each fit, even though $adj.R^2$ in each case is almost identical. For example, the values of A differ by 5 orders of magnitude, and the values of σ_0 differ by 3 orders of magnitude. Because of the large variation between parameters, it is not possible to extract any meaningful results from the trends of each parameter with applied force.

12.4.2.3 Discussion of models applied to I-V behaviour

Both models discussed in sections 12.4.2.1 and 12.4.2.2 have been successfully applied to other composite materials. In particular, the random resistor network model has been applied to a range of different physical systems, including discontinuous thin gold films [230], carbon black and wax composites [232] and epoxy resin/graphite nanosheet composites [234]. In these cases, the superposition of a linear and a quadratic term is sufficient to accurately model the I-V response.

	σ_0	A	m	B	$adj.R^2$
Fit 1	2.92×10^{-6}	1.93×10^{-6}	1.50	0	0.9976
Fit 2	1.12×10^{-3}	6.18×10^{-11}	2.19	98	0.9970

TABLE 12.1: Fit parameters σ_0, A, m and B for two visually similar fits to the experimental $J-E$ data obtained at a force of 3.45 N, which show similar goodness-of-fit (adj.R^2) values.

He and Tjong investigated both the RRN model and the tunnelling model, for composite materials of polyethylene or PVDF with conductive carbon nano-fibres or graphite flakes. The RRN model provided an adequate description of the I-V properties, although deviations in the low-field region were observed. When applying the tunnelling model, a statistically improved fit was achieved at the low-field region due to the inclusion of the exponential term $\exp(-B/E)$. Furthermore, the fit parameters could be linked to the effect of increasing the volume fraction of conductive particles within the composite. For example, they found that both parameters A and σ_0 increased with increasing conductive content. Furthermore, the tunnelling barrier height B was found to decrease with increasing filler content, and this was attributed to a reduced distance between neighbouring particles in the composite. Errors on the parameters were not quoted.

Previous work by Webb was focussed on another force-sensitive conducting polymer composite produced by Peratech Holdco Ltd [85, 233, 245]. In this case, the sensor comprised a screen-printable ink with a high loading of both acicular conducting particles and spherical insulating particles. Webb successfully applied both a RRN model and the tunnelling model to this composite. For the RRN model, it was observed that as the compression of the ink was increased, both the linear and quadratic conductance increased. However, above 1 N the quadratic conductance levelled off whilst the linear component continually increased. When the tunnelling model was applied, it was found that both parameters σ_0 and A increased with force, although A showed indication of levelling off at the highest forces. Overall, the linear contribution to the current decreased with force, whilst the non-linear (tunnelling) contribution increased. This behaviour was attributed to decreasing physical separation between the acicular conductive particles, resulting in narrower tunnelling barriers and increased tunnelling conduction. The parameter m was found to vary in the range 2–3, whereas here, for the transparent composite, m fluctuated in the range 1.5–2.2.

Furthermore, Webb also performed a preliminary investigation into the I-V behaviour of the transparent conductive material which is the focus of this thesis. However, in that instance the composite contained spontaneous agglomerations of conductive acicular particles, instead of the pre-formed granules which were developed throughout this thesis. Additionally, the experimental set-up was very different to that used here, where the compression force was applied to a large area of the PS layer. The experimental design was such that the effects of increasing contact area between PS layer and electrode could not be ruled out. Despite this, Webb found a large degree of electrical hysteresis between increasing and decreasing voltage sweeps, particularly in the first sweep, and noise in the current at large voltages. These features were present in the I-V sweeps performed here, as discussed in section 12.4. Overall, Webb found that parameters A and σ_0 increased with increasing force, although the associated errors were often large. The linear contribution to the total current density was found to increase with force, whilst the non-linear contribution decreased with force. This is

in agreement with the results found here, upon application of the RRN model, as shown in Fig. 12.14(b). Similarly, the exponent m was found to be close to 2, also in agreement with the values presented here. The parameter B was not discussed. For both models, residual analysis revealed a poor fit in the low-field region.

Here, the RRN model was applied successfully to data obtained for the 0.5 mm test area. However, the tunnelling model could not be fitted to the data without forming large errors on each parameter. The experimental equipment was designed such that the effect of increasing the contact area between probe and PS layer was mitigated. The PS layer, within the test area, was capped with a chromium/copper/gold electrode which created intimate contact over the rough surface topography of the PS layer. Therefore, each granule within the test area contributed to the current flow even if it was not in contact with the probe. However, the contact resistance between the probe and the test area could not be ruled out, as in essence a two-point probe measurement system was created. The contact resistance can be highly sensitive to the quality of the contact created between the surfaces. When one, or both, surfaces are topologically rough, the contact area will increase with increasing force as more surface asperities are brought into contact. The contact resistance therefore depends on the force applied. This effect was not accounted for here. Realistically, the measured I-V curves also include a contribution from the I-V behaviour of the probe/capping electrode contact. Other potential issues encountered during measurement were discussed in section 12.3. Briefly, these include degradation of both the granules and the capping electrode with increasing force. Fundamentally, this is a complicated and variable composite system, where the limitations of the experimental method, and any conclusions drawn must be recognised. In any future work, these effects need to be investigated thoroughly before any definite conclusions about the conduction networks within the granules can be made.

In summary, both a phenomenological and a physical model were applied to the I-V sweeps performed on the 0.5 mm test area of the PSRTs. The phenomenological model, comprising a linear and a quadratic term provided a good fit to the data, although residual analysis suggested that a better fit may be achieved with the inclusion of higher order terms. It was found that, above 0.7 N the linear contribution to conduction increased with increasing force, whereas the non-linear contribution decreased. Below 0.7 N, it was believed that issues arising from a non-zero contact resistance may have dominated. In the physical model, any non-linear contribution to the current density could in theory be linked to quantum tunnelling effects. However, the model could not be successfully applied and in many cases each parameter exhibited a large error. It was shown that two visually similar fits, with the same statistical goodness-of-fit value, could predict very different values of the parameters, giving little confidence in the application of such a model.

12.5 Measurement of flicker noise

Electrical noise within a composite material may provide a means to probe the nature of the electrical conduction within that composite. This was introduced previously in chapter 8. Flicker noise is a frequency dependent oscillation of a measurable quantity (for example current) that can be linked with fluctuations in conductivity within a material. In conducting polymer composites, the flicker noise may be strongly dependent on the filler fraction of conductive particles. Compression of such a composite forces conductive particles closer together and hence may also affect the measured flicker noise. Here, the transparent ink containing the nanocomposite granules was printed in a 6 mm sensor format, as shown earlier in Fig. 9.4. Sensors were printed for both $G3$ and $G4$ PS layers. The granule number density within these layers, and their electrical functionality in a four-wire touchscreen format, were previously reported in chapter 10. Force was applied to the sensors using the custom-built rig as shown in Fig. 9.9 and the flicker noise was measured over a 2 second period, then repeated 20 times. The power spectrum of the noise was calculated as per equation 8.26. It is important to note that in this experimental design the effect of increasing contact area between electrode and PS layer with increasing force (and hence increasing the number of granules contacted) could not be ruled out.

Fig. 12.19(a) shows the power spectrum obtained for sample $G3$, for applied masses of 50 and 500 g, approximately corresponding to forces of 0.5 and 5 N. Fig. 12.19(b) shows the power spectra for sample $G4$ at the same forces. The power spectrum of the flicker noise is larger for an applied load of 5 N than for 0.5 N, for both samples. This relates to the increased current which flows through the sensor under 5 N load (resulting in a lower resistance). On a log-log scale, the flicker noise appears linear with a gradient equal to that of the coefficient γ. For

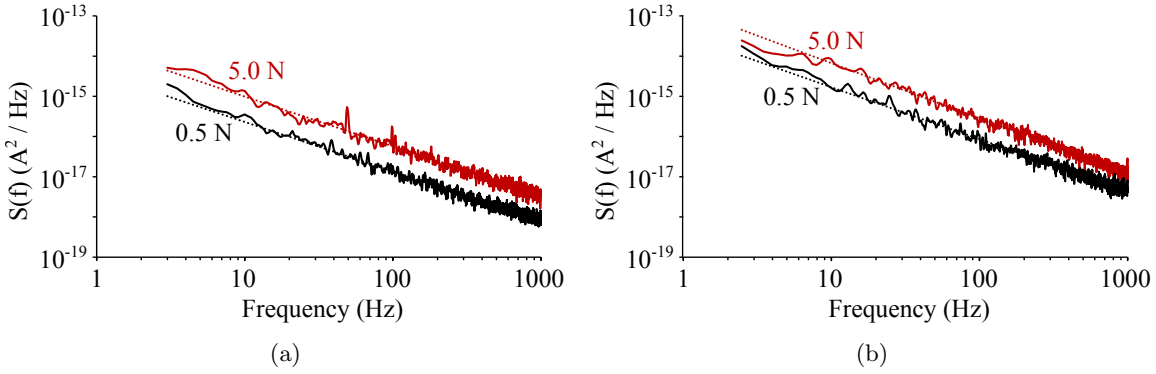

FIGURE 12.19: Graphs showing the noise power spectra for current fluctuations in samples (a) $G3$ and (b) $G4$ when the sensors were subject to 0.5 N (solid black line) and 5 N (solid red line) applied force. The dashed lines represent a linear relationship (note the log-log scale) from which the gradient yields γ.

sample $G3$, γ was calculated as 1.227 ± 0.005 and 1.54 ± 0.01 for 0.5 and 5 N respectively. For sample $G4$, γ was 1.292 ± 0.005 and 1.371 ± 0.005 for 0.5 and 5 N respectively.

The flicker noise was analysed for three sensors each of $G3$ and $G4$. Fig. 12.20(a) shows the average current passing through the sample with increasing applied force. As the force was increased the current also increased, and hence the resistance decreased. On average, sample $G4$ showed a larger current flow than for sample $G3$. This is due to the increased granule number density within sample $G4$, which allows for a greater number of conduction pathways between the upper and lower ITO electrodes. Fig. 12.20(b) shows all calculated values of γ for each sensor at each force. From the graph, there is no apparent trend between γ and force. Instead, the value of γ fluctuates in the range 1.2–1.8.

In the literature, a change in γ with increasing conductive content in a composite material has been used to draw conclusions regarding trapping states within the composite. For example, Williams *et al.* report, for insulating/conducting polymer blends, increasing the conductive fraction above the percolation threshold results in a decrease in γ [255]. A smaller γ indicates a multiplicity of trap states with an extended density of states within each trap. This result is then attributed to the fact that, for a smaller conductive fraction, fewer of these states are sampled during charge transport through the composite. Here, the disorder in the calculated γ values gives no physical insight into the presence of trapping states (if any).

As well as the value of γ, the magnitude of the noise response has also been used to probe conduction within composites. According to equation 8.34, the power spectrum $S(f)$ obeys a scaling law dependent on the resistance of the composite, R, raised to the exponent ω. Typically, R is changed by altering the conductive fraction of the composite above the percolation threshold. Here, R was varied by applying force to 6 mm sensors. The expression

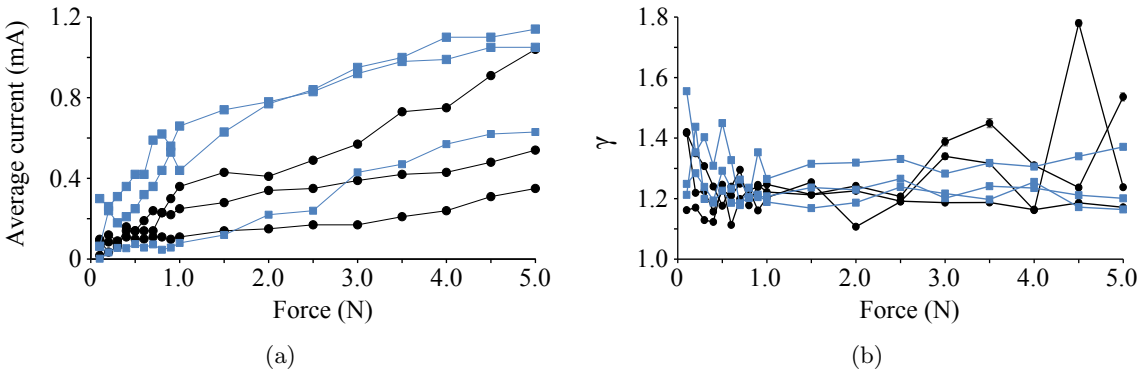

FIGURE 12.20: Graphs showing (a) the average current flow through each sensor and (b) the calculated γ value for each sensor, as a function of applied force. The black circles represent $G3$ sensors and the blue squares represent $G4$ sensors. Lines are drawn between data points as a guide to the eye.

$\frac{S(f)}{I^2} = R^{\omega}$ was analysed by measuring the power spectrum at frequencies of 10, 100 and 1000 Hz. The resistance was calculated from the fixed voltage (2.5 V and the average current passing through the sensor at each applied force.

Fig. 12.21 evaluates the relation $\frac{S(f)}{I^2} = R^{\omega}$ for three 6 mm sensors of sample $G3$, where the relative noise amplitude is evaluated at frequencies of 10, 100 and 1000 Hz. The graph is plotted on a log-log scale, such that the dashed lines represent linear relationships where the value of the gradient is equal to ω. Note that rather than extract $S(10Hz)$, $S(100Hz)$ and $S(1000Hz)$ from the experimental data, the previously determined values of γ were used to calculate an approximate value. This is because experimentally $S(f)$ showed large peaks at certain frequencies (sometimes at 100 Hz) and therefore calculating an approximate value from the measured γ value ensured that these peaks were not sampled during this analysis. In Fig. 12.21(c) there is a peak in the calculated value of $log(S(f)/I^2)$, for each frequency, located close to $log(R) = 4.4$. This peak can be traced back to the force-resistance response observed for this sensor, where at the lowest loading of 10 g (0.1 N) the resistance was initially low but then increased to a much larger value at the next increment of force (0.2 N).

From the figure, for each sensor the values of the scaling exponent ω, calculated at each frequency of 10, 100 and 1000 Hz, are mostly in agreement, within error. This confirms the applicability of the $1/f^{\gamma}$ model. However, when comparing across different $G3$ sensors at the same frequency, large differences between the values are observed. For example at a frequency of 100 Hz, sensors 1, 2 and 3 exhibited an ω value of 1.4±0.2, 1.0±0.1 and 2.3±0.5. These values do not agree within error and suggest a large amount of variation in the noise properties of the individual sensors.

In the literature, the exponent ω has been linked to the type of conduction occurring within the composite [288–290]. For example Breeze *et al.* studied the flicker noise characteristics of a carbon black/polymer composite [254]. They found that, when plotting the noise of the resistivity fluctuations for different sample resistivities (driven to higher values by increasing the temperature of the composite), two regimes could be observed. In the non-metal regime (high resistivity) the value of ω was 2.77. At low resistivities ω decreased and this was attributed to the onset of percolative conduction and quantum tunnelling mechanisms. A similar transition between two values of ω was also observed by Pierre *et al.* for copper/polymer composites [290].

Here, such analysis cannot be performed, due to the large variations observed between ω from sensor to sensor. The limitations of the experimental design prevent any further analysis. This is because, in the sensor and test rig design used for noise measurements, the effect of increasing contact area between electrode and PS layer cannot be ruled out. The application of force to the upper ITO electrode pushes it into contact with the PS layer, and the contact

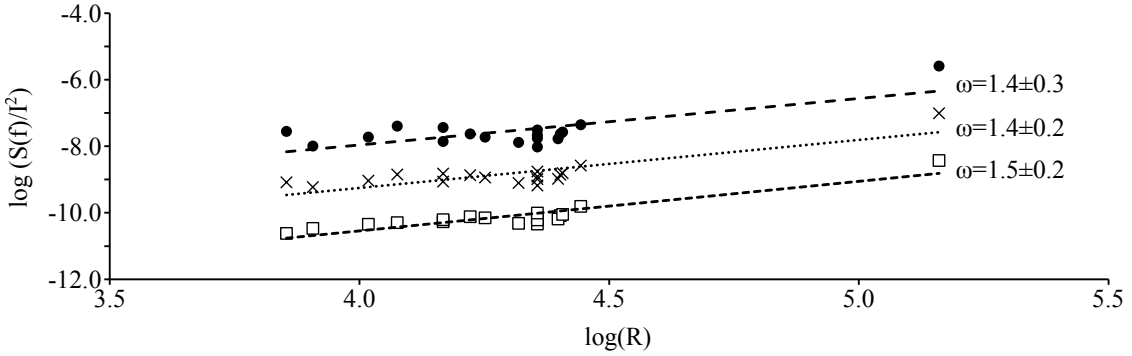

(a) Sensor 1

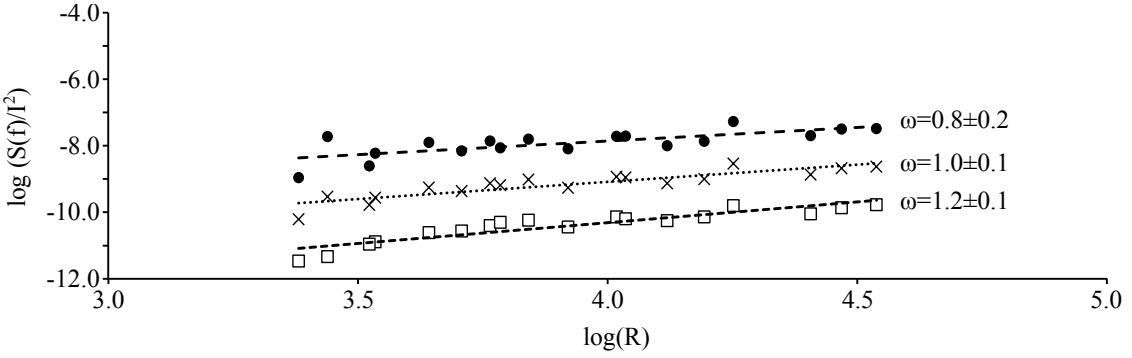

(b) Sensor 2

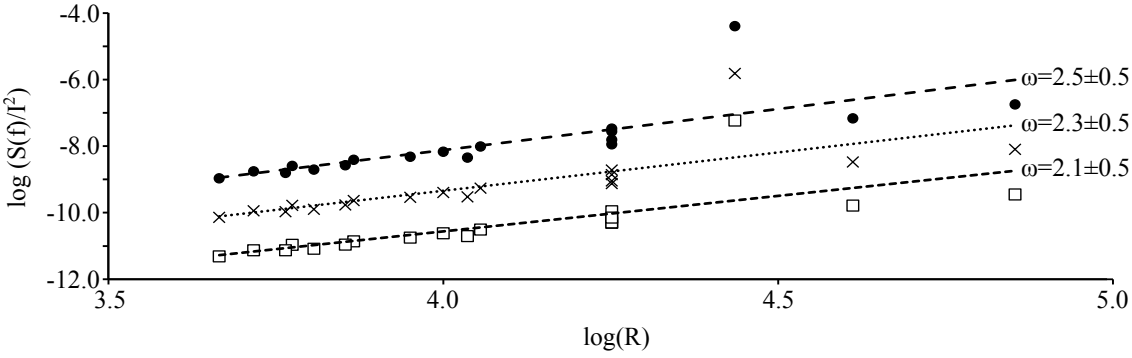

(c) Sensor 3

FIGURE 12.21: Graphs showing the magnitude of the flicker noise at frequencies of 10 Hz (black circles), 100 Hz (crosses) and 1000 Hz (open squares) as a function of the resistance through the sensor, for samples (a) 1, (b) 2 and (c) 3. This is expressed on a log-log scale to allow extraction of the scaling coefficient ω.

area created is dependent on the force applied. Therefore, in the experiment performed here the measured noise is likely to be a summation of the contact noise and the noise through the granule composites. It is impossible to draw any reliable conclusions about the nature of the conduction through the composites without first quantifying the noise contribution of the ITO/PS layer contact. In future work, it would be beneficial to repeat these measurements

using the test rig developed for the measurements presented in sections 12.3 and 12.4 in this chapter. Then, the effect of increasing the contact area between probe and PS layer could be partially mitigated.

12.6 Summary of part II

Part II of this thesis has presented a significant body of work designed to investigate and characterise the physical basis of any force-induced resistive response of both the touchscreen ensemble and the individual nanocomposite granules. Previously, the fabricated granules were found to possess a complex internal structure comprising conductive particles separated by polymer binder and air voids. When the granules are subject to a force, compression of the granule may open up additional conduction pathways, thus decreasing the resistance through the granule. Additionally, increasing the force on the upper ITO electrode creates contact with an increasing number of granules within the PS layer, which also acts to decrease the resistance.

The functional performance of touchscreen test devices were investigated in chapter 10, where a number of parameters were devised in order to compare the response as a function of granule loading. A control test device, containing agglomerated nanoparticles instead of pre-formed granules, was also considered. It was found that both the electrical properties and optical transmission through the touchscreen could be linked to the distribution of granules within the PS layer. An increased number density of granules resulted in a larger value of optical haze. Additionally, increasing the number density also produced a less variable F-R response over the touchscreen surface but resulted in a higher sensitivity, or a more 'switch-like' response.

To better understand the contact between flexible ITO electrode and PS layer during operation of the touchscreen, a model simulation was developed which enabled the number of granules contacted by the electrode to be modelled as a function of force, allowing the prediction of the F-R response of the touchscreen. The model provided a reasonable prediction of the shape of the F-R response seen in experimental test devices, although it underestimated the resistance, particularly at higher forces. In the model any force-sensitivity intrinsic to the granules was neglected, suggested this phenomena must be accounted for in order to produce a more accurate model.

To assess the intrinsic force sensitivity of the granules, test areas on the PS layer of the PSRT devices were fabricated by evaporating chromium/copper/gold capping electrodes and net forces of up to 3.45 N were applied to the test area. By varying the size of the test areas the force exerted on each individual granule could be further controlled. For example, at the maximum SCTP force of 3.45 N, the force exerted on the granules in the 0.5 mm test area was

largest, due to the small number of granules contained within this area. Two key observations were made. The first was that the resistance through the test area was dependent upon the size of the test area. This was linked to the number of granules contained within the test area, where larger test areas contained more granules. As each granule may be modelled as a resistor in parallel with its neighbours, the more granules that are contacted by the probe the lower the overall resistance. This observation was used to predict the resistance of a single granule as 0.5–30 MΩ. The large variation in this value resulted from the inherent variation in the resistance of the test area at initial contact with the probe. An estimate of granule resistance is useful for simulations of the force-sensitive response of the touchscreens. For example, Fig. 11.2(a) in chapter 11 showed the effect of varying the granule resistance on the calculated F-R response of the PSRT devices.

The second observation was that the magnitude of the F-R response was also linked to the size of the test area. The smallest test area (0.5 mm) exhibited the largest percentage change in resistance between initial contact with the probe and maximum applied force. This change was significantly smaller for the 2 and 1 mm test areas. Again, this was attributed to the difference in force exerted on the individual granules. By assuming that each granule protruded above the PS surface by the same height, the force exerted by the probe is distributed equally between all granules. Therefore the force per granule is larger in the smaller test area. When these granules are subjected to high forces, additional pressure-induced conduction pathways within the granule may be triggered.

Due to the experimental design, the force exerted on each granule was very high (a maximum of 16±4 mN). Unfortunately, this exceeded the average granule fracture strength of 10.6±0.3 mN previously determined in chapter 7, such that granule degradation or breakage during testing cannot be ruled out. This may also be a cause of the observed poor repeatability of the F-R response of all test areas. Furthermore, the forces exerted on the granules here are likely to be much larger than for standard operation of the touchscreen device. From the model presented in chapter 11, it may be expected that the largest force a granule will experience is at first contact between the ITO and PS layer, when the contact area is smallest and hence the number of granules contacted is low.

In order to probe the underlying conduction mechanisms responsible for any pressure-sensitive resistance response, the I-V characteristics of the test areas were investigated by performing 10 I-V sweeps at each force. Hysteresis between increasing and decreasing force cycles was evident in most sweeps performed, however the magnitude and persistence of the hysteresis during repeated testing was greatest for the 0.5 mm test area. In some cases, the hysteresis could be explained by charge trapping mechanisms, however in other instances the hysteresis may have been caused by a non-constant current flow. By allowing the granule resistance to settle for a fixed period of time prior to measurement this effect may be confirmed.

To investigate the physical mechanisms behind the observed force-sensitive I-V response in the 0.5 mm contacts two models were fitted to the data. The first, the random resistor network model, was applied successfully. Here, the total current was split into a linear and a non-linear term, with the latter represented by a quadratic function. Analysis of the linear and quadratic conductances with applied force showed that, above 0.7 N, the linear contribution to total current increased, and the non-linear contribution decreased. An increase in linear charge transport mechanisms at the expense of the non-linear charge transport may be caused by granule compression creating more direct (percolative) conduction pathways between neighbouring particles. A similar effect has been found in other composite materials. However, the RRN model is phenomenological and can offer no significant physical insight into the nature of the non-linear conduction pathways. A second model, derived from the physical basis of quantum tunnelling processes, was also applied. Here, the non-linear term was represented by a power law and exponential function, whose parameters could give physical insight into the type and nature of the tunnelling process. Unfortunately, this model could not be fitted well to the experimental data and large variations in most model parameters were obtained.

Additionally, the flicker noise through 6 mm sensors of samples $G3$ and $G4$ was measured. However, neither the noise exponent γ or the magnitude of the noise could be used to draw any conclusions regarding the conduction mechanisms within the granules. This was attributed to the limitations of the test procedure (in both the geometries of the samples used and the method of applying force to the sensors).

Finally, whilst pressure-sensitivity is suggested by the results obtained in this chapter, two important points must be taken into consideration. The first is that any pressure-sensitive conduction is only realised at high forces, well beyond that experienced during normal operation of the touchscreen device. If this intrinsic pressure sensitive feature is to be utilised in the PSRT response, it is necessary to redevelop the granules such that this feature may be unlocked at lower forces. The second point is that the results obtained here cannot, with absolute certainty, be attributed as being intrinsic to the granules. The composite system itself is complicated and highly variable, and the limitations of the experimental design did not account for all possible external sources of pressure sensitivity (for example in the contact resistance between probe and capping electrode). In future work, it may be prudent to remove this effect in order to re-examine the pressure sensitive nature of the granules.

Chapter 13

Conclusions and Future Work

In this thesis, the design and development of new ink components for resistive sensors, primarily for touchscreen applications, was presented. Part I described the design, fabrication and analysis of nanocomposite granules, which were incorporated into the ink. Then, part II discussed the functional performance of the granules when printed to form resistive touchscreen sensors, as well as the physical basis of the force-dependent resistive response of both the touchscreen ensemble and the individual nanocomposite granules. The main conclusions from part I and part II are discussed in the following sections, along with suggestions for future work.

13.1 Conclusions and future work from part I

Here, the aim was to fabricate and analyse new nanocomposite granules for use in the printed pressure-sensitive resistive layer within the touchscreen sensors. In previous versions of the touchscreen, developed by Peratech Holdco Ltd., nanoparticle clusters formed during blending of the ink components. These provided the pressure-sensing properties of the touchscreen. In this thesis, these were replaced by pre-formed nanocomposite granules which offered improved functionality through increased control over the granule size, internal structure and mechanical properties. For example, control over the size distribution of the granules allowed their size to be matched to the printed ink thickness, which was important for the electrical functionality of the sensor. The internal porosity of the granules also linked to the electrical functionality through the possible creation of pressure-enhanced conduction pathways, and the fracture strength of the granules linked to their overall durability under repeated application of force. A thorough understanding of these characteristics allowed links to be made to the theory of granulation, developing an understanding of how the granule properties

could be tailored through altering the starting constituents or the operation parameters of the granulation process.

As well as fabricating the granules, it was necessary to devise and implement a range of analytical tools in order to quantify their size, structure and strength. The method of measuring the size distribution of granules was given particular emphasis in chapter 5. Through most of this thesis, the granules were imaged using SEM microscopy, with the relevant size and shape parameters extracted manually from the digital images using image analysis software. This technique was compared against commercially available particle size measurement systems which used the measurement principles of static and dynamic image analysis and laser diffractometry. It was important to understand the limitations of size analysis through SEM microscopy against these alternative techniques which allowed rapid, automated measurement of a large sample size of granules. For instance, whilst SEM imaging was slow and time-consuming, it allowed high-resolution visualisation of the granule topography and surface roughness. Although manual measurement of the granules limited the sample size measurable, the user could easily distinguish close or overlapping granules on the image, which automated measurement systems struggled to achieve. In fact, it was found that the main disadvantage of SEM imaging and manual image analysis was the poor representation of bimodal granule size distributions. High magnifications were necessary to resolve small granules and to allow accurate readings of granule size, which meant that larger granules were under-represented within the images. However, the commercially available instruments often struggled to measure small granules less than 10 µm in size, where effective dispersion of the granules was crucial.

Focussed ion beam (FIB) milling was an important tool for revealing the internal structure of the granules. Determining granule porosity was important, as a high porosity suggested that the granules may be compressible under applied force. This may have promoted pressure-enhanced conduction pathways within the granule. Furthermore, FIB milling often revealed complex and unusual granular structures. In some cases, FIB milling provided direct evidence of granule growth by the coalescence of several smaller granule nuclei. It also revealed the presence of concentric binder rings, which suggested growth by layering mechanisms. This was exemplified in Fig. 6.6 and Fig. 7.4 which show high-resolution detail of granule internal structures which were directly linked to predictions of granulation theory. In fact, in the field of granulation there is very little published work in the literature by which FIB milling was used as a tool to investigate internal granule structure, and alternative methods have not offered the high-resolution detail as shown in the images presented in this thesis. It was therefore shown that FIB milling was a viable technique to reveal complex structure of the nanocomposite granules produced here, and is clearly applicable to other granulation studies.

Additionally, compressive loading tests on individual granules were performed to assess their mechanical properties, using dedicated equipment available at Leeds University. Unfortunately the equipment did not offer sufficient resolution to determine the elastic deformation properties of the granules, and the smallest granules that could be tested were 75–100 µm in size. Despite these limitations, this technique provided some measure of the fracture strength of granules produced from a range of constituent materials and under different operating conditions.

Chapters 6 and 7 presented an in-depth study of how changing the constituent material properties and the operating variables impacted on the granule size, structure and strength. It was found that using spherical antimony-doped tin dioxide (ATO) nanoparticles promoted a well-defined granulation mechanism, where key processes such as nucleation, coalescence, layering and breakage could be readily observed. Furthermore, the induction time (that is the time during which granules exist in the nuclear state with no significant growth) was longer, and significant growth occurred only after 15 minutes in the granulating vessel. Conversely, when using acicular ATO nanoparticles the growth process was less well-defined and rapid growth by coalescence occurred in the early stages of the process. This resulted in larger, heavily agglomerated granular structures, which are not conducive to effective dispersion when blending with the screen-printable ink. Considering the polymeric binding agent, granules fabricated with the silicone binder exhibited a larger fracture strength than those fabricated with either carbon or water-based binders. The carbon-based binder resulted in a shortening of the induction time and rapid growth occurred sooner. Although a complex relationship between the binder quantity and the growth kinetics of the granules was observed, a silicone binder quantity of 10 % by mass was the maximum quantity that produced a stable, predictable granulation process that limited the degree of granule breakage. The key result of chapter 6 was therefore the development of an optimised granule 'recipe', consisting of spherical ATO nanoparticles and 10 % silicone binder by mass.

Throughout chapter 7, this 'optimum recipe' was further defined through consideration of the granulation process, namely through altering the granulation energy, through the rotational speed of the dual asymmetric centrifuge (DAC), and the residence time in the DAC. These parameters were intimately linked, as a lower rotational speed resulted in a longer induction time. In practical terms, this meant that a longer 'window of opportunity' existed during which the surface roughness and porosity both decreased although the overall granule size showed little variation. This result was highlighted in Fig. 7.1(a) and Fig. 7.9(a) for a rotational speed of 2000 rpm. As an extension of this principle, the regime map shown in Fig. 7.13 summarised an extensive body of work that considered the average granule size for a wide range of granulation speeds and times. From this, the induction time was determined as a function of rotational speed, as shown in Fig. 7.14. Overall, this chapter described how the properties of the granule nuclei may be tailored to 'pre-set' their electrical characteristics

through their internal porosity. Finally after the induction time, when rapid growth had occurred, the granules exhibited strange surface indentations, giving a warped 'golf-ball' shape. Whilst these large granules had no direct application within the scope of this thesis, it was noted that granules with this unusual feature have not been observed within the field of granulation, but may yet be relevant to pharmaceutical applications where an increased surface area is beneficial for effective granule dissolution.

Whilst part I of this thesis gave an in-depth study into granule formation, further work may extend the current understanding by investigating additional parameters known to affect the granulation process, or by improvement of the methods utilised in this thesis. For example, the surface energy of the constituent particles plays an important role in the wetting properties of the liquid binder. By altering the surface energy of either the particles or the binder phase, the granule properties may be further controlled. Previous work suggests that poor wetting characteristics lead to higher granule porosities, which may allow a greater degree of control over the granule compressibility and their electrical response. Additionally, only one type of constituent particle was considered (ATO), and two different shapes (spherical and acicular) were investigated. There exists a wealth of other electrically active nanoparticles, with a wide range of shapes, which may be trialled. Similarly for the liquid binder, only three insulating binders were considered. Future work could extend the range of binder considered, and also consider electrically active binders such as conductive polymers (for example polyaniline) or even polymers which exhibit a pressure-sensitive resistive response (for example PVDF).

Future work may also look to improve the method by which the mechanical properties of the granules are assessed. Here, the limitations of the equipment meant that only the granule fracture strength could be quantified. However, by measuring the elastic properties of the granule through the Young's modulus a greater understanding of the compressible nature of the granules could be gained. It is envisaged that changing the properties and the amount of the liquid binder phase may also impact on the compressible nature of the granules. This in turn would lead to greater control over the functional granule properties when they are subsequently incorporated into the touchscreen sensor. By controlling both their porosity and the compressibility, the effect on the electrical conduction through the granule as a function of applied force may be investigated.

13.2 Conclusions and future work from part II

In part II of this thesis, the granules were incorporated into an ink that was printed to form the pressure sensing (PS) layer of a resistive touchscreen sensor, and both the functional performance of the touchscreen and the physical basis of the force-sensitivity of the resistance response were investigated.

Chapter 10 considered the optical transmission through the PS layer, and the force-resistance (F-R) behaviour of the touchscreen assembly. An important part of this investigation was a comparison with a control scenario, where the PS layer contained agglomerates of the nanoparticles which were formed during blending of the screen-printable ink. By using pre-formed granules, the optical transmission through the PS layer was improved, when compared to the control scenario. This was linked to the number density (i.e. the number of granules/agglomerates per unit area within the PS layer) and the size of the agglomerates or granules within the layer. The number density of the spontaneously formed agglomerates in the control was higher, compared with the same mass loading of the new pre-formed granules. From this, it was clear that the average size of the granules was larger than the average size of the agglomerates.

Without the granulation stage, agglomerates with a wide size distribution are formed during blending of the ink, which can also leave unagglomerated nanoparticles in the PS layer. When the agglomerates were smaller than the thickness of the printed PS layer they did not contribute to the electrical conduction through the layer (as they could not make contact with the flexible electrode) however they provided scattering centres for light transmitted through the layer. Through considerations of both Rayleigh and Mie scattering theory, it was shown that individual nanoparticles and small agglomerates less than 0.1 µm in size promoted Rayleigh scattering, where incident light was scattered approximately equally in all directions. When the natural agglomerates or pre-formed granules were greater than 1 µm in size, light scattering was predominantly in the forward direction. This important result was shown in Fig. 8.11. In touchscreen applications, diffuse scattering needs to be minimised so that the touchscreen does not impact on light transmission from the underlying display. Here, it was shown that diffuse scattering (measured from the optical haze) could be minimised for a given particulate loading by first granulating the ATO nanoparticles prior to inclusion in the ink. In this way the number of unagglomerated or small agglomerates present in the layer was reduced, which limited the number of scattering centres scattering light to large angles.

The number density of granules within the layer was also linked to the electrical functionality of the touchscreen. This functionality was assessed by the definition of empirical parameters, describing the hysteresis between increasing and decreasing force sweeps, the variation in the force-resistance (F-R) response across the sensor surface, and the sensitivity of the F-R response (i.e. how quickly it switched from a high to low resistance state with application of force). PS layers were fabricated with different number densities of granules. High number densities meant that a larger number of granules contacted the flexible electrode at any given time, so that the resistance was less sensitive to local variations in granule number. This resulted in a decrease in the variability parameter. However, the sensitivity parameter increased because, with large numbers of granules in the PS layer, the resistance quickly

saturated to a minimum value. This was summarised in Fig. 10.11. In this case, a high sensitivity was not beneficial for pressure-sensitive applications, where instead a controlled and predictable decrease from high to low resistance states is preferred.

Chapter 11 presented a model simulation of the F-R response of a touchscreen assembly, by considering the interplay between the flexible ITO electrode and the PS layer. From an understanding of the mechanical properties of the sensor components, the deflection of the flexible electrode was calculated as a function of applied force, as presented in Fig. 11.1(a). The contact area was approximated by assuming that contact occurred when the deflection of the ITO electrode exceeded the depth of the air-gap between electrode and PS layer. With knowledge of the number density of granules within the PS layer, the number of granules contacted by the electrode as a function of applied force was calculated. Then, by assuming that the granules behaved as resistors in parallel the F-R response of the PSRT was estimated. As a first approximation, intrinsic pressure-sensitivity of the granules was neglected. A comparison was made between the F-R response calculated using this model and that observed experimentally, and was presented in Fig. 11.5. The magnitude of the F-R response observed experimentally could not be accounted for by just considering the increasing number of granules contacting the electrode. The model may be more accurate if it included the effect of pressure-sensitive conduction pathways within the granules, activated through applied force. Nevertheless, the model was useful predictive tool for understanding how sensor parameters such as the depth of the air-gap and the thickness of the flexible ITO electrode would impact on the F-R response.

Chapter 12 described an experimental study of the intrinsic pressure-sensitivity of the electrical conductivity of the granules. Here, the aim was to understand and quantify the physical basis of any pressure-enhanced conduction within the granules. To achieve this, an experimental technique was developed so that the number of granules contacted by the electrode remained constant with applied force. This was achieved by evaporating electrical contacts ('capping electrodes') onto defined 'test areas' of the PS surface, to electrically link all granules within that region. Then, force was applied using spring-contact test probes, whose diameter matched that of the capping electrodes. The F-R response of test areas of varying size were measured, for both increasing and decreasing force. Overall, as the size of the test area decreased, the percentage decrease in resistance between initial contact and the maximum force increased. Significant evidence of a force-sensitive resistance was evident for the smaller test areas, as was shown in Fig. 12.4. Smaller test areas meant that the force imparted by the probe was spread over fewer granules, such that each granule experienced a larger compressive force.

Overall, the repeatability of the F-R response of the test areas was poor. When removing the force, the resistance rarely attained its original value, and this was also found for repeated

force sweeps on the same test area. Additionally, different test areas with the same size did not show identical F-R behaviour. This behaviour was partly attributed to the intrinsic variability within the complex granule network in the test areas, and partly to limitations in the experimental design. Because of the geometry of the samples, the resistance was measured using a two-point method, so contact resistance between probe and capping electrode could not be neglected. This contact resistance was likely to be dependent on the force applied, and therefore may have partly obscured the F-R properties of the granules.

To understand the physical basis of the pressure-sensitive conduction the current-voltage (I-V) characteristics of the test areas were analysed. As for the F-R response, the I-V behaviour also showed variation in the form of hysteresis, where differences in current flow were observed between increasing and decreasing voltage sweeps. This effect was maximised for smaller test areas, where the hysteresis also remained during repeated sweeps on the same test area. Charge trapping mechanisms could be attributed to the instances where the current on the up-sweep was lower than for the down-sweep, which often occurred in the first voltage sweep performed at each applied force. Here, trap sites within the granule were filled as voltage was initially ramped up. When the sites were full, subsequent current flow contributed to the electrical current even when the voltage was then decreased. However, in many instances the current flow on the up-sweep was slightly larger than for the down-sweep. This was harder to explain and is not yet fully understood, although it could be linked to a dynamic granule resistance which was changing throughout the measurement period.

In an attempt to better understand the conduction behaviour, the decreasing voltage sweeps were analysed by fitting two models to the IV data. The random resistor network (RRN) model gave an excellent statistical fit to the data. Here, the total current was modelled as the sum of a linear and quadratic dependence on voltage. Above 0.7 N, it was shown that the linear contribution to the current increased with force at the expense of the non-linear contribution, as shown in Fig. 12.14. This was attributed to an increasing number of direct, percolative, conduction pathways forming as the granule was compressed, as the constituent particles within the granule were brought closer together. However, due to the limitations of the model the exact physical nature of the non-linear conduction pathways could not be determined. To this end a second model, derived from the physical principles of quantum tunnelling mechanisms, was also applied to the IV data. In this model, the non-linear contribution to current was directly linked to the specific tunnelling mechanism, as well as the magnitude of the tunnelling current and the probability of successful tunnelling events. Unfortunately, this model did not fit well to the data and large variations in the model parameters were obtained, giving limited physical insight. Finally, it is important to note that, whilst this chapter suggested that pressure-sensitive conduction within the granules may occur, the forces required to activate this response are significantly larger than what the granules experienced during standard operation of the touchscreen sensor.

In future work, it is necessary to first modify the experimental design such that the contact resistance between the probe and the capping electrode is negated, by utilising a four-point measurement system. When contact resistance is eliminated, the magnitude of the F-R response of the granules should be determined with greater certainty. This would also remove the contribution of the contact resistance on the IV sweeps. Measurements of the electrical flicker noise using the same experimental set-up for direct granule contact may also shed light on the nature of electrical conduction. In this thesis, the flicker noise measurements could not give conclusive information on the nature of the electrical conduction. This is partly because the experimental set-up used measured the flicker noise through a full sensor device. This meant that the increasing contact area between probe and sensor with increasing applied force could also have contributed to the noise characteristics.

In the work presented in chapter 10, only one configuration of PS layer was tested. By extending the range of granule number densities tested, additional data could also be collected in order to corroborate the results presented here. This would confirm the link between the granule distribution within the PS layer and the variability and sensitivity of the F-R response.

In order to bring together the results from parts I and II of this thesis, in future work the PS layers could be fabricated from granules with different physical properties. For example, by extending the work presented in chapter 12 to granules with different porosities, the link between porosity and electrical conduction within the granule may be better understood. Granules which exhibit a large degree of elastic deformation under applied force may lead to enhanced conduction through quantum tunnelling mechanisms. From a full understanding of how internal structure may be used to tailor the electrical response of the granule, and therefore of the touchscreen assembly as a whole, the full potential of application-tailored granules may be unlocked. This would enable the fabrication of pressure-sensitive touchscreens whose resistance response could be controlled solely by modification of the functional granules contained within, through a detailed understanding of the granulation process.

Throughout this thesis, one particular device geometry was considered. Here, the nanocomposite granules were assembled into a touchscreen device, where the granule-containing layer was sandwiched between two transparent electrodes. The focus of the thesis was on developing the granule-containing layer, and tailoring the individual granules and the distribution of the granules to control the functional force-sensitive response. In this regard, chapter 10 showed how it was possible to modify the light transmission through the PS layer, and also the variability and the sensitivity of the force-sensitive resistance of the device, through control of the granule distribution within the PS layer. Chapter 12 showed how force-sensitive

conduction mechanisms within each individual granule may also contribute to the overall response of the touchscreen device, although in this case the effect was shown to be significant only at larger forces beyond the standard operating conditions of a touchscreen.

However, it is important to note that the functional response may also be tailored through optimisation of the device geometry. For example in the force sensing interface developed by 3M, it was demonstrated that the sensitivity of the response was dependent on the air gap between electrode and sensing interface, as shown in Fig. 2.9. Similarly, in the work presented here in chapter 11, simulations showed that the force sensitivity could be tailored through adjusting the depth of the air gap. In addition, other device parameters such as the flexibility (Young's modulus) and thickness of the electrode substrate can also be used to tailor the electrical response of the touchscreen. For example, when detection of larger forces is necessary, a combination of thick, inflexible electrodes coupled with a larger air gap may be implemented. For highly sensitive detection of the lightest touches, a thin flexible electrode with a small air-gap may be used. In future work, each of these parameters should be explored and linked to the predictions of the simulation.

Finally, other device geometries such as the 6 mm circular sensors (see section 9.2.5), may also be worthy of future development. These sensors represent discrete, force-sensing buttons, as opposed to a continuous location-tracking touchscreens. In chapter 2, the concept of hybrid touch sensing was introduced. Here, location sensing is achieved through (usually) projected capacitive sensing, and force sensitivity is realised through the addition of discrete force sensors underneath the interface. The force signals detected by each sensor can be used to calculate the total force the user imparts to the interface. If these sensors were themselves transparent, this principle can be extended to transparent interfaces (touchscreens) where the force sensors lie directly underneath the cover glass, above the display. This method of force-detection is of particular interest as it can be integrated into the capacitive sensing systems which currently dominate the touch sensing market.

Appendix A

Calculation of Beam Deflections

This Appendix describes the derivation of equations 8.2 and 8.3 presented in chapter 8. The principles of such derivations are described in detail in many engineering text books dealing with statically indeterminate beam systems [209, 291–293].

Consider a uniformly distributed load w, applied non-centrally to a beam of length L between positions a and b, such that the total force applied is $w \times (b - a)$. This is shown in Fig. A.1(a). First, it is necessary to determine the bending moment M, which is then inserted into equation 8.1. This will be dependent on the reactive moments at the supports, M_A and M_B, as well as the reaction force supplied by the support, R_A and R_B.

The bending moment can be determined by considering the free body diagram of the beam, as is shown in Fig. A.1(a). However, due to the complex nature of the loading scenario, it is useful to use the principle of superposition for determining M. The principle of superposition

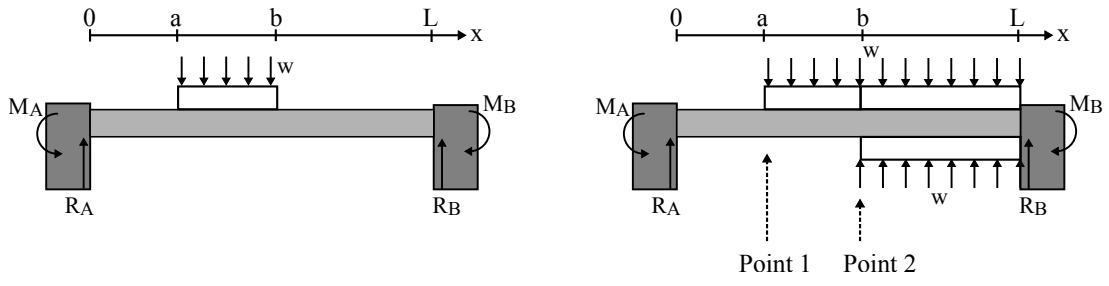

(a) (b)

FIGURE A.1: Schematic of a uniformly distributed load applied non-centrally to a beam of length L between positions a and b. M_A and M_B are the bending moments at points A and B, at each end of the beam, and similarly R_A and R_B are the reaction forces. The beam loaded as shown in (b) is equivalent to that shown in (a), through the principle of superposition.

states that the loaded beam shown in Fig. A.1(b) is equivalent to that shown in Fig. A.1(a). The latter system is much simpler to analyse. Working left to right along the beam::

$$M = M_A - R_A x + \frac{w[x-a]^2}{2} - \frac{w[x-b]^2}{2} \tag{A.1}$$

The terms in square brackets are Macauley terms and act to simplify the expression [291]. They are only activated when x is larger than a or b, respectively, such that the term inside the square bracket is always positive. When x is smaller than a or b, the term inside the bracket becomes zero and does not contribute to M. Hence, the third term in equation A.1 is only 'switched on' when point 1 in Fig. A.1(b) is reached. Until this point, $[x-a]$ is negative and therefore is set to zero. Similarly, at point 2, $[x-b]$ is switched on. This term counteracts the previous term for all beam lengths greater than b, as is required for the principle of superposition.

Also, note that by considering the beam from right to left, a similar expression would be calculated using the terms M_B and R_B.

Then, using equation 8.1:

$$EIy'' = -M = -M_A + R_A x - \frac{w[x-a]^2}{2} + \frac{w[x-b]^2}{2} \tag{A.2}$$

This can be integrated twice, *w.r.t* x, to obtain an expression for y, the beam deflection. Note that when integrating, the Macauley terms are treated as variables, i.e. these terms are integrated *w.r.t* $[x-a]$ and $[x-b]$:

$$EIy = \frac{R_A x^3}{6} - \frac{M_A x^2}{2} - \frac{w[x-a]^4}{24} + \frac{w[x-b]^4}{24} + Cx + D' \tag{A.3}$$

By using the boundary conditions that both y and y' are 0 when $x = 0$ or $x = L$, the constants C and D are set to zero.

Now, it is necessary to derive terms for M_A and R_A. This is done by considering an infinitesimal portion of the uniform distributed load ∂x a distance x along the beam, as shown in Fig. A.2. In the limit $\partial x \to 0$, ∂x can be treated as a point load. R_A and M_A can be easily calculated for point loads. Using the approach described in [209], it can be shown that:

$$dM_A = -w\partial x \times \frac{x(L-x)^2}{L^2} \tag{A.4}$$

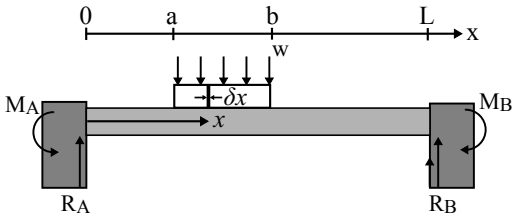

FIGURE A.2: Schematic of a uniformly distributed load applied non-centrally to a beam of length L between positions a and b. When calculating M_A and R_A, an infinitesimal part of the uniformly distributed load, ∂x, at a distance x along the beam, is considered. In the limit $\partial x \to 0$, ∂x can be treated as a point load.

Therefore:

$$M_A = \int dM_A = \int_a^b \frac{w}{L^2} x(L-x)^2 dx. \tag{A.5}$$

By integrating this equation between a and b the following result is obtained:

$$M_A = \frac{-w}{L^2}\left[\frac{L^2}{2}\left(b^2-a^2\right) - \frac{2L}{3}\left(b^3-a^3\right) + \frac{1}{4}\left(b^4-a^4\right)\right]. \tag{A.6}$$

Similarly, for R_A a similar approach is considered. Using the approach described in [292], it can be shown that:

$$R_A = \int dR_A = \int_a^b \frac{w}{L^3}(L-x)^2(L+2x)dx. \tag{A.7}$$

By integrating this equation between a and b the following result is obtained:

$$R_A = \frac{w}{L^3}\left[L^3\left(b-a\right) - L\left(b^3-a^3\right) + \frac{1}{2}\left(b^4-a^4\right)\right]. \tag{A.8}$$

Bibliography

[1] R. S. Dahiya, G. Metta, M. Valle, and G. Sandini, "Tactile Sensing; From Humans to Humanoids," *IEEE Transactions on Robotics*, vol. 26, pp. 1–20, Feb 2010.

[2] M. L. Hammock, A. Chortos, B. C. K. Tee, J. B. H. Tok, and Z. Bao, "25th anniversary article: The evolution of electronic skin (E-Skin): A brief history, design considerations, and recent progress," *Advanced Materials*, vol. 25, no. 42, pp. 5997–6038, 2013.

[3] S. J. Dempsey, M. Szablewski, and D. Atkinson, "Tactile sensing in human–computer interfaces: The inclusion of pressure sensitivity as a third dimension of user input," *Sensors and Actuators A: Physical*, vol. 232, pp. 229–250, 2015.

[4] The Economist, "Planet of the phones." [Magazine], 28 Feb 2015. Available online at http://www.economist.com/news/leaders/21645180-smartphone-ubiquitous-addictive-and-transformative-planet-phones, accessed Nov 2015.

[5] Apple Inc., "Apple unveils Apple Watch–Apple's most personal device ever," 2014. [Press Release] Available online at https://www.apple.com/uk/pr/, accessed Apr 2015.

[6] C. Lussey, P. J. Laughlin, A. Graham, D. Bloor, and D. J. Lussey, "Pressure sensitive polymer composite material adapted for touch screen," Mar 7 2013. US Patent App. 14/007,232.

[7] D. Lussey, "Polymer composition," Jan 23 1998. US Patent 6,291,568.

[8] D. Bloor, K. Donnelly, P. J. Hands, P. J. Laughlin, and D. Lussey, "A metal-polymer composite with unusual properties," *Journal of Physics D: Applied Physics*, vol. 38, no. 16, pp. 2851–2860, 2005.

[9] D. Bloor, A. Graham, E. J. Williams, P. J. Laughlin, and D. Lussey, "Metal-polymer composite with nanostructured filler particles and amplified physical properties," *Applied Physics Letters*, vol. 88, no. 10, p. 102103, 2006.

[10] P. J. W. Hands, P. J. Laughlin, and D. Bloor, "Metal–polymer composite sensors for volatile organic compounds: Part 1. Flow-through chemi-resistors," *Sensors and Actuators B: Chemical*, vol. 162, no. 1, pp. 400–408, 2012.

[11] A. Graham, P. J. Laughlin, and D. Bloor, "Metal–polymer composite sensors for volatile organic compounds: Part 2. Stand alone chemi-resistors," *Sensors and Actuators B: Chemical*, vol. 177, pp. 507–514, 2013.

[12] D. Lussey, D. Bloor, P. J. Laughlin, A. Graham, and C. Hilsum, "Electrically responsive composite material, a method of manufacture and a transducer produced using said material," May 28 2013. US Patent 8,449,974.

[13] V. Subramanian, J. B. Chang, A. de la Fuente Vornbrock, D. C. Huang, L. Jagannathan, F. Liao, B. Mattis, S. Molesa, D. R. Redinger, D. Soltman, S. K. Volkman, and Q. Zhang, "Printed electronics for low-cost electronic systems: Technology status and application development," in *34th European Solid-State Circuits Conference*, pp. 17–24, IEEE, 2008.

[14] W. J. Guan, Y. Li, Y. Q. Chen, X. B. Zhang, and G. Q. Hu, "Glucose biosensor based on multi-wall carbon nanotubes and screen printed carbon electrodes," *Biosensors and Bioelectronics*, vol. 21, no. 3, pp. 508–512, 2005.

[15] L. Setti, A. Fraleoni-Morgera, B. Ballarin, A. Filippini, D. Frascaro, and C. Piana, "An amperometric glucose biosensor prototype fabricated by thermal inkjet printing," *Biosensors and Bioelectronics*, vol. 20, no. 10, pp. 2019–2026, 2005.

[16] C. Reig and E. Avila-Navarro, "Printed antennas for sensor applications: A review," *Sensors Journal, IEEE*, vol. 14, no. 8, pp. 2406–2418, 2014.

[17] L. L. Lavery, G. L. Whiting, and A. C. Arias, "All ink-jet printed polyfluorene photosensor for high illuminance detection," *Organic Electronics*, vol. 12, no. 4, pp. 682–685, 2011.

[18] T. Unander and H. E. Nilsson, "Characterization of printed moisture sensors in packaging surveillance applications," *Sensors Journal, IEEE*, vol. 9, no. 8, pp. 922–928, 2009.

[19] H. Andersson, A. Manuilskiy, T. Unander, C. Lidenmark, S. Forsberg, and H. E. Nilsson, "Inkjet printed silver nanoparticle humidity sensor with memory effect on paper," *Sensors Journal, IEEE*, vol. 12, no. 6, pp. 1901–1905, 2012.

[20] M. Li, Y. T. Li, D. W. Li, and Y. T. Long, "Recent developments and applications of screen-printed electrodes in environmental assays – A review," *Analytica Chimica Acta*, vol. 734, pp. 31–44, 2012.

[21] W. Shen, "Properties of SnO_2 based gas-sensing thin films prepared by ink-jet printing," *Sensors and Actuators B: Chemical*, vol. 166, pp. 110–116, 2012.

[22] G. Walker, *Interactive Displays: Natural Human-Interface Technologies*, ch. Touch Sensing, pp. 27–106. John Wiley & Sons, 2014.

[23] M. Ramuz, B. C. K. Tee, J. B. H. Tok, and Z. Bao, "Transparent, optical, pressure-sensitive artificial skin for large-area stretchable electronics," *Advanced Materials*, vol. 24, no. 24, pp. 3223–3227, 2012.

[24] S. J. Woo, J. H. Kong, D. G. Kim, and J. M. Kim, "A thin all-elastomeric capacitive pressure sensor array based on micro-contact printed elastic conductors," *Journal of Materials Chemistry C: Materials for optical, magnetic and electronic devices*, vol. 2, no. 22, pp. 4415–4422, 2014.

[25] A. Diaz-Lantada, C. G. Bris, P. L. Morgado, and J. S. Maudes, "Novel system for bite-force sensing and monitoring based on magnetic near field communication," *Sensors*, vol. 12, no. 9, pp. 11544–11558, 2012.

[26] W. Tao, T. Liu, R. Zheng, and H. Feng, "Gait analysis using wearable sensors," *Sensors*, vol. 12, no. 2, pp. 2255–2283, 2012.

[27] T. Someya and T. Sekitani, "Printed skin-like large-area flexible sensors and actuators," *Procedia Chemistry*, vol. 1, no. 1, pp. 9–12, 2009. Proceedings of the Eurosensors XXIII conference.

[28] H. Yousef, M. Boukallel, and K. Althoefer, "Tactile sensing for dexterous in-hand manipulation in robotics-A review," *Sensors and Actuators A: Physical*, vol. 167, no. 2, pp. 171–187, 2011.

[29] M. I. Tiwana, S. J. Redmond, and N. H. Lovell, "A review of tactile sensing technologies with applications in biomedical engineering," *Sensors and Actuators A: Physical*, vol. 179, pp. 17–31, 2012.

[30] S. A. Brewster and M. Hughes, "Pressure-based text entry for mobile devices," in *Proceedings of the 11th International Conference on Human-Computer Interaction with Mobile Devices and Services*, p. 9, ACM, 2009.

[31] G. Wilson, C. Stewart, and S. A. Brewster, "Pressure-based menu selection for mobile devices," in *Proceedings of the 12th International Conference on Human Computer Interaction with Mobile Devices and Services*, pp. 181–190, ACM, 2010.

[32] K. Zhang, K. Douros, H. Li, H. Li, and Y. Wei, "Systems and methods for pressure-based authentication of an input on a touch screen," Mar 3 2011. US Patent App. 12/548,983.

[33] E. J. V. Backlund, H. Bengtsson, H. Heringslack, J. Sassi, O. K. Thörn, and P. Åberg, "User interface with three dimensional user input," Jan 7 2014. US Patent 8,625,882.

[34] S. Heo and G. Lee, "Force gestures: Augmenting touch screen gestures with normal and tangential forces," in *Proceedings of the 24th Annual ACM Symposium on User Interface Software and Technology*, pp. 621–626, ACM, 2011.

[35] G. Walker, "A review of technologies for sensing contact location on the surface of a display," *Journal of the Society for Information Display*, vol. 20, no. 8, pp. 413–440, 2012.

[36] R. Phares and M. Fihn, *Handbook of Visual Display Technology*, ch. Introduction to touchscreen technologies, pp. 935–974. Springer, 2012.

[37] G. Barrett and R. Omote, "Projected-capacitive touch technology," *Information Display*, vol. 26, no. 3, pp. 16–21, 2010.

[38] C. Kittel and P. McEuen, *Introduction to Solid State Physics*, vol. 8. Wiley New York, 1976.

[39] V. E. Bottom, "Measurement of the piezoelectric coefficient of quartz using the Fabry-Perot dilatometer," *Journal of Applied Physics*, vol. 41, no. 10, pp. 3941–3944, 1970.

[40] X. B. Wang, C. Song, D. M. Li, K. W. Geng, F. Zeng, and F. Pan, "The influence of different doping elements on microstructure, piezoelectric coefficient and resistivity of sputtered ZnO film," *Applied Surface Science*, vol. 253, no. 3, pp. 1639–1643, 2006.

[41] A. Decharat, S. Wagle, and F. Melandsø, "Effect of polymer electrode thickness on the acoustical properties of all-screen printed piezoelectric PVDF copolymer transducers," *Japanese Journal of Applied Physics*, vol. 53, no. 5S3, p. 05HB16, 2014.

[42] A. V. Shirinov and W. K. Schomburg, "Pressure sensor from a PVDF film," *Sensors and Actuators A: Physical*, vol. 142, no. 1, pp. 48–55, 2008.

[43] T. Julien, "Flexo-printed piezoelectric PVDF pressure sensors," 2012. Masters Thesis, Department of Chemistry, Tampere University of Technology, Tampere, Finland.

[44] T. Papakostas and N. White, "Screen printable polymer piezoelectrics," *Sensor Review*, vol. 20, no. 2, pp. 135–138, 2000.

[45] K. Omote, H. Ohigashi, and K. K. Koga, "Temperature dependence of elastic, dielectric, and piezoelectric properties of "single crystalline" films of vinylidene fluoride trifluoroethylene copolymer," *Journal of Applied Physics*, vol. 81, no. 6, pp. 2760–2769, 1997.

[46] C. Rendl, P. Greindl, M. Haller, M. Zirkl, B. Stadlober, and P. Hartmann, "PyzoFlex: Printed piezoelectric pressure sensing foil," in *Proceedings of the 25th Annual ACM Symposium on User Interface Software and Technology*, pp. 509–518, ACM, 2012.

[47] M. Zirkl, G. Scheipl, B. Stadlober, P. Hartmann, M. Haller, C. Rendl, and P. Greindl, "PyzoFlex: A printed piezoelectric pressure sensing foil for human machine interfaces," in *SPIE Organic Photonics & Electronics*, pp. 883124–883124, International Society for Optics and Photonics, 2013.

[48] H. K. Kim, S. G. Lee, and K. S. Yun, "Capacitive tactile sensor array for touch screen application," *Sensors and Actuators A: Physical*, vol. 165, no. 1, pp. 2–7, 2011.

[49] H. K. Kim, S. G. Lee, J. E. Han, T. R. Kim, S. U. Hwang, S. D. Ahn, I. K. You, K. I. Cho, T. K. Song, and K. S. Yun, "Transparent and flexible tactile sensor for multi touch

screen application with force sensing," in *International Solid-State Sensors, Actuators and Microsystems Conference*, pp. 1146–1149, 2009.

[50] K. Kim, K. Shin, J. H. Han, K. R. Lee, W. H. Kim, K. B. Park, B. K. Ju, and J. J. Pak, "Deformable single wall carbon nanotube electrode for transparent tactile touch screen," *Electronics Letters*, vol. 47, no. 2, pp. 118–120, 2011.

[51] Samsung, *User Manual TL220 v1.2*, 2009. [User Manual] Available online at: http://www.samsung.com/us/support/owners/product/EC-TL220ZBPRUS accessed Nov 2015.

[52] R. J. Miller, S. Bisset, T. P. Allen, and G. Steinbach, "Object position detector," Dec 20 1994. US Patent 5,374,787.

[53] R. N. Rao, P. B. Tilley, A. V. Tungare, and Y. Wei, "Device and method for automated use of force sensing touch panels," Nov 21 2013. US Patent App. 13/038,235.

[54] S. Vadagave, S. Vojjala, and H. El-Khoury, "User interface with child-lock feature," Jun 26 2014. WO Patent App. PCT/US2013/070,333.

[55] D. A. Soss, "Advances in force-based touch panels," *Information Display*, vol. 23, no. 12, pp. 20–24, 2007.

[56] J. Elwell, "P-200L: Late-news poster: Sensing touch by sensing force," in *SID Symposium Digest of Technical Papers*, vol. 38, pp. 312–314, 2007.

[57] A. Mölne, "Integrated pressure sensitive lens assembly," Sep 18 2012. US Patent 8,269,731.

[58] D. E. Brown, C. D. Brown, and A. L. Mölne, "Integrated feature for friction less movement of force sensitive touch screen," Mar 27 2012. US Patent 8,144,453.

[59] R. Schediwy and K. Inscore, "Force sensing input device and method for determining force information," Jan 21 2014. US Patent 8,633,911.

[60] J. Wang and R. W. Lindeman, "ForceExtension: Extending isotonic position-controlled multi-touch gestures with rate-controlled force sensing for 3D manipulation," in *2013 IEEE Symposium on 3D User Interfaces (3DUI)*, pp. 3–6, 2013.

[61] C. Rendl, P. Greindl, K. Probst, M. Behrens, and M. Haller, "Presstures: Exploring pressure-sensitive multi-touch gestures on trackpads," in *Proceedings of the 32nd Annual ACM Conference on Human Factors in Computing Systems*, pp. 431–434, ACM, 2014.

[62] Apple Inc., "Apple unveils all-new MacBook," 2015. [Press Release] Available online at https://www.apple.com/uk/pr/, accessed Apr 2015.

[63] J. T. Bernstein, A. Cieplinski, B. W. Degner, D. Kerr, P. Kessler, P. Puskarich, M. H. Coelho, and A. Pance, "Touch pad with force sensors and actuator feedback," Jan 21 2014. US Patent 8,633,916.

[64] N. Parivar and W. C. Westerman, "Gesture and touch input detection through force sensing," Jan 30 2014. US Patent App. 13/559,577.

[65] Y. Ogawa, "Pressure sensitive stylus pen," Oct 15 1996. US Patent 5,565,632.

[66] F. L. Lu, P. H. Wu, Z. P. He, R. S. You, and C. W. Pan, "Stylus and capacitive pressure sensing element employed therein," Mar 6 2014. US Patent App. 13/654,627.

[67] F. Fado, T. L. Wong, G. F. Verrier, R. L. Donaldson, and P. D. Kowalewski, "Digitizing stylus having capacitive pressure and contact sensing capabilities," Aug 1 1995. US Patent 5,438,275.

[68] Y. Fukushima, "Pressure sensitive element and a stylus pen with pressure sensitive function," May 27 1997. US Patent 5,633,471.

[69] B. L. Weaver and K. M. Kropp, "Stylus with pressure sensitive membrane," Nov 8 2012. US Patent App. 13/102,457.

[70] Z. J. Zeliff, Y. H. Li, K. Perpich, Y. T. Huang, and K. Y. Lu, "Stylus with pressure sensor," Dec 5 2013. US Patent App. 13/909,479.

[71] Y. Stern, R. Zachut, Y. Tzafrir, E. Mann, O. Tamir, and A. Kalmanovich, "Pressure sensitive stylus for a digitizer," Sep 17 2013. US Patent 8,536,471.

[72] G. Largillier, "Developing the first commercial product that uses multi-touch technology," *Information Display*, vol. 23, no. 12, pp. 14–18, 2007.

[73] D. R. Cairns, G. P. Crawford, and A. F. Chernefsky, "P-7: Wear resistance of indium tin oxide coatings on polyethylene terephthalate substrates for touchscreen applications," *SID Symposium Digest of Technical Papers*, vol. 32, no. 1, pp. 574–577, 2001.

[74] H. Li, Y. Wei, H. Li, S. Young, D. Convey, J. Lewis, and P. Maniar, "Late-news paper: Multitouch pixilated force sensing touch screen," *SID Symposium Digest of Technical Papers*, pp. 455–458, 2009.

[75] H. Li, P. Maniar, and Y. Wei, "Transparent force sensor and method of fabrication," Jan 31 2013. US Patent App. 12/725,699.

[76] G. Goncalves, L. Hirsch, P. Joguet, J. Olivier, and G. Wantz, "Method for the production of a transparent film, in particular for a transparent array-type tactile sensor," Sep 13 2012. WO Patent App. 12/050,439.

[77] J. S. Leng, W. M. Huang, X. Lan, Y. J. Liu, and S. Y. Du, "Significantly reducing electrical resistivity by forming conductive Ni chains in a polyurethane shape-memory polymer/carbon-black composite," *Applied Physics Letters*, vol. 92, no. 20, p. 204101, 2008.

[78] X. L. Xie, Y. W. Mai, and X. P. Zhou, "Dispersion and alignment of carbon nanotubes in polymer matrix: A review," *Materials Science and Engineering R: Reports*, vol. 49, no. 4, pp. 89–112, 2005.

[79] B. W. Steinert and D. R. Dean, "Magnetic field alignment and electrical properties of solution cast PET-carbon nanotube composite films," *Polymer*, vol. 50, no. 3, pp. 898–904, 2009.

[80] R. Divigalpitiya, D. E. Livingstone, R. S. Moshrefzadeh, and E. M. Cross, "Pressure activated switch and touch panel," Oct 26 2004. US Patent 6,809,280.

[81] R. Divigalpitiya, P. J. Chen, D. A. Kanno, G. Miholics, V. Patel, and M. T. Scholz, "Force sensing membrane," Aug 28 2007 Aug 28. US Patent 7,260,999.

[82] F. N. Eventoff, "Electronic pressure sensitive transducer apparatus," Feb 2 1982. U.S. Patent 4,314,227.

[83] S. Yaniger, "Stannous oxide force transducer and composition," Mar 22 1994. U.S. Patent 5,296,837.

[84] B. Krivopal, "Pressure sensitive ink means, and methods of use," Nov 23 1999 Nov. U.S. Patent 5,989,700.

[85] A. J. Webb, "Nanoscale morphology and electrical behaviour of a pressure sensitive ink," 2010. Masters Thesis, Department of Physics, Durham University, UK.

[86] N. K. Rana, "Application of force sensing resistor (FSR) in design of pressure scanning system for plantar pressure measurement," in *Second International Conference on Computer and Electrical Engineering (ICCEE'09)*, vol. 2, pp. 678–685, 2009.

[87] B. Choi, H. R. Choi, and S. Kang, "Development of tactile sensor for detecting contact force and slip," in *IEEE/RSJ International Conference on Intelligent Robots and Systems*, pp. 2638–2643, 2005.

[88] E. R. Miranda and M. M. Wanderley, *New Digital Musical Instruments: Control and Interaction Beyond the Keyboard*, vol. 21 of *The Computer Music and Digital Audio Series*, pp. 109–152. AR Editions, Inc., 2006.

[89] S. I. Yaniger, "Force sensing resistors: A review of the technology," in *Electro International, 1991*, pp. 666–668, 1991.

[90] C. M. A. Ashruf, "Thin flexible pressure sensors," *Sensor Review*, vol. 22, no. 4, pp. 322–327, 2002.

[91] A. Hollinger and M. M. Wanderley, "Evaluation of commercial force-sensing resistors," in *Proceedings of International Conference on New Interfaces for Musical Expression*, 2006.

[92] C. Lebossé, P. Renaud, B. Bayle, and M. de Mathelin, "Modeling and evaluation of low-cost force sensors," *IEEE Transactions on Robotics*, vol. 27, no. 4, pp. 815–822, 2011.

[93] I. D. Rosenberg, A. Grau, C. Hendee, N. Awad, and K. Perlin, "IMPAD: An inexpensive multi-touchpressure acquisition device," in *CHI'09 Extended Abstracts on Human Factors in Computing Systems*, pp. 3217–3222, ACM, 2009.

[94] S. N. Bathiche, "Computer keyboard with quantitatively force-sensing keys," Aug 14 2007. US Patent 7,256,768.

[95] L. Shi, Y. Feng, and C. C. Sun, "Massing in high shear wet granulation can simultaneously improve powder flow and deteriorate powder compaction: A double-edged sword," *European Journal of Pharmaceutical Sciences*, vol. 43, no. 1, pp. 50–56, 2011.

[96] J. Sruti, C. N. Patra, S. Swain, K. C. Panigrahi, A. P. Patro, S. Beg, S. C. Dinda, and M. E. B. Rao, "Improvement in the dissolution rate and tableting properties of cefuroxime axetil by melt-granulated dispersion and surface adsorption," *Acta Pharmaceutica Sinica B*, vol. 3, no. 2, pp. 113–122, 2013.

[97] H. Javaheri, P. Carter, and A. A. Elkordy, "Wet granulation to overcome liquisolid technique issues of poor flowability and compactibility: A study to enhance Glibenclamide dissolution," *Journal of Pharmaceutics and Drug Development*, vol. 1, no. 5, pp. 1–12, 2014.

[98] I. N. Tikhonova, A. M. Popov, N. V. Tikhonov, and V. V. Tikhonov, "Harnessing the capabilities of spray granulation in the food industry for the production of functional foods," *Procedia Chemistry*, vol. 10, pp. 419–423, 2014.

[99] M. M. Hanafi, S. M. Eltaib, and M. B. Ahmad, "Physical and chemical characteristics of controlled release compound fertiliser," *European Polymer Journal*, vol. 36, no. 10, pp. 2081–2088, 2000.

[100] S. P. E. Forsmo, A. J. Apelqvist, B. M. T. Björkman, and P. O. Samskog, "Binding mechanisms in wet iron ore green pellets with a bentonite binder," *Powder Technology*, vol. 169, no. 3, pp. 147–158, 2006.

[101] E. M. Holt, "The properties and forming of catalysts and absorbents by granulation," *Powder Technology*, vol. 140, no. 3, pp. 194–202, 2004.

[102] S. M. Iveson, J. D. Litster, K. Hapgood, and B. J. Ennis, "Nucleation, growth and breakage phenomena in agitated wet granulation processes: A review," *Powder Technology*, vol. 117, pp. 3–39, 2001.

[103] A. D. Salman, M. Hounslow, and J. P. K. Seville, *Granulation*. No. 11 in Handbook of Powder Technology, Elsevier Science B.V., 2007.

[104] J. D. Litster and B. J. Ennis, *The Science and Engineering of Granulation Processes*, vol. 15 of *Particle Technology Series*. Springer Science & Business Media, 2004.

[105] E. Y. Bormashenko, *Wetting of Real Surfaces*, vol. 19 of *Studies in Mathematical Physics*. Walter de Gruyter, 2013.

[106] T. Schæfer and C. Mathiesen, "Melt pelletization in a high shear mixer: IX. Effects of binder particle size," *International Journal of Pharmaceutics*, vol. 139, pp. 139–148, 1996.

[107] A. C. Scott, M. J. Hounslow, and T. Instone, "Direct evidence of heterogeneity during high-shear granulation," *Powder Technology*, vol. 113, pp. 205–213, 2000.

[108] D. M. Newitt and J. M. Conway-Jones, "A contribution to the theory and practice of granulation," *Transactions of the Institute of Chemical Engineers*, vol. 36, no. 422, 1958.

[109] C. D. Willet, M. J. Adams, S. A. Johnson, and J. P. K. Seville, "Capillary bridges between two spherical bodies," *Langmuir*, vol. 16, pp. 9396–9405, 2001.

[110] H. Rumpf, *Agglomeration, AIME*, ch. The Strength of Granules and Agglomerates, pp. 379–418. Interscience, New York, 1964.

[111] S. M. Iveson and J. D. Litster, "Fundamental studies of granule consolidation Part 2: Quantifying the effects of particle and binder properties," *Powder Technology*, vol. 99, pp. 243–250, 1998.

[112] B. J. Ennis, G. Tardos, and R. Pfeffer, "A microlevel-based characterization of granulation phenomena," *Powder Technology*, vol. 65, no. 1–3, pp. 257–272, 1991.

[113] L. X. Liu, J. D. Litster, S. M. Iveson, and B. J. Ennis, "Coalescence of deformable granules in wet granulation processes," *A.I.Ch.E. Journal*, vol. 46, no. 3, pp. 529–539, 2000.

[114] S. M. Iveson and J. D. Litster, "Growth regime map for liquid-bound granules," *A.I.Ch.E. Journal*, vol. 44, no. 7, pp. 1510–1518, 1998.

[115] S. M. Iveson, P. A. L. Wauters, S. Forrest, J. D. Litster, G. M. H. Meesters, and B. Scarlett, "Growth regime map for liquid-bound granules: Further development and experimental validation," *Powder Technology*, vol. 117, no. 1–2, pp. 83–97, 2001.

[116] J. S. Ramaker, M. A. Jelgersma, P. Vonk, and N. W. F. Kossen, "Scale-down of a high-shear pelletisation process: Flow profile and growth kinetics," *International Journal of Pharmaceutics*, vol. 166, no. 1, pp. 89–97, 1998.

[117] K. van den Dries, O. M. de Vegt, V. Girard, and H. Vromans, "Granule breakage phenomena in a high shear mixer; Influence of process and formulation variables and consequences on granule homogeneity," *Powder Technology*, vol. 133, no. 1-3, pp. 228–236, 2003.

[118] G. I. Tardos, M. Irfan-Khan, and P. R. Mort, "Critical parameters and limiting conditions in binder granulation of fine powders," *Powder Technology*, vol. 94, no. 3, pp. 245–258, 1997.

[119] S. T. Keningley, P. C. Knight, and A. D. Marson, "An investigation into the effects of binder viscosity on agglomeration behaviour," *Powder Technology*, vol. 91, no. 2, pp. 95–103, 1997.

[120] R. Ho, S. E. Dilworth, D. R. Williams, and J. Y. Y. Heng, "Role of surface chemistry and energetics in high shear wet granulation," *Industrial and Engineering Chemistry Research*, vol. 50, pp. 9642–9649, 2011.

[121] F. Thielman, M. Naderi, M. A. Ansari, and F. Stepanek, "The effect of primary particle surface energy on agglomeration rate in fluidised bed wet granulation," *Powder Technology*, vol. 181, pp. 160–168, 2008.

[122] D. Zhang, J. H. Flory, S. Panmai, U. Batra, and M. J. Kaufman, "Wettability of pharmaceutical solids: Its measurement and influence on wet granulation," *Colloids and Surfaces A: Physicochemical and Engineering Aspects*, vol. 206, pp. 547–554, 2002.

[123] O. Planinšek, R. Pišek, A. Trojak, and S. Srčič, "The utilization of surface free-energy parameters for the selection of a suitable binder in fluidised bed granulation," *International Journal of Pharmaceutics*, vol. 207, pp. 77–88, 2000.

[124] A. C. Scott, M. J. Hounslow, and T. Instone, "An investigation into the kinetics of liquid distribution and growth in high shear mixer agglomeration," *Powder Technology*, vol. 97, pp. 246–257, 1998.

[125] J. D. Osborne, R. P. J. Sochon, J. J. Cartwright, D. G. Doughty, M. J. Hounslow, and A. D. Salman, "Binder addition methods and binder distribution in high shear and fluidised bed granulation," *Chemical Engineering Research and Design*, vol. 89, pp. 553–559, 2011.

[126] G. K. Reynolds, C. A. Biggs, A. D. Salman, and M. J. Hounslow, "Non–uniformity of binder distribution in high-shear granulation," *Powder Technology*, vol. 140, pp. 203–208, 2004.

[127] B. M. J. Tan, Z. H. Loh, J. L. P. Soh, C. V. Liew, and P. W. S. Heng, "Distribution of a viscous binder during high shear granulation – Sensitivity to the method of delivery and its impact on product properties," *International Journal of Pharmaceutics*, vol. 460, no. 1–2, pp. 255–263, 2014.

[128] M. Fujiwara, M. Dohi, T. Otsuka, K. Yamashita, and K. Sako, "Influence of binder droplet dimension on granulation rate during fluidized bed granulation," *Chemical and Pharmaceutical Bulletin (Tokyo)*, vol. 61, no. 3, pp. 320–325, 2013.

[129] S. M. Iveson, J. D. Litster, and B. J. Ennis, "Fundamental studies of granule consolidation Part 1: Effects of binder content and binder viscosity," *Powder Technology*, vol. 88, pp. 15–20, 1996.

[130] P. J. T. Mills, J. P. K. Seville, P. C. Knight, and M. J. Adams, "The effect of binder viscosity on particle agglomeration in a low shear mixer/agglomerator," *Powder Technology*, vol. 113, no. 1–2, pp. 140–147, 2000.

[131] H. Zhai, S. Li, D. S. Jones, G. M. Walker, and G. P. Andrews, "The effect of the binder size and viscosity on agglomerate growth in fluidised hot melt granulation," *Chemical Engineering Journal*, vol. 164, no. 2-3, pp. 275–284, 2010.

[132] A. Johansen and T. Schæfer, "Effects of physical properties of powder particles on binder liquid requirement and agglomerate growth mechanisms in a high shear mixer," *European Journal of Pharmaceutical Sciences*, vol. 14, pp. 135–147, 2001.

[133] A. Johansen and T. Schæfer, "Effects of interactions between powder particle size and binder viscosity on agglomerate growth mechanisms in a high shear mixer," *European Journal of Pharmaceutical Sciences*, vol. 12, no. 3, pp. 297–309, 2001.

[134] T. Schæfer and D. Johnson and A. Johansen, "Effects of powder particle size and binder viscosity on intergranular and intragranular particle size heterogeneity during high shear granulation," *European Journal of Pharmaceutical Sciences*, vol. 21, pp. 525–531, 2004.

[135] M. B. Mackaplow, L. A. Rosen, and J. N. Michaels, "Effect of primary particle size on granule growth and endpoint determination in high-shear wet granulation," *Powder Technology*, vol. 108, pp. 32–45, 2000.

[136] R. Ramachandran, M. A. Ansari, A. Chaudhury, A. Kapadia, A. V. Prakash, and F. Stepanek, "A quantitative assessment of the influence of primary particle size polydispersity on granule inhomogeneity," *Chemical Engineering Science*, vol. 71, pp. 104–110, 2012.

[137] P.C. Knight and A. Johansen and H. G. Kristensen and T. Schæfer and J. P. K. Seville, "An investigation of the effects on agglomeration of changing the speed of a mechanical mixer," *Powder Technology*, vol. 110, no. 3, pp. 204–209, 2000.

[138] D. Oulahna, F. Cordier, L. Galet, and J. A. Dodds, "Wet granulation: The effect of shear on granule properties," *Powder Technology*, vol. 130, no. 1—3, pp. 238–246, 2003.

[139] N. Rahmanian, M. Ghadiri, X. Jia, and F. Stepanek, "Characterisation of granule structure and strength made in a high shear granulator," *Powder Technology*, vol. 192, no. 2, pp. 184–194, 2009.

[140] N. Rahmanian, A. Naji, and M. Ghadiri, "Effects of process parameters on granules properties produced in a high shear granulator," *Chemical Engineering Research and Design*, vol. 89, no. 5, pp. 512–518, 2011.

[141] H. G. Merkus, *Particle Size Measurements: Fundamentals, Practice, Quality*. Springer Science & Business Media, 2009.

[142] M. Batzill and U. Diebold, "The surface and materials science of tin oxide," *Progress in Surface Science*, vol. 79, no. 2, pp. 47–154, 2005.

[143] Z. Q. Li, Y. L. Yin, X. D. Liu, L. Y. Li, H. Liu, and Q. G. Song, "Electronic structure and optical properties of Sb-doped SnO_2," *Journal of Applied Physics*, vol. 106, no. 8, p. 083701, 2009.

[144] G. Jain and R. Kumar, "Electrical and optical properties of tin oxide and antimony doped tin oxide films," *Optical Materials*, vol. 26, no. 1, pp. 27–31, 2004.

[145] N. Naghavi, C. Marcel, L. Dupont, J. B. Leriche, and J. M. Tarascon, "On the electrochromic properties of antimony–tin oxide thin films deposited by pulsed laser deposition," *Solid State Ionics*, vol. 156, no. 3, pp. 463–474, 2003.

[146] M. I. B. Bernardi, S. Cava, C. O. Paiva-Santos, E. R. Leite, C. A. Paskocimas, and E. Longo, "Comparison of blue pigments prepared by two different methods," *Journal of the European Ceramic Society*, vol. 22, no. 16, pp. 2911–2919, 2002.

[147] D. W. Kim, D. S. Kim, Y. G. Kim, Y. C. Kim, and S. G. Oh, "Preparation of hard agglomerates free and weakly agglomerated antimony doped tin oxide (ATO) nanoparticles by coprecipitation reaction in methanol reaction medium," *Materials Chemistry and Physics*, vol. 97, no. 2, pp. 452–457, 2006.

[148] J. Zhang and L. Gao, "Synthesis and characterization of antimony-doped tin oxide (ATO) nanoparticles," *Inorganic Chemistry Communications*, vol. 7, no. 1, pp. 91–93, 2004.

[149] J. Zhang and L. Gao, "Synthesis and characterization of antimony-doped tin oxide (ATO) nanoparticles by a new hydrothermal method," *Materials Chemistry and Physics*, vol. 87, no. 1, pp. 10–13, 2004.

[150] Permaset, "PermaPrint Premium." [Technical Data Sheet]. Available online at: http://www.permaset.com.au/permaprint-premium/ (accessed May 2015).

[151] Dow Corning, "Xiameter® RTV-4234-T4 Base and Xiameter® T4/T4 O Curing Agent." [Product Data Sheet]. Available online at: www.xiameter.com/EN/Products/Pages/ProductLanding.aspx, accessed May 2015.

[152] F. Tenambergen, C. H. Maruiama, and K. Mäder, "Dual asymmetric centrifugation as an alternative preparation method for parenteral fat emulsions in preformulation development," *International Journal of Pharmaceutics*, vol. 447, no. 1, pp. 31–37, 2013.

[153] U. Massing, S. Cicko, and V. Ziroli, "Dual asymmetric centrifugation (DAC)–A new technique for liposome preparation," *Journal of Controlled Release*, vol. 125, no. 1, pp. 16–24, 2008.

[154] H. Schulz, B. Schimmoeller, S. E. Pratsinis, U. Salz, and T. Bock, "Radiopaque dental adhesives: Dispersion of flame-made Ta_2O_5/SiO_2 nanoparticles in methacrylic matrices," *Journal of Dentistry*, vol. 36, no. 8, pp. 579–587, 2008.

[155] H. Chen, O. Jacobs, W. Wu, G. Rüdiger, and B. Schädel, "Effect of dispersion method on tribological properties of carbon nanotube reinforced epoxy resin composites," *Polymer Testing*, vol. 26, no. 3, pp. 351–360, 2007.

[156] R. Fuhrer, C. M. Schumacher, M. Zeltner, and W. J. Stark, "Soft iron/silicon composite tubes for magnetic peristaltic pumping: Frequency-dependent pressure and volume flow," *Advanced Functional Materials*, vol. 23, no. 31, pp. 3845–3849, 2013.

[157] M. Landin, P. York, M. J. Cliff, R. C. Rowe, and A. J. Wigmore, "Scale-up of a pharmaceutical granulation in fixed bowl mixer-granulators," *International Journal of Pharmaceutics*, vol. 133, no. 1, pp. 127–131, 1996.

[158] M. Landin, P. York, M. J. Cliff, and R. C. Rowe, "Scale-up of a pharmaceutical granulation in planetary mixers," *Pharmaceutical Development and Technology*, vol. 4, no. 2, pp. 145–150, 1999.

[159] J. D. Litster, K. P. Hapgood, J. N. Michaels, A. Sims, M. Roberts, and S. K. Kameneni, "Scale-up of mixer granulators for effective liquid distribution," *Powder Technology*, vol. 124, no. 3, pp. 272–280, 2002.

[160] G. M. Walker, C. R. Holland, M. N. Ahmad, J. N. Fox, and A. G. Kells, "Drum granulation of NPK fertilizers," *Powder Technology*, vol. 107, no. 3, pp. 282–288, 2000.

[161] M. Cavinato, R. Artoni, M. Bresciani, P. Canu, and A. C. Santomaso, "Scale-up effects on flow patterns in the high shear mixing of cohesive powders," *Chemical Engineering Science*, vol. 102, pp. 1–9, 2013.

[162] B. Y. Shekunov, P. Chattopadhyay, H. H. Y. Tong, and A. H. L. Chow, "Particle size analysis in pharmaceutics: Principles, methods and applications," *Pharmaceutical Research*, vol. 24, no. 2, pp. 203–227, 2007.

[163] W. Pabst and E. Gregorova, "Characterization of particles and particle systems." [Technical Report], 2007. Institute of Chemical Technology, Prague.

[164] A. Rawle, "The importance of particle sizing to the coatings industry Part 1: Particle size measurement," *Advances in Colour Science and Technology*, vol. 5, no. 1, pp. 1–12, 2002.

[165] ISO 13322-1, "Particle Size Analysis – Image Analysis Methods – Part 1: Static image analysis methods," 2004. Available online at http://www.iso.org/iso/, accessed May 2015.

[166] J. I. Goldstein, D. E. Newbury, P. Echlin, D. C. Joy, C. Fiori, and E. Lifshin, *Scanning Electron Microscopy and X-ray Microanalysis. A Text for Biologists, Materials Scientists, and Geologists*. Plenum Publishing Corporation, 1981.

[167] M. Loretto, *Electron Beam Analysis of Materials (2nd Ed.)*. World Society Studies, Springer Netherlands, 1993.

[168] P. J. Goodhew, J. Humphreys, and R. Beanland, *Electron Microscopy and Analysis*. CRC Press, 2000.

[169] Retsch Technology, *Particle Analyzer CAMSIZER XT*. Available online at: http://www.retsch-technology.com/rt/products/, accessed May 2015.

[170] H. C. van de Hulst, *Light Scattering by Small Particles*, ch. 9: Rigorous scattering theory for spheres of arbitrary size (Mie theory). Courier Corporation, 1957.

[171] D. L. Phillips, "A technique for the numerical solution of certain integral equations of the first kind," *Journal of the ACM*, vol. 9, no. 1, pp. 84–97, 1962.

[172] S. Twomey, *Introduction to the Mathematics of Inversion in Remote Sensing and Indirect Measurements*, ch. Algebraic and geometric aspects of functions and function space. Elsevier, 2013.

[173] S. Röthele and H. Naumann and M. Heuer, "The application of Fraunhofer diffraction below 1 µm to particle size analysis from 0.1 µm to 2000 µm." [Technical Report], 1990. Available online at: https://www.sympatec.com/EN/LaserDiffraction_Process/Publications.html, accessed May 2015.

[174] P. A. L. Wauters, R. V. de Water, J. D. Litster, G. M. H. Meesters, and B. Scarlett, "Growth and compaction behaviour of copper concentrate granules in a rotating drum," *Powder Technology*, vol. 124, no. 3, pp. 230–237, 2002.

[175] A. B. Abell, K. L. Willis, and D. A. Lange, "Mercury intrusion porosimetry and image analysis of cement-based materials," *Journal of Colloid and Interface Science*, vol. 211, no. 1, pp. 39–44, 1999.

[176] S. Eckhard and M. Nebelung, "Investigations of the correlation between granule structure and deformation behavior," *Powder Technology*, vol. 206, no. 1, pp. 79–87, 2011.

[177] L. Farber, G. Tardos, and J. N. Michaels, "Use of x-ray tomography to study the porosity and morphology of granules," *Powder Technology*, vol. 132, no. 1, pp. 57–63, 2003.

[178] P. Lu, J. J. Lannutti, P. Klobes, and K. Meyer, "X-ray computed tomography and mercury porosimetry for evaluation of density evolution and porosity distribution," *Journal of the American Ceramic Society*, vol. 83, no. 3, pp. 518–522, 2000.

[179] C. Bacher, P. M. Olsen, P. Bertelsen, and J. M. Sonnergaard, "Compressibility and compactibility of granules produced by wet and dry granulation," *International Journal of Pharmaceutics*, vol. 358, no. 1, pp. 69–74, 2008.

[180] AZoNano, "Physical characterization of materials using mercury intrusion porosimetry by micromeritics." [Technical Report]. Available online at: http://www.azonano.com/articles.aspx, accessed May 2015.

[181] H. Giesche, "Mercury porosimetry: A general (practical) overview," *Particle & Particle Systems Characterization*, vol. 23, no. 1, pp. 9–19, 2006.

[182] U. Rattanasak and K. Kendall, "Pore structure of cement/pozzolan composites by x-ray microtomography," *Cement and Concrete Research*, vol. 35, no. 4, pp. 637–640, 2005.

[183] S. P. Rigby, P. I. Chigada, J. Wang, S. K. Wilkinson, H. Bateman, B. Al-Duri, J. Wood, S. Bakalis, and T. Miri, "Improving the interpretation of mercury porosimetry data using computerised X-ray tomography and mean-field DFT," *Chemical Engineering Science*, vol. 66, no. 11, pp. 2328–2339, 2011.

[184] J. Hsieh, *Computed Tomography: Principles, Design, Artifacts, and Recent Advances*. SPIE Bellingham, WA, 2009.

[185] E. N. Landis and D. T. Keane, "X-ray microtomography," *Materials Characterization*, vol. 61, no. 12, pp. 1305–1316, 2010.

[186] I. U. Bhuiyan, J. Mouzon, S. P. E. Forsmo, and J. Hedlund, "Quantitative image analysis of bubble cavities in iron ore green pellets," *Powder Technology*, vol. 214, no. 3, pp. 306–312, 2011.

[187] N. Rahmanian and M. Ghadiri, "Strength and structure of granules produced in continuous granulators," *Powder Technology*, vol. 233, pp. 227–233, 2013.

[188] L. Holzer, F. Indutnyi, P. H. Gasser, B. Münch, and M. Wegmann, "Three-dimensional analysis of porous $BaTiO_3$ ceramics using FIB nanotomography," *Journal of Microscopy*, vol. 216, no. 1, pp. 84–95, 2004.

[189] S. Deshpande, A. Kulkarni, S. Sampath, and H. Herman, "Application of image analysis for characterization of porosity in thermal spray coatings and correlation with small angle neutron scattering," *Surface and Coatings Technology*, vol. 187, no. 1, pp. 6–16, 2004.

[190] J. Subero and M. Ghadiri, "Breakage patterns of agglomerates," *Powder Technology*, vol. 120, no. 3, pp. 232–243, 2001.

[191] S. Antonyuk, M. Khanal, J. Tomas, S. Heinrich, and L. Mörl, "Impact breakage of spherical granules: Experimental study and DEM simulation," *Chemical Engineering and Processing: Process Intensification*, vol. 45, no. 10, pp. 838–856, 2006.

[192] Y. S. Cheong, M. J. Adams, A. F. Routh, M. J. Hounslow, and A. D. Salman, "The production of binderless granules and their mechanical characteristics," *Chemical Engineering Science*, vol. 60, no. 14, pp. 4045–4053, 2005.

[193] G. Pharr, "Measurement of mechanical properties by ultra-low load indentation," *Materials Science and Engineering: A*, vol. 253, no. 1–2, pp. 151–159, 1998.

[194] D. G. Bika, M. Gentzler, and J. N. Michaels, "Mechanical properties of agglomerates," *Powder Technology*, vol. 117, no. 1, pp. 98–112, 2001.

[195] J. S. Wallace and J. Ilavsky, "Elastic modulus measurements in plasma sprayed deposits," *Journal of Thermal Spray Technology*, vol. 7, no. 4, pp. 521–526, 1998.

[196] L. X. Liu, D. Golchert, N. W. Page, D. Page, and J. D. Litster, "Strength and attrition resistance of agglomerates and particulate coatings," *Powder Technology*, vol. 130, no. 1, pp. 415–420, 2003.

[197] S. Antonyuk, J. Tomas, S. Heinrich, and L. Mörl, "Breakage behaviour of spherical granulates by compression," *Chemical Engineering Science*, vol. 60, no. 14, pp. 4031–4044, 2005.

[198] N. Rahmanian, M. Ghadiri, and Y. Ding, "Effect of scale of operation on granule strength in high shear granulators," *Chemical Engineering Science*, vol. 63, no. 4, pp. 915–923, 2008.

[199] A. Hassanpour, C. C. Kwan, B. H. Ng, N. Rahmanian, Y. L. Ding, S. J. Antony, X. D. Jia, and M. Ghadiri, "Effect of granulation scale-up on the strength of granules," *Powder Technology*, vol. 189, no. 2, pp. 304–312, 2009.

[200] M. Marigo, D. L. Cairns, J. Bowen, A. Ingram, and E. H. Stitt, "Relationship between single and bulk mechanical properties for zeolite ZSM5 spray-dried particles," *Particuology*, vol. 14, pp. 130–138, 2014.

[201] P. Kippax, "Appraisal of the laser diffraction particle-sizing," *Pharmaceutical Technology*, vol. 3, pp. 88–89, 2005.

[202] B. H. Kaye, D. Alliet, L. Switzer, and C. Turbitt-Daoust, "The effect of shape on inter-method correlation of techniques for characterizing the size distribution of powder. 1. Correlating the size distribution measured by sieving, image analysis, and diffractometer methods," *Particle & Particle Systems Characterisation*, vol. 14, no. 5, pp. 219–224, 1997.

[203] S. F. Yap, M. J. Adams, J. P. K. Seville, and Z. Zhang, "Single and bulk compression of pharmaceutical excipients: Evaluation of mechanical properties," *Powder Technology*, vol. 185, no. 1, pp. 1–10, 2008.

[204] N. Passerini, B. Albertini, M. L. González-Rodríguez, C. Cavallari, and L. Rodriguez, "Preparation and characterisation of ibuprofen–poloxamer 188 granules obtained by melt granulation," *European Journal of Pharmaceutical Sciences*, vol. 15, no. 1, pp. 71–78, 2002.

[205] M. A. Ansari and F. Stepanek, "The effect of granule microstructure on dissolution rate," *Powder Technology*, vol. 181, no. 2, pp. 104–114, 2008.

[206] G. Leofanti, M. Padovan, G. Tozzola, and B. Venturelli, "Surface area and pore texture of catalysts," *Catalysis Today*, vol. 41, no. 1, pp. 207–219, 1998.

[207] L. H. U. Andersson and T. Hjertberg, "Silicone elastomers for electronic applications. I. Analyses of the noncrosslinked fractions," *Journal of Applied Polymer Science*, vol. 88, no. 8, pp. 2073–2081, 2003.

[208] M. Bardin, P. C. Knight, and J. P. K. Seville, "On control of particle size distribution in granulation using high-shear mixers," *Powder Technology*, vol. 140, no. 3, pp. 169–175, 2004.

[209] T. H. G. Megson, *Structural and Stress Analysis*. Butterworth-Heinemann, 2005.

[210] P. J. Flory, "Molecular size distribution in three dimensional polymers: I: Gelation," *Journal of the American Chemical Society*, vol. 63, pp. 3083–3090, 1941.

[211] S. R. Broadbent and J. M. Hammersley, "Percolation processes," *Mathematical Proceedings of the Cambridge Philosophical Society*, vol. 53, no. 3, pp. 629–641, 1957.

[212] I. J. Youngs, "Exploring the universal nature of electrical percolation exponents by genetic algorithm fitting with general effective medium theory," *Journal of Physics D: Applied Physics*, vol. 35, no. 23, pp. 3127–3137, 2002.

[213] H. Scher and R. Zallen, "Critical density in percolation processes," *The Journal of Chemical Physics*, vol. 53, no. 9, pp. 3759–3761, 1970.

[214] W. Bauhofer and J. Z. Kovacs, "A review and analysis of electrical percolation in carbon nanotube polymer composites," *Composites Science and Technology*, vol. 69, no. 10, pp. 1486–1498, 2009.

[215] G. M. Nasr, H. M. Osman, M. Abu-Abdeen, and A. I. Aboud, "On the percolative behavior of carbon black-rubber interlinked systems," *Polymer Testing*, vol. 18, no. 7, pp. 483–493, 1999.

[216] V. I. Roldughin and V. V. Vysotskii, "Percolation properties of metal-filled polymer films, structure and mechanisms of conductivity," *Progress in Organic Coatings*, vol. 39, no. 2, pp. 81–100, 2000.

[217] X. Jing, W. Zhao, and L. Lan, "The effect of particle size on electric conducting percolation threshold in polymer/conducting particle composites," *Journal of Materials Science Letters*, vol. 19, no. 5, pp. 377–379, 2000.

[218] J. Vilčáková, P. Sáha, and O. Quadrat, "Electrical conductivity of carbon fibres/polyester resin composites in the percolation threshold region," *European Polymer Journal*, vol. 38, no. 12, pp. 2343–2347, 2002.

[219] T. Ota, M. Fukushima, Y. Ishigure, H. Unuma, M. Takahashi, Y. Hikichi, and H. Suzuki, "Control of percolation curve by filler particle shape in Cu-SBR composites," *Journal of Materials Science Letters*, vol. 16, no. 13, pp. 1182–1183, 1997.

[220] M. Knite, V. Teteris, A. Kiploka, and J. Kaupuzs, "Polyisoprene-carbon black nanocomposites as tensile strain and pressure sensor materials," *Sensors and Actuators A: Physical*, vol. 110, no. 1, pp. 142–149, 2004.

[221] B. C. K. Tee, C. Wang, R. Allen, and Z. Bao, "An electrically and mechanically self-healing composite with pressure-and flexion-sensitive properties for electronic skin applications," *Nature Nanotechnology*, vol. 7, no. 12, pp. 825–832, 2012.

[222] A. Ferreira, P. Cardoso, D. Klosterman, J. A. Covas, F. W. J. V. Hattum, F. Vaz, and S. Lanceros-Mendez, "Effect of filler dispersion on the electromechanical response of epoxy/vapor-grown carbon nanofiber composites," *Smart Materials and Structures*, vol. 21, no. 7, p. 075008, 2012.

[223] L. He and S. C. Tjong, "Nonlinear electrical conduction in percolating systems induced by internal field emission," *Synthetic Metals*, vol. 161, no. 5, pp. 540–543, 2011.

[224] H. Bar, M. Narkis, and G. Boiteux, "The electrical behavior of thermosetting polymer composites containing metal plated ceramic filler," *Polymer Composites*, vol. 26, no. 1, pp. 12–19, 2005.

[225] D. S. McLachlan, "Equations for the conductivity of macroscopic mixtures," *Journal of Physics C: Solid State Physics*, vol. 19, no. 9, pp. 1339–1354, 1986.

[226] D. S. McLachlan, "An equation for the conductivity of binary mixtures with anisotropic grain structures," *Journal of Physics C: Solid State Physics*, vol. 20, no. 7, pp. 865–877, 1987.

[227] C. R. Lin and Y. D. Lee, "Strain-dependent dynamic properties of filled rubber network systems," *Macromolecular Theory and Simulations*, vol. 5, no. 6, pp. 1075–1104, 1996.

[228] C. R. Lin, Y. C. Chen, and C. Y. Chang, "A links-nodes-blobs model for conductive polymer composites," *Macromolecular theory and simulations*, vol. 10, no. 4, pp. 219–224, 2001.

[229] A. K. Gupta and A. K. Sen, "Nonlinear DC response in composites: A percolative study," *Physical Review B*, vol. 57, no. 6, pp. 3375–3388, 1998.

[230] Y. Gefen, W. H. Shih, R. B. Laibowitz, and J. M. Viggiano, "Nonlinear behavior near the percolation metal-insulator transition," *Physical Review Letters*, vol. 57, no. 24, pp. 3097–3100, 1986.

[231] A. Celzard, G. Furdin, J. F. Mareche, and E. McRae, "Non-linear current-voltage characteristics in anisotropic epoxy resin-graphite flake composites," *Journal of Materials Science*, vol. 32, no. 7, pp. 1849–1853, 1997.

[232] R. K. Chakrabarty, K. K. Bardhan, and A. Basu, "Nonlinear I-V characteristics near the percolation threshold," *Physical Review B*, vol. 44, no. 13, pp. 6773–6779, 1991.

[233] A. J. Webb, M. Szablewski, D. Bloor, D. Atkinson, A. Graham, P. Laughlin, and D. Lussey, "A multi-component nanocomposite screen-printed ink with non-linear touch sensitive electrical conductivity," *Nanotechnology*, vol. 24, no. 16, p. 165501, 2013.

[234] H. Lin, W. Lu, and G. Chen, "Nonlinear DC conduction behavior in epoxy resin/-graphite nanosheets composites," *Physica B: Condensed Matter*, vol. 400, no. 1, pp. 229–236, 2007.

[235] M. A. Lampert and P. Mark, *Current Injection in Solids.* Academic Press, 1970.

[236] S. M. Sze and K. K. Ng, *Physics of Semiconductor Devices.* John Wiley & Sons, 2006.

[237] P. N. Murgatroyd, "Theory of space-charge-limited current enhanced by Frenkel effect," *Journal of Physics D: Applied Physics*, vol. 3, no. 2, pp. 151–156, 1970.

[238] A. Graham, "Electrical properties and vapour sensing characteristics of a novel metal-polymer composite," 2008. PhD Thesis, Department of Physics, Durham University, UK.

[239] D. K. Roy, *Quantum Mechanical Tunnelling and its Applications.* World Scientific, 1986.

[240] M. Lenzlinger and E. H. Snow, "Fowler-Nordheim tunneling into thermally grown SiO_2," *Journal of Applied Physics*, vol. 40, no. 1, pp. 278–283, 1969.

[241] G. A. Niklasson and K. Brantervik, "Analysis of current-voltage characteristics of metal-insulator composite films," *Journal of Applied Physics*, vol. 59, no. 3, pp. 980–982, 1986.

[242] Z. Chiguvare, J. Parisi, and V. Dyakonov, "Current limiting mechanisms in indium-tin-oxide/poly3-hexylthiophene/aluminum thin film devices," *Journal of Applied Physics*, vol. 94, no. 4, pp. 2440–2448, 2003.

[243] Y. L. Chiou, J. P. Gambino, and M. Mohammad, "Determination of the Fowler-Nordheim tunneling parameters from the Fowler-Nordheim plot," *Solid-State Electronics*, vol. 45, no. 10, pp. 1787–1791, 2001.

[244] F. H. A. El-kader, S. A. Gaafer, K. H. Mahmoud, S. I. Mohamed, and M. F. H. A. El-kader, "Electrical conduction in (polyvinyl alcohol/glycogen) blend films," *Polymer Composites*, vol. 30, no. 2, pp. 214–220, 2009.

[245] A. J. Webb, "Temperature dependence and touch sensitivity of electrical transport in novel nanocomposite printable inks," 2014. PhD Thesis, Department of Physics, Durham University, UK.

[246] A. J. Webb, D. Bloor, M. Szablewski, and D. Atkinson, "Temperature dependence of electrical transport in a pressure-sensitive nanocomposite," *ACS Applied Materials & Interfaces*, vol. 6, no. 15, pp. 12573–12580, 2014.

[247] A. K. Raychaudhuri, "Measurement of 1/f noise and its application in materials science," *Current Opinion in Solid State and Materials Science*, vol. 6, no. 1, pp. 67–85, 2002.

[248] J. H. Scofield, J. V. Mantese, and W. W. Webb, "1/f noise of metals: A case for extrinsic origin," *Physical Review B*, vol. 32, no. 2, pp. 736–742, 1985.

[249] H. Liu, E. Lhuillier, and P. Guyot-Sionnest, "1/f noise in semiconductor and metal nanocrystal solids," *Journal of Applied Physics*, vol. 115, no. 15, p. 154309, 2014.

[250] A. A. Balandin, "Low-frequency 1/f noise in graphene devices," *Nature Nanotechnology*, vol. 8, no. 8, pp. 549–555, 2013.

[251] R. A. Sayer, J. D. Engerer, N. S. Vidhyadhiraja, and T. S. Fisher, "Length and temperature dependent 1/f noise in vertical single-walled carbon nanotube arrays," *Journal of Applied Physics*, vol. 113, no. 14, p. 144306, 2013.

[252] F. N. Hooge, T. G. M. Kleinpenning, and L. K. J. Vandamme, "Experimental studies on 1/f noise," *Reports on Progress in Physics*, vol. 44, no. 5, p. 479, 1981.

[253] U. N. Nandi, C. D. Mukherjee, and K. K. Bardhan, "1/f noise in nonlinear inhomogeneous systems," *Physical Review B*, vol. 54, no. 18, pp. 12903–12914, 1996.

[254] A. J. Breeze, S. A. Carter, G. B. Alers, and M. B. Heaney, "1/f noise through the metal-nonmetal transition in percolating composites," *Applied Physics Letters*, vol. 76, no. 5, pp. 592–594, 2000.

[255] A. T. Williams, P. Farrar, A. J. Gallant, D. Atkinson, and C. Groves, "Characterisation of charge conduction networks in poly (3-hexylthiophene)/polystyrene blends using noise spectroscopy," *Journal of Materials Chemistry C*, vol. 2, no. 9, pp. 1742–1748, 2014.

[256] P. Kratochvíl, *Classical Light Scattering from Polymer Solutions*. No. 5 in Polymer Science Library, Elsevier, 1987.

[257] T. R. Giraldi, M. T. Escote, A. P. Maciel, E. Longo, E. R. Leite, and J. A. Varela, "Transport and sensors properties of nanostructured antimony-doped tin oxide films," *Thin Solid Films*, vol. 515, no. 4, pp. 2678–2685, 2006.

[258] H. C. van de Hulst, *Light scattering by small particles*. Courier Corporation, 1957.

[259] E. J. McCartney, "Optics of the Atmosphere: Scattering by Molecules and Particles," *New York, John Wiley and Sons, Inc.*, vol. 1, 1976.

[260] S. Prahl, "Mie scattering calculator." Freely available applet, 2012. Available online at: http://omlc.org/calc/mie_calc.html, accessed July 2015.

[261] T. Wriedt, *The Mie Theory: Basics and Applications*, ch. Mie Theory: A Review, pp. 53–71. Springer, 2012.

[262] R. L. Weiher and R. P. Ley, "Optical properties of indium oxide," *Journal of Applied Physics*, vol. 37, no. 1, pp. 299–302, 1966.

[263] C. G. Granqvist and A. Hultåker, "Transparent and conducting ITO films: New developments and applications," *Thin Solid Films*, vol. 411, no. 1, pp. 1–5, 2002.

[264] P. Lippens and U. Muehlfeld, "Indium Tin Oxide (ITO): Sputter Deposition Processes," in *Handbook of Visual Display Technology* (J. Chen, W. Cranton, and M. Fihn, eds.), pp. 779–794, Springer Berlin Heidelberg, 2012.

[265] B. G. Lewis and D. C. Paine, "Applications and processing of transparent conducting oxides," *MRS Bulletin*, vol. 25, no. 8, pp. 22–27, 2000.

[266] R. E. Treharne, "RF magnetron sputtering of transparent conducting oxides and CdTe/CdS solar cells," 2011. PhD Thesis, Department of Physics, Durham University, UK.

[267] K. A. Sierros and S. N. Kukureka, "Mechanical integrity of touch-screen components," *Journal of the Society for Information Display*, vol. 17, no. 11, pp. 947–952, 2009.

[268] K. A. Sierros, N. J. Morris, S. N. Kukureka, and D. R. Cairns, "Dry and wet sliding wear of ITO-coated PET components used in flexible optoelectronic applications," *Wear*, vol. 267, no. 1, pp. 625–631, 2009.

[269] D. R. Cairns and R. P. Witte II and D. K. Sparacin and S. M. Sachsman and D. C. Paine and G. P. Crawford and R. R. Newton, "Strain-dependent electrical resistance of tin-doped indium oxide on polymer substrates," *Applied Physics Letters*, vol. 76, no. 11, pp. 1425–1427, 2000.

[270] D. S. Hecht, D. Thomas, L. Hu, C. Ladous, T. Lam, Y. Park, G. Irvin, and P. Drzaic, "Carbon-nanotube film on plastic as transparent electrode for resistive touch screens," *Journal of the Society for Information Display*, vol. 17, pp. 941–946, 2009.

[271] D. Jung, S. K. Lee, K. H. Lee, D. Burk, L. J. Overzet, S. Y. Choi, and G. S. Lee, "A temperature-independent multi-walled carbon-nanotube sheet electrode for transparent touch screen," in *19th International Workshop on Active-Matrix Flatpanel Displays and Devices (AM-FPD)*, pp. 99–100, IEEE, 2012.

[272] J. Y. Lee, S. T. Connor, Y. Cui, and P. Peumans, "Solution-processed metal nanowire mesh transparent electrodes," *Nano Letters*, vol. 8, no. 2, pp. 689–692, 2008.

[273] S. Bae, H. Kim, Y. Lee, X. Xu, J. S. Park, Y. Zheng, J. Balakrishnan, T. Lei, H. R. Kim, Y. I. Song, *et al.*, "Roll-to-roll production of 30-inch graphene films for transparent electrodes," *Nature Nanotechnology*, vol. 5, no. 8, pp. 574–578, 2010.

[274] A. Hobby, "Fundamentals of screens for electronics screen printing," *Circuit World*, vol. 16, no. 4, pp. 16–28, 1990.

[275] K. Jost, D. Stenger, C. R. Perez, J. K. McDonough, K. Lian, Y. Gogotsi, and G. Dion, "Knitted and screen printed carbon-fiber supercapacitors for applications in wearable electronics," *Energy & Environmental Science*, vol. 6, no. 9, pp. 2698–2705, 2013.

[276] F. C. Krebs, C. Frederik, M. Jørgensen, K. Norrman, O. Hagemann, J. Alstrup, T. D. Nielsen, J. Fyenbo, K. Larsen, and J. Kristensen, "A complete process for production of flexible large area polymer solar cells entirely using screen printing—first public demonstration," *Solar Energy Materials and Solar Cells*, vol. 93, no. 4, pp. 422–441, 2009.

[277] C. Gray, J. Wang, G. Duthaler, A. Ritenour, and P. S. Drzaic, "Screen printed organic thin film transistors (OTFTs) on a flexible substrate," in *International Symposium on Optical Science and Technology*, pp. 89–94, International Society for Optics and Photonics, 2001.

[278] S. Abbott, *How to be a Great Screen Printer*. MacDermid Autotype, 2008. e-book available online at http://www.fespa.com/knowledge/technical-library/how-to-be-a-great-screen-printer, accessed June 2015.

[279] F. Zicarelli, "Capability, limits and considerations for screen printing." [Online article], Nov 2012. Available online at http://www.printedelectronicsworld.com/articles/4885/capability-limits-and-considerations-for-screen-printing, accessed June 2015.

[280] T. A. Germer, J. C. Zwinkels, and B. K. Tsai, *Spectrophotometry: Accurate Measurement of Optical Properties of Materials*, vol. 46 of *Experimental Methods in the Physical Sciences*. Elsevier, 2014.

[281] F. W. Billmeyer and Y. Chen, "On the measurement of haze," *Color Research & Application*, vol. 10, no. 4, pp. 219–224, 1985.

[282] T. A. Roberts and J. K. Beddow, "Some effects of particle shape and size upon blinding during sieving," *Powder Technology*, vol. 2, no. 2, pp. 121–124, 1968.

[283] A. Kirubanandham and S. Basu, "On characterization of mechanical deformation in flexible electronic structures." [Application Note], August 2012. Available online at: http://cp.literature.agilent.com/litweb/pdf/5991-1040EN.pdf, accessed Nov 2015.

[284] K. Alzoubi, M. M. Hamasha, S. Lu, and B. Sammakia, "Bending fatigue study of sputtered ITO on flexible substrate," *Journal of Display Technology*, vol. 7, no. 11, pp. 593–600, 2011.

[285] L. Kogut and K. Komvopoulos, "Electrical contact resistance theory for conductive rough surfaces," *Journal of Applied Physics*, vol. 94, no. 5, pp. 3153–3162, 2003.

[286] L. Kogut and K. Komvopoulos, "Electrical contact resistance theory for conductive rough surfaces separated by a thin insulating film," *Journal of Applied Physics*, vol. 95, no. 2, pp. 576–585, 2004.

[287] L. Lam, J. Swingler, and J. McBride, "The contact resistance force relationship of an intrinsically conducting polymer interface," in *Proceedings of the 50th IEEE Holm Conference on Electrical Contacts and the 22nd International Conference on Electrical Contacts*, pp. 304–311, 2004.

[288] J. Planès and A. François, "Percolation scaling, inhomogeneity, and defects in polyaniline blends: A 1/ f noise diagnosis," *Physical Review B*, vol. 70, no. 18, p. 184203, 2004.

[289] C. Chiteme, D. S. McLachlan, and I. Balberg, "1/f or flicker noise in cellular percolation systems," *Physical Review B*, vol. 67, no. 2, p. 024207, 2003.

[290] C. Pierre, R. Deltour, J. V. Bentum, J. A. A. J. Perenboom, and R. Rammal, "Electrical-conduction mechanisms in polymer-copper-particle composites. II (1/f)-noise measurements in the percolation limit," *Physical Review B*, vol. 42, no. 6, p. 3386, 1990.

[291] E. J. Hearn, *Mechanics of materials 1: An Introduction to the Mechanics of Elastic and Plastic Deformation of Solids and Structural Components*, ch. Slope and Deflection of Beams, pp. 105–106. Butterworth-Heinemann, 1997.

[292] J. M. Gere and S. P. Timoshenko, *Mechanics of Materials*, ch. Statically Indeterminate Beams, pp. 535–576. Chapman & Hall, 5th ed., 1991.

[293] R. J. C. a. C. G. A. P. P. Benham, *Mechanics of Engineering Materials*, ch. Statically Indeterminate Beams, pp. 211–234. Harlow Longman Group, 1996.